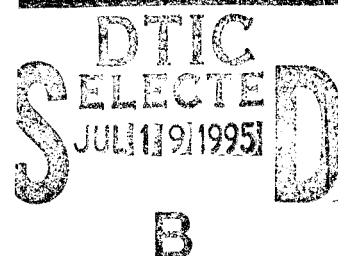


AGARD

ADVISORY GROUP FOR AEROSPACE RESEARCH & DEVELOPMENT

7 RUE ANCELLE, 92200 NEUILLY-SUR-SEINE, FRANCE

**AGARD CONFERENCE PROCEEDINGS 564****High Power Microwaves (HPM)**

(les Micro-ondes de forte puissance (MFP))

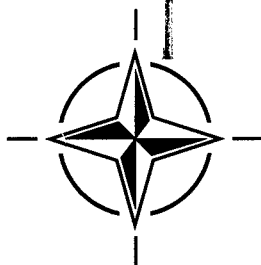
*Papers presented at the Sensor and Propagation Panel Symposium,
held in Ottawa, Canada 2-5 May 1994.*

*(This meeting was held jointly with NATO DRG Panel 1/RSG.1 on
Tactical Implications of High Power Microwaves)*

DISTRIBUTION STATEMENT A

Approved for public release
Distribution Unlimited

19950718 005

**NORTH ATLANTIC TREATY ORGANIZATION**

AGARD

ADVISORY GROUP FOR AEROSPACE RESEARCH & DEVELOPMENT

7 RUE ANCELLE, 92200 NEUILLY-SUR-SEINE, FRANCE

AGARD CONFERENCE PROCEEDINGS 564

High Power Microwaves (HPM)

(les Micro-ondes de forte puissance (MFP))

Papers presented at the Sensor and Propagation Panel Symposium,
held in Ottawa, Canada 2-5 May 1994.

*(This meeting was held jointly with NATO DRG Panel 1/RSG.1 on
Tactical Implications of High Power Microwaves)*



North Atlantic Treaty Organization
Organisation du Traité de l'Atlantique Nord

The Mission of AGARD

According to its Charter, the mission of AGARD is to bring together the leading personalities of the NATO nations in the fields of science and technology relating to aerospace for the following purposes:

- Recommending effective ways for the member nations to use their research and development capabilities for the common benefit of the NATO community;
- Providing scientific and technical advice and assistance to the Military Committee in the field of aerospace research and development (with particular regard to its military application);
- Continuously stimulating advances in the aerospace sciences relevant to strengthening the common defence posture;
- Improving the co-operation among member nations in aerospace research and development;
- Exchange of scientific and technical information;
- Providing assistance to member nations for the purpose of increasing their scientific and technical potential;
- Rendering scientific and technical assistance, as requested, to other NATO bodies and to member nations in connection with research and development problems in the aerospace field.

The highest authority within AGARD is the National Delegates Board consisting of officially appointed senior representatives from each member nation. The mission of AGARD is carried out through the Panels which are composed of experts appointed by the National Delegates, the Consultant and Exchange Programme and the Aerospace Applications Studies Programme. The results of AGARD work are reported to the member nations and the NATO Authorities through the AGARD series of publications of which this is one.

Participation in AGARD activities is by invitation only and is normally limited to citizens of the NATO nations.

The content of this publication has been reproduced directly from material supplied by AGARD or the authors.

Accession For	
NTIS GRA&I	<input checked="" type="checkbox"/>
DTIC TAB	<input type="checkbox"/>
Unannounced	<input type="checkbox"/>
Justification	
By	
Distribution	
Availability Codes	
Dist	Avail and/or Special
A-1	

Published March 1995

Copyright © AGARD 1995
All Rights Reserved

ISBN 92-836-0012-6



Printed by Canada Communication Group
45 Sacré-Cœur Blvd., Hull (Québec), Canada K1A 0S7

High Power Microwaves (HPM)

Theme

This symposium was selected by the Panel in response to the new NATO strategies and technology needs, and in accordance with the technology issues identified by the AASC. Close coordination with the AGARD Avionics Panel resulted in the choice of this subject. In addition, cooperation with another NATO body working in the field of HPM (the DRG) resulted in co-chairmanship of this Symposium.

EMC-related problems are of increasing concern to the military community, due to both the major role of sophisticated electronics in systems, and to the diversity of radiating devices. Unwanted disturbances of military systems have thus sometimes been experienced. Furthermore, very high peak power generators operating at microwave frequencies are already available in the laboratory and the possible development of microwave weapons has to be considered.

Some of the related topics are already documented, and so an extrapolation of available results may only be needed: such is the case for the coupling mechanisms of an incident pulse to a target, which at low frequencies is a classical NEMP (Nuclear Electro-magnetic Pulse) related problem.

On the other hand, specific aspects have also to be accounted for, like the peak power handling capability of transmission lines, antennas, and of the atmosphere.

The symposium identified the state-of-the-art in these rapidly changing areas.

Topics covered:

- High Peak Power Generators
- Transmission Line and Antenna Peak Power Handling
- Atmospheric Microwave Breakdown
- Target Coupling Mechanisms
- Components and Subsystems Vulnerability
- Hardening Against HPM
- Test Facilities

Les micro-ondes de forte puissance (MFP)

Thème

Le thème du symposium a été choisi par le Panel pour répondre aux nouvelles stratégies de l'OTAN et aux besoins technologiques tels qu'exprimés par l'AASC.

Le choix du sujet résulte d'un travail de coordination étroite mené avec le Panel d'avionique. En outre, le Panel a coopéré avec un autre organisme de l'OTAN, le Groupe sur la Recherche pour la Défense (le GRD), travaillant dans le domaine des micro-ondes de forte puissance, ce qui a eu pour résultat la co-présidence de ce symposium.

Les problèmes liés à la compatibilité électromagnétique EMC sont considérés de plus en plus comme un sujet d'inquiétude d'une part par la communauté militaire, et d'autre part, en raison du rôle prépondérant de l'électronique sophistiqué au niveau des systèmes et de la diversité des dispositifs rayonnants. Ainsi, certains systèmes militaires ont parfois subi des perturbations non prévues. En outre, des générations à puissance de crête très élevée fonctionnant à des hyperfréquences sont déjà disponibles au niveau des laboratoires et il faut en tenir compte pour de possibles développements d'armes hyperfréquence.

Un certain nombre de ces sujets ont déjà été traités et nous n'avons besoin que d'une extrapolation des résultats disponibles: tel est le cas pour les mécanismes de couplage pour une impulsion frappant une cible, ce qui, à base fréquence, est un problème classique lié au NEMP (impulsion électromagnétique nucléaire).

D'autre part, il faut également tenir compte de certains aspects spécifiques tels que la capacité d'acheminement de la puissance de crête sur des lignes de transmission, des antennes et de l'atmosphère.

Le symposium a défini l'état de l'art dans ces domaines en évolution constante.

Sujets traités:

- les générateurs à puissance de crête élevée
- la capacité d'acheminement à puissance de crête des lignes de transmission et des antennes
- les mécanismes de couplage de cible
- la vulnérabilité des pièces et des sous-systèmes
- le durcissement contre les hyperfréquences à haute puissance
- les installations d'essais

Sensor and Propagation Panel

Chairman: Prof. D.H. HÖHN
FGAN
Forschungsinstitut für Optik
Schloss Kressbach
D-7400 Tübingen
Germany

TECHNICAL PROGRAMME COMMITTEE

Co-Chairmen:

Mr. F. Christophe (FR)
Dr. P.W. Reip (UK)

Programme Committee Members:

Dr. J. Agee, US
Lt. Col. A. Cassara, IT
Dr. W.A. Flood, US
Dr. S. Kashyap, CA
Dr. A. Lanusse, FR
Dr. R. Little, UK
Dr. J. Nitsch, GE
Dr. D. Sérafin, FR

PANEL EXECUTIVE

Lt. Col. R. Cariglia, IAF

Mail from Europe:
AGARD-NATO
Attn: SPP Executive
7, rue Ancelle
92200 Neuilly-sur-Seine
France

Mail from US and Canada:
AGARD-NATO-SPP
PSC 116
APO AE 09777

Tel: 33 (1) 47 38 57 68
Telex: 610176
TGelefax: 33 (1) 47 38 57 99

DRG Panel 1

DRG Panel 1 on Long-Term Scientific Studies

Chairman: Ir. G.A. Willemsen (NL)

Vice-Chairman Dr. K. Gardner (NATO IS)

Secretary: Mr. D. Stamatopoulos (NATO IS)

Members: Dr. R.S. Thomas (CA)
Mr. N. Krarup-Hansen (DE)
ICA P. Desvergues (FR)
B. Dir. V. Wenthe (GE)
Ir. R.F.M.J. Broeders (NL)
Dr. J.A. Grimshaw (UK)
Dr. J. Iafrate (US)

DRG Panel 1/RSG.1 on the Tactical Implications of High-Power Microwaves

Chairman: Dr. P.W. Reip (UK)

Members: Dr. S. Kashyap (CA)
Mr. E. Krogager (DE)
Mme. F. Etling (FR)
Dr. J. Nitsch (GE)
Cdr. G. Giancarli (IT)
Ir. C.D. de Haan (NL)
Col. B. Crane (US)

Mailing Address:

Head, Defence Research Section
Defence Support Division
NATO Headquarters
1110 Brussels
Belgium

Tel: [32](2)728-4420
Fax: [32](2)728-4103
Telex: 23-867

Preface

The last 40 years has seen an unprecedented and unparalleled growth in the development and use of electronics. Associated with this has been an increase in concerns over electromagnetic compatibility (EMC), and this has led to a corresponding growth in legislation to maintain standards, as well as in the test facilities to licence hardware of all types, from aircraft control systems to consumer electronics.

The use of electronics in military systems has paralleled that in the consumer industry, even though the leadtimes to get systems and subsystems into service are much longer. If anything the problems of EMC were realised earlier, and strenuous efforts have been and continue to be made to counter not only the EMC problem, but also to harden against the threat from nuclear EMP and lightning, as well as the more directed threats from our own or other EW systems.

Why, therefore, has the subject of High Power Microwaves come to such prominence over the last few years. There are possibly three factors which contribute to this, namely:

- evidence (some qualitative; some quantified) that these waveforms can affect electronically rich systems
- the increase in the use of electronics in mission critical application, in both weapons and weapon platforms
- the developments in HPM source technology which have seen major reductions in size as well as increases in efficiency

In isolation these could be considered as merely extra data points for consideration. However taken together this *may* be considered to indicate a potential for the development of new offensive systems which could be used to affect the performance of weapon systems.

The question to be answered is whether these systems are the “golden bullet” — methods of attack which are applicable to a wide range if not all weapon systems and platforms, or whether they are applicable to only classes of weapons, or in the minimal case are only effective against single systems. The question of whether they could be cost-effectively deployed remains as an additional and vital issue.

Much work remains to be carried out, and groups such as the NATO AC243 Panel 1, RSG1 are taking the first steps internationally to address these issues; this symposium was another major step. It brought together the current state of the art in the major technologies which have a direct bearing on the current situation, and will stand as a reference point in the understanding and development of these technologies.

This symposium was jointly sponsored by AGARD and the Defence Research Group (DRG) of NATO. These proceedings are also published by DRG as AC/243 (Panel 1) TP/4, Vol. I (unclassified) and Vol. II (classified).

Dr. P.W. Reip
Chairman NATO AC243 Panel 1 RSG 1
WX2 Electronic Warfare Division
DRA Fort Halstead, Sevenoaks, Kent, TN13 2AL, UK

Contents

	Page
Theme/Thème	iii
Sensor and Propagation Panel	iv
DRG Panel 1	v
Preface	vi
 SESSION I — GENERATORS Session Chairman: Dr. W.A. Flood 	
Present and Future Trends in High Power Generation by R. van Heijster and J.M. Schouten	1
High-Power Microwave Development in Russia by S. Gauthier	2
High Efficiency Backward-Wave Oscillators for High Power Microwave Generation: Present Status and Future Trends by E. Schaamiloglu, J. Gahl, C. Fleddermann, D. Shiffler, L. Moreland, C. Grabowski, T. Cavazos, B. Wroblewski and W. Wilbanks	3
Applications of Relativistic Klystron Amplifier Technology by M. Friedman, V. Serlin, M. Lampe and R. Hubbard	4
A Compact and Light-Weight Magnetron by T. Treado and P.D. Brown (NOT AVAILABLE FOR PUBLICATION)	5
Photoinjector-Driven Chirped-Pulse Free Electron Maser by G.P. Le Sage, F.V. Hartemann, H.X.C. Feng, S.N. Fochs, J.P. Heritage, N.C. Luhmann Jr, M.D. Perry and G.A. Westenskow	6
Investigations into Sub-ns Pulse Generation using Ferrite-Loaded Coaxial Lines by H.R. Bolton, J.E. Dolan, A.J. Shapland, D.M. Parkes, K. Trafford and B. Kerr	7
Transient Antenna Design Parameters for Optimising Radiated Pulse by A.P. Lambert, S.M. Booker and P.D. Smith	8
 SESSION II — COUPLING Session Chairmen: Dr. A. Lanusse & Dr. J. Nitsch 	
Analysis of Interaction of HPM with Complex Structures by S. Kashyap and A. Louie	9
A Procedure Based on Line Theory for Calculating Surface Currents and Coupling into the Interior of Large Objects by E. Arnold	10
Frequency-Domain Analysis of Nonlinearly Loaded Thin-Wire Antennas and Networks by K.M. Noujeim, S.G. Zaky and K.G. Balmain	11

HPM Coupling to a Cylindrical Target with Selected Built-in Components by M. Magg and J.B. Nitsch	12
Coupling Measurements on Intelligent Missiles at Microwave Frequencies by Ch. Braun, P. Guidi and H.U. Schmidt	13
High Power Microwave Hazard Facing Smart Ammunitions by J. Bohl	14
Calculation and Measurement of HPM Fields Scattered by a Target with Openings by S. Kashyap, M. Burton and A. Louie	15
Analyse du couplage par une technique de mesure rapide de champ proche (Coupling Analysis by a Rapid Near Field Measurement Technique) by B. Chevalier and D. Sérafin	16
Investigation of RF Coupling with UWB Radar by A.J.E. Taylor, R.A. Clement, C. Hall and D.M. Parkes	17
Design, Construction and Calibration of Sensors for HPM Measurements by J.S. Seregelyi and S. Kashyap	18
Electromagnetic Shielding Properties of Composite Materials by C.L. Gardner, R. Apps and A.J. Russell	19
Hardening Against a Combined Electromagnetic Threat by M. Dion, C. Gardner, S. Kashyap	20
SESSION III — PROPAGATION Session Chairman: Dr. S. Kashyap	
Modeling and Numerical Simulation of Microwave Pulse Propagation in Air Breakdown Environment by J. Kim, S.P. Kuo and P. Kossey	21
A Review of Nonlinear Electromagnetic Propagation Effects by J. Lo Vetri, M.S. Wartak and R. Siushansian	22
Spectral Variation of High Power Microwave Pulse Propagating in a Self-Generated Plasma by A. Ren, S.P. Kuo and P. Kossey	23
Nonlinear Optical Emission and Scattering in Micrometer-Sized Droplets by G. Chen, M. Mazumder, J.C. Swindal, K. Schaschek and R.K. Chang	24
Micron-Sized Droplets Irradiated with a Pulsed Carbon Dioxide Laser: Measurements of Explosion and Breakdown Thresholds by R.L. Armstrong, A. Biswas, R.G. Pinnick and J.D. Pendleton	25
Calculating the 3-D Absorbed Power Distribution Inside a Human Body that is Illuminated by an Incident EM Field using the WCG-FFT Method by A.P.M. Zwamborn	26

SESSION IV
Session Chairman: Dr. J. Agee

Critical Heat Flux Panel Experiments	27†
by J.E. Beraun, K.F. Raymond, J.S. Orlins and F.A. Rigby	
Upgrading of the RF Tubes of the Present State of the Art	28
by G. Faillon	
La sensibilité des transistors à effet de champ aux impulsions hyperfréquences (Sensitivity to Field Effect Transistors to Microwave Pulses)	29*
by D. Lazaro, J.C. Mollier, A. Roizes and F. Christophe	
The Numerical Modelling of Near-Field HPM Target Coupling	30
by A. Soubeyran, J.P. Estienne, J.P. Bœuf and A. Ravier	
Estimation théorique de la vulnérabilité des mines enfouies aux MFP (Theoretical Estimation of the Vulnerability of Buried Mines to HPM)	31*
by A. Roizes, F. Christophe, J. Grando, J. Mametsa, A. Sarremejean & J. Brettes	
Laboratoire d'essais Fier de fort niveau hyperfréquence	32
by J.P. Brasile, G. Jean-François and M. Simon	
Paper 33 withdrawn	33
Paper 34 withdrawn	34
Radial Accelatron, a New Low-Impedance HPM Source	35
by M.J. Armann	

* Published in Classified Volume

† Paper 27 (unclassified) is printed in both volumes because the discussion sheet relating to this paper is classified.

PRESENT AND FUTURE TRENDS IN HIGH POWER GENERATION.

Rob M.E.M. van Heijster
Physics and Electronics Laboratory TNO
P.O. Box 96864
2509 JG The Hague
The Netherlands (1)

Jan M. Schouten
Naval Electronics and Optics Establishment
P.O. Box 1260
2340 BG Oegstgeest
The Netherlands (2)

1. SUMMARY

Modern warfare requires high levels of microwave power for various applications. Semiconductors are only suitable for low and medium power levels, for high power generation microwave tubes are still the most effective solution.

The feasibility of high power levels is mainly dependent on technology. The topics are given below:

- Tube type
- Tube design
 - Electron beam
 - Efficiency & cooling
 - Operating voltage.
- Energy storage

The reliability requirements are strongly related to the modes of operation.

Tube designs, production techniques and maintenance greatly determine tube reliability. Good power supply design can strongly increase tube reliability and hence system reliability. New power supply topologies also necessitate protection systems for the tube to run under high power conditions.

The procurement costs, the limited lifetime of the tube and the necessary maintenance are the main cost-drivers. Tube design and efficient maintenance procedures will increase the lifetime of the tube. The build-in test equipment of the power supply will reduce maintenance costs.

New cathodes and higher efficiencies will allow for higher output power. Reliability and lifetime will be increased by new technologies and "smart" power supplies, the latter also being responsible for decreasing maintenance costs.

2. ABBREVIATIONS

The abbreviations used throughout the text are explained in this section.

BIST	Build-in Self Test
CFA	Cross Field Amplifier, a tube type family.
CW	Continuous Wave
EC	European Community
EMI	Electro Magnetic Interference
EOL	End Of Life
EW	Electronic Warfare
FEA	Finite Element Analysis
HV	High Voltage
HVPS	High Voltage Power Supply
MEOB	Naval Electronics and Optics Establishment
MPM	Microwave Power Module
MTBF	Mean Time Between Failure
MTTF	Mean Time To Failure
MTTR	Mean Time To Repair
OE	Operational Envelop
OP	Operation Point
RSG	Research Study Group
TNO	Netherlands Organization for applied scientific research
TNO-FEL	TNO Physics and Electronics Laboratory
TWT	Travelling Wave Tube, a tube type.

3. INTRODUCTION

Modern warfare requires high levels of microwave power for various applications. Semiconductors are only suitable for low and medium power levels, for high power generation microwave tubes are the most effective solution. The paper will give an overview of present and future trends in high power microwave systems, based on electron beam tubes.

Modern warfare requires high levels of microwave power, often in combination with wide bandwidth and high duty cycles. For many years, the generation of high power levels was the domain of microwave tubes, such as: Magnetrons, Klystrons, CFA's and TWTs.

- (1) Rob van Heijster is project manager at TNO Physics and Electronic Laboratory (TNO-FEL). He is chairman of RSG-19 on "Micro- and millimeter wave tubes".
- (2) Jan Schouten is deputy head of the RADAR and EW department of the Naval Electronics and Optics Establishment (MEOB) of the Royal Netherlands Navy. He is also a member of RSG-19.

In the past years, the reliability of the microwave tubes and the related power supplies proved to be limited. High maintenance cost and the vulnerability to single point failures accelerated the design of solid state replacements in the 70's. The design of new tube technology and HVPSs (High Voltage Power Supply) ceased.

The development of high power solid state amplifiers in D, E and F band amplifiers started. The designers made use of medium power amplifiers, called books, the power of which was combined. This made the solid state amplifier very reliable and user friendly.

The design of solid state microwave amplifiers had to rely on:

- The development of the combiner.
The design of combiners, specially the Wilkinson combiner proved to be very successful. The bandwidth, combining losses and power handling were well predictable and the production method well within the present technology.
- The availability of transistors.
The development of high frequency high power transistors slowed down. The expected 200 to 400 W transistor was only met in the D-band. For the other bands the power stopped at 150 W (E/F band) to 5 W (J-band). The large quantities of transistors required in the high power amplifiers brought the price of the amplifiers out of the range of many users.

The interest in the use of microwave tubes returned. System designers took full advantage of:

- The development and studies in scandate cathodes;
- The use of dedicated cathode-types in specific tubes;
- Improved brazing technology and tube processing;
- Increased understanding of the operational use by the manufacturer;
- The fine tuning of the HVPS, the protection circuits and R.F. circuits to the tube.

Within NATO, RSG-19 is assigned to develop a new standard for the reliability of high power microwave tubes.

For the assessment of the various reliability aspects of tubes and their HVPS the concept of the OE (Operational Envelop) is a useful tool. It also helps to adept the feasibility of tube and HVPS concepts.

This paper will first address the concept of the OE. Feasibility, reliability and cost-effectiveness are the three aspects that will be covered next.

4. OPERATIONAL ENVELOP

To model all various aspects of tube reliability, RSG-19 introduced the "operational envelop" concept. Three definitions will clarify this concept:

- Operation point (OP):
Any combination of voltages and currents (temperatures, shock, vibration etc. may also be included) that is applied to the tube or is present on the HVPS.
- Valid operation point:
Any OP that the tube or HVPS can handle for prolonged time (the specified lifetime).
Valid OPs are often subject to time constraints, their validity is restricted to a given pulse width and/or duty cycle.
- Operational envelop:
The boundary of the set of all valid OPs.

As long as the tube is operated within the OE, the stress factors are within the limits and the (well designed) tube will exhibit a good reliability.

During switch-on, the tube will run under a number of OPs, varying from "all voltages zero" to the chosen OP. All OPs should be within the OE.

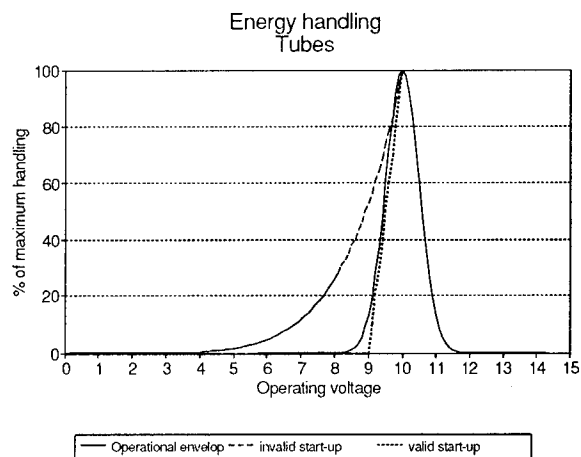


Fig. 1. Operational envelop with valid and invalid start-up curve.

An example is given in fig. 1. A given tube can handle 100 % energy at 10 kV, due to beam defocussing the energy handling capacity is decreased for other voltages. This leads to the shown OE. Two switch-on curves are given. One clearly has OPs outside the OE, so it is an invalid start-up curve. The other remains within the OE, giving a valid start-up.

5. FEASIBILITY

The feasibility of high power levels is mainly dependent on technology. The topics are given below:

- Tube type
The requirements for coherency, stability and bandwidth mainly determine the most suitable tube type and hence the maximum obtainable peak power.
- Tube design
New tube designs and production techniques allow for higher power levels. Three aspects require our special attention:
 - Electron beam
The electron beam converts DC power to RF power. The ability to generate and focus high energy electron beams is of major influence on the power level that can be achieved. We will focus on modern cathode design and cathode materials to investigate how the beam current can be increased.
 - Efficiency & cooling
Increasing system efficiency allows for more output power at the same level of dissipated heat. Better cooling implies a higher level of allowable dissipation and hence output power.
 - Operating voltage.
Higher operating voltages increase output power, however they also increase the electron velocity and hence require a major change in tube design. This limits the operating voltage in being a tool to increase output power.
- Energy storage
High peak power levels require large energy storage and cause, due to fast switching, high levels of Electro Magnetic Interference (EMI). Modern techniques to store and control energy, under both operational and error conditions, will be addressed.

The system specification is the technical translation of the operational requirement. This specification dictates the class of tube and the technology to be used in the tube. In this paragraph the tube type, design, power supply and interface will be discussed.

5.1 Tube type

The tube class is driven by:

- 1 Frequency and bandwidth;
This determines the use of a TWT, klystron or magnetron etc.. For a wide frequency band, up to 2 octaves, a TWT will be the best choice. For a limited bandwidth but tuneable over a 4 to 5 % bandwidth, a klystron is a good choice. A magnetron will be the best alternative for up to 3 % bandwidth.
- 2 Power output;
For the power output and the related duty cycle a TWT and klystron is capable of delivering medium peak powers (200 kW) with duty cycles up to 20%. The use of a magnetron will give high peak powers (1 MW) but low duty cycles up to 1%.

- 3 Stability;
Stability in a tube depends strongly on the power supply of the system. For stable, good AM and PM noise figures <-100dBc/Hz the TWT and klystron is the best choice. For a magnetron special measures have to be taken in a coherent system, -60 dBc/Hz can be reached.
- 4 Reliability;
The reliability of the three tube classes mentioned above depends on the stress that is applied to the tube. This will be discussed further in paragraph 6.

An overview is given in table 1.

	TWT	Klystron	Magnetron
Freq. tuning	External source	External source	Fixed/ tuned
Bandwidth	Octave(s)	Tuneable w.r.	Tuneable s.r.
Peak power	Medium	Medium	High
Duty cycle	Up to CW	Up to CW	1% max.
Coherency	Excellent	Excellent	Poor
AM/PM noise in dBc/Hz	<-100	<-110	<-60
Stability	Depending on external source	Depending on external source	0.2%
Reliability	20.000 hrs	20.000 hrs	3.000 hrs

Table 1, Overview tube types
w.r. = wide range, > 3 %.
s.r. = small range, < 3 %.

5.2 Tube design

The system application plays a major role in the design of a high power tube. It dictates the materials and the constructions to be applied to the tube. Each application has its own specific design restraints. A search radar will be operational during a long period of time. A tracking and illumination radar will be used during a short period of time only. EW systems are active over short periods and are in a Standby mode for a long period. This is also the case with fire control and illumination radars whose reliability must be very high upon activation. Systems that are in standby for long periods, often exhibit arcing. Due to the long standby hours, ions may be collected around the cathode and the evaporation of barium oxide out of the cathode may pollute the ceramics and grid structure. Applying the HV (High Voltage) to the tube an arc may be induced by those effects. Failure will cause extreme danger to the platform on which the radar and/or EW is mounted.

In communication systems the operational use is different from the earlier mentioned systems. The tube is in the operational mode for long periods of time. The ions produced are collected by the beam and the evaporation of barium oxide is less due to the beam cooling of the cathode surface and the equal temperature over the gun parts. During the design of the cathode

special measures on, cathode material, oxide, B or M type cathode, grid and thermal stress and stability have to be taken.

The platform that carries the system will dictate the mechanical stress applied to the tube. Land-based systems do not show high shock and vibration levels. Missile applications show high levels of shock, vibration and acceleration during the start. Fighter airplanes will shock and vibrate over a long period of time. Tubes on board ships will see low frequency vibrations over long periods of time. The three described situations all require special attention to the construction of the different parts in a tube. Restrictions apply to design also. In missile and fighter applications the weight of the tube and its power supply will be limited while for land-based and shipborne applications the weight is less stringent. This implicates that the tube designer has to be aware of the platform on which the tube will be used. Finite Element Analysis (FEA) proves a valuable instrument here. It allows the tube designer to predict the mechanical strength of his design and to simulate the impact of various stimulations.

The second part of this paragraph will focus on future strategies and techniques to cope with the above-mentioned problems.

5.2.1 Strategy

Future trends will focus on an increasing use of computer aided design. Libraries of tube parts (e.g. cathodes, RF-structures etc.) will be built up. A new tube will be designed by using the library-parts. More attention will be paid to the tube parts during their design, since they can be used in many tube designs. This will result in thorough FEA and thereby good mechanical strength, in good electric figures, in high reliability and in as simple as possible manufacturing. The manufacturer can easily adapt a given tube design to specific user requirements.

The users will tend to apply standard tube types and HVPS. The manufacturers can produce larger quantities of these standard products at lower costs. This allows for the application of many tubes, mini-tubes or MPMs (Microwave Power Module) in a high power amplifier to increase output power.

5.2.2 Cathode

Tube development will benefit from improved cathode design. Higher current densities and longer lifetimes are required. The development of coatings for the cathode, to lower the work function, are under investigation. Scandate proves to be very successful. Research is still required as the understanding of the physics is still not fully understood. A new development is the Field Emission Cathode Array (see fig. 2). High current densities can be reached in a medium vacuum environment. Figures of 40 to 400 A per square centimeter are attainable in a vacuum of $1.10 \cdot 10^{-6}$ torr. Heaters are not required for this type of cathodes. TaSi₂ is a basic material for this type of cathodes. The limitation is the short life of the cathode. This is due to the relative fast deterioration of the tips in the TaSi₂ array. Further research using other materials and alloys are proceeding.

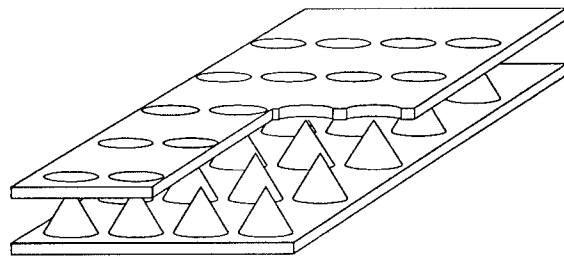


Fig. 2. Field Emission Cathode Array.

5.2.3 Cooling

The cooling of the tube has a major effect on the power handling of the tube. By efficient cooling of the R.F. structure, the power handling can be improved by at least 3 db. There are three distinctive groups of R.F. structure: Helix, Coupled Cavity and Ring Bar. In the coupled cavity and ring bar tubes the cooling of the structure is limited by the surface area of the structure. In the helix tube the heat transfer from the structure is limited by the heat resistance of the isolation material between the helix and the body. In general Beryllium Oxide or Aluminium Oxide is used. The use of diamond rods is under investigation, which promises a reduction of the heat resistance by a factor of 4. FEA proves a valuable instrument here. It allows the tube designer to predict the thermal behaviour of his design and to simulate the impact of various thermal stimuli.

5.2.4 Focussing

Higher efficiency and improved focussing will reduce the energy absorbed in the RF-structure of the tube. Stronger and more reliable magnets, such as Samarium Cobalt magnets, are key elements. Due to the reduced thermal load of the RF-structure, the tube output power can be increased.

5.2.5 Structure

The use of special plastic mandrills for manufacturing the RF-structures are investigated. This technology makes use of a mandrill on which material, such as copper, is electroformed thereby creating the RF-structure. The mandrill is etched out of the structure and the RF-structure remains. Due to the limited amount of brazing high accuracy and high yield can be reached by this technique. It will also reduce the RF-losses in the structure and improve the R.F. efficiency.

5.2.6 Microwave Power Module

Hybrid technology combines the best of two worlds, the high power of the microwave vacuum tube and the gain of the solid state amplifier. To increase power (gain) of a tube higher electron velocities are required. This implies an increase of the operating voltage of the tube. There are a number of disadvantages. Higher voltages will add extra difficulties to the design and reliability of the power supply and increase the complexity of the design and production of the tube. In solid

state higher gains are available. By combining the gain of the solid state amplifier and the power output of the tube a cost effective solution can be found. The low gain of the tube will reduce the high voltages of the tube. When the HVPS is added to the combination of tube and solid state amplifier the MPM is obtained. The MPM has the advantage of no external HV connection and no complex wiring, only three connections have to be made: input, output and power (e.g. 28 or 270 Vdc).

So far this approach has been seen in medium power amplifiers of 200 W and frequencies up to 18 GHz. The AM/PM noise performance of the MPM is only fair due to the poor stabilization of the HVPS. The high power per cubic centimeter rating results in stringent cooling requirements. It can be foreseen that a further development to higher power levels is achievable. Future developments will focus on improvement of AM/PM noise performance and cooling.

MPMs are perfectly suited for active phased array applications, where each antenna element (or set of antenna elements) requires its power amplifier. The advantages and disadvantages of the MPM versus solid state amplifiers is given in table 2.

	MPM	Solid state
Power	50 W	5 W
Efficiency	40 %	15 %
AM/PM noise	fair	good

Table 2, Comparison of an average MPM versus solid state.

The increased power of the MPM can be used either to decrease the number of units or to increase output power, depending on system requirements. both MPM and solid state amplifier require extensive cooling systems.

5.2.7 Mini tube

A way of increasing the system power output is the use of multiple mini tubes. The voltage required with mini-tubes is reasonably low, about 4 kV. By combining the power in a Wilkinson combiner or Rothman lens and using multiple power supplies, a reliable high power amplifier will be designed.

5.2.8 Dual mode tube

The development of dual mode tubes started in the 80's. The difficulties with the design of the vacuum envelope and gun slowed it down. New interest, specially for the designs from the former eastern block countries, can be seen in this type of tubes.

5.2.9 Klystron

The limited instantaneous bandwidth has been a disadvantage of klystrons. New developments in the E.C. have been started on the design of inter active klystrons. This design will give the klystron a bandwidth comparable to that of a TWT.

5.2.10 Magnetron

One of the life shortening effects in the magnetron is the wear-out of the cathode and the secondary emission of the cathode stem area. The improvements of the cathode material follow the

trends shown for TWT and klystron. The effect of secondary emission can greatly be reduced by adding an appropriate coating to the cathode stem and by decreasing the stem temperature.

5.3 Power supply

The feasibility of a microwave power generator is not limited by the voltage and current ratings of today's HVPS. More important however is the protection and control of the power supply. The power supply should be kept within its OE under all conditions. The OE of the HVPS should include that of the tube, so the power supply can never be damaged by any operation condition of the tube. Both control and protection greatly enlarge the HVPS OE.

Present HVPS developments benefit from resonant switching converter topologies, that have among others the following advantages:

- Low EMI.
Due to the sinusoidal current EMI is reduced;
- Low stored energy.
The resonant converter allows for higher switching frequencies which, in combination with low EMI, leads to simple output filters with a low amount of stored energy;
- Tight control.
The high operating frequency and simple filtering allow for high control bandwidth and tight converter control;

The low converter EMI allows for fast acting control and protection circuits without the disadvantage of erroneous operation. Semiconductor protection devices are available that can react in nanoseconds and can handle several hundreds of amperes. They can make the HVPS virtually insensitive to the most extreme tube OP: the HV-arc.

The sinusoidal converter current reduces the electrical stress on the converter semiconductors which on the one hand increases reliability and on the other hand allows for an increased power handling. Also the switching losses are reduced resulting in a higher efficiency and, consequently, smaller heatsinks.

The high frequencies allow for small capacitors, transformers and, due to the sinusoidal current, simple filtering.

Future trends will bring small and efficient power supplies. The main design effort will be on protection and control. The OE will be widened by adequate protection. The control electronics will be programmed to exactly monitor the OP and keep it within the OE unconditionally.

5.4 Interface

The power supply has two major tasks in relation with the tube, it should deliver enough power and it should keep the tube unconditionally within the tube OE.

Tight control of the OE will gradually allow for higher output power without over-stressing the sensitive parts of the tube. Tube design will be influenced by this trend, and gradually go

towards tubes that allow for very high powers in return for a very narrow OE.

The OE will become more and more important in the future. It enlarges the possibilities of power tubes at the expense of increased risk to destroy tube or HVPS in case the OE is not properly maintained.

5.5 Energy storage

The energy, necessary to generate high power microwave levels, is drawn from the HVPS. The energy, supplied by power invertors, is temporarily stored in capacitors. In case of tube, the stored energy is uncontrollably released into the tube, which can be destroyed eventually. There are several techniques to avoid this energy release:

- Application of a crowbar.
- Limitation of energy storage.
- Application of HV switches.

These techniques are discussed more in detail below.

5.5.1 Crowbar

A crowbar is the conventional solution to avoid excessive energy release. It provides a low impedance pad for the energy source, thereby diverting the energy off the tube. Crowbars however show several drawbacks:

- Their reliability is limited due to sensitivity to wear;
- Their ability to "fire" is often not unconditional;
- Their reaction time is fair, a part of the stored energy is still released in the tube before the crowbar fires;
- The operation principle implies high currents compared to the operating current;
- The operation principle implies high current rise-times, the resulting EMI may easily cause damage to HVPS electronics.

5.5.2 Limited energy storage

The energy storage is limited to the maximum rating for the tube. This state of the art technique requires electronic circuits to compensate the effect of limited energy storage. Modern semiconductor technology provides high bandwidth components with sufficient voltage and current rating to enable these control circuits. The compensation electronics guarantee operation within the OE.

5.5.3 HV switch

HV-switches between energy storage and tube can block the energy release. Certain tube types (CFAs) require the switch also to switch the tube on and off. The conventional switches have drawbacks about equal to the already mentioned crowbar. To avoid these drawbacks, the HV-switch is often replaced by a low voltage, high current switch combined with a pulse transformer.

Future developments will bring the stacked transistor topologies. This emerging technology enables fast reacting reliable switches that can handle high voltages and high current levels. Today these switches still are bulky, in the near future they will be available in the same size as conventional switches. Stacked transistor topologies also enable control of rise- and

fall-times, thereby reducing the amount of EMI. Moreover, operation within the OE, both under operating and error conditions, can be guaranteed by adequate control of the stacked transistor system.

6. RELIABILITY

The reliability requirements are strongly related to the modes of operation. The paper will address various aspects, including Mean Time Between Failure (MTBF) and the certainty that a tube will run upon switch-on.

Tube designs, production techniques and maintenance greatly determine tube reliability. Good power supply design can strongly increase tube reliability and hence system reliability. New power supply topologies also include the necessary protection systems for the tube to run under high power conditions.

This chapter will focus on reliability of power tubes and HVPS. The system reliability is not only determined by the sole reliability of the tube and HVPS but also by the tube-HVPS interaction. The concept of the OE is a useful tool to describe the various reliability aspects.

6.1 Tube

The TWT is taken as example, since it has all functions in physically separated areas:

- Electron generation in the cathode;
- Beam control in the grid;
- Beam focussing & acceleration;
- RF is generated/amplified in the RF structure;
- Electron collection in the collector.

Other tube types have some or all of these elements. The CFA family generally lacks beam control and focussing, electron collection is done by the RF structure. The klystron has the same outline as a TWT, however the RF structure is distinctive and they often lack a beam control grid.

In relation to general tubes, the MTBF of high power tubes is more related to:

- 1 Cathode stress.
High output power requires high current densities in the electron beam and thus at the cathode surface. This asks for new cathode (micro-) structures and materials. It can be necessary to operate the cathode at elevated temperatures. The latter will decrease cathode life and increase the out-gassing process.
- 2 Electrical stress.
High power tubes generally run under high voltages. This makes the tube sensitive to flash-overs due to gas in the vacuum envelope or contamination of the ceramics. Eventually this will lead to the inability of the tube to withstand the HV.
- 3 Thermal stress of the helix.
Due to imperfections in beam focussing a part of the electron beam is intercepted by the RF structure. The high speed of the electrons causes high heat dissipation in the RF structure.

4 Thermal stress of the collector(s).

All energy supplied to the tube is either converted to RF-energy or to heat. Almost all heat is, under normal conditions, dissipated in the collector. Overheating may cause the collector to melt or to evaporate metal (copper) which will form conductive layers on isolating ceramics. Collector cooling therefore is an crucial factor in tube reliability.

5 Vacuum.

Due to (thermal) stress in the brazing and/or hot spots anywhere in the tube, micro-leaks can develop, thereby causing loss of vacuum. High surface temperatures of parts inside the vacuum envelop can cause out-gassing, thereby destroying the vacuum. Also the evaporation of barium out of the cathode can have this effect.

Under certain circumstances, a "quick-start" is applied to the tube. The OE is "widened" to include the OPs with high inrush currents which can be done with special cathode and heater design. Special grids can keep the tube from operating thereby allowing for a fast switch-on of the HV.

The certainty that a tube will run upon a "quick-start" can be checked by the BIST (Build-in Self Test) of the HVPS. The heater can be tested upon resistance, where the quality of the vacuum can be proved with a static HV test. Tubes, equipped with an ion pump, can maintain their vacuum and allow for an easy check of the quality of the vacuum.

Tube technology nowadays moves to a "narrowing" of the OE in favour of an increased reliability. Better knowledge of thermal cathode behaviour can result in an OE that, under strict control of the OP locus, will allow for quick-start.

6.2 HVPS

HVPS reliability is, of course, subject to general reliability aspects that apply for all electronic devices. Due to its high power and voltage handling some specific aspects are noteworthy:

1 Electrical stress.

Semiconductors are used as close as possible to their maximum ratings, which requires adequate derating to meet the reliability specifications. The sinusoidal currents of resonant converters lack high dV/dt and dI/dt which reduces the electrical stresses.

2 Thermal stress.

Most of the components are operated close to their maximum operating temperature, once more requiring derating. Resonant converters, running with sinusoidal currents however exhibit greatly reduced switching losses that allow for reduced operating temperatures and enhanced reliability.

3 Switching

The high voltage levels implicate high levels of stored energy in parasitic capacitances. This energy is released upon switching and can destroy semiconductors. Resonant converter topologies can reduce rise-times, thereby reducing the current through the parasitic capacitors. This also can compensate certain parasitic capacitances.

4 EMI

The high pulsed output power causes high levels of EMI, which can destroy other parts of the HVPS. Once again rise-time reduction can reduce EMI.

BIST equipment does not increase reliability in statistical terms. A failure cannot be avoided by BIST. The certainty that both tube and HVPS will run upon switch-on however can greatly be increased by proper BIST procedures. This reliability aspect is especially important for missile systems, fire control and EW systems, since they are (only) switched on when life-threatening situation occurs.

6.3 Tube-HVPS control.

Tubes and HVPS strongly interact. As far as reliability is concerned, malfunction of either one can destroy the other. The increase of reliability depends on the HVPS that has to fulfil four requirements:

- It has to keep the tube within the tube OE;
- It has to keep itself within the HVPS OE;
- It has to be able to withstand all the tube's possible operating points, including arcing (=short circuit of the HVPS!). The HVPS OE itself should be wide enough to enclose all the tube's operating points;
- It has to be fail-safe: never should the tube be put in an invalid OP due to power supply failure.

The above-mentioned requirements can be met by new power supply technology. The power supply control has, apart from regular HVPS functions, four major tasks in tube & HVPS control:

- Monitor the OP of the tube;
- Compare the OP with the internally stored OE;
- Take corrective actions to keep the OP within the OE;
- Shut-down the power supply in case the OP is near the edge of the OE. At shut-down, the OP should remain within the OE.

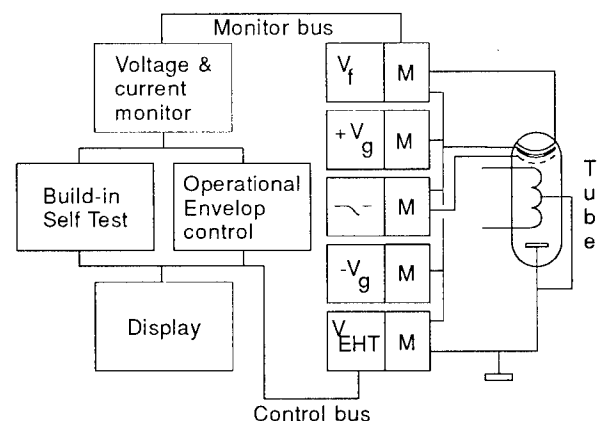


Fig. 3. Power supply with full OE control and BIST.

Given the above mentioned guide-lines concerning reliability of tube, HVPS and their interaction, a power supply was designed at FEL-TNO in the Netherlands. This power supply has extensive control electronics to guard the OE and BIST to check the power supply and the TWT. It has a display panel indicating

which part of the TWT or HVPS is malfunctioning. The prototype still meets all reliability requirements after a more than four year test period. The lay-out of the HVPS is given in fig. 3.

6.4 Mini-tube

At a first glance, the choice between a "mini" and a "normal" tube has no impact on reliability. The mini-tube however works with lower electron speeds and hence lower voltages. This factor enables a significant increase in reliability of both tube and HVPS.

The major drawback of the mini is its relatively low peak output power. The mini is easier to produce, especially in series production, which allows for a lower price and a strict quality program. The mini has the potential to run at a significant lower dollar per watt rating than its bigger opponent. Even with the extra costs of combiners, large amounts of power can be generated cost-effectively by using a sufficient number of minis.

The mini will be the future solution in many RF power generators.

6.5 Microwave power module

The consists of a solid-state pre-amplifier, a (mini) TWT and a HVPS, all combined in one housing, see fig. 4.

The MPM further increases the reliability that is obtained by the use of mini-tubes:

- The gain is obtained by the solid state amplifier so the gain requirement for the tube is minimal. The tube designer can concentrate on reliability instead of on gain.
- The MPM runs at lower voltage than the mini tube.
- The tube and the HVPS can be perfectly matched with respect to their OE.
- Maintenance personnel does not have to handle HV-parts, which both increases reliability and safety.

The MPM has, as already stated, a lower power rating than the mini. For the same reasons however, their dollar to watt rating can be reasonable. The main application for MPM is the phased array antenna that benefits from the multiple amplifier concept and from the power combination that is done "in free space".

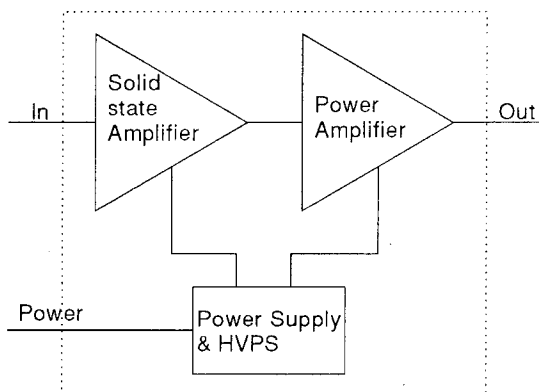


Fig. 4. The Microwave Power Module.

7. COST-EFFECTIVENESS

The procurement costs, the limited lifetime of the tube and the necessary maintenance are the main cost-drivers. Tubes also require maintenance when they are non-operating or in storage.

Production technology is in an on-going process of decreasing production costs, however tubes are labour-intensive to produce which strongly limits the effect of production technology on tube procurement costs.

Tube design and efficient maintenance procedures will increase the lifetime of the tube. The build-in test equipment of the power supply will reduce maintenance costs.

The maintenance cost of a system is not only the cost of repair and periodic maintenance, but also the cost of the logistic system.

The repair of the microwave tube is complicated and can in general only be done by the manufacturer at high expenses. The microwave tube has to be returned to the tube manufacturer for analysis and repair. This causes long turn-around times, meaning extra investments in spares tubes.

Repair of the defective HVPS may be performed by the maintenance organization of the system owner or may be contracted to the system manufacturer, requiring spare HVPSs due to long turn around times.

Maintenance personnel can only perform a limited fault analysis. A key factor is the limited time available for repair. A system has to be operational within the specified MTTR, often less than 1 hour. The maintenance engineer however has to determine whether tube or HVPS is defect. Effective HVPS BIST however can give a quick, good and well specified analysis of the fault.

Periodic maintenance can greatly be reduced by BIST. As long as tube and HVPS are operated within the OE, there is no objection to use the tube as a test load for the HVPS and/or the HVPS as a test device for the tube. This however requires auto-calibrating facilities, fail-safe BIST and fail-safe OE control. Human interference, if necessary, then is limited to maintenance that requires specific equipment.

Periodic maintenance can also be reduced by training of the maintenance engineer in fault diagnostics on microwave tubes and HVPS. The basic principles on microwave tube theory and tube maintenance has to be part of his education.

Tubes do change their OE over lifetime. Maintenance engineers often report increased lifetime due to slightly changed voltage settings. When aging is included in the OE programmed in the HVPS, this can increase tube lifetime. The operation within the OE itself also increases lifetime.

Failure data comprise a great amount of information regarding reliability and MTTF. With data, obtained from BIST, maintenance engineers (following a well defined procedure) and factory repair engineers, an in-depth analysis of the failures can

be made. Here the use of HV and STANDBY hours is of major importance and a real MTBF can be calculated. Special circumstances such as land-based and ship- or airborne, type of system fire control, illumination, search radar or jammer, have to be taken into account. The results of the analysis have to be available to the system user, tube manufacturer and/or the system designer. Depending on the results of the analysis operational procedures, system modifications or tube modifications have to be discussed.

8. CONCLUSIVE REMARKS

New cathodes and higher efficiencies will allow for higher output power. Reliability and lifetime will be increased by new technologies and "smart" power supplies, the latter also being responsible for decreasing maintenance costs.

After a decreasing interest in the use of high power vacuum tubes in the 70's and 80's, new developments started in the field of cathode technology, efficiency, power supplies and tube-HVPS interfaces. This brought the tube back into the newly developed systems as a reliable microwave power source.

The combining of power, as is common practice for high power solid state amplifiers, showed its benefits at the introduction of the mini tube. The marriage of the low power solid state amplifier and the mini tube resulted in the MPM, a versatile and easy to use power amplifier.

The development of new tube technologies will depend on the performance requirements of systems. The active phased array antenna act as a technology push into the development of MPMs.

The OE will be increasingly important for tube and HVPS design and development. Future developments will benefit from tight OE control. Close corporation between the designers of tube, HVPS and system is necessary to formulate the OE.

New technologies as scandate cathodes will allow for higher output power. Tube designers will take advantage from OE control to further increase output power.

Effective BIST will reduce maintenance costs.

The power amplifier of the future will consist of a number of (cheap) standard tubes, in most cases mini tubes or MPMs. The system will be virtually maintenance free, indicating the defective tube or HVPS part in case of a failure. The latter results in repair by replacement.

DISCUSSION

E. SCHWEICHER

Do the cooling problems you mentioned about HEMT's or MESFET's explain the cooling difficulties encountered by TI and Westinghouse in the development of the active phased array antenna of the radar of the ATF F-22 ?

AUTHOR'S REPLY

I am not in a position to discuss the problems that are encountered during the development of the F-22 radar system. However TNO-FEL has a vast experience with the development of active phased array antennas, as for example used in the PHARUS universal SAR radar. Cooling of active phased arrays is difficult due to :

- the low efficiency of the semiconductor power amplifier
- the high power density involved
- the (virtual) absence of conduction cooling in two-dimensional array's. A medium (e.g. air, water or freon) is used to transport heat. This leads to an elaborate cooling system.

The higher efficiency of MPM's give them a strong advantage as far as cooling is concerned. The required cooling capacity for MPM can be down to 50 % when compared to a solid state amplifier with the same RF output power.

E. SCHWEICHER

What do you think about the power capability and the reliability of HEMT's and especially pseudomorphic HEMT's ?

AUTHOR'S REPLY

The amount of heat that can be dissipated by a HEMT (or any other transistor) is limited by its chip surface. The efficiency and chip surface determine the power capability of the HEMT. In relation to other semiconductors the efficiency is the main factor. However in relation with MPM's the chip surface becomes a main factor, since it cannot be increased beyond a given limit.

As my presentation indicates, almost any reliability can be achieved, as long as operation is limited to a given operational envelop. For HEMT's this will in general mean that high reliability is achieved for a limited temperature range, input voltage range and supply voltage range. When the device is "pushed to its limits" the reliability will decrease.

HIGH-POWER MICROWAVE DEVELOPMENT IN RUSSIA

Sylvain Gauthier,
National Defense Headquarters, DSTI,
101 Colonel By Drive, 18ST
Ottawa, Ontario, Canada, K1A 0K2

SUMMARY

This is a survey of Russian research and development in high-power microwave (HPM) sources. It emphasizes those sources of nanoseconds pulse duration time which have potential weapon as well as radar applications. It does not cover the whole range of Russian HPM research and development but concentrates on those aspects which may lead to military applications. Russian investigators have achieved many world firsts in HPM generation; for example, a multiwave Cerenkov generator with a peak output power of 15 gigawatts. Their successes are based on their impressive capability in pulsed power technology which has yielded high-current generators of terawatt peak power. They have transformed the energy of these currents into microwave radiation using tubes of both conventional and novel designs exploiting relativistic electron beams. Recently, the development of high-current mini-accelerators has moved relativistic electron-beam (REB) HPM

generation out of the laboratory and enabled the development of deployable military systems with peak powers in the gigawatt range. As a result, they now see development of a REB-based radar systems as one of the most promising directions in radar systems. Details of such a system are described and the implications for HPM weapons are considered.

INTRODUCTION

This briefing is on HPM development in Russia and is presented at the unclassified level. The paper starts by a brief review of the most active Russian research groups working on HPM technology. This is followed by Russian development in high-current accelerators used to drive HPM devices. Then, the slow-wave devices such as magnetron, backward-oscillator (BWO), multiwave Cherenkov generator (MWCG), and relativistic diffraction generator (RDG) are examined, and finally, a brief review of fast-wave and plasma devices is presented.

RUSSIAN INSTITUTES

The Institute of Applied Physics (IPF) in Nizhniy Novgorod, formerly Gorky, is seen as the leading Russian institute in the area of HPM technology. This institute has worked on most types of HPM devices such as slow-wave and fast-wave. The only area in which they have not been working is in plasma devices. The IPF is internationally known for its development of fast-wave devices such as gyrotrons, and cyclotron autoresonance masers (CARM), which have produced the highest average power in the mmw band.

In Tomsk, the Institute of high-current (ISAH) has been working extensively on development of slow-wave devices such as BWO, MWCG, and RDG. They have focused on the wavelength band 0.8-3cm. This institute has been working on HPM generation in both single pulse and repetitive operation, and as part of this program, they have developed compact repetitive accelerators. This institute is well-known for its research in multiwave devices which have produced the highest peak power in both centimeter and mmw bands.

The Institute of Nuclear Physics (IYAF), also located in Tomsk, specializes in development of relativistic magnetron, vircators, and resonator-storage sources. They have been

working mainly in the s-band (3-GHZ). This institute is a key center for development of compact repetitive accelerator based on linear induction accelerator. These systems have been used to drive their relativistic magnetron in repetitive operation.

In Moscow, the Institute of General Physics (IOF) has been working extensively on HPM plasma devices such as plasma filled devices, plasma Cherenkov masers (PCM), Vircators. This institute has also developed a very successful system based on plasma for the conversion of HPM radiation into electrical current [1]. The IOF is also known to have worked on some fast wave devices such as gyrotrons and free electron lasers (FEL). The Moscow Radiotechnical Institute is another group that has been active in HPM research. Their main interest has been mainly in Vircator and plasma devices. It is suspected that a close cooperation exists between the IOF and the Moscow Radiotechnical Institute, since they have been working on similar devices.

HIGH-CURRENT ACCELERATORS

Russian scientists have been very successful in the development of compact accelerators used to drive their HPM devices in repetitive operation. The ISAH, and the IYAF in Tomsk are two key Russian institutes in developing compact repetitive accelerators. The ISAH started its development of

compact accelerators in the late 1960's [2]. They were intended specifically to drive relativistic BWO. By the late 1970's, the Russians came up with the SINUS-series of small-size accelerators based on capacitive storage line. Since that time, the ISAH has developed many models of its SINUS-accelerators which are able to generate beam currents with several gigawatts of peak power. Pulselength ranges from a few nanoseconds to tens of nanoseconds. Originally, the repetition rate was limited to 50 pulses per seconds (pps). In 1990, the ISAH succeeded to operate these accelerators at a repetition rate of 1000pps [3]. This was made possible through their analysis of the high-voltage spark gap behaviour in repetitive operation. Russian scientists found out that these switches are destabilized by the appearance of a gas region near the electrodes. By removing it at the repetition rate of operation, the numbers per pulses per seconds was increased to 1000HZ.

The key-feature of the Sinus-accelerators is the tesla-transformer used to charge the capacitive storage-line. The transformation factor makes possible the use of a low-voltage capacitor as primary source. As a result, the accelerators are more compact, and capable of repetitive operation. In the past, the ISAH has been using the spark gap, and thyatron as high power switches in these accelerators. Recently, however, they have been using thyristors which are

high-power semiconductor switches. This is significant, since Russia is the world leader in development of high-power semiconductor switches. Use of these switches is likely to make the accelerators more compact and capable of higher repetition rates.

Since the mid 1980's, the ISAH and IYAF have been working on a new design of high-current accelerators based on inductive storage line which is capable of a two order increase in density energy storage [4]. This is particularly important for development of compact accelerators. The key components for magnetic storage accelerators is the opening switches which must change quickly from a state of very low-resistance to very high-resistance. Originally, the ISAH has been using plasma-opening switches which they have been extensively working on. In 1987, The ISAH succeeded to operate a small-size accelerator capable of generating beam current at a 25 gigawatts peak power level, with pulselength of 80 nanoseconds duration time [5]. Since the early 1990's, the Russians have used solid-state semiconductor switches as opening switches. They have already obtained an electron beam with maximum energy of 400 KeV, and a current of 6 KA, when the pulse duration was 30 nanoseconds. As opposed to plasma-opening switches, the semiconductor switches offers greater simplicity of construction, stability of parameters, and the

possibility of repetitive operation. These switches can find wide usage not only in small-size accelerators but also in large ones.

The Russians have also developed compact repetitive sources of high voltage current based on linear induction accelerators [6]. These accelerators have been developed by the Institute of Nuclear Physics in Tomsk, and have been used to drive their relativistic magnetrons [7]. Repetition rates up to 100pps in steady state, and 160pps in a train of three pulses have been produced in these accelerators.

In pulsed power technology, Russia is substantially ahead of the West in development of magnetic cumulative generators (MCG) which are driven by explosive charges [8] [9]. They have produced the world record in generation of single current pulse with an energy of 100 megajoules and current of 300MA. The pulselength of these generators is about 20 microsecond which is also relatively fast when compared to large capacitor facilities which range in the millisecond duration time. One hundred megajoules of energy is quite impressive, when we think that a state-of-the-art large capacitor facility using about 250 tons of capacitors can only produced 10 MJ per pulses. Russia has developed a desk-size version of MCG, 16 inches-wide by 40 inches-long (40 X 110 cm), which can be incorporated into missile systems.

SLOW-WAVE DEVICES

Relativistic magnetrons

Russian research in relativistic magnetrons have been very extensive. The small-size of a magnetron, and its high reliability, stability and efficiency are key features that have been driven Russian research. In late 1970's, peak power at the gigawatt level with efficiencies of 40 percent were already produced in relativistic magnetrons [10]. In the late 1980's, Russia was able to generate a peak power at the 10 gigawatt level from their magnetron [6].

In 1989, Russia created a world first by operating a relativistic magnetron at an operating frequency as low as 1.2 GHZ [11]. Microwave radiation of 130ns duration time at the 210MW peak power was produced. The efficiency of the relativistic magnetron was 6 percent. Russian scientists said that this research has been driven by potential HPM application in the decimetric band which seems to indicate a new trend in Russian HPM research.

In 1987, Russian scientists operated a relativistic magnetron in repetitive mode [7]. Peak power of 360MW at a repetitive rate of 160pps in a train of three pulses was produced at that time. In the experiment, they used as a source of high-voltage their new linear-induction accelerators which is very compact. Since 1987, Russian

scientists have continued to investigate repetitive operation of relativistic magnetrons.

Relativistic Backward-wave oscillator (BWO)

BWO is one of the HPM devices in which Russia has been working the most. They were the first microwave devices to be driven by relativistic current, back in 1973. By late 1970's, these devices almost reached their maximum capability in terms of peak power microwave. Research to increase the peak power capability of BWO led to the development of oversize waveguide structures, and then of Multiwave Cherenkov generators which will be examined later. Russian research in BWO has been concentrated on increasing the efficiency of these devices, and operating them in a repetitive mode.

The Russians have shown, theoretically and experimentally, that the maximum efficiency of BWO using regular electrodynamic structures is around 20 percent. In early 1980's, they started investigating the use of irregular structures to produce an inhomogeneous coupling over the interaction space [12]. Inhomogeneous coupling is obtained by increasing the amplitude of the periodical structure. In the first experiment a peak power of 320MW with an efficiency of 29 percent was produced from an irregular BWO tube. A similar BWO with regular structure

produced only 20 MW of peak power with an efficiency of 11 percent. Since that time, Russian scientists have shown that the use of inhomogeneous coupling can increase the efficiency above 50 percent. In 1992, the Russians showed that BWO efficiency can be further increased by use of inhomogeneous phase velocity [13]. This is obtained by increasing the periodicity of the electrodynamic structure. Russia has found that the electron beam transfers the greater part of its energy at the beginning of the interaction space. As the electron beam loses its kinetic energy, a certain equilibrium is reached between the beam and the electromagnetic wave; and the conditions for efficient energy transfer are less and less favourable. In increasing the phase velocity of the wave, this equilibrium is broken, and transfer of the electron beam energy is optimized over the entire interaction space. The Russians have verified experimentally their new theory. They have produced in the 3.2 cm band, a peak power of 200MW with pulselength of 12 ns, and efficiency of 40 percent. This was close to their theoretical prediction for this specific case, and confirms the possibility of increasing the efficiency of BWO through the use of inhomogeneous phase velocity. Russia have shown that for moderated relativistic electron beams, $\gamma=2$, efficiency can be as high as 70 percent. As opposed to inhomogeneous coupling which has been considered only for ultra-relativistic electron beam, this new

techniques is valid for moderated relativistic electron beam such as those used in compact repetitive accelerators.

Relativistic BWO have been the first Russian HPM devices to be operated in repetitive operation. The Russians have been using the SINUS-series of compact repetitive accelerators to drive these BWO. In 1978, peak power of 100MW at rep-rate of 50pps was produced from the relativistic BWO. During the 1980's, repetitive BWO produced gigawatt peak power of nanoseconds pulses at a repetitive rate of up to 100pps.

Advanced radars

In 1992, the Russian had already developed a high-power short-pulse radar based on their repetitive relativistic BWO [14]. The radar transmitted up to 100pps at the gigawatt peak power level. Frequency of operation was of 10GHZ and pulselength was only of 5 nanoseconds. In field testing, the radar was able of detecting aircraft targets flying at 50 meters above the ground, up to a distance of 50 KM. The radar systems has also enhanced capabilities for detection of small ship targets. Russia concluded that used of HPM devices in radar systems is a new and extremely promising direction in contemporary system.

High repetition rate

Russians are working very hard to increase the repetition rate of the repetitive HPM devices. In 1990, the ISAH in Tomsk has been able to operate relativistic BWO and Orotron devices at a repetitive rate as high as 1000pps [3]. The key system for this research is the compact repetitive accelerators that ISAH has designed and manufactured. This accelerators can produces beam currents up to 5KA, and electron energy up to 800 KeV, with pulselength of 10-20ns. The relativistic BWO was operated at the 3-cm wavelength band, and the orotron was operated at the 8mm wavelength band. Radiated pulselength was around 15ns for both HPM devices. In their experiments, the Russians first used a regular BWO. In single pulse operation, peak power of 600MW and efficiency of 15 percent was produced. At high repetition rates, peak power and efficiency dropped to about 300MW and 7.5 percent, respectively. Russian scientists have also investigated repetitive operation of irregular BWO. At a repetitive rate of 100pps, they produced a peak power of 500MW at efficiency of 20 percent. This is a three fold increase in efficiency over the previous regular BWO. In their investigation of orotrons, single pulse operation produced a peak power of 200MW and efficiency of about 12 percent. At a repetition rate of 1000pps, peak power of 100MW and efficiency of about 6 percent were produced. This research in HPM devices at a high repetition rate is likely

to lead to the development of advanced high power radar and jammers.

Multiwave Cherenkov generators (MWCG)

In the early 1980's, Russian scientists started a series of experimental investigations to increase the peak power and length of microwave radiation from BWO [15]. Finally, the ISAH came up with a new device, called a multiwave Cherenkov generator, consisting of an oversize waveguide structure containing two periodic sections separated by a drift space. The first section modulated the electron beam which imposes its structure on the radiated field of the second section. In 1983, a peak power of 5GW was produced in the 3cm wavelength band. Pulselengths were of 30 to 50ns, and efficiency was around 10 percent. In 1987, Russia produced from their MWCG, a peak power as high as 15GW with efficiency of 50 percent [16]. This was the highest peak power produced up to that time, and is still the highest published in Russian literature. Pulselength of the radiated wave was 70ns which means that the each pulse has one kilojoule of energy. This is very high as compared to a few joules seen for radar applications. Another Russian HPM device that is known to have produced around kilojoule of energy per pulse is the relativistic diffraction generator (RDG) [17]. It has produced gigawatt peak powers 60GHZ. Pulselength was as

long as 700ns. In fact, RDG are very promising for generation of microsecond duration at the GW peak power.

Dielectric Cherenkov Masers (DCM)

In 1983, Russia showed that DCM can be used as HPM generators [18]. At that time, peak power of 580MW at the 3cm wavelength were produced. Pulselength were of 55ns, bandwidth of 17 percent, and efficiency of 17 percent. Since that time, Russia research in DCM has been very extensive. They have shown that efficiency in DCM can be as high as 40 percent. The extreme simplicity of DCM is one the key factors driving Russian research in DCM. In early 1990's, Russian scientists set up a new direction in DCM by showing that they can be used as an ultra-broadband HPM amplifier [19]. This capability has not been known before since previous experiments on DCM have been using propagation channels with diameter superior to the radiated wavelength. For such conditions the beam-wave coupling fall off rapidly as the frequency increases. As a result, broad band amplification is not possible. If the propagation channel diameter is inferior to the radiated wavelength then beam-wave coupling is virtually independent of the frequency. As a result, ultra-broadband amplification is possible. In experiments, 40db of gain was obtained with bandwidths as large as 40-50 percent at 10GHZ and higher.

Russians have used electron beam energies typical of compact accelerators, which might indicate the intention of developing repetitive DCM.

PLASMA-DEVICES

Vircator is one of the most promising HPM devices due to its simplicity and compactness of construction [20]. One of the key advantages of Vircator is their simple frequency tuning, which can be done by varying the external magnetic field, or the vircator geometry such as the space anode-cathode. Experimentally, these devices have produced peak powers at the GWs level, in the frequency range 1-10GHz with efficiency up to 20 percent. Some of the best achievements of the IYAF in Vircator research are shown in table 1.

In 1989, the IYAF in Tomsk developed a new type of monochromatic HPM generators based on a vircator devices coupled to an electromagnetic resonator-storage [21]. Basically, the electromagnetic energy is slowly accumulated, and then rapidly extracted. This increases considerably the peak power of the initial radiation. Although this scheme is a new design for HPM devices, the use of resonator-storage to increase peak powers of microwave radiation is much older. In fact, the IYAF has been working on resonator-storage driven by conventional microwave source for more than two decades. On the other

hand, this is the first record of a resonator-storage system driven by a relativistic source. The IYAF claimed that resonator-storage is very promising for development of long-range impulse radars which have strong capability detecting stealth targets.

Experimentally, the vircator generated a frequency spectrum of 2.7-3GHz with a peak power of 20MW. The accumulation time was 250 nanoseconds, and the energy was extracted in 10 nanoseconds. The peak power at the resonator-storage output was as high as 400MW. This is very promising as a source of HPM radiation due to the simplicity and compactness of this new system. An interesting result of the experiment is the generation of a very monochromatic radiation from a wide-frequency source. Monochromatic radiation would be very difficult to obtain from a vircator alone, and is very important in radar applications. The Russians consider that vircator/resonator-storage are very promising as HPM sources of nanoseconds coherent radiation at the gigawatt peak power level with a rep-rate up to 1000pps.

FAST-WAVE DEVICES

The Institute of Applied Physics (IPF) is a world leader in the development of fast-wave devices such as gyrotrons. According to the Russians, gyrotrons are currently the only devices capable

of generating MW output power at frequency higher than 100GHZ [22]. Some of the best results of the IPF are given in Table 2. In the early 1990's, the Russians said that a gyrotron with a frequency operation up to 80GHZ with output power of 0.5MW and pulse duration of around one second had been developed. They were then working on similar devices but with higher output power and at higher frequency. In figure 2, some estimations of the maximum output from gyrotron devices as a function of the ratio of the diameter of the waveguide and the radiated wavelength is shown. More than one MW output is seen as possible for gyrotron operating at a frequency of 300 GHZ.

In the late 1980's, Russian interest in cyclotron autoresonance masers (CARM) increased significantly [23]. The Institute of Applied Physics said that theoretical calculations have shown that for the 1-2mm wave band (150GHZ-300GHZ), average power of 1-10MW are possible. In 1990, the IPF hoped to get such average power in the nearest future. We have no information on the current level of this technology in Russia.

CONCLUSION

Russia is currently among the world leaders in development of HPM technology. The future of Russian research in HPM is full of uncertainty due to the Russian economic problems.

However, we suspect that it will remain a high priority due to its military value.

TABLE 1. VIRCATORS FROM IYAF

Peak power (GW)	F (GHZ)	efficiency (%)	pulse-length (ns)	H field (KG)
1.2	2.9	17	120	
0.3	3.1	13	1000	
1.5	3.1	6	30	1.8
5.4	5.4	4	30	5.4

TABLE 2. GYROTRONS FROM IPF

frequency (GHZ)	power (MW)	efficiency (%)	pulse-length (ms)
82	1.5	36	0.1
100	2.1	30	0.1
143	1.0	47	0.1
167	0.5	30	1.0

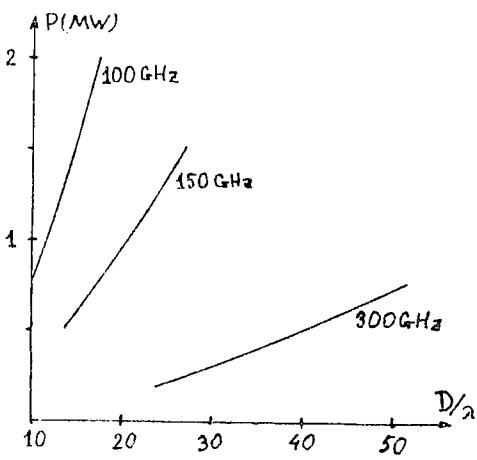


FIGURE 2. Estimation of maximum power from gyrotron

REFERENCES

1. Askaryan, G.A., Batanov, G.M., **"Plasma-burst conversion of intense microwave radiation and supplying power to space stations"**, Soviet Technical Letters, 15(4), April 1989, pp 294-296.
2. Mesyats, G.A., **"Vacuum discharge effects in the diodes of high-current electron accelerators"**, IEEE transactions on Plasma Science, Vol 19, No. 5, Oct. 91, pp 683-689.
3. Bykov, N.M., Mesyats, G.A., **"Relativistic periodically pulsed microwave oscillators"**, Eighth International Conference on High-Power Particle Beams (BEAMS 1990), July 1990, pp 1141-1146
4. Kovalchuk, B.M., Mesyats, G.A., **"Generator of high-power nanosecond pulses with a vacuum line and a plasma interrupter"**, Soviet Physics Dokl., Oct. 85, pp 879-880.
5. Arbuzov, A.I., Bystritskii, V.M., **"The application of a plasma erosion opening switch to a nanosecond generator at the power level of 10 GW"**, IEEE Transactions on Plasma Science, Vol. PS-15, No. 6, Dec 1987, pp 674-677.
6. Usov Yu.P., **"The development and application of charged particle high power accelerators in Nuclear Physics Institute Tomsk"**, BEAMS 1990, July 1990, pp 264-271.
7. Vasilev V.V., Didenko, A.N., **"Relativistic magnetron operating with a pulse train"**, Soviet Technical Letters, 13(6), June 1987, pp 317-318.
8. **"EMP weapons lead race for non-lethal technology"**, Aviation Week & Space Technology, May 24, 1993, pp 61.
9. **"Russia leads in pulse weapons"**, Jane's Defence Weekly, 10 Oct 1992, pp 5.
10. Granatstein, V.L., **"High-power Microwave Sources"**, Artech House, 1987.
11. Sulakshin, A.S., Fomenko, G.P., **"Relativistic magnetron for the 30-cm wavelength range"**, Soviet Physics Letters, 15(11), Nov 1989, pp 887-888.
12. Elchaninov, A.S., Kovalev, N.F., **"Highly efficient relativistic backward-wave tube"**, Pisma Zh. Tekh. Fiz., 6, April 1980, pp 443-447.
13. Korovin, S.D., Rostov, V.V.,

- "Relativistic backward wave tube with variable phase velocity", Soviet Tech. Lett., 18(4), April 1992, pp 265-266.**
14. Bunkin, B.V., Elchaninov, A.S., **"Radar based on a microwave oscillator with a relativistic electron beam", Sov. Tech. Lett., 18(5), May 1992, pp 299-300.**
 15. Bugaev, S.P., Kanavets, V.I., **"Relativistic Cherenkov generator", Sov. Tech. Lett. 9(11), Nov 1983, pp 596-597.**
 16. Bugaev, S.P., Cherepenin, V.A., **"Relativistic multiwave cerenkov generators", IEEE Transactions on Plasma Science, Vol. 18, No. 3, June 1990, pp 525-536.**
 17. Bugaev, S.P., Cherepenin, V.A., **"Investigation of a millimeter-wavelength-range relativistic diffraction generator", IEEE Trans. on Plasma Science, Vol. 18, No. 3, June 1990, pp 518-524.**
 18. Didenko, A.N., Borisov, A.R., **"Cerenkov radiation of high-current relativistic electron beams", Sov. Tech. Lett., 9(1), January 1983, pp 26-27.**
 19. Chirkov, K.A., Shlapakovskii, A.S., **"Dielectric cerenkov maser as an ultrabroad-band high-power microwave amplifier", Sov. Tech. Phys.Lett., 17(10), Oct 1991, pp 682-684.**
 20. Rukhadze, A.A., Tarakanov, V.P., **"Vircators", Radioteknika i Elektronika, No 3, 1992, pp 385-396.**
 21. Grigoryev, V.P., Fomenko, G.P., **"Experimental and theoretical investigations of generation of electromagnetic emission in the vircators", BEAMS 1990, July 1990, pp1211-1216**
 22. Flyagin, V.A., Nusinovich, G.S., **"Gyrotrons for ECHR: State-of-the-art and prospects", BEAMS 1990, July 1990, pp 307-311**
 23. Bratman, V.L., Petelin, M.I., **"Millimeter wavelength CARM: Problems and perspectives", Eighth International Conference on High-Power Particle Beams (BEAMS 1990), July 1990, pp 1129-1134.**

DISCUSSION

E. SCHWEICHER

How does the frequency jitter of relativistic magnetrons compare to the frequency jitter of conventional magnetrons ?

AUTHOR'S REPLY

I really don't know. I have been following the technology from a general point of view without going much into details.

F. CHRISTOPHE

En complément de cet impressionnant panorama des travaux russes sur les générateurs de puissance, avez-vous des informations sur les travaux dans le domaine des antennes ?

AUTHOR'S REPLY

Je sais que les russes ont travaillé sur des antennes à très large bande de fréquence (ultra-wideband) telles que les "cornets" et les log-periodic. Cependant, ces travaux ne semblent pas être destinés aux transmissions des ondes de hautes puissances.

Translation:

Q.

In addition to this impressive overview of Russian work on power generators, do you have any information on work in the field of antennas ?

A.

I know that the Russians have worked on ultra-wideband antennas, such as horn antennas and log-periodic antennas. However, this work does not seem to be aimed at high power wave transmission.

High Efficiency Backward-Wave Oscillators for High Power Microwave Generation: Present Status and Future Trends

E. Schamiloglu, J. Gahl, C. Fleddermann, D. Shiffler, L. Moreland,
C. Grabowski, T. Cavazos, B. Wroblewski, and W. Wilbanks

Department of Electrical and Computer Engineering
University of New Mexico
Albuquerque, NM, 87131, USA

Summary

The efficiency of high peak power microwave generation in vacuum X-band backward-wave oscillators is described. Nonuniform slow wave structures are driven by the Sinus-6, a short pulse, repetitive relativistic electron beam accelerator. Peak microwave power exceeding 500 MW at 9.45 GHz has been measured in an 8 ns pulse. The corresponding beam-to-microwave power conversion efficiency was 17%, although efficiencies approaching 25% have been achieved at lower power levels. The ability to acquire a large amount of data using the Sinus-6 accelerator facilitates comparisons with electromagnetic particle-in-cell simulations and analytical theories. In a companion set of experiments, a modified PI-110A single shot electron beam accelerator is used to study backward-wave oscillators with parameters comparable to the Sinus-6 experiments, except at pulse durations approaching 0.5 μ s. The goal of these studies is to extend the duration of microwave generation in high power backward-wave oscillators to several hundreds of nanoseconds. Technological innovations, such as ferroelectric cathodes and thin film metallic coatings, are expected to yield significant advances in long pulse operation.

1. Introduction

High power backward-wave oscillators (BWOs) have been studied experimentally and theoretically for about 25 years (Ref 1). The resurgence in interest in these classical microwave tubes coincided with the development of pulsed high current relativistic electron beam accelerators. Researchers in the United States primarily use single shot electron beam accelerators whose energy store is a Marx bank (Ref 1). The electron beams propagate through slow wave structures with uniform ripple amplitudes and periods, transported by a strong axial magnetic field. Researchers in the Former Soviet Union, on the other hand, developed several generations of repetitively-pulsed electron beam accelerators based on Tesla transformer technology with very high coupling efficiencies (Ref 1). In addition, they developed complicated slow wave structures which were motivated by theoretical analyses showing that nonuniform BWOs can be designed to yield higher beam-to-microwave power conversion efficiencies than uniform BWOs (see Refs 2 and 3, and references therein). In a nonuniform BWO, variations in the coupling impedance or

phase velocity affect the interaction between the electron beam and electromagnetic modes along the length of the tube. The coupling impedance between the slow space charge wave on the electron beam and the surface harmonic of the backward TM_{01} mode can be modified by varying the ripple amplitude, or by varying the magnetic field distribution within the tube. The phase velocity of this harmonic can be varied along the length of the tube by gradually changing the period of the ripples. The efficiencies for converting input beam power into RF radiation using uniform BWOs have been reported to be as large as 15% (Ref 2). Work in the former Soviet Union on nonuniform BWOs has shown experimental measurements of RF efficiencies exceeding 40%, and theoretical predictions indicate efficiencies may reach 75% in the absence of space charge effects (Refs 2 and 3).

The high power BWO program at the University of New Mexico seeks to define the physics of efficient microwave generation in uniform and nonuniform BWOs in both the short pulse and long pulse regimes. Basic understanding is gained from experiments using the Sinus-6, a repetitively-pulsed relativistic electron beam accelerator developed jointly by the High Current Electronics Institute (Tomsk, Russia) and the Institute of Electrophysics (Ekaterinburg, Russia). This basic understanding is then transferred to the PI-110A long pulse experiments. It is expected that technological innovation will lead to advances in long pulse BWO operation beyond the 100 ns barrier that researchers have typically faced (Ref 1).

2. Sinus 6 Experiments

The experiments using the Sinus-6 described below seek to quantify the use of a shallow ripple-amplitude initial section of a nonuniform BWO as a prebuncher to increase the microwave generation efficiency.

Figure 1 is a cut-away diagram of the Sinus-6. The Tesla transformer (1) steps up the voltage from 300 V to 700 kV. An open ferromagnetic core is used in the Tesla transformer, which provides a high coupling coefficient between the transformer windings. The pulse forming line is contained within the Tesla transformer, permitting both increased efficiency and an overall compact system. The high voltage switch (2) is a nitrogen-filled spark gap, which is pressurized to 16 atmospheres. By adjusting the pressure the spark gap voltage can be varied from 350 to 700 kV. The oil-filled

adiabatic transmission line (3) matches the $22\ \Omega$ impedance of the pulse forming line to the $\approx 100\ \Omega$ impedance of the vacuum diode. The magnetically insulated coaxial diode uses an explosive-emission graphite cathode (2 cm diameter with a 1 mm annular wall thickness). A uniform magnetic field up to 3.0 T in magnitude, used to confine the electron beam, is generated by a pulsed solenoid system (4). The pulsed system provides a magnetic field pulse duration of 3 ms and requires 10 s to recharge. The Sinus-6 can generate electron beams at a pulse repetition rate of 200 Hz, but is presently operating at 0.1 Hz due to constraints imposed by the magnetic field system.

The Anode-Cathode ($A - K$) gap spacing and applied magnetic field were held constant and the resultant diode impedance was about $125\ \Omega$, depending on the cathode potential. The electron beam pulse has a full width, half maximum (FWHM) temporal duration of about 12 ns. Cathode voltages are measured using a capacitive divider, and beam currents are measure using a Rogowski coil. By adjusting the pressure in the spark gap, cathode voltages from 400 to 650 kV are generated with corresponding beam currents ranging from 3 to 5 kA.

Total peak radiated power measurements were made using both a semiconductor microwave detector and a crystal diode detector (set-up shown schematically in Fig 2). Power density measurements were made 1.6 m downstream from a conical horn antenna which has a maximum diameter of 15 cm. The total power was calculated by numerically integrating the radiation pattern that was experimentally mapped. The radiated frequency was measured by heterodyning the RF signal against a known oscillator frequency.

The basic tube studied in this work is a nonuniform amplitude configuration referred to as the "Long Tube". This tube is a two stage slow wave structure constructed from individual rings for each ripple period, and was designed based on the work of Kovalev and colleagues (Ref 2). Each ring is a trapezoidally shaped annulus with a width of 1.5 cm (corresponding to a ripple period of 1.5 cm) and a maximum radius of 1.65 cm. Four different rings were used, and their parameters are listed in Table 1.

In addition to this basic tube, variations referred to as Short Tubes #1-#3 were also studied to elucidate the role of the initial stage of the Long Tube. As is evident from Table 2, the short tubes are variations of the second stage of the Long Tube. These short tubes have a start current in the range of the start current for the Long Tube.

A typical mode pattern radiated by the Long Tube and measured 1.6 m from the output antenna is shown in Fig 3. The beam parameters

used were 500 kV and 4 kA, and each data point was the average of 3 to 5 shots. The calculated TM_{01} radiation pattern (Ref 4) for a total peak power of 500 MW is indicated by the solid line in Fig 3. For comparison, the data points were integrated numerically to yield a total power of 450 MW, in good agreement with the calculated mode pattern. Since the radiation pattern was found to be insensitive to slight changes in frequency, it was sufficient to measure the power density at the maximum electric field in order to ascertain the total radiated power.

Figure 4 shows the dependence of peak radiated power using the Long Tube on electron beam current. Each data point represents the average of 5 shots and the error bar represents the typical scatter in the data. The beam current was changed by varying the pressure in the spark gap switch and the applied voltage to the cathode. The $A - K$ gap and applied magnetic field were held constant for all shots. The results from Long Tube over a range of parameters are summarized in Table 3. In this parameter scan the measured frequency remained constant at 9.45 ± 0.05 GHz.

At beam currents above 4 kA air breakdown near the output window was observed. Time-integrated photographs showed a bright annular ring of plasma consistent with a TM_{01} radiation mode pattern. In order to suppress the air breakdown, a gas bag filled with SF_6 was placed in front of the horn antenna. The amplitude and pulse duration from the crystal diode detector were observed to increase when the gas bag was used. Figure 4 shows the effect of using a gas bag on the microwave power measurements.

To elucidate the role of the prebuncher on the efficiency of the Long Tube, experiments were performed with various short tubes (parameters summarized in Tables 1 and 2). Sections of cutoff pipe were added to the modified tubes to ensure that the $A - K$ gap and the tapered magnetic field at the end of the tube remained constant. The beam parameters were approximately 4 kA and 500 kV, which were chosen to avoid air breakdown associated with the Long Tube. Data showing the peak output microwave power generated by the Long Tube and the three short tubes are given in Table 2. It is clear that none of the short tubes are as efficient as the Long Tube, and Short Tube #2 is the most efficient, with an efficiency of about 15%. Consistent with the lower relative powers indicated, air breakdown was never observed with the short tubes, even when they were driven at the highest input beam powers. Because the growth rate of the RF fields must decrease with the difference between the beam current and the start current, it can be inferred from the RF pulse widths in Table 2, that the start currents for the Long Tube is between the start currents for Short Tubes #2

and #3. Therefore, the increased efficiency of the Long Tube is a result of the prebuncher and cannot be attributed to the ratio of beam current to start current.

TWOQUICK (Ref 5) particle-in-cell (PIC) simulations provided a comprehensive picture of the prebunching of the electron beam in the initial section of the nonuniform amplitude slow wave structure. The results from the PIC simulations indicate that, in addition to the surface harmonic of the backward wave, the forward traveling volume harmonics may play an important role in the energy exchange process in the BWO. Based on these results it may be possible to design an uniform BWO where the forward traveling volume harmonics can serve the role of a prebuncher (Ref 6).

3. PI-110A Experiments

The accelerator used in the UNM Long Pulse BWO Experiment is a modified Physics International Pulserad 110A. An 11-stage Marx bank with an energy storage capacity of 2.75 kJ is used as the main energy store and initial pulse forming device in the accelerator. The Blumlein which previously followed the Marx bank has been replaced with an LC filter network. When erected, the Marx bank and the LC network together form a 2-stage pulse forming network (PFN). An equivalent circuit for this is shown in Fig 5. The pulse duration and impedance of the accelerator in this configuration are approximately 500 ns and 40 Ω , respectively. A balanced resistive voltage divider (not shown in the figure) has been placed between the Marx bank and the LC network to monitor the Marx voltage. The electron gun immediately follows the LC filter network, and its configuration is nearly identical to the one on the Sinus-6. The cathode holder is stainless steel and is curved to follow the magnetic field lines. At the end of the holder is a 2 cm-diameter carbon knife-edge tip from which an annular electron beam is emitted. Either 6 or 7 field coils can be placed around the slow wave structure to produce a guiding field for the electron beam. The field strength on axis is typically 3.0 T. After traveling through the slow wave structure, the electron beam follows the magnetic field lines to the beam dump, which consists of a section of stainless steel screen surrounded by a larger, concentric section of copper pipe that is lined with carbon on its inner surface. The microwaves that are produced in the slow wave structure travel past the screen into another section of circular waveguide, and then to a conical horn where they are radiated into an *anechoic* measurement area.

Two Rogowski coils are used to monitor the beam current, one around the cathode holder and the other to be located just upstream of the beam dump. In addition, a capacitive voltage divider has recently been installed just behind the first Rogowski coil to enable

measurement of the cathode voltage during experiments. To measure the microwave radiation, two different kinds of detectors have been used. One is a simple \dot{B} probe which directly measures the magnetic field intensity of the microwave radiation. The other detector is similar to the one presently being used on the Sinus-6 experiments. It consists of a small piece of a semiconductor material placed inside a short section of waveguide. Before the accelerator is fired, a negative voltage pulse having an amplitude of approximately 50 V and a duration of 100-120 μ s is sent to the detector. When microwaves enter the waveguide and impinge upon the semiconductor, the impedance of the semiconductor changes, causing a ripple in the amplitude of the reflected voltage pulse. From the amplitude of the ripple the power density of the incident microwave radiation can be determined.

Long pulse vacuum BWO experiments have begun using uniform slow wave structures. Initial results from these experiments yielded microwave pulses with FWHM durations exceeding 100 ns. Typical signals from the first Rogowski coil and the microwave detector (\dot{B} probe) are shown in Fig 6. The radiated power was estimated to be about 10 MW. By positioning the \dot{B} probe at various angles with respect to the center axis of the horn, a crude map of the radiation was obtained and indicated that the radiation is emitted in the TM_{01} mode. Frequency measurements have not been performed at this time. However, several PIC code simulations of the slow wave structure were performed and the results indicated a frequency of approximately 10 GHz. It should be noted that there was evidence of breakdown inside the slow wave structures on these shots.

4. Technological Innovations

The extension of microwave radiation in long pulse, high power BWOs beyond the typical 100 ns timescale is dependent on technological innovations. Two innovations that are being studied as part of the program at the University of New Mexico are ferroelectric cathodes and thin film metallic and ceramic coatings. Ferroelectric cathodes are potentially a new source of electrons for high power, electron beam-driven microwave devices. These cathodes have the potential to extend the pulse duration of high power BWOs beyond the 100 ns regime. Typically high power BWO experiments utilize explosive emission cathodes. These cathodes form plasmas which can expand into the anode-cathode gap and hence cause a change in the diode impedance. Furthermore, plasmas and neutrals inherent to the explosive emission process can adversely affect the BWO interaction over time scales longer than 10's of nanoseconds. Ferroelectric ceramics have the potential for providing sufficient

current to operate a BWO without the above problems (Ref 7).

Ferroelectrics are materials possessing a spontaneous electric dipole moment when the temperature is below the Curie temperature and above the Curie-Weiss temperature. Since these materials have a spontaneous dipole moment, ferroelectrics may be characterized by a bulk surface charge density which depends upon the magnitude and direction of the polarization of the sample. These materials are promising as advanced cathode materials because it is possible to liberate electron charge from the sample. The emission mechanism consists of the following sequence of events. The material is placed in a state very close to a phase transition. A large electric field is then applied across the cathode. If the electric field is of the proper polarity, a phase transition occurs, causing the cathode to become paraelectric and forcing the spontaneous electric dipole moment to zero. When the phase transition occurs, a large amount of surface charge remains momentarily unscreened on the surface of the cathode. This charge may be liberated as electrons. For example, the ferroelectric lead lanthanum zirconate titanate (PLZT) has a surface charge of 55 mC/cm^2 , corresponding to about 10^{14} electrons/ cm^2 . Furthermore, since the amount of unscreened charge is initially quite large, the emission energy of electrons from the surface can lie in the kilovolt range.

The ferroelectric experiment at the University of New Mexico consists of a ferroelectric sample placed in the triode configuration shown in Fig 7. A circular grid 0.27 cm in diameter with 20% transmission forms the emitting surface on the top of the PLZT wafer. The thickness of the wafer is 0.33 mm and the grid and plate are separated by 2.7 cm. The cathode contact on the back of the wafer is grounded. The drive circuitry is also shown in Fig 7. A bias voltage, used to produce a preset dipole moment in the sample, is applied to the grid, and the pulsed coercive field is applied through a coupling capacitor. A DC voltage of up to 20 kV is applied between the plate and the cathode contact. Current viewing resistors (CVRs) provide measurements of the grid current and plate current, while a current toroid and Rogowski coil have been used to measure current in the grid-cathode gap. Voltage measurements are obtained using resistive dividers.

Preliminary results from these experiments indicate that the initial state of the ferroelectric clearly affects the electron emission process. Emission occurs only when the ferroelectric becomes saturated. Electron charge on the order of 10^5 of milliCoulombs have been measured at electric fields on the order of 10 kV/cm. Ferroelectric cathodes compatible with high current accelerators are expected to be developed during the course of this investigation.

Finally, in an attempt to increase the threshold electric field for vacuum breakdown in slow wave structures, a quasi-DC experiment was performed to study the effectiveness of ion sputter-deposited thin film metallic and ceramic coatings on planar electrodes. Electric fields as high as 60 kV/mm were sustained across a 1 mm gap for pulse durations approaching 10 μs . It is believed that electron emission was suppressed by the 500 nm thick coatings because whiskers were covered and localized field enhancements were minimized (Ref 8).

Future trends in efficient high power microwave generation using vacuum BWOs will incorporate new physics, such as carefully taking advantage of the backward and forward propagating volume harmonics of the TM_{01} mode, as well as technological innovation in the form of ferroelectric cathodes and novel thin film coatings.

5. References

1. Benford, J. and Swegle, J., "High-Power Microwaves", Boston, MA, Artech House, 1992, Chap 6, and references therein.
2. Kovalev, N.F. and Petrukhina, V.I., "Ultra-relativistic Carcinotron with a Jump in Beam-rf Coupling", *Electr. Techn. SVCH*, vol. 7, 1977, pp 101-105, (in Russian), and references therein.
3. Korovin, S.D., Polevin, S.D., Roitman, A.M., and Rostov, V.V. "Relativistic backward wave tube with variable phase velocity", *Sov. Tech. Phys. Lett.*, vol. 18, 1992, pp 265-266.
4. Koslover, R.A., Computer code "TM0n", SEAC, Albuquerque NM, 1988.
5. Seidel, D.B. and Pointon, T.D., Sandia National Laboratories, private communication.
6. Moreland, L.D., Schamiloglu, E., Lemke, R.W., Korovin, S.D., Rostov, V.V., Roitman, A.M., Hendricks, K.J., and Spencer, T.A., "Efficiency of High Power Vacuum BWOs using Nonuniform Slow Wave Structures", to appear in *IEEE Trans. Plasma Sci.*, Special Issue on High Power Microwaves, 1994.
7. Riege, H., "Electron Emission from Ferroelectrics—A Review", *Nucl. Instrum. Methods*, vol. A340, 1994, pp 80-89.
8. Mayberry, C.S., Wroblewski, B., Schamiloglu, E., and Fleddermann, C.B., "Suppression of Vacuum Breakdown using Thin Film Coatings", to appear in *J. Appl. Phys.*, 1994.

Illustrations

Table 1. Parameters of slow wave structure rings.

Ring Type	Maximum Radius [cm]	Minimum Radius [cm]	Average Radius [cm]	Ripple Amplitude [cm]	Ripple Period [cm]
A	1.65	1.45	1.550	0.100	1.50
B	1.65	1.38	1.515	0.135	1.50
C	1.65	1.20	1.425	0.225	1.50
D	1.65	1.15	1.400	0.250	1.50

Table 2. Summary of tube configurations.

	Tube Configuration	Relative Power	Crystal Diode Detector Pulse Width [ns]	Frequency ± 0.05 [GHz]
Long Tube	A-A-B-B-B-C-C-C-D-D-C	1.0	8.7	9.45
Short Tube #1	C-C-C-D-D-C	0.2	7.2	9.60
Short Tube #2	C-C-C-C-D-D-C	0.7	7.7	9.50
Short Tube #3	C-C-C-C-C-D-D-C	0.5	10.0	9.60

Table 3. Summary of Long Tube results.

Cathode Voltage [kV]	Beam Current [kA]	Input Power [GW]	Total Peak Power [MW]	RF Conversion Efficiency	Diode Impedance [ohms]
475	3.49	1.66	371	0.22	136
508	3.83	1.95	420	0.22	133
533	4.06	2.16	453	0.21	131
566	4.39	2.48	487	0.20	129
576	4.52	2.60	494	0.19	128
601	4.86	2.92	519	0.18	124
627	5.19	3.26	545	0.17	121

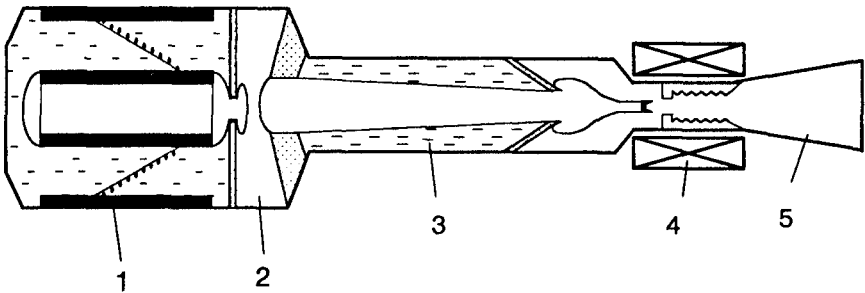


Fig 1. Cut-away diagram of Sinus-6. (The various components are described in the text.)

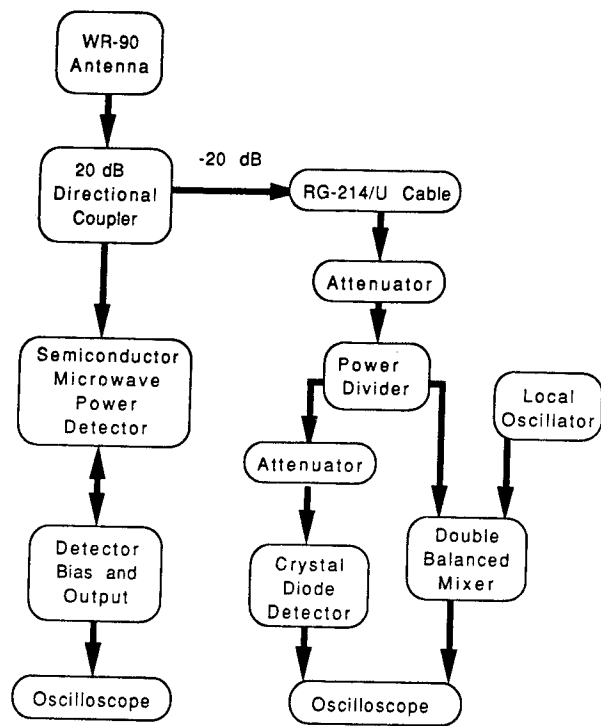


Fig 2. Block diagram of power measurement scheme.

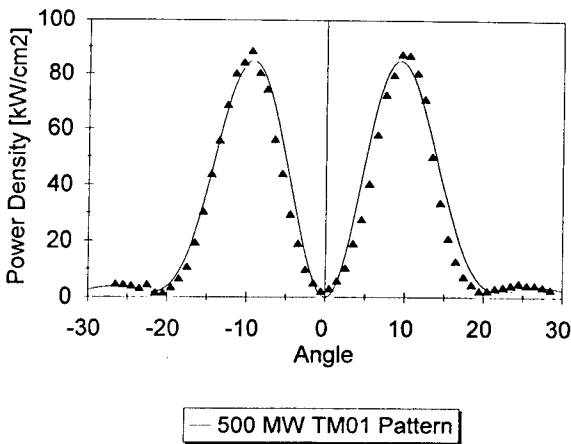


Fig 3. Radiation pattern from Long Tube.

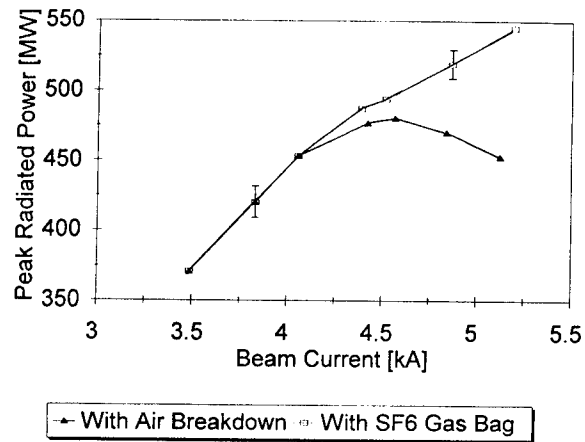


Fig 4. Dependence of power radiated from Long Tube on beam current.

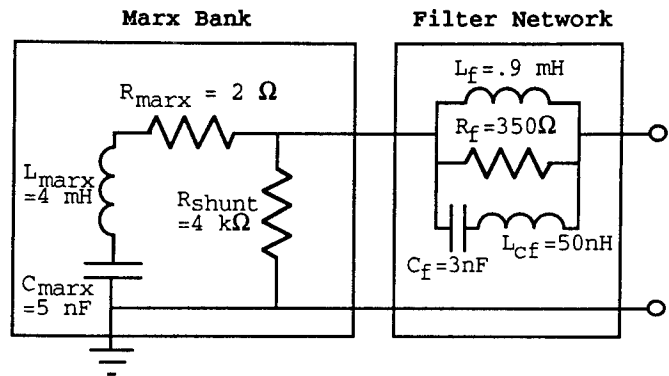


Fig 5. Equivalent circuit of modified PI-110A.

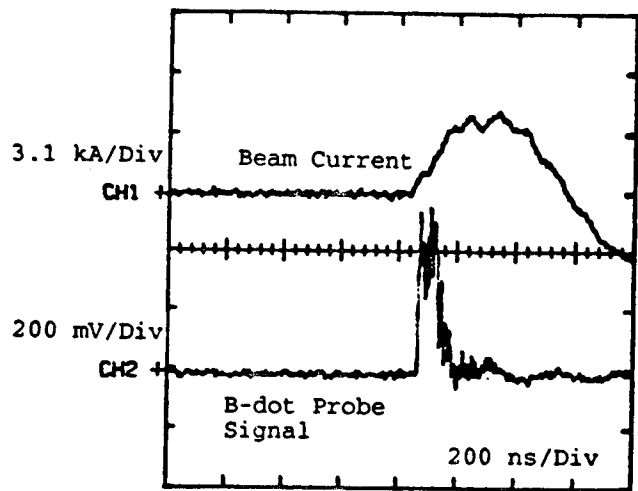


Fig 6. Typical output radiation from long pulse experiment measured using \dot{B} probe.

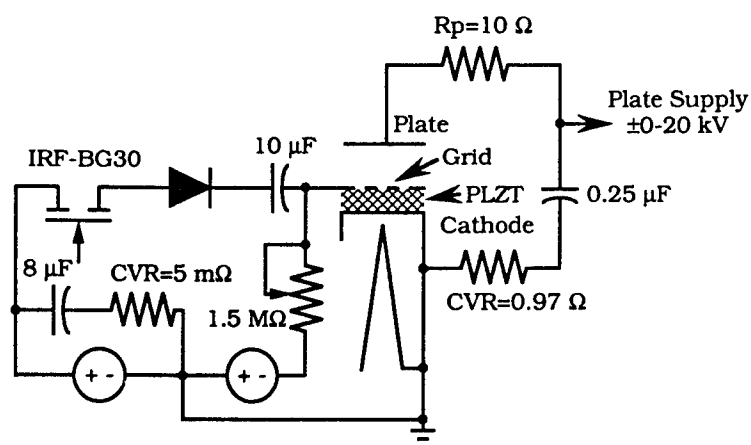


Fig 7. Configuration for ferroelectric cathode experiment.

Acknowledgements

This work is supported by U.S. Air Force Office of Scientific Research Grant F49620-94-1-0087DEF and Air Force Office of Scientific Research Instrumentation Grant F49620-93-1-0585. Acquisition of the Sinus-6 was funded by the Air Force Phillips Laboratory, Advanced Weapons and Survivability Directorate, Air Force Materiel Command, Kirtland AFB, New Mexico. Particle-in-cell simulation support was provided by Dr. R. W. Lemke (Sandia National Laboratories, Albuquerque, New Mexico).

Applications of Relativistic Klystron Amplifier Technology

M. Friedman, V. Serlin, M. Lampe, R. Hubbard

Plasma Physics Division, Naval Research Laboratory, code 6732
Washington D.C. 20375

1. SUMMARY

Over the past decade, development of the relativistic klystron amplifier (RKA) at NRL boosted high power microwave (HPM) technology by an order of magnitude. RKA has set world records in peak RF power generation. Using RKAs, microwave power in excess of 10 GW has been generated, at a frequency of 1.3 GHz and with energy of 1 kJ per pulse.

Even though the NRL RKA constitutes a major advance over previous HPM technology, practical applications continue to be limited by size, cost and immobility of the equipment; relatively low efficiency (35%); breakdown at high power level, particularly in the output gaps; and unfavorable power scaling at frequencies above 1 GHz. However, we developed plans for a new generation of RKAs that will leapfrog all of these limitations, providing a technology with the following characteristics: (1) Compact, cheap, and efficient. (2) Avoiding gap breakdown. (3) Equally efficient from .5 to 10 GHz (>75%).

This development can be achieved by using two major innovations:

- (1) An annular "triaxial" RKA structure to modulate the electron beam. This innovation provides the desired power, frequency and compactness.
- (2) An inductively loaded wide gap to efficiently modulate the electron beam and to extract microwave with high efficiency (>75%), while avoiding breakdown and DC space charge limits.

A triaxial RKA could also be designed with an impedance of 1 ohm or less, which could be ideal for matching to an explosive generator. Such a device would be sufficiently compact for use in a missile or an airborne bomb. The microwave output would be overwhelming (possibly > 1MJ). A single shot could irradiate an area hundreds of meters across, with microwave energy more than sufficient to wipe out electronics. This would permit blackout of ships, bases or missiles.

2. BACKGROUND

The physics of intense relativistic electron beams (IREBs) is governed by the beam electric and magnetic self fields. There are many applications of IREBs that exploit these self fields; for example high power microwave (HPM) generation⁽¹⁻⁴⁾. The U.S. Department

of Defense has an interest in this area of research and supported our effort for the last fifteen years. A new family of high power microwave generators, named Relativistic Klystron Amplifier⁽⁴⁾ / Oscillator⁽¹⁾ (RKA/RKO), emerged from this research utilizing the self fields to modulate IREBs and to generate pulsed RF with peak power in the multi-gigawatt range. Moreover, we found (experimentally and theoretically) that these devices can operate in different modes:

- (1) An amplifier⁽³⁾ with a gain of 50 dB and with phase stability of better than 2° .
- (2) An oscillator⁽⁵⁾ with a frequency agility of 10% between pulses and with fast tuning capabilities.
- (3) Low or high beam impedance (1 ohm - 200 ohm).
- (4) Short or long pulse duration (nanoseconds to microseconds).

All of this can be achieved at frequencies equal or lower than 10 GHz and with an efficiency > 40% (the efficiency may reach 70% which is, theoretically, the highest efficiency of classical klystrons).

In this paper we describe RKA/RKO devices with the characteristics outlined above. In chapter 1 we describe DC processes that govern IREBs in drift tubes and influence operations of RF tubes. In chapter 2 we discuss the RF characteristics of the two gaps used to modulate an IREB and extract RF power. Chapter 3 describes the physics of RKA/RKO devices and how they differ from classical klystrons. Chapter 4 describes an RKA of a triaxial geometry. Chapter 5 describes a future frequency-agile RKO with a frequency bandwidth > 10%. Chapter 6 presents some applications of the RKA technology.

3. DC PHENOMENOLOGY

In this chapter we describe the DC physics of propagation of Intense Relativistic Electron beams (fig. 1). A practical way to transport an un-neutralized IREB is to immerse it in a strong external axial magnetic field. We assume here that:

- (a) The focusing axial magnetic field is infinitely large.
- (b) The IREB is in equilibrium and its parameters are time independent
- (c) The electron flow is laminar and does not support virtual cathode and counter streaming electrons.
- (d) The drift region through which the IREB propagates is made out of infinitely conducting materials but it is axisymmetric in geometry.
- (e) The self magnetic field is of little importance and does not affect IREB propagation.

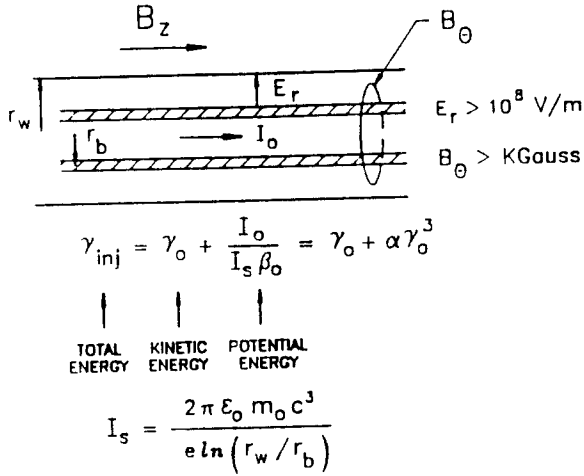


Figure 1 Geometry and fields of a propagating IREB

Under this assumptions one can calculate the potential energy $e\Phi$ associated with IREB propagation and the kinetic energy of an electron E_k in the IREB.

$$eV_0 = (\gamma - 1)m_0 c^2 = e\Phi(r_b) + E_k = e\Phi(r_b) + (\gamma_0 - 1)m_0 c^2 \quad (1)$$

where, eV_0 is the injected energy of the electrons: $(\gamma - 1)m_0 c^2$.

The potential energy is found by solving simultaneously Poisson's and the continuity equations. For example, the height of a potential hill created by a stream of a thin annular electron beam with a current I_0 propagating at a radius r_b inside a smooth metallic drift tube of radius r_w is

$$\Phi(r_b) = -\frac{(I_0 / v_0)}{2\pi\epsilon_0} \ln(r_w / r_b) \quad (2)$$

where, v_0 is the streaming velocity. Equations 1 and 2 can be solved numerically for v_0 .

Some conclusions can be drawn from this analysis.

(a) The potential energy increases (and v_0 decreases) when I_0 and/or (r_w / r_b) increases.

(b) When an axisymmetric gap in the drift tube is introduced, a potential hill is created in the gap preventing slow electrons from crossing the gap (electrostatic insulation⁽⁶⁾ of high voltage gap), but, at the same time, reducing the electron kinetic energy. These effects have been observed experimentally and play important parts in the operation of RKA/RKO devices.

(c) The potential energy residing in the IREB is large and can reach a value $e\Phi(r_0) = (\gamma - \gamma^{1/3})m_0 c^2$, which is

larger than the kinetic energy $E_k = (\gamma - 1)m_0 c^2 = (\gamma^{1/3} - 1)m_0 c^2$. We showed⁽³⁾ that the large potential energy helped in the modulation process of IREB but that RF energy could not be extracted from this potential energy. Since gaps are used in RKA/RKO to modulate an IREB and to extract RF energy from the modulated IREB, it is very important to design them so as to take into account the above two effects.

Two geometries for gaps have been used in RKA/RKO devices:

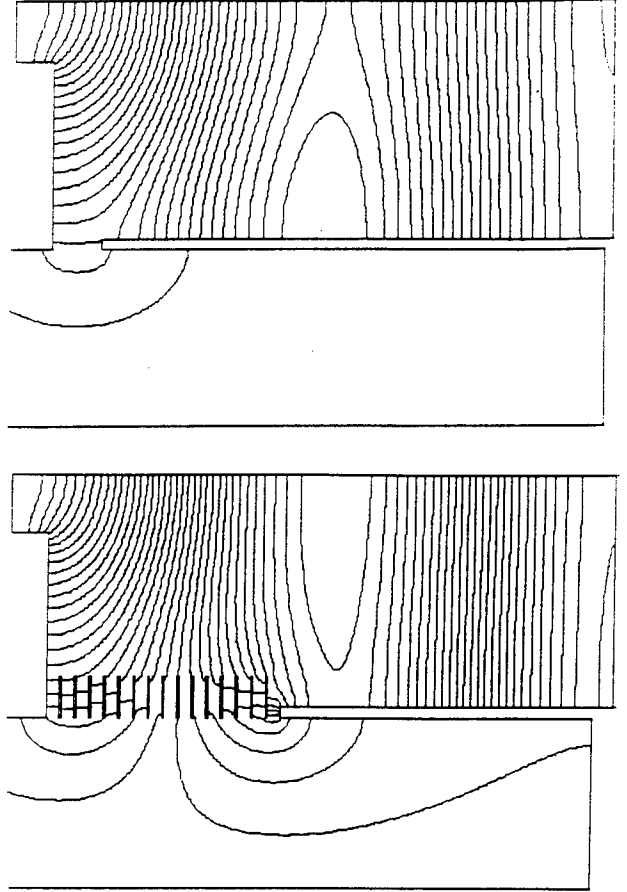


Figure 2 Narrow and extended gap geometries

(a) A narrow gap (fig. 2 top) with a length smaller than a quarter of a wavelength. Its precise length is a compromise between a long gap needed for electrostatic insulation and a short gap needed for reducing the potential energy. This length was found by trial and error and it is typically (for the high power L-band RKA discussed below) 2 cm. In an extraction gap of such a length an electron beam of a current of 30 kA and an energy of 1 MeV will have 30% of the total energy in potential energy. This energy can not be converted to RF energy and is lost as heat and X-rays.

(b) An extended-interaction gap with a length equal or larger than half a wavelength. To reduce the potential energy in an electron beam propagating through a long

gap we stacked the gap with thin grounded metallic washers (Fig.2 bottom). The presence of the washers was to increase the so called limiting current or, alternatively, decrease the potential energy residing in the beam. The reduction in the potential energy is accompanied by an increase in the kinetic energy. Since the washers are connected inductively to ground, the gap RF field is not affected.

4. CHARACTERISTICS OF RF GAPS.

In order to generate a high RF power RKA/RKO devices have to handle large DC currents. This is being achieved by using an annular IREB that propagate close to the drift tube walls. In this geometry the potential energy (and the kinetic energy) changes considerably with small changes in any one of the experimental parameters i.e.

$$\frac{\Phi}{\partial \Phi / \partial (\text{PARAMETER})} = \bigcirc (\text{PARAMETER})^{(3)}$$

The larger the potential energy is, the more sensitive it becomes to changes in the experimental parameters. This property is *unique* to RKA/RKO, however, it does not require IREBs, as it can be also achieved with a mildly relativistic intense electron beam.

When an RF voltage superimposed on the gap, electrons will gain and lose velocity, not only from the RF field but also from changes in the potential energy. The potential energy during the acceleration phase will decrease with further electron acceleration. The potential energy will increase during the deceleration phase with a further slowing down of electrons. At the limit of a sufficiently high RF voltage at the gap, the increase in potential energy during the deceleration phase will be so large as to cut momentarily beam propagation (the gate effect⁽³⁾).

In most klystron-like devices the RF voltage applied on a gap is unidirectional, and the gap length has to be less than a quarter of a wavelength to be effective in beam modulation. This sets limitations on the voltage and frequency that can be applied on the gap. We are investigating different cavities in which the gap length is more than half a wavelength (Fig. 2 bottom). Here, the gap electric field is bi-directional. Due to finite transit time electrons will "see" mostly a unidirectional electric field.

As stated earlier, the long gap is stacked with thin metallic washers. The purpose of the washers is to neutralize the DC space charge of the beam, while sustaining the longitudinal RF field which couples the beam to the cavity, or extracts RF energy from the beam. With appropriate choice of RF mode, it appears that a gap width exceeding half a wavelength can be used for high frequency modulation of IREBs, as well as for extraction of RF energy from the modulated

beam with high efficiency.

The gaps and cavities have been chosen so as to accommodate a large diameter annular electron beam. In the past we have used coaxial cavities. In this geometry the wavelength was proportional to the beam diameter, which in turn was proportional to the current. Hence, the RF power was proportional to the wavelength (or even to the wavelength to the power of $n>1$). Lately we have found that this power law does not exist in triaxial cavities. In the future, triaxial cavities will be used for RKA/RKO. These triaxial cavities can support many RF modes, most of them being dangerous to the RKA operation. The TE modes will not be excited if high tolerance in the symmetry of the experimental parameters, such as geometry, electron beam, and magnetic field can be maintained. Two additional modes can be excited in the system (figure 3). These modes combine the separate

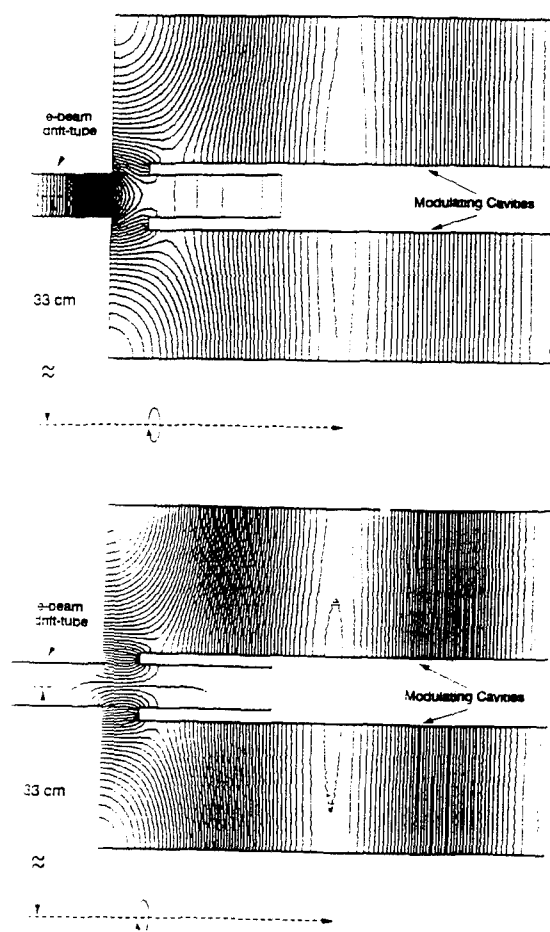


Figure 3 SUPERFISH simulations showing different modes in the triaxial RKA. The radial electric field vectors in the coaxial cavities are parallel (top) and anti-parallel (bottom).

TEM coaxial modes in each of the radially opposing

cavities. The two modes differ by the relative directions of the radial electric field vectors in two radially opposing cavities; parallel or anti-parallel. The RF power of one mode, for which the radial electric field vectors are parallel, will leak out from the gaps to the drift tube as a propagating TEM mode. This mode is not useful to modulate an electron beam and can be harmful to the RKA operation. The other mode combines the two coaxial electric field configurations to generate a TM mode in the drift tube. This TM mode is below cutoff and can be used to modulate the beam. At first glance the two modes seem to have the same resonance frequency and can exist simultaneously in the triaxial RKA. However, using the SUPERFISH computer code we found that this degeneracy was removed due to a different gap capacitance associated with each mode. The resonance frequencies of these modes differ by 20 MHz, and since the RKA is an amplifier, the external RF source can be tuned to generate the required electric field configuration.

5. THE PHYSICS OF RKA/RKO (LINEAR PICTURE)

The bunching mechanism of an electron beam of any energy and current occurs after a velocity modulation was imposed on the electron beam, and after propagation through a drift region. The modulation of the electron beam can be described as an interference of two space charge waves that are excited by the RF voltage. At low current, the dispersion relation curves of these waves are symmetric with respect to the beam line $\omega/kv_0=1$, $k=2\pi/\lambda$. At high current level, where the electric self field of the beam is large, the dispersion relation curves are not symmetric with respect to the beam line. This asymmetry makes the bunching mechanism for RKAs unique and novel. The RF current and voltage at a distance z from the excitation point are:

$$I_1 = j(V_{10}/Z)\sin(\alpha\mu\theta) \quad (4)$$

$$V_1 = V_{10}(\cos(\alpha\mu\theta) + j\xi\sin(\alpha\mu\theta))$$

Where V_{10} is the applied RF voltage, $\theta = \omega\delta z/\beta_0 c$, and α , μ , δ , and $\xi (<0)$ depend on the experimental parameters. Using the relativistic Tonk's theorem⁽⁷⁾ together with equation 4 one gets

$$\text{Real}(\oint \mathbf{E}_1 \times \mathbf{H}_1 d\mathbf{S} + \xi(V_{10}/Z)\sin^2(\alpha\mu\theta)) = 0 \quad (5)$$

where, E_1 and H_1 are the RF electric and magnetic field components and S is the drift tube cross section. The above relationship means that during IREB propagation dc energy is converted to ac kinetic energy, which in turn is converted to electromagnetic energy, so as to maintain power conservation.

In contrast, for a low density classical electron beam

eq.5 will become

$$\oint \mathbf{E}_1 \times \mathbf{H}_1 d\mathbf{S} = 0 \quad (6)$$

Theory and particle simulations were performed, showing that even at the non-linear region, the IREB modulation is strongly affected by the self electric field in a way to increase the amplitude of the electron bunches. Experiments showed full electron beam modulation at frequencies of 1.3 and 3.5 GHz.

It is well known that RF power can be extracted from modulated electron beams. We will now describe the operation of high power RKAs.

5.1. The NRL RKA operation at a frequency of 1.3 GHz.

The present high power RKA at NRL consists of four parts (Fig. 4):

1. A source that generates an IREB. The electron beam is annular in shape, 13.2 cm in diameter, and 0.4 cm thickness. An external axial magnetic field, $B_z = 10$ kgauss, focuses and guides the electron beam in drift regions that are evacuated to a base pressure of 10^{-5} Torr.
2. The second part of the device is a multi-mode coaxial cavity that is loaded with RF energy from a 500 kW RF source for a duration of 1.5 microseconds. The stored energy generates an oscillating gap voltage with an amplitude of 30 kV and with a 1.3 GHz frequency. Current modulation appears after the electron beam propagates through the cavity. At any point z downstream the amplitude of the modulation is

$$I_1 = [1.5 \cdot \sin(0.04 \cdot z)]_{\text{kA}}$$

3. The third part of the RKA is a coaxial cavity that is placed downstream. The gap of the cavity is positioned at a place for which I_1 is maximum ($=1.5$ kA). The cavity has a characteristic impedance of 10 ohms and its length could be varied under "hot" operation (i.e. a mechanically tuned cavity). The mutual interaction between the cavity and the partially modulated electron beam results in boosting the RF current amplitude in the beam to at least 17 kA.

4. The last part of the device is an RF converter, transforming the electron kinetic energy into an RF pulse. Reproducible RF pulses with peak power of 6 GW and 140 nsec duration, have been generated. Higher RF pulses, of peak power > 15 GW were also obtained⁴. However, the operation at the high power level was erratic in nature⁵. We showed⁷ that these power levels are upper limits for an RKA with the geometry shown in figure 1.

5.2. High frequency RKA⁸.

At NRL, we have attempted to scale the RKA operation to frequencies of 3.5 GHz and 9.4 GHz. We found that the output power scales as the (wavelength)⁻ⁿ where $n > 1$. At 3.5 GHz we demonstrated full modulation of the

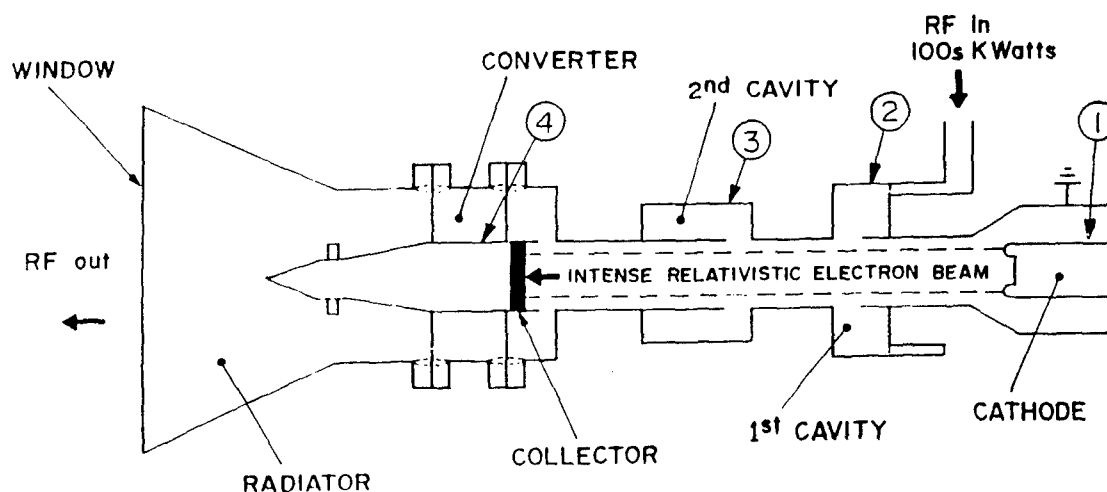


Figure 4 Schematics of the High Power Relativistic Klystron Amplifier.

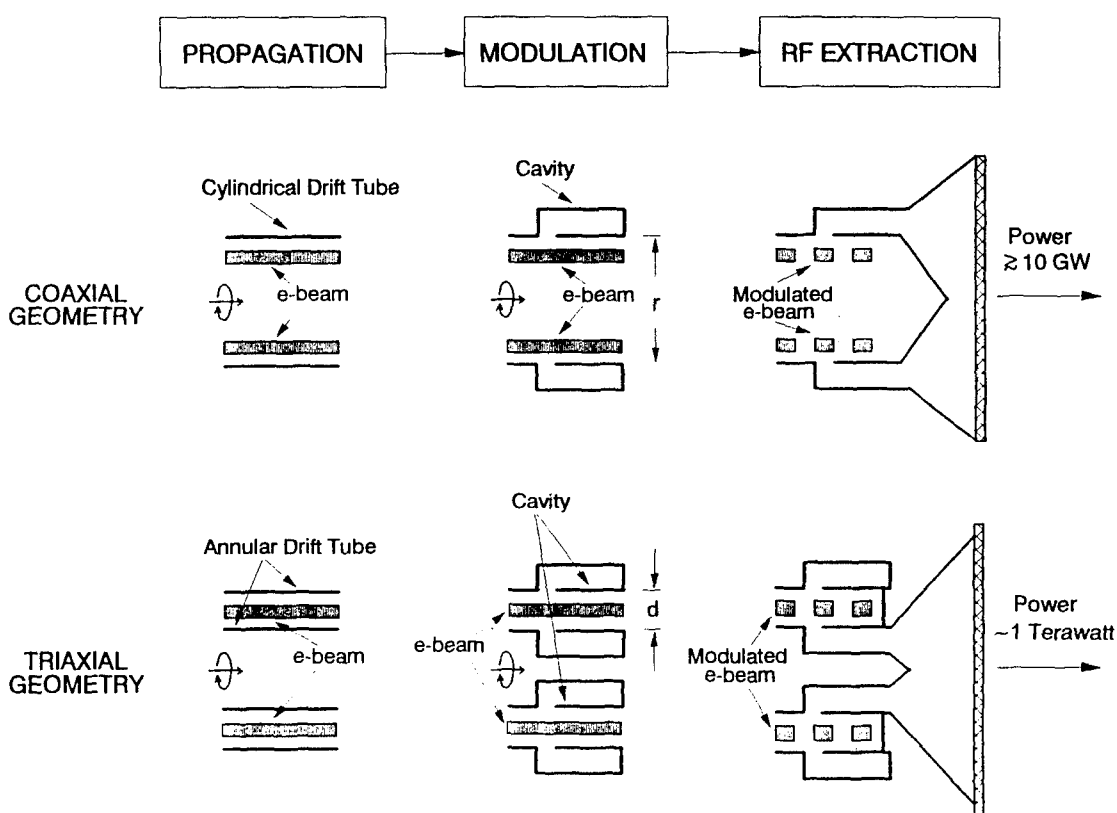


Figure 5 Comparison of coaxial RKA (old) vs. triaxial RKA (new) in propagation, modulation and RF extraction (from left to right).

intense electron beam with excellent phase stability, but the extracted RF power level was around 10% of the DC beam power. When an additional passive cavity was inserted in the RF structure, in front of the converter, and was tuned to the 3.5 GHz, the efficiency

increased to >60%, but only for a duration of 50 nsec.

The 9.4 GHz RKA did show beam modulation, but operated erratically even at low power (< 500 MW). These experiments clearly show the limitations of the

present coaxial RKA geometry:

5.3. Limitations of coaxial RKAs.

During the last three years we have investigated the erratic behavior of RKAs at high power and/or high frequency. We found many effects that contribute to this behavior. For example:

- (1) Beam loading of high voltage gaps influences the effective gap length, the resonance frequency, and the "Q" of the cavities.
- (2) Alterations of the electrical and magnetic properties of stainless steel under intense x-ray bombardment, strong quasi-DC magnetic field, and high power RF electromagnetic energy. The stainless steel was used as a construction material of the RKA.
- (3) Emission of electrons from surfaces subjected to high RF electric field.

These and other problems led us to the conclusion that we have reached the power and frequency limits of the present coaxial RKA. Any further improvement of operation should involve radical modifications of the RKA.

6. NEW DEVELOPMENT - THE TRIAXIAL RKA⁹

We are now conducting research in the RKA technology with a goal of achieving operation at high power and with high efficiency. A geometry for RKA which can handle higher DC power and generate higher RF power is a triax. In this geometry the annular electron beam is surrounded on the outside and inside by metallic structures. Figure 5 compares the "new" and "old" structures. One can see two major differences between the two structures: 1. The presence of a grounded conductor inside the electron beam can increase the propagating beam current by a factor of two (since the so called limiting current is twice as high). 2. The new RKA can be of a large radius, since the cutoff wavelength does not depend on it. The shortest wavelength that can be generated is equal to twice the separation between the inner and outer structures (which can be very small - of the order of 1 cm.). A large diameter RKA can handle a large diameter electron beam of high current and a high power. Theoretically, there is no limitation on the current and power handling capabilities of the new RKA, and the output power is independent of the frequency (as long as the wavelength is larger than twice the separation between the two structures).

The critical parts of the new RKA are: (1) A high voltage pulse generator. (2) A diode. (3) Magnetic field coils (to confine the electron beam), and (4) The RF structure. Figure 6 shows schematically the new Triaxial RKA operating in a single pulse mode. It consists of a Marx generator (marked 1 in fig. 6) charging a Blumlein transmission line of 7 ohm

impedance and electrical length of 140 nsec. (marked 2).

The electron beam emerging from the diode will be of 500 kV voltage and of 70 kA current (total power 35 GW). It will be confined and guided by magnetic field coils (marked 5 in fig. 6).

The RF structure surrounding the electron beam consists of an annular drift tube, in which four gaps feeding coaxial cavities (with the same resonance frequency) are inserted (marked 6-9 in fig. 6). One of this cavities (marked 6) is energized by an external RF source. (The triaxial RKA is in the construction stage. Parts 1 to 4 were built and are being tested. One magnetic field coil was purchased. We hope to finish the construction in a few months).

Using a large diameter intense relativistic electron beam can give us a better control of the length of the RKA, especially at high frequencies. From the RKA equations one can find that a large diameter annular intense relativistic electron beam is necessary for a non-vanishing length of a high frequency RKA. The length of an RKA is of the order of

$$L = [(\beta_0 c) / (4f\delta)] / \alpha\mu \quad (7)$$

where $\beta_0 c$ is the beam velocity, δ and $\alpha\mu$ depend on the DC beam parameters and on the geometry. Typically $1 < \delta < 2$ and $\alpha\mu$ is proportional to Δ/R , where Δ is the width of the annular channel inside which the beam propagates and R is the beam radius. Hence, the requirement will be for small Δ and large R so as to have L of the order of 10 cm or larger. For such parameters the beam RF impedance will be around 1 ohm. This low impedance will necessitate new kinds of cavities and HV gaps.

The interaction between the IREB and the cavities of the triaxial RKA at a frequency of 1.3 GHz was modeled using a simulation code and was discussed in an earlier paper. Similar calculations¹⁰ were performed at 11 GHz to confirm the high frequency capabilities of the triaxial RKA. The geometry shown in fig. 7 consists of an annular channel in which two coaxial cavities were inserted. These cavities were tuned to a frequency of 11 GHz. A 30 kA IREB of 10 cm radius propagated inside the channel. RF power was pumped into the cavity at 11 GHz and an oscillating voltage of 50kV amplitude was established across the gap. At 20 cm downstream the current profile was

$$I = (30 + 10 \cos(\omega t)) \text{ [kA]} \quad (8)$$

The calculations are in excellent agreement with the RKA theory.

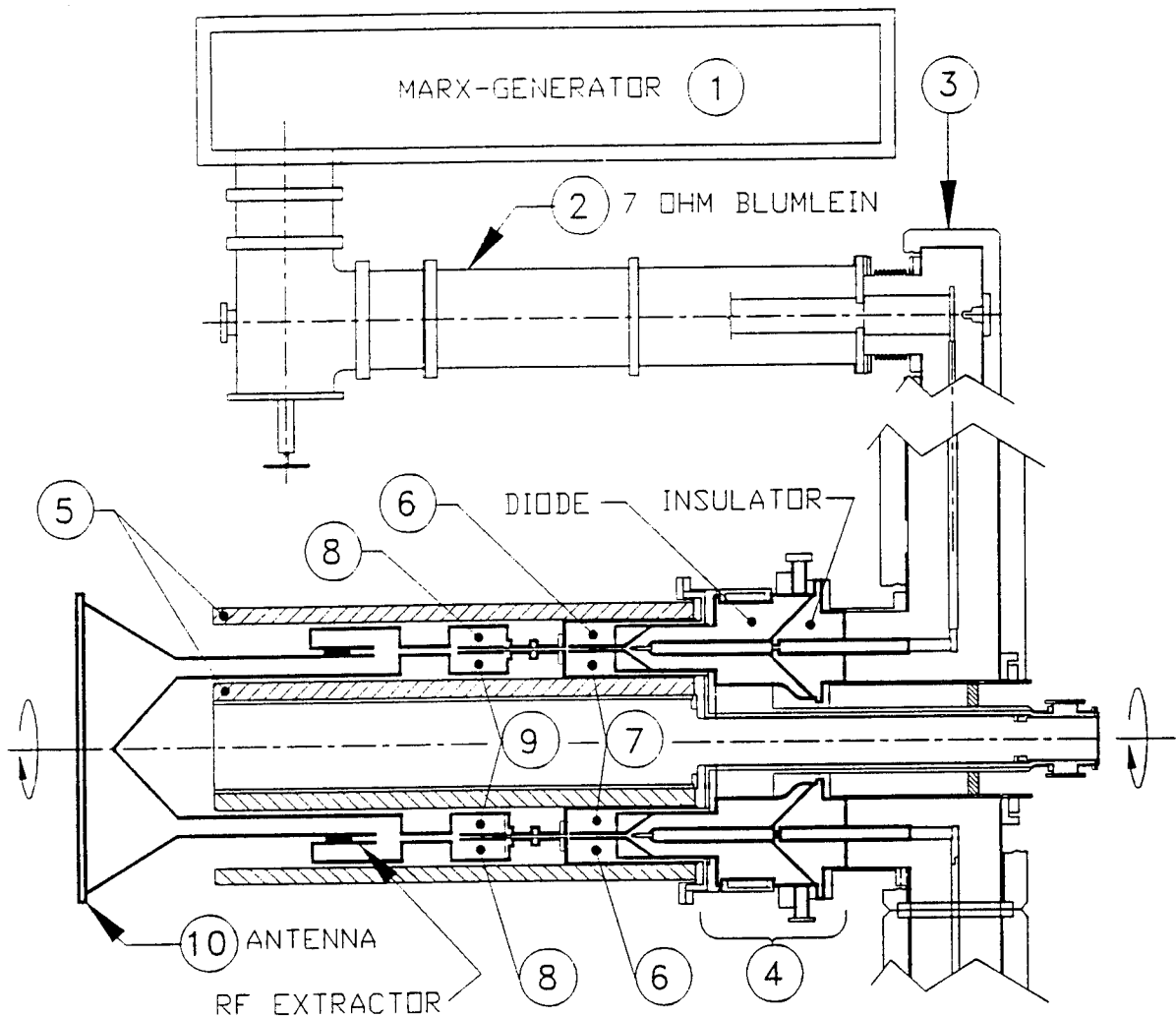


Figure 6 Schematics of the Triaxial RKA.

7. A FREQUENCY-AGILE RELATIVISTIC KLYSTRON OSCILLATOR (RKO)

A frequency tunable klystron oscillator was first built in the 1940's. The device consists of two cavities traversed by an electron beam. RF feedback channel connected the two cavities. The device was brought into oscillation when the real part of sum of the circuit admittance and beam admittance was < 0 . The frequency of oscillation was determined by equating the imaginary part of the total admittance to zero. Beam admittance depended on the transit time, and hence, on the velocity of the electrons and the distance between the cavities. These early devices utilized changes in beam voltage for change in transit time to induce frequency tuning.

A frequency agile RKO utilizes an IREB with a high potential energy. The potential energy can be varied by a change in geometrical parameters, such as beam radius (Eq. 1). This in turn changes the kinetic energy

of the electrons and their transit time.

A local change in the axial magnetic field can compress or de-compress the radial dimension of the IREB at the region between the two cavities. This in turn changes the electron velocity and the transit time, resulting in a frequency shift. The schematic of a frequency-agile RKO is shown in Fig. 8. Here, two coaxial, quarter-wavelength cavities are connected back to back by inductive loops. The inter-gap distance is about half a wavelength. An annular IREB propagates through the two gaps. An axial magnetic field focuses the beam and an additional magnetic field is used to compress and de-compress the IREB in the inter-gap region. The admittance of the electrical circuit is,

$$Y_c = j\omega C + (jZ_c \cot(\omega L/c))^{-1} \quad (9)$$

where Z_c is the characteristic impedance of the cavities.

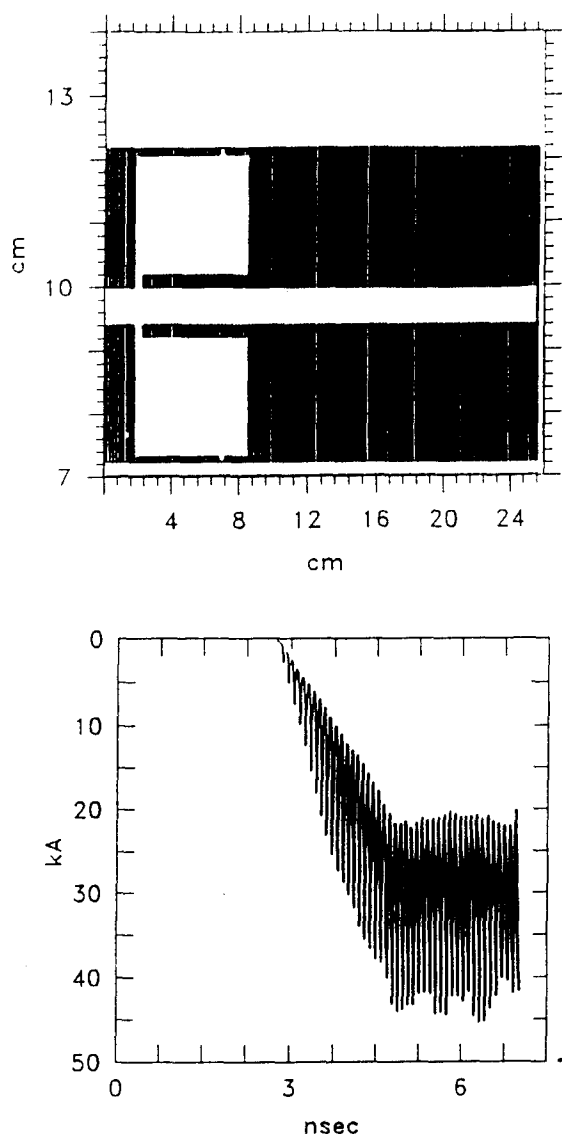


Figure 7 Computer simulation of an RKA operation at a frequency of 11 GHz. Beam current 30 kA and electron energy 500 keV. (top) geometry of simulation. (bottom) Modulated current.

The electronic admittance is,

$$Y_e = j \sin(\alpha \mu \theta) \exp(j\theta) / Z ; \theta = \omega \delta L / \beta_0 c \quad (10)$$

where, α , μ , δ , and L are parameters depending on the geometry and beam current and voltage. As mentioned before the frequency is determined by equating the sum of the imaginary parts of the admittances to zero and the start of oscillation occurs when the sum of the real part of the admittances is less than zero. Varying the intensity of the auxiliary magnetic field will change

beam radius according to Busch's theorem

$$r_b^2 B = \text{constant} \quad (11)$$

Equations 9-11 can be solved numerically. For example, Fig. 9 shows an S-band RKO frequency tuning curve as a function of the intensity of the inter-gap magnetic field. Beam voltage 250 kV, current 4 kA, and inter-gap spacing of 6 cm.

A somewhat similar device was built by us in 1983 in which the tuning mechanism was successfully investigated for IREB modulation at a frequency of 300 MHz.

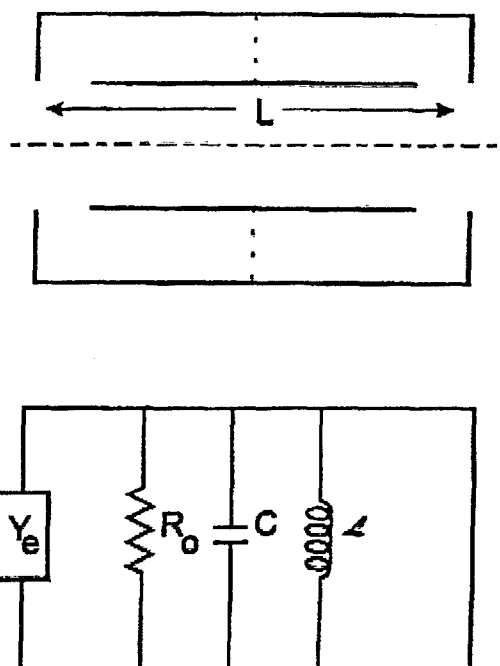


Figure 8 Simple cavity (top) and equivalent circuit (bottom)

8. APPLICATION OF RKAs.

Even though the ongoing research in RKA/RKO was geared for generating high peak RF power (>10 GW, >1 kJ/pulse), the research revealed that these devices can also operate in different modes, such as :

- (a) high frequency: $f \approx 10$ GHz
- (b) high efficiency: $>50\%$
- (c) rep-rated:
- (d) frequency agility:
- (e) long pulse duration:
- (f) low or high beam impedance:

For applications, factors such as weight, cost, reliability, ease of operation, etc. have to be looked at and compared with existing technology. RKA/RKO can be used as a HPM weapon source to blind C⁴I drones and satellites, disrupting the operation of cruise missiles. In a more

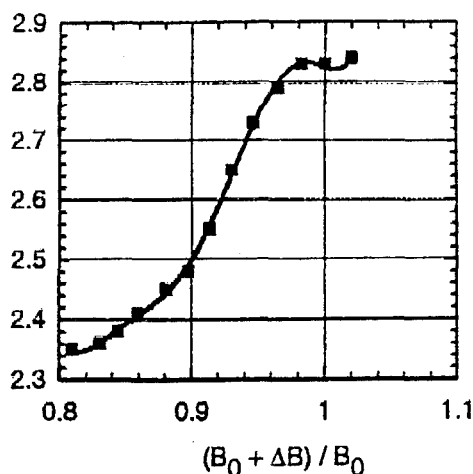


Figure 9 Frequency tuning with magnetic field for a 250-keV beam

exotic application, an RKA/RKO can be an ideal match load to an explosive generator power source. In yet another application, an RKA can power a high-gradient particle accelerator. We have already built an electron accelerator with an average voltage gradient of 60 MV/meter accelerating 200 A of electrons to 60 MeV.

Acknowledgements: This work was supported by ONR and by BMDO-IST/HDL.

9. REFERENCES

1. Friedman, M., Serlin, V., Drobot, A. and Seftor, L., "Self Modulation of Intense Relativistic Electron Beam", *J. of Appl. Phys.* 56, 9, September 1, 1984 pp 2459-2474.
2. Friedman, M., and Serlin, V., "Modulation of Intense Relativistic Electron Beams by an External Microwave Source", *Phys. Rev. Lett.* 55, 26, 23 December 1985, pp 2860-2863.
3. Friedman, M., Serlin, V., Krall, J., and Lau Y. Y., "Externally Modulated Intense Relativistic Electron Beams", *J. Appl. Phys.* 64, 7, 1 October 1988 pp 3353-3379.
4. Friedman, M., Serlin, V., Krall, J., and Lau Y. Y., "Efficient Generation of Multi-Gigawatt RF Power by a Klystron-like Amplifier", *Rev. Sci. Instrum.*, 61, 1, 1 January 1990 pp 171-181.
5. Friedman, M., and Serlin, V., "Generation of a Modulated Intense Relativistic Electron Beam with a Frequency Tunable by a Magnetic Field", *Rev. of Sci. Instrum.* 55, 7, July 1984, pp 1074-1076.
6. Friedman, M., and Serlin, V., "Electrostatic Insulation of a high Voltage Gap", *IEEE Trans. Electr. Insul.*, 23, 1, 1 January 1988 pp 51-56.
7. Bers, A., and Penfield, P., "Conservation Principles for Plasmas and Relativistic Electron Beams", *IRE Trans. Electron Devices* ED-9, 1, 1 January 1962 pp 12-21.
8. Serlin, V., Friedman, M., Krall, J., and Lau, Y. Y., "Relativistic Klystron Amplifier II - High Frequency Operation", *Proc. SPIE*, 1407, 20-24 January 1991, pp 8-12.
9. Friedman, M., Serlin, V., Krall, J., and Lau, Y. Y., "Relativistic Klystron Amplifier I - High Power Operation", *Proc. SPIE*, 1407, 20-24 January 1991, pp 2-7.

Photoinjector-Driven Chirped-Pulse Free Electron Maser

*G.P. Le Sage, F.V. Hartemann, H.X.C. Feng,
S.N. Fochs, J.P. Heritage
and N.C. Luhmann, Jr.*

University of California, Davis CA 95616
M.D. Perry and G.A. Westenskow
Lawrence Livermore National Laboratory
P.O. Box 808, L-637
Livermore California 94550
UNITED STATES

Summary

An ultra-short pulse, millimeter-wave free electron maser experiment is currently underway at UC Davis and Lawrence Livermore National Laboratory. A 8.5 kG, 30 mm period helical wiggler is used to transversally accelerate a train of one hundred 5 MeV, 0.25 nC, 1 ps duration micro bunches synchronously energized by a 20 MW, X-band photocathode RF linac. The photocathode is irradiated by a burst-mode, UV laser system which produces up to 100 pulses at 207 nm, with an energy of 10 mJ per pulse, and a pulse duration of 200 fs, at a repetition rate of 2.142 GHz. This system includes a 400 fs jitter synchronously modelocked AlGaAs semiconductor laser oscillator which is amplified by an eight-pass Ti:Al₂O₃ chirped pulse laser amplifier. The output of this amplifier is subsequently frequency quadrupled into the UV. Because the electron micro bunches are shorter than the radiation wavelength, the system coherently synchrotron radiates and behaves essentially as a prebunched FEM. In addition, by operating in a waveguide structure at grazing, where the bunch axial velocity in the wiggler matches the group velocity of the electromagnetic waves, one obtains output radiation pulses which are extremely short, and have greatly enhanced peak power. The device operates in the TE₁₂ mode of a cylindrical waveguide, and will produce up to 2 MW of coherent synchrotron radiation power at 140 GHz, in a 15 ps FWHM pulse. The -3 dB instantaneous interaction bandwidth extends from 125 GHz to 225 GHz. The output pulse is chirped over the full interaction bandwidth. One of the major potential applications of such a device is an ultra-wideband millimeter-wave radar.

List of Symbols

E_z	axial electric field
β	normalized particle velocity
β_g	normalized group velocity
γ	normalized particle energy
λ	wavelength
Δz	bunch length
$\Delta \tau$	pulse duration
q	bunch charge
P	power
I_p	peak current
c	speed of light

1 Introduction

Ultra-short, high power millimeter-wave and far infrared pulses of coherent radiation have numerous applications ranging from chemistry and solid state physics, to the next generation of ultra-wideband radar systems. Theoretical investigation of the waveguide interaction in a helical, pulsed wiggler of a micro bunch which is shorter than a radiation wavelength [1,2] has demonstrated distinct sets of characteristics. The first well known case includes the Doppler upshifted, and downshifted interactions, where the output pulse width is dominated by the slippage length [3] between the electron bunch, and the electromagnetic wave. In the case of two distinct interaction frequencies, the Doppler upshifted and downshifted interactions are given by

$$\omega^{\pm} = \gamma_{//}^2 \beta_{//} k_w c \left[1 \pm \beta_{//} \sqrt{1 + \left[\frac{\omega_c}{\gamma_{//} \beta_{//} k_w c} \right]^2} \right],$$

while the corresponding pulse durations are governed by the slippage times which are evaluated as follows

$$\Delta \tau(\omega^{\pm}) = \frac{L}{c} \left[\left| \frac{1}{\beta_{//}} - \frac{1}{\beta_g(\omega^{\pm})} \right| \right].$$

The alternate case, which is the grazing interaction, occurs when the waveguide dispersion relationship is utilized to match the group velocity of the electromagnetic wave to the axial velocity of the electron bunches. In this configuration, slippage is equal to zero and the output pulse duration is expected to be considerably shorter. Indeed, in the grazing case, the pulse length is shortened, because of the extremely wide instantaneous bandwidth of the interaction. In this case, the output RF pulse is chirped, and the pulse length is dominated by the waveguide dispersion relationship. The pulse duration can be estimated as follows

$$\Delta \tau \approx \frac{N_w l_w}{c} \frac{1}{\beta_{//}^3 \gamma_{//}^2} \frac{\Delta \omega}{\omega^*}.$$

The waveguide dispersion relationship showing the two interaction regimes is shown in Fig. 1.

Currently, a dielectric loaded FEM structure is being theoretically investigated, which can produce yet shorter RF pulses, since the grazing interaction can be met at an inflection point of the dispersion relation [4]. In this case, the group velocity dispersion $\frac{\partial \beta_g}{\partial \omega}$ becomes zero, and the only limitations remaining on the ultimate output pulse duration correspond to higher-order corrections. The interaction within the dielectric loaded rectangular waveguide structure is shown schematically in Fig. 2.

2 Multibunch X-Band Photoinjector

The multibunch photoinjector currently under development at LLNL is a 1 1/2 cell, standing wave p-mode structure, operating at 8568 MHz. The gun design is optimized through the use of the LANL codes SUPERFISH and PARMELA [5] to achieve a normalized emittance of $< 5 \pi$ mm-mrad. The RF source is a 20 MW, SLAC Klystron with pulse characteristics of 2.5 μ s pulse length, and a 1 Hz repetition rate. Electron bunches are produced by a train of UV laser pulses spaced by 467 ps (every fourth RF cycle) striking a high quantum efficiency (~5%) Cesium Telluride photocathode [7]. These micro bunches are quickly accelerated by the high electric field at the cathode surface of the half cell [6]. The laser system which produces the UV laser pulses is based on a gain modelocked AlGaAs diode laser oscillator, operating at 829 nm with a multiple quantum well saturable absorber, and driven by an RF signal which is actively synchronized with the klystron RF pulse. The timing jitter of the laser system is 400 fs. The 200 fs pulses produced by the laser system are subsequently amplified to 100 μ J by a Ti:Al₂O₃ chirped pulse amplifier, and frequency quadrupled into the UV. The overall system arrangement is shown schematically in Fig. 3. By irradiating the photocathode with a train of laser pulses, locked to the phase of the standing wave RF within the accelerator cavity, a train of micro bunches are produced with the advantageous characteristics of reduced charge per bunch, and increased overall charge of the bunch train. Typically, the coherence factor of radiation spectral power density scales as

$$\exp \left[- \left[\frac{\pi \Delta Z}{\beta \lambda} \right]^2 \right],$$

while the radiated power scales quadratically with the bunch charge q through the relationship

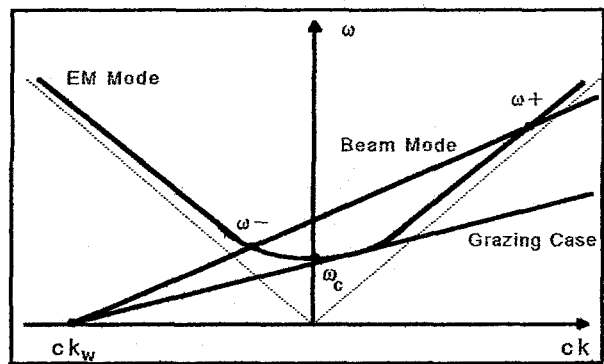
$$P \propto q^2 \exp \left[- \left[\frac{\pi \Delta Z}{\beta \lambda} \right]^2 \right].$$

This multi-bunch scheme directly applies to the FEM application, where reduced bunch charge improves space charge degradation of the bunch, as it travels through the wiggler, and where the synchrotron radiation from each micro bunch coherently contributes to the power of the output pulse. A proof-of-principle experiment has also demonstrated a scheme where multiple electron bunches can be produced by using a metallic photocathode as an integral mirror in an optical cavity [8]. For the experimental parameters described in Table 1, the normalized spectral power density for the grazing case is shown in Fig. 4. The temporal characteristics of the output pulse is shown in Fig. 5.

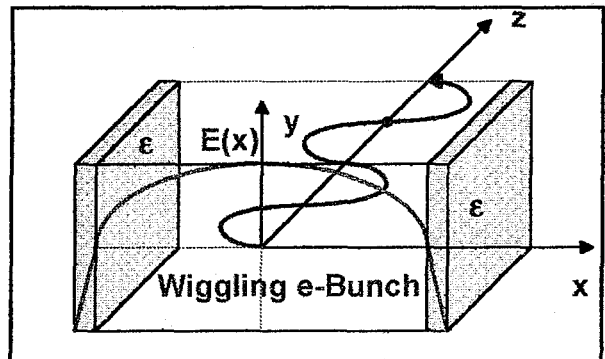
Acknowledgments

This work is supported in part by Rome Laboratory (ATRI) under Grant No. F30602-94-2-0001, in part by

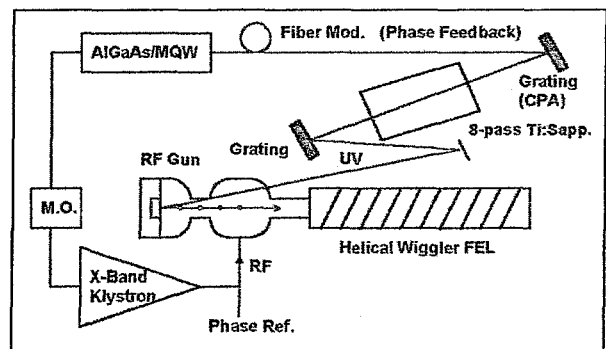
ARO under Grant No. DAAHO4-93-0084 and in part by LLNL/LDRD Contract No. W-7405-ENG-48.



1. FEL dispersion



2. Dielectric Loaded FEM Structure.



3. Experimental Arrangement

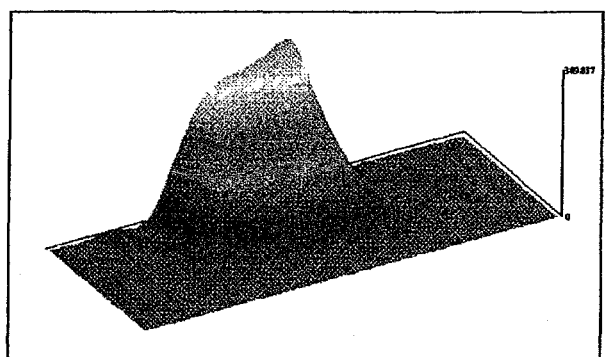


Fig 4. Normalized Spectral Power Density at Grazing

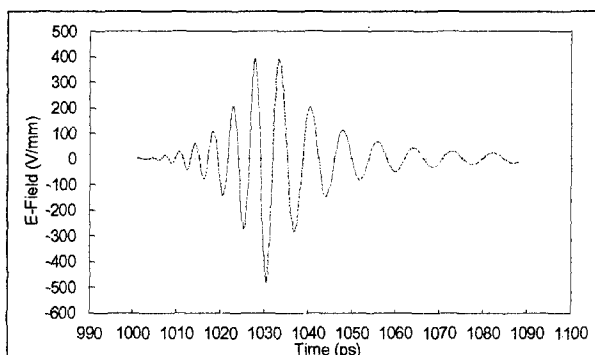


Fig 5. Temporal E-Field at Grazing

Microbunch Energy	5 MeV
Microbunch Charge	0.25 nC
Microbunch Length	0.3 mm
Peak Current	250 A
Wiggler Period	30 mm
Wiggler Field	8.5 kG
Number of Periods	10
Grazing Frequency	140 GHz
Waveguide Mode	TE ₁₂
Waveguide Cutoff	40 GHz

6. Table: FEL characteristics

References

- [1] "Time and Frequency Domain Analysis of Superradiant Coherent Synchrotron Radiation in a Waveguide FEL", A. Gover, F. V. Hartemann, G. P. Le Sage, N. C. Luhmann, Jr., R. S. Zhang, and C. Pellegrini, Phys. Rev. Lett. 72, 1192 (1994)
- [2] "Coherent Synchrotron Radiation in a Cylindrical Waveguide with a Helical Wiggler", F. V Hartemann, G. P. Le Sage, D. B. Mc Dermott, and N. C. Luhmann, Jr., Phys. Plasmas 1, 1306 (1994)
- [3] "A review of free-electron lasers", Roberson and Sprangle, Physics of Fluids B, January 1989
- [4] "Transform-Limited Pulses of Coherent Synchrotron Radiation in a Dielectric-Loaded Waveguide Free-Electron Maser", G. P. Le Sage, F. V. Hartemann, H. X. C. Feng, S. N. Fochs, and N. C. Luhmann, Jr., in progress
- [5] Los Alamos Accelerator Code Group, Poisson/Superfish group of codes, Parmela group of

codes, Los Alamos National Laboratory, Los Alamos, New Mexico

[6] "Design of the Laser-Driven RF Electron Gun for the BNL Accelerator Test Facility", Kirk T. McDonald, IEEE Transactions on Electron Devices, Vol. 35, No. 11, November 1988

[7] "Photocathodes for Free Electron Lasers", Steven H. Kong, et. al., Conference Proceedings, 16th International Free Electron Laser Conference, Stanford University, Stanford, Ca., August 1994

[8] "Coherent photoelectron bunch generation and quantum efficiency enhancement in a photocathode optical resonator", F. V. Hartemann et. al., Appl. Phys. Lett. 65 (19), 7 November 1994

INVESTIGATIONS INTO SUB-NS PULSE GENERATION USING FERRITE-LOADED COAXIAL LINES

H.R. Bolton, J.E. Dolan, A.J. Shapland

ELSYM Department

University of Wales College of Cardiff

P.O. Box 917, Cardiff CF2 1XH, UK

D.M. Parkes, K. Trafford, B. Kerr

Defence Research Agency

St. Andrews Road

Great Malvern, Worcestershire WR14 3PS, UK

SUMMARY

Systems such as Pockels Cell drivers and UWB radar require electrical pulses of <200 ps rise-time and amplitude of 10kV or greater into 50 ohms. Desired p.r.f.'s may be 50kHz or higher in burst mode. The output rise-time of high power and p.r.f. capable pulsers is generally of the order 2-20ns, and ferrite-loaded coaxial lines are one means of reducing the leading edge 10-90% rise-time to the order of 100-200ps.

The development of the fast-rising leading edge in ferrite lines is due to the non-linearity of the magnetic medium, and the consequent formation of an 'electromagnetic shock front' at the pulse leading edge. Over the past decade, the use of magnets to bias the ferrite has been found to improve output rise-time and amplitude characteristics considerably. Steady-state analyses made by Soviet analysts in the 1960's do not explain the magnet-biased ferrite line characteristics, and a numerical approach will be presented which shows how the microwave characteristics of the ferrite may be combined with the TEM transmission line equations to model electromagnetic shock wave propagation in such ferrite-loaded lines. It now appears reasonably clear that ferrite lines may be effectively modelled and designed in terms of parameters including the ferrite saturation magnetisation, and the dimensions of the line and the ferrite beads. Second order effects such as conductor and dielectric losses may also be taken into account if required.

1. INTRODUCTION

The phenomenon of pulse sharpening which may occur along ferrite-loaded coaxial lines has been exploited since the 1950's. The combination of ferrite lines - 'shock lines' - with relatively slow primary switches such as thyratrons can give sub-nanosecond rise-times, with applications including Pockels cell drivers, e-beam drivers, and ultra wide-band radar systems. Ferrite lines have generally been operated using a d.c. current bias passed along the coaxial centre conductor, making their

operation analogous to that of a single-turn coaxial magnetic switch, albeit one in which switching times are short relative to transit-times through the device. Reported output amplitudes and rise-times had been gradually developed from around 2ns@10kV in 1981 [1] to 500ps @250kV in 1982 [2] and 300ps @70kV in 1990 [3].

This relation to magnetic switch operation initially makes an explanation of the pulse sharpening process in terms of the non-linear B-H properties of the ferrite cores appear attractive. The slope of the B-H curve would give the phase velocity in the line as a function of the instantaneous current amplitude, and so the development of the propagating waveform with time could be assessed. However, the analysis breaks down because of the inevitable conclusion that the higher amplitude parts of the wave must catch up with the lower amplitude parts, implying that the wavefront becomes infinitely steep. This cannot actually occur because of the finite relaxation or switching time of the ferrite magnetisation, and it was shown in the early 1960's [4,5] that, analogous to the well-known 'sonic boom' in air, a 'shock front' will develop at the leading edge of the propagating pulse, which represents the limiting ferrite switching profile subject to the shock front amplitude. The rise-time across such a shock front may be related to the amplitude of the input pulse and the ferrite switching coefficient in an elegant closed-form analysis, and the effective propagation velocity of the shock front may also be calculated. However, while this approach enables the observed rise-times in d.c. current biased lines to be accounted for quite well, the necessary line length for a shock front to develop to maximum amplitude and minimum rise-time can only be assessed very approximately. The development of d.c. current-biased ferrite lines to give output pulse voltages of 50-200kV at rise-times of 300-500ps [2,3] has therefore been on a somewhat empirical basis.

The usefulness of the ferrite line pulse sharpening technique at relatively low voltages was considerably extended when Dave Parkes of DRA Malvern discovered that bar magnets placed around a d.c. current-biased

ferrite line operating at 10kV into 50ohms could reduce the output rise-time from around 1ns to the order of 200ps. Investigations of this striking effect led to various conclusions, amongst which are that the d.c. current bias is largely superfluous in conjunction with magnets, that the magnets are of most importance towards the output end of the ferrite line, and that the toroidal ferrite beads most susceptible to the effect are physically rather small, and generally of extremely square-loop characteristics, as used historically in computer memory devices. The use of a solenoid to bias the ferrite line axially has been found to give similar results to the use of magnets. It turns out that the observed rise-times in magnet-biased lines cannot be accounted for in terms of the magnetisation reversal behaviour assumed in the above-mentioned shock front theory. A particular characteristic distinguishing the effects of magnet or solenoidal bias from d.c. current bias is that the shock front waveforms tend to show oscillations after the initial rising edge. Together with the low-loss, square-loop characteristics of the MgMn composition memory beads, and the predominantly axial alignment of the bias fields, this led to the suggestion that the extremely fast rise-times occurring might relate to the stimulation of gyromagnetic precession behaviour in the ferrite similar to that exploited in non-reciprocal microwave devices such as circulators and isolators [6].

These observations led us into the process of development of a novel model for the estimation of pulse propagation and rise-time in ferrite lines. Given the doubtful utility of the standard B-H curve and small signal permeability ferrite characteristics, it was important to deal with

- (a) the fundamental magnetisation mechanisms involved in the generation of the extremely fast output rise-times, and
- (b) how to link these pulse magnetisation processes with an analysis of the TEM wave propagation process which must occur in the coaxial transmission line.

Our present objectives under a current contract may be summarised as follows;

- * theoretical elucidation of observed phenomena
- * comparison and development of experiment and theory
- * establishing rise-time/voltage characteristics and limits
- * development of line design and construction techniques

This paper briefly outlines the theoretical model evolved to describe ferrite line behaviour [7], and then describes some of our experimental progress in generating fast pulses using magnetically biased ferrite lines [8].

Implementation of practical systems at high p.r.f.'s requires consideration of thermal management issues in particular. The shock front development process involves absorption of energy from the input pulse leading edge, which then dissipates as heat, having a first-order effect on line behaviour due to the temperature-dependence of the ferrite magnetic properties. Inhibition of corona by the use of suitable dielectrics is also of major importance. One aspect of magnet-biased ferrite lines is that the shock front waveform is intrinsically oscillatory. With regard to applications where overshoot may be intolerable, investigations are being made into the effects on the shock front profile of lossy dielectrics and of conductive ferrite types.

2. FERRITE LINE MODEL

The exploitation of the non-linear properties of ferrites in transmission lines as a means of pulse sharpening was probably first outlined by Katayev in a 1959 patent, and 'Electromagnetic Shock Waves' (1964), also by Katayev [5], remains almost by default the standard work on the subject. The essence of pulse sharpening action in shock lines is somewhat analogous to the steepening of sea waves as they run into shoaling water. The ferrite non-linearity causes an increase of TEM phase velocity with pulse amplitude, and, as the input pulse travels down the line, a narrow fast-switching or 'spin-reversal' region develops at the pulse leading edge, generally termed the 'shock front'. The technique has been characterised by Oicles [9] as one of 'pulse carving', in that the process of generating the fast rise-time leading edge involves erosion of the waveform profile by progressive energy absorption into the medium.

2.1 Gyromagnetic theory

An explanation of the fast rise-time properties of magnet-biased ferrite lines arose from the realisation that the bias may saturate the ferrite magnetisation axially. The effect of the pulsed circumferential H-field in addition to the static bias field is then to cause coherent rotation of the magnetisation from axial to near-circumferential alignment. This suggested that the ferrite pulse behaviour might be best described in terms of damped precession of the molecular level magnetic dipoles around the net applied magnetic field.

At an atomic level, the orbital electrons have a quantised level of spin, which gives the electron quantised levels of both angular momentum and magnetic moment. In ferrimagnetic materials, the vector combination of the electron spin alignments across the entire molecule results in a net and permanent value for the angular momentum and magnetic moment terms. Short-range spin coupling forces mean that this net magnetic dipole moment behaves as a vector quantity of fixed amplitude which varies its orientation subject to applied fields.

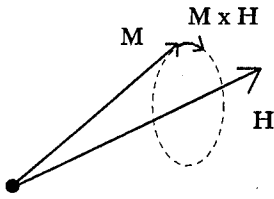
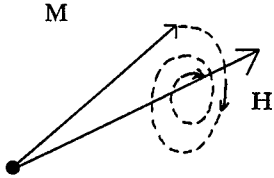
(a) precession of \mathbf{M} around \mathbf{H} due to $\mathbf{M} \times \mathbf{H}$ term(b) spiral of \mathbf{M} towards \mathbf{H} due to additional $\mathbf{M} \times \mathbf{M} \times \mathbf{H}$ term

Fig. 1 Landau-Lifshitz model of magnetisation vector rotation.

Subject to external bias fields sufficiently strong to overcome internal forces and saturate the material, the bulk (macroscopic) magnetisation behaviour and the molecular level magnetisation behaviour may become essentially equivalent. Under these conditions the Landau-Lifshitz (L-L) form of dynamic magnetisation equation is appropriate;

$$\frac{d\mathbf{M}}{dt} = -\gamma\mu_0(\mathbf{M} \times \mathbf{H}) - \frac{\alpha\gamma\mu_0}{M_s}(\mathbf{M} \times \mathbf{M} \times \mathbf{H}) \quad (1)$$

where the vector terms \mathbf{M} and \mathbf{H} represent the material magnetisation and the applied magnetic field in three dimensions. M_s and γ are the ferrite saturation magnetisation and gyromagnetic ratio respectively. The $\mathbf{M} \times \mathbf{H}$ term in Eq. 1 represents precession of \mathbf{M} around \mathbf{H} , while the $\mathbf{M} \times \mathbf{M} \times \mathbf{H}$ term represents the rotation of \mathbf{M} towards eventual alignment with \mathbf{H} . This process is indicated in Fig. 1.

The gyromagnetic ratio is the ratio of the electron spin magnetic moment to the angular momentum, which controls the magnetic dipole's dynamic response to an applied magnetic field; for all ferrites this is effectively a constant, given by $\gamma = -1.76 \times 10^{11}$ (rads/sec/Tesla).

The relative magnitude of the $\mathbf{M} \times \mathbf{M} \times \mathbf{H}$ 'damping' term is given by the magnitude of the damping factor, α .

The magnitude of both pulsed and bias fields, in the range 10-100kA/m, means that detailed low-amplitude B-H curves are superfluous to the pulsed magnetisation description [5]. Initially, we envisaged that the shock front wavefronts observed in axially biased ferrite lines would be explained in terms of the above magnetisation equation for the ferrite, with the pulsed $I/2\pi r$ field term

due to the coaxial current stimulating precession of \mathbf{M} around the static axial bias field during the progressive alignment of \mathbf{M} with the net \mathbf{H} -field existing at peak current. The coupling of the L-L equation to the transmission line equations follows in section 2.2.

2.2 Transmission line equations

Since the transmission line being analysed is coaxial, there is no doubt that the principal mode must be TEM, and so there was no compelling reason to propose magnetisation modes other than axysymmetric. Maxwell's equations may be written down in differential form for the propagation of one-dimensional plane waves along the z-axis as

$$\frac{dE_y}{dz} = -\frac{dB_x}{dt} \quad (2)$$

and

$$\frac{dH_x}{dz} = \epsilon_0\epsilon_r \frac{dE_y}{dt} \quad (3)$$

where the x-and y-axes represent the circumferential and radial directions respectively. Since \mathbf{B} may be written as

$$\mathbf{B} = \mu_0(\mathbf{H} + \mathbf{M}) \quad (4)$$

it is useful to write Eq. 2 as

$$\frac{dE_y}{dz} = -\mu_0 \left(\frac{dH_x}{dt} + \frac{dM_x}{dt} \right) \quad (5)$$

where $\frac{dM_x}{dt}$ will be found from the L-L equation.

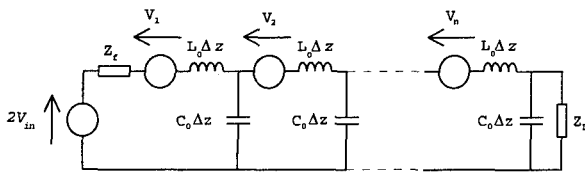
Rewriting Eqs. 3 and 5 with E_y and H_x in terms of voltage and current gives

$$-\frac{dV}{dz} = L_0 \frac{dI}{dt} + b \frac{dM_x}{dt} \quad (6)$$

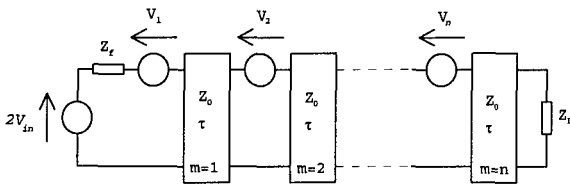
and

$$-\frac{dI}{dz} = C_0 \frac{dV}{dt} \quad (7)$$

where L_0 and C_0 represent the coaxial inductance and capacitance per-unit length, and b is the radial thickness of the ferrite. For numerical solution, discretisation will be into elements of Δz ; the discretised equivalent circuit for Eqs. (6) and (7) is then shown in Fig. 2(a). The voltage sources $V_1 \dots V_n$ represent the rate of change of circumferential magnetic flux, calculated for each section from the product of dM_x/dt with the ferrite cross-sectional area, $b\Delta z$. We have found that a direct time-stepping solution of the network of Fig. 2(a) is unsatisfactory, due to the natural oscillations which occur



(a) equivalent circuit-based



(b) transmission line element-based.

Fig. 2 Coaxial transmission line models

in the L-C loops. It is therefore advantageous to replace each linear L-C pair by a linear transmission line section with transit time $\tau = \Delta z \sqrt{L_0 C_0}$ and characteristic

impedance $Z_0 = \sqrt{L_0 / C_0}$, as shown in Fig 2(b). Solution

of this network proceeds in terms of time-stepping solution of the L-L magnetisation equation for each of the n elements, together with the propagation along the transmission line chain of voltage pulses resulting from

(a) the voltage at the input end of the line and

(b) changes in the n voltage sources representing the ferrite magnetisation.

The effect of the line current on the ferrite magnetisation is thus by means of the $H = I/2\pi r$ term on $d\mathbf{M}/dt$ in the L-L equation; conversely, $d\mathbf{M}_x/dt$ determines the voltage V_m in the transmission line network. The magnetisation-driven voltage sources clearly represent, in discretised form, the mechanism by which pulse energy may be reflected and absorbed by the magnetic medium in the actual ferrite line. The simulation may represent any input voltage waveforms and values of axial bias field, transmission line dimensions, ferrite dimensions, and values of ferrite saturation magnetisation.

3. INITIAL RESULTS

Fig. 3 shows a comparison of the measured and simulated output voltage waveforms from a 60cm length line feeding into a 50ohm load, for the measured input voltage waveform shown. The line i.d. and o.d. were 0.75mm and 2.4mm respectively, and the MgMn ferrite bead i.d. and o.d. were 0.785mm and 1.35mm. The capacitance per unit length was calculated in terms of the high-frequency permittivities of the heatshrink insulation layer and of the ferrite, taken as 2.1 and 12.0 respectively. The $4\pi M_s$ value for the ferrite was 0.25T.

The axial bias field was taken as 0.02T. The value of α was taken as 0.2. Although the predicted output waveform was reasonable overall, the predicted shock front rise-time was over 500ps, and it was immediately apparent that the measured shock front rise-time of around 150ps was not forthcoming from the model. The problem now was that since all the parameters in the model except α were well-defined by measurement, only α remained as a variable. We found that increasing α radically above unity would give shorter rise-times, but such an increase could not be justified realistically, given the definition of α in terms of the standard measurement of gyromagnetic resonance linewidth, ΔH , subject to d.c. bias field, H_0 , as $\alpha = \Delta H / 2H_0$, which yields values of α in the range 0.001-0.1 for low-loss ferrites. Further, the L-L equation is of doubtful validity for values of α over unity[10].

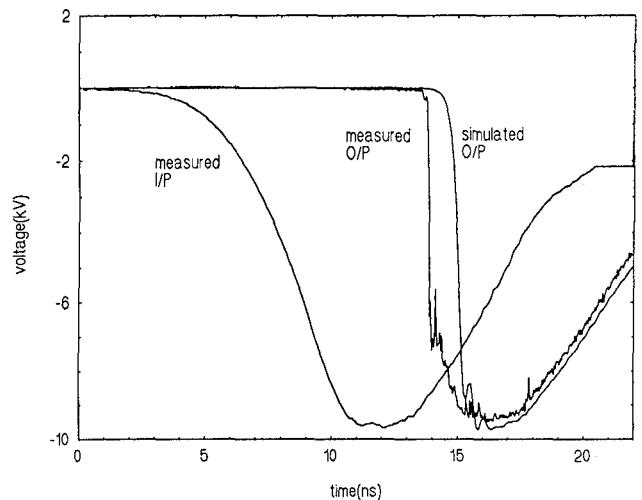


Fig. 3 Measured and simulated I/P and O/P waveforms; L-L model contains pulse $H=I/2\pi r$ and static axial bias terms.

4. THE RADIAL DEMAGNETISATION EFFECT

It seemed that, although the model linked the coherent precession of the magnetisation around the pulsed field to the shock front rise-time, this did not in itself account for the fast rise-times. It then occurred to us that coherent precession of the magnetisation term around the axial and circumferential bias field would in fact lead to a transient component of magnetisation directed radially outward from the bead surface, as shown in Fig. 4. Firstly, the shape of the bead must then cause a partial demagnetisation term. Secondly, because the magnetic flux penetration depth into copper over nanosecond timescales is extremely low, currents must be induced in the coaxial conductors to mirror the radial magnetisation

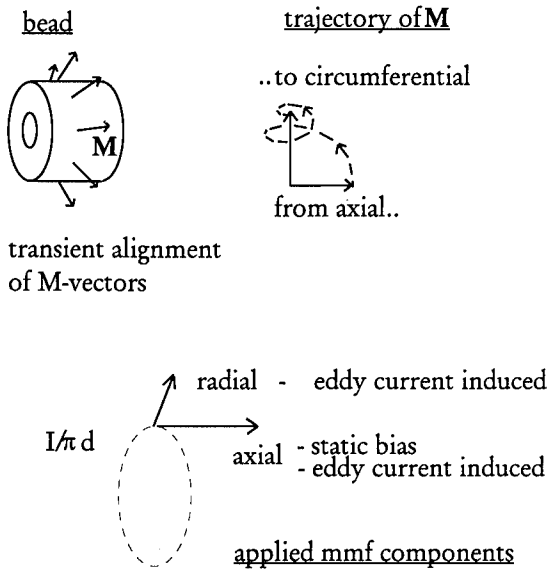


Fig.4 Showing transient radial orientation of magnetisation during pulsed precession from axial to radial alignment.

and ensure complete radial flux cancellation at the conductor surface. A third H-term in the solution of the L-L equation was therefore proposed, defined as

$$H_y = -M_y \quad (8)$$

The effect of this term on the waveform is shown in Fig. 5. The predicted rise-time is reduced to about 150ps, agreeing well with the measured value. The effect of the radial demagnetisation term on the rise-time may be explained with reference to the additional components of dM/dt which are generated through the presence of H_y in the L-L equation.

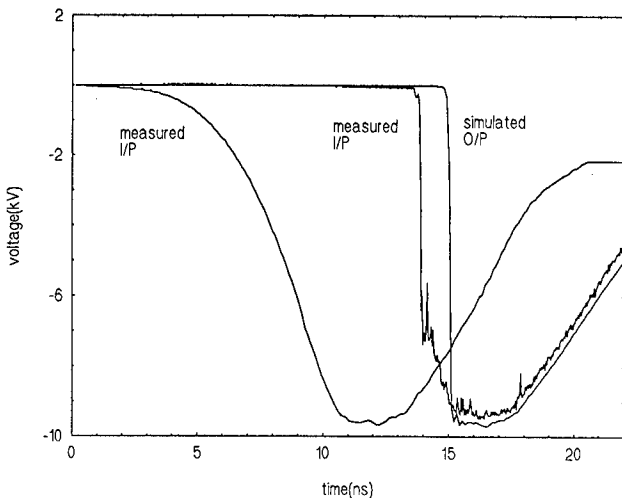


Fig. 5 Measured and simulated I/P and O/P waveforms; L-L model also including radial induced term $H_y = -M_y$.

5. THE SOLENOIDAL INDUCED FIELD TERM

Both in the above simulation, and with simulations of other ferrite lines, we have consistently found that the predicted shock front position using the above formulation is delayed relative to the measured shock front, as seen in Figs. 3 and 5 above. When the ferrite magnetisation is pulsed out of axial alignment, a large voltage would be induced in a solenoidal loop placed around the ferrite line. In fact, the coaxial outer conductor acts as a short-circuit turn, and so we can see its effect as being to prevent any net change of axial flux over short timescales relative to the conductor L/R decay time. However, since the ferrite cross-sectional area (end-view) is less than the overall coaxial cross-section, the demagnetisation term on the ferrite induced by this will be less than 100%. We therefore tried the effect of including the following solenoidal-current-driven, axial H-term in the L-L simulation;

$$H_z = -k\Delta M_z \quad (9)$$

where k is an axial demagnetisation factor in the range $0 < k < 1$. The result of running the simulation with $k=0.5$ is shown in Fig. 6. In simulating other lines, values of k around 0.5 also give reasonable agreement. In general terms, the effect of including the above term may be

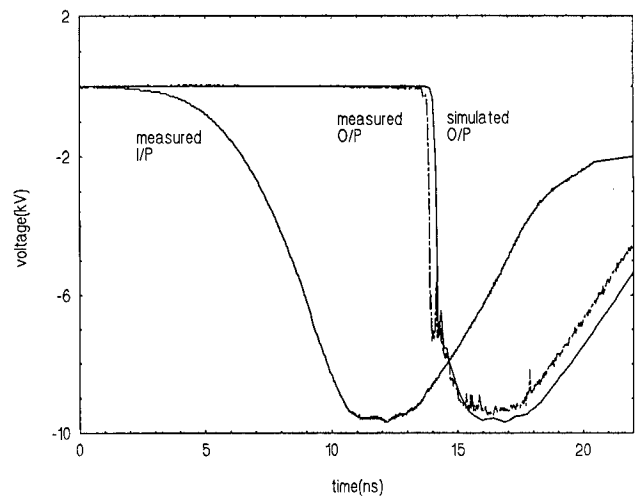


Fig. 6 Measured and simulated I/P and O/P waveforms; L-L model also including radial term $H_y = -M_y$ and axial term $H_z = -0.5\Delta M_z$.

seen as causing a reduced angle of swing of M away from its initial axial alignment.

It was not at first obvious whether the radial demagnetisation term proposed in section 4 might arise primarily from geometric effects or induced currents. Considerations of symmetry suggest that, if it were current-driven, the induced current patterns would have to be solenoidal. Since the induced solenoidal field term

described in this section is required in the model to account for the experimentally observed shock front delays, this suggests that the radial demagnetisation term does in fact arise primarily from induced solenoidal currents. In the longer term, a finite-element solution in cylindrical coordinates might well be useful in relating these effects more exactly.

6. EXPERIMENTAL INVESTIGATIONS

A particular aim of our work has been to establish whether or not the magnetic biasing technique could be extended to ferrite types other than computer memory cores. While the magnetic dipole-based model appeared to account for the rise-times observed in memory core lines, it was not clear whether factors such as the highly square-loop characteristics of the MgMn memory beads, and the very short axial length (0.4mm) of the individual beads, were also of importance in the fast rise-time characteristics of the lines. Effectively, we had little idea as to whether the validity of the model would extend to other ferrite types, or even to other dimensions and proportions of ferrite beads. If it did, we would expect risetimes of below 200ps @10kV for bead sizes of up to 3-4mm o.d., with clear practical advantages in terms of line fabrication, cost, etc.

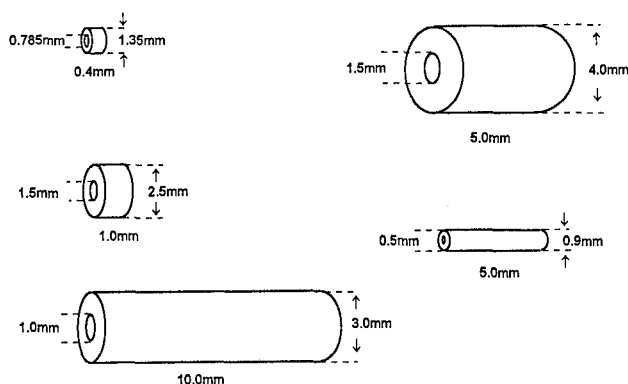


Fig. 7 Some bead sizes and shapes tested.

Ferrite compositional types available off-the-shelf in small bead or tube form include NiZn, MgMn, and MnZn. The range of bead sizes we have experimented with at the 10kV level is illustrated in Fig. 7. Our problem in assessing various ferrite types as candidates for use in shock lines was that the small-signal bandwidth characteristics follow the same pattern in all ferrites, while the differences in B-H loop characteristics suggested no clear relation to the observed gyromagnetic behaviour in ferrite lines.

The experimental system is outlined in Fig. 8. The Bournlea Instruments Model 3153 pulse generator is a thyatron-switched, resonant charge line unit, generating a negative going output pulse into 50ohms of around 4.5ns 10-90% fall-time, and amplitude variable up to

11.5kV. A Tektronix 11801A digital sampling oscilloscope with SD-26 sampling head giving bandwidth/risetime figures of 20GHz/17.5ps is used to monitor the output pulse waveforms. A capacitive (D-dot) pick-up is used to derive the trigger signal for the 11801A from the 3153 output pulse. This minimises the timing jitter on the measured waveforms, which is then around 20ps pk-pk. Type URM 67 single-braid 50ohm coaxial cable is used to link the high voltage system elements. A cable length of at least 15m between the pulser and the ferrite line is required to give the necessary pre-trigger delay for the 11801A. While magnets have several advantages such as compactness, low cost, and low weight, the use of a d.c. current-driven solenoid enables more easily reproduced results and also a more precise characterisation of the bias field. Values of free-space axial field in the range 0-40kA/m may be established on the axis of the solenoid used at present.

The ferrite line output pulse is measured through a series of coaxial, 50ohm, 20GHz bandwidth attenuators. These also act as a matched load for the pulse. Advantages of using attenuators rather than D-dot or B-dot pick-ups are that the calibration is extremely good, problems of frequency-dependent attenuation of the measured pulse are reduced, and the need for integration of the waveform is eliminated. For low p.r.f. work, a Barth model 202 and a model 142 unit act as the high voltage attenuators. These are capable of absorbing 10kV pulses at low pulse widths, albeit at only 2W mean power. For higher p.r.f. work, a 1GHz, 200W Bird attenuator is used at the front end, but the bandwidth and rise-time of the measurement system deteriorates.

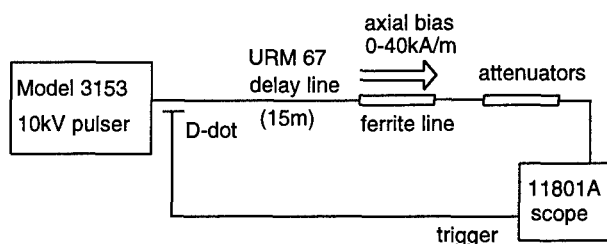


Fig. 8 System outline.

Experiments comparing lines using MgMn memory beads, and using some small NiZn tubes which we obtained with an o.d. of 0.9mm and length of 5mm, gave rise-times of below 200ps in each case. This tended to support the model, and suggested that the axial length of the individual beads has little if any effect on the gyromagnetic response. However, attempts to extend these results to larger beads were not initially successful at all. The application of magnetic bias only marginally improved rise-times below 1ns; in some lines using RFI suppression bead types such as Mullard FX1242, the bias actually worsened rise-times.

The lack of positive results initially led us to try to account for the slow responses of large beads in terms of possible effects and factors including multi-moding (TE or TM modes), the nature of the bead material, and possible interaction between the shock front axial length and the bead dimensions for larger beads. However, a complicating factor in our original line of approach was that we focussed on the use of cascaded lines, with the view that the overall line length could thus be minimised. The input rise-time to the magnet-biased line was then of the order of 1ns. A problem which we only gradually became aware of was that of waveform attenuation through the interfaces between line sections, which represent complex 3-D transitions, particularly for faster pulse rise-times. It became clear that it would be desirable to minimise the number of ferrite line sections.

A single line of 1m length was therefore designed with the aid of the novel transmission line model outlined previously, using ferrite beads each of i.d. 1.5mm, o.d. 2.5mm, and length 1mm, and saturation flux density 0.35T, to sharpen the 4.5ns input pulse directly to the final output rise-time. The line would be subjected to a uniform axial bias of around 20kA/m over its entire length. Two lines were built; (a) using a particular NiZn bead type which had not been tried before, and (b) with 70cm of a second NiZn grade at one end followed by 30cm of a MnZn grade. Both lines (a) and (b) gave overall waveforms very similar to the design curves, as shown in Fig 9. The output pulse leading edges for both

is also explained by low loss gyromagnetic behaviour in the MnZn beads at the output end, modified by eddy-current limited diffusion of the pulsed magnetic fields into the relatively conductive MnZn beads. Reversing line (b) so that the non-conductive NiZn beads are at the output end gives relatively long shock front rise-times of around 500ps, which may be explained simply in terms of lossier gyromagnetic behaviour of this NiZn ferrite type.

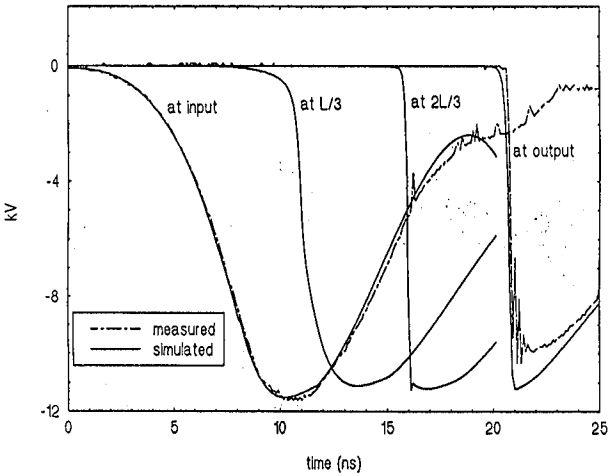
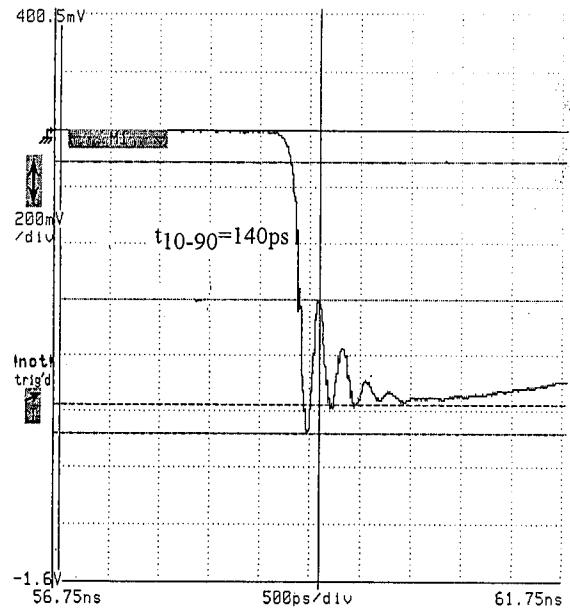
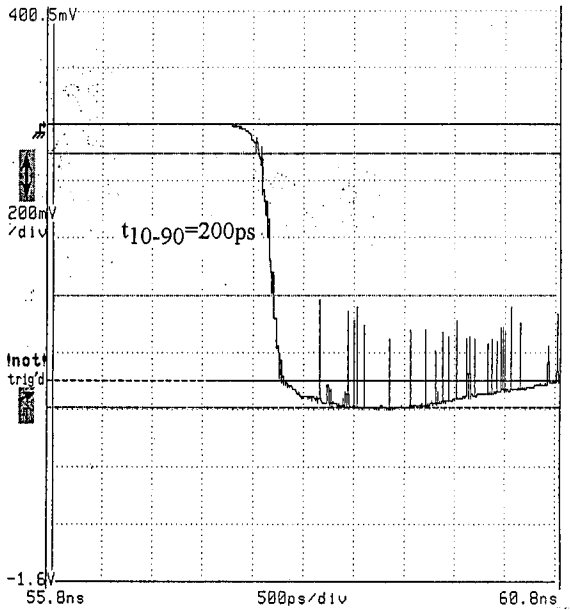


Fig. 9 Design curves and experimental input/output waveforms.

lines are shown in fig. 10; the leading edge amplitude and rise-time are 12kV/140ps at 11.5kV nominal output for line (a) and 10kV/200ps for line (b). For line (a), the underdamped 140ps rise-time pulse can be related to low-loss gyromagnetic behaviour of the ferrite. For line (b), we think that the smooth 200ps rise-time waveform



(i) line(a)



(ii) line(b)

Fig. 10 Measured line output waveform leading edges.

7 DISCUSSION

These results showed clearly that the rise-time obtained from a ferrite line in fact relates principally to the particular gyromagnetic characteristics of the ferrite bead used, and especially the damping factor, α . We have since been able to use beads of very large aspect ratio (1mm i.d. and 3mm o.d.) and 10mm length to obtain waveforms similar to those of Figs. 9 and 10. This indicates that the individual bead dimensions do not significantly interact with the gyromagnetic phenomena, although of course detailed effects relating to the necessary strength of bias field to overcome inter-bead reluctances may well occur.

8 DESIGN RULES

Using the novel simulation model, we have generated a set of theoretical curves for rise-time as a function of the ratio of line voltage to mean bead diameter (Fig. 11). These show that the rise-time reduces progressively as the pulse amplitude is increased, and that higher values of B_{sat} will give faster rise-times.

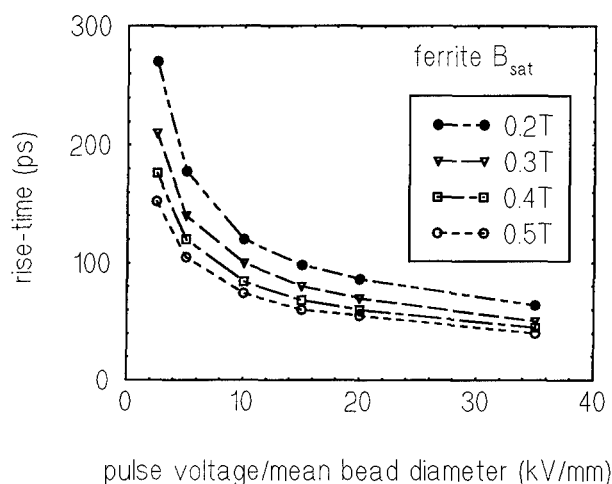


Fig.11 Theoretically predicted rise-time as a function of peak pulse voltage to mean bead diameter.

However, the major limitation on rise-times may be expected to be the breakdown electric stress at the centre conductor, which will determine the peak operating voltage. At present we have operated line sections at 16MV/m peak stress, but not for extended periods. It is clear that peak levels will be critically dependent upon the quality of dielectric impregnation around the ferrite beads.

Modelling shows that the necessary line lengths scale with input pulse rise-time. A question which arises is whether the application of magnet bias is always beneficial. Both from modelling and from experiment,

we have found that it is generally possible to obtain a lower output rise-time from a magnet-biased line; however, the necessary line length for a magnet-biased line becomes a factor of 2-4 longer than for an unbiased line of the same ferrite type. As an example, for a 10kV, 4.5ns rise-time input pulse, the output rise-time from a 10cm length unbiased ferrite line using type FX1242 beads is 1.6ns@10kV. Using magnet bias, the output rise-time for the same bead type is reduced to about 600ps; however, the minimum line length for this to occur is 35cm. In some circumstances, the ability to use a short line length may outweigh the faster output rise-times obtained using bias, and this will represent a design trade-off.

An area of ongoing interest is to establish the intrinsic ferrite parameters which give low-loss gyromagnetic behaviour. We have made a tentative connection between fast output rise-times and low values of ferrite coercivity, H_c , but how this relates to the detailed ferrite chemical composition and grain structure of the ferrites is not yet apparent.

9 CONCLUSIONS

Rise-times down to 140ps at around 10kV have been achieved using various types and sizes of ferrite beads in magnetically biased ferrite lines. The operation of such ferrite lines has been effectively explained in terms of a novel transmission line model incorporating a gyromagnetic description of the pulsed ferrite magnetisation behaviour, and line lengths may be designed to match the input pulse waveform. The importance of a low-loss gyromagnetic characteristic has been established, and it is expected that increased pulse voltages will lead to lower rise-times. The practical operating limits for peak voltage stress in such lines remain to be established.

10 ACKNOWLEDGEMENTS

This work is supported by the Defence Research Agency, Malvern, UK.

© British Crown Copyright 1994 /DRA

Published with the permission of the Controller of Her Britannic Majesty's Stationery Office.

11 REFERENCES

- [1] Weiner, M., Silber, L., 'Pulse sharpening effects in ferrites', IEEE Trans. Magnetics, 1981, MAG-17, pp.1472-1477.
- [2] Shvets, V.A., 'Nonlinear multichannel pulse-sharpening line containing ferrite rings with

nonrectangular hysteresis loop', Instruments and Experimental Techniques, 1982, pp908-912.
(1982, Pribory i Tekhnika Eksperimenta, No 4, pp116-119)

[3] Seddon, N. and Thornton, E., 'A high-voltage, short rise-time pulse generator based on a ferrite pulse sharpener', Rev. Sci. Instrum., 1988, Vol 59, pp2497-2498.

[4] Ostrovskii, L.A., 'Formation and development of electromagnetic shock waves in transmission lines containing unsaturated ferrite', Soviet Physics - Technical Physics, 1964, Vol 8, No. 9, pp805-813.
1963, (Zhurnal Tekhnicheskoi Fiziki, Vol 33, No 9)

[5] Katayev, I.G., 'Electromagnetic Shock Waves', 1966, Iliffe Books Ltd., London.

[6] Benson, T.M., Pouladian-Kari, R., and Shapland, A.J., 'Novel operation of ferrite loaded coaxial lines for pulse sharpening applications', Electronics Letters, 1991, Vol 27, No.10, pp861-863.

[7] Dolan, J.E., Bolton, H.R., and Shapland, A.J., 'Analysis of ferrite line pulse sharpeners', Proc. 9th IEEE Pulsed Power Conf., 1993.

[8] Dolan, J.E., Bolton, H.R., and Shapland, A.J., 'Development of ferrite line pulse sharpeners', Proc. 9th IEEE Pulsed Power Conf., 1993.

[9] Oicles, J., Electromagnetic shock lines for ultrafast high voltage pulse generators, LLNL int. comm. April 1984.

[10] Gyorgy, E.M., 'Rotational model of flux reversal in square loop ferrites', J. Appl. Phys., 1957, Vol 28, 1011-1015.

TRANSIENT ANTENNA DESIGN PARAMETERS FOR OPTIMISING RADIATED PULSE

A.P. Lambert

S.M. Booker

P.D. Smith

Department of Mathematics and Computer Science

University of Dundee

Dundee DD1 4HN, UK

1. INTRODUCTION

Antenna structures capable of supporting (essentially) transverse electromagnetic (TEM) spherical waves are characterised by their frequency independence over a wide band width, making them ideal candidates for transient field generation and reception. In particular, the triangular plate configuration of the TEM horn is of interest for a variety of directive wide band applications, including nuclear EMP simulation [1], impulsive field detection [2], ultrawideband radar pulse transmission [3], and feeds for paraboloidal reflector antenna systems [4]. The basic design for such structures is based on that of idealised, infinitely long, conical antennas. However, in producing practical antennas, which optimise the required characteristics of the radiated pulse train, several modifications to the original design are possible. This paper will discuss two particular features of the TEM horn design: the prediction of the characteristic impedance for a given structure and the effect of the horn profile on the output pulse.

2. THE CHARACTERISTIC IMPEDANCE

An accurate estimation of the characteristic impedance of a given transient antenna is desirable for two main reasons. Firstly, by ensuring that the structure is correctly matched to the rest of the system, maximum power transfer to the active radiating elements is guaranteed. Secondly, the (possibly corruptive) effects of late-time reflections, due to mismatch at the antenna-free space interface, can be reduced by suitable tailoring of the characteristic impedance at the end of the antenna. The original theoretical work on this topic was by Carrel [5]. However, experiment and subsequent re-examination of the analysis has shown his results for the TEM horn to be in error, [6]. Consequently, two alternative methods for estimating the characteristic impedance have been developed: a new conformal mapping technique, [7], and a numerical treatment, based upon the electric field integral equation (EFIE), which is suitable for a variety of TEM structures, [8]. These two methods will be described and the results of both shown to be in excellent agreement with those obtained experimentally, by time domain reflectometry (TDR).

2.1 Numerical Impedance Estimates

The original theoretical work on TEM horns, [5], predicted that a structure with plates of apex angle 40° , separated by an angle of 27° , would have a character-

istic impedance of 100Ω . However, TDR measurements on this structure, [6], suggested an impedance of approximately 140Ω . In order to reduce the measured impedance of a horn (with plates of apex angle 40°) to 100Ω the separation of the plates had to be reduced to approximately 16° . In order to investigate this discrepancy an alternative approach to the determination of transient antenna impedance was required. Here we describe the numerical approach developed for this purpose and validate it for a variety of canonical structures (of known impedance). The numerical estimates of TEM horn impedance are found to verify the TDR measurements, suggesting that the analytical results of [5] are in error.

2.1.1 The Model

The approach we shall follow is one based on a time-domain solution of the EFIE. Such an approach has been used previously to solve transient scattering problems for an arbitrary surface, e.g. [9]. It has also been exploited in the calculation of far-field radiation from an arbitrary surface driven by a transient source, [10].

Consider an arbitrary surface, S , subject to an incident electric field $\vec{E}^i(\vec{r}, t)$. Let S be perfectly conducting and surrounded by a lossless homogeneous medium of constant permittivity ϵ and permeability μ , the speed of light in this medium being c . The field induces a surface current $\vec{J}(\vec{r}, t)$ and surface charge $\rho(\vec{r}, t)$ on S .

Let us define a vector potential by

$$\vec{A}(\vec{r}, t) = \frac{\mu}{4\pi} \int_S \frac{\vec{J}(\vec{r}', t - |\vec{r} - \vec{r}'|/c)}{|\vec{r} - \vec{r}'|} dS', \quad (1)$$

and a scalar potential $\phi(\vec{r}, t)$ similarly.

The field radiated by the surface distributions, $\vec{E}^s(\vec{r}, t)$, can be represented in terms of these potentials. Further, since the total electric field tangential to a perfectly conducting surface is zero, $(\vec{E}^i + \vec{E}^s)^{tan} = 0$, we may derive the EFIE

$$\vec{E}^i(\vec{r}, t)^{tan} = \left[\nabla \phi(\vec{r}, t) + \frac{\partial \vec{A}(\vec{r}, t)}{\partial t} \right]^{tan} \quad (2)$$

In addition we may derive a continuity equation

$$\frac{\partial \rho}{\partial t}(\vec{r}, t) + \nabla_S \cdot \vec{J}(\vec{r}, t) = 0, \quad (3)$$

where ∇_S is the surface divergence on S .

Equations (2) and (3) are sufficient to determine a solution for \bar{J} and ρ , given suitable initial and boundary conditions. The transient voltage source, $V(t)$, can be introduced to the model via a suitable representation for \bar{E}^i .

2.1.2 Application of the method of moments

In order to solve (2) and (3) numerically using the time-domain method of moments we must select spatial basis functions for \bar{J} and ρ , together with a suitable testing procedure. The basis functions we choose are those described by Rao et al [11]; these have several useful properties. We outline here how these functions may be used to determine the behaviour of S subject to a voltage source $V(t)$.

Let us define a grid on S with N_c triangular patches arranged such that the grid has N_e internal edges (edges common to two patches). If E_n is the n th internal edge with mid-point \bar{r}_n^e , $1 \leq n \leq N_e$, then denote by T_n^+ / T_n^- the two triangles adjacent to E_n . Let the centroids of these triangles be $\bar{r}_n^{c+} / \bar{r}_n^{c-}$ and let the vertices not on E_n be $\bar{r}_n^{v+} / \bar{r}_n^{v-}$. See Figure 1.

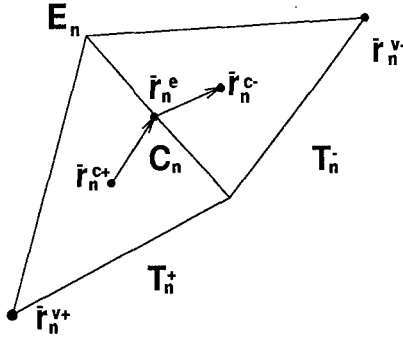


Figure 1 The triangle pair and parameters.

Using this grid we may define a set of spatial basis functions for the surface current, $\bar{f}_n(\bar{r})$, $1 \leq n \leq N_e$, which are piecewise linear over the internal edges of the grid. We may also define a set of spatial basis functions for the surface charge, which are piecewise constant on the triangles of the grid. The surface current may thus be approximated by

$$\bar{J}(\bar{r}, t) \approx \sum_{n=1}^{N_e} I_n(t) \bar{f}_n(\bar{r}), \quad (4)$$

where $I_n(t)$ are expansion coefficients, to be computed. The surface charge will have a similar approximate representation as a sum over the N_c centroids of the grid.

The continuity equation, (3), may be discretised using these approximations, by point-matching at the centroid of each triangular patch. The vector potential \bar{A} , and scalar potential ϕ , may also be approximated

from these representations for \bar{J} and ρ , using (4) and its scalar analogue.

To discretise the EFIE we consider the edge E_n , $1 \leq n \leq N_e$, of the grid (Figure 1). Integrating each side of (2) along a piecewise linear contour C_n , from \bar{r}_n^{c+} to \bar{r}_n^{c-} via \bar{r}_n^e , we find

$$\frac{\partial}{\partial t} \int_{C_n} \bar{A}(\bar{r}, t) \cdot d\bar{l} + \Delta\phi = \int_{C_n} \bar{E}^i(\bar{r}, t) \cdot d\bar{l}, \quad (5)$$

where $\Delta\phi = \{\phi(\bar{r}_n^{c-}, t) - \phi(\bar{r}_n^{c+}, t)\}$. The integral on the left hand side may be approximated from the value of \bar{A} at the mid-point of C_n

$$\int_{C_n} \bar{A} \cdot d\bar{l} \approx \bar{A}(\bar{r}_n^e, t) \cdot (\bar{r}_n^{c-} - \bar{r}_n^{c+}). \quad (6)$$

For an arbitrary incident field the right hand side of (5) may be approximated by a similar testing procedure. This is the approach adopted in [9]. Here however we may be more exact.

Let us define a strongly localised incident electric field by

$$\bar{E}^i(\bar{r}, t) = V(t) \delta(\bar{r} - \bar{r}_p^e) d\bar{l}, \quad (7)$$

where $d\bar{l}$ is a unit vector lying tangential to the contour C_p at \bar{r}_p^e , the mid-point of edge E_p . Then the right hand side of (5) gives $V(t)$ for edge p and 0 for all other edges. Hence, we have effectively introduced a voltage source, $V(t)$, at the p th internal edge of our grid.

The discretised forms of (2) and (3) form a coupled system of discrete equations which may be solved using a marching-in-time approach similar to that outlined in [9].

2.1.3 Canonical Structures

Having developed a model to simulate a radiating surface subject to a voltage source we now validate it, by simulating a variety of canonical structures. We firstly choose the V-conical antenna (VCA), see [12], because it highlights the two principal difficulties in applying the model. Firstly, care must be taken when defining a grid to approximate the antenna surface, if stable, accurate solutions are to be obtained. Secondly, although the VCA is a TEM structure, any practical antenna will be finite and its impedance frequency dependent; we must therefore derive and interpret the impedance spectrum of the antenna in a consistent and meaningful manner. Another advantage of the VCA is that analytical and experimental results for the antenna impedance have been found to be in excellent agreement, see [12]

The VCA design is depicted in the inset in Figure 2. It consists of an infinitely long cone, of apex half-angle θ , cut down to leave two curved plates, of azimuth half-angle ϕ ; thus, two parts of the full conical surface, each of azimuthal extent $\pi - 2\phi$, are removed. These

plates may be driven against each other by a source at the cone apex to produce TEM waves. Figure 2 depicts the feed region of the mesh used to simulate a VCA of apex half-angle $\theta = 70^\circ$ and azimuth half-angle $\phi = 45^\circ$. The x -axis forms the axis for the cone. The grid is viewed obliquely from a line in the xy -plane at an angle of 50° to the cone axis.

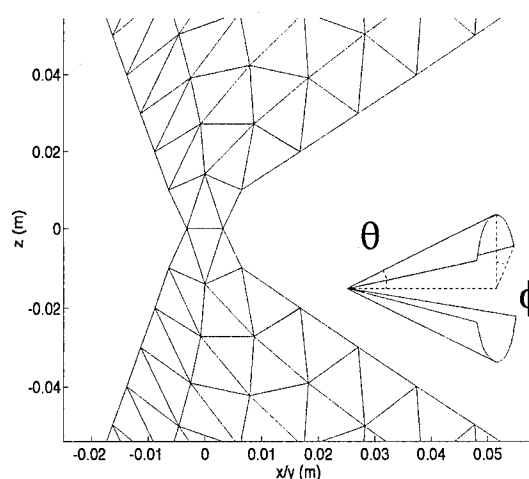


Figure 2 Oblique view of VCA grid feed region.

It may be seen that, although the antenna surface is faithfully reproduced away from the cone apex the feed region is simulated by a flat vertical region (in the yz -plane) of six triangles. The voltage source is applied via the edge at $z = 0$. This proves to be the most effective way of feeding the desired waveform onto the antenna surface, for the following reasons.

If a single voltage source, at an edge in the xy -plane, is used then a flat vertical region is necessary in order to ensure stability. If the triangular patches adjacent to the feed edge are allowed to incline away from the z -axis then their centroid separation decreases. This will tend to reduce the range of solution stability; for a sufficiently small (although relatively large) θ no stable solution is possible, see reference [6]. The introduction of two, well-separated sources is no remedy to this problem. The region between these sources can not be removed entirely from consideration and the desired waveform can not be induced on the antenna surface with any acceptable degree of accuracy.

The feed arrangement of Figure 2 not only ensures stability of solution, even for relatively small angles, but also provides an accurate estimate of the feed current and antenna impedance.

The grid of Figure 2 is that of a 0.15 m VCA with $\theta = 70^\circ$, and $\phi = 45^\circ$. Shen et al, [12], found that the characteristic impedance of a VCA was independent of θ ; it may be seen, therefore, that the impedance of our structure is that of a self-complementary fin antenna, $Z = 60\pi \Omega \approx 188.5 \Omega$. In order to estimate numerically the impedance of this structure a 1V error

function of approximate risetime 0.2 ns was simulated at the feed edge of the grid. The resulting feed current is depicted in Figure 3.

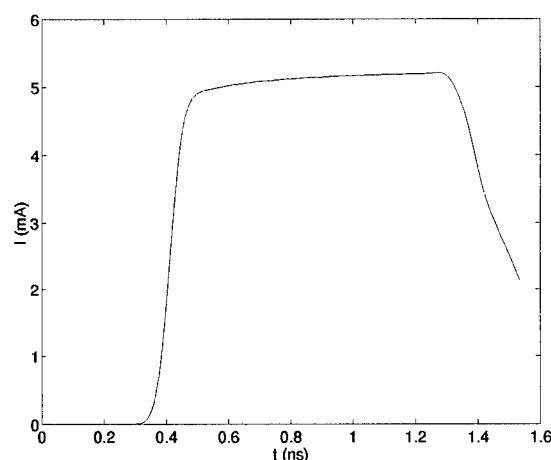


Figure 3 VCA feed current: $\theta = 70^\circ$, $\phi = 45^\circ$.

It may be seen that this current well approximates the voltage waveform although some frequency dependence is apparent before the first reflection from the cone termination, at ~ 1.3 ns. This is to be expected since our structure is finite whereas the ideal VCA is infinitely long. However, it is also expected that a high-frequency limit will exist for the impedance which will equal the characteristic impedance of the infinite structure.

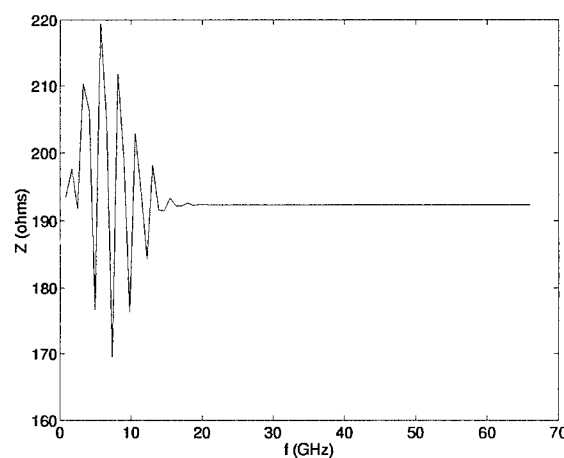


Figure 4 VCA impedance: $\theta = 70^\circ$, $\phi = 45^\circ$.

In order to determine the frequency spectrum of the impedance we neglect the feed current affected by cone termination, after ~ 1.3 ns, and then apply a discrete Fourier transform to the applied voltage and feed current data for this initial interval. The resultant impedance spectrum is depicted in Figure 4. It is apparent that a high-frequency limit exists and closer inspection reveals it to be $Z \approx 192.3 \Omega$. This represents an error of 2% compared with the known characteristic impedance.

One other thing which may be noted from Figure 4 is

that the impedance diverges from the limit only at 20 GHz and below; this corresponds to a range of wavelengths 0.015 m or greater. Noting that the antenna is 0.15 m long, frequency components corresponding to wavelengths of less than an order of magnitude below the antenna length behave as though the structure were infinite. This is to be physically expected in the early-time behaviour.

Simulations on VCAs with $\phi = 45^\circ$ were performed across the range of apex half-angles $30^\circ \leq \theta \leq 90^\circ$; the error in the calculated impedance never exceeded 2% of the known value. Further simulations across a range of apex half-angles $30^\circ \leq \theta \leq 90^\circ$ for VCAs with $\phi = 20^\circ$ have predicted a high-frequency limit within 1.1% of the known value.

In order to verify the model further a grid was designed to simulate a 0.4 m biconical antenna of apex half-angle 46.9° . Such a structure is well known to have a characteristic impedance of $Z = 100 \Omega$, e.g. [13]. A high-frequency limit was again apparent in the calculated impedance spectrum and had value 101.9Ω within 2% of the established result. Similar agreement was found also with other biconical antennas.

From the simulations performed thus far, using this numerical method, it is clear that the characteristic impedance of a TEM antenna may be estimated reliably to within a few percent.

2.1.4 The TEM Horn Impedance

Having validated the numerical approach to transient antenna impedance for a variety of structures, we now note the results of simulating a TEM horn antenna of plate apex angle 40° . For a plate separation of 27° we find that the impedance estimated by the above model is 148Ω . This accords well with the TDR measurement of approximately 140Ω . To numerically estimate an impedance of 100Ω , for a TEM horn with plates of apex angle 40° , we require a plate separation of slightly less than 16° , again in good agreement with the TDR measurements.

2.2 Analytical Impedance Calculation

It must be noted, from section 2.1.4, that the numerical estimate for TEM horn impedance is 48 % greater than the analytical value due to [5]. In view of the expected error for such numerical simulations (typically a few per cent) the results of [5] appear to be clearly in error. This view is supported by the TDR measurements of TEM horn impedance. For this reason, the approach of [5] was re-examined and errors identified in the original approach. We now describe a revised analytical calculation of TEM horn impedance, due to a correction of [5].

2.2.1 The Infinite Noncoplanar Fin

The TEM horn antenna results from truncating the plates of an idealised, infinitely long, noncoplanar fin

antenna, at a certain finite length. The characteristic impedance of the horn is then the impedance of the TEM modes supported on the idealised noncoplanar fin. We begin this section by describing some properties of the idealised structure.

An infinite, noncoplanar fin antenna is a conical structure which supports spherical transverse electromagnetic (TEM) waves. Employing the usual $e^{j\omega t}$ time convention, the magnetic field \vec{H} for conical structures may be written in the form

$$\vec{H} = j\omega\epsilon\nabla \times \left(\vec{r} e^{-jkr} \Pi(\theta, \phi) \right)$$

where \vec{r} denotes the unit vector in the radial direction, the wavenumber k is given by $k = \omega\sqrt{\mu\epsilon}$ and the angular function $\Pi(\theta, \phi)$ satisfies the two-dimensional Laplace equation

$$\left[\sin\theta \frac{\partial}{\partial\theta} \left(\sin\theta \frac{\partial}{\partial\theta} \right) + \frac{\partial^2}{\partial\phi^2} \right] \Pi(\theta, \phi) = 0 \quad (8)$$

Thus, the non-zero components of the electric and magnetic fields corresponding to the transverse electromagnetic (TEM)-mode excited in the structure, are given by:

$$E_\theta = \frac{1}{r} \frac{\partial^2 \Pi_{er}}{\partial r \partial \theta} \quad H_\theta = \frac{j\omega\epsilon}{r \sin\theta} \frac{\partial \Pi_{er}}{\partial \phi} \quad (9)$$

$$E_\phi = \frac{1}{r \sin\theta} \frac{\partial^2 \Pi_{er}}{\partial r \partial \phi} \quad H_\phi = -\frac{j\omega\epsilon}{r} \frac{\partial \Pi_{er}}{\partial \theta} \quad (10)$$

This means that, in structures of this sort, the three-dimensional problem of determining the electric and magnetic fields (and other related quantities) can be reduced to one of solving Laplace's equation for the scalar function $\Pi(\theta, \phi)$ in two dimensions, subject to the appropriate boundary conditions prescribed by the particular antenna configuration. Conformal mapping techniques provide a useful tool in solving field problems of this type and the following sections will now explain the application of these techniques to the noncoplanar fin antenna, with particular emphasis on the calculation of the characteristic impedance of such a structure as a function of its angular dimension.

2.2.2 Conformal Mapping Approach

Consider a pair of infinite, noncoplanar fins which have a common apex O such that the fins are normal to the plane passing through the centre line of each fin, as shown in Figure 5. The half-angle of the fins is ψ_o and the plane of each fin is inclined at an angle of $\theta_o/2$ to the vertical axis ($\theta = 0$), with $0 < \theta_o < \pi$. Denoting the surfaces of the fins satisfying $|\phi| < \pi/2$ and $|\pi - \phi| < \pi/2$ as S_1 and S_2 respectively, then, in truncated form, this geometry describes a triangular plate antenna, fed at the origin, with potentials of $V_o/2$ and $-V_o/2$ applied to S_1 and S_2 respectively.

The boundary condition for $\Pi(\theta, \phi)$ on S_1 , is given by [12]:

$$\frac{V_o}{2} = \lim_{r \rightarrow 0} \int_0^{\theta_o/2} -r E_\theta d\theta \quad (11)$$

and a similar expression holds for S_2 . Upon substitution of E_θ from (9), it follows that

$$\Pi(\theta, \phi) = \begin{cases} jV_o/2k & \text{for any point } P \in S_1 \\ -jV_o/2k & \text{for any point } P \in S_2 \end{cases} \quad (12)$$

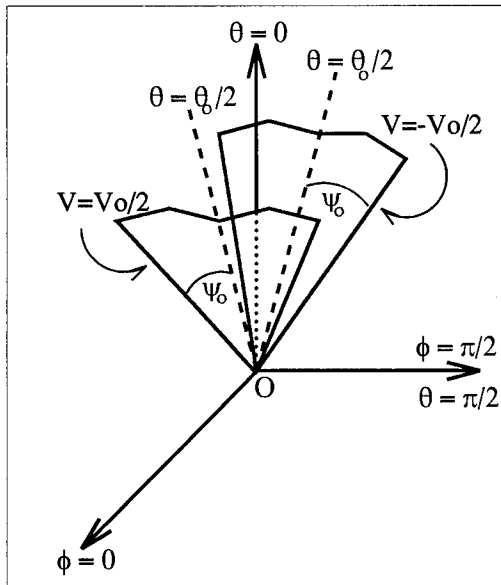


Figure 5 Fin arrangement

Thus, for this particular conical structure, the boundary value problem to be solved is equation (8), subject to the condition (12).

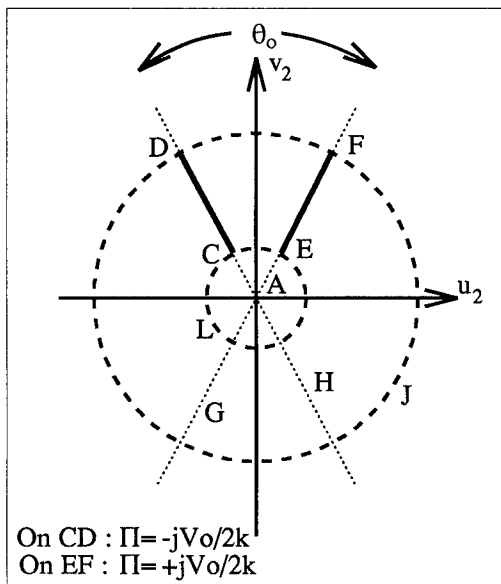


Figure 6 w_2 -plane

The first stage of the analysis is to convert the structure of Figure 5 into a related two-dimensional form. Now, the standard mapping $\rho = \tan \frac{\theta}{2}$, $\phi_c = \phi$, transforms the surface of any sphere $r = \text{constant}$ into the

cylindrical coordinate plane (ρ, ϕ_c) , such that the radial lines $\phi_c = \text{constant}$ describe the spherical coordinate ϕ and the concentric circles $\rho = \tan \theta/2$ correspond to the spherical coordinate θ . By applying this mapping and making use of the change of variables $u_1 = \rho \cos \phi_c$, $v_1 = \rho \sin \phi_c$, the noncoplanar fin structure is transformed into a pair of circular arc segments CD and EF in the w_1 -plane, where EF, CD denote the mapping of fins S_1 and S_2 respectively (- see [5] for a full description of this procedure).

The second stage is to transform these circular arcs into rays in the w_2 -plane, as shown in Figure 6. This is done by means of the bilinear transformation, [5]

$$w_2 = \frac{j + w_1}{1 + jw_1} \quad (13)$$

which maps the fins CD and EF to the pair of rays shown by the solid lines, with $R^{-1} < \rho < R$, $\theta = \pi/2 \pm \theta_o/2$, and R given by $R = \sqrt{(1 + \sin \psi_o)/(1 - \sin \psi_o)}$.

The next stage in Carrel's analysis was to map the structure of Figure 6 onto two collinear slits, by applying the power transformation

$$\sigma = (Rw_2)^{\pi/\theta_o} \quad (14)$$

and then rotating the resulting structure about the origin, in order to align the slits along the real axis. Now, in order for Laplace's equation to be guaranteed invariant under a mapping $\sigma = f(w_2)$, this mapping must be analytic, invertible, possess continuous second derivatives in the domain D_{w_2} and satisfy $f'(w_2) \neq 0$ in D_{w_2} , [14]. However, the transformation (14) violates the invertibility condition because the boundary conditions are incorrectly specified. A discussion of this point is given in [7].

2.2.3 New Approach

An alternative approach to that of Carrel is the application of the principal logarithm, [14], to the function $e^{-j\pi/2} w_2$:

$$w_3 = \text{Log}(e^{-j\pi/2} w_2), \quad w_2 \neq 0 \quad (15)$$

where the argument is such that $-\pi < (\arg(w_2) - \pi/2) \leq \pi$.

This mapping transforms the w_2 -plane into the situation shown in Figure 7 where, as before, the thick lines CD and EF represent the mapping of the fins. The region of interest consists of the infinite strip lying between the shaded boundaries $v_3 = \pm j\pi$. Due to the electrical and geometrical symmetry of Figure 7, attention can be restricted a single quadrant, and so, taking a conductor to be any surface in the w_3 -plane on which the potential functions $\Pi(u_3, v_3)$ is constant, the second quadrant of Figure 7 may be redrawn, as shown in Figure 8, with the shaded regions denoting conducting boundaries and the field lines as shown.

Figure 8 may be converted into a pair of unequal slots on the real axis, as shown in Figure 9, by applying the Schwarz-Christoffel transformation, [16]:

$$w_3(w_4) = \epsilon + \delta \int_0^{w_4} \frac{(w_4 - \alpha) dw_4}{\sqrt{w_4(w_4 - 1)(w_4 - \beta)(w_4 - \gamma)}} \quad (16)$$

where $\alpha, \beta, \gamma, \delta$ and ϵ are constants related to the geometry of the structure and $1 < \alpha < \beta < \gamma$.

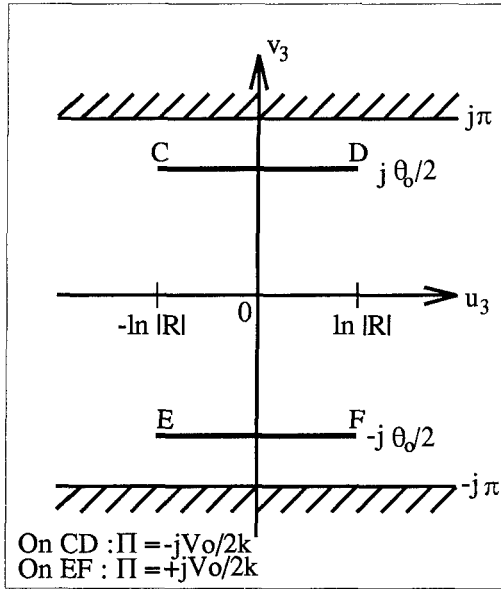


Figure 7 : Fin structure after applying principal logarithm mapping

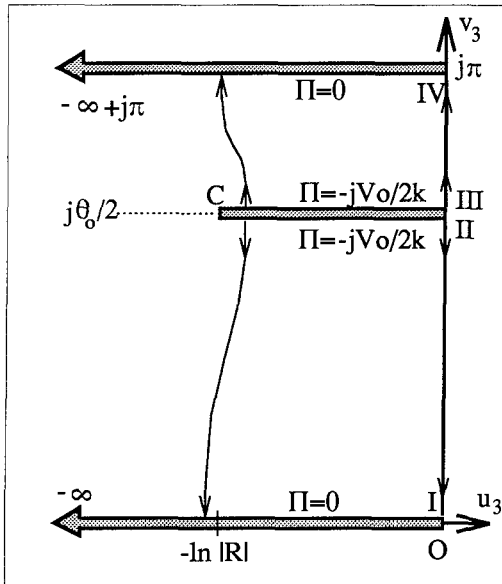


Figure 8 : Second quadrant of Figure 7

In order to determine $\alpha, \beta, \gamma, \delta$ and ϵ , coordinates of appropriate points in the w_3 -plane, and their images in the w_4 -plane, are substituted into equation (16). Since $w_3(0) = 0$, $\Rightarrow \epsilon = 0$ and, from the coordinates of the remaining points II, C, III and IV, a set of 4 equations in the 4 unknowns α, β, γ and δ is obtained. For the purposes of later calculations, these 4 equa-

tions are re-expressed in terms of elliptic integrals of the first and third kinds, [17], giving, after considerable manipulation, a set of equations for the w_4 -plane relating the unknowns, α, β, γ and δ to the physical parameters, θ_0 and ψ_0 , of the system.

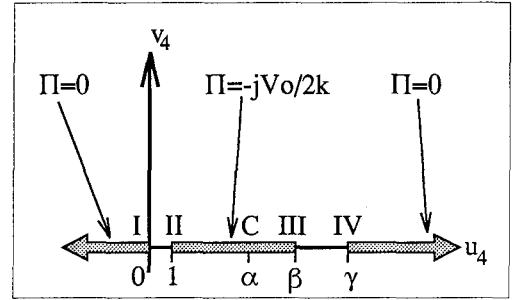


Figure 9 : After Schwarz-Christoffel transformation

Referring to Figure 9, the structure at this point consists of two unequal, collinear slots along the real axis: the dimensions of the slots being determined by the values of α, β, γ and δ . These slots can be mapped onto the more conventional geometry of Figure 10 by means of a bilinear transformation, which has the property of mapping any three points in the w_4 -plane onto three arbitrary points in the w_5 -plane.

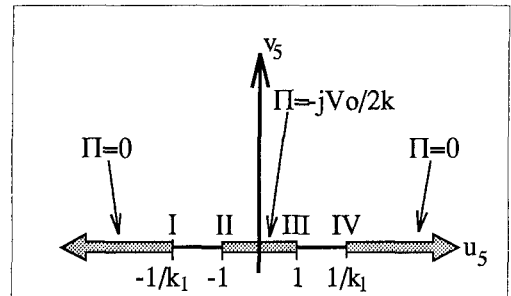


Figure 10 : Collinear slots, in w_5 -plane, after bilinear mapping

The crossproduct of the transformation is of the form:

$$\frac{(w_4 - 0)(1 - \beta)}{(w_4 - \beta)(1 - 0)} = \frac{(w_5 + 1/k_1)(-1 - 1)}{(w_5 - 1)(1/k_1 - 1)}$$

where the value of k_1 is fixed by setting $w_4(IV) = \gamma \Rightarrow w_5(IV) = 1/k_1$. Hence, the following relationship between k_1, β and γ is obtained:

$$\gamma(\beta - 1)k_1^2 - 2\{\gamma(1 + \beta) - 2\beta\}k_1 + \gamma(\beta - 1) = 0 \quad (17)$$

for which the negative root satisfies the required condition that $|k_1^2| < 1$. The final mapping applied to the structure is standard and converts the symmetrical, collinear slots of Figure 10 into a rectangle in the upper half-plane, by means of the Schwarz-Christoffel transformation:

$$w_6(w_5) = \int_0^{w_5} \frac{dw_5}{\sqrt{(1 - w_5^2)(1 - k_1^2 w_5^2)}} \quad (18)$$

The result is shown in Figure 11, where $K \equiv K(k_1)$ and $K' \equiv K(k_1')$ denote complete elliptic integrals of the first kind with modulus k_1 and complementary modulus $k_1' (= \sqrt{1 - k_1^2})$, respectively.

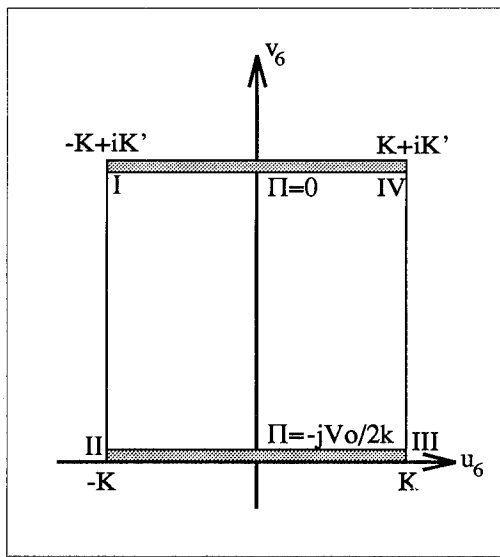


Figure 11 : Final structure in w_6 -plane

Thus the original infinitely long, triangular plate antenna structure has been mapped, by a series of conformal transformations, onto a pair of parallel plates in the w_6 -plane: the associated electric field being mapped *entirely* into the interior of the rectangle I-II-III-IV. It follows that the electric field is uniform within the rectangle, with the potential being given by

$$\Pi(\theta, \phi) = -\frac{jV_0}{2k} \left[1 - \frac{v_6}{K'} \right] \quad (19)$$

Analytic expressions for the components of the electric and magnetic field are specified by (9), (10) and (19). However, fully explicit analytic expression for $\partial\Pi(\theta, \phi)/\partial\theta$ and $\partial\Pi(\theta, \phi)/\partial\phi$ are not available because w_4 is *implicitly* defined in terms of w_3 in equation (16). The noncoplanar fin is thus less tractable than the V-conical antenna, as studied by Shen [12], for which the field expressions are fully explicit.

Nevertheless, although explicit expressions for the electric and magnetic field components are unavailable, the characteristic impedance may be derived directly by examination of Figure 11. For a transmission line, the characteristic impedance is given by, [18],

$$Z_o = \eta\epsilon/C$$

where C is the capacitance per unit length, η is the intrinsic impedance of the medium inside the transmission line and ϵ is the permittivity. Therefore, for the parallel plate configuration of Figure 11, the characteristic impedance is

$$Z_o = \eta d/b$$

where d is the distance between the plates and b is the width of the plates. Note that this is the *exact* solution; there are no fringing effects, because the total electric field in the w_5 -plane is mapped into the *interior* of the period rectangle in the w_6 -plane. Upon substitution, the final expression for the characteristic impedance of the noncoplanar fin antenna is

$$Z_o = \eta \frac{K'}{2K} \quad (20)$$

where k_1 , the modulus of the elliptic integrals K and K' , is obtained from equation (17).

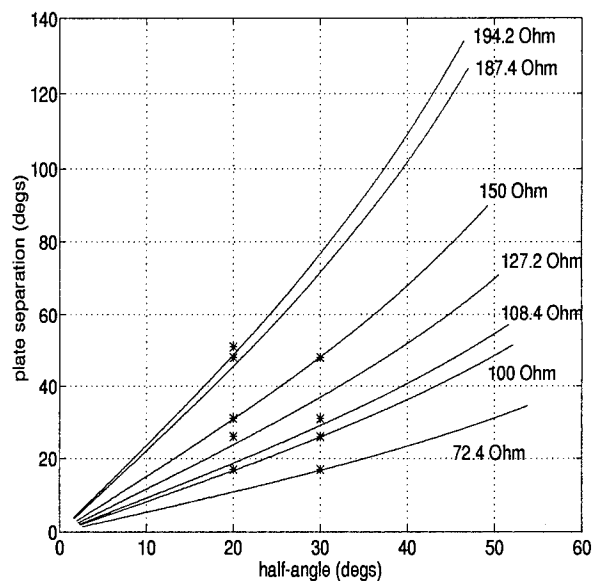


Figure 12 : Calculated Z_o curves for free-space antenna structure with experimental values (*)

2.2.4 Solution Procedure

In section 2.2.3, an expression was derived for the characteristic impedance of a noncoplanar antenna, in terms of elliptic integrals of the first kind. The general form of this equation is common to several other conical antenna configurations, such as the V-conical, [12] and the coplanar fin antenna, [5]. However, in contrast to the two above-mentioned cases, the modulus k_1 of the elliptic integrals in (20) is not directly related to the physical features of the antenna but is instead related to θ_o and ψ_o via the intermediate parameters β and γ , which arise during the w_4 -plane mapping. This means that an indirect approach to the solution of (20) has to be taken.

Essentially, the solution procedure chooses a particular value for the free-space characteristic impedance Z_o , thereby determining the modulus k_1 and then fixes the value of γ . The remaining unknowns α , β and δ are then determined by solving the appropriate equations, finally yielding a plate separation angle θ_o and a plate half-angle ψ_o corresponding to these selected values. By repeating the exercise for a range of γ values, a plot of θ_o vs. ψ_o is then obtained (*i.e.* for a fixed impedance, θ_o is determined as a function of ψ_o).

2.2.5 Theoretical and Experimental Results

A Fortran program was written to evaluate the various quantities in the above-mentioned solution procedure, the elliptic integrals being calculated using Numerical Recipes, [19], routines. The output of the program is a curve of plate separation angle, θ_o , vs half-angle, ψ_o , for a specified free-space characteristic impedance value. Figure 12 shows a selection of these curves (solid lines), corresponding to a range of Z_o .

In order to verify these results, Time Domain Reflectometry (TDR) measurements were also carried out, using a triangular plate of either 20° or 30° half-angle, supported at various elevation angles to a ground plane: the structures therefore having half of the corresponding free-space characteristic impedance. A Tektronix 11801A oscilloscope was used to display plots of ρ , a dimensionless parameter related to the characteristic impedance as follows:

$$Z = Z_{ref} \frac{1 + \rho}{1 - \rho} \tag{21}$$

where $Z_{ref} = 50\Omega$. By means of cursors, measurements of ρ were taken at the apex of the antenna, the accuracy in ρ being ± 0.04 (non-dimensional) units. Tables 1 and 2 below list the various elevation angles, equal to half the corresponding free-space separation angles, and their associated ρ and Z_o values.

0.3m plate - 30° half-angle			
Elevation angle	ρ	$Z_o(\Omega)$	$\Delta Z(\Omega)$
8.5°	-0.16	36.2	± 2.97
13.0°	0.0	50.0	± 4
15.5°	0.04	54.2	± 4.34
24.0°	0.2	75.0	± 6.25

Table 1

1.0 m plate - 20° half-angle			
Elevation angle	ρ	$Z_o(\Omega)$	$\Delta Z(\Omega)$
8.5°	0.0	50.0	± 4.00
13.0°	0.12	63.6	± 5.17
15.5°	0.2	75.0	± 6.25
24.0°	0.304	93.7	± 8.27
25.5°	0.32	97.1	± 8.64
40.5°	0.4	116.7	± 11.1

Table 2

Also listed are the errors, ΔZ , in the final impedance values, calculated from (21). These results are plotted in Figure 12, along with the corresponding predicted impedance curves.

Some of the experimental points in Figure 12 do not lie exactly upon the predicted curves; however, when measurement error is taken into account it is found that all of the points lie well within the predicted lower and upper impedance bounds. For example, the 20° half-angle, 13° elevation antenna, has a predicted free-space impedance value of 130Ω ; and measured value

lies in the range $(63.6 \pm 5.17) \times 2 \Omega$. By contrast, Carrel's calculations erroneously predict the impedance of this antenna to be 100Ω .

2.3 Conclusion

In this section two new approaches to the determination of transient antenna impedance have been described. One, a new conformal mapping approach, is applicable to TEM horn antennas. This analysis has identified the source of the error in the original treatment of such structures by Carrel, [5], and has demonstrated that, by a different choice of transformations, a correct expression for the impedance can be determined. The other numerical approach, based on a numerical solution of the EFIE, is applicable to a wide range of transient antennas. Both methods have been verified by comparison with experimental (TDR) measurements and are in excellent agreement with these. As a result, a strong degree of confidence in the prediction of TEM impedances has been established.

3. HORN PROFILING

In order to maximise the power radiated by a TEM horn, or similar aperture antenna, two criteria must be borne in mind. Firstly, it is desirable to match the impedance of the antenna, at the feed-point, to that of the transmission line feeding it. The impedance of the line is matched to that of the power source, or generator, and is thus pre-determined. Secondly, it is desirable to match the impedance of the antenna, at the radiating aperture, to that of free-space; again this impedance is fixed. It proves most efficient to match the impedance of the antenna to that of the transmission line. This ensures a maximum transfer of power from the source to the radiating elements. The impedance of such lines, typically 50Ω , differs significantly from that of free-space, $120\pi \Omega \approx 377 \Omega$. The impedance mismatch between the radiating aperture and the free-space surrounding it means that the transfer of power from antenna to free-space is not efficient. It can also give rise to potentially corruptive late-time reflections in the radiated pulse train.

If the impedance of the antenna feed-point is to be matched to the generator and the feed-line then any improvement to radiation from the aperture must result from a variation in impedance along the antenna arms. If the impedance of the antenna were increased towards the radiating aperture (and the aperture mismatch lessened) then the power radiated by the antenna might be increased, and any corruption of the pulse train by late-time reflections reduced.

There are two ways in which the antenna impedance might be varied along the arms: continuously and discretely. An example of the latter approach is the tri-impedance horn described in [20]. One limitation on the effectiveness of such a design is the abrupt change in impedance at discrete points along the antenna

arms. Such abrupt changes in the antenna impedance will necessarily give rise to reflected signals and power losses. Although these might be sufficiently small that a significant gain in radiated power could be achieved, it might be that a continuous change in impedance along the antenna arms would be more effective in increasing the power radiated by the antenna.

One way to effect a continuous increase in the impedance of a TEM horn, or similar aperture antenna, is to *flare* the plates away from each other. This will smoothly increase the impedance of the antenna, since the effective angular separation of the antenna arms is continuously increasing, towards the aperture. In this section we describe the effects of an exponential flaring of an aperture antenna, on its radiated far-field. We adopt a numerical approach, based on the electric field integral equation (EFIE), suitable for the simulation of directive, transient antennas, see [10]. (This approach is similar to that of section 2.1 but employs an injected current model, for the antenna feed, rather than a voltage source).

3.1 The V-cut antenna

In order to rigorously investigate the effects of an exponential flaring on the radiated far-field of an aperture antenna, we must first determine a suitable antenna design. The obvious choice of a triangular plate TEM horn (or non-coplanar fin antenna) is unsuitable. We wish to investigate a range of antenna lengths, for a given pulsewidth, but long surface antennas (of 10 pulsewidths or more) prove to be prohibitively computationally expensive.

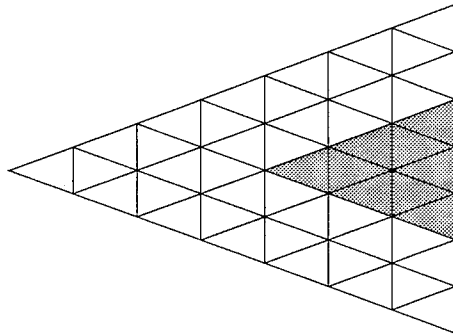


Figure 13 Mesh design of V-cut antenna.

Instead, we consider a V-cut antenna. This is essentially a linear-type antenna with two arms running out from the feed-point. It can be created from a triangular plate TEM horn antenna by removing a central, triangular portion of each plate, leaving a V or A shape (see Figure 13). The number of patches required to mesh a V-cut will increase linearly with length, rather than as the square of antenna length, as is the case for surface antennas. The computational burden of a V-cut antenna is therefore much smaller than that of a TEM horn, or similar surface antenna.

Despite this great difference in computational burden however, there is a great similarity in the behaviour of V-cut and TEM horn antennas. The majority of the current propagating along the plates of a TEM horn is confined to the edges. Thus, if a central portion of each plate is removed then the essential physics of the antenna will remain unaltered. The V-cut remains an aperture antenna, radiating the derivative of an applied transient pulse. The only significant difference lies in the lack of a small current contribution to the centre of the radiating aperture of the V-cut antenna. This which makes the V-cut slightly less directive than the full-plate structure. However, the V-cut antenna design provides a powerful computational tool for investigating the behaviour of aperture antennas, the computational burden associated with such a design being comparatively small.

3.2 Exponential flaring

We now describe the nature of the exponential flaring itself. We assume that the azimuth (ground) plane of the antenna is the xy -plane and that the axial line (boresight) is the positive x -axis. We take the origin of our coordinate system to be at the feed-point of the antenna. The surface of the V-cut antenna may now be described by a profile in the xz -plane. For the unflared antenna this profile is given by:

$$z = \pm lx, \quad 0 \leq x \leq L_x, \quad (22)$$

where $l = \tan \theta$, each flat plate making an angle of θ with the azimuth plane. θ will be called the launch angle of the antenna or the plate elevation angle. L_x is the length of the projection of the plate onto the x -axis; this is determined from the actual plate length a . For unflared V-cut antenna plates, $L_x = a \cos \theta$.

We may now introduce an exponential flaring to the antenna design by defining the plate profile in the following manner:

$$z = \pm \left(\frac{\exp(\alpha lx) - 1}{\alpha} \right), \quad 0 \leq x \leq L_x, \quad (23)$$

where, again, $l = \tan \theta$. α is a variable parameter which determines how rapidly the profile of the antenna flares; if x and z are measured in m then α is measured in m^{-1} . L_x , the length of the plate profile projected onto the x -axis, must now be determined from the arc-length of the profile. For an antenna of plate length a :

$$a = \int_0^a ds = \int_0^{L_x} \sqrt{1 + \left(\frac{dz}{dx} \right)^2} dx, \quad (24)$$

which may be solved numerically for L_x .

The profile determined by equation (23) has the following property. If x is small then $z \approx lx$. Hence, near the origin (or near the feed-point of the antenna), the profile approximates a flat plate of launch angle θ . This means that the impedance of the feed region

of the antenna can be well matched to a feed-line of constant impedance. The exponential increase in the profile should continuously increase the impedance of the antenna towards the radiating aperture, as is desired.

It may also be noted that:

$$\lim_{\alpha \rightarrow 0} \left(\frac{\exp(\alpha l x) - 1}{\alpha} \right) = l x, \quad (25)$$

so that the unflared profile of equation (22) is a limiting case of the general, exponentially flared profile of equation (23).

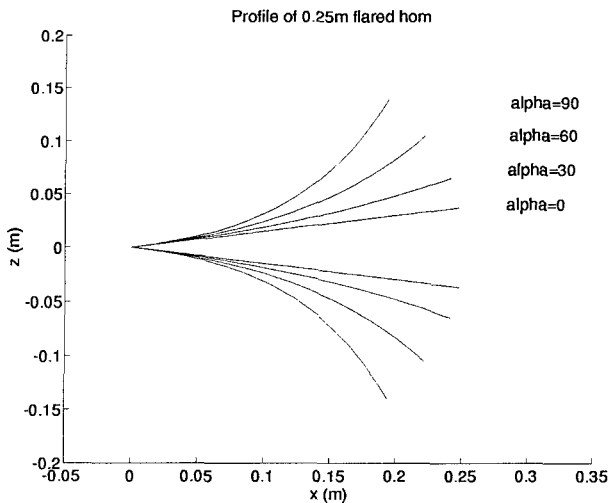


Figure 14 Flared profile of 1/4 m horn.

Figure 14 depicts the profile of a 1/4 m V-cut antenna of launch angle 8.5° , for a range of α ($\alpha = 0 \text{ m}^{-1}$, $\alpha = 30 \text{ m}^{-1}$, $\alpha = 60 \text{ m}^{-1}$ and $\alpha = 90 \text{ m}^{-1}$). It is clear that the feed region of each profile does indeed approximate a flat plate of elevation 8.5° , even for the most rapidly flaring profile, $\alpha = 90 \text{ m}^{-1}$. It is also clear that, for such a range of α , the *effective* plate separation angle at the radiating aperture (given by the angle between the x -axis and a line tangential to the end of the profile) can be considerably larger than 8.5° . Hence the impedance of the flared V-cut can vary considerably along its length.

3.3 Results For Flaring Simulations

In order to assess the effect of an exponential flaring on the radiated far-field of a general, transient, aperture antenna a range of lengths (compared with the transient pulsewidth) are investigated.

The driven antenna behaviour is simulated using the electric field integral equation approach described in [10], with a current fed across the apex edge of each plate. The (equivalent) applied voltage, for all simulations, is taken to be a pulse step (error function) of magnitude $\sim 4 \text{ kV}$ and risetime $\sim 100 \text{ ps}$. All antenna designs are V-cuts of impedance 50Ω (launch angle 8.5° , plate apex half angle 20°). The (isocles) triangular patches of the antenna mesh are approximately 0.75 cm long, with a base of approximate width

0.55 cm and an apex angle of 40° . The arms of each V-cut mesh consist of 3 rows of patches and are therefore $\sim 1.65 \text{ cm}$ wide at the aperture; the perpendicular arm width is approximately $1.65 \cos 20^\circ \approx 1.55 \text{ cm}$. Four lengths of plate are simulated: 0.20 m (approximately 6.7 pulsewidths in length); 0.33 m (~ 11 pulsewidths); 0.50 m (~ 16.7 pulsewidths); and 1.00 m (~ 33.3 pulsewidths). The plate length is never so small as to be comparable with the width of the applied pulse, hence none of the antenna designs is electrically short. The antennas may therefore be assumed as supporting TEM (spherical) waves.

The results of flaring these four V-cut antenna designs are depicted in Figures 15, 16, 17 and 18.

It is clear that flaring the plates of an aperture antenna, according to an exponential law, can significantly increase the peak radiated field, without necessarily distorting the radiated waveform.

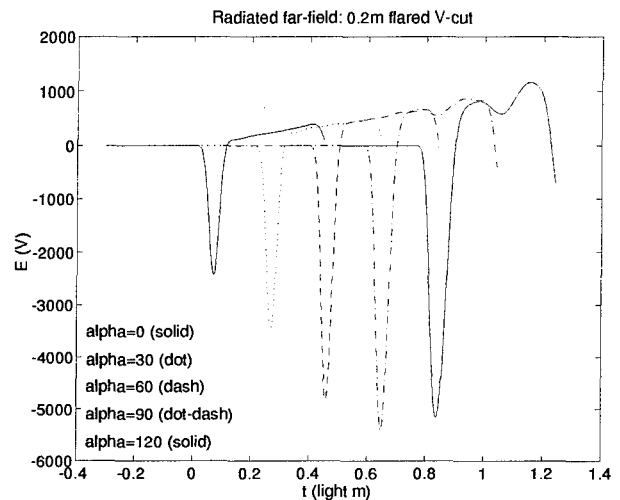


Figure 15 Flared 1/5 m V-cut far-field.

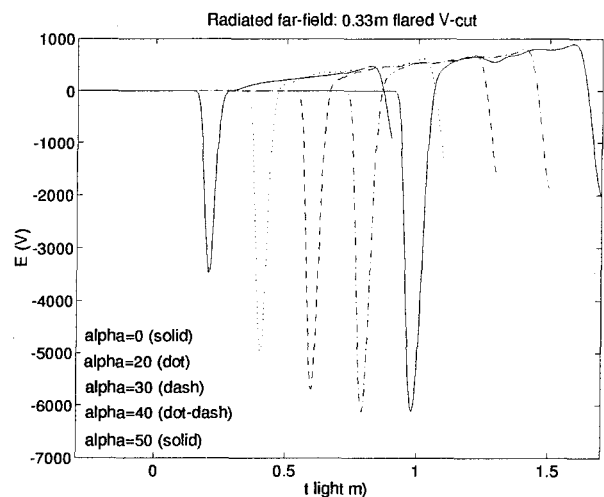


Figure 16 Flared 1/3 m V-cut far-field.

The most significant increase in the magnitude of the radiated far-field is for the shorter antenna designs. In the case of the 0.20 m antenna the peak far-field

increases by more than a factor of 2.2, whilst for the 0.33 m structure the increase exceeds a factor of 1.7. The longer antennas show a less pronounced effect. In the case of the 0.50 m V-cut, the peak far-field increases by a factor of ~ 1.4 , and for the 1.00 m V-cut the increase is by a factor of ~ 1.3 .

The radiated waveform is also more distorted in the case of these longer antennas. For the 0.20 m and 0.33 m V-cut simulations, no significant change in the radiated waveform is apparent with increasing α . For the 0.50 m V-cut antenna there is no appreciable waveform distortion for $\alpha \leq 20 \text{ m}^{-1}$; however, as this value of α is passed, the pulsewidth of the waveform begins to broaden ($\alpha = 30 \text{ m}^{-1}$). In the case of the 1.00 m antenna however a considerable distortion of the radiated waveform is apparent even for $\alpha = 10 \text{ m}^{-1}$ which produces the peak far-field strength. The radiated waveform for a flaring of $\alpha = 20 \text{ m}^{-1}$ is fundamentally different to that for the unflared 1.00 m V-cut with $\alpha = 0 \text{ m}^{-1}$.

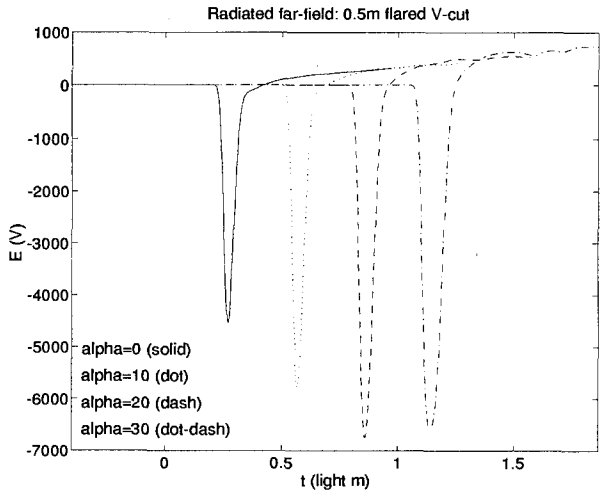


Figure 17 Flared 1/2 m V-cut far-field.

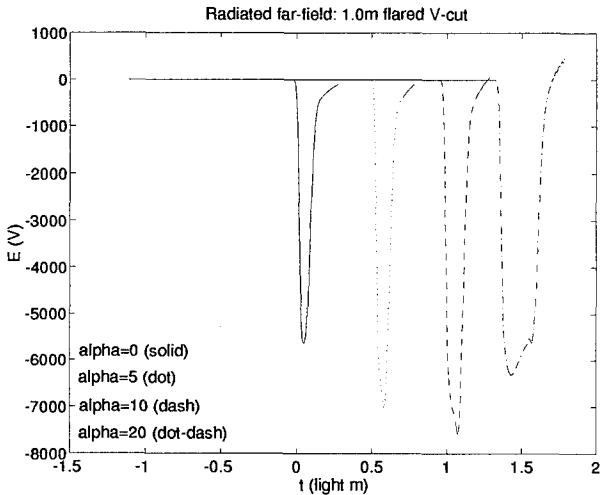


Figure 18 Flared 1 m V-cut far-field.

There are at least two significant phenomena which could cause a distortion of the radiated waveform from

the time-derivative expected for a TEM horn of small launch angle, at comparatively large values of α .

Firstly, it is clear from Figure 14 that the surface of a flared V-cut antenna is not defined by radial lines, as is the case for an unflared antenna. Hence the flared V-cut antenna will not strictly be a TEM antenna. Since the surface of the antenna varies smoothly however, it might be thought that a TEM spherical wave introduced at the (locally radial) feed region might be transmitted along the antenna without suffering appreciable dispersion. This would appear to be true of the shorter antennas, Figures 15 and 16. There will be a critical flaring beyond which TEM modes of propagation could not be supported as far as the aperture, however. If such a flaring were exceeded then dispersion of the different frequency components would become an important consideration.

Secondly, for large values of the flaring parameter α , the antenna plates become steeply inclined to the azimuth (ground) plane near the aperture. The antenna will then be, essentially, a coplanar fin antenna (or TEM horn of large elevation) rather than a low elevation TEM horn antenna. Whilst the latter structure will radiate the time-derivative of the applied voltage, the former structure radiates a faithful copy of the voltage waveform (see, for instance, [21] or [20]). A similar phenomena can be observed in the case of transient radiation from wide-angle biconical antennas (see [22]). Hence, as α increases, a transition in the radiated far-field might be expected, from the time-derivative of the applied bias to a faithful copy of that waveform. It might be noted, in this context, that the far-field of the greatly flared, long antenna ($\alpha = 20 \text{ m}^{-1}$, Figure 18) appears to be developing a step-like character.

It would be difficult to tell from these results exactly which kind of waveform distortion might be physically significant for this particular range of parameters. More importantly however, it is clear that, for the shorter antennas (0.20 m and 0.33 m), no such effects are predicted. It must also be remembered that these designs gave the most significant increase in peak radiated field strength, with flaring.

3.4 Conclusion

It is clear that flaring, according to an exponential law, can significantly improve the radiated field of an aperture antenna. In particular, for shorter TEM antennas the peak radiated far-field can more than double under an optimal flaring. In such a case the radiated waveform remains essentially unaffected by plate curvature. In contrast, for longer antennas the peak radiated field increases by only a factor of 1.3, or so. In addition, the radiated waveform suffers considerable distortion compared with that of the unflared structure.

4. CONCLUSION

In producing practical TEM antennas for wide band applications two considerations are important. The first is a correct understanding of the behaviour of the idealised, infinite TEM structure on which the antenna is based. The second is an understanding of how to optimise the practical antenna, created by truncating that infinite structure. Only when *both* aspects of antenna design have been properly addressed can an optimal design be reliably produced.

In this paper we have considered both of these aspects for a TEM horn antenna. We have demonstrated analytical and numerical methods for calculating the characteristic impedance of a TEM horn; these methods verify earlier experimental measurements. We have also demonstrated the potential of profiling the horn for improving the radiated far-field of such antennas.

5. ACKNOWLEDGEMENT

This work was supported by the Defence Research Agency, UK.

References

- [1] J.J.A. Klaasen, *Outline of a Nuclear EMP Simulator for Ships (EMPSIS)*, Proceedings of the 10th International Zurich Symposium on Electromagnetic Compatibility, pp 317-322, 1993.
- [2] M. Kanda, *Time-Domain Sensors for Radiated Impulse Measurement*, IEEE Trans. Antennas Propagat., AP-31, pp 438-444, 1983.
- [3] D.M. Parkes, M.F. Lewis, R.L.S. Devine, K. Trafford and D. Richardson, *Practical Measurements using Ultrawideband Radar*, Ultrawideband Radar, SPIE Vol 1631, pp 232-242, 1992.
- [4] E.G. Farr and C.E. Baum, *Prepulse Associated with the TEM Feed of an Impulse Radiating Antenna*, Sensor and Simulation Notes, Note 337, 1992.
- [5] R.L. Carrel, *The Characteristic Impedance Of Two Infinite Cones Of Arbitrary Cross Section*, IRE Trans. Ant. Prop., AP-6, pp 197-201, 1958.
- [6] S.M. Booker and A.P. Lambert, *A Consideration of the Impedance of TEM Antennas*, DRA Research Report 3, University of Dundee, April 1993.
- [7] A.P. Lambert, S.M. Booker and P.D. Smith, *Calculation of the Characteristic Impedance of TEM Horn Antennas by Conformal Mapping Techniques*, submitted to IEEE Trans. Antennas Propagat.
- [8] S.M. Booker, A.P. Lambert and P.D. Smith, *A Determination of Transient Antenna Impedance via a Numerical Solution of the Electric Field Integral Equation*, submitted to Journal of Electromagnetic Waves and Applications.
- [9] B.P. Rynne, *Time Domain Scattering from Arbitrary Surfaces Using the Electric Field Integral Equation*, J. Electromag. Waves and Applic., Vol 5, pp 93-112, 1991.
- [10] A.P. Lambert and S.M. Booker, *The Simulation of Fields Radiated by Directive, Transient Antennas*, DRA Research Report 2, University of Dundee, December 1992.
- [11] S.M. Rao, D.R. Wilton and A.W. Glisson, *Electromagnetic Scattering by Surfaces of Arbitrary Shape*, IEEE Trans. Antennas Propagat., AP-30, pp 409-418, 1982.
- [12] H.M. Shen, R.W.P. King and T.T. Wu, *V-Conical Antenna*, IEEE Trans. Antennas Propagat., Vol. AP-36, pp 1519-1525, 1988.
- [13] S.A. Schelkunoff and H.T. Friis, *Antennas, Theory and Practice*, Wiley, New York, 1952.
- [14] L.A. Rubinfeld, *A First Course in Applied Complex Variables*, John Wiley and Sons, New York, 1985.
- [15] B.A. Fuchs and B.V. Shabat, *Functions of a Complex Variable and Some of their Applications*, Volume 1, Pergamon Press, Oxford, 1964.
- [16] A. Jeffrey, *Complex Analysis and Applications*, CRC Press, Florida, 1992.
- [17] I.S. Gradshteyn and I.M. Ryzhik, *Tables of Integrals, Series, and Products*, Corrected and Revised Edition, Academic Press, London, 1980.
- [18] R.E. Collin, *Field Theory of Guided Waves*, 2nd Edition, IEEE Press, New York, 1991.
- [19] W.H. Press, S.A. Teukolsky, W.T. Vetterling and B.P. Flannery, *Numerical Recipes in Fortran*, 2nd edition, Cambridge University Press, Cambridge, 1992.
- [20] P.D. Smith, *Transient Antennas*, MOD Report 7, University of Dundee, March 1989.
- [21] P.D. Smith and D. M. Parkes, *Compact and Directive Transient Antennas*, Proceedings of the 7th Int. Conf. Ant. Prop., pp 558-561, 1991.
- [22] C.W. Harrison, Jr and C.S. Williams, Jr, *Transients in Wide-angle Conical Antennas*, IEEE Trans Antennas Propagat., AP-13, pp 236-246, 1965.

ANALYSIS OF INTERACTION OF HPM WITH COMPLEX STRUCTURES

S. Kashyap and A. Louie
 Defence Research Establishment Ottawa
 Ottawa, Ontario, Canada
 K1A 0Z4

ABSTRACT

This paper concerns the use of time- and frequency-domain methods for computing the interaction of high power microwaves with simple and complex structures. Effects of various factors — the geometric modelling of the structure, the Fourier transformation, the shape of the incident pulse, etc. — on the CPU-time and the accuracy of the solution are demonstrated. Results of our computations for various structures are presented.

INTRODUCTION

Use of time-domain methods such as the FDTD for modelling a wide variety of electromagnetic interaction problems has been increasing in popularity for a number of years. Application of the FDTD method has included modelling very complex structures such as the human body, microstrip and microwave structures, radar cross-section computations and inverse scattering [1]. Response can be obtained directly in the time domain, or in the frequency domain through a fast Fourier transformation (FFT).

Frequency-domain codes such as the NEC [2] and JUNCTION [3] have also been extensively used for electromagnetic analysis of a wide variety of structures. Response obtained in the frequency domain can be converted to time domain using an inverse fast Fourier transformation (IFFT).

The choice between a frequency-domain method and a time-domain method for modelling and analyzing a specific electromagnetic interaction is not always straightforward. This paper investigates the effect of a number of factors on the accuracy of the solution obtained. These factors include incident field wave shape, geometric modelling of the structure, Fast Fourier Transformation (FFT or IFFT), and computer time considerations.

PROCEDURE

Figure 1 shows some of the cylindrical structures with apertures and slots chosen for this study. A plane wave with a Gaussian waveform is assumed to be incident on the structure. The FDTD method is used to compute time-domain fields at various points inside and outside the cylinder for two incident plane wave polarizations. Frequency-domain response is obtained by taking an FFT of the time-domain response, with de-convolution of the incident waveform, resulting in a waveform-independent frequency response (i.e. the transfer function). This response is then compared with the frequency domain response obtained by the moment method implementation of the electric field integral equation (EFIE).

Since both the FDTD method and the EFIE method have been well described in the literature only a minimal description essential for this paper is given here. The theme of this paper is the *comparison* of frequency-domain results obtained from the two methods, rather than the intricacies of the methods themselves.

a. FDTD Method:

The FDTD method is a direct implementation of the time-dependent Maxwell's equations:

$$\begin{aligned}\epsilon \frac{\partial \mathbf{E}}{\partial t} + \sigma \mathbf{E} &= \nabla \times \mathbf{H} \\ \mu \frac{\partial \mathbf{H}}{\partial t} &= -\nabla \times \mathbf{E}\end{aligned}\quad (1)$$

The finite-difference procedure proposed by Yee [4] positioned the \mathbf{E} and \mathbf{H} fields at half-step intervals around a unit cell (Yee cell), where \mathbf{E} and \mathbf{H} are evaluated at alternate half time steps, effectively giving centred difference expression for both space and time derivatives. For example, taking one of the three partial differential equations associated with each of the vector equations above gives

$$\begin{aligned}\frac{\partial E_z}{\partial t} &= \frac{1}{\epsilon} \left(\frac{\partial H_y}{\partial x} - \frac{\partial H_x}{\partial y} - \sigma E_z \right) \\ \frac{\partial H_z}{\partial t} &= \frac{1}{\mu} \left(\frac{\partial E_x}{\partial y} - \frac{\partial E_y}{\partial x} \right)\end{aligned}\quad (2)$$

Rewriting them in finite difference form yields a complete system of six finite-difference equations which then provides a computational scheme: the new value of a field vector component at any point depends only on its previous value and on the previous values of the components of the other field vector at adjacent points. Thus at any given time step the computation can proceed one point at a time for a single processor, or several points at a time for a machine with parallel processors.

b. EFIE Method:

Reference [5] describes a simple and efficient numerical procedure for scattering by arbitrarily shaped bodies, using the moment method to solve the electric field integral equation (EFIE). The object surface is modelled as a finite union of planar triangular patches. Because of the EFIE formulation, this procedure is applicable to both open and closed surfaces. It has been applied to a wide variety of electromagnetic interaction problems and has yielded excellent correspondence with measurement and other numerical methods. In JUNCTION, the EFIE approach is extended to analyze an arbitrary configuration of conducting wires and bodies. The algorithm developed [5] can handle wire-to-wire, surface-to-surface, and wire-to-surface junctions. A modified version of JUNCTION is used here as the "EFIE method".

PLANE WAVE FORM

In this study, the time-domain incident wave on a structure is a Gaussian plane wave (Figure 2a). Figure 2b shows the frequency spectrum of this pulse. Note that 1% and 0.1% of peak value are reached at about 2.9 GHz and 3.6 GHz, respectively. A narrower time-pulse will have a wider frequency spectrum.

GEOMETRIC MODELLING

All electromagnetic simulation codes require the structure to be represented geometrically in a specified manner. DIDECDREO is a program used for this purpose. It creates wire grid, surface patch and cell models for electromagnetic interaction analysis. Figure 3 shows a block diagram of the DIDECDREO structure. The program allows a structure to be created or altered interactively. Several files can be merged

together, allowing the creation of complicated structures by parts. The results associated with one or multiple input or output files can be displayed dynamically on one or more viewports. The structure to be analyzed can be input in various ways. Numerical entry of vertices on a keyboard, digitization of a blueprint with a graphics tablet, input files of one of the EM analysis programs (NEC, EFIE, FDTD, etc.), a built-in library of shapes which can be merged, and AutoCAD DXF files are the present means for creating a structure. Once a structure has been stored in DIDECD format, the program allows one to create input files for a number of electromagnetic analysis codes such as NEC (Numerical Electromagnetic Code), TWTDA (Thin Wire Time Domain Analysis Code), EFIE (Electric Field Integral Equation Code) and FDTD (Finite Difference Time Domain Code). Figure 4 shows a cylindrical structure modelled as triangular patches for analysis using the EFIE code. Figure 5 shows the same cylinder as a union of Yee cells for analysis using the FDTD code.

EFIE RESULTS FOR A CYLINDER WITH OPENINGS

Figure 6 shows a cylinder with an aperture and three slots used in the study. It also shows a rectangular metal plate to simulate a circuit board. Three configurations of the connection between the cylinder and the metal plate, as well as two different pulse directions, are used. Figure 7 shows some of the EFIE results for one of the configurations at 1.1 GHz. It shows a three dimensional E-field plot at a transverse section at the centre of the cylinder. It also shows the corresponding E-field contour plot. The three dimensional plot and the contour plot show the distribution of E-fields in and around the cylinder and the concentration of these fields at the slots.

FDTD RESULTS AND COMPARISON IN THE FREQUENCY DOMAIN

The surface of the cylinder and plate occupies about 2800 Yee cells, centrally located within an FDTD cell space of 81×81×81 cells. The centre of the cylinder is chosen for comparison and only the Ez-field is shown for both axial and transversal illuminations. A Gaussian pulse as described before is assumed to be incident on the cylinder. Figures 8 and 9 show the Ez-field obtained from a Fast Fourier transformation with de-convolution of the incident pulse. For comparison the corresponding results from the EFIE-based JUNCTION method are also shown. The comparison between the two methods is very good. Some disagreement exists between the peak magnitude at the resonance frequencies.

CPU-TIME CONSIDERATIONS AND MODELLING GUIDELINES

We have shown that in computer simulations of the interaction of electromagnetic waves with geometric structures, both time- and frequency-domain codes may be used. The two independent methods are comparable — as long as proper precautions are taken — and can be used as verification of the accuracy of each other.

From an efficiency, i.e. CPU-time economy, point of view, the FDTD method with an incident Gaussian pulse is the approach of choice. For this example, running EFIE takes about 4 hours of CPU-time on a VAX 6420 *for each frequency*, running FDTD with the Gaussian pulse (2049 time steps) takes 14 hours. Other geometric configurations also have a similar CPU-time ratio, that the CPU-time taken for EFIE(one frequency) :: FDTD(Gaussian) is 1::3.5.

The reason that FDTD(Gaussian) is the most efficient is that the time-domain response decays back to zero rapidly, and that after a complete run, one can Fourier-transform the results (with de-convolution of the Gaussian pulse) and obtain the field response *for all frequencies* (within the wide frequency spectrum of the Gaussian pulse). In other words, in the time it takes EFIE to run less than four frequencies, the process

$$\begin{aligned} &\text{FFT/Gaussian [FDTD(Gaussian)]} \\ &= \text{EFIE(all frequencies)} \end{aligned}$$

gives the whole frequency spectrum of responses. Because frequency-domain response comparison, with FFT(FDTD) versus EFIE, has been shown to be reasonably accurate, this process is a reliable and time-saving method in obtaining frequency-domain data.

Thus, in summary, the merits of the FDTD method with an incident Gaussian pulse, followed by a time-to-frequency Fourier transform, are:

- a. large frequency content of the incident pulse,
- b. pulse decays down to zero rapidly, minimizing running time, and
- c. efficiency: one time run to obtain all frequencies.

(Note, however, there is nothing “magical” about the Gaussian pulse itself: any time-domain pulse of narrow pulse width would share the same merits. The Gaussian pulse is chosen because of its simple analytic form and because it is a “standard”.) The main disadvantage is due to computer resources, that only the chosen field quantities at several specified points are written to the output (although all six field components at all the Yee cells are evaluated at each time step, due to the

constraint of the size of the output file only those chosen ones are written out). The code must be run again for computation of other field components and at other points. (As a contrast, in EFIE the currents on all the edges are stored in an output file. So the field values at any other points *at the same frequency* can be calculated from this “currents file” and EFIE does not have to be rerun.)

Time-domain response comparison has some inherent inaccuracies, mainly due to the fact that difference equations are by definition *approximations* to differential equations. In FDTD versus IFFT(EFIE), care has to be taken in finding the correct field locations for direct comparisons.

Finally, it must be remembered that discretization errors can be significant. In the FDTD approach one must keep in mind that the minimum reliable wavelength is ten times the size of the Yee cell (hence setting the limit for the maximum reliable frequency). Also, using smaller cells (hence more cells), within the limit of the host computer, to model the geometric object may improve the accuracy of the comparison. The availability of the field quantities only at discrete points due to the lattice structure can create some problems. In the frequency-domain code EFIE, discretization affects both the high and the low frequencies: on the one hand there is the one-fifth wavelength rule, setting the limit for the maximum frequency, and on the other hand at low frequencies there must be enough spatial resolution to reflect highly varying fields in neighbourhoods of “boundary edges”. It must be remembered that the discretization guidelines of “10 cells/ λ ” and “edges $\leq \lambda/5$ ” are “traditional” ones based on experience from many studies in computational electromagnetics. They are sometimes more stringent than necessary and useful results may be obtained even above the high-frequency threshold. This is why in sometimes we may present the high-frequency results well above the threshold. The point of caution is that if the guidelines are violated, one must seek independent verification of the results obtained.

CONCLUSIONS

In this study, the penetration of HPM inside an cylinder with openings and loaded with a rectangular metal plate has been studied. The FDTD code has been used to calculate the time-domain response for a Gaussian pulse. Comparison, in the frequency domain, has been made with the results obtained by using the frequency-domain method EFIE. Effects of various factors such as wave shape, structure discretization, and fast Fourier transformation on CPU-time and accuracy of the results were discussed. Guidelines for using the time-domain and the frequency-domain codes were suggested. It was found to be more efficient in most cases to use the time-domain method.

REFERENCES

- [1] A. Taflove and K. R. Umashankar, "The Finite-Difference Time-Domain Method for Numerical Modeling of Electromagnetic Wave Interactions with Arbitrary Structures", *Progress in Electromagnetic Research*, Elsevier, 1990.
- [2] G. L. Burke and A. J. Poggio, "Numerical Electric Code (NEC) — Method of moments", *Naval Ocean Systems Centre, Technical Document 116*, 1977.
- [3] S.-U. Hwu and D. R. Wilton, "Electromagnetic Scattering and Radiation by Arbitrary Configurations of Conducting Bodies and Wires", *University of Houston, Technical Report 87-17*, 1988.
- [4] K. S. Yee, "Numerical Solution of Initial Boundary Value Problem involving Maxwell's Equations in Isotropic Media", *IEEE Transactions on Antennas and Propagation*, AP-14, 302-307, 1966.
- [5] S. M. Rao, D. R. Wilton, and A. W. Glisson, "Electromagnetic Scattering by Surfaces of Arbitrary Shape", *IEEE Transactions on Antennas and Propagation*, AP-30, 409-418, 1982.

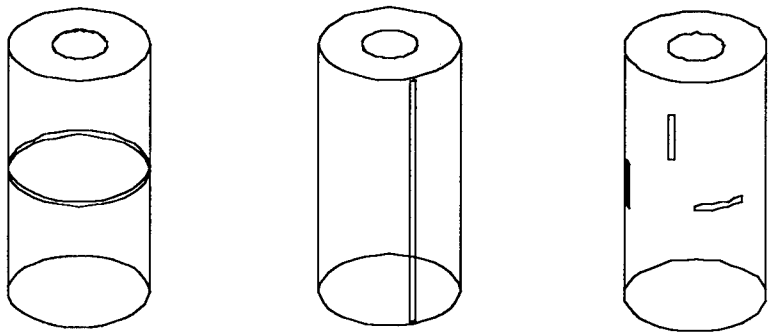


Figure 1. Some of the cylindrical structures under study.

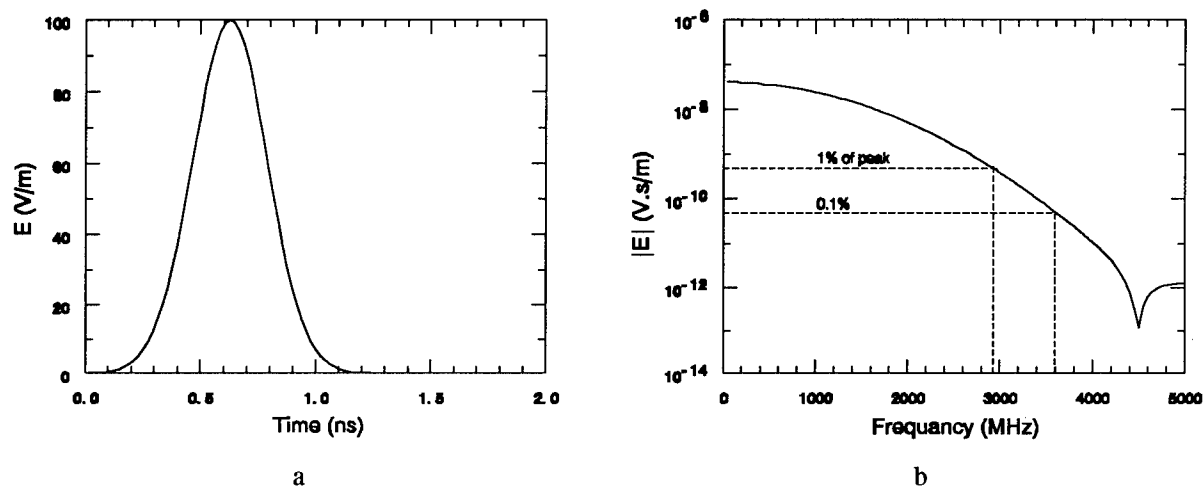


Figure 2. Gaussian pulse in time and frequency domains.

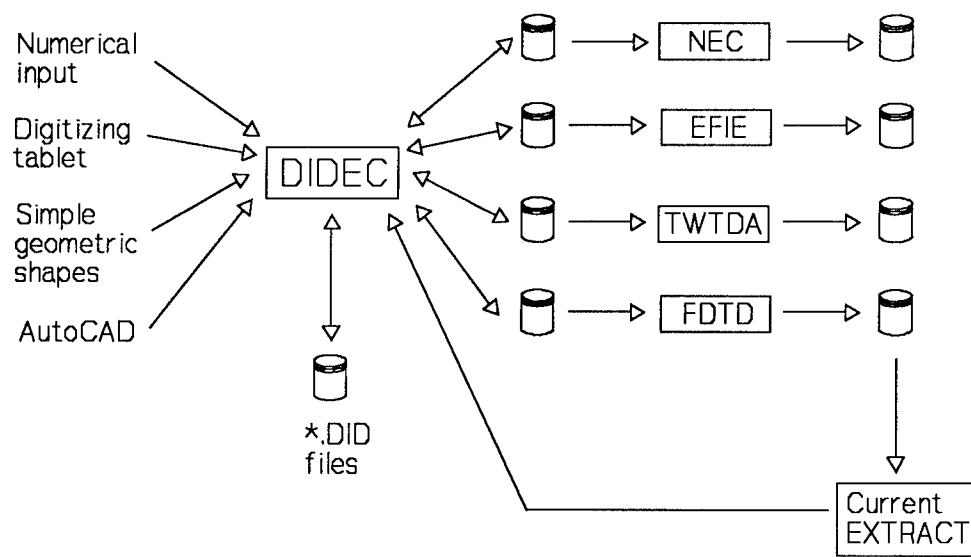


Figure 3. The block structure of the geometric modelling DIDECDREO program.

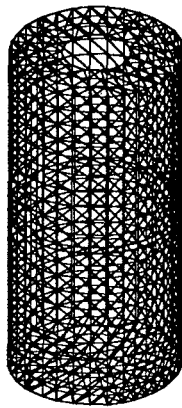


Figure 4. Example of a triangular surface-patch model for EFIE.

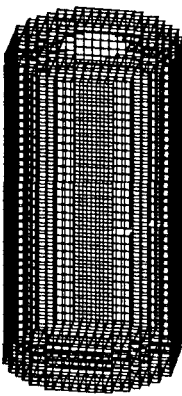


Figure 5. FDTD model of the same cylinder.

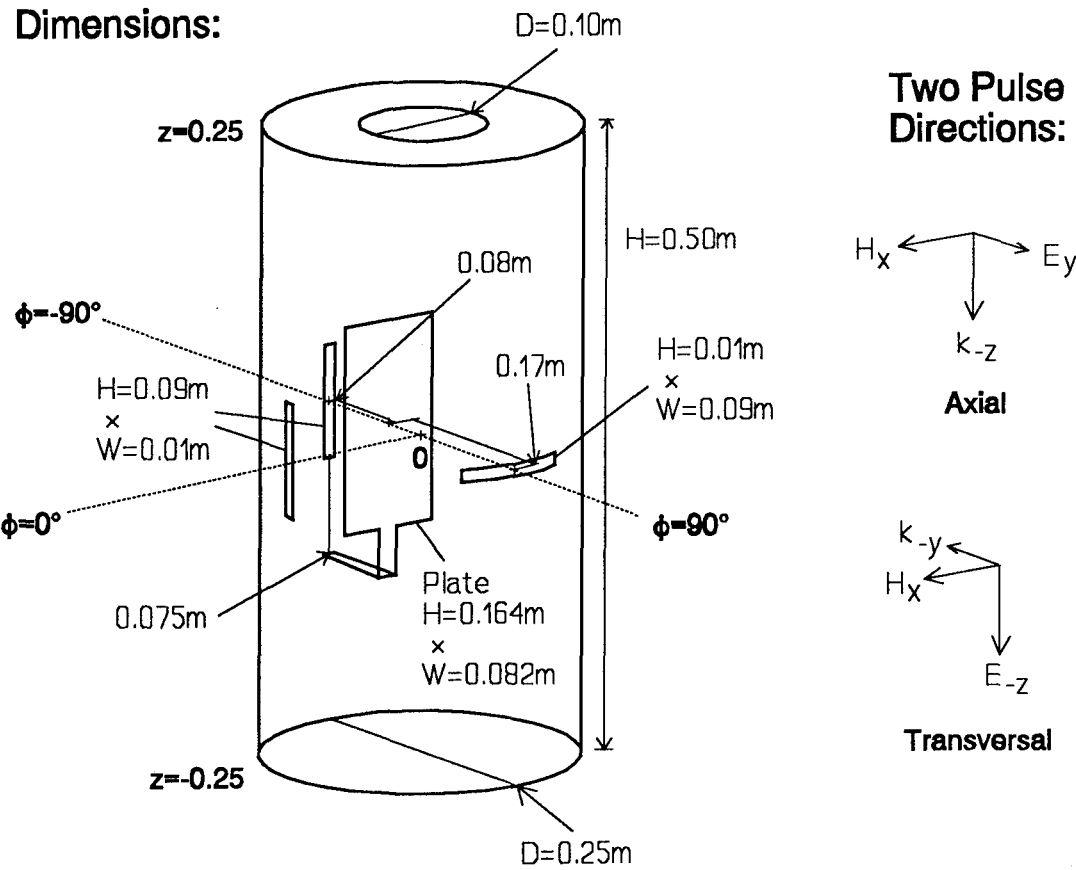


Figure 6. Cylinder dimensions and pulse orientations

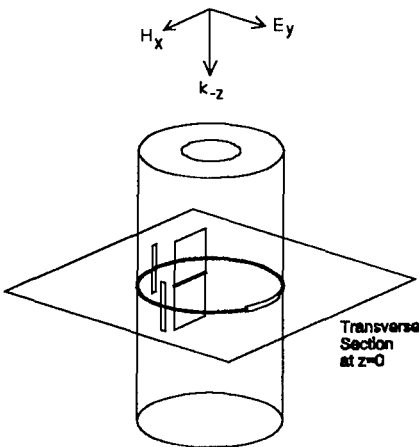
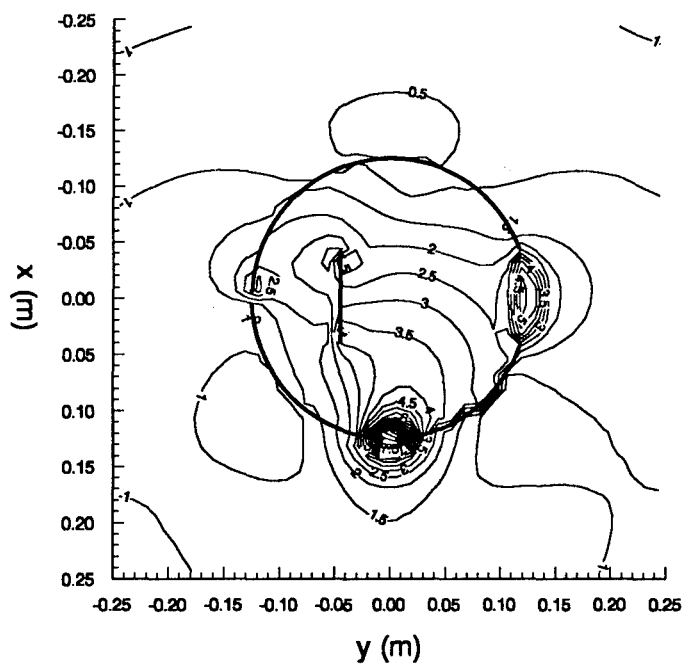
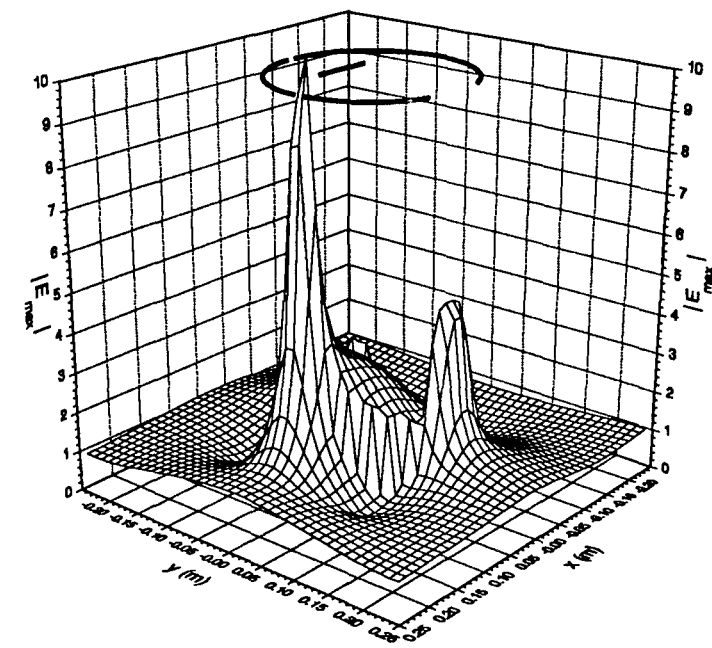


Figure 7. E-field in and around a cylinder with slots and floating plate.

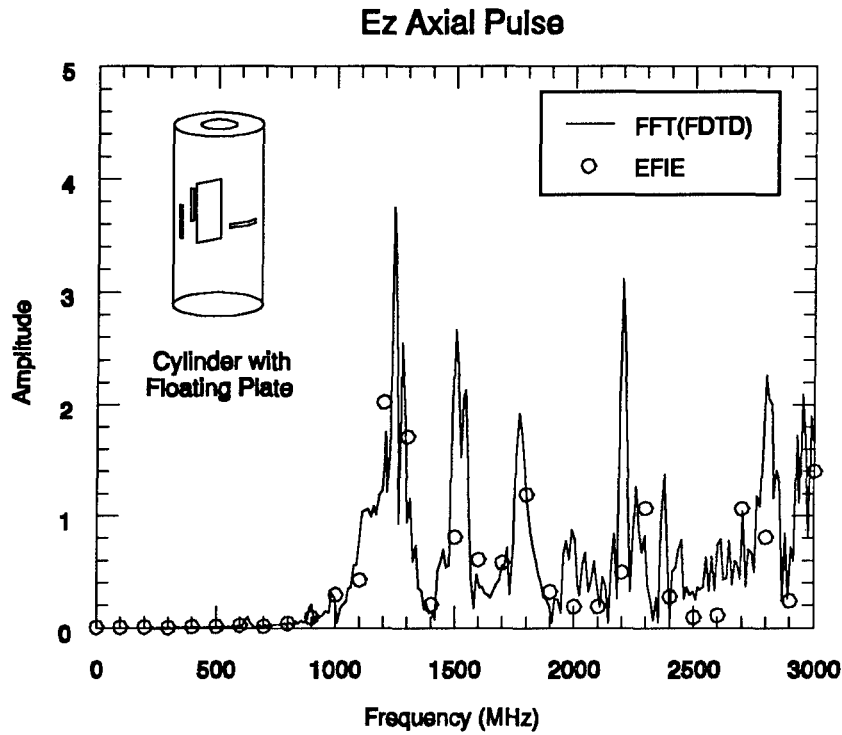


Figure 8. Ez-field at the centre of cylinder under an axial pulse:
FDTD versus EFIE in frequency domain

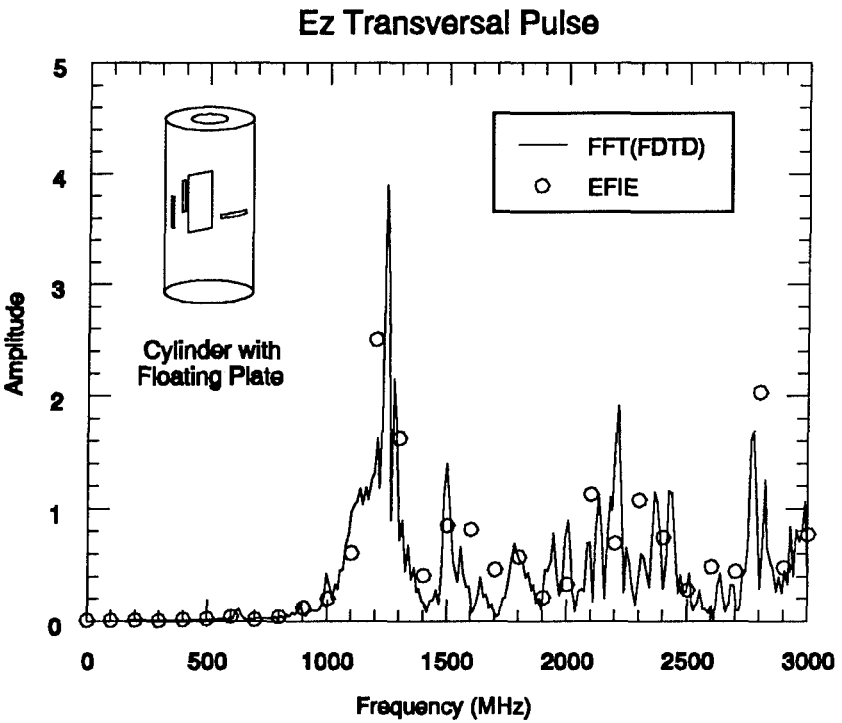


Figure 9. Ez-field at the centre of cylinder under a transversal pulse:
FDTD versus EFIE in frequency domain

DISCUSSION

MALABIAU

- 1/ Quelle est la fréquence maximale correspondant à la discrétisation effectuée sur le modèle de frégate qui a été présenté ?
- 2/ Quelle est la taille maximale des matrices utilisés dans les calculs ?

AUTHOR'S REPLY

- 1/ La discrétisation a été effectuée pour pouvoir être valide jusqu'à 100 MHz environ.
- 2/ La taille maximale des matrices est de 5000 à 10000 x 10000.

E. SCHWEICHER

Did you validate your code by calculating the pulse response of a perfect conducting spherical target ?

AUTHOR'S REPLY

Yes, the code was validated for a number of targets, including a perfect conducting sphere.

Translation:

Q.

1. What is the maximum frequency of the digitizing carried out on the model of the frigate which was presented ?
2. What is the maximum size of the matrixes used in the calculations ?

A.

1. Digitizing was carried out for validation up to about 100MHz.
2. The maximum size of the matrices is 5000 to 10 000 x 10 000.

A PROCEDURE BASED ON LINE THEORY FOR CALCULATING SURFACE CURRENTS AND COUPLING INTO THE INTERIOR OF LARGE OBJECTS

E. Arnold
VR3 E213
Deutsche Aerospace AG
Sedanstrasse 10
89070 Ulm
Germany

SUMMARY

For objects, which are too large to be calculated with the MM or the FDTD an approximation based on line theory was developed. For calculating an object a wire grid model is made. This model is described by Z-Matrix coefficients which are calculated approximately using line theory. The coupling of the wires are taken into account. Having the Z-matrix it takes less effort to determine the currents at some special points of the object.

Though the procedure is designed for the calculation of big objects compared to a wavelength, some results for simple objects are shown and compared with the results received by different methods.

1 INTRODUCTION

The use of the MM or the FDTD for calculating currents on the surface and on the inner parts of a metallic body is often limited by the ratio size of object / wavelength or the fineness of the modelling. If the size increases or the shape gets more complicated the effort for calculation grows, too. For such objects an approximation based on line theory was developed. The object is seen to be a wire grid model and the wires are considered as coupled transmission lines. Line theory is always applicable if the current distribution on the object's surface can be approximated by a superposition of forward and backward running waves induced by discrete sources or incoming fields.

It is a widespread opinion that line theory is only applicable if the wires run parallel at a small distance to a perfect conducting plane. This opinion arises from the usual way to derive the line equations assuming a TEM propagation of the wave on the wire. Actually it can be shown under weaker assumptions that the line equations are a rather good approximation of the current distribution in a wire. If a wire is near to a perfect conducting plane the line parameters L' and C' are real. If the distance increases L' and C' become complex.

2. THE BASIS OF THE CALCULATION

2.1 THE TRANSMISSION LINE EQUATIONS

The basis of the procedure are the equations of a straight wire located above a perfect conducting plane. The current in the wire is induced by an incoming field \vec{E}^{inc} . Then the line equations are

$$\begin{aligned} \frac{d^2 U}{ds^2} - \gamma^2 * U &= \frac{d}{ds} (\vec{E}^{inc} * \vec{e}) \\ \frac{d^2 I}{ds^2} - \gamma^2 * I &= -\frac{1}{Z} * (\vec{E}^{inc} * \vec{e}) \end{aligned} \quad (1)$$

$$\gamma^2 = (R' + j\omega L') * (G' + j\omega C')$$

$$Z^2 = \frac{R' + j\omega L'}{G' + j\omega C'}$$

The solution of the equations is

$$U(s) = e^{-\gamma*s} * (C_1 + P(s)) + e^{\gamma*s} * (C_2 + Q(s)),$$

$$I(s) = \quad (2)$$

$$\frac{1}{Z} * \{ e^{-\gamma*s} * (C_1 + P(s)) - e^{\gamma*s} * (C_2 + Q(s)) \}$$

with

$$P(s) = \frac{1}{2} * \int_{s_a}^s (\vec{E}^{inc} * \vec{e}) * e^{\gamma*t} * dt,$$

$$Q(s) = \frac{1}{2} * \int_s^{s_e} (\vec{E}^{inc} * \vec{e}) * e^{-\gamma*t} * dt,$$

$$s_a \leq s \leq s_e.$$

I is the current in the line, U is the voltage between the line and the perfect conducting plane, s is the length parameter, s_a and s_e are the length parameter values of the starting point and the end point of the line, Z is the line impedance, γ is the propagation constant and \vec{e} is the unit vector in the direction of the wire. R' , L' , G' and C' are the line parameters and C_1 , C_2 are constants from the integration of the differential equations (1) needed to connect loads on both ends of the line.

The incoming field \vec{E}^{inc} has no special assumptions. \vec{E}^{inc} could be a plane wave or it could be a field of a source located in the vicinity of the line.

We consider now a single wire in the vicinity of other wires. The currents in the other wires produce a field \vec{E}^{inc} , which induces a current distribution in the single wire. If we look in this way at all wires, we get a pair of equations of the form (1) for every wire, and all equations together form a coupled system of integral equations. In principle this system is directly solvable, but because of the large effort required for this, we prefer to calculate an approximate solution.

2.2 DESCRIPTION OF AN ENSEMBLE OF WIRES BY A Z-MATRIX

In fig. 1a we see as an example the wire grid model of a piece of a plane. The ends of the wires are called nodes. If two or more wires belong to a node, we shorten these wires at the node a tiny bit until every wire is isolated. If a wire touches the perfect conducting plane it is shortened too. After this procedure the wire grid model appears as a passive electrical device made by isolated straight wires. Each end of a wire is a port of this device. The device for the model of fig. 1a

is shown in fig. 1b. If we assume that only nonradiating loads are connected at the ports, the port voltages are a linear function of the port currents and this function is commonly called the Z-matrix. If the wire grid model consists of N wires, the device has $2N$ ports and the rank of the Z-matrix is $2N$. If the device is influenced by a linear polarized plane wave generated by a distant source, the Z-matrix has an additional column (3), and if the plane wave is elliptically polarized the Z-matrix has 2 additional columns. The Z-matrix for a linearly polarized incoming plane wave is shown in equation (3).

For the calculation we connect the ports by small pieces of wire to get back the wire grid model. Because these wires are very small, they are nonradiating.

(3)

$\begin{pmatrix} U_1 \\ U_2 \\ \vdots \\ U_{2N} \end{pmatrix}$

normal Z-matrix of a device with 2N ports

=

$\begin{pmatrix} z_{11} & z_{12} & z_{13} & \dots & z_{1,2N} & z_{1,2N+1} \\ z_{21} & z_{22} & z_{23} & \dots & z_{2,2N} & z_{2,2N+1} \\ \vdots & \vdots & \vdots & \ddots & \vdots & \vdots \\ z_{2n,1} & z_{2n,2} & z_{2n,3} & \dots & z_{2n,2N} & z_{2n,2N+1} \end{pmatrix}$

normal Z-matrix of a device with 2N ports

*

$\begin{pmatrix} I_1 \\ I_2 \\ \vdots \\ I_{2N} \end{pmatrix}$

column for the plane wave

$\vec{E}^{inc}(0) * \vec{p}$

$\vec{E}^{inc}(0)$ is the incoming plane wave at the origin of the coordinate system (a different point can be chosen, but then the phase of the coefficients $z_{i,2N+1}$ will be different). \vec{p} is the unit vector in the direction of polarisation of \vec{E}^{inc} .

We call the matrix of equation (3) the "extended Z-matrix".

Fig. 1a: Wire grid model of a plane area (Example with 40 wires)

Fig 1b: Device made by wires of the model of Fig. 1a (80 ports)

2.3 DETERMINATION OF THE MATRIX-COEFFICIENTS - COUPLING OF WIRES

If the coefficients z_{ij} of equation (3) are determined exactly and if the other assumptions, pointed out in section 2.2, are realized, the matrix contains the coupling of the wires. But because some assumptions are normally more or less non-compliant, our solution will have certain inaccuracies. Therefore we will not spend much effort in the calculation of the z_{ij} but determine them approximately.

The coefficient z_{ij} defines the voltage at the i^{th} port when a certain current flows into the j^{th} port and all other ports are open. This follows simply from (3). To determine z_{ij} we first disconnect all sources and loads from all ports. Then we connect a voltage source at the i^{th} port and calculate by use of (2) the current distribution I_i on the wire which belongs to the port, assuming all other wires are not present. On the other wires this current produces an incoming field \vec{E}^{inc} , which is due to the voltage U_j at the j^{th} port. The voltage is calculated again by use of equation (2). From this we have

$$z_{ij} = \frac{U_j}{I_i}.$$

By calculating z_{ij} in this way the currents on all wires are neglected, which do not belong to the i^{th} port or the j^{th} port. The error produced by this approximation is small if the neglected currents are small. Because all ports except the j^{th} port are open, the neglected currents are considerably smaller than the current of the i^{th} port. This is particularly true if the length of the wires is less than a third of a wavelength. Furthermore our results show that the distance between the i^{th} and the j^{th} wire has to be larger than one third of the length of the longer of both wires.

If the matrix (3) were a Y- or an S-matrix the determination of the matrix coefficients by a similarly simple procedure would produce considerably larger currents on the other wires. Therefore the errors would be much larger than when using a Z-matrix.

To determine the coefficients $z_{i,2N+1}$ in the column for the incoming plane wave we first open all ports again and calculate by (2) the current distribution on all wires not belonging to the i^{th} port. By doing this we neglect again the coupling of the wires. All these currents produce a field. Then we calculate the sum of all these fields, superpose it with the incoming plane wave and calculate the voltage U_i at the i^{th} port by using (2). Then we get by (3)

$$z_{i,2N+1} = \frac{U_i}{E^{inc}(0) \cdot \vec{p}}.$$

3. THE CALCULATION OF A LARGE OBJECT

We explain the procedure with the simple cylinder of fig. 2a. The cylinder is situated on a perfectly conducting plane. It is subjected to an incoming plane wave which is polarized parallel to the cylinder axis. Inside the cylinder there are 2 wires. The 1st wire protrudes from the cylinder through a hole in the roof. The 2nd wire is completely inside the cylinder. Both wires end at the bottom and are loaded there with 50 Ohms against the ground plane. The results of some calculations with this cylinder are shown in section 5.

In the 1st step we make a wire grid model of the object as shown in fig. 2b. Every wire is considered to be a transmission line and is coupled with other wires. Its properties are described by the line parameters R' , L' , G' and C' . For each wire we

Fig. 2a: Cylinder

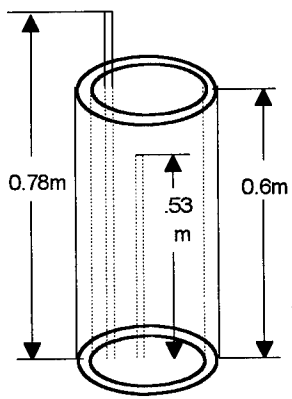


Fig 2b: Wire grid model of the exterior

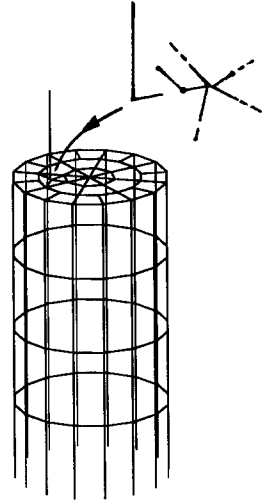
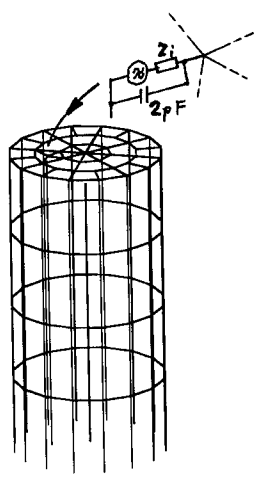


Fig. 2c: Wire grid model of the interior



receive R' , L' , G' and C' by 2 simple calculations of a monopole with the NEC2 program.

For calculating a large object the object is divided into several parts. The coupling between wires of different object parts is neglected. In the example of Fig. 2 a 1st object part could be the roof with the wire protruding from the cylinder, a 2nd object part could be all the wires being perpendicular to the ground plane and a 3rd part could be all the wires lying parallel to the ground plane.

In the 2nd step we calculate for all wires of the 1st object part the extended Z-matrix using the procedure of section 2.3. Then we eliminate from the matrix all the rows and columns belonging to ports, whose nodes belong only to this object part, by connecting the ports by tiny pieces of wire according to the connections at the wire grid model. (Besides these nodes there are other nodes which belong to 2 or more object parts.) For doing this with a Z-matrix we need only little effort. Afterwards every remaining "port" of the Z-matrix belongs to a node, which belongs to other object parts, too. The elimination leads normally to a significantly smaller rank of the matrix.

In the 3rd step we calculate the extended Z-matrix for the 2nd object part. Then the 1st and the 2nd Z-matrices are combined to give a common Z-matrix. This also needs only little effort.

The 3rd step is repeated with the next object part until all object parts are combined. Then we calculate voltage and current at those ports where we want to know the surface currents.

In fig. 2c we see the model for the coupling into an object. We come back to this example in section 5.

4. DETERMINATION OF LINE PARAMETERS

The properties of a line are normally described by the line parameters R' , L' , G' and C' . Instead of these parameters the complex propagation constant γ and the complex line impedance Z can also be used. Using γ and Z has some advantage for the determination of the parameters, because the change of the current and voltage as a result of a change of a parameter can easily be predicted (1). With the procedure mentioned in 4.2 the advantage is obvious.

4.1 COMPARISON OF THE CURRENT DISTRIBUTION ON A MONOPOLE AND ON A LINE

The attenuation constant $Re(\gamma)$ ($Re(\gamma)$ denotes the real part of γ), the phase velocity v_p and the line impedance Z have to be determined very carefully. The prevailing investigations have shown that the parameters of a straight wire are nearly independent of the wire's length, but are strongly dependent on the frequency. Since the determination of the attenuation is difficult using short wires, the wires used are about 10 wavelength long. Fig. 3 shows the current distribution on the monopole of fig. 4 for the cases of transmitting and receiving according to NEC2 and to the line model. The line is considered to be homogenous. The parameters were determined by the procedure of section 4.2. The diameter of the monopole was 0.2m. At the "open" end of the line a capacitive load was connected, producing a reflection factor of $r = 0.6 * e^{-j50^\circ}$.

Fig.3a: Current distribution on the monopole of fig. 4 for transmitting due to NEC2 and the line model ($f=100$ MHz)

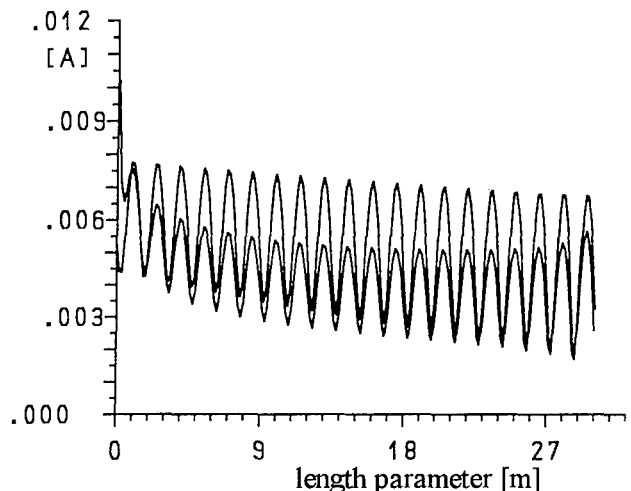
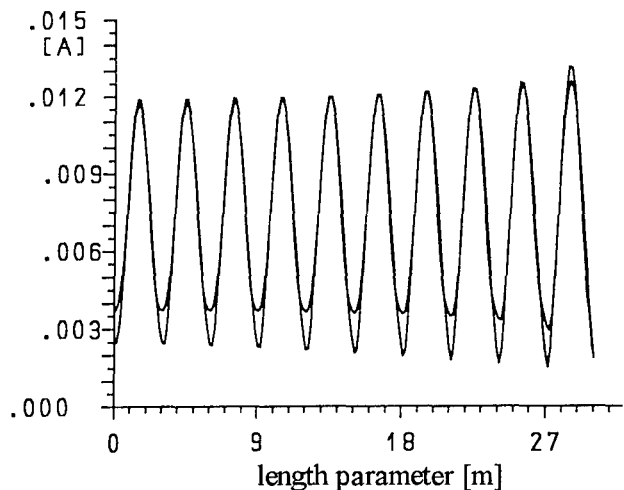


Fig.3b: Current distribution on the monopole of fig. 4 for receiving due to NEC2 and the line model ($f=100$ MHz)



Though the currents of the receiving case show quite good coincidence, the differences in the transmitting case are considerable. Obviously the capacitive coupling one can see by the strong decrease in the result of NEC2 in fig. 3a, is not included in the line model. A better coincidence would be reached by an appropriate capacitor connected parallel to the source. However this capacitor is not necessary for the determination of the line parameters. For the line model we used the following parameter values:

$$Re(\gamma) = 0.012 \frac{1}{m}, v_p = 3 * 10^8 \frac{m}{s}, Z = 138 * e^{-j15^\circ} \Omega .$$

They are equivalent to (4)

$$R' = 76.5 \Omega/m, \quad L' = 0.444 \mu H/m, \\ G' = -0.385 * 10^{-2} 1/(\Omega * m), \quad C' = 23.4 \text{ pF/m} .$$

Though G' is negative, the line is a passive device. A negative G' is normal for thick wires.

4.2 HOW TO DETERMINE THE LINE PARAMETERS

At the moment we receive the line parameters with an interactive procedure described in the flow chart of fig. 5. Therein the current distribution on a monopole calculated by NEC2 and by the corresponding line model for the transmitting and the receiving case are compared. The parameters of the line are varied until the current distributions coincide sufficiently well. The monopole is shown in fig. 4. The procedure makes use of the transmitting case as well as the receiving case. Each parameter is estimated from the case which shows the more significant influence. Until now we have only considered wires in surrounding air. For this we have obtained the best results if $v_p = 3 * 10^8 \frac{m}{s}$.

At some frequencies in the receiving case the wire shows beside the "normal mode" a relatively strongly stimulated "second mode". If this happens, the user must try to estimate the parameters for the normal mode.

Fig. 5: Flow chart to get the line parameters (Compare the current distribution of NEC2 and of the line model)

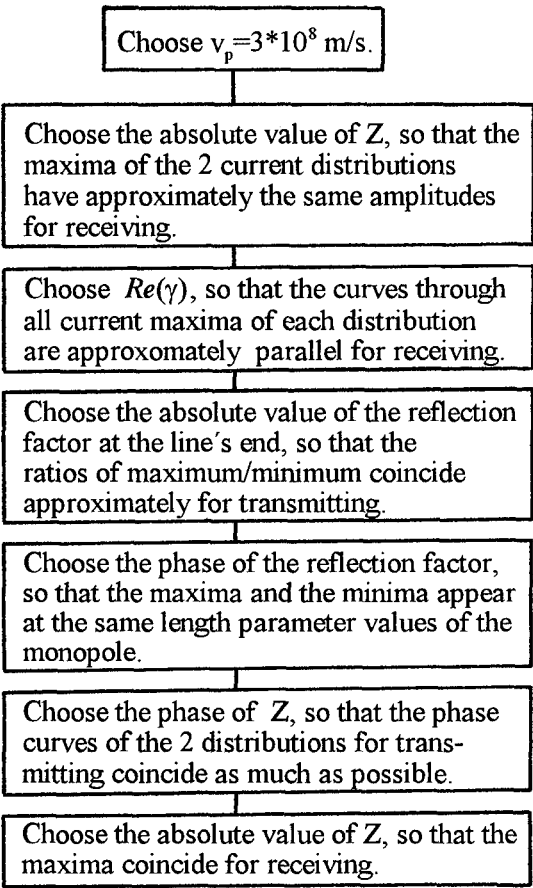
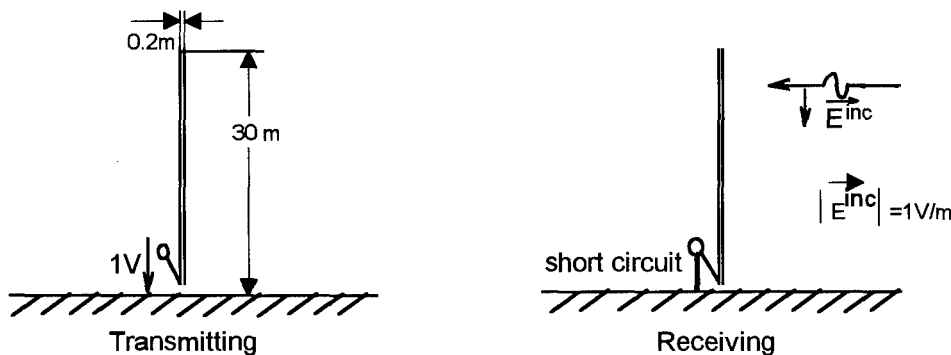


Fig 4: NEC model for calculating the current distribution on a monopole



4.3 DETERMINATION OF THE LINE PARAMETERS FOR A FREQUENCY BAND

The line parameters determined with the above mentioned procedure are not very exact, since most criteria are not significant and the estimation depends on the experience of the user. Therefore we recommend performing the procedure with several frequencies of a sufficiently wide frequency range and filter the results. Fig. 11 shows an example. There the parameters were determined at 6 frequency points in the range from 100 MHz to 1000 MHz . The parameters for the required frequencies are then received from the filtered curves.

According to theoretical reflections one can presume that the true dependence of the parameters as a function of frequency is not so smooth as shown in fig. 11.

5. COMPARISON OF RESULTS FOR SIMPLE OBJECTS CALCULATED WITH NEC2 AND THE LINE MODEL

From section 3 we conclude that the current distribution on monopoles in the receiving case can be quite well approximated by solutions of the line equation (2). According to the reflection principle this holds for dipoles in free space also.

Fig 6: Square loop (6m x 6m) in free space influenced by an incoming wave (f=100 MHz)

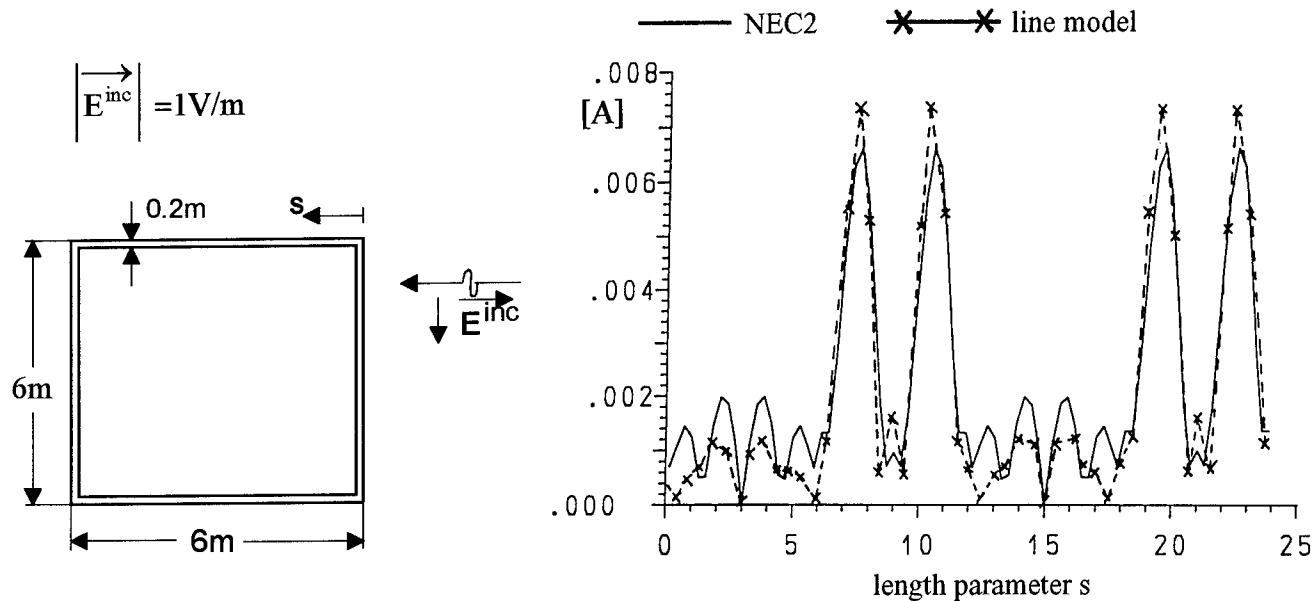


Fig. 7: Rectangular loop (1m x 3m) in free space influenced by an incoming plane wave (f=100 MHz)

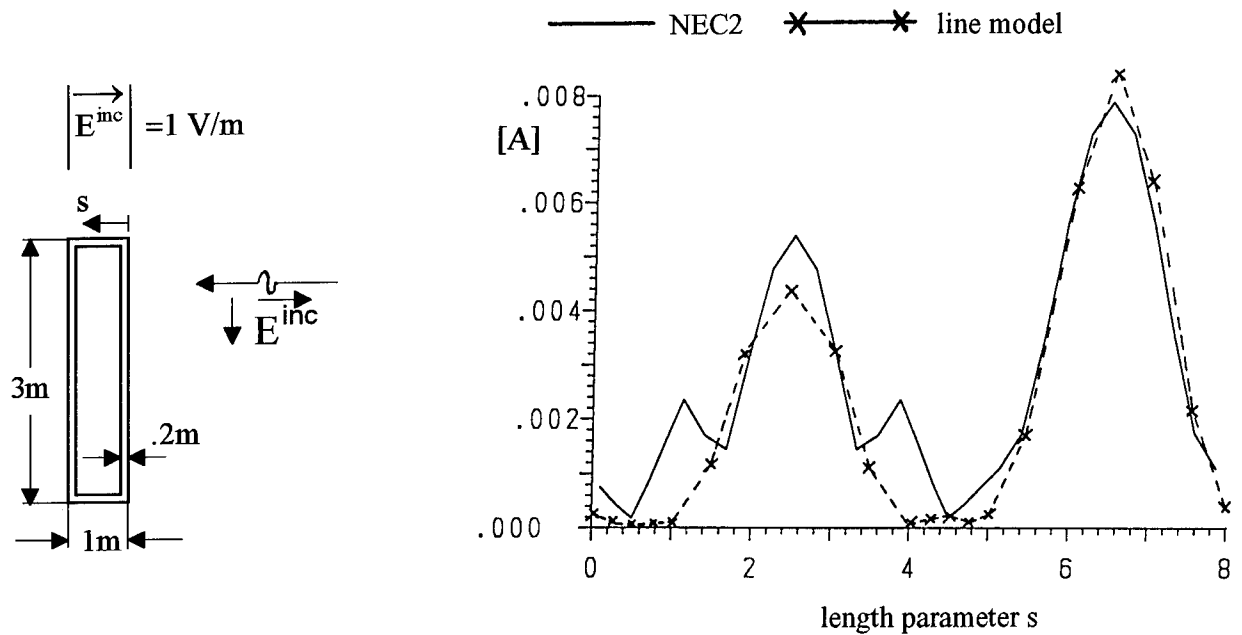
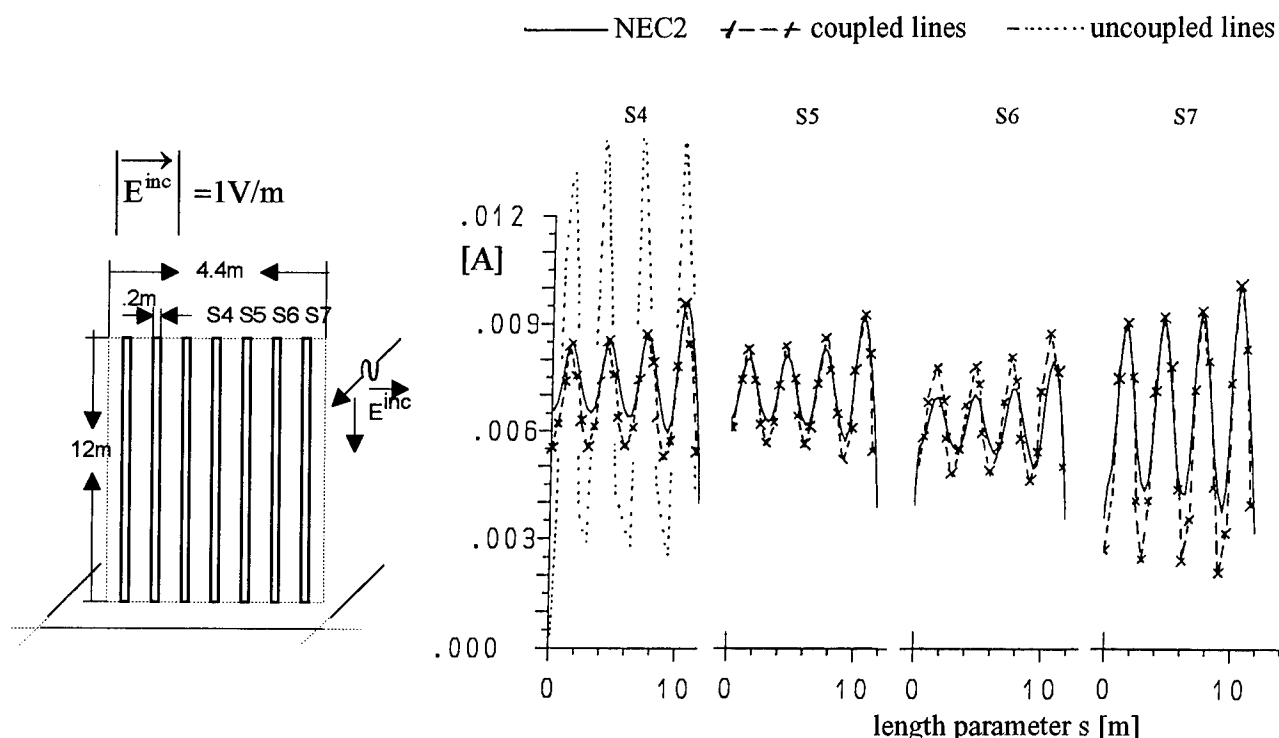


Fig 8: Wire grid model of a plane area (12m x 4.4m), 7 wires perpendicular to a perfectly conducting ground plane influenced by an incoming plane wave



The dipole can be considered as the one wire of a 2nd wire line, where the 2nd wire is situated so far parameters of the dipole result from those of the monopole according the reflection principle.

In fig 6., fig. 7 and fig. 8 we compare the current distribution of simple objects calculated by NEC2 with those calculated by the line model. The solid curves show the results of NEC2. The results of the line model are marked by "x". For all examples the line parameters are given by (4).

6. COMPARISON WITH AN EXAMPLE FROM LITERATURE

The cylinder of fig. 2a is an example treated in /1/. It is situated on a perfectly conducting ground plane and is induced by an incoming plane wave with 1 V/m, polarized parallel to the cylinder axis. Unfortunately in /1/ the thickness of the two 0.78m (driven wire) and 0.53 m (receiving wire) wires is not defined. With the line model the diameters of these wires are set to 2 mm. The coupling into the interior of the cylinder takes place via the driven wire protruding the roof of the cylinder.

The results shown in fig. 9 are taken from /1/. The result of the calculation was obtained with a FDTD program. The curves of fig. 9a show the voltage at the end of the driven wire when the end of the receiving wire is loaded with 50 Ohm against the ground. The load of the driven wire is not explicitly given in /1/. One can probably conclude from the description of the measurement that the load is chosen to be 50 Ohms also. Fig. 9b shows the voltage at the end of the receiving wire when the driven wire is loaded with 50 Ohms. In this case the receiving wire is probably loaded with 50 Ohms too. Fig. 10a and fig. 10b show the results of the line model. Driven and receiving wires are both loaded with 50 Ohms. For convenience these figures contain the results of the measurement of /1/ also.

The present cylinder is not a typical example for the calculation method demonstrated here since the object is relatively small.

The line parameters of the model are determined according to the procedure described in section 4. Fig. 11 shows the line parameters of the driven and the receiving wire as a function of frequency. The calculation of the voltages at the end of the

Fig. 9a: Voltage at the end of the driven wire from /1/

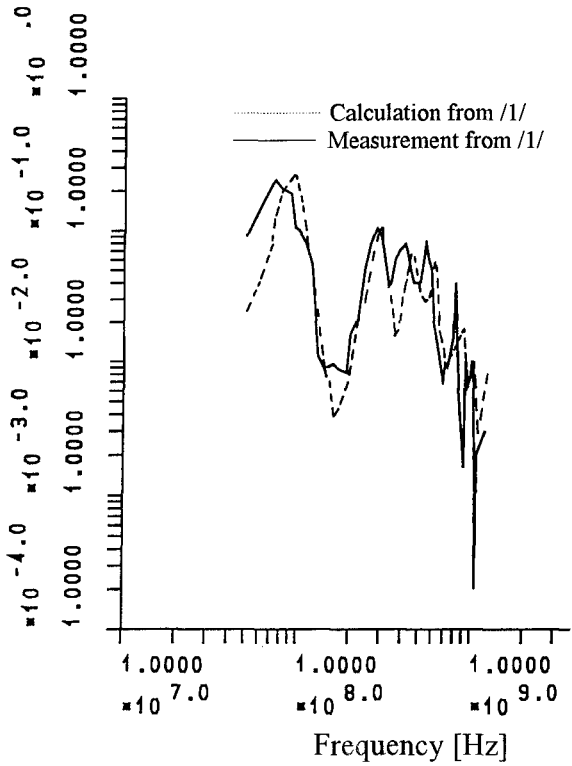


Fig. 9b: Voltage at the end of the receiving wire from /1/

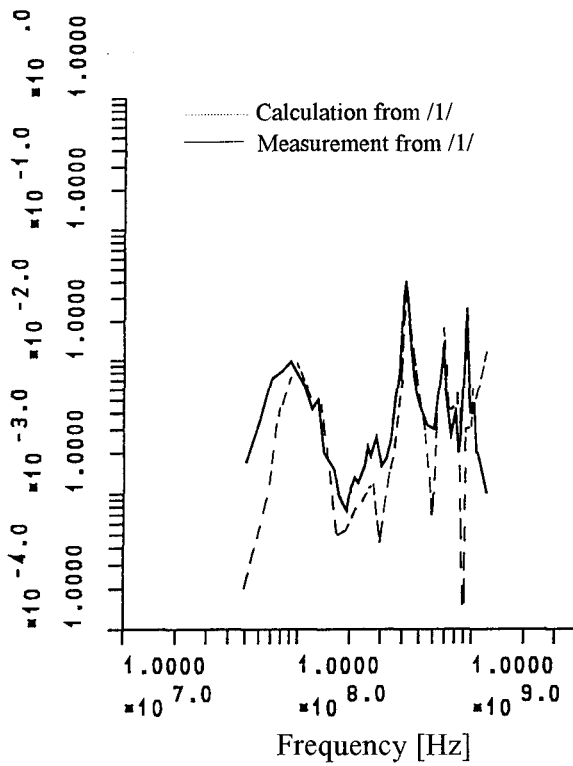


Fig. 10a: Voltage at the end of the driven wire received by the line model

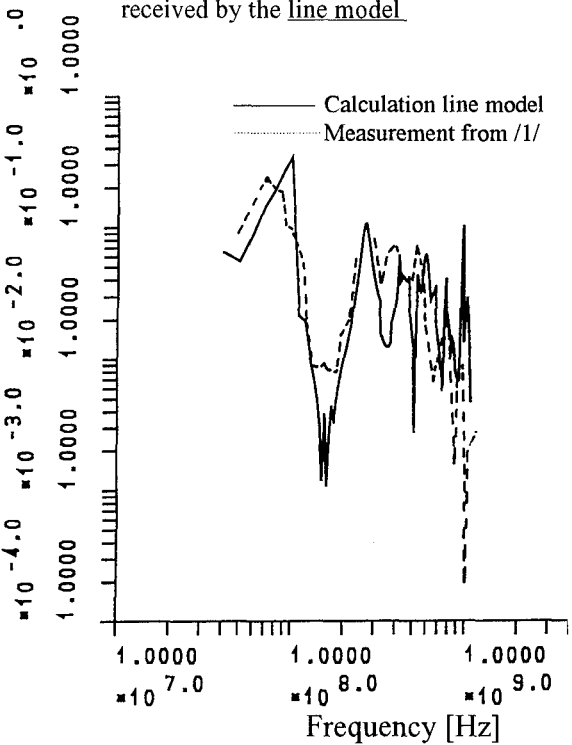
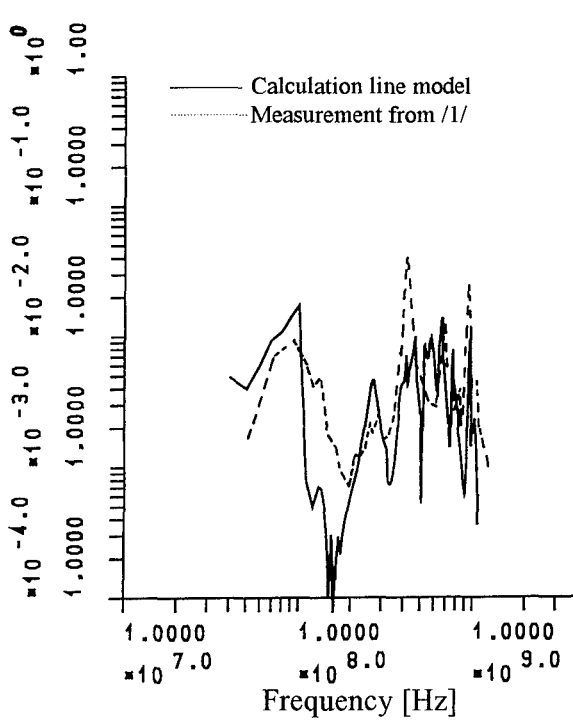


Fig.10b: Voltage at the end of the receiving wire received by the line model



driven and receiving wire was performed in 2 steps. In the 1st step the driven wire was cut close above the roof and the voltage between its remaining end and the roof was calculated. Then a short circuit was connected between the cut end and the roof and the current was calculated. Voltage and current defines a Norton-Generator used in the 2nd step. In the 2nd step we consider the cylinder from the interior. We close the hole in the roof and connect the Norton-Generator between the driven wire and the roof. Parallel to the Norton-Generator we connect a capacitance with about 2 pF to compensate for the difference between the current distribution of a wire and its line model in the vicinity of the source. This difference we have already seen in fig 3. At the upper end of the receiving wire we add another capacitance of about .5 pF against the ground to adjust the reflection factor at the end of the wire to reality. Then we calculate the voltages of the 2 wires. For the 2nd step we use the same line parameters as for the 1st step.

For the calculation of the 1st step the whole wire grid model was imaged to a single Z-matrix. In the 2nd step we decomposed the object into 3 parts. The 1st part consists of a few wires on both sides of the Norton-Generator. The 2nd part consists of the roof, the vertical wires of the cylinder and the receiving and the driven wire. The 3rd part consists of all remaining horizontal wires.

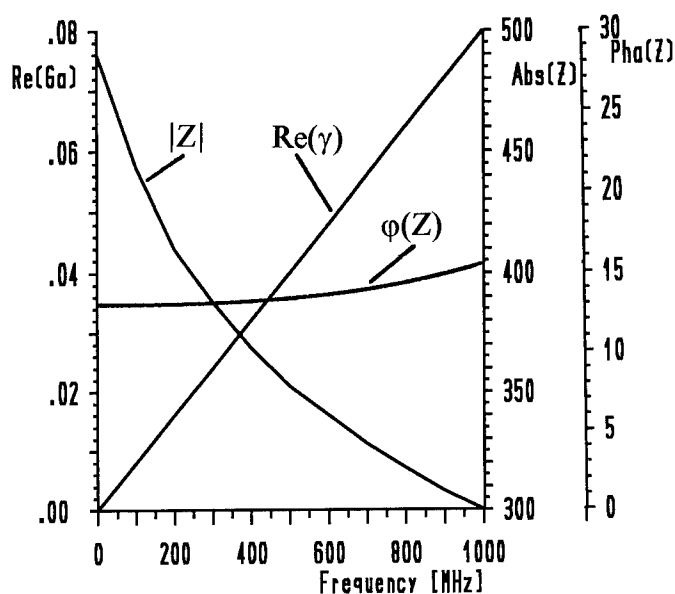
Special calculations with other objects showed that relatively small pieces of wire on both sides of a generator may not be coupled with other wires. Therefore here they comprise the 1st object part.

7. PROBLEMS

The current distribution on an object is approximated quite well by the line model if the wires are parallel. But there is a problem if lines are cascaded. We will show this problem in the following example.

We first consider a straight line with a certain length. The line is fed at one end and has a certain current distribution. Then we cut the line into 2 halves, so that now 2 lines exist. When we

Fig. 11: Line parameter for a large frequency band (driven wire and receiving wire)



connect the 2 lines again at the cutting point they show an essentially higher current as the single line before, when taken coupling of the lines into account. If the coupling is suppressed, the 2 lines exactly show the same current distribution. Obviously the coupling in the direction of the line is already included in the line equations.

In the program the problem is avoided by automatically suppressing the coupling between 2 lines, which are directly connected. In cases when the coupling is desired, for example when the 2 lines run in opposite directions, the coupling can be restored by an additional short line connected between the 2 lines.

References

- /1/ C. D. Turner, L. D. Bacon: Comparison of Experimental and Numerical Results on Microwave Coupling Into Cylindrical Enclosures
IEEE Int. Symp. on EMC, Aug. 2. - 4. 1988, Session 4B, pp 205-209
Seattle (State Washington)

DISCUSSION

P. ZWAMBORN

Could you indicate the residual EM field inside a closed surface ? (the "leakage" of your thin-wire model)

AUTHOR'S REPLY

There is no leakage. The calculation runs in 2 steps. In the 1st step we calculate the current on the outer surfaces. In doing this the relative small current inside is neglected. From the calculation we receive a Norton Generator.

In the second step we look to the cylinder from inside. The cylinder is totally closed and we have no direct penetration of the outer field. The field inside is induced exclusively by the Norton Generator.

E. SCHWEICHER

Does your method apply to the scattering of an incident wave by a FSS (Frequency Selective Surface) ?

I am interested by your response because I had a PhD student who solved exactly Maxwell's equations for that problem by means of successive approximations.

AUTHOR'S REPLY

I'm not deeply involved in this subject. I think it depends on the selection mechanism. If the surface is made by resonant patches or dipoles, I think you can apply the method.

LABAUNE

When dividing the elements in families, are you sure that this division is always correct ?

AUTHOR'S REPLY

In doing this you can make big mistakes. This therefore needs some experience. The user has to know whether the mistakes are tolerable. Normally 2 wires which are perpendicular to each other have essentially less coupling than 2 wires which are parallel. You can test the mistake in a simple way : transform your result from the frequency domain to the time domain and look how good causality will be.

FREQUENCY-DOMAIN ANALYSIS OF NONLINEARLY LOADED THIN-WIRE ANTENNAS AND NETWORKS

Karam M. Noujeim, Safwat G. Zaky and Keith G. Balmain

Department of Electrical and Computer Engineering

University of Toronto

10 King's College Road

Toronto, Ontario M5S 1A4

Canada

Abstract Electronic devices are susceptible to a wide variety of high-level electromagnetic interference signals, from medium to microwave frequencies. The ability to assess the susceptibility of these devices to interference using computational techniques is an important asset to the designer. An essential ingredient in this process is the ability to combine linear field computations with nonlinear circuit analysis.

A frequency-domain-based computer program, known as TWIRE, has been developed for the periodic steady-state analysis of thin-wire antennas and scatterers loaded with nonlinear circuits. In addition to linear and nonlinear resistors, capacitors, and inductors, these circuits may contain transformers, diodes, transistors, N -port networks, etc. The computer program is based on an S -parameter technique that combines the thin-wire method of moments with a frequency-domain-based nonlinear circuit simulator employing harmonic balance.

The program is applicable to arbitrary-size wire networks and antenna structures loaded with circuits such as amplifiers, attenuators, detectors, filters, multipliers, and mixers. The program has been tested on various nonlinearly loaded antenna structures. Its predictions are found to be in agreement with measured results, and with analytical results published in the literature.

1. Introduction

The widespread use of electronic circuits in computer and communication systems requires that such circuits operate in close proximity. Very often, these circuits are sources of interfering electromagnetic energy, and interact with each other adversely. The ability to assess the immunity of these circuits to electromagnetic interference using computational techniques is an important asset to the designer.

When an electronic circuit is exposed to interfering electromagnetic energy, currents are induced in the cables attached to the circuit, and in the various conducting traces connecting the circuit's electronic components. The amplitudes of these currents might be high enough so as to cause the electronic components to malfunction, or even fail.

In order to predict the effects of electromagnetic interference on the components of an electronic circuit, this paper combines linear electromagnetic field analysis with nonlinear circuit analysis. First, field analysis using the Richmond-Tilston thin-wire method of moments [1-4] is performed to determine the induced currents and an equivalent network of the field-exposed cables and conducting traces of the circuit. Then, the

induced currents and the equivalent network thus found are combined with the electronic components, and the resulting system is analyzed using SPECTRE [5], a nonlinear circuit analysis program employing the method of harmonic balance.

The computer program SPECTRE can be used to find the periodic steady-state response of nonlinear circuits driven by single-frequency, or at most dual-frequency excitations. Here, dual-frequency excitation means that the source of the field, say a voltage generator, has an impressed voltage with two single-frequency spectral components. Alternatively, the two single-frequency excitations could originate from two separate generators. A practical example would be intermodulation interference from two mobile transmitters. Another example would be the interference in a single-frequency driven electronic circuit caused by a nearby single-frequency transmitter.

2. Analysis technique

Given a thin-wire structure loaded with electronic components in a dual-frequency (ω_1 and ω_2) impressed electromagnetic field, the following steps are applied:

- (a) On the wire structure, N ports are defined corresponding to the N ports of the electronic components connected to the wire structure.
- (b) The electronic components are removed.
- (c) The S -matrix of the N -port wire structure is determined at zero frequency using the following:
 - i) Norton's equivalent circuit theorem generalized to N -port networks.
 - ii) The nodal admittance formulation [6].
 - iii) Y -matrix to S -matrix conversion.
- (d) At the radian frequencies $m\omega_1 \pm n\omega_2$, where m and n are non-negative integers, the S -matrix of the N -port wire structure immersed in the dual-frequency electromagnetic field is determined using the following:
 - i) The thin-wire method of moments.
 - ii) Norton's equivalent circuit theorem generalized to N -port networks.
 - iii) Y -matrix to S -matrix conversion.
- (e) The N ports are shorted. Then, the currents that flow through these ports at the fundamental frequencies ω_1 and ω_2 are determined using the following:

- i) The superposition theorem.
- ii) The thin-wire method of moments.

The currents thus determined will be referred to as the field-equivalent current sources. The wire structure is now equivalent to an N -port network represented by an $N \times N$ S -matrix loaded with these current sources.

- (f) The electronic components are connected to the N -port equivalent network, and the resulting system is analyzed using SPECTRE.

For a nonlinearly loaded thin-wire structure in impressed single-frequency (ω_1) electromagnetic fields, ω_2 is set to zero in (d) and (e).

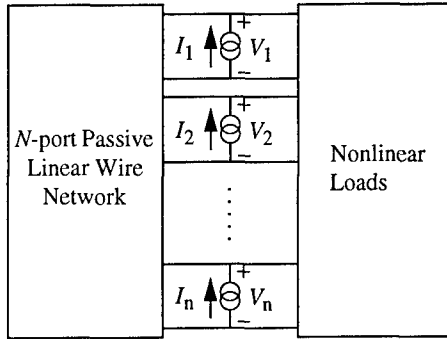


Figure 1. Equivalent representation of a nonlinearly loaded thin-wire structure in impressed electromagnetic fields.

3. Results

3.1 Example 1

The first example selected for analysis is shown in Fig. 2 and consists of a dipole antenna center-loaded with a Zener diode. The dipole height is $L = 0.2734$ m, and the wire radius is $R = 0.00184$ m. A uniform, single-frequency plane wave with peak electric field amplitude E_0 and frequency $f = 300$ MHz is incident on the wire structure. The electric field is parallel to the dipole antenna. The i - v characteristic of the Zener diode is approximated using the plot shown in Fig. 2.

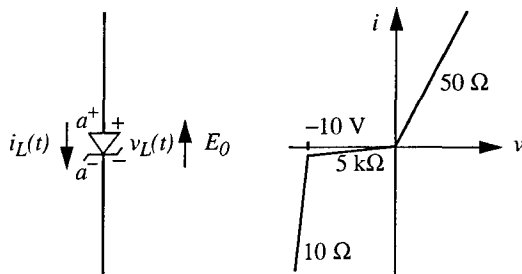


Figure 2. Dipole antenna loaded with a Zener diode, and the Zener diode approximate i - v characteristic.

The steady-state current $i_L(t)$ through the Zener diode, as derived by Liu and Tesche [7] is given by

$$i_L(t) = i_{sc}(t) - \int_{-\infty}^t y_{in}(t-\tau) v_L(\tau) d\tau \quad (1)$$

where

$y_{in}(t)$ = The inverse Laplace transform of the input admittance $Y_{in}(s)$ of the antenna.

$v_L(t)$ = The voltage across the nonlinear load as a function of $i_L(t)$.

$i_{sc}(t)$ = The time-dependent short-circuit current at the antenna port induced by the time varying incident plane wave, striking the antenna at $t = 0$.

Equation (1) contains a convolution integral over the entire past history of the antenna port, and may be solved for the steady-state current using a time-stepping technique [7].

By applying the analysis technique developed in Section 2 to the field-exposed antenna structure of Fig. 2, the equivalent circuit shown in Fig. 3 results. Then, for $E_0 L = 10, 12.5$, and 100 volts where E_0 is the peak electric field amplitude, the computer program TWIRE is used to determine the periodic steady-state current through the Zener diode. For each of these cases, the normalized currents as determined by TWIRE, and by Liu and Tesche are shown in Fig. 4. The first fifteen harmonics of the fundamental frequency f were chosen in constructing the waveforms obtained by TWIRE for each case since it was found that a larger number of harmonics results in less than 1% change in the current waveforms.

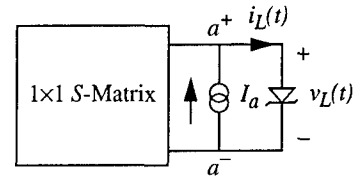


Figure 3. The equivalent circuit of the antenna structure shown in Fig. 2.

When $E_0 L = 10$ volts, the electromagnetic field excitation is not strong enough to drive the Zener diode into reverse breakdown, and Fig. 4a shows the rectifying nature of the diode. When $E_0 L = 12.5$ volts, Fig. 4b shows the normalized steady-state current through the Zener diode at the onset of reverse breakdown. When $E_0 L$ is increased to 100 volts, the Zener diode reverse breakdown is evident from the normalized steady-state current plot of Fig. 4c.

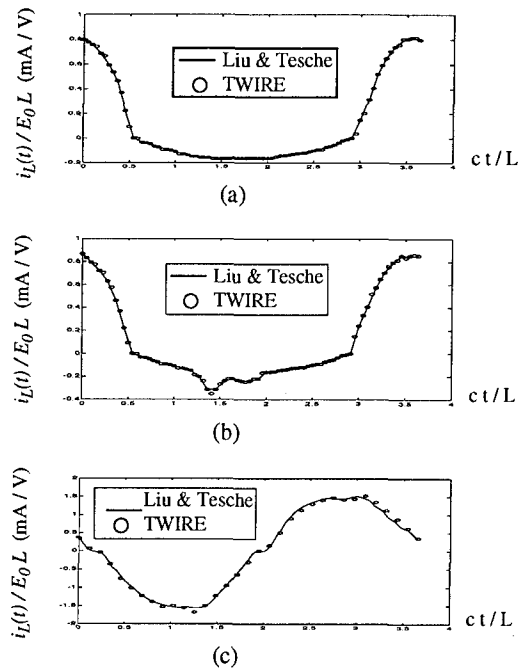


Figure 4. The normalized current waveform through the nonlinear load for (a) $E_0 L = 10$ V, (b) $E_0 L = 12.5$ V, and (c) $E_0 L = 100$ V.

The normalized periodic steady-state currents obtained using TWIRE are in agreement with those determined by Liu and Tesche. For a wire structure with a large number of nonlinearly loaded ports, the time-stepping technique developed by Liu and Tesche becomes inefficient as it requires convolution over the entire history of each port.

3.2 Example 2

The third example chosen for analysis consists of a nonlinearly loaded dipole antenna immersed in a dual-frequency E -field, and is shown in Fig. 5.

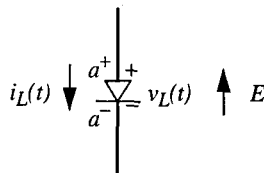


Figure 5. A diode-loaded dipole antenna immersed in a dual-frequency impressed field at $f_1 = 141.25$ MHz and $f_2 = 159.32$ MHz.

The dipole antenna has a radius $R = 0.003$ m and a height $L = 0.966$ m. It is center-loaded with a diode whose i - v characteristic is approximated by

$$i(t) = a v(t) + c v^3(t) \quad (2)$$

where $a = -0.00008$ A/V and $c = 0.00392$ A/V³. The dual-frequency E -field is parallel to the axis of the dipole antenna and is of intensity E given by

$$E = 0.25 (\cos 2\pi f_1 t + \cos 2\pi f_2 t) \quad (3)$$

where $f_1 = 141.25$ MHz and $f_2 = 159.32$ MHz.

In order to determine the steady-current through the diode of Fig. 5, Schuman [8] solved a space-time-domain integro-differential equation using a time-marching procedure carried out over 2560 segments in time.

By applying the analysis technique developed in Section 2, the dual-frequency field-exposed antenna structure shown in Fig. 5 may be represented by the equivalent circuit of Fig. 6 in which two field-equivalent current sources are used to account for the impressed fields at frequencies f_1 and f_2 . Fig. 7 shows the current waveforms through the nonlinear load as determined by TWIRE, and by Schuman.

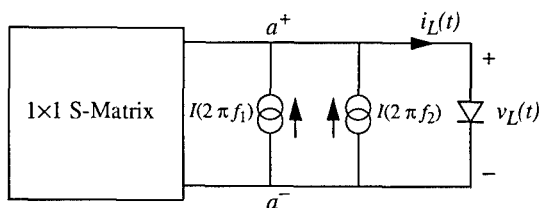


Figure 6. The equivalent circuit of the diode-loaded dipole antenna of Fig. 5.

In Fig. 7, the slow envelope has a frequency $f_2 - f_1$. The fast oscillations have a frequency at which the dipole is approximately half-wavelength-long. The magnitude of the FFT of the load current waveform was determined using TWIRE, and is plotted against frequency as shown in Fig. 8. This plot displays the intermodulation and harmonic components at $2f_1 \pm f_2$, $2f_2 \pm f_1$, $3f_1$, and $3f_2$.

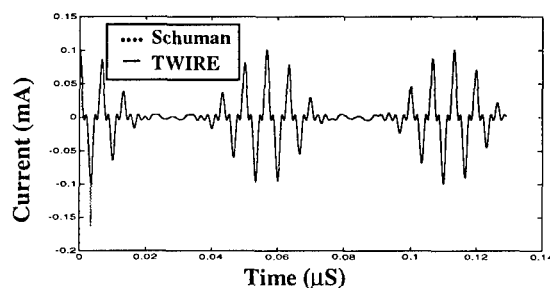


Figure 7. The diode current waveform of the dipole antenna structure shown in Fig. 5 when immersed in a dual-frequency impressed field at $f_1 = 141.25$ MHz and $f_2 = 159.32$ MHz.

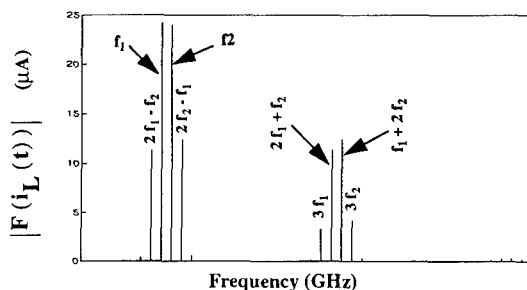


Figure 8. The magnitude of the FFT of the load current waveform shown in Fig. 7 as determined using TWIRE. This plot displays the intermodulation and harmonic components at $2f_1 \pm f_2$, $2f_2 \pm f_1$, $3f_1$, and $3f_2$.

The steady-state current waveform through the nonlinear load obtained using TWIRE is in agreement with that obtained by Schuman. For field-exposed antenna structures with a large number of nonlinear loads, Schuman's technique becomes very inefficient as it involves the solution of a large number of integro-differential equations over thousands of time segments.

4. Conclusions

An S -parameter-based technique has been developed and used to combine the thin-wire method of moments program with the SPECTRE frequency-domain nonlinear circuit analysis program employing harmonic balance. The technique has been tested on various nonlinearly loaded antenna structures, and the simulation results are in very close agreement with analytical results published in the literature.

The combined field-circuit program may be used to determine the periodic steady-state response of nonlinearly loaded thin wires exposed to single or dual-frequency electromagnetic fields.

5. References

- [1] J. H. Richmond, "Radiation and scattering by thin-wire structures in the complex frequency domain," Ohio State University ElectroScience Lab., Rep. NASA CR-2396, May 1974.
- [2] J. H. Richmond, "Computer program for thin-wire structures in a homogeneous conducting medium," Ohio State University ElectroScience Lab., Rep. NASA CR-2399, June 1974.
- [3] M. A. Tilston, and K. G. Balmain, "On the suppression of asymmetric artifacts arising in an implementation of

the thin-wire method of moments," *IEEE Trans. Antennas Propagat.*, vol. AP-38, pp. 281-285, Feb. 1990.

- [4] M. A. Tilston, and K. G. Balmain, "A multiradius, reciprocal implementation of the thin-wire moment method," *IEEE Trans. Antennas Propagat.*, vol. AP-38, no. 10, pp. 1636-1644, October 1990.
- [5] K. S. Kundert, and A. Sangiovanni-Vincentelli, "Simulation of nonlinear circuits in the frequency domain," *IEEE Trans. Comp.-Aid. Des.*, vol. CAD-5, pp. 521-535, Oct. 1986.
- [6] J. Vlach, and K. Singhal, *Computer Methods for Circuit Analysis and Design*, Van Nostrand Reinhold, 115 Fifth Avenue, New York, N. Y., 1983.
- [7] Liu T. K., and Tesche F. M., "Analysis of antennas and scatterers with nonlinear loads," *IEEE Trans. Antennas Propagat.*, vol. AP 24, no.2, March 1976.
- [8] Schuman H., "Time-domain scattering from a nonlinearly loaded wire," *IEEE Trans. Antennas Propagat.*, vol. AP 22, pp. 611-613, July 1974.
- [9] J.-J. Laurin, S. G. Zaky, and K. G. Balmain, "EMI-induced delays in digital circuits: prediction," *IEEE International Symposium on Electromagnetic Compatibility*, Aug. 17-21, 1992, pp. 443-448.

6. Acknowledgment

The authors express their appreciation for the support and interaction provided by Bell Canada, and Bell-Northern Research, and in particular by Mr. M.M. Cohen. Additional support was provided by the Natural Sciences and Engineering Research Council of Canada.

DISCUSSION

S. KASHYAP

Could you please comment on the difference between the experimental and twire results ?

AUTHOR'S REPLY

We used a theoretical representation of the diode obtained from a commercially available library of solid-state devices. We did not independently verify that the diode used exactly matches the representation used and therefore suspect that diode variability is the main cause of the observed difference.

A further possibility is that the laboratory setup requires a better arrangement of absorbing material to reduce reflections.

J. LOVETRI

I have two question. The first is : do you think that the discrepancy between the measured results and calculated may be due to direct field coupling into the diode which was modeled by the nonlinear circuit analysis program ?

The second is (I am not quite clear on this point) : when you replace the field problem by a Norton equivalent network, do you replace the impedance by a numerical value or by a function which depends on ω . The reason I ask is that the intermodulation frequencies coming from the nonlinear circuit will, in general, see a different impedance.

AUTHOR'S REPLY

The dimensions of the diode are very small compared to a wavelength and also small compared to the wire segment length in the folded monopole. Therefore direct field coupling to the diode should be negligible.

The field circuit problem is first solved for every harmonic frequency needed and also for every intermodulation frequency. Therefore frequency variation of network element properties is fully incorporated in the method.

HPM Coupling to a Cylindrical Target with Selected Built-In Components

M. Magg

IABG m.b.H.

Einsteinstr. 20

D-85521 Ottobrunn, Germany

J.B. Nitsch

NBC Defense Research and Development Institute

P.O. Box 1142

D-29623 Munster, Germany

SUMMARY

A numerical simulation of HPM coupling to small missiles is described. The main interest is in the currents induced on the interior cabling in the resonance region. The results of the numerical simulation agree very well with real measurements performed on a test model. For a more realistic missile design we will find a very big reduction of the HPM coupling into the missile if its metallic fin system is replaced by a non-conducting one. Finally, we comment on the relation between maximum possible response and the shape of the incident microwave pulse.

1. INTRODUCTION

The electromagnetic resonance region of a target system is of particular interest for HPM coupling. If one succeeds in tuning the frequency of the illuminating wave to a resonance of the target system one will generally amplify the electromagnetic stress for vulnerable components inside the target system [Ref. 1].

Resonances appear at various steps of the electromagnetic coupling mechanism.

- The surface current induced by the illuminating wave on the outer side of the target hull shows resonance bumps closely related to the length scales which determine the external geometry of the target [Refs. 2, 3].
- Slots in the metallic target hull which allow the electromagnetic wave to enter into the interior region will be especially permeable if half the wavelength fits the slot length.
- The target interior with its metallic components and cabling supports very pronounced cavity resonances. Depending on the location and orientation of the electronic component under study these resonances show up in the voltage across its ports.

In this article we are interested in small missiles as possible targets for HPM. Their geometrical dimension (about 1 m in length) is such that all different types of resonance phenomena tend to overlap.

In one of the investigated missile designs the fin system for flight control penetrates the topological separation between shielded inside and unshielded outside. Under such circumstances it is no longer helpful to break the coupling problem into an exterior

and an internal step. Back radiation from inside the target is no longer small.

Complex problems like this can be solved either by measuring the coupling in a real experiment or by numerical simulation.

In this paper we advocate the latter method.

The quantities we are looking for are the currents produced by the HPM illumination in the interior cabling of the missile. For power consideration see Ref. 4. Our study assumes linearity throughout the whole coupling mechanism although in principle it is possible to include non-linear material properties.

In section 2 we analyze the HPM coupling to a wire inside a cylindrical cavity and compare the results of the numerical simulation with a real measurement.

Section 3 deals with a more detailed missile design and estimates the effect of replacing its metallic fin system by a non-conducting version.

Section 4 comments on the question of optimum HPM pulse shape.

Finally, a short summary of the results is given.

2. COUPLING TO A WIRE INSIDE A CYLINDRICAL CAVITY

The coupling of an incident electromagnetic wave to some target is conveniently formulated in terms of the corresponding transfer function:

$$T(f) = \frac{V_i(f)}{E_p^{inc}(f)} \quad (1)$$

In this definition $E_p^{inc}(f)$ is the amplitude of the incident continuous wave with frequency f and a given polarization P at the position assigned for the target. The illumination of the target by that wave causes the voltage V_i across a port of a vulnerable electronic device inside the target, after steady state conditions are achieved.

Note that in this case T has the dimension of a length. The voltage V_i comprises both the amplitude and the phase delay with respect to the incident wave, hence T is a complex function of the frequency f and the polarization P . Obviously, the transfer function is closely related to the concepts of shielding and damping factors which we will not use here.

We assume the target contains a wire connecting two electronic boxes in the inside (see Fig. 1). One box is close to the head, the other close to the tail. Both boxes short-circuit the wire via a small impedance to the target hull.

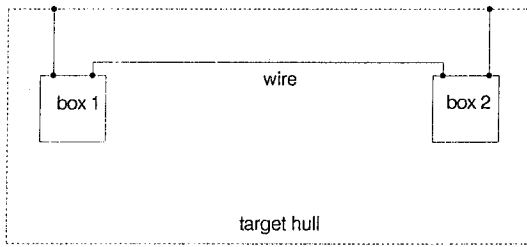


Fig. 1. Target interior

Under these frequently applicable conditions the transfer admittance of the wire

$$T_Y(f) = \frac{I_w(f)}{E_p^{inc}(f)} \quad (2)$$

is of crucial interest. The current I_w is measured at the port of the device of interest. Again the current is defined relative to the phase of the incident c-w signal.

Solving the transmission line problem for the wire and the target hull one can convert the transfer function into the transfer admittance and vice versa.

To investigate the coupling into the target interior one usually factorizes the problem into an exterior and an interior part [Ref. 5]:

$$T_Y(f) = T_i(f) \cdot T_e(f) \quad (3)$$

The exterior transfer function T_e is the ratio of the actual field or current surface density at a small aperture or narrow slot on the outside of the target hull (after steady state is reached) over the amplitude of the incident wave. Taking polarization indices into account T_e is a complex matrix and T_i a complex vector.

The interior transfer function T_i is the ratio of the current I_w to that external field or current surface density. If there are several penetration paths into the target each path gives rise to a term like (3). The

complete results for T_Y is then given by the sum over all the individual paths.

The factorization (3) will be of practical importance if the penetration path from the outside region to the interior region is narrow, e.g. only a few narrow slots or small apertures perforate the metallic target hull. Under this condition T_e will change only very little if all slots and apertures are closed and only the exterior of the target is seen by the incident wave. If the exterior geometry of the target is simple enough an analytical treatment for a resonance decomposition of the exterior transfer function may be manageable [Refs. 2, 3]. The resonance poles of the exterior transfer function for the flat ended cylinder are well known [Ref. 3].

As a simple well defined reference object we took a slotted cylindrical cavity with a single wire. The cylinder is 50 cm long and 25 cm in diameter. Halfway between the two flat endcaps the cylinder jacket has a thin circumferentially oriented slot of 35° angular extent. In the plane fixed by the cylinder axis and the slot center there is a wire at a distance of 4 cm parallel to the cylinder axis. The wire is shortened at both endcaps. The computer generated model of this configuration is shown in Fig. 2. The upper half of the cylinder is taken away to present the interior. The model uses a spatial resolution down to 5 mm which is sufficient for this electromagnetic simulation. We simulated a broad side illumination of this cylinder. The propagation vector at the incident wave is parallel to the direction pointing from the center of the slot to the center of the cylinder. The polarization is orthogonal to the slot.

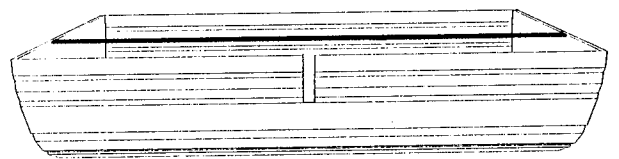


Fig. 2: Computer model of a slotted, cylindrical cavity with wire parallel to axis (top half removed)

The resulting exterior transfer function T_e as a function of the frequency is presented in Fig. 3. This transfer function refers to a point 0.3 m in front of the slots center. The polarization for T_e was that of the incident wave. The humps of the graph fit the low lying circumferential TE and meridional TM surface resonance modes as expected from that illumination [Ref. 3].

The exterior transfer function T_e is of crucial interest when dealing with the frequency dependence of the radar back scattering cross section. Except for the

peak at 210 MHz all other narrow spikes on the back of the broad humps are due to the reradiation of the cavity resonances via the circumferentially oriented slot. Obviously, the factorization into exterior and interior problem will be useful only if this reradiation is small and can be neglected.

The transfer admittance of the wire inside the cylinder for broadside incidence is shown in Fig. 4. The transfer admittance refers to the current on the wire 1 cm away from the endcaps.

The most prominent spikes are produced by the TEM modes followed by some of the TM modes. Note TE-modes do not support a current in strictly axial parallel wires hence they do not show up in the transfer admittance. The relative weight at which the individual TEM or TM resonance respectively contribute to the transfer admittance tends to follow the exterior transfer function. This illustrates the factorization property (3).

Changing the distance of the wire relative to the cylinder axis shifts the TM resonance contributions to the transfer admittance up to 10 % on the frequency axis.

The results presented in Figs. 3 and 4 are obtained by employing a commercial state of the art finite difference time domain code for Maxwell's equations on a middle class computer work station [Ref. 6]. Fig. 5 shows the same transfer admittance as measured by a real experiment [Ref. 7]. Both results agree very well. The conspicuous differences in the height of narrow peaks are due to different frequency resolution and slightly different measurement positions in both experiments. Some tiny sharp spikes which appear in Fig. 5 and are missing in Fig. 4 can be attributed to TE-modes. They contribute in the „real“ experiment because there the wire was not absolutely parallel to the cylinder axis.

Taking into account the sensitivity of the transfer admittance to minor variations of the wire location, computer simulation has proven to be a fast, reliable and cost efficient method to measure transfer functions.

If a slot of length l in a big planar shield is illuminated by an orthogonal polarized wave with a wave length longer than

$$2 \cdot l \quad (4)$$

a short wire bridging the slot at its center will carry the following current:

$$i_{bridge} = l \cdot \frac{E^{inc}}{Z_o} \quad (5)$$

In this formula Z_o denotes the impedance of free space. The transfer admittance of that little bridge across the slot is:

$$T_Y = \frac{l}{Z_o} \quad (6)$$

The circumferentially oriented slot of our cylinder has a length of 0.076 m. The same slot in a planar shield would produce a transfer admittance of 2×10^{-4} A x m/V. This is much less compared to what is received by the wire in the cylinder at resonance frequencies.

The characteristic impedance of the wire at a distance of 4 cm parallel to the cylinder axis is about $250 \Omega \pm 10 \%$ depending on the exact value for the diameter of the wire.

The transfer admittance of the wire close to the cylinder endcap transforms into the following transfer function for the voltage between wire and cylinder hull halfway between the two endcaps:

$$T_{center} = 250 \Omega \cdot T_Y \quad (7)$$

Near resonance we get:

$$T_{center} = 0,375 m \quad (8)$$

This again is significantly more than what is expected from the geometrical length of the slot alone.

3. MICROWAVE COUPLING TO A MISSILE

Perhaps the most important penetration path for a microwave signal into a small missile is via its stabilizers and flight control fins. These fins get usually extended through narrow slots in the missile hull. They are connected by some handles with a steering device in the missile. Fig. 6 shows a computer model of such a missile. One half of the hull is removed to reveal the missiles interior. The missile model taken has a length of 63 cm and a diameter of 26 cm. Its interior is divided into 3 compartments by metallic partition walls. Only the middle compartment has a direct connection to the exterior since it houses 4 flight control fins.

A wire connects the missiles tail cap with the front compartment. At both ends the wire is shortened to the hull; most of its way the wire runs within 0.5 cm distance from the hull's inner side. The wire enters and leaves the middle compartment via small ducts in the partitions. There was no direct conducting connection between the wire and the fin system. Spatial resolution of this computer model was 2.5 mm.

We simulated a head-on illumination of that missile measuring the wire current in all 3 compartments. The corresponding transfer admittances for the middle and the tail compartment are presented in Figs. 7 and 8, respectively. The transfer admittance reflects basically the resonance spectrum of the missile's interior which was computed independently using a numerical electromagnetic eigenmode solver program. The lowest spike at around 140 MHz is caused by the fin system which extends from the middle compartment to the missile outside. The 140 MHz spike pops up in the missiles exterior transfer functions as well. An example is presented in Fig. 9 which displays the magnetic transfer function as measured at the pole of the hemispherical frontcap. The component shown is parallel to incident magnetic field of the wave.

Comparing the transfer admittance as measured in the poorly shielded middle compartment with the transfer admittance in the separated tail compartment one learns that most of the induced current follows the wire and penetrates the partition walls. Capacitive leak off at the wire ducts is not very efficient.

The maximum of transfer admittance in the fin compartment is 1.2×10^{-3} A/(V/m) at a frequency of 1.57 GHz. In the tail compartment one still finds 0.85×10^{-3} A/(V/m) at 1.83 GHz.

The wire 0.5 cm apart from the hull inside has a characteristic impedance of about 140 Ω. This means in the middle of the tail compartment one can expect a transfer function for the voltage between wire and hull of 0.12 m.

An obvious way to reduce the coupling is to replace the metallic fins and fin handles by non-conducting counterparts. The effect of this action can be seen in Fig. 10 which displays the transfer admittance in the fin compartment for non-metallic fins. The geometry including the slots was not changed.

The overall effect is a reduction of the coupling to the wire by 40 dB relative to the metallic fin system. The current in the tail compartment is even more reduced. The most prominent effect of this action on the external transfer function (Fig. 11) is the vanishing of the fin resonance spike at 140 MHz on the back of the lowest meridional exterior body resonance.

For a missile with metallic fins the factorization (3) of the transfer function into interior and exterior part loses its practicability. From the topological point of view the distinction between shielded and unshielded regions becomes ambiguous. At the resonance of the fin system this distinction loses its meaning completely.

As a possible alternative for a non-conducting fin system a coating of the inner side of the fin compartment with absorbing material was suggested. Assuming a 1 cm thick layer of conventional HF absorber material we find a satisfactory damping of the resonances between 1.5 and 2.5 GHz. However, the strong lower lying resonance suffer only very little suppression.

4. SPECTRAL ENGINEERING

The maximum magnitude of the transfer admittance as a function of frequency constitutes an upper bound for the induced current relative to the incident electric field whatever spectrum is used for the incident pulse. Obviously, in order to get close to the maximum current one has to tune the incident signal precisely to the highest resonance in the transfer admittance and limit the bandwidth to about the halfwidth of the resonance peak.

In the real world this optimizing strategy runs a high risk to fail.

Usually, the resonance structure of a possible target is only poorly known. Fine tuning would require the frequency resolution not to be worse than a few MHz. Very often the target resonance one tries to excite sits in the lower part of the resonance spectrum where prominent resonance spikes are sparse.

Very likely the attempt to maximize the responding current of a vulnerable target component by using fine tuned, narrow banded signals will end with at least 20 dB less than what was expected because one has hit only the footing of the resonance one was aiming at.

The physical characteristics of the HPM source provide a further obstacle to obtain maximum response. For various source types the pulse length is quite limited, i.e. 100 ns. The corresponding frequency bandwidth is then 40 MHz at least. This limits the fine tuning and lowers the actually achievable response.

Taking into account the finite pulse length in time it is of interest how long the triggered response at a vulnerable port inside the target persists.

Because of the many contributing cavity resonances with vastly different decay times this response does not follow a simple exponential law. Roughly, one may characterize the length of the signal response by the time $t_{1/2}$ it takes from its peak amplitude to come down to half that value.

As examples we selected two types of microwave pulses. Both are gaussian pulses with a carrier frequency of 1.5 GHz. The short 10 ns pulse has a bandwidth of 354 MHz, the bandwidth of the „long“ 100 ns pulse is 10 times smaller. These two pulse types are used to illuminate the missile of Fig. 6 head-on with a peak strength of 1 V/m. The resulting currents on its head to tail wire are summarized in Table 1.

The table also contains the current strength obtained by a cw illumination. It can be seen that the currents induced by finite length pulses were considerably weaker than those induced by ideally tuned cw illumination. The length of current response is almost uncorrelated to the length of the incident pulse.

Assume a digital circuit is connected to the end of the wire in the tail compartment. The risk that the short microwave pulse triggers toggling in this circuit may be as high as for the long pulse.

	metallic fin system			non-metallic fin system		
	cw	long pulse	short pulse	cw	long pulse	short pulse
fin compartment	1200/-	98/30	95/150	9/-	0.9/30	3/30
tail compartment	850/-	15/35	32/300	4/-	0.3/40	0.07/500

Table 1: Current on wire inside missile
The current is described in the form peak amplitude in μA / $t_{1/2}$ in ns.
The illuminating wave had a maximum field strength of 1 V/m.

5. CONCLUSIONS

This study gives an example of the capabilities of a numerical simulation of microwave coupling into missiles. Spatial resolution down to the mm scale allows quite realistic modeling.

The numerical method is especially helpful in cases where other solution techniques are not practicable and actual measurement is too involved.

The fin system of a missile is identified as a very efficient penetration path into all compartments of a missile. This path can be almost stopped up if the fin system is made out of non-conducting material.

For realistic pulse shapes the coupling of an illuminating microwave to the inside of a missile falls short of the theoretical maximum by a factor of approximately 10.

A narrowbanded signal tuned to the lower part of the resonance region of a small missile runs a high risk to achieve only a poor response because it may miss the sparse resonance peaks in that frequency band.

REFERENCES

- [1] C.E. Baum, „Maximization of Electromagnetic Response at a Distance“, IEEE Trans. Electromagnet. Compatibility, Vol. 34, No. 3, pp. 148 - 152, August 1992.
- [2] C.E. Baum, „The Singularity Expansion Method“, in Topics in Applied Physics, Vol. 10, L.B. Felsen Ed., Berlin Germany, Springer Verlag, 1986, pp. 129 - 179.
- [3] H.M. Überall, C.R. Schumacher, X.L. Bao, „Resonant Attenuation in Electromagnetic Wave Scattering from Conducting Elongated Objects“, IEEE Trans. Electromag. Compatibility, Vol. 35, No. 4, pp. 466 - 471, November 1993.
- [4] K.S.H. Lee, Fang-Chou Yong, Trends and Bounds in RF Coupling to a Wire inside a Slotted Cavity“, IEEE Trans. Electromag. Compatibility, Vol. 34, No. 3, pp. 466 - 471, November 1993.
- [5] C.E. Baum, „Electromagnetic Topology: A Formal Approach to the Analysis and Design of Complex Electronic Systems“, Proceedings of the EMC Symposium, Zürich, pp. 209 - 214, March 1981.
- [6] The MAFIA collaboration, „Users' Guide MAFIA, Version 3.x“, CST GmbH, Lauteschlägerstr. 38, D-64289 Darmstadt, Germany.
- [7] Ch. Braun, W. Ochs, H.V. Schmidt, „Low Level Microwave Field and Current Coupling Measurements on/into a Generic Missile Model“, Fraunhofer-Institut für Naturwissenschaftlich-Technische Trendanalysen, D-53864 Euskirchen, Germany, 1991.

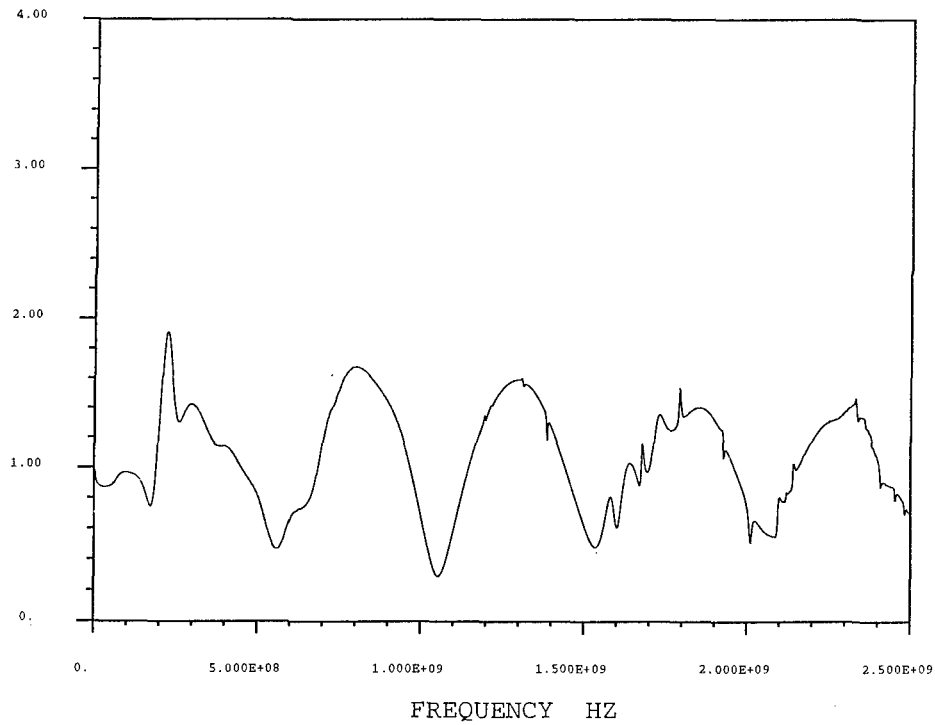


Fig. 3: Exterior transfer function T_e of cylindrical cavity for broadside illumination

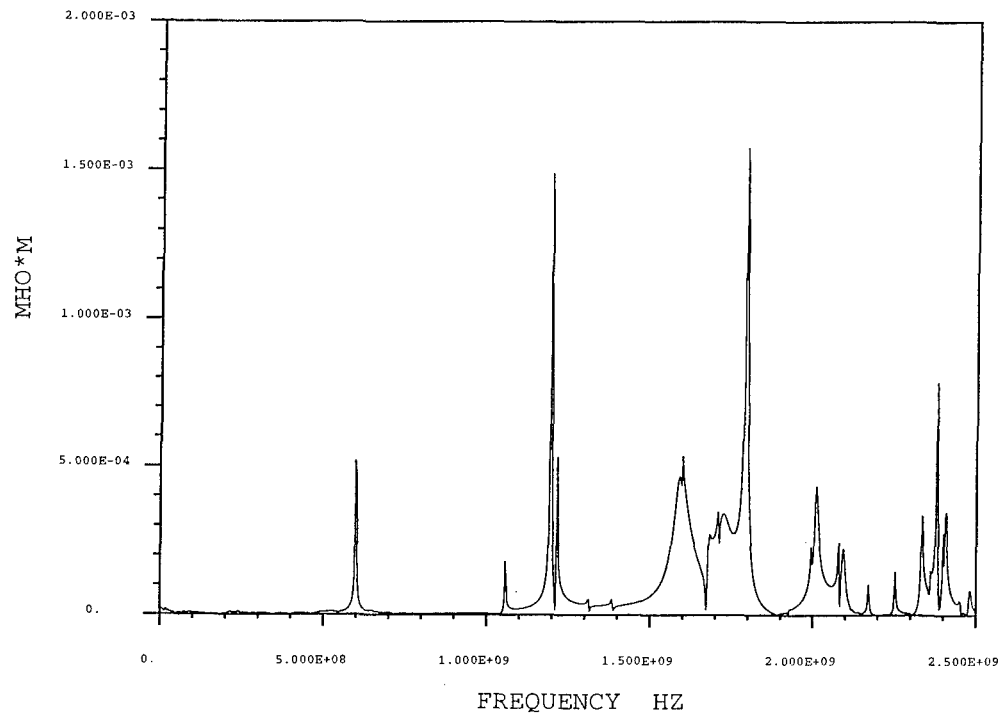


Fig. 4: Transfer admittance T_y of wire inside cylindrical cavity.
Distance of wire to axis 4 cm.

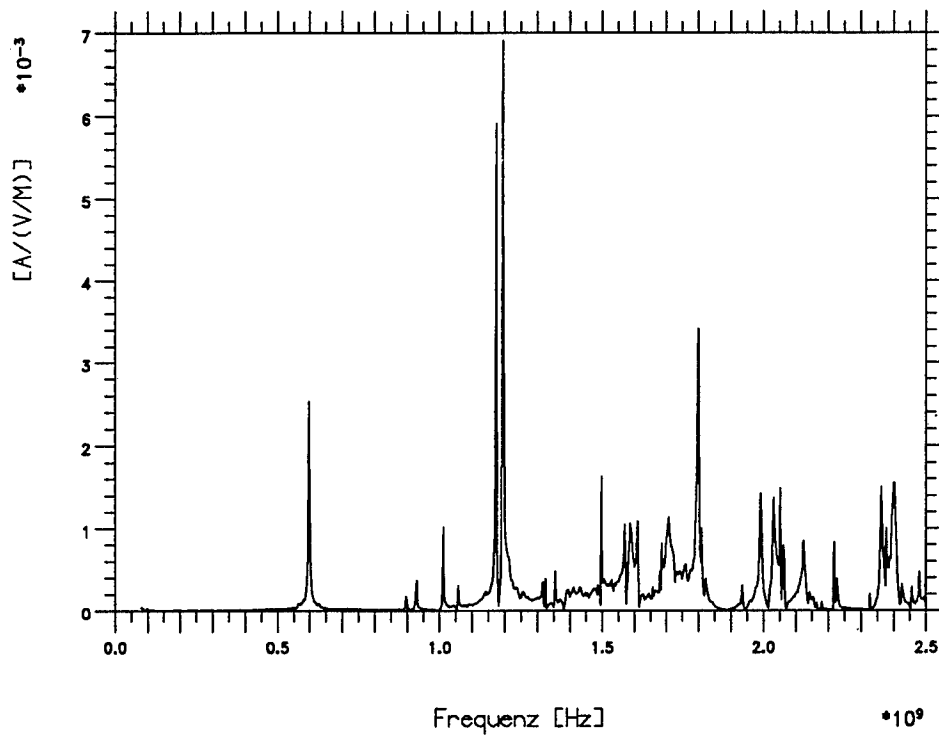


Fig. 5: Same transfer admittance as in Fig. 4 but measured by experiment. Distance of wire to axis about 4.5 cm.

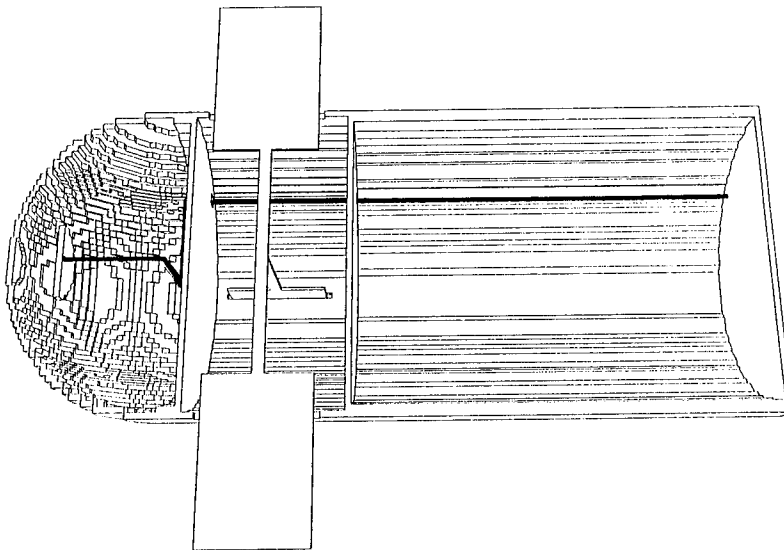


Fig. 6: Computer model of a small missile with extendable fins and 3 compartments. Wire runs from head to tail. Half of the hull is removed to display the inside.

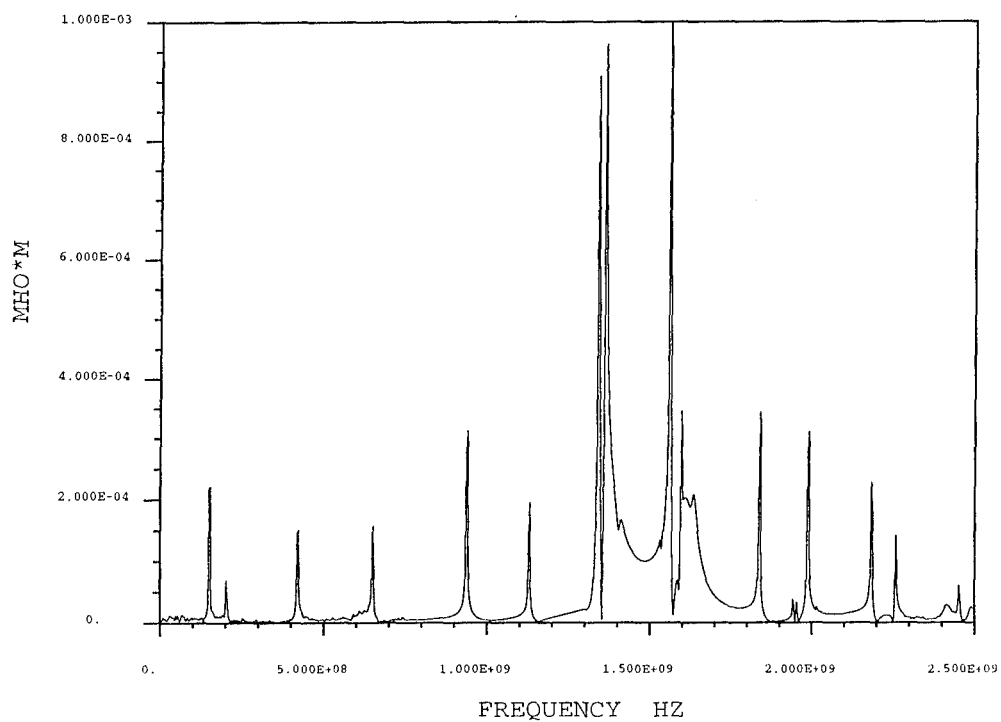


Fig. 7: Transfer admittance of wire in the fin compartment of small missile for head-on illumination

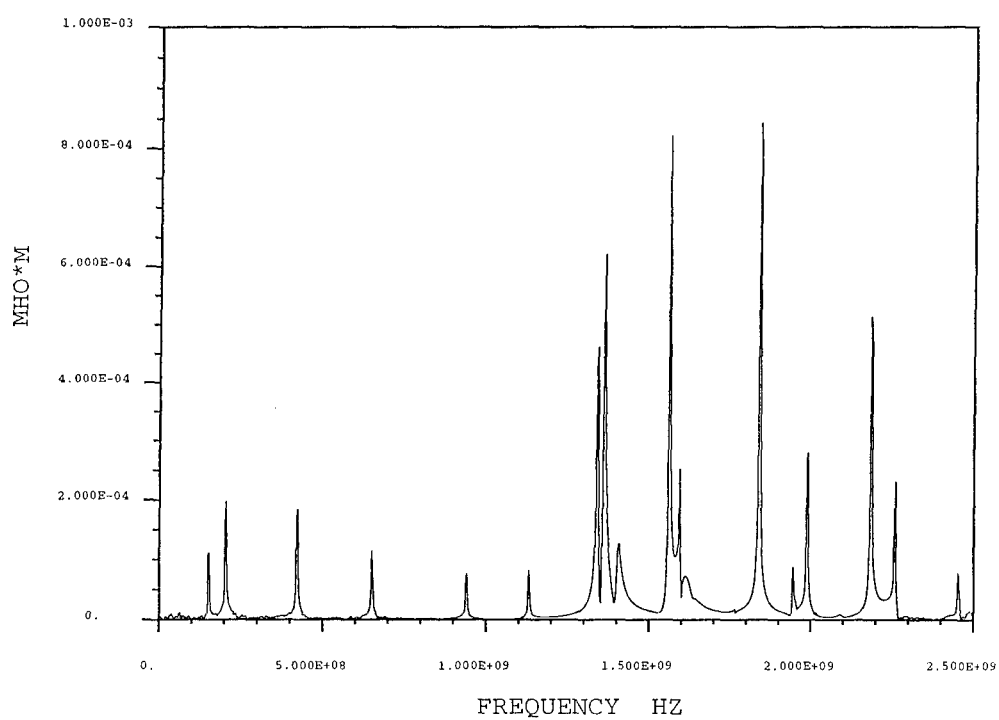


Fig. 8: Transfer admittance of wire in the tail compartment of small missile for head-on illumination

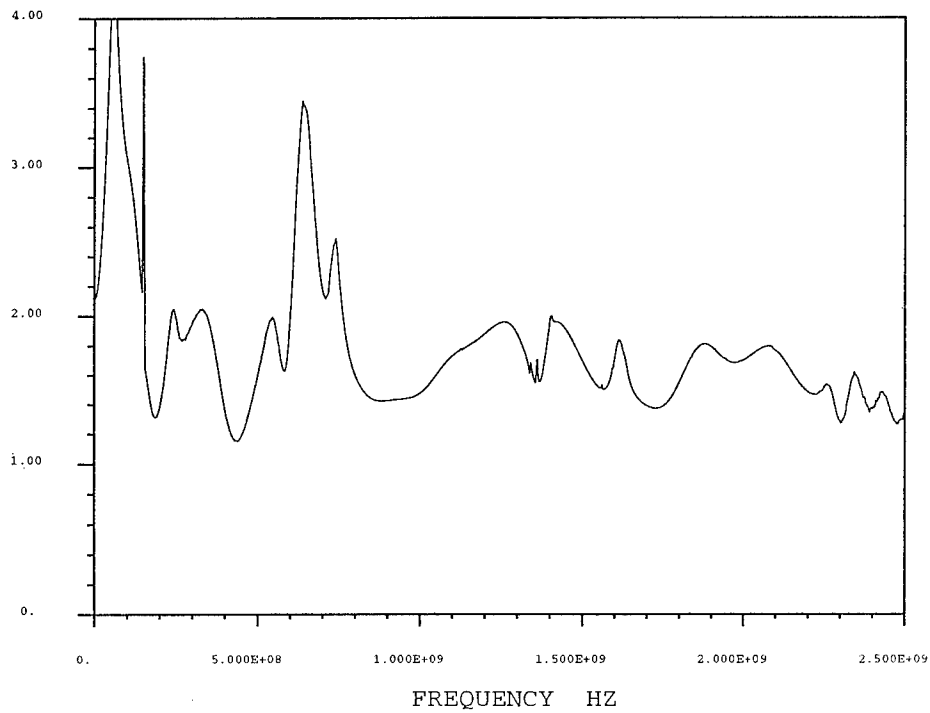


Fig. 9: Exterior magnetic transfer function of small missile for head-on illumination. Polarization same as for incident wave.

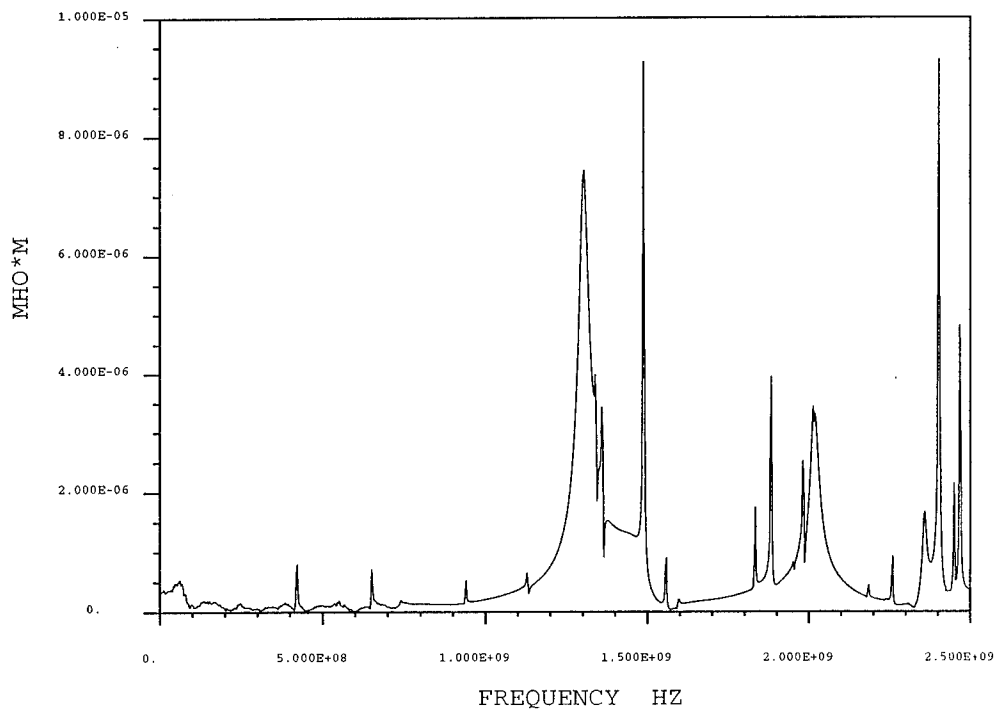


Fig. 10: Same transfer admittance as in Fig. 7, however, fin system is non-conducting

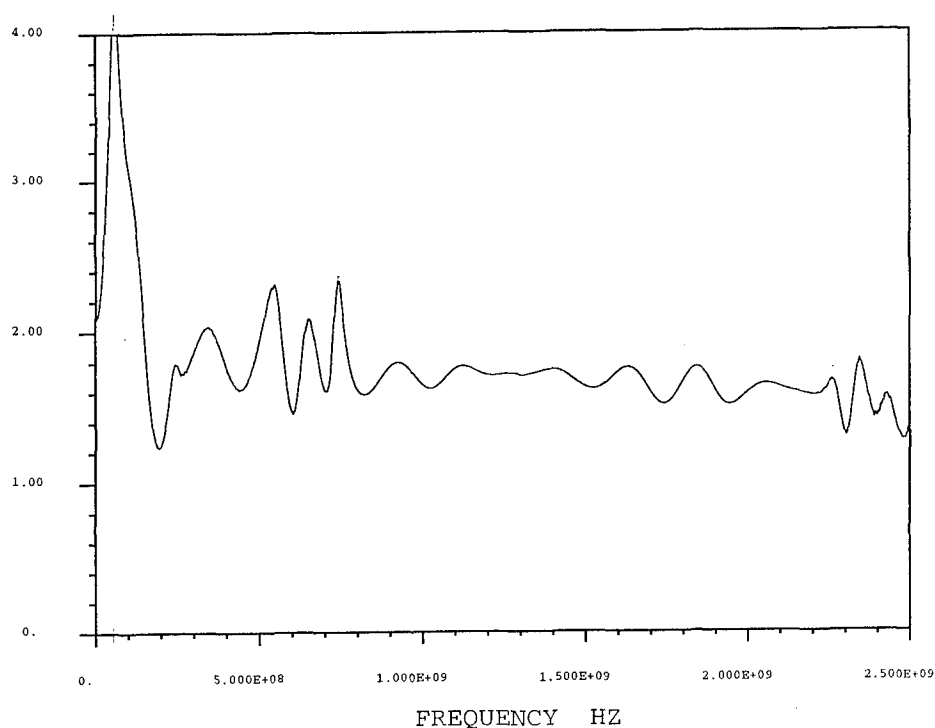


Fig. 11: Same exterior transfer function as in Fig. 9, however, fin system is non-conducting

DISCUSSION

P. FUERXER

Les spécialistes de l'acoustique des salles ont éliminé l'effet de résonances fines non significatives en utilisant des sons hululés c'est-à-dire modulés en fréquence. Pensez-vous que cette approche pourrait être utile dans le calcul des couplages électromagnétiques ? Cette remarque s'applique de façon générale à la démarche actuelle basée sur les calculs sur ordinateur et pas seulement aux résultats présentés dans cet exposé qui a particulièrement bien mis en valeur les problèmes et leur complexité.

Translation:

Room acoustics specialists have eliminated the effects of fine, non significant resonances by using warbled sounds i.e. frequency modulated sounds. Do you think that this approach could be useful for the calculation of electromagnetic couplings ? This remark applies in a general way to the present approach based on computer calculations and not simply on the results presented in this paper, which was particularly good at exposing the problems in all their complexity.

Coupling Measurements on Intelligent Missiles at Microwave Frequencies

Ch. Braun

P. Guidi

H.U. Schmidt

Fraunhofer Gesellschaft INT

Appelsgarten 2

D-53881 Euskirchen

Germany

1. SUMMARY

This paper describes our low power microwave coupling measurements on terminally guided missiles in the frequency range between 10 ... 8000 MHz. The *plane wave excitation* experiments have been carried out in our field coupling facility, which consists of a asymmetric triplate transmission line with maximum field levels of about 40 V/m in the working volume.

As test objects we examined five (semi) autonomous guided missiles. Three of them, former experimental studies from the Diehl company (GE), are presented in this paper. The test objects were positioned in the simulator in three orthogonal orientation with respect to the external field and were not connected to a power supply (inactive condition).

In order to be able to systematically analyze the interaction of the external electromagnetic fields with the avionics and its wiring, we had to divide the investigations into three independent phases, namely, external interaction with the fuselage, mode of penetration to the interior of the missile and excitation of the electrical systems and the cabling.

The *coupling paths* depend very much on the design principles of the airframe. The main threat identified was back door coupling via those *wings* and *fins*, which are not attached galvanically to the outer surface of the hull. Because of flight guidance, these parts are fastened through slots to the bearings of the motor drives inside the missile. The dominant *cable resonances* sometimes can be traced back to the resonances of the wings and/or fins and the type of cabling. Another threat was coupling via the long *slots* required for the folding wings. These shafts penetrate the whole body and enable the external fields to couple into the interior. The peak amplitudes at the ends of the cables were found to be between 50 ... 500 [$\mu\text{A}/(\text{V/m})$], depending on the test object.

2. INTRODUCTION

The INT is one of about 47 institutes of the Fraunhofer-Gesellschaft (FhG), a non-profit organisation for the advancement of applied research. The INT is under contract of the Ministry of Defence. The main areas of research are related to nuclear radiation and electromagnetic effects. Our group investigates electromagnetic coupling to large conducting structures and systems. To this end, we work with various electromagnetic field codes (NEC, MAFA, CONCEPT) and do plane wave excitation measurements with a self-developed field-coupling facility.

Since 1985 we have conducted with this field simulator a great variety of tests on rather simple structures such as antennas and cylinders as well as on more complicated objects such as scale-models of aircraft (MRCA, EFA) and ship (frigate F122).

Advanced guided missiles require sophisticated technologies with a considerable number of sensors and electronic devices. Autonomous and semi-autonomous missiles need antennas (electromagnetic, optical). Via these components electromagnetic fields can couple into the *interior* of such a projectile. The guidance principles of those missiles necessitate slots, cracks and interfaces for wings and fins, which cause further disturbing fields within the hull. These unwanted fields give rise to interferences and resonances on the cabling and on components, which may degrade the performance of the whole system.

Some typical effects on guided missiles due to high power electromagnetic fields are disturbances of target identification and tracking, influence on the inertial measuring unit or generation of unwanted motions of the rudder. These interferences have different consequences, dependent on the guidance principle. For example, the missile can lose its target (IR seeker), leave its steering range (laser beam rider) or can be disturbed in its operating sequence. Furthermore the interfering fields within the airframe can impair electronic devices or even destroy them. The unwanted ignition of pyrotechnic elements (squibs) might be another awful consequence.

In view of this threat the German MOD initiates a *research project* to investigate the coupling mechanisms onto and system performances on available missiles under analytical, numerical and experimental aspects. In 1992, the German MOD asked some of his laboratories and an industrial company (Diehl R thenbach, GE) to investigate and assess the HPM threat to missiles. The task for INT was to

- *measure the coupling of plane waves* in the frequency range between .01 ... 8 GHz
- on the airframe (hull, wings, fins)
- through apertures into the interior
- onto cables and components
- *determine the transfer functions* with respect to the external field
- *find out the dominant coupling paths*
- *ascertain the dominant resonance frequencies*
- *cooperate* on establishing *test plans* for the susceptibility measurements with considerable higher electromagnetic fields on the active missiles in view of the measured resonance frequencies. These tests will be carried out in another test facility (WTD 81 Greding, GE).

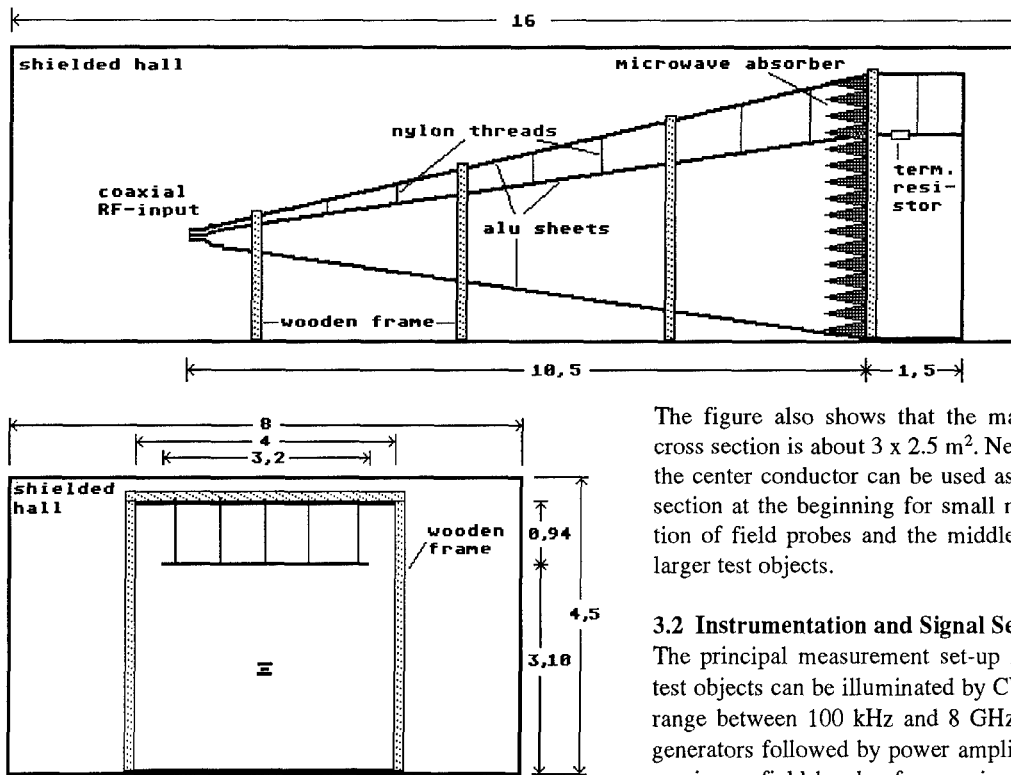


Fig.3.1: Side view and cross section of the TEM wave guide of the INT (units in meter)

3. INT FIELD COUPLING FACILITY

All measurements were done with our field simulator. It was built in 1984 and served at first as a tool to carry out scale model measurements [1,2]. For example, we examined a 1/50-scale model of the German F 122 frigate, a 1/20-scale model of the EFA aircraft and a 1/10-scale model of the MRCA. Since then the equipment was permanently improved and is currently used mainly for real size tests on missiles.

3.1 TEM Wave guide

We use an open tapered TEM cell. To enlarge the test volume, the septum was not placed in the middle, but at approximately 3/4 of the height of the cell. The design is illustrated in Fig.3.1. The simulator consists of a

- source (coaxial input)
- launcher which provides a transition from the circular coaxial output of the source to the unsymmetric rectangular triplate geometry of the line
- long *pyramidal shaped* section of transmission line maintaining the width-to-plate separation ratio to provide a constant impedance ($50\ \Omega$) along the length of the line while gradually changing the cross-sectional dimension. This section is the actual simulator and includes the *test volume*
- short *parallel plate region*, where resistors and absorbers are placed.

At low frequencies, a *resistor network* in series with the center conductor and equal to the characteristic impedance of the transmission line provides a matched termination for energy propagating on the line. At high frequencies, a wall of e.m. energy *absorbing material* placed across the output end of the line provides a non-reflecting termination.

The figure also shows that the maximum working volume cross section is about $3 \times 2.5\ \text{m}^2$. Nearly the whole area under the center conductor can be used as test volume: the smaller section at the beginning for small models or for the calibration of field probes and the middle and the end section for larger test objects.

3.2 Instrumentation and Signal Sensing

The principal measurement set-up is shown in Fig.3.2. The test objects can be illuminated by CW-fields in the frequency range between 100 kHz and 8 GHz. Digital tuneable sweep generators followed by power amplifiers are used to produce maximum field levels of approximately 40 V/m in the main working volume. In the front part of the simulator this leads to about 200 V/m.

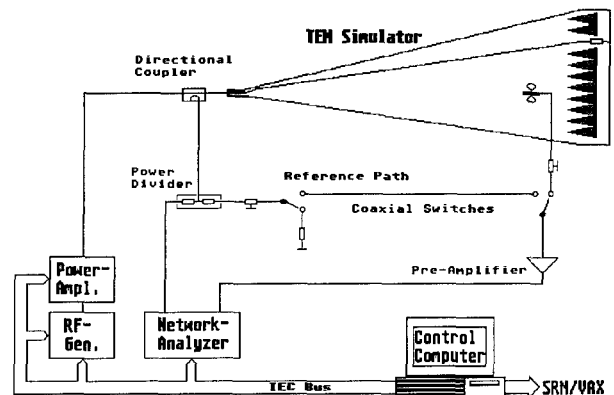


Fig.3.2: Principal measurement set-up

As receiver we use two different vector network analyzers. All devices are controlled and read out via IEC-Bus by a desktop computer (HP9000). Data recording and processing are also performed with this computer or can be done by a DEC computer (VAX).

For surface and free field measurements we use *electrically small* e.m. field sensors. Because these sensors are operated below the cut-off frequency, its output voltage is directly proportional to the frequency. Consequently these probes are referred to as D-dot or B-dot sensors, depending on whether they respond to the electric or magnetic field.

Partially we use AFWL-designed sensors, but because of their high costs we use them in the main for the calibration of our laboratory-made sensors. For *small* test objects with *curved* surfaces it is necessary to rely on miniaturized sensors which are specially fabricated by us. For the electric field they usually take the form of conical monopoles or dipoles, for the magnetic fields we use shielded half loops or loops. These self-made sensors must be individually calibrated.

CW testing means exciting the system with a single frequency and measuring the response of the system (magnitude and phase) at this frequency. This procedure is then repeated at a sufficient number of frequencies f over a broad frequency range to define the *system transfer function* $T(f)$ (ratio of system response to exciting signal). It is defined as the relationship that describes, as a function of frequency, the response (e.g. voltage $V(f)$) at a measurement point *within* a given system that would be produced by the application of an e.m. field $E_e(f)$ *external* to the system, that is

$$T(f) = V(f) / E_e(f).$$

4. COUPLING MEASUREMENTS

4.1 General

The reason for these investigations was the threat to missiles illuminated by electromagnetic fields. Low power (microwave) coupling measurements are conducted in order to determine the transfer functions of specific test points. The measurement of the *charge and current densities* indicates the field distribution on the test object and the main structure resonances (fuselage, wing, fin). These fields penetrate through apertures into the interior of the hull causing *interference fields*, which either directly influence the electronic components or induce disturbing currents on the cabling. This second effect can also impair or destroy connected devices. The *cable resonances* help to find out the coupling paths.

In this paper we show measurement results of *three missiles* in the frequency range between 10 ... 8000 MHz. The outer dimensions of the test objects are in the order of 100 cm, so we restricted the surface field measurements to frequencies up to 2500 MHz, with a resolution of 2.5 MHz. Because of the small apertures in the hull and the short cable lengths between the different components we had to extend the frequency range up to 8 GHz for the fields within the missile and the currents on the cables. Up to 4 GHz we select a resolution of 5 MHz, in the range between 4 and 8 GHz the resolution was 10 MHz.

The quantities measured and shown in this paper are frequency dependent *transfer functions*. Due to the above mentioned definition the relationship in case of the magnetic surface field H_s is $T_{Hs}[A/V] = H_s/E_e$, and in case of the electric field E_s this leads to $T_{Es}[] = E_s/E_e$, which is dimensionless. In case of wire current I the relationship is $I[A/(V/m)] = I/E_e$.

Although the network analyzers always record magnitudes and phases we will show in this report only the magnitudes of the transfer functions because of better clarity. Differentiating sensors (B-dot, D-dot) are not very sensitive at low frequencies, so at weak coupling the transfer functions show at the beginning (mostly below 100 MHz) distinct behaviour.

As the different test objects were available to us only for limited time, we could not perform all the measurements we are interested in, but had to concentrate us to fundamental investigations.

4.2 Orientation to the External Field

During its flight the missile can be in every orientation to an external electromagnetic field. So we illuminated the test objects successively with plane waves of three different

polarisations. For this reason the DUT was, depending on its weight, either suspended with nylon threads or positioned on a Styrofoam stand in the TEM wave guide in three orthogonal directions with respect to the incident field. Fig.4.1 shows as an example the missile IPAS in the rear part of the simulator in the positions P, S, and T:

- P: E-field parallel to fuselage
 - S: E- and H-field perpendicular to the fuselage
 - T: E-field perpendicular and H-field parallel to fuselage.
- In orientation P fuselage resonances will be excited, whereas in S and T the resonances of the wings and fins dominate.

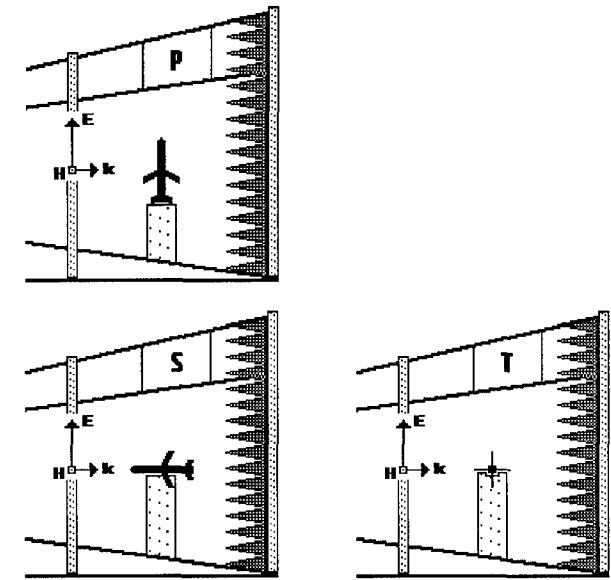


Fig.4.1: Test object in three orthogonal directions (P, S, T) in the rear part of the TEM simulator

4.3 Possible Coupling Paths

Remote controlled projectiles need antennas (e.g. radar seeker) or optical receivers (e.g. optical seek head). Via these radomes and windows electromagnetic fields can couple into the interior. In addition the guidance principles necessitates further apertures, such as deep slots for wings, which often penetrate the whole fuselage. In Fig.4.2 typical openings are depicted. These axial and circumferential slots can be excited by surface currents and act as sources for interfering fields.

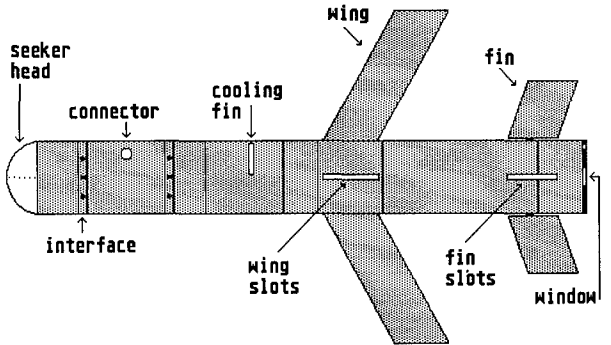


Fig.4.2: Possible apertures in the hull of a missile

The wings and fins act as antennas and can also cause disturbing fields within the system. An example is shown in Fig.4.3. The two or four fins are attached to the drive shafts of the motors, which are located inside the missile close together with the cabling and electronic components. In the figure the electric field is orientated parallel to the fin (worst

case, in our notation S or T), so maximum excitation of the rudder takes place. The current, flowing along the shaft and the drive unit to the structure cause magnetic fields which interfere with the nearby wires and electronic devices.

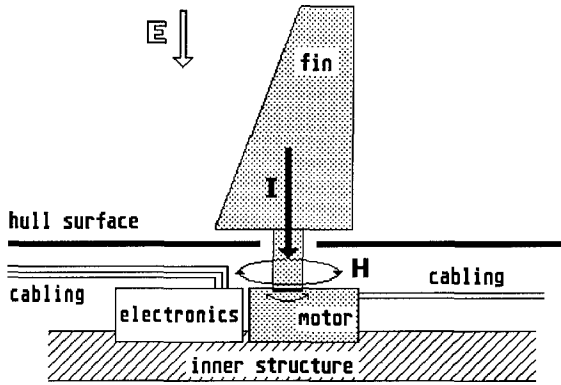


Fig.4.3: Typical coupling path 'fin-cabling-inner structure'

4.4 Test Objects

This paper presents our investigations on three missiles with different guidance systems developed by the Diehl company:

- *Bussard* is a terminally guided mortar shell with semi-active seeker (measured in winter 1992/93)
- *IPAS* is a terminally guided sub ammunition for a dispenser weapon; it will be taken by an aircraft in the vicinity of the target area (measured in April 1993)
- *EAP* is a terminally guided missile shot off from a howitzer. Its guidance system is based on a mm-wave seeker head (measured in autumn 1993).

Besides the *Bussard* all the test objects were in working order.

For the measurements the missiles were not equipped with pyrotechnic elements (squibs) and the warhead. These parts have been replaced by reproductions and connected to the cabling. Signal lines to these substituted components were terminated with their real impedances, power lines with the corresponding loads. All our experiments were carried out without power supply (inactive condition).

To measure surface fields or cable currents we need sensors to be mounted on selected locations on the outer structure or within the airframe. If we were not allowed to damage the surface for this purpose, we had to make reproductions of particular parts of the structure. The determination of fields or cable currents within the structure often was practicable only by removing of some system components.

5. COUPLING MEASUREMENTS ON BUSSARD

5.1 Description

In Fig.5.1 the outline and dimensions of the *Bussard* are depicted. Behind the window made out of acrylic glass is the semi-active laser seeker. In the rear part of the nose and in the central structure the signal and control electronics, thermal batteries and acceleration pick ups are situated. Between the central structure and the warhead there are four wings, which are folded down during transport and storage. These *folding wings* require slots penetrating the whole airframe, so that the central structure is divided into four *chambers*. These cells are filled with electronics, batteries, cabling etc.

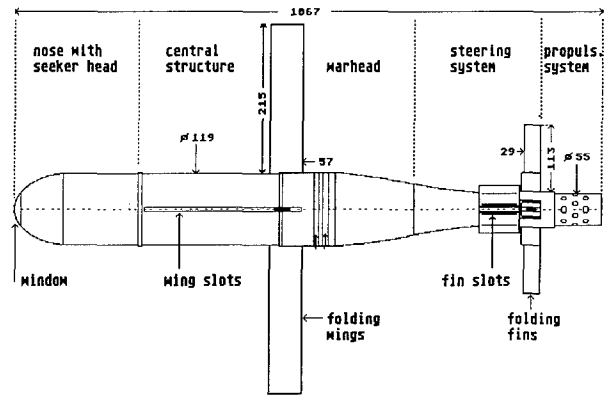


Fig.5.1: Outline and dimensions of the *Bussard*

The overall dimension are about 107 cm with a diameter of 12 cm (central structure), the weight is nearly 17 kg. Our *test object* was a not operational demonstration model. Important circuit boards and parts of the cable network were missing.

5.2 Surface Field Measurements

5.2.1 Location of measuring points

If it was not allowed to drill the structure for fixing the sensors and it was not possible in lack of time to reproduce all interesting parts, the selection of the measuring points was restricted. Fig.5.2.1 shows the eight chosen locations at the surface of the *Bussard*. Three of them are on one of the wings ($M1$, $M2$, $M3$). $M4$ and $M5$ are located near the center and the front part, respectively. On the fin there are two measuring points ($M6$, $M7$). $M8$ is situated at the rear of the test object.

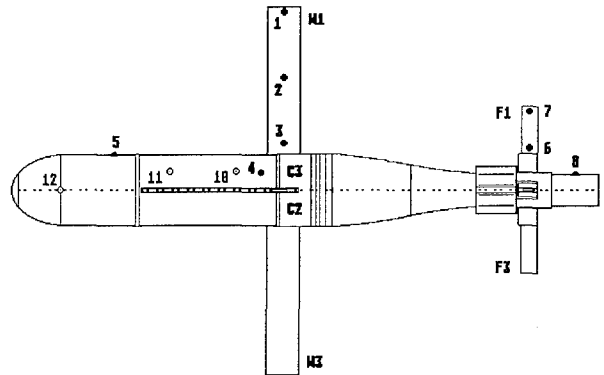


Fig.5.2.1: Location of the eight measuring points at the surface of the *Bussard* ($M10$, $M11$ and $M12$ are in the interior)

The current densities were measured in *axial* direction (along the axis of the test object) as well as in the direction perpendicular to this axis, i.e. parallel to the wings and fins. In this paper this direction is called *tangential*. As sensors for the surface charge and current densities we use small conical monopoles and shielded half loops. The electric field is measured on $M1$, $M5$, $M7$ and $M8$ (end parts of the structure), whereas the magnetic field is examined on nearly all points (besides $M1$, $M7$).

5.2.2 Surface fields in position P, T and S

In position **P** the wave hits the side of the test object and the E-field is parallel to the fuselage (see Fig.4.1). Due to this orientation it can be expected that the dominant *surface currents* are in axial direction. The transfer function in Fig.5.2.2

shows this component near the center, the peak amplitude is 41 [mA/V]. The tangential current is not depicted, because the amplitudes are very low and reach only 5 [mA/V].

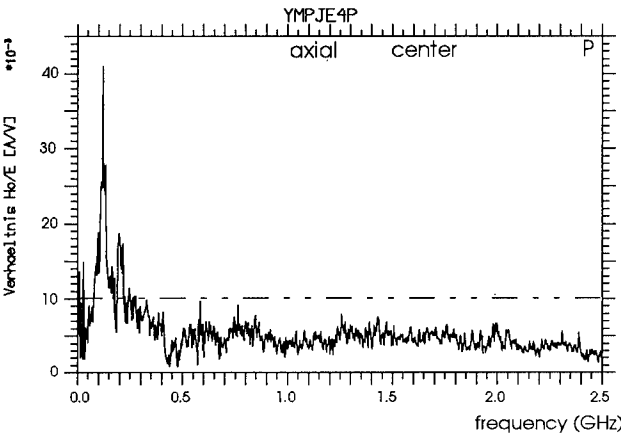


Fig.5.2.2: Surface current density H_s/E_e (axial component) near the center (M4) in position P

The further measurements show, that nearly at all points this characteristic frequency at 125 MHz can be detected, even at the basis of the wing and the fin, so it can be called as *fuselage resonance*.

The *electric fields* on the hull of the test object have similar shapes with the same resonance frequency, the maximum of 25 [] is attained at the rear.

In position T the plane wave is again impinging on the side of the Bussard, but now the electric field is perpendicular to the fuselage and therefore parallel to two of the wings and the fins. In this orientation the resonances of the tail units should be excited and the tangential surface currents dominant.

That can be validated with the transfer function in Fig.5.2.3 showing the tangential current on the basis of the wing (M3). The resonance at 242.5 MHz also appears at the electric field on the top of the wing, so this frequency can be called as *wing resonance*. At M3 the surface current reaches its maximum at 47 [mA/V], whereas the highest electric field strength of 12 [] is found on the top of the wing. On the short fin no definite resonances are visible, neither at the magnetic nor at the electric field. There are some higher amplitudes between 500 ... 1000 MHz, which may be influenced by the fin dimensions.

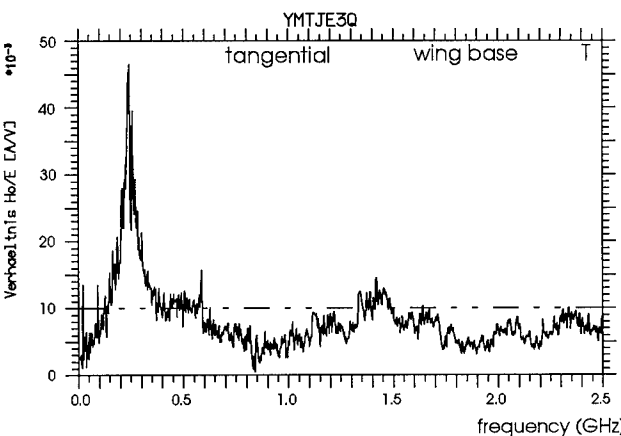


Fig.5.2.3: Surface current density H_s/E_e at the basis of the wing (M3) in position T

By rotating the test object in its horizontal position at 90° orientation S is reached, where the plane wave hits the nose and where also the magnetic field is perpendicular to the fuselage. In this position surface fields similar to those of the T orientation are induced, although the field strengths are somewhat lower.

The *results* of all these surface field measurements indicate, that in position P on nearly all examined measuring points the fuselage resonance at about 125 MHz is detectable. Further resonances didn't occur, in contrast to the S and T orientation, where apart from the wing and fin resonances a lot of further peak values is observed. The wing resonance was determined to 242.5 MHz, whereas no definitive fin resonance could be excited. The field strengths induced in position P generally are lower than those in the other two positions.

5.3 Interior Field Measurements

5.3.1 Location of measuring points

An advantage of the not fully equipped test object was that, on certain places within the hull, there was enough space to mount field sensors. Because of the special design characteristics of the Bussard hull two main *coupling paths* arise. External fields can penetrate into the interior through the *glass window* in the seeker head as well as through the deep *slots* in the central structure.

To measure these fields, one of the measuring points (M12, see Fig.5.2.1) was fixed 9 cm behind the *window* opening (diameter 7 cm) on a partition wall. For this reason the reproduction of the seeker system was removed.

Two further measuring points are in one of the four *double chambers* (each chamber: l=109mm, r=52mm) in the central structure, normally filled with electronics and cabling. The perspective drawing in Fig.5.3.1 shows such a chamber which is divided by a partition with two apertures at the upper ends. In the rear chamber there is a big wall opening provided for the spring mechanism for deploying the wing. Obviously an external field can couple easily through the wing slots (width 8mm) and the spring openings into the rear chamber (M10) and through the small apertures in the partition into the front chamber, where M11 is situated.

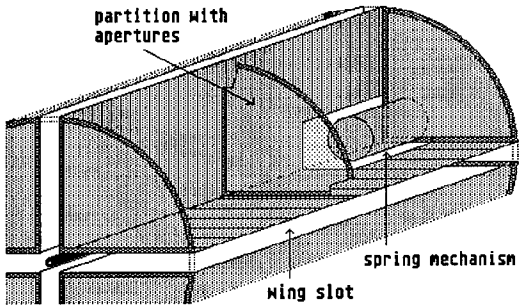


Fig.5.3.1: Perspective drawing of an empty chamber

Fig.5.3.2 shows schematically the examined field components in the chamber. With a free field sensor the indicated components H_a and H_t of the *magnetic field* in the room center are measured, whereas with a monopole *electric surface fields* on the cover of the chamber are determined. For the measurements all parts were moved out.

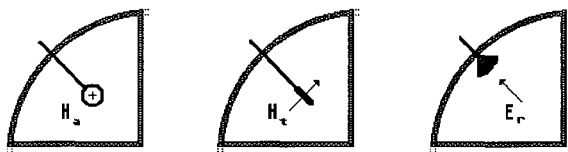


Fig.5.3.2: Schematic arrangement of the H- and E-field sensors in the chamber

5.3.2 Fields behind the window

If the electric field vector is oriented parallel to the fuselage (P) maximum fields will be excited on the ends of the hull. The field on the nose penetrates through the glass window and causes at the wall (M12) maximum magnetic field strengths of 7 [mA/V]. In orientation S the wave impinges directly upon the window. In this case the highest amplitudes (16 [mA/V]) could be measured. The transfer function in Fig.5.3.3 shows significant resonances only at 4890, 6020 and 7200 MHz. In position T the wave hits the missile on the side, so the induced field is only 3 [mA/V]. In the general shape all curves resemble each other and have no remarkable amplitudes below 2 GHz.

The highest electric fields (9 []) on M12 are created in position P. Due to Fig.5.3.4 below the main resonance at 2600 MHz no field coupling occurs. The field strengths in the other two orientations again have similar shape but considerable lower amplitudes (about factor of 6).

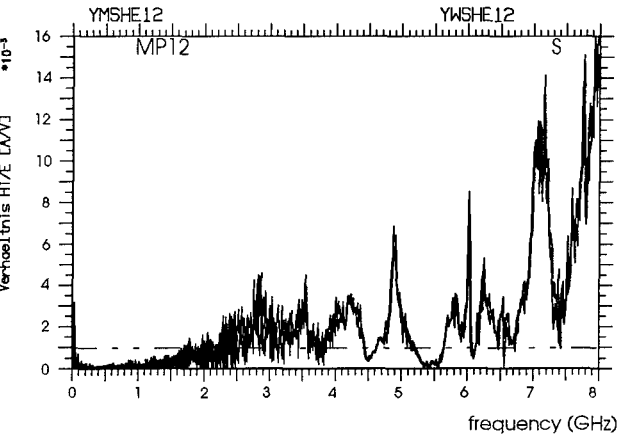


Fig.5.3.3: Magnetic surface field H_s/E_e behind the window in position S (M12)

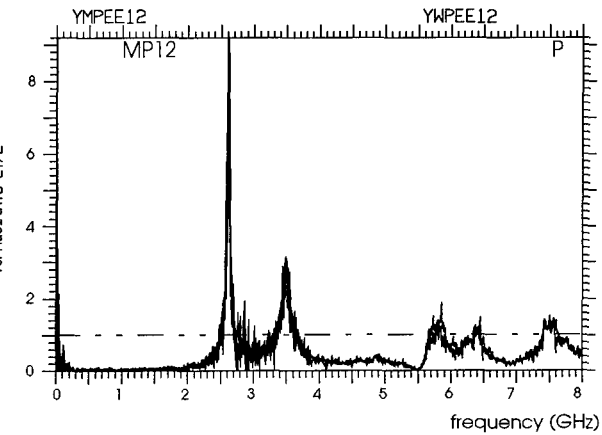


Fig.5.3.4: Electric surface field E_s/E_e behind the window in position P (M12)

5.3.3 Fields within the chamber

At first the tangential components H_t of the magnetic field are considered. In the two positions S and T the external electric field is oriented parallel to two opposite wings, so that on the surface a high current is flowing perpendicular to the wing slots exciting high disturbing fields in the slots. Fig.5.3.5 shows that in T position in the middle of the rear chamber (M10) magnetic fields in the order of 12 [mA/V] are created with the dominant resonance at 4100 MHz. Only a fraction of the field couples into the front chamber (M11). Fig.5.3.6 indicates that only 20 % of the field penetrates into the 'shielded' chamber.

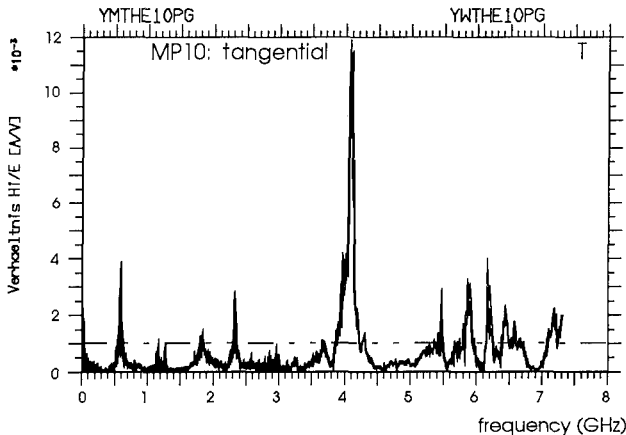


Fig.5.3.5: Magnetic field H_t/E_e in the middle of the rear chamber (M10) in position T

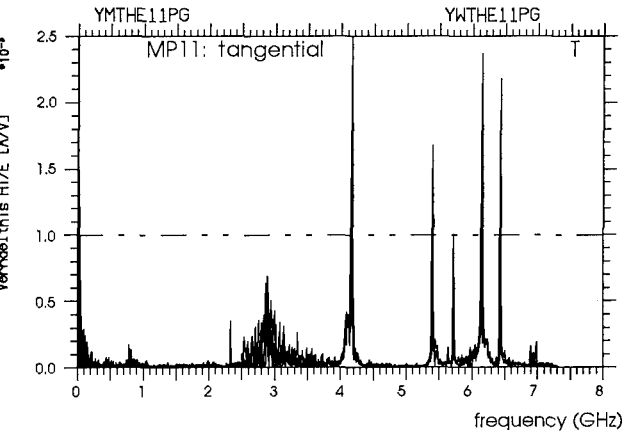


Fig.5.3.6: Magnetic field H_t/E_e behind the partition in the middle of the front chamber (M11) in position T

By comparing the two curves it can be seen, that the frequencies below 4 GHz cannot penetrate the small apertures in the partition. These slots act like a filter, so only certain sharp resonances are allowed to pass.

The internal fields in position S are smaller and attain only 50 % of those in T. In P, where the external surface current flows parallel to the long slots, inner field strengths of only 3 [mA/V] are created. These main resonances are similar in all three field orientations. It is noticeable, that in contrast to the rear chamber in the front chamber the induced fields are relatively independent from the orientation of the external fields.

For the axial magnetic field components similar effects are observed although partly at other frequencies.

The electric field in the double chamber was measured on the inner surface of the cover. Into the rear chamber (M10) in all three field orientations fields are produced which resemble each other in shape. The maximum values reach 0.6 [] in P and S, whereas in position T the resonances are much higher (factor of 3.5). In the chamber behind the partition (M11) only one sharp resonance at 3350 MHz can be stimulated.

5.4 Current Measurements on Cables

5.4.1 Selected cables

Finally we examined the field induced currents on selected cables in the Bussard. Because in our test object important components and parts of the cabling were removed by Diehl, we had to chose some relevant lines with the help of the block diagram. The search criterions were cable length and function of the connected components.

We selected four cables of different length and lay them, beginning in the seeker head, in the missile. Fig.5.4.1 shows schematically the routes of the wires. All cables are running through one of the chambers in the central structure parallel to the existing cable bundles and are terminated at each end by a 50 Ω resistor.

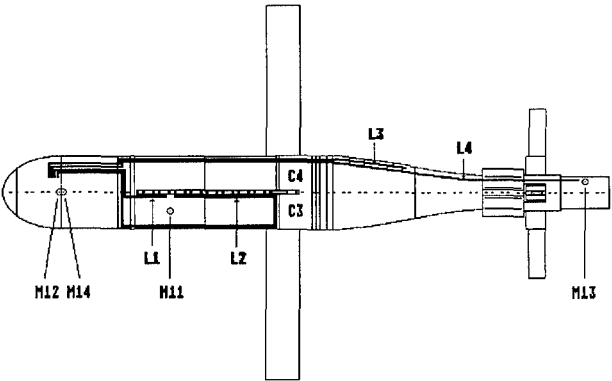


Fig.5.4.1: Route of the four selected lines L1, L2, L3 and L4 in the test object

Line L1 (30 cm) and L2 (80 cm) run on two typical ways into the chamber and end at measuring point M11 on the cover. L3 (65 cm) and L4 (95 cm) are going to the warhead and the steering system, respectively. These cables reproduce signal and power lines which connect different components in the missile.

At the current measurements we use two different line terminations. The 50 Ω resistor is intended to represent the high in-/output impedance of a connected (electronic) component, whereas the short circuit is a reproduction of a low impedance device. Fig.5.4.2 depicts the four typical configurations we have measured. We examined both the short circuit current I_0 and the current I_{50} through a 50 Ω load. The other ends of the lines are always terminated by a 50 Ω resistor.

In the nose the cables end either in front of the partition wall (M12) or behind it (M14). In the first case the left ends of the lines are illuminated by the interior field coupled through the window, in the second case they cannot be affected by a disturbing field at its left. In the following only a small fraction of the extensive measurements we have carried out are presented and summarized.

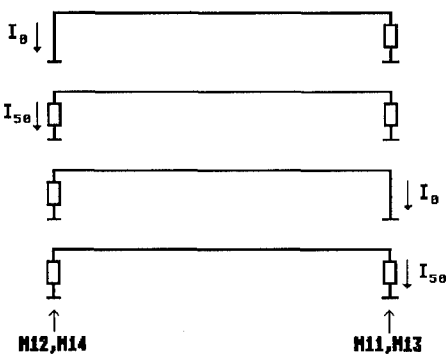


Fig.5.4.2: Typical current measurements on the lines with different terminations

5.4.2 Induced cable currents

In position P the main resonances of the short circuit currents I_0 at the left ends (M12) reach amplitudes between 400 ... 470 [μA/(V/m)]. As an example Fig.5.4.3 shows line L4. On the other wires similar currents are induced and it could not be observed a dependence on length because the wire ends in the nose act as antennas reproducing basically the penetrating fields. The high currents, however, are not transferred to the right sides in M11 and M13. There they differ in the resonance frequencies as well as in the amplitudes. For example the current I_0 on L1 reaches at M11 a maximum value of only 57 [μA/(V/m)]. The lowest currents are induced on the right end of L4, see Fig.5.4.4.

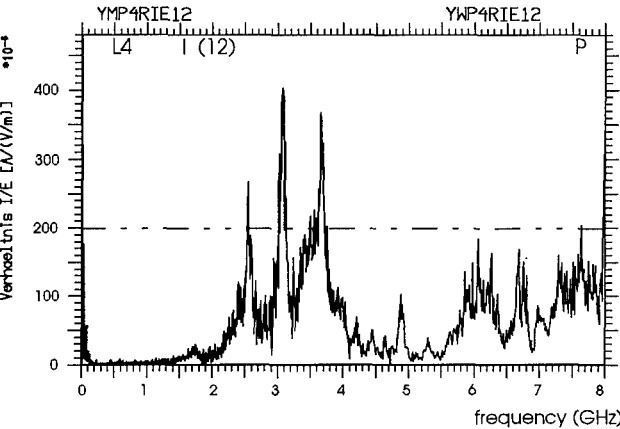


Fig.5.4.3: Short circuit current I_0/E_e on the left side (M12) of line L4 in position P

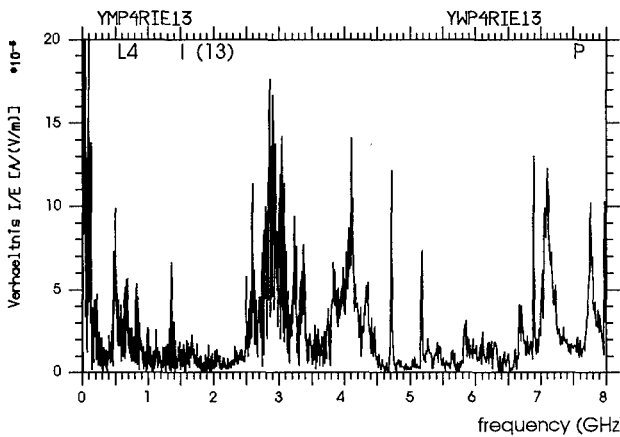


Fig.5.4.4: Short circuit current I_0/E_e on the right side (M13) of line L4 in position P

To exclude the antenna effect of the left ends the wires are terminated on the back of the partition (M14), so no field coupling can occur. The currents measured now are at a factor of 20 lower than in front of the wall. It could also be shown that on the right end of line L4 similar currents are flowing not depend on whether the left side is illuminated or not. The measured currents I_{50} through the $50\ \Omega$ resistor show similar behaviour.

In orientation S the short circuit currents I_0 again reach peak amplitudes of about $400\ [\mu\text{A}/(\text{V}/\text{m})]$, the number of resonances is higher on all examined wires, however. In position T lower fields are coupled into the nose, so at the left ends of the wires currents of only $120\ [\mu\text{A}/(\text{V}/\text{m})]$ are induced.

5.4.3 Distribution of the resonances

The main objective of the cable measurements was to identify *typical resonances* which may cause malfunctions in the missile. These frequencies serve as a basis for the *test plan* for the susceptibility measurements on an active missile. Therefore at the end of our cable measurements the results had to be summarized. For this reason all resonances induced on the four wires are considered, independent of the orientations to the external field (P, S, T), the terminations (I_0 , I_{50}) and the places of the measuring points (M11 ... M14).

It turned out that innumerable resonances were excited. In addition most of the peaks occur frequently. To get a better overview of the correlation between the cable resonances and the outer and inner structure resonances of the Bussard, we will show both the *amplitude distribution* and the *frequency probability* of the resonances.

For clarity the amplitude spectrum in Fig.5.4.5 only shows peak values greater than $25\ [\mu\text{A}/(\text{V}/\text{m})]$. In the frequency range below 1 GHz only small resonances of about $12\ [\mu\text{A}/(\text{V}/\text{m})]$ are observed with the exception of peaks around 600 MHz which have values up to $50\ [\mu\text{A}/(\text{V}/\text{m})]$. Between 1 ... 2 GHz maxima up to $100\ [\mu\text{A}/(\text{V}/\text{m})]$ are excited. Above 2 GHz the amplitudes are increasing steeply.

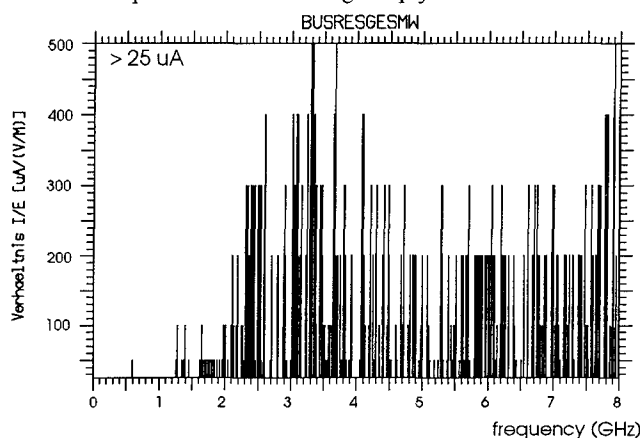


Fig.5.4.5: Amplitude spectrum of the summarized resonances on the four lines in the Bussard (only peaks $> 25\ [\mu\text{A}/(\text{V}/\text{m})]$)

The frequency probability in Fig.5.4.6 shows those peaks occurring more than five times. It is obvious that the small resonances around 600 MHz must be considered because of their frequent appearance.

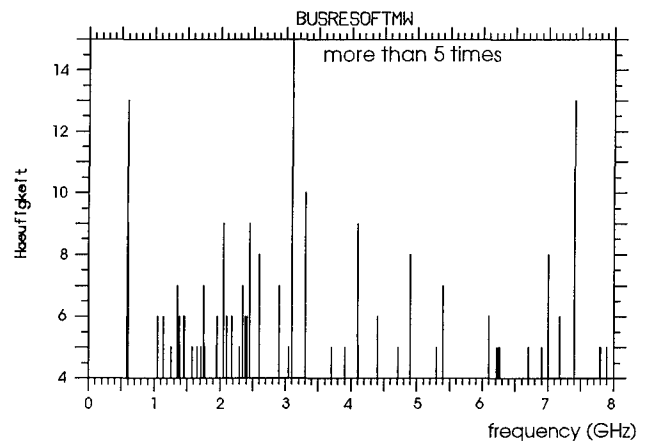


Fig.5.4.6: Frequency probability of the summarized resonances on the four lines in the Bussard (only for peaks occurring more than five times)

It was also examined if the coupled *field resonances* in the nose and the chambers also appear on the *lines*. As a result for the rear chamber it turned out, that mainly the room resonances at 600, 1250, 3000, 4100, 7000 and 7180 MHz are repeatedly excited on the wires. For the front chamber this was the case for 3300, 5400, 6100 and 7000 MHz, for the nose the resonances agreed often at 2600, 4900, 7000 and 7400 MHz.

A correlation between *wire* and *structure resonances* could not be observed, neither for the fuselage nor for the wings and fins. That means that the rudders of the Bussard are not responsible for the wire currents, but that the fundamental *coupling path* leads through the window and the wing slots.

6. COUPLING MEASUREMENTS ON IPAS

6.1 Description

Fig.6.1 shows the outline and dimensions of the IPAS. The test object was an operating model but not fitted with the mmW-seeker. The unit in the middle of the fuselage called *opto-coupler* is used only during the susceptibility tests at the WTD 81. This component transmits via glass fibres signals from the SPU, IMU and the steering system to the measuring equipment. The unit in the rear is for *filtering* the external power lines during the susceptibility tests.

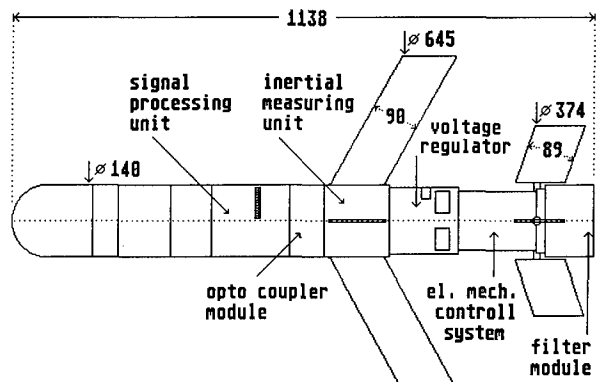


Fig.6.1: Outline and dimensions of the IPAS

At our examinations the test object was not powered. The missile has four fixed wings and four moveable fins. On the surface there are four slots at the rear for the fins and one

opening near the center. This slot serves as cooling fin for the SPU and is covered by a metal mesh. Because of the short measuring time of only three weeks we could measure the surface fields only in two positions (P, S) and the interior fields not at all. For the same reason the current measurements could only be carried out between 10 ... 2500 MHz.

6.2. Surface Field Measurements

6.2.1 Location of measuring points

As at the Bussard we were not allowed to drill the structure for fixing the sensors. So the selection of the measuring points was limited to the nine places shown in Fig.6.2.1. Five of them (M1, M2, M3, M5, M6) are on the hull, M10 and M11 on one of the wings and M12 and M13 on one of the fins. The current densities were again measured both in axial and 'tangential' direction (see Bussard, Fig.5.2.1).

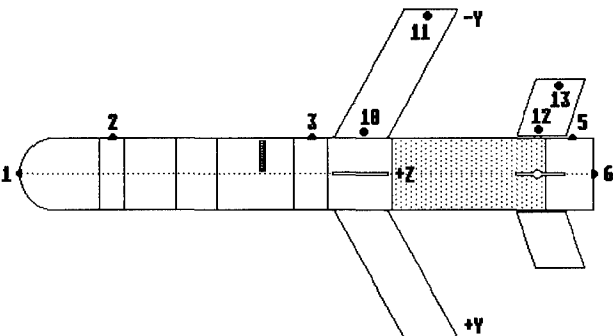


Fig.6.2.1: Location of the nine measuring points on the surface of the IPAS

6.2.2 Surface fields in position P and S

In position P the wave hits the side of the test object. The E-field is parallel to the fuselage, so the surface current is dominant in axial direction. The transfer functions of this component show peaks at 120 MHz. This resonance appears at all places of the hull, so it could be called as fuselage resonance of the IPAS.

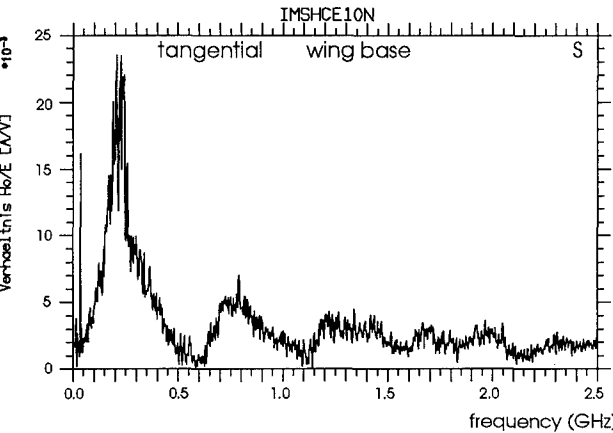


Fig.6.2.2: Surface current density H_s/E_e (tangential component) on the base of the wing (M10) in position S

In position S the plane wave is impinging on the nose and both the E- and H-field are perpendicular to the body. In addition the E-field is parallel to two of the rudders and therefore is able to excite their resonances. The tangential current density measurements were done at M3 and M10, whereas charge densities were determined on the top of the wing (M11) and the fin (M13). The results of these measure-

ments show that the wing resonance appears at 207 MHz (Fig.6.2.2), whereas it could not be determined a single fin resonance. There is a lot of peaks between 400 ... 900 MHz and around 1700 MHz which may be assigned to the fin.

6.3 Current Measurements

6.3.1 Selected cables

The different components within the IPAS are connected together via cable bundles. The inner construction is very compact and normally there is no room to fix sensors for current measurements. In two components, however, built in for test purposes by Diehl and serving as connection to the outside world, there is enough space available.

The first unit named *opto-coupler* (see Fig.6.1) is connected via five cable bundles of different length to meaningful components (e.g. IMU, SPU) within the missile. At our measurements the box was empty besides the connector strip, so we were able to determine the cable currents terminated at the socket. Fig 6.3.1 shows schematically the cables to the unit with their impedances. At the end of the low-impedance lines we determined the short circuit current I_0 and at the end of the high-impedance lines the current I_{50} at a 50 Ω resistor. For the I_0 measurements we selected three cables (L3, L12, L20) and for the I_{50} measurements four cables (L7, L10, L16, L17). The numbering relates to the pin numbers.

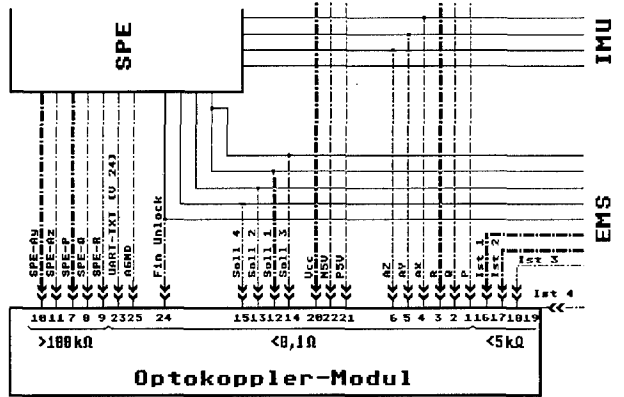


Fig.6.3.1: Cables to the opto-coupler module (selected lines bold)

At the susceptibility tests in Greding (WTD 81) the filter module in the rear of the IPAS is connected to the power supply (Fig.6.3.2). For our purposes we removed the filters behind the connector strip and measured the short circuit current I_0 on three selected lines (Lb, Ln, Lv).

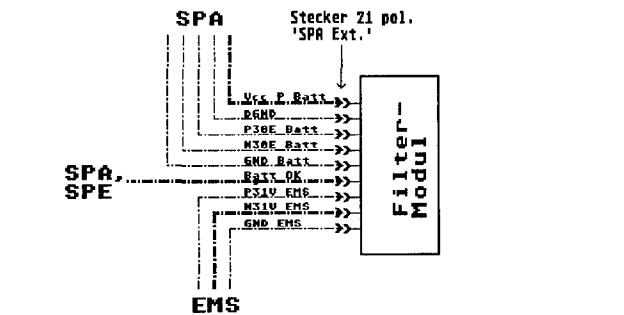


Fig.6.3.2: Cables to the filter module (selected lines bold)

6.3.2 Induced cable currents at the opto-coupler

The short circuit current I_0 at the end of line $L3$ was examined in all three IPAS positions P, S and T. It turned out, that in position T (E-field parallel to the rudders) the highest currents with maximum amplitudes of $19 \mu\text{A}/(\text{V/m})$ have been induced (Fig.6.3.3). In this orientation also in other examined missiles the highest currents had been measured.

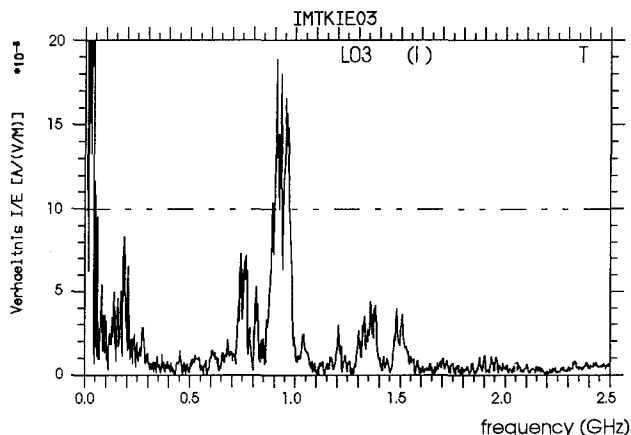


Fig.6.3.3: Short circuit current I_0/E_e at the end of line $L3$ in position T

Besides corresponding resonances around 200 MHz on all of the three tested cables further peaks at different frequencies are excited. No relation between resonance frequencies and cable length could be observed, because the various lines are not terminated at a single point but are branched repeatedly.

The same remarks are valid analogously for the currents I_{50} . Nevertheless the two lines $L16$ and $L17$ have the same length and are situated in the same bundle partly different resonances are measured at their ends. The reasons may be the variable locations within the bundle with respect to the disturbing field and different terminations.

The highest currents are induced on line $L7$ ($35 \mu\text{A}/(\text{V/m})$). It is remarkable that at these measurements in the center of the airframe most of the resonances are excited below 1 GHz and only few appear at higher frequencies. Above 1.5 GHz only isolated resonances can be observed.

6.3.3 Induced cable currents at the filter module

In the rear part of the IPAS external fields are able to penetrate through the four openings for the fin shafts. In addition currents can flow via the shafts to the inner structure causing disturbing fields (see Fig.4.3). Therefore in this region high current amplitudes can be expected.

This prediction is confirmed by the short circuit currents on the three examined lines. For example on line Lb the maximum reaches $61 \mu\text{A}/(\text{V/m})$. Again the highest peaks are around 200 MHz and maximum currents are induced in position T. In contrast to the results in the center of the IPAS in the rear part a lot of resonances is excited above 1 GHz.

6.3.4 Distribution of resonances

If we had to establish a test plan for the susceptibility measurements, we summarized the results of the cable measurements to get an overview over the typical resonances. Again all resonances induced on the cables are considered, inde-

pendent of the orientations to the external fields, the terminations and the place of the connector strip (center, rear).

The amplitude spectrum for the IPAS in the measured frequency range between 10 ... 2500 MHz is shown in Fig.6.3.4. All frequencies greater than $1 \mu\text{A}/(\text{V/m})$ and recognizable as resonances are plotted. The spectrum shows big resonances around 100 and 200 MHz and between 600 ... 1000 MHz, which can be related to the structure resonances. That means that the coupling to the interior mainly occurs via the wings and the fins. Frequencies above 1 GHz have lower amplitudes and appears rarely, as the frequency probability describes.

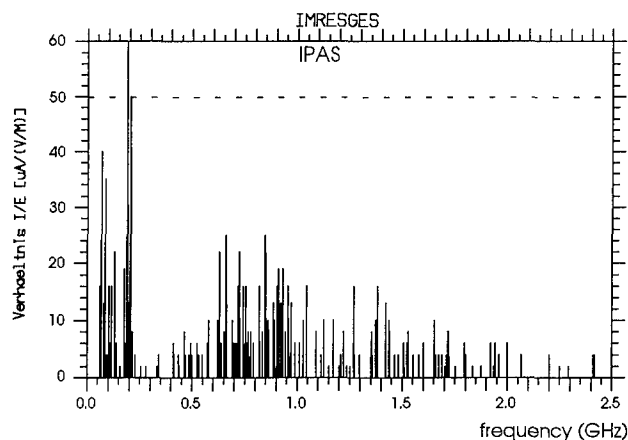


Fig.6.3.4: Amplitude spectrum of the summarized resonances on the examined ten lines in the IPAS

This behaviour of the IPAS is quite different to the Bussard. Fig.6.3.5 is an extract of Fig.5.4.5. It shows the amplitude spectrum of the Bussard only between 10 ... 2500 MHz with all measured resonances greater than $6 \mu\text{A}/(\text{V/m})$. Here the main resonances begin at approximately 1 GHz and rise in amplitude with increasing frequency. Furthermore in a selected frequency range the maximum peaks are at least a factor of 5 higher than those of the IPAS. Whereas on the cables of the Bussard resonances are excited up to 8 GHz, the induced currents in the IPAS are getting lower by increasing frequency.

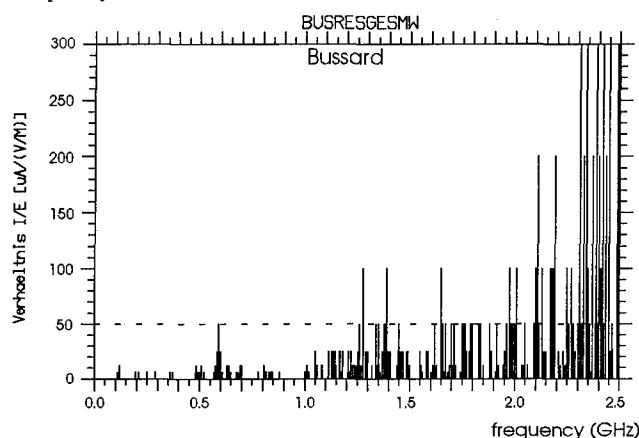


Fig.6.3.5: Amplitude spectrum of the summarized resonances on four typical lines in the Bussard

From these results we can conclude that at the various test objects different coupling paths exist causing characteristic resonances on the lines. Therefore it is necessary to examine further missiles.

7. COUPLING MEASUREMENTS ON EAP

7.1 Description

In Fig.7.1 the outline and dimensions of the EAP are depicted. The test object was an operating model but like the IPAS not fitted with the seeker. The projectile is made of steel with a high degree of hardness and weighs nearly 45 kg. The overall length is about 90 cm with a diameter of 15.4 cm. The missile has four moveable fins and only two wings. These parts are folded down during transport and storage in *slots* penetrating the whole airframe. The two slots for the wings and two of the fins have the dimensions of 382x15 mm, the two slots for the other fins are smaller (229x10 mm).

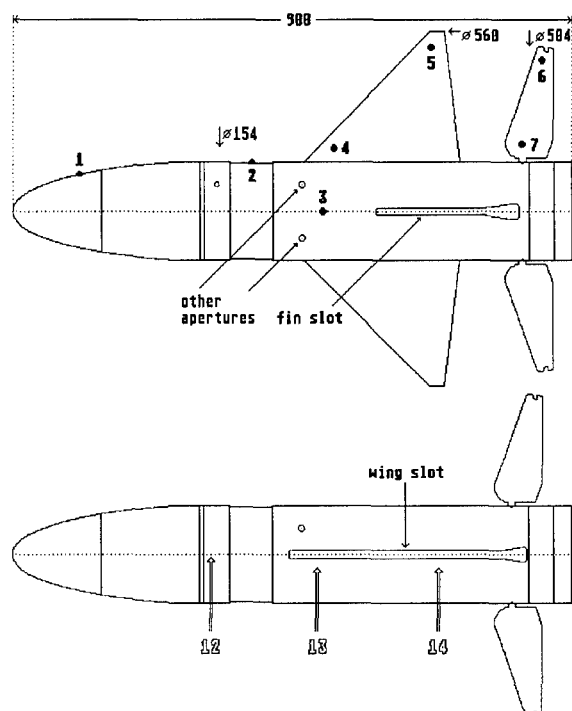


Fig.7.1: Outline and dimensions of the EAP with measuring points and openings

In the front section instead of the seeker a time generator is situated. In the middle section of the missile the signal and control electronics, voltage control and different pick ups are located, whereas the rear section is equipped with the electromechanical control system and thermal batteries. The last two sections are linked together by connectors. The measurements on the EAP were carried out a few months ago and in lack of time are still not fully evaluated.

7.2 Surface Fields

The *measuring points* of the surface fields are also shown in Fig.7.1. Current densities were determined on the fuselage (M2, M3) and on the base of one of the wings (M4) and fins (M7), both in axial and 'tangential' direction (see Bussard, Fig.5.2.1). The charge densities were examined on the ends of the structure (M1, M5, M6).

In position **P** the E-field is parallel to the body so we get the *fuselage resonances*. On the EAP the peaks appear at 130 MHz, both in the axial current direction and in the electric field on the nose (M1) of the test object. The maximum current density of 26 [mA/V] arises on M2, the peak electric field of 19 [] is measured on the nose.

In position **S** the E-field is parallel to the two wings and two of the fins. The main resonances in tangential current direction are excited at 300 MHz on M3 and M4. As this frequency also appears at the top of the wing, it could be identified as *wing resonance*. In contrast to the Bussard and the IPAS measurements it could be now observed a relatively sharp *resonance* around 450 MHz on the base and the top of the *fin*.

The wing and fin resonances in position **T** differ from those in the **S** position. Now we have measured maxima at 250 MHz for the *wing* and around 400 MHz for the *fin*. Such a change in frequency was observed neither at the Bussard nor at the IPAS. This different behaviour may be explained with the missing of two wings.

In each of the three orientations the highest current densities are at 26 [mA/V]. In **S** and **T** the electric surface fields are lower than in position **P** and reach their peaks at the wing tip at only 10 [].

7.3 Interior Field Measurements

7.3.1 Location of measuring points

The EAP has four slots of different length penetrating the whole airframe, similar to the Bussard. Through the holes and slots (Fig.7.1) the cabling, electronics and system components can be seen, so we had to determine the fields within the EAP coupled through the various apertures.

As indicated already in Fig.7.1 we have measured interior fields in three different locations (M12, M13, M14). Fig.7.3.1 shows schematically the place of the E-field sensor (M12) near the electronics. Measuring point M13 is in the center of a chamber filled with electronic devices and cabling. Fig.7.3.2 shows the location of the free field sensor. The penetrating H-field is measured in axial (H_a) and tangential (H_t) direction. Also seen are the possible coupling paths through the slots. Further magnetic fields are determined within one of the shafts (H_p) and in the crossing of these shafts (H_a), as indicated in Fig.7.3.3.

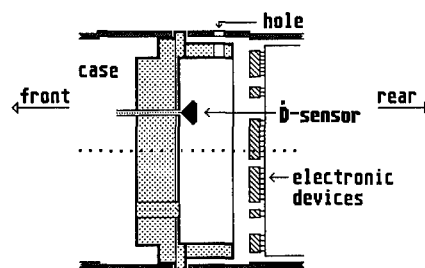


Fig.7.3.1: E-field measurement on M12 near electronic devices

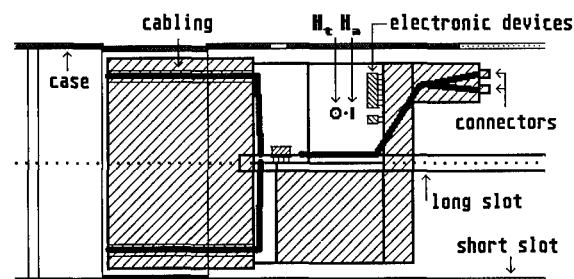


Fig.7.3.2: H-field measurement in the center of a chamber (M13)

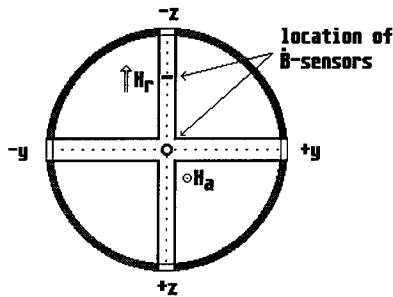


Fig.7.3.3: H-field measurements within a shaft and in the intersection (M14)

7.3.2 Summary of the results

We have done a lot of interior field measurements. The main results can be summarized as follows:

- M12: The small hole in the case (Fig.7.1) has no influence on the electric fields near the electronic circuits. The peak values of the E-field of about 0.45 [] are generated in positions P and S at 340 MHz. In T the main resonance at 525 MHz has an amplitude of 0.86 [].
- M13: The peak magnetic fields in the chamber are in position T (1.5-2.2 [mA/V]) higher than in P (0.7-1.4 [mA/V]) and S (0.7-0.8 [mA/V]). The main resonances are observed around 500 and 2800 MHz.
- M14: In the shaft the peak magnetic fields again reach in T (6.4-19.0 [mA/V]) higher values than in P (1.5-2.7 [mA/V]) and S (2.0-2.8 [mA/V]). The principal resonances are around 600, 900 and 3100 MHz.

All measurements show, that in position *T* the coupled interior fields are generally higher than in *P* and *S*. In addition in *T* more resonances at higher frequencies are excited.

Regarding the correlation between the resonances of the *outer structure* and the *inner fields* the following can be concluded:

- In position *P* (E-field parallel to fuselage) on M12 a high resonance at 135 MHz is observed, which can be assigned to the *fuselage resonance*. The same is with resonances at 130 and 150 MHz measured in the shaft (M14).
- In positions *S* and *T* (E-field parallel to wings and fins) in the chamber (M13) and the shaft high peaks at 245 and 295 MHz are excited. These frequencies correspond to the *wing resonances*. Definite fin resonances could not be identified.

7.4 Current Measurements

As already mentioned the EAP measurements are not completely analyzed yet, that is the case especially for the current measurements on selected cables. We examined at the ends of seven low impedance lines the *short circuit currents* I_0 in the frequency range between 10 ... 8000 MHz. The wires are running from the front to the rear section. So far we have summarized some results between 10 ... 2500 MHz.

First of all Fig 7.4.1 shows the *amplitude spectrum* of the seven lines with peak values greater than 6 [$\mu\text{A}/(\text{V/m})$]. As at the IPAS resonances corresponding to the structure resonances (130, 250, 300, 400, 450 MHz) could be observed. But additionally a broad frequency band appears around 600, 1450 and 1950 MHz. The comparison with the amplitude spectrum of the IPAS (Fig.6.3.4) and the Bussard (Fig.6.3.5) shows, that the peak values nearly reach the current strengths of the Bussard. But at the EAP the maxima are in the lower frequency range.

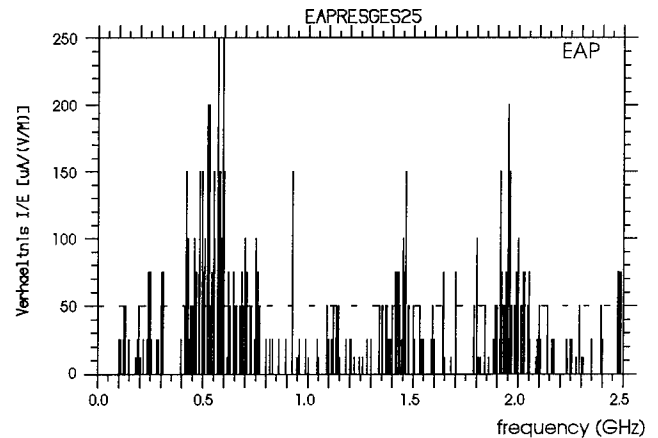


Fig.7.4.1: Amplitude spectrum of the summarized resonances on the examined seven lines in the EAP

If we compare the *frequency probability* in Fig.7.4.2 with the amplitude spectrum we noticed that a lot of frequencies shows unique appearance. Only few resonances are excited more than two times.

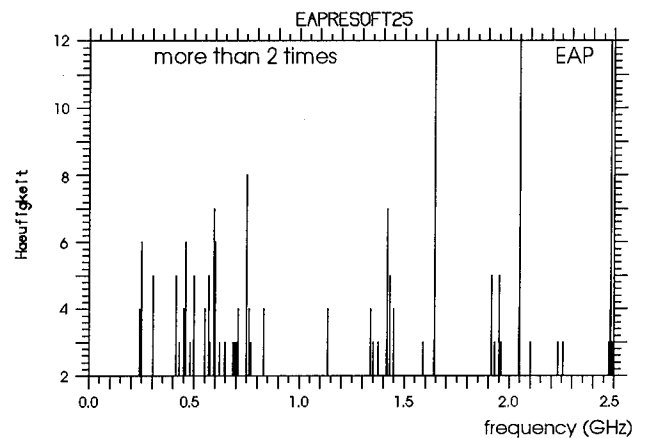


Fig.7.4.2: Frequency probability of the summarized resonances on the examined seven lines in the EAP (for peaks occurring more than two times)

REFERENCES

- [1] Braun, Ch., Graf, W., Schmidt, H.U.: "A Scale-Model Simulator for System Tests", 1992 Joint Symposia IEEE/APS, URSI, Nuclear EMP Meeting, Chicago (USA), 18.-25. July 1992
- [2] Braun, Ch.: "Design of a Broadband Wave Guide for EMP Scale-Model Measurements (in German)", PhG-INT (internal report 6/84, 1984)

DISCUSSION

MALABIAU

- 1/ Quel est le coefficient de sélectivité Q des résonances observées ?
- 2/ Quel est le Q le plus élevé qui a été mesuré ?
- 3/ Les résonances observées sont-elles reproductibles en amplitude et avec quelle précision ?

Translation:

1. What is the coefficient of selectivity Q of the resonances observed ?
2. What was the highest Q measured ?
3. Are the resonances observed reproducible in amplitude and if so, with what degree of accuracy ?

P.A. KOSSEY

You mentioned that your institute also uses numerical codes to calculate or predict the coupling of EM fields to structures, etc. Have there been any attempts to compare any aspects of your experimental results with such theoretical modeling, to help validate the models ?

AUTHOR'S REPLY

We have calculated the structure resonances ; but we couldn't calculate cable currents because of the complexity of the interior (electronics, etc).

We can calculate currents on a cable in an idealized cylinder.

High Power Microwave Hazard Facing Smart Ammunitions

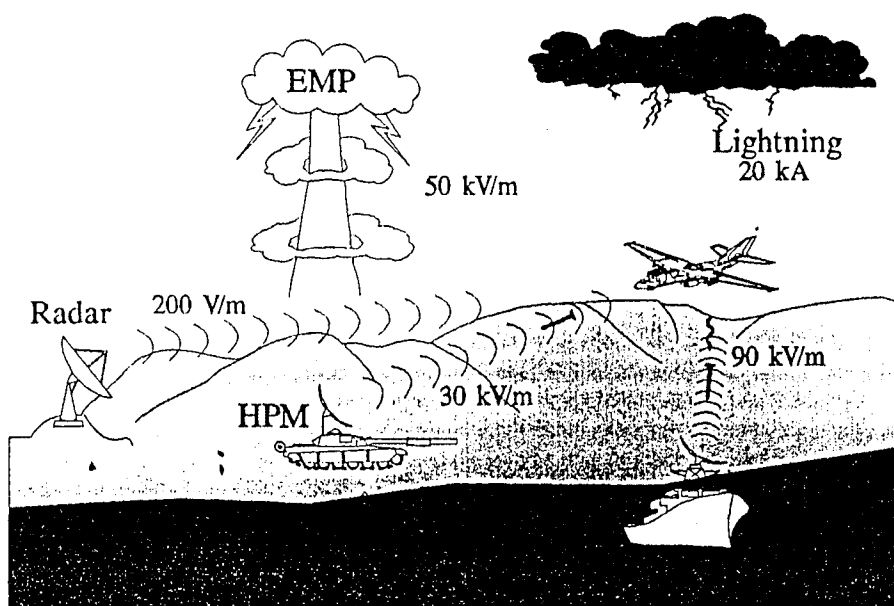
Dipl.-Ing. J. BOHL
DIEHL GmbH & Co.
Department: M-ELK3
Fischbachstr. 120
D-90552 Roethenbach/Pegn.
Germany

High Power Microwave Hazard Facing Smart Ammunitions

1. Introduction

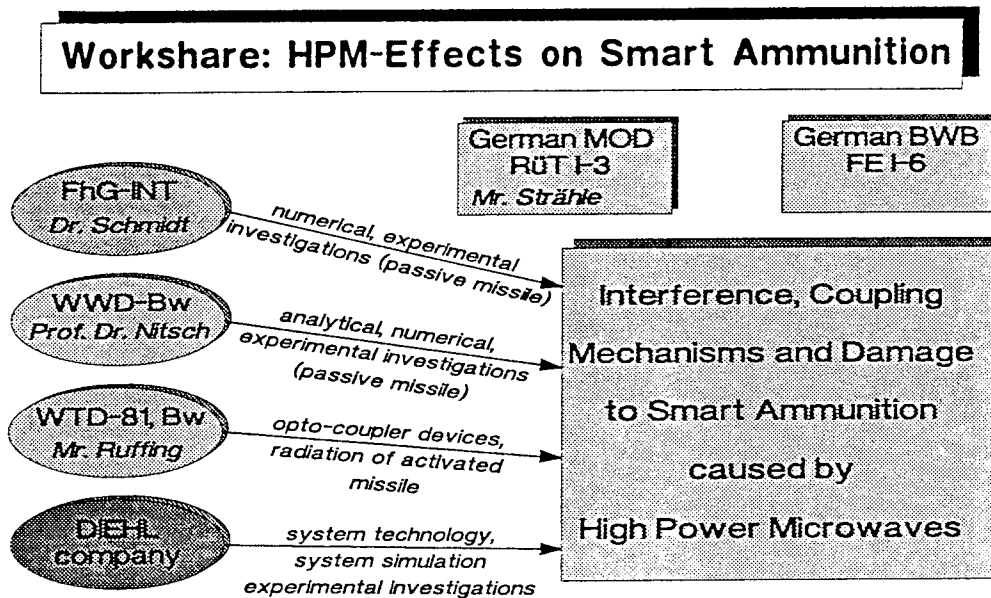
The battle field of the present and even more the one in future will be characterized by the use of weapon systems with a high degree of electronics, computers and sensors, designed and built to keep not only the man out of the loop! But the higher the technology used for smart weapon systems, the more these systems are endangered by numerous sources of hazard. One of those sources is the threat caused by induced or natural electromagnetic fields. These threat factors can be generated by natural, civil and military environment.

Ammunition Endangered through High Power Microwaves, Generated by Natural, Civil and Military Environment



In principle there are two main applications which must be considered in military applications: Firstly, weapon systems, that is, high power microwave sources as well as intelligent electromagnetic radiation systems to defeat ammunition on the battle field and secondly, the hardening of the own smart ammunition systems and missiles against the interference sources created by the different types of electromagnetic fields. The following will discuss the possible electromagnetic coupling effects on smart ammunition and missiles and their typical interference caused on the electronics and sensor level. Real time 6-DOF simulations show the flight mission which may be compromised depending on the coupled electromagnetic fields.

The German MOD has established a research program where smart ammunitions with different seeker systems are investigated in respect of the coupling effects on smart ammunition caused by high power microwaves. This program considers all available resources and know how in Germany. The systems are investigated by analytical, numerical and experimental methods with passive and activated missiles.

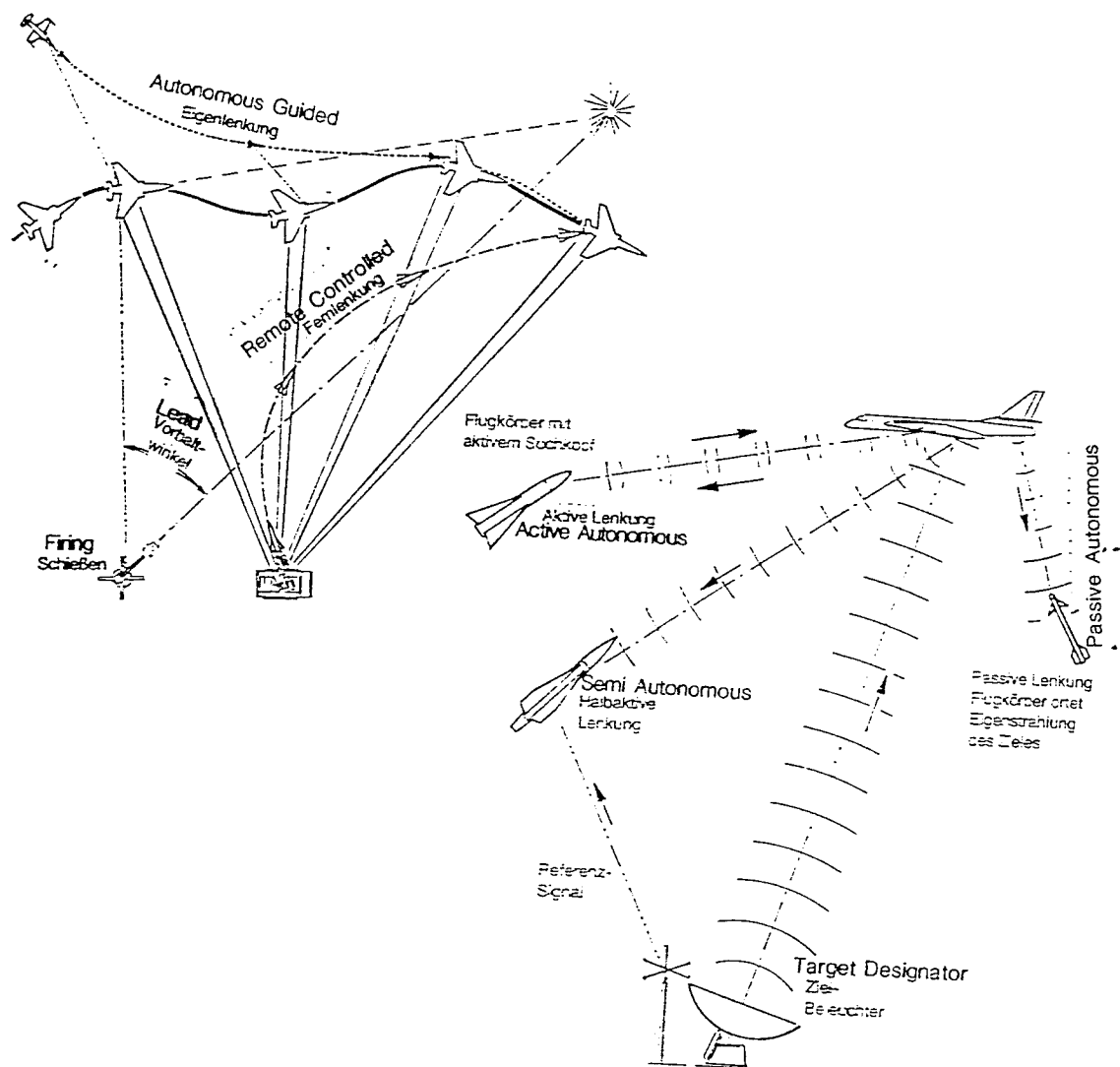


2. Smart Ammunition Systems

Smart ammunitions typically have a number of electronics, sensors, electromechanics and mechanics on board which are necessary for a controlled, autonomous flight for a successful mission. The smart ammunition and missile technology distinguish between semi autonomous and autonomous guided ammunition and missiles. The advance in the electronic and sensor technology is mainly represented by a change from analog to digital operated systems with a high degree of computerization with processor technology. The future belongs to the autonomous fire and forget systems where an active or passive seeker system is on board. The man should be out of the loop in direct combat situations.

In principle ammunition and missiles can be classified as follows:

- unguided ballistic ammunition/missiles
- programmed flight of ammunition/missiles; the data for the nominal flight path are stored in the missile's computer
- semi autonomous guided ammunition/missiles controlled via radio, wire, laser spots (laser designator), laser beams, video systems etc., the control and guidance data are transmitted to the missile from the firing station in an interactive manner
- autonomous guided, fire and forget ammunition and missiles with different search and detection sensors (IR, mmW, and the like) on board; the powerful, miniaturized computers control the target search and target discrimination algorithms select the target and guide the missile to the target (target track with final homing).



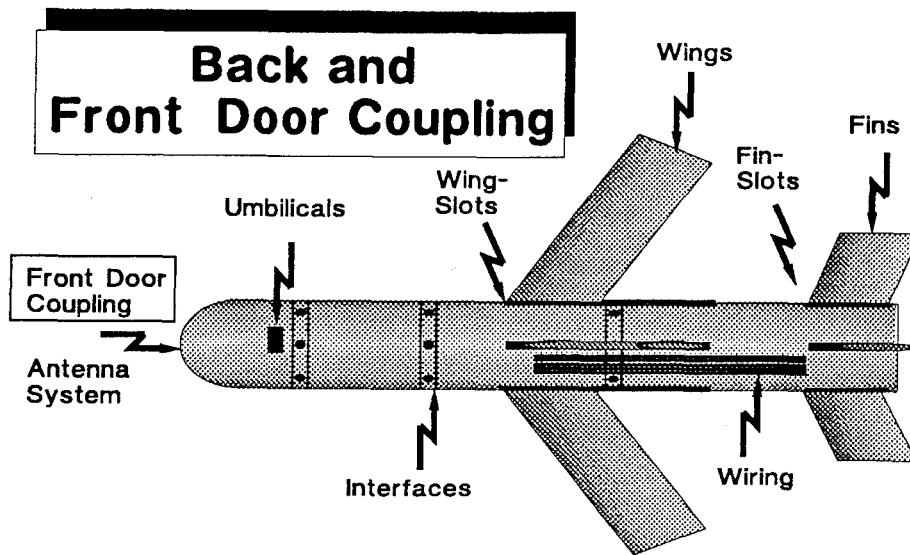
Typical Hardware/Sensor of Guided Ammunition

Semi Autonomus	Autonomus
<ul style="list-style-type: none">Airframe (Wings, Fins and Body)Control Actuation System/ElectronicsVoltage Regulator with BatteriesElectrical NetworksReceiving Transmitting System for Missile Commands and/or Missile DeviationWarhead with Safe and Arm UnitGyros and Acceleration SensorsPropellant System	<ul style="list-style-type: none">Airframe (Wings, Fins and Body)Control Actuation System/ElectronicsVoltage Regulator with BatteriesElectrical NetworksWarhead with Safe and Arm UnitGyros and Acceleration SensorsSignal Processor UnitAuto PilotPropellant SystemActive or Passive Seeker System (mmW, IR, ...)

3. Back and Front Door Couplings

Smart ammunition systems normally do have intended and inadvertent paths of micro wave transmissions. An intended path of micro wave transmissions (Front Door) is - for example - the subsystem "mmW seeker section with the antenna system" or the IR-seeker.

Nearly all smart ammunitions need wings for the aerodynamic lift and for stabilization. Furthermore control fins are necessary to guide and maneuver the system with the goal to hit the searched and tracked target. Barrel or tube launched systems require folded wings and fins which are deployed after launch. This means that the body has to be designed with a number of slots. For initialization of the missiles before launch, umbilicals are necessary. All these described system-specific designs are called "Back Door" coupling possibilities.



These systemspecific extremities, slots, umbilicals, antennas and wirings but also the body of the missile itself must be considered as antennas which respond to the electrical field.

The wing and fin slots respond best to the magnetic field component, whereas the wings and fins respond best to the electrical field component. The coupled electromagnetic field, or the current induced by the electromagnetic field, is lead to the inside of the ammunition over the fins, wings and slots affecting electronical components depending on the frequency, field strength, polarization, modulation frequency and modulation degree of the propagated electromagnetic field.

The critical resonances due to the outer dimensions of the ammunition can be estimated in advance. It must be distinguished between

- outer body resonances due to
 - missile length ($\lambda/2$ -antenna)
 - missile circumference (λ -antenna)
- resonance possibilities due to
 - slots in the structure of the missile
 - wings and fins of the missile

The slots can be considered as ($\lambda/2$)-antennas where the electromagnetic field can cause resonance in the missile. The best coupling effect can be achieved when the H-field is oriented in parallel to the slots. The control fins also act as antennas. The best coupling effect can be achieved when the E-field is oriented in parallel to the fins. This is also true of the wings. The control fins normally extend into the inside of the missile, where the fin control actuators with the control electronics are located. In this case the fin length must be considered as ($\lambda/4$)-antennas. The surface current induced on the fins is transmitted via the fin root to the inside of the ammunition and acts there as a secondary radiation source on the wiring and electronics. The same effect occurs when the wings have a connection inside the missile body. This is normally the case when folded wings are used.

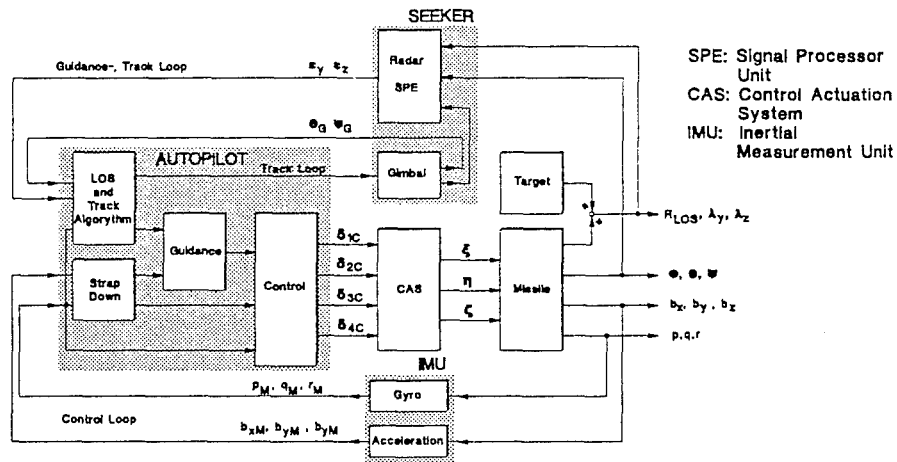
Another possible design version has the wings mounted directly on the surface of the missile structure. Now the length of the wings or fins must be considered as ($\lambda/2$ -antennas). The coupled surface current on the wings is now passed on to the missile's body.

4. The Guidance and Control System of Smart Ammunitions

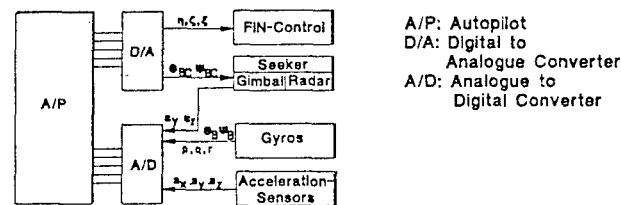
The missile guidance and control components are tasked with guiding the missile after stabilization to a target area and acquiring a target with subsequent final homing. The guidance and control loop of smart ammunition is designed with different layers of control loops which have different tasks. These control loops are more or less sensitive to electromagnetic radiation interference and can lead to the loss of the target.

The complex guidance and control system of smart ammunition shows hierachical structure and exists of a number of cascaded control loops, the most interesting one being the guidance loop, the control loop and the track loop.

Structure of a Complex Guidance and Control System



Overall Guidance and Control Schematic



Control Loop

The control loop is tasked with ensuring IPAS roll control in the three axes (roll, yaw and pitch).

This includes:

Stabilizing the roll movement (attenuation)

Achieve and maintain an inertially predetermined flight attitude (attitude hold)

Controlled angle of incidence of ammunition for ensuring the required accelerations

The computation of the actual flight attitude deviations from desired values is effected by means of the signals supplied by the IMU. The discrepancies as determined will be translated into appropriate actuation signals d1c, d2c, d3c, d4c by the control algorithms and transmitted to the control actuator system.

Since perturbations of both the IMU signals and the actuator system would be passed into the control loop directly, they present a potential hazard to the control loop function.

Guidance Loop

The guidance loop is superposed to the control loop described earlier. It is responsible for the IPAS Center of Gravity movement (trajectory).

For orientation during the navigation phase the guidance loop makes use of the position and velocity data computed by the strap-down algorithms out of the IMU signals. Deviations from the desired trajectory are eliminated by the guidance regulator due to appropriate acceleration commands to the control loop. Any interference on the level of the inertial sensor system will produce navigation errors which, depending on nature and value of those factors, may cause the ammunition to miss the target area (mission failure).

After target acquisition the guidance signals will be computed based on the target miss distance data e_y and e_z as measured by the seeker (deviations from the aimpoint in the seeker field of vision). In order to minimize the miss distance values also in the case of rapidly moving targets the proportional navigation is used as a guidance method. The line of sight rate data needed for this guidance law (change IPAS to target line of sight) are estimated by means of a special algorithm (LOS algorithm).

In addition to the measured target miss distance values o_G and w_G of the seeker frame system the IPAS roll data p_m q_m r_m are processed. Accordingly, any interference of the IMU signals would cause an error in the estimation of the line of sight rate and, hence, improper operation of the guidance loop.

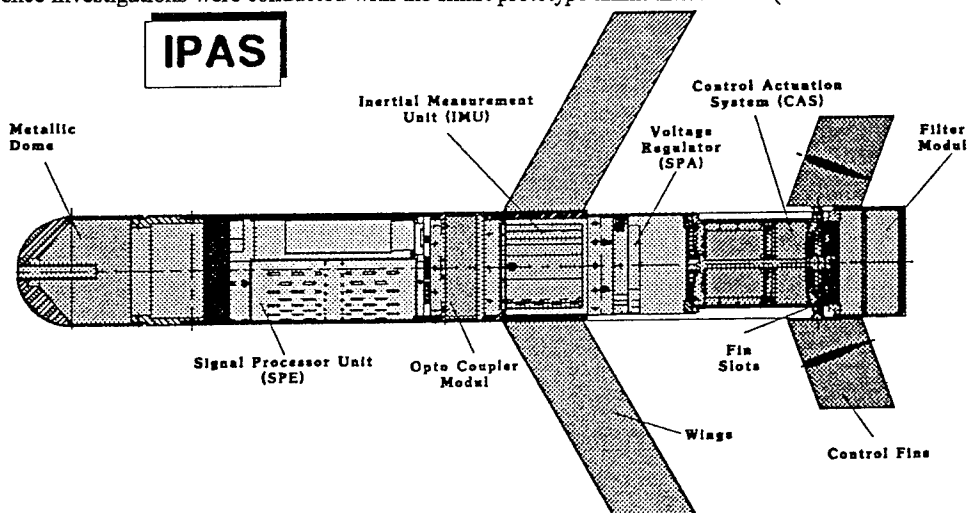
Tracking Loop

During the end game, a constant line of sight is required between the seeker and the target. Therefore, seeker frame system-to-target tracking is required. Since the position of the aimpoint in the seeker field of vision, which is only ± 1.5 degrees (linear range) is determined by both the target movement and the IPAS in-flight movement, the tracking algorithm must use the roll rate measured via the IMU.

The processing of roll rate measurement data subject to interference will, however, cause malfunctions to the seeker tracking process which may, in the worst case, result in target loss and, hence, IPAS end game failure.

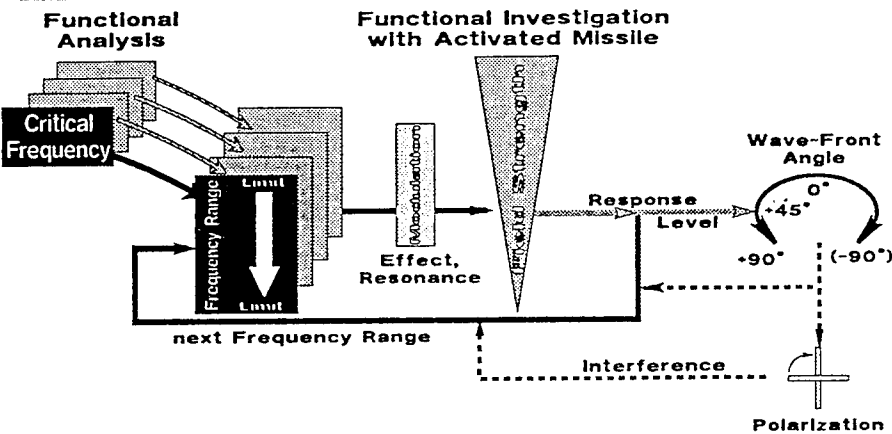
5. Interferences of Investigated Radiated Smart Ammunition with Electromagnetic Fields

Interference investigations were conducted with the smart prototype ammunition IPAS (Smart Antitank Submunition)



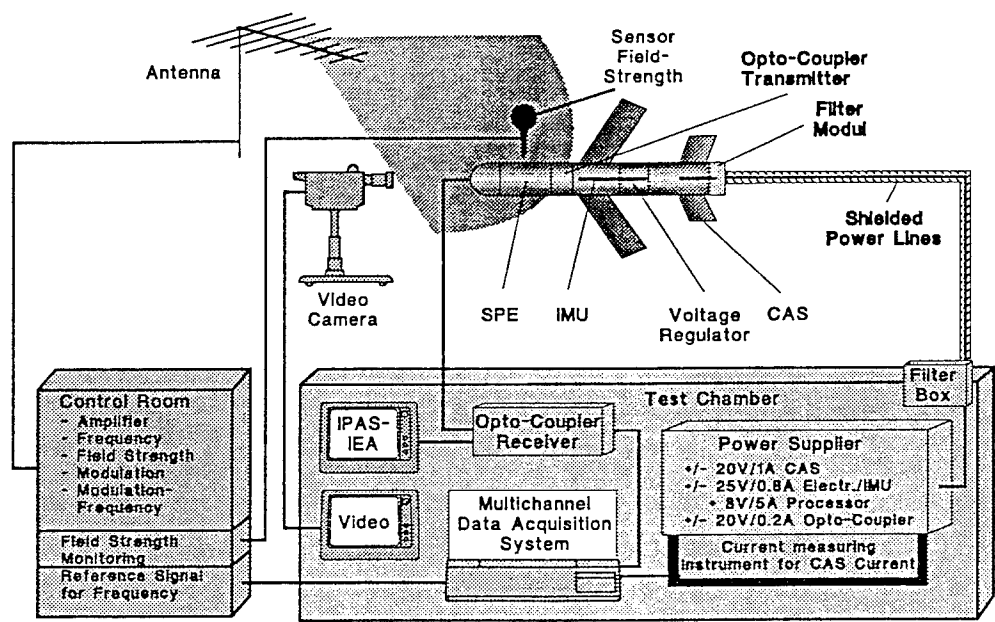
For the first investigation step the system was operated without the seeker. The front door coupling effect was prevented by using a metallic nose instead of the dome. This ensured that only the back door effects due to the fins, finslots, wings and missile structure could be investigated. The interferences on the electronics due to electromagnetic field radiation were measured. Real time 6-DOF simulations showed performance limitations for the ammunition.

Methodology for EMI-Tests

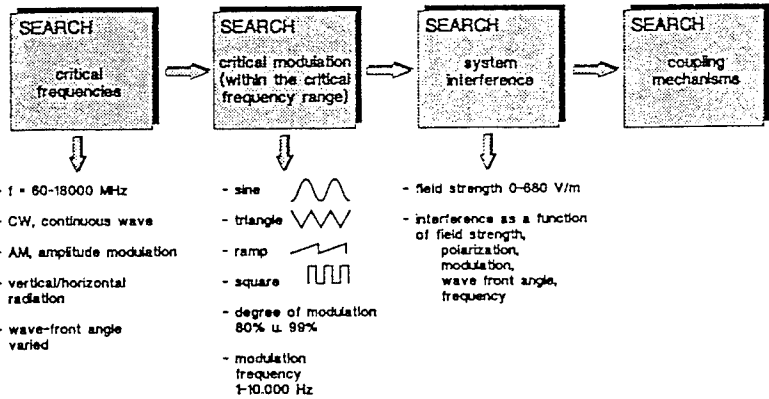


During the radiation tests the investigated ammunition was activated. All relevant guidance and control signals were transmitted via an optocoupler device and recorded. The power supply lines were also decoupled from the missile. No flight abnormal additional devices interfered the system during radiation.

Test Set-up

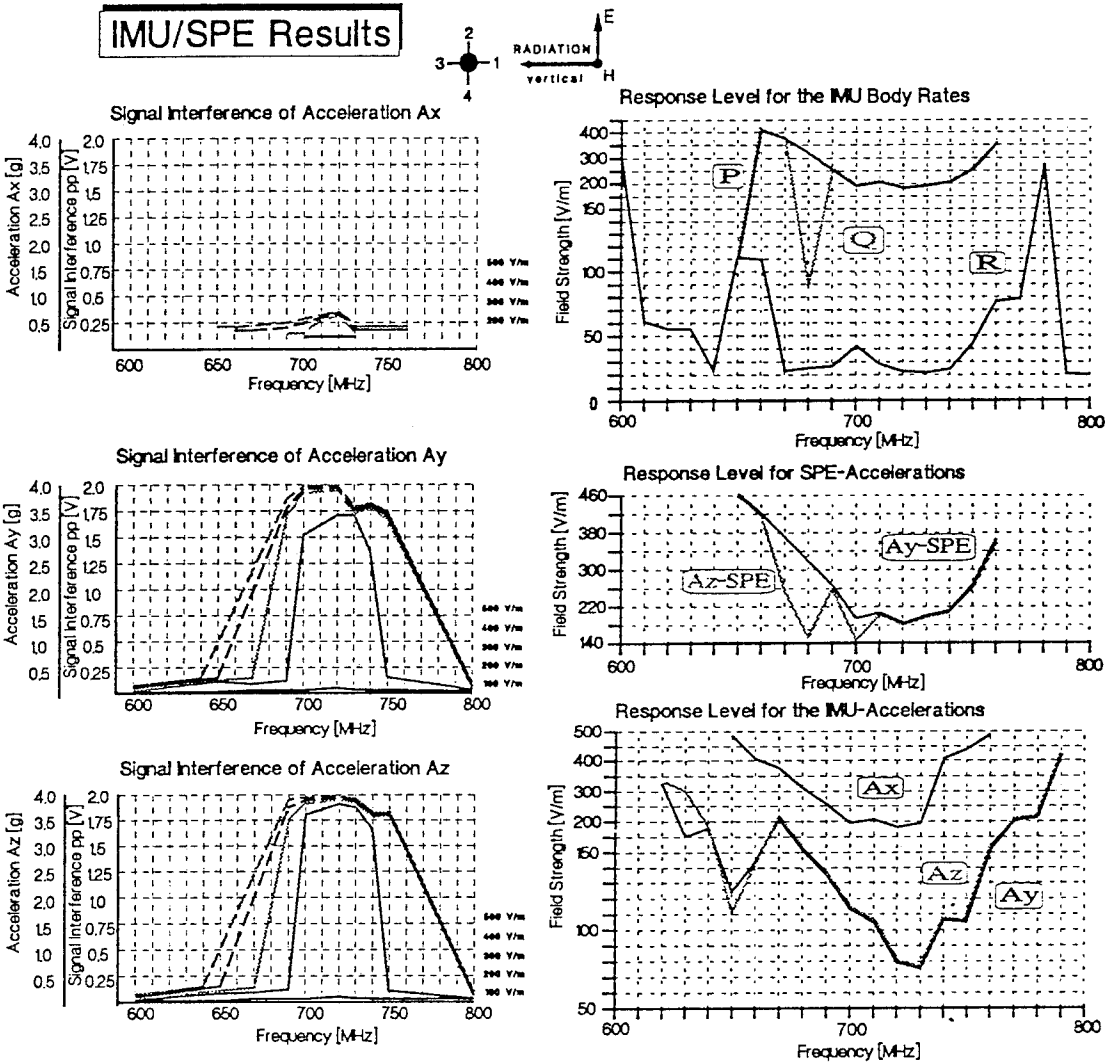


Procedure for EMI-Test with Activated IPAS



The experimental radiation investigations with the activated IPAS showed, that this ammunition could be affected by interference only via the control fins and the slots in the structure for the control fins. The kind of modulation and the modulation frequency played the essential role for the missile electronic's susceptibility to interfere. The fins act like one side short-circuited dipoles. Due to the negligible fin slot dimensions nearly the whole system interference was caused through the resonances of the fins. The signal interference of the missile show a rather big damping working forwards from the rear (CAS) to the front of the missile.

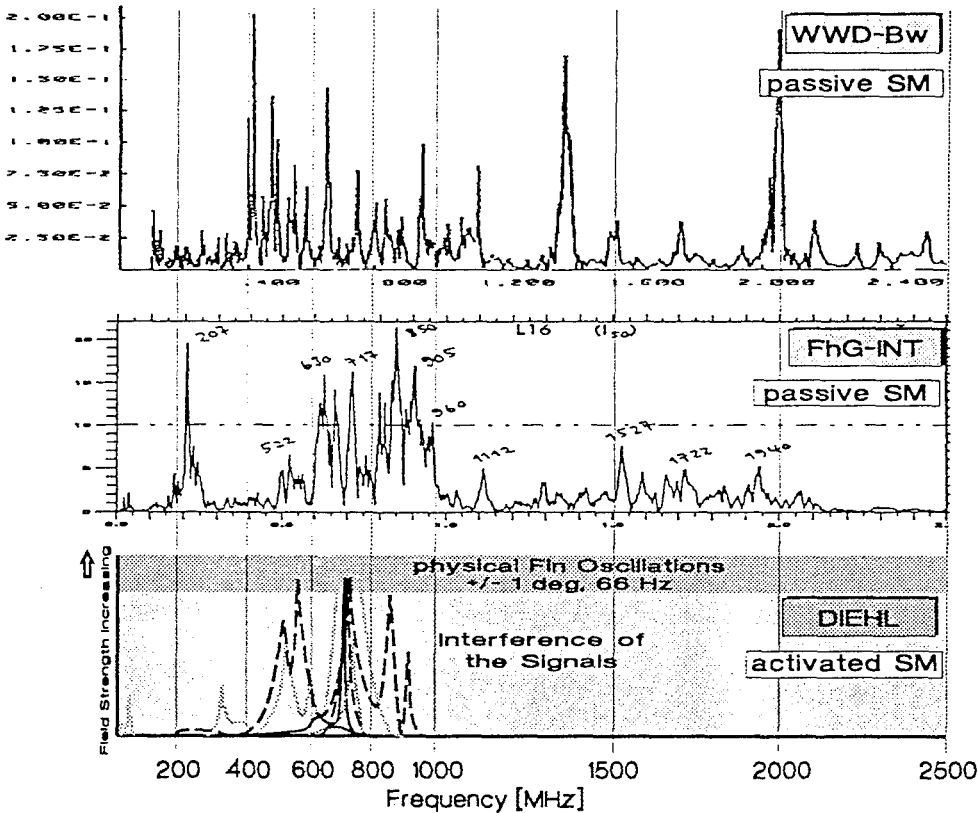
Without any modulation of the carrier frequency the electronics of the system couldn't be interfered at all. The following system signals were subject to interference: the fin deflection signals of the control actuation system, the gyro and acceleration signal of the IMU (Inertial Measurement Unit) and the digitalized acceleration and gyro signals inside of the Signal Processor Unit (SPE).



First of all the investigation test results measured at the activated ammunition were compared with investigation test results measured at the passive ammunition - resonances on wiring and cavity responses at different locations inside the missile - and also the theoretical and numerical investigation results.

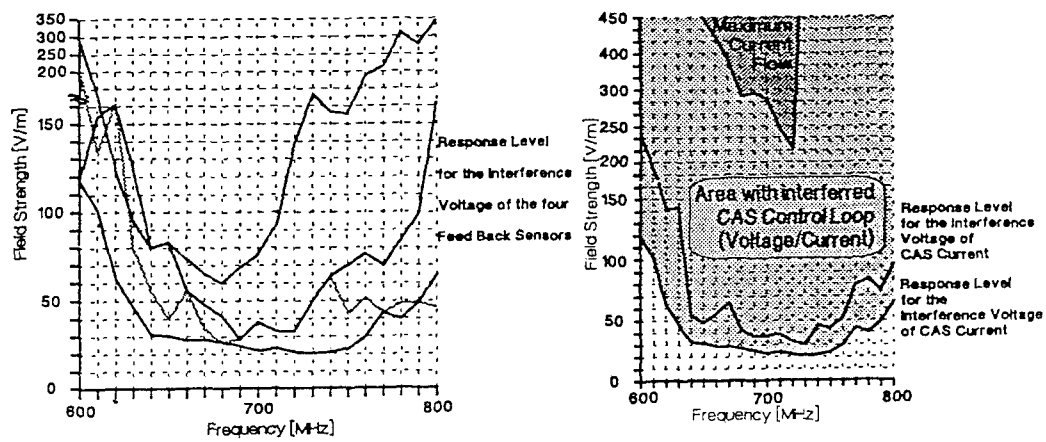
The predictions due to the outer dimensions of the ammunition matched the measured interferences on the level of the system electronics to a very large extent. But not all predicted and measured resonances at the passive ammunition cause an interference with the system electronics. Only system tests with activated electronics can quantify the predicted interference potential. In the case the radiation of the ammunition can cause interferences with system signals the performance limitation of the flight path must be evaluated by the system simulation which considers the measured signal interference.

Comparison of different Investigation Aspects

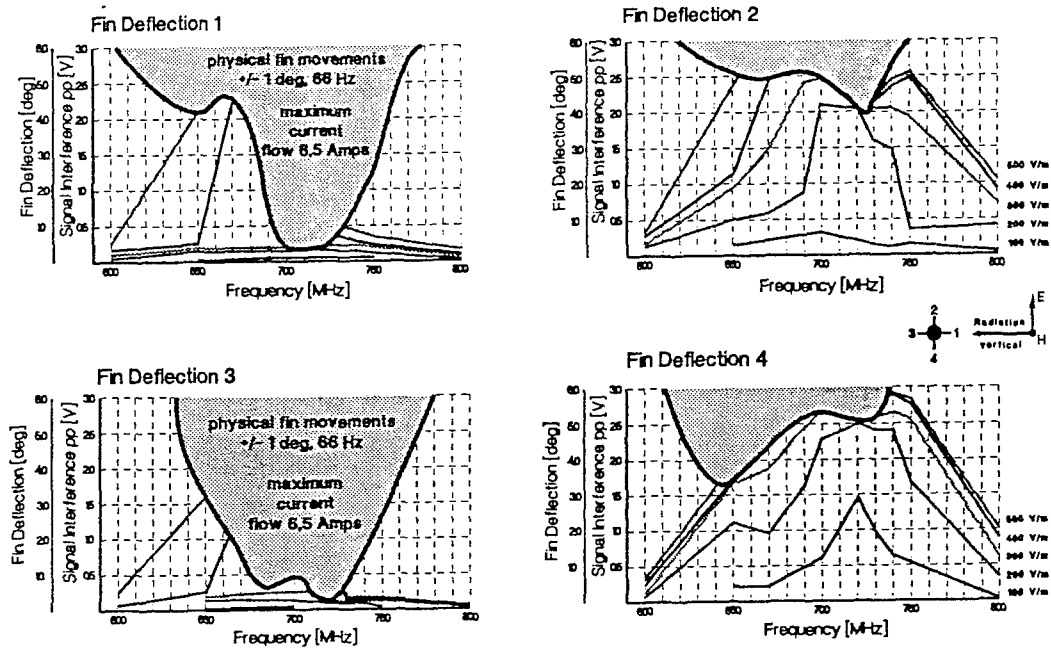


WWD-Bw: Cavity Resonance at CAS
 FhG-INT: Wire-Resonance at CAS
 DIEHL: CAS System Interference

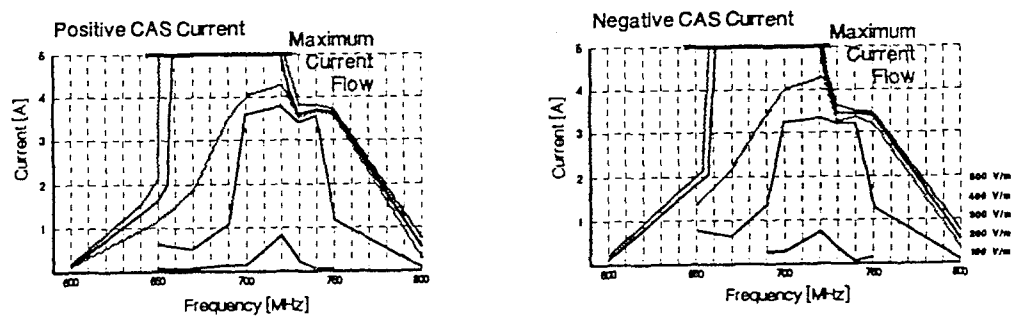
Response Level for the Interference of CAS



Interferences of Fin Deflection Signals



Interference of CAS Current

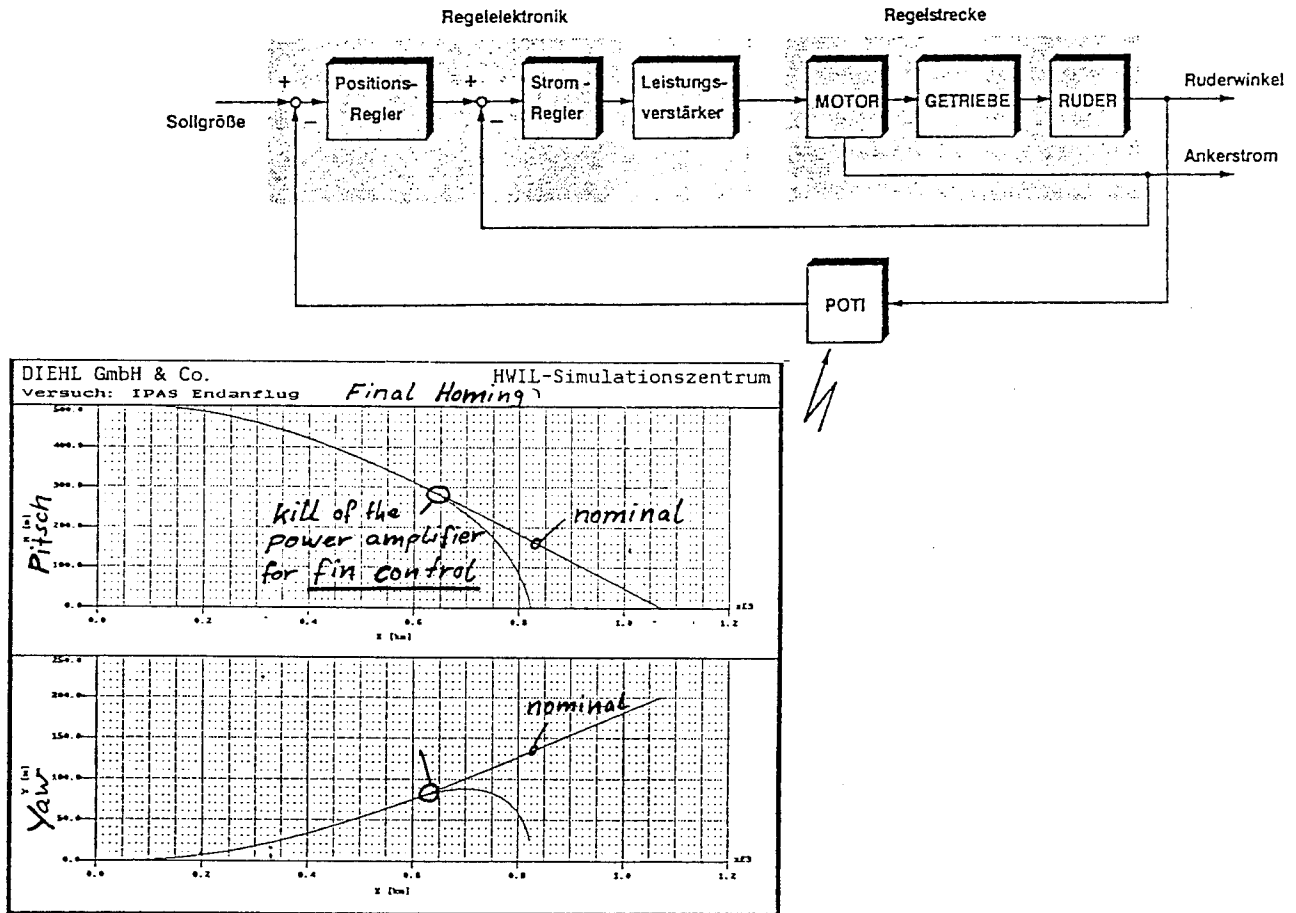


6. System Simulations due to the Interference caused by high Power Microware

The system simulation was conducted in different steps. The interference was considered for the most sensitive "Final Homing Phase" of the missile's flight path.

a.) The interference measured at the Control Actuation System (CAS) only.

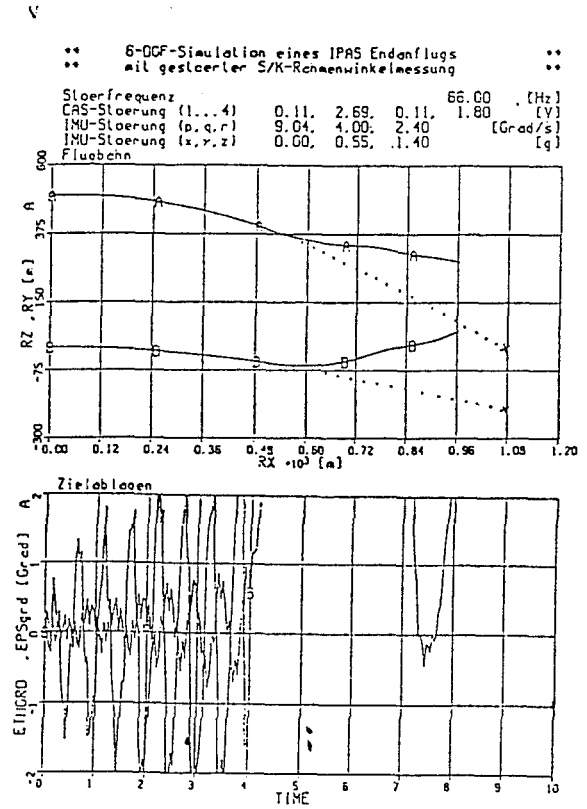
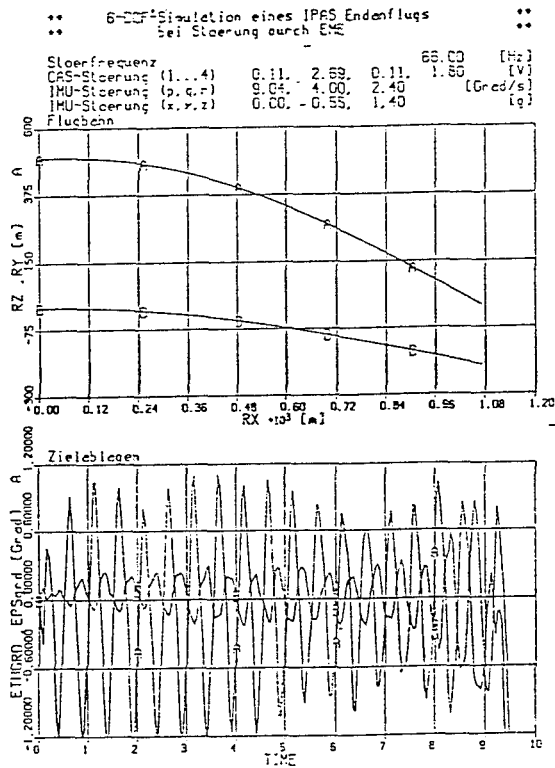
The oscillating resonances itself on the servo control loop hardly interferes with the flight path. But these oscillations cause an increased current flow in the power amplifiers which are designed to withstand the maximum current flow for only a few seconds. Any damage to the power amplifier will immediately interrupt the flight mission.



- b.) Interference measured at the IMU-signals (body rates and accelerations) only. These signals are the inputs for the guidance and control loop.
- c.) Simulation runs with combined interference from CAS and IMU.
- d.) Theoretical interference of the gimbal signal to interfere with the track loop

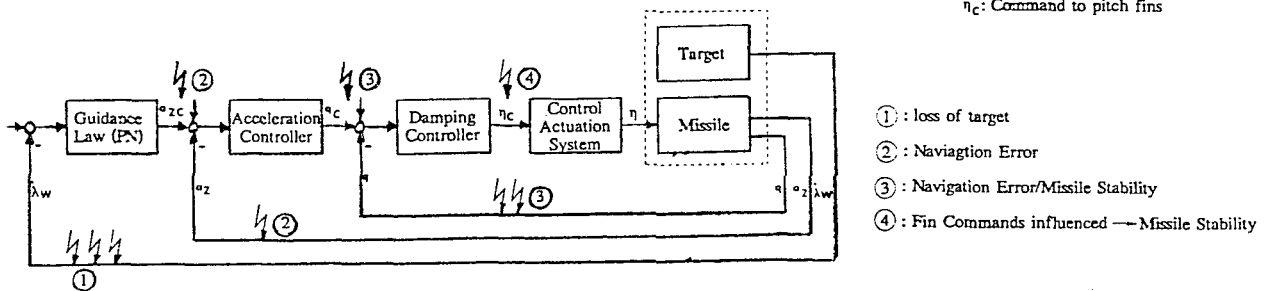
The simulation results which considered the interference with the CAS- and IMU-signals showed that the missile's flight path hardly could be degraded in performance. The reason for this effect is that the interferences on the signals have an oscillating character. Much better effects for system interferences can be reached if the signals show offset shifts.

A closer look at the internal state variables show that the CAS- and IMU-signal interferences have a strong influence on the track loop. The nominal deviation within the sight of view is about $\pm 0.15^\circ$ in comparison to the jammed sight of view which reaches the limit of about $\pm 1.2^\circ$. In case the interference causes a deviation greater than 1.2° the target is lost and the flight mission can not be fulfilled. An interference of 3 % on the gimbal signals lead to a loss of the target already.



Follow on investigation with an integrated seeker will verify the influence on the missile's flight path due to the front door coupling effects.

Interference of the Guidance and Control Loop



The most sensitive signals in the guidance and control loop of the smart ammunition can be found in the track loop or the interference with the gimbal signals which influence the line of sight signal and lead to a loss of the target.

CALCULATION AND MEASUREMENT OF HPM FIELDS SCATTERED BY A TARGET WITH OPENINGS

S. Kashyap, M. Burton, and A. Louie

Defence Research Establishment Ottawa

Ottawa, Ontario, Canada

K1A 0Z4

ABSTRACT

This paper concerns the computation and measurement of HPM fields inside and outside a structure with openings. RCS computations and measurements are made for a number of targets. The computations use both frequency-domain and time-domain methods, and the results are then compared with those measured in an anechoic chamber. An attempt is made to correlate various quantities such as the RCS, the scattered fields inside a structure, and the time-domain scattered far-fields. It is shown that some of the scattered far-field quantities may be used to identify the target scattering centres, the frequencies at which maximum coupling occurs, and the cut-off frequencies of a target.

INTRODUCTION

Structures such as airplanes, helicopters, and missiles represent an important class of targets for HPM coupling analysis and measurements, since they have apertures and slots through which the HPM fields may enter the structure. Scattered fields near such objects (inside and outside) are affected by the size and location of the openings. Scattered far-fields (e.g. RCS) are also affected by the nature of the openings. Thus the measurement and calculation of the fields near a target and the RCS in the frequency and time domains may provide information on the scattering and coupling properties of a target.

Ling, Lee and Chou have used a shooting and bouncing ray approach to look at the RCS of open waveguides [1] and other complicated objects [2]. Pathak and Burkholder [3] have analyzed the electromagnetic scattering of open-ended waveguides using a combination of asymptotic and modal techniques. These approaches are generally valid when the structure dimensions are large compared to the wavelength.

In this paper, the fields inside a structure and the RCS are calculated using a moment method solution of the electric field integral equation (EFIE) in the frequency domain. The correlation between the internal fields and

the RCS is studied. Time-domain RCS is then obtained by multiplying the frequency-domain RCS with the spectrum of an appropriate pulse and taking an inverse Fourier transform. This time-domain response reveals information on the location of the scattering centres of the target. The time-domain response and the frequency-domain response are then used to obtain time-frequency distributions (TFDs), which in turn reveal new information on the target, such as the identification of the target cut-off frequencies.

FREQUENCY-DOMAIN RESPONSE

Figure 1 shows some of the objects used in the study. A plane electromagnetic wave illuminates the structures. Reference [4] describes a simple and efficient numerical procedure for scattering in frequency domain by arbitrarily shaped bodies, using the moment method to solve the electric field integral equation (EFIE). The object surface is modelled using planar triangular patches (for example, Figure 2). Because of the EFIE formulation the procedure is applicable to both open and closed surfaces. This procedure has been applied to a wide variety of electromagnetic interaction problems and has yielded excellent agreement between this, other numerical methods, and exact analytic formulations. In JUNCTION [5], the EFIE approach is extended to analyze an arbitrary configuration of conducting wires and bodies. The algorithm developed can handle wire-to-wire, surface-to-surface, and wire-to-surface junctions. Both near-field and far-field quantities such as the RCS can be computed. A modified version of JUNCTION is used here as the "EFIE method".

Figure 3 shows the computed electric field in and around a cylinder with openings for plane wave incidence at 9.0 GHz. It shows the reflected and the transmitted fields along the axis of the cylinder. Figure 4 shows both the computed and measured RCS of the cylinder from 2 to 18 GHz. Figure 5 shows a plot of the peak field magnitude inside the cylinder at different frequencies, compared with the RCS. It shows a correspondence between the peak field magnitude and the RCS:

whenever the RCS is high, the field inside the structure is low. In simple objects like the one used in this example, and for this angle of incidence, this correspondence may be explained by using simple laws of reflection and transmission of EM waves. The correspondence may be used for predicting coupling to an object from far field quantities.

TIME-DOMAIN RESPONSE

Time-domain behaviour of the fields or the time-domain RCS can be obtained by multiplying the frequency-domain response with the spectrum of an appropriate incident pulse and taking an inverse Fourier transform. Figure 6 shows the time-domain impulse response RCS for a cylinder open at one end. It shows the location of the scattering centres of the target. The first peak corresponds to the leading edge (or the open end) of the target and the second peak corresponds to the trailing edge (or the closed end) of the target. The magnitude of the peaks is related to the magnitude of the reflection from the leading and the trailing ends.

TIME-FREQUENCY DISTRIBUTIONS

The time-domain and the frequency-domain responses give important information on the electromagnetic scattering properties of a target. Use of time-frequency distributions (TFDs) [6] gives further information on a target which neither the time- nor the frequency-domain response is able to provide alone. TFDs are obtained by computing a short-time Fourier transform of the time-domain response $f(t)$ or the frequency-domain response $F(\Omega)$ as follows:

$$S(\tau, \Omega) = \int f(t) g(t-\tau) e^{-j\Omega t} dt$$

$$S(\tau, \Omega) = \frac{e^{-j\Omega \tau}}{2\pi} \int F(\omega) G(\Omega - \omega) e^{j\tau \omega} d\omega$$

where $g(t)$ and $G(\Omega)$ are the window function in time and frequency domain, respectively.

Figure 7 shows a TFD obtained by computing a short-time Fourier transform from the time-domain impulse response. Frequency-domain and time-domain responses are also shown along the two axes. From the TFD, one can easily identify the leading and the trailing edges of the structure. In addition one can also identify the cut-off frequencies of the cylindrical cavity at 3.5 and 10.2 GHz. This information is not available from the time- or frequency-domain response alone and can be used to further characterize a structure using far-field quantities.

CONCLUSIONS

In this paper frequency- and time-domain responses of a structure have been computed using the moment method and inverse Fourier transformation. Both near field and far field quantities were computed. In the cases considered, there is a correspondence between the fields inside a structure and the RCS. Time-domain RCS was computed and has been shown to provide information on the location of the scattering centres of the target. Time-frequency distributions were also computed and it has been shown that the TFDs provide more information (such as the cut-off frequencies) on a target than that provided by the frequency- and the time-domain responses alone. Thus study of far field quantities (for example, RCS) in the frequency domain, in the time domain, and as TFDs can all reveal important target information, such as the frequencies at which the maximum coupling occurs and the cut-off frequencies.

REFERENCES

1. Ling, H., Lee, S. W., and Chou, R. C., "High Frequency RCS of Open Cavities with Rectangular and Circular Cross-sections", *IEEE Trans. Antennas Propagat.*, AP-37, 1989, pp. 648-654.
2. Lee, S. W. et al, "XPATCH: A High Frequency Electromagnetic Prediction Code and Environment for Complex Three-Dimensional Objects", *IEEE Antennas and Propagation Magazine*, Vol. 36, No. 1, Feb. 1994, pp. 65-69.
3. Pathak, P. H. and Burkholder, R. J. "Modal, Ray and Beam Techniques for Analyzing the EM Scattering by Open-Ended Waveguide Cavities", *IEEE Trans. Antennas Propagat.*, AP-37, 1989, pp. 637-647.
4. S. M. Rao, D. R. Wilton, and A. W. Glisson, "Electromagnetic Scattering by Surfaces of Arbitrary Shape", *IEEE Trans. Antennas Propagat.*, AP-30, 1982, pp. 409-418.
5. S.-U. Hwu and D. R. Wilton, "Electromagnetic Scattering and Radiation by Arbitrary Configurations of Conducting Bodies and Wires", *University of Houston, Technical Report 87-17*, 1988.
6. Moghadder, A. and Walton, E. K., "Time-Frequency Distribution Analysis of Scattering from Waveguide Cavities", *IEEE Trans. Antennas Propagat.*, AP-41, 1993, pp. 677-680.

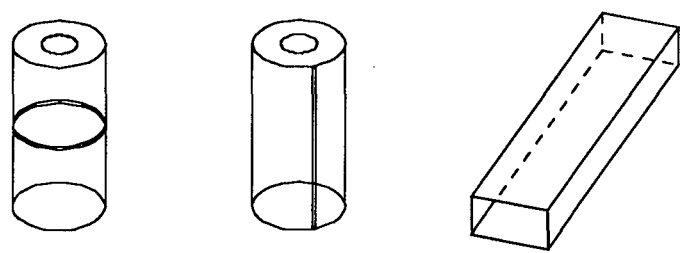


Figure 1. Some of the objects used in this study.

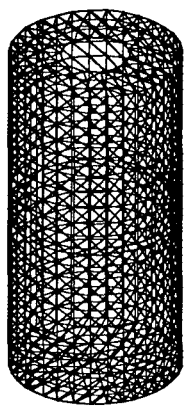


Figure 2. Example of a triangular surface-patch model for EFIE.

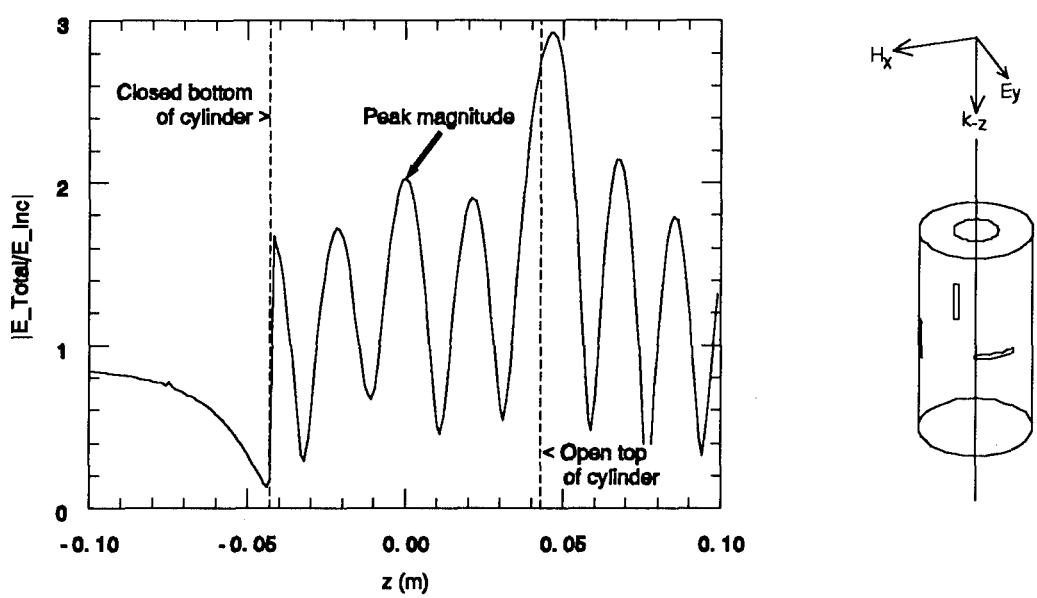


Figure 3. Total electric field along an axis of a cylinder with openings, for plane wave incidence.

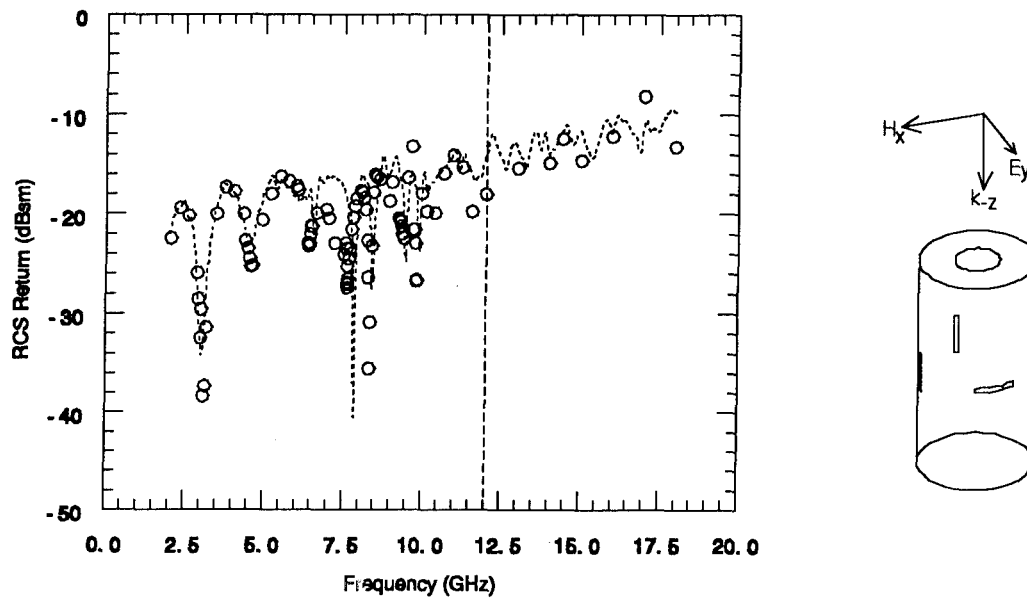


Figure 4. RCS of the cylinder with a hole and three slots.
Dashed curve = Measurement. Circles = EFIE.
Vertical dashed line = $\lambda/5$ simulation limit.

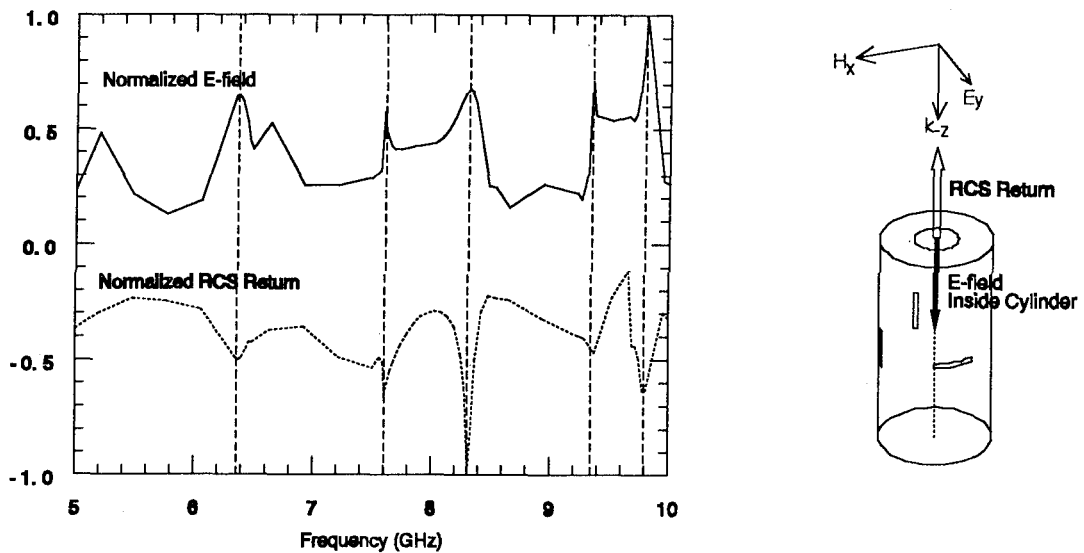


Figure 5. RCS return versus peak magnitude of the E-field inside the cylinder.
Dotted curve = RCS return normalized to peak value -1.0.
Solid curve = Peak magnitude of the total electric field inside the cylinder, normalized to maximum value +1.0.
Vertical dashed lines = Minimum RCS return and maximum E-field frequencies.

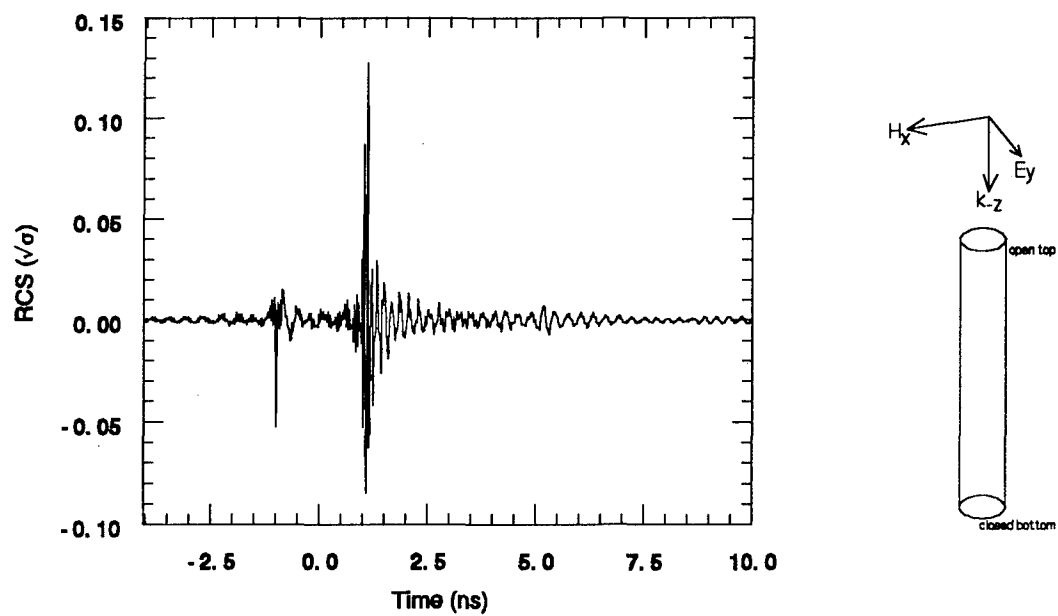


Figure 6. Time-domain RCS (i.e. back-scattered far-field) of a cylinder with one open end.

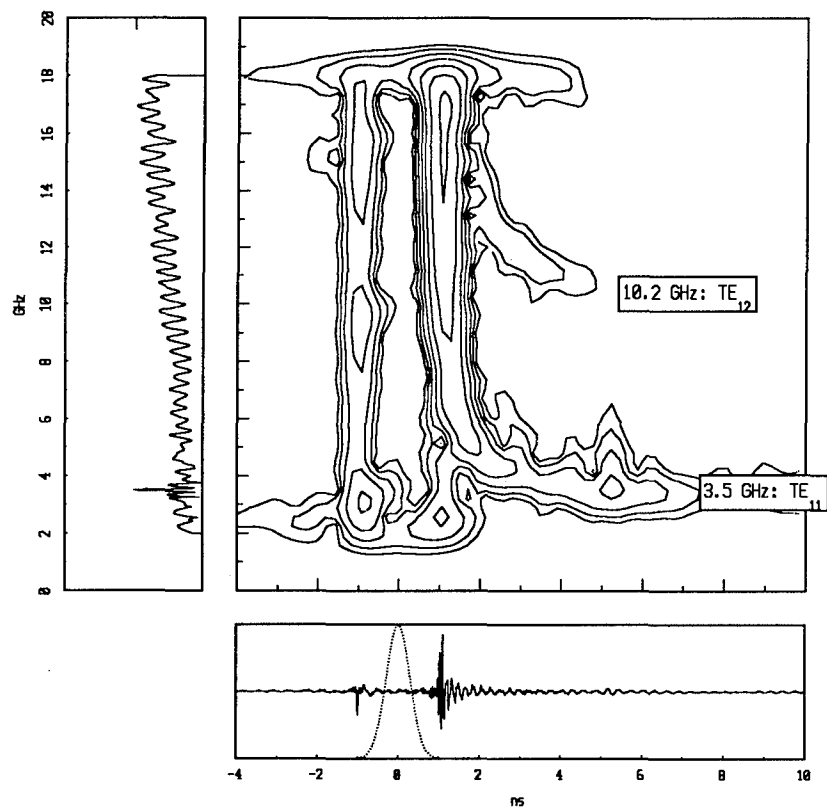


Figure 7. TFD of the cylinder with one open end. Frequency domain and time domain responses are shown along the vertical and horizontal axis, respectively. The dotted curve represents the window function in the time domain.

DISCUSSION

P.D. SMITH

How does noise affect the determination of cutoff frequencies (of the hollow tube or box) in the time frequency calculation ? How much noise can be added before these disappear ? Does it work for real data as well as numerically calculated data ?

AUTHOR'S REPLY

The method works for calculated and measured results. The data for TFD's was obtained from measured results. Noise affects (measurement noise) if it can not be gated out and is in the same time location as that required for the determination of the cut-off frequencies.

P.D. SMITH

How well were the aperture slots represented in your calculations ? Where they one cell thick ? Does this accurately model true aperture size ?

AUTHOR'S REPLY

Along the narrow direction, we use 1 or 2 edges. We use an implementation of END where the tangential boundary condition can be applied on each cell and the object can be infinitesimally thin.

U. LAMMERS

The methodologies you described apply to radar cross-section modeling independent of power. Are you investigating phenomena that apply to high microwave power in particular, such as non-linear effects of imperfect metallic junctions ?

AUTHOR'S REPLY

We have not looked at the non-linear effects of imperfect metallic junctions. Some work at the university of Toronto does look at some non-linear effects.

P. ZWAMBORN

- 1/ Is the relation power density inside the cylinder versus R.C.S. perhaps a better way to distinguish the relation inside E-field and R.C.S.
- 2/ How have you solved the causality problems caused by the windowing process before taking the inverse FFT ?
- 3/ Can you indicate the resolution in determining the cut-off frequency ?

AUTHOR'S REPLY

- 1/ Thank you for your suggestion. We will also look at the power density VS RCS
- 2/ There are a number of techniques for taking IFFT of a band-limited signal. We use some of these techniques.
- 3/ Resolution depends upon a number of factors including window width, length of the structure, noise, type of the window. We are investigating the effect of these factors.

Analyse du couplage par une technique de mesure rapide de champ proche (Coupling analysis by a rapid near field measurement technique)

B. Chevalier, D. Sérafin
Délégation Générale pour l'Armement
Direction des Recherches, Etudes et Techniques
Centre d'Etudes de Gramat
46500 Gramat
France

1. SUMMARY

This paper presents a method for coupling analysis allowing to determine the worst case of stress (frequency, polarization and attitude angles) of a target by an electromagnetic wave. The approach is based on the determination of the radiated pattern of the device under test, considered as a transmitting antenna, using near field measurements. The coupling can be determined using the reciprocity theorem.

2. INTRODUCTION

The interaction between an electromagnetic wave and a target happens through antennas and shielding defects (apertures, connectors, discontinuities...).

If it is quite easy to determine the coupling via the antennas (front door), it is more difficult to estimate the same quantity for a component or a specific equipment inside the structure (back door).

Usual experimental methods simulate as faithfully as possible the coupling conditions: direct illumination of the object. However, these techniques present some constraints:

- necessity to illuminate the device in its entirety (great dimensions)
- difficulties for modifications of attitude angles.

So, we have chosen an indirect method to determine the coupling using near field measurements. The advantages of such a technique are:

- compact range
- arbitrary polarization and attitude angle
- rapidity.

A spherical measurement device has been chosen because of the complexity of the systems to be tested.

3. THE COUPLING CROSS SECTION

To characterize the coupling between the incident wave and a target, we introduce the notion of Coupling Cross Section (CCS):

$$\sigma = \frac{W_r}{P_{inc}}$$

Where σ is the Coupling Cross Section (cm^2)

W_r is the received power at the considered point
(Watts)

P_{inc} is the incident power density (W/cm^2)

The Coupling Cross Section is determined using the an-

tenna theory; the object is considered in reception and transmission mode (fig. 1).

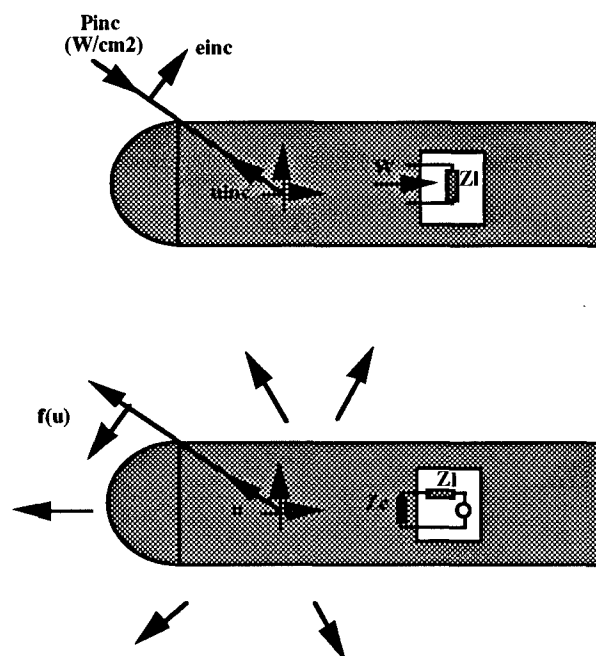


figure 1 : CCS definition for a device under a microwave illumination and the reciprocal problem

For a considered test point, the CCS is given by:

$$\sigma(u) = \frac{\lambda^2}{4\pi} \rho_{ch} \rho_{pol}(u) G(u)$$

Where λ is the wavelength (cm)

ρ_{ch} is the load factor representing the relative adaptation between the load impedance Z_l of the internal component and the input impedance Z_e of the object considered as a transmitter
 ρ_{pol} is the polarization factor
 $G(u)$ is the gain

The Coupling Cross Section depends on three primary parameters (fig. 2):

- frequency
- attitude angle
- polarization

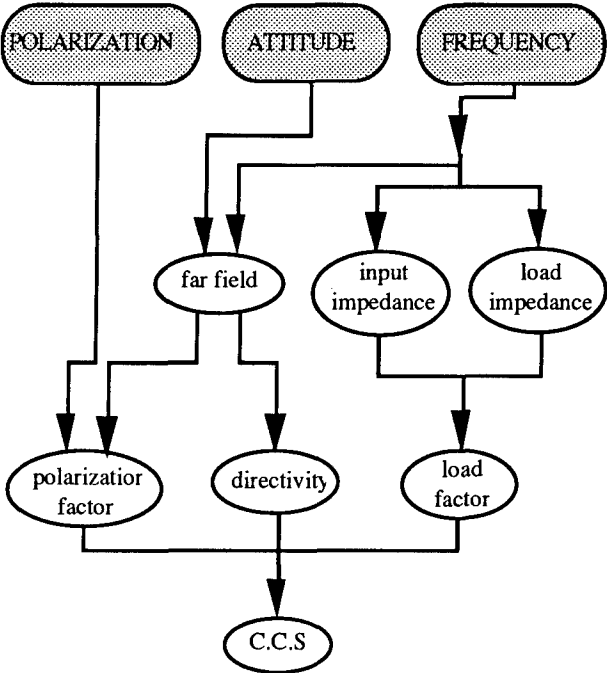


figure 2 : flow chart for the CCS analysis

4. NEAR FIELD MEASUREMENT DEVICE

The development of a near field measurement device, the SOCRATE facility, has made possible the entire analysis of Coupling Cross Sections between 100 MHz and 4 GHz for objects less than 2 meters in diameter.

This device has been set in an anechoic chamber to simulate free space environment (fig. 3).

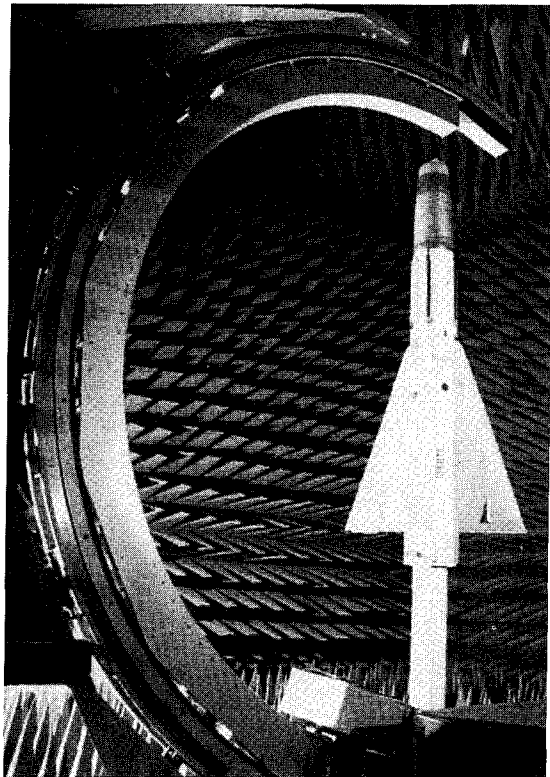


figure 3 : SOCRATE device

The frequency range is divided in two subbands - 100 MHz to 1 GHz and 1 GHz to 4 GHz - using different measurement techniques.

4.1 Low band : 100 MHz - 1 GHz

The measurements of the field transmitted by the system under test are achieved by means of a wide band antenna moved mechanically on the meridian. The antenna is composed of two capacitive loaded elements. They are put at 90° each other in order to do measurements in two polarizations.

The antenna displacement allows to achieve the measurements for all the considered elevations while the different azimuths are obtained with the positionner on which the object is set.

Because of the dead angle due to the positionner, the elevation measurements can only be done between 0° (the vertical) and 170°.

4.2 High band : 1 GHz - 4 GHz

Here, the field measurements are performed by means of a semi-circular array composed of a retina and a wide band collector (fig. 4). The retina and the collector use the modulated scattering technique [1].

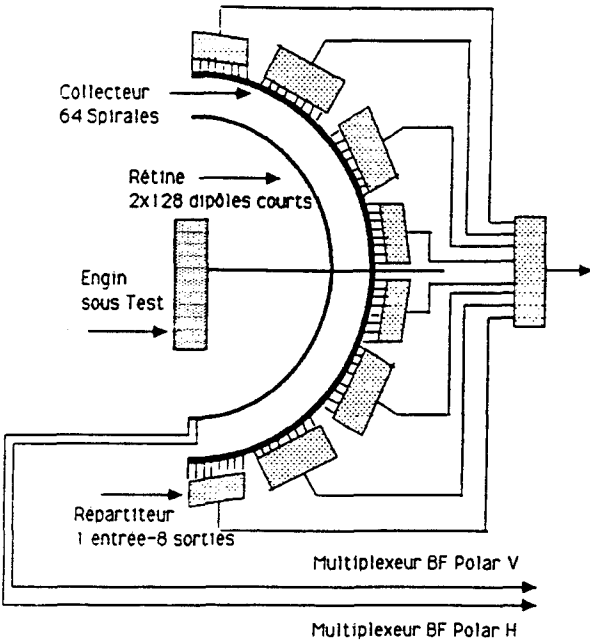


figure 4 : H.F. band, near field measurement device

The retina is composed of 128 dual polarized probes (fig. 5). Each probe is made of two dipoles loaded by a PIN diode. The two dipoles are put at 90° each other in order to measure the two polarizations of the radiated electromagnetic field. The dipoles are directed at 45° from the vertical in order to balance the couplings between the two linear, orthogonal polarizations. The horizontal and vertical components are calculated by addition and subtraction of the measured fields.

The collector is composed of 64 spiral antennas (fig. 5). Each spiral collects the field radiated by two couples of cross dipoles.

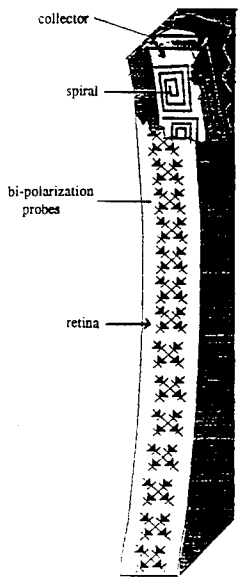


figure 5 : partial view of the retina-collector entity

The low frequency modulation of one of the dipoles through its associated PIN diode produces a perturbation of the electromagnetic field. This perturbation is picked up by the collector. So we have a modulated microwave signal at the output of the collector. The magnitude and the phase of this signal are proportional to the magnitude and the phase of the electric field at the modulated dipole location. The electromagnetic field distribution is measured rapidly at the retina location by a successive modulation of all the PIN diodes.

Such a technique avoid mechanical displacement of a probe as the use of a microwave multiplexer.

The figure 6 shows the bloc diagram for the measurements using the modulated scattering technique.

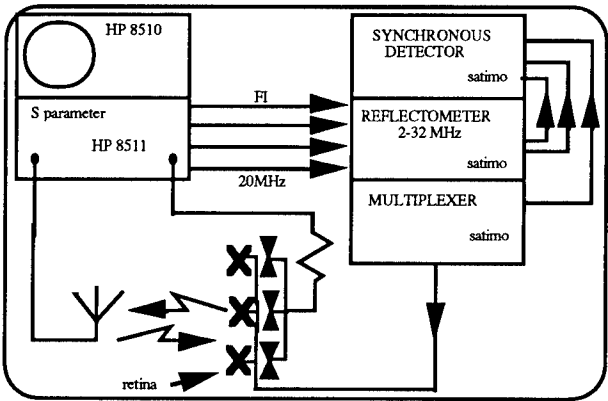


figure 6 : modulated scattering technique bloc diagram

The multiplexer achieves the sequential modulation of the PIN diodes on the retina. The reflectometer (vectorial voltmeter) picks up the modulated signal at the output of the collector. The dual synchronous detector (which is the B.F. part of the receiver in the modulated scattering technique) allows to restore the two orthogonal components of the measured electric field.

Because of the dead angle due to the positionner, the eleva-

tion measurements can only be done between 0° (the vertical) and 175°.

5. COUPLING CROSS SECTION ANALYSIS

5.1 Principle of determination of the CCS

The figure 7 shows the way to follow for the determination of the Coupling Cross Section.

We need to measure two quantities to determine the Coupling Cross Section of a system:

- the input impedance at the considered feeding point
- the near field radiated by the device

The input impedance is classically measured with a network analyser.

The SOCRATE facility permits to measure the near field radiated on a sphere (2 meters in diameter) around the object under test.

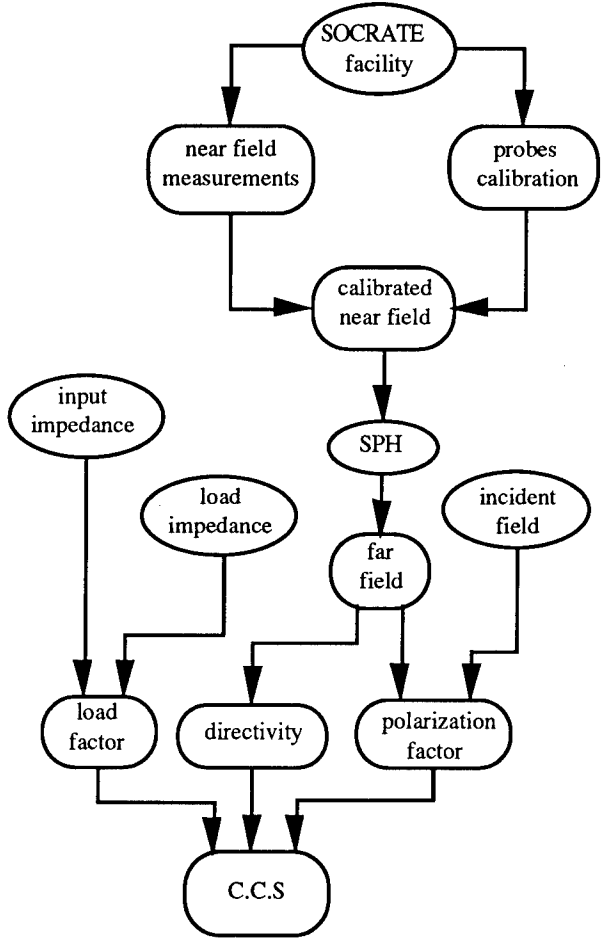


figure 7 : CCS determination using near field measurements

Firstly, each probe of SOCRATE is calibrated using reference antennas for which the radiated patterns are well known. After that, the near field radiated by the device under test can be measured and corrected.

A spherical near field to far field transformation (SPH program) is then used to obtain the radiated pattern of the device.

Using the reciprocity theorem, the Coupling Cross Section is then calculated from the input impedance and the radiated pattern of the device under test.

These operations are repeated for all the frequencies of interest.

5.2 Results

To show the interest of SOCRATE for coupling analysis, we have chosen a cylinder ($h = 496\text{mm}$, $\phi = 245\text{mm}$) presenting four apertures (fig. 8):

- one horizontal slot ($9\text{cm} \times 1\text{cm}$) on the Ox axis direction
- two vertical slots ($1\text{cm} \times 9\text{cm}$); one on the $-Ox$ axis direction and one on the $-Oy$ axis direction
- one circular aperture ($\phi=10\text{cm}$) located at the top of the cylinder.

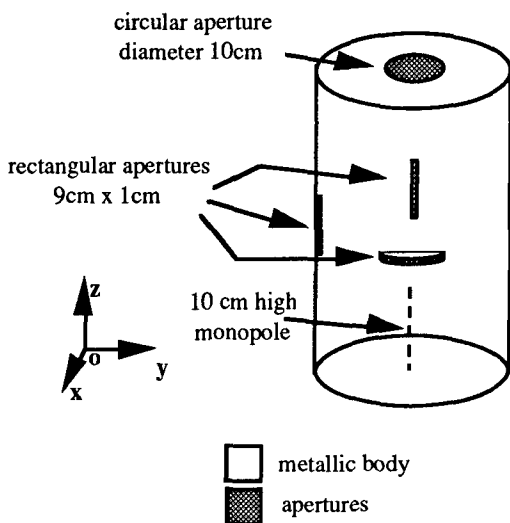


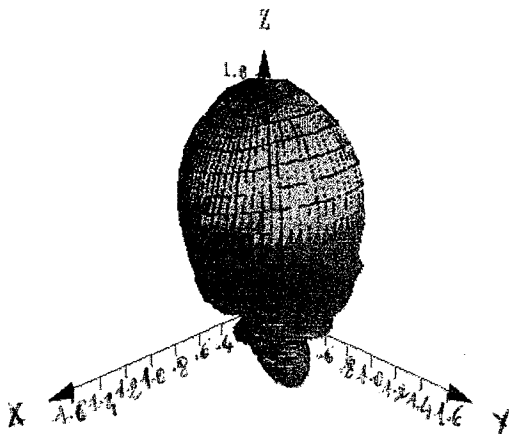
figure 8 : generic object

The cavity is excited by a 10cm high monopole. It is centered on the base of the cylinder.

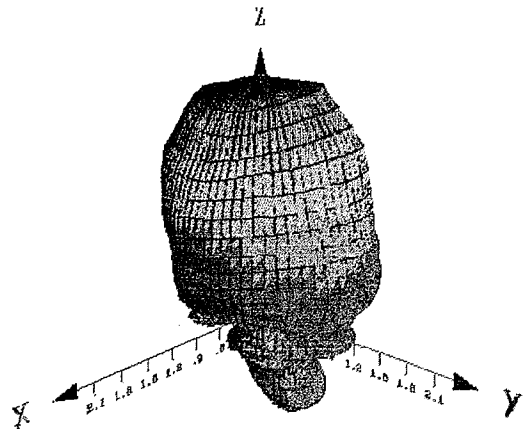
The figure 9 shows the 930 MHz patterns obtained at the different steps in the determination of the Coupling Cross Section:

- near field
- far field
- Coupling Cross Section.

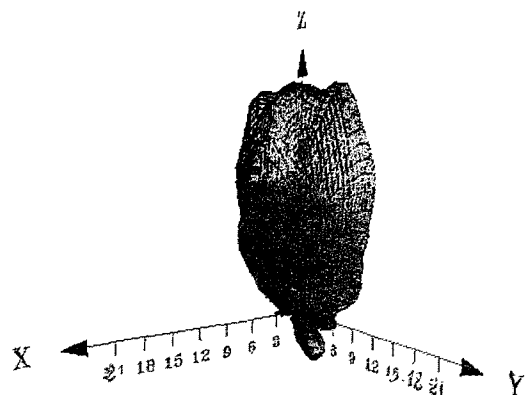
This frequency corresponds to the TM_{010} mode of the cavity.



a) measured near field



b) calculated far field



c) calculated C.C.S : max = 30 cm^2

figure 9: $f = 930\text{ MHz}$

The Coupling Cross Section diagrams (fig. 9,10 and 11) show important variations of attitude angles and coupling levels with small variations of frequency around a resonance mode of the cavity.

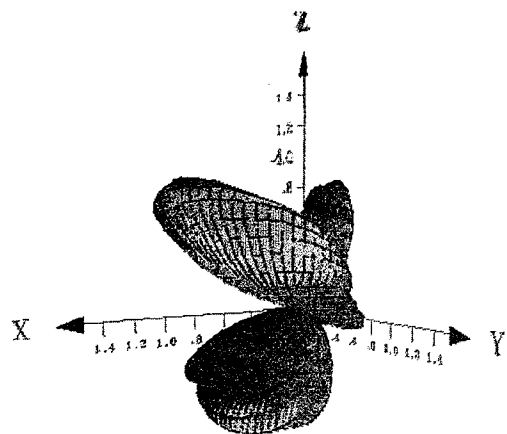


figure 10 : C.C.S at $f = 920\text{ MHz}$: max = 1.6 cm^2

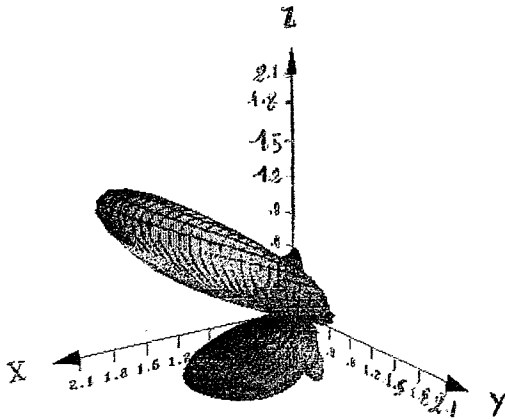


figure 11 : C.C.S at $f = 940 \text{ MHz}$: $\text{max} = 1.7 \text{ cm}^2$

The figures 12 and 13 show respectively the Coupling Cross Section diagrams at 1.5 GHz - TM_{110} mode - and 2.5 GHz - TM_{311} mode -.

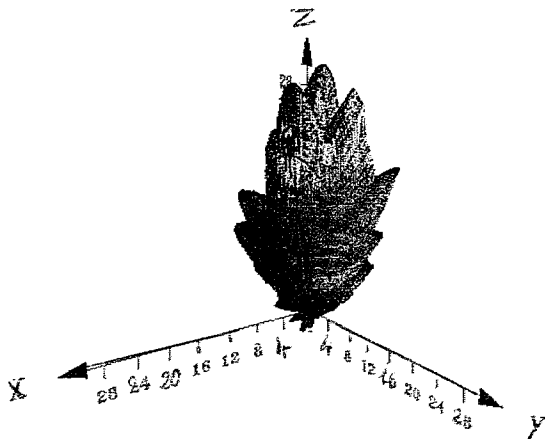


figure 12 : C.C.S at $f = 1.5 \text{ GHz}$: $\text{max} = 30 \text{ cm}^2$

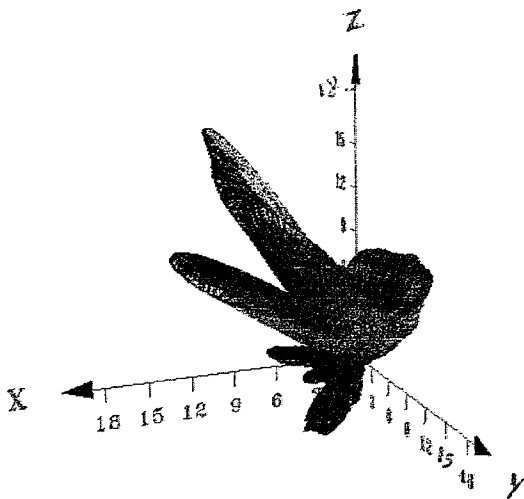
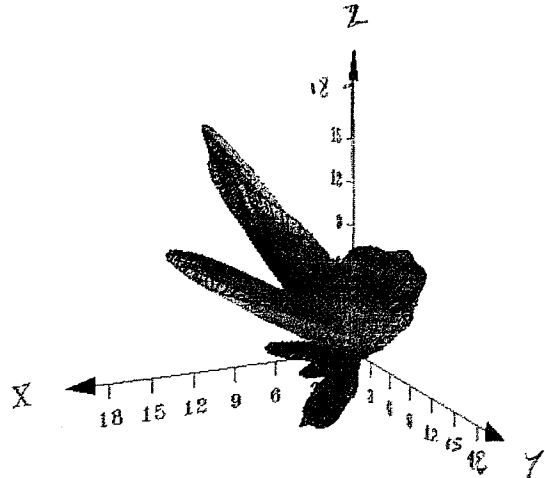


figure 13 : C.C.S at 2.5 GHz : $\text{max} = 20 \text{ cm}^2$

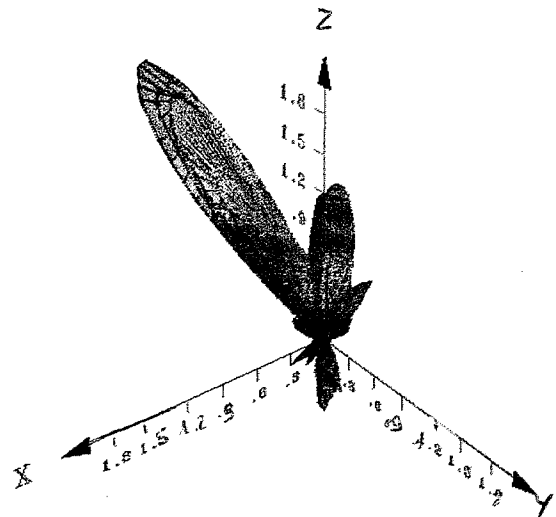
We can observe on figures 9 to 13 that the CCS diagrams become more directive when frequency increases.

The Coupling Cross Sections drawn on figure 9 to 13 represent a combination of the two polarizations along θ (elevations) and ϕ (azimuths).

Each polarization can be isolated in order to determine, for each frequency, the preferential polarization for coupling and its associated attitude angles (fig. 14).



a) θ polarization, $\text{max} = 19 \text{ cm}^2$



b) ϕ polarization, $\text{max} = 2 \text{ cm}^2$

figure 14 : C.C.S at $f = 2.5 \text{ GHz}$

6. CONCLUSION

We have presented in this paper an original method for coupling analysis using rapid near field measurements.

The results presented, obtained with a generic object, prove the interest of such a method for the determination of the worst cases of coupling - frequency, polarization and attitude angle - between an electromagnetic wave and a

target in the microwave frequency domain.

Associated with this coupling analysis, the C.E.G. is developing a method for the localization of leakage points using a near field to very near field transformation.

The combine use of these two analyses will allow to define the hardening techniques necessary to protect the systems against electromagnetic threats.

REFERENCES

[1] J. Ch. Bolomey, B. J. Crown, G. Fine, L. Jofre, ..., " Rapid Near Field Antenna Testing via Arrays of Modulated Scattering Probes ", IEEE Transactions on Antennas and Propagation, Vol. 36, N°6, June 88, pp 804 - 813.

DISCUSSION

P. ZWAM BORN

Could you comment on the mutual coupling inside your antenna between different elements and the coupling between antenna and object ?

AUTHOR'S REPLY

The mutual coupling between the different elements of the device is taken into account by the calibration. To avoid coupling between the antenna and the object, the object has to be included in a sphere of 2 meters in diameter ; the diameter of the antenna being 4 meters.

A. SOUBEYRAN

Comment est faite l'extrapolation du champ proche en champ lointain ?

AUTHOR'S REPLY

La transformation champ proche-champ lointain revient à faire une transformée de Fourier en coordonnées sphériques.

Translation:

Q.

How is extrapolation from near-field to far-field performed ?

A.

Near-field to far-field conversion involves the use of a Fourier transform using spherical coordinates.

INVESTIGATION OF RF COUPLING WITH UWB RADAR

A.J.E.Taylor
R.A.Clement
Defence Research Agency
Fort Halstead
Sevenoaks
Kent TN14 7BP, U.K.

and

C.Hall
D.M.Parkes
Defence Research Agency
Malvern
Worcester WR14 3AS, U.K.

SUMMARY

Direct experimental investigation of the coupling of microwaves to military systems involves technically difficult instrumentation of the equipment. The problems associated with instrumenting the equipment can be avoided by exploiting the properties of ultrawideband radar. Illumination of a target by a short duration, fast risetime electromagnetic pulse results in a back scattered response which is formed by a combination of the early reflections of the incident pulse, and later natural resonances of the object. We compare experimental and computational studies of the responses of a generic missile seeker head in order to assess what impulse radar reveals about coupling to a target.

1. INTRODUCTION

Given the increased likelihood of disturbances of military systems by microwave radiation, more attention has to be paid to the way in which the radiation couples with both existing and new equipment. Any technique which enables investigation of coupling without extensive, and costly, instrumentation of the equipment is obviously a boon for the understanding of coupling, and for this reason we have been using ultrawideband (UWB) radar to investigate coupling. The ultrawideband testing procedure involves repetitively illuminating the target with a fast rise time pulse and averaging the return signal in the time domain. The early return signal contains information related to the physical dimensions of the object and the late return signal contains information about the natural resonances of the object. In this paper we apply both experimental and computational approaches to characterising the information about target coupling contained in the return signal.

As a test case we have used a representative missile seeker head, which consists of a hollow metal cylinder, 50 cm long and 25 cm in diameter, with a 10 cm diameter aperture at one end and with three 9 cm by 1 cm slots midway along its axis.

2. EXPERIMENTAL RESULTS

In the experimental setup the target is supported above one end of a ground plane, and illuminated by a pulse fed into an antenna which is located at the other end of the ground plane. The D - dot probe lies between the antenna and the target. A full description of the experimental arrangement is given in Parkes, Lewis, Devine, Trafford and Richardson (1992).

The results for two orientations of the test object are shown in figure 1. The difference in the latencies between the clearly discernable first and second reflections corresponds to twice the time taken for the pulse to travel from the front surface to the back. In the case of end illumination the difference is 3.68 ns, which corresponds to a distance 0.551 m, and in the case of broadside illumination the difference is 2.2 ns, which corresponds to a distance of 0.33 m. These distances are larger than the physical dimensions of the object because they are the distances involved in travelling round the object.

3. COMPUTATIONAL RESULTS

In the computational model, the ground plane was not included, in order to reduce the workspace involved. The target was illuminated by a plane wave with a gaussian time course, and the electric field in the far field was calculated using Fluid Gravity Engineering's implementation of the finite difference scheme for solving Maxwell's equation which was described by Yee (1966), with the boundary conditions described by Mur (1981) and far field calculations according to the scheme introduced by Yee, Ingham and Shlager (1991). The orientation of the test object was changed in steps of 45 degrees and the range of surfaces facing the antenna are shown in figure 2. The polarisation of the electric field was vertical, in keeping with the experimental situation.

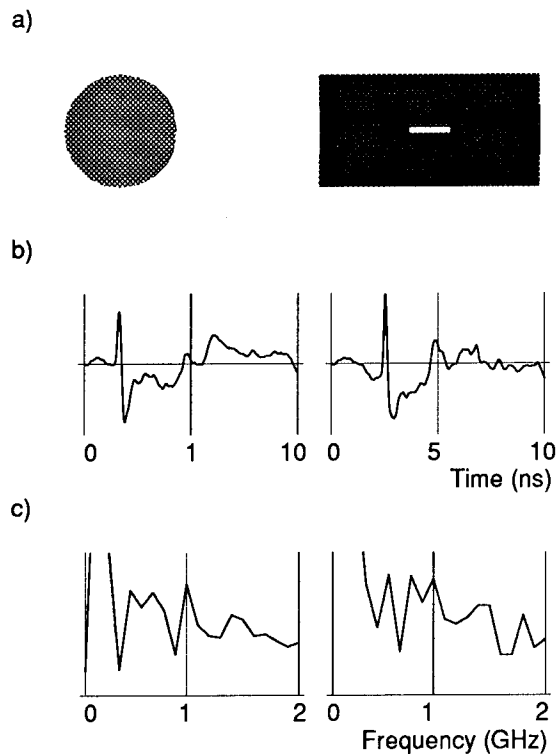


Figure 1. Experimental results obtained with ultrawideband radar. a) Aspect of the target facing the antenna and probe. b) Integrated time domain responses from D-dot probe. c) Fourier transforms of time domain responses.

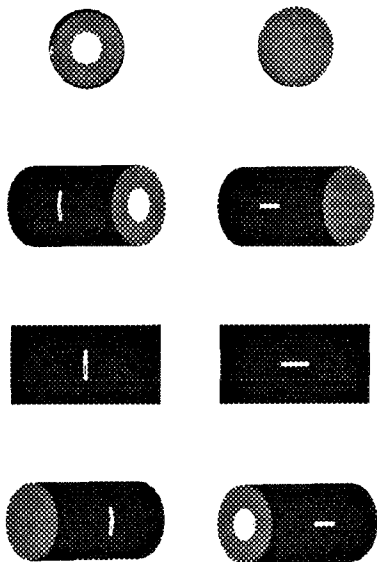


Figure 2. Array of orientations of the test object used in the computational study. In all the subsequent figures, the results of the calculations are presented according to the order of this array.

Figure 3 shows the first 10 ns of the calculated time domain responses. The reflections are largest at the orientations (0, 90, 180 and 270 degrees) when the metallic surface is normal to the incident pulse and reflects the pulse directly back in the measurement direction. There is good agreement between the latencies of the reflections in the experimental and

computational results for the corresponding end and side illumination cases, in keeping with the findings of Cloude, Smith, Milne, Parkes and Trafford (1992), who investigated the responses from a number of different targets.

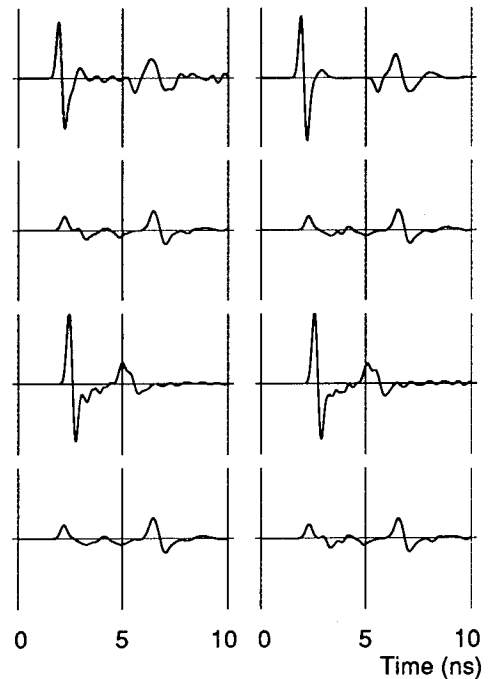


Figure 3. Relative amplitudes of the computed time domain responses for the array of orientations of the test object shown in figure 2.

Figure 4 shows the the Fourier transforms of the time domain responses. It is clear that the surface currents which are supported by the test object are not limited to a single body length resonance. For end illumination, there are peaks in the responses at multiples of 0.21 GHz (0.42, 0.63 and 0.84), and with side illumination, there are peaks in the responses at multiples of 0.36 GHz (0.36, 0.72 and 1.08). These peaks arise when multiples of the half wavelength can be fitted round the object.

The responses of the test object were computed for 100 ns after excitation by the pulse, and the Fourier transforms of the responses after the initial 25 ns, when the reflections of the incident pulse have passed, are shown in figure 5. The frequencies of the resonances are of interest because they correspond to the cavity modes of a closed cylinder of the same size as the test object. The information in the late response remains to be exploited experimentally, because the absolute amplitudes of the peaks are a factor of a hundred times smaller than those of the early part of the response.

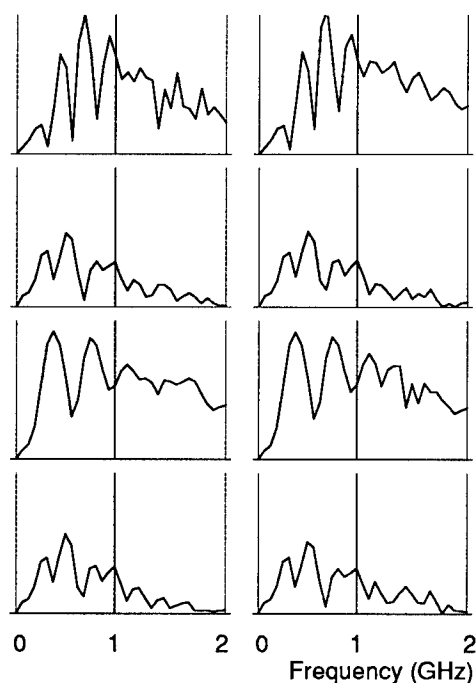


Figure 4 Relative amplitude spectra of the computed responses for the array of orientations shown in figure 2.

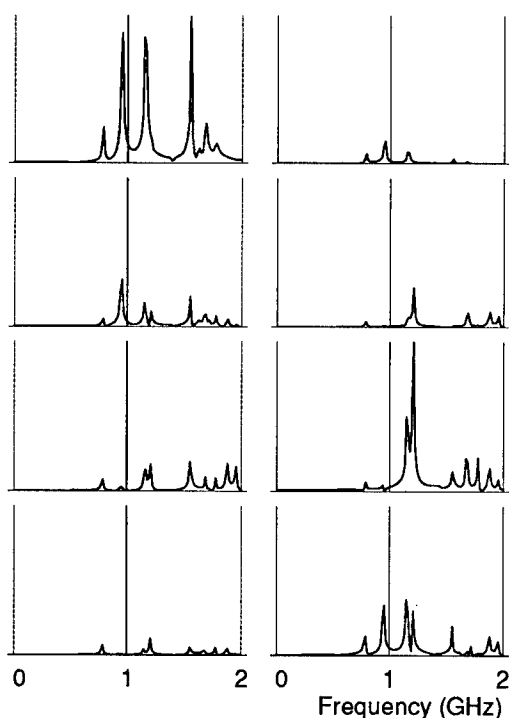


Figure 5. Relative amplitude spectra of the later time domain responses for the array of orientations of the test object shown in figure 2.

4. CONCLUSION

We have found agreement between experimental and computational investigations of the early part of the time domain response of a test target to ultrawideband radar. Fourier analysis of the early responses reveals the frequencies at which surface currents are supported by the test object. The technique of ultrawideband radar also has the potential to identify internal resonances of the object, as these

are present in the Fourier transform of the late part of the response.

5. REFERENCES

- Cloude, S., Smith P., Milne A., Parkes D.M. and Trafford K. (1992) Analysis of Time domain ultra wideband radar signals. Proceedings of SPIE Pulse Engineering Conference 1631. Los Angeles, USA, January 22-23, 1992.
- Mur, G. (1981) Absorbing boundary conditions for the finite-difference approximation of the time-domain electromagnetic-field equations. IEEE Transactions EMC - 23, 377-382.
- Parkes D.M., Lewis M.F., Devine R.L.S. , Trafford K. and Richardson D. Practical measurements using ultrawideband radar. Proceedings of SPIE Pulse Engineering Conference 1631, 232-242. Los Angeles, USA, January 22-23, 1992.
- Yee K.S. (1966) Numerical solution of initial boundary problems involving Maxwells equations in isotropic media. IEEE Transactions AP - 14, 302-307.
- Yee K.S., Ingham D. and Shlager K. (1991) Time domain extrapolation to the far field based on FDTD calculation. IEEE Transactions AP - 39, No. 3.

Acknowledgement We thank A. Milne and S.Taylor of Fluid Gravity Engineering for helpful advice on applying their code to this problem.

DISCUSSION

D. PEEBLES

In view of the different frequency responses given by the target body when illuminated by horizontally and vertically polarized signals, does the author think that illuminated by cross-polarized signal would be benefit (or circularly polarized signal, if that were possible) ?

AUTHOR'S REPLY

Not sure about circular polarisation, probably best to use alternate H&V polarisation pulses, since one advantage of method is to pass only a single pulse over the target, simplifying analysis.

D. NITSCH

In the early time you calculated the outer resonances of the body. Can you comment on the damping of the circumferential modes compared to the axial (meridional) ones ?

AUTHOR'S REPLY

I have not checked but feeling that axial damping would be faster.

D. NITSCH

I would expect the contrary.

E. SCHWEICHER

- 1/ What is the pulse width ?
- 2/ What was the pulse generator you used ? Is it a transmission line discharged by an avalanche transistor ?
- 3/ What is the jitter of the used pulse generator ?

AUTHOR'S REPLY

- 1/ 300 ps half width
- 2/ Kentech step. Yes.
- 3/ ≈ 1 ps trigger/pulse. ≈ 5 ns pulse/pulse

Design, Construction and Calibration of Sensors for HPM Measurements

J.S. Seregelyi and S. Kashyap
 Defence Research Establishment Ottawa
 3701 Carling Avenue
 Ottawa, Ontario, Canada
 K1A 0Z4

1. SUMMARY

The measurement of High Power Microwave (HPM) coupling is an important diagnostic tool in the understanding of HPM interaction with complex structures. The quantities of interest include the electric and magnetic fields both in free space and at (or near) the surface of a body. The sensors used must be small in order to cause minimal perturbation of the ambient field and to function over as wide a bandwidth as possible. In addition, the signal-to-noise ratio (SNR) must be as large as possible. This paper presents an engineering overview of the design and construction of various HPM sensors presently used at the Defence Research Establishment (DREO). Calibration methods for such sensors will also be briefly discussed.

2. PREFACE

Although the operating principles of common electromagnetic sensors are easily found in the literature [1, 2], the details of construction are often omitted. This is particularly true for sensors to be used in the multi-GHz region where the required dimensions are typically only a few millimeters.

In addition, once a sensor has been constructed, there remains the difficulty of accurately establishing its calibration factor. Ideally, the sensor is "calibrated by ruler". In other words, the response can be established either analytically or numerically such that given a certain physical geometry, the calibration factor is known. However, the fabrication process often introduces deviations from theory which can not be easily discounted. For example, a finite thickness ground plane, a truncated ground plane, co-axial leads or dielectric support assemblies may influence the results of measurement. As a result, it is often more accurate to measure a sensor response. The question of how to establish an accurate electric or magnetic field then becomes an issue.

This paper is intended as an engineering review of the construction and calibration techniques used at DREO and will discuss some of the details mentioned above.

3. SENSOR TYPES

3.1 Electric Field

3.1.1 Monopole/Dipole

Figure 1 is a schematic representation of one half of a biconical dipole sensor. The 5 mm dipole is tapered at 47° to create a 100 Ω impedance. The top of the electrode is rounded in an effort to minimize the resonance due to the finite height. The base of the electrode is connected to the inner conductor of a 25 cm long, 50 Ω co-axial line which is feed through a square brass tube and is terminated with a modified SMA connector. The dipole is completed with a second assembly which is identical except that it is tapped to receive the 2-56 flat head screws used to hold the unit together. In addition, commercial feed-through or bulkhead SMA connectors are often permanently added to the sensors for two reasons. The first is so the SMA connection on the sensor (which was slightly modified to accept the 0.034" diameter co-axial cable from the dipole) does not vary with time or degrade the contacts of the high quality SMA or 3.5 mm cables used in the lab. The second is so a supporting plate can be attached to the sensor leads.

The response of the dipole described above is shown in Figure 2. This measurement was made in an anechoic chamber using a broadband horn antenna as a source. From this figure it can be seen that the upper -3 dB point of the sensor is at approximately 7 to 8 GHz and that the resonance is above 12.5 GHz (upper limit of the measurement).

3.1.2 Patch Antenna

The operating principles of a patch antenna are discussed in detail in References [3, 4]. At DREO these sensors are used in two modes. In the first, the centrally fed patch is oriented horizontally such that the electric field is perpendicular to the radius as shown in Figure 3. In this mode of operation, the lower frequency pick up is emphasized and the sensor has a very large, relatively uniform response from 100's of kHz to the TM_{01} resonance which is determined by setting $n=0$ and $m=1$ in the equation,

$$f_{nm} = \frac{X_{nm} c}{2\pi a_e \sqrt{\epsilon_r}}$$

where

$$a_0 = a \sqrt{1 + \frac{2t}{\pi a \epsilon_r} \left(\ln \frac{\pi a}{2t} + 1.7726 \right)},$$

$$X_{nm} = \text{roots of } J'_n(x) = 0,$$

c is the speed of light, ϵ_r is the dielectric constant, a is the patch radius and t is the patch thickness. The responses of two patch sensors are shown in Figure 4. Both sensors have a 2.5 cm radius but differ in dielectric type and thickness as identified on the plot. From these and other responses (not shown) it has been determined that a thinner dielectric and a higher dielectric constant increases the capacitance of the sensor and, therefore, moves the -3 dB point to a lower frequency. Unfortunately, the sensor pick up is also reduced resulting in a poorer SNR.

In the second mode of operation the patch is used at much higher frequencies. A typical response is shown in Figure 5 where the various f_{nm} resonances of the patch can clearly be seen. It is obvious from this response that the sensor cannot be used in this mode without some form of signal processing. If using a network analyzer, the simplest way to do this is to calibrate the sensor response into the reference field measurement and normalize all remaining measurements with respect to this. One advantage of patch antennas is that they can be designed with any commercial software drawing package and fabricated in the same way as printed circuit boards. They can also be designed to conform to a surface.

3.2 Magnetic Field

3.2.1 Loop Probe/Surface Field Probe

The probes used for magnetic field measurements are discussed in detail in References [5, 6]. As depicted in Figures 6 and 7, they may be used in surface field or free field modes and are basically co-axial cables which are formed into a loop. The outer conductor is circumferentially cut at the top (and bottom) of the loop so that the inner conductor will respond to the magnetic field but is shielded from the electric field. The pick-up of these sensors can be modelled by the simple equation

$$\ell \frac{di(t)}{dt} + R i(t) = \mu_0 A \frac{dH(t)}{dt} \quad (1)$$

which has time and frequency domain solutions of;

$$i(t) = \frac{\mu_0 A}{\ell} \left(\exp(-Rt/\ell) * \frac{dH(t)}{dt} \right)$$

$$|I(f)| = \frac{2\pi\mu_0 A H(f)}{R} \sqrt{\frac{f^2}{1 + (2\pi\ell f/R)^2}}$$

where i is the loop current, H is the magnetic field, $A = \pi a^2$ is the loop area, R is the sum of the radiation and termination resistance, $\mu_0 = 4\pi \cdot 10^{-7}$ [A/m], r is the wire radius and ℓ is the loop inductance given by

$$\ell = a\mu_0 \left[\ln \left(\frac{8a}{r} \right) - 2 \right].$$

Comparison of the response measured in a TEM cell to that calculated is shown in Figure 8.

If the radiation and termination resistance in the loop are very small, the value of R in Eq. 1 becomes negligible and the equation reduces to

$$\ell \frac{di}{dt} = \mu_0 A \frac{dH}{dt}$$

$$i(t) = \frac{\mu_0 A}{\ell} H(t)$$

The advantage of such a sensor is that, like the horizontal patch antenna discussed earlier, this sensor has a very flat response from 10's of kHz into the GHz range or, in other words, the current in the loop is directly proportional to the magnetic field - not it's derivative. Figure 7 depicts a modified ground plane sensor which incorporates a 1 GHz Tektronix current probe in place of the 50 Ω cable. Although this probe significantly reduces the required dynamic range of the measurement, it does not do so by enhancing the pick-up at the lower frequencies but by attenuating the higher frequencies and, as such, decreases the SNR in this range.

4. GENERATION OF FIELDS FOR CALIBRATION

As mentioned previously, it is often difficult to calibrate a sensor using theoretical parameters because of deviations in the simple theory caused by practical considerations in fabrication, calibration and application. As a result, a sensor should be calibrated by measuring its response in a known field. The obvious difficulty is how to establish such a field.

Although there is no means of establishing an exact magnitude, a number of ways exist by which to generate a reasonably well known field value. The Transverse Electromagnetic (TEM) cell [6] is one of these. This device is basically a truncated, rectangular transmission line as depicted in Figure 9 and can be operated from DC to its first resonance determined by the cell dimensions. Unfortunately, the bandwidth is inversely proportional to the size of the cell and, therefore, since a sensor must be much smaller than the septum height or width in order to minimize perturbation of the field, the amount of useful testing which can be done in a TEM cell at high frequencies is very limited.

The other factor to consider is that the field along a cross-section of the cell is not completely uniform but varies according to Figure 10. The sensor calibration must take into account this field variation in addition to the reflections and standing waves which are induced at virtually all frequencies because of the difficulty in inducing and terminating an ideal TEM mode in the cell. This is a result of the geometrical discontinuities inherent to the ends of the cell and is particularly true of very small cells because input connectors, dielectric supports etc. cannot be scaled down to account for the smaller dimensions. In addition, the relative errors in the machining and assembly processes become larger in these smaller cells.

One means of minimizing the effects of the reflections is to test in the time domain. An impulse test may potentially be designed so that the sensor response can be established before any major reflection has an opportunity to alter the excitation field. This adds an added degree of difficulty to the design of a TEM cell since operation in the frequency domain requires a short cell which maximizes the usable bandwidth (first major resonance is inversely proportional to the cell length). However, operation in the time domain requires that a cell be as long as possible to maximize the temporal separation between the initial field excitation and the reflection from the back taper.

An alternative which avoids this problem is to make use of what is referred to as a GTEM cell [7]. Like a TEM cell, this is also a rectangular transmission line; however, it is essentially only the front taper of the TEM cell which is directly terminated in a resistive load and absorbing material. Since the discontinuities in the cell have been removed, the associated resonances are also gone. However, the cross-sectional field uniformity is still similar to that of Figure 10 and must be accounted for. The situation is aggravated by the fact that the septum is tapered and off-centered in the working volume.

The response of the DREO GTEM cell (1 m long) is shown in Figure 11. The dimensions of this cell are much larger than an equivalent bandwidth TEM cell thus allowing much larger sensors to be tested (or alternatively, a small sensor to perturb the ambient field much less). The primary disadvantage of this cell is that the field magnitude rapidly deviates a few dB both spatially and with respect to frequency. Fortunately, there are no deep nulls in the field values and the response of a sensor can be numerically recovered without any significant difficulties.

Finally, a method which essentially eliminates the possibilities of resonances entirely is to calibrate in an anechoic chamber or an open field site with a standard gain horn antenna as a source. Here too the unwanted reflections from nearby surfaces must be kept under control. One can improve the measurements by using time domain gating.

5. SUMMARY

An overview of the various types of electromagnetic sensors used at DREO has been presented with an emphasis on the engineering aspects of sensor design. The electric field is generally measured with a dipole/monopole, however the patch antenna is available as an alternative under certain circumstances. The primary sensor for the magnetic field is a single turn loop used either in free space or on the surface of a structure. A brief discussion of calibration requirements using TEM and GTEM cells, anechoic chambers and open field test site has also been presented.

6. ACKNOWLEDGMENT

The authors wish to thank R. Apps and A. Walsh for their assistance with sensor assembly and testing.

7. REFERENCES

1. Kraus J.D. "Antennas", 2nd Ed., McGraw-Hill Book Co., 1988 (ISBN 0 07 035422 7).
2. King R.W.P. and Harrison C.W. "Antennas and Waves: A Modern Approach", Cambridge, MA, The MIT Press, 1969 (SBN 262 11033 4).
3. James J.R. and Hall P.S. "Handbook of Microstrip Antennas", London, UK, Peter Peregrinus Ltd., 1989 (ISBN 0 86341 150 9)
4. Pozar D.M. "Considerations for Millimeter Wave Printed Antennas", IEEE Trans. on Antenna and Propagation, Vol. AP-31, No. 5, Sept. 1983, pp. 740-747.
5. Pearson L.W. and Lee Y.M. "An Experimental Investigation of the King Surface Current Probing Technique in a Transient Application", AFWL SSN 265, Dec. 1979.
6. Kanda M. and Orr R. "Generation of Standard Electromagnetic Fields in a TEM cell", NBS Technical Note 1319, Aug. 1988.
7. Hansen D., Wilson P., Konigstein D. and Schaer H. "A Broadband Alternative EMC Test Chamber Based on a TEM-Cell Anechoic-Chamber Hybrid Concept", International Symposium on Electromagnetic Compatibility, 1989, Paper 8p1-A2.

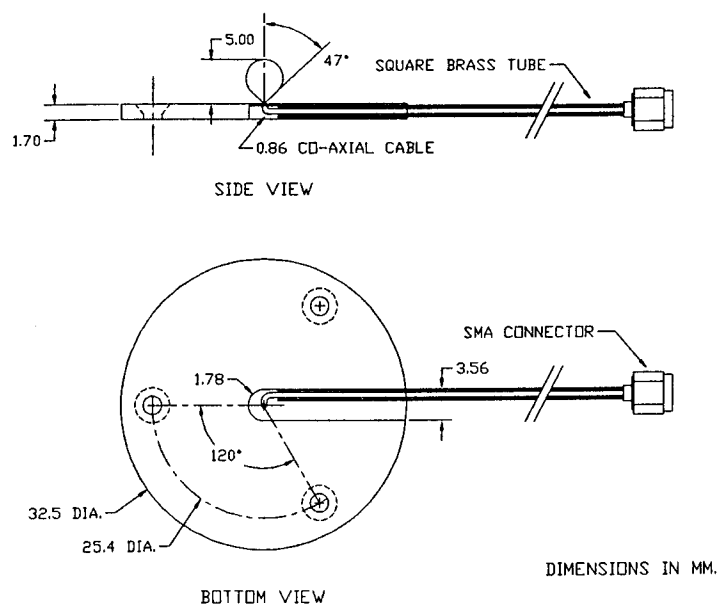


Figure 1: Schematic representation of one half of a dipole. The electrode is 5 mm long and is rounded to minimize the inherent resonance. The other half of the dipole is identical except that it is tapped to receive the assembly screws.

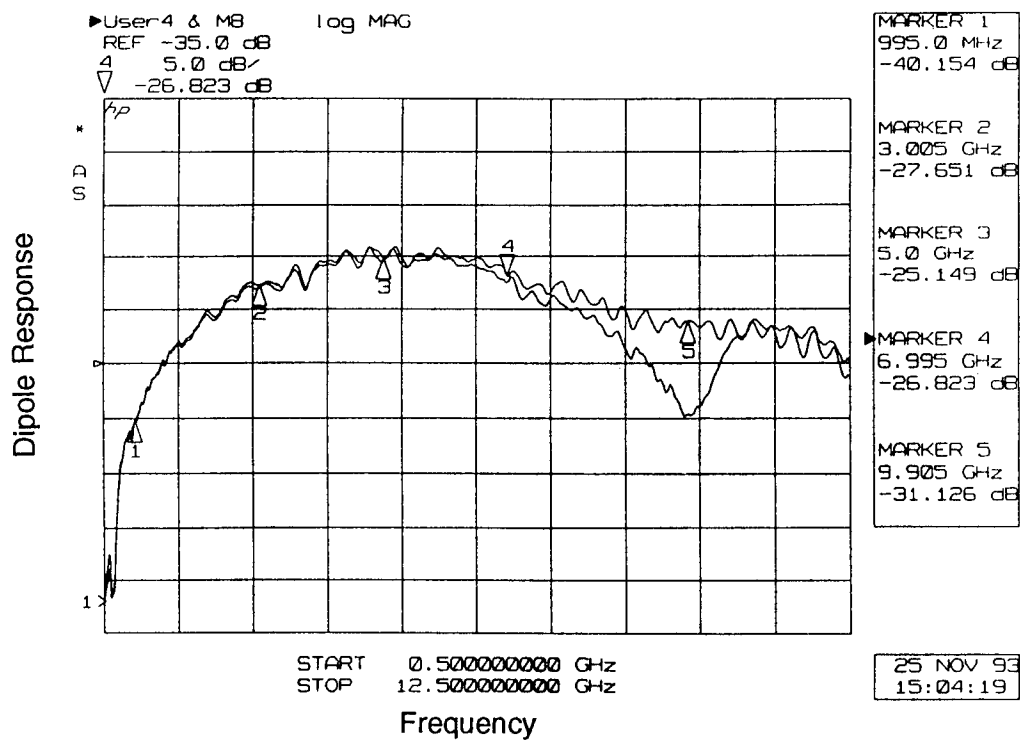


Figure 2: Response of the dipole depicted in Fig. 1. The measurement was made in an anechoic chamber with a standard gain horn antenna as a source. Although both sensors are physically virtually identical, there is clearly a difference in the response.

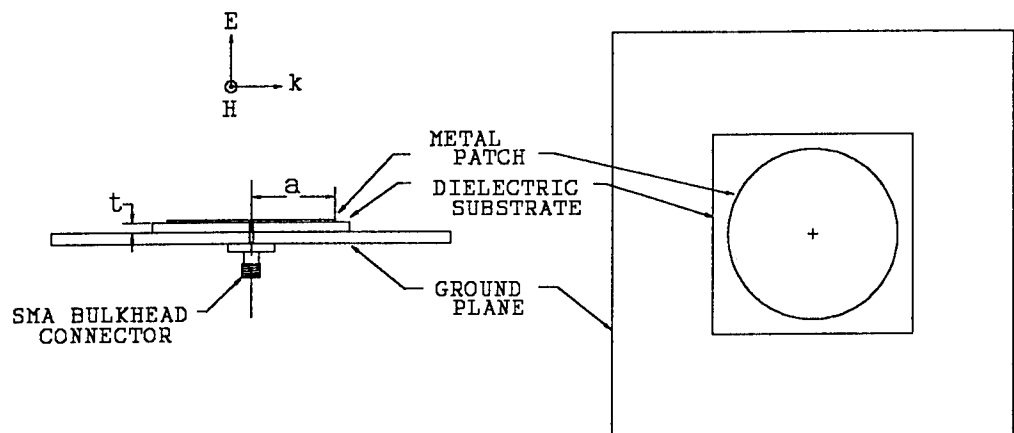


Figure 3: A schematic representation of a patch antenna. The radius of the (in this case) circular patch is " a " and the thickness of the dielectric is " t ". In order to emphasize the lower frequency response, a central feed point has been chosen.

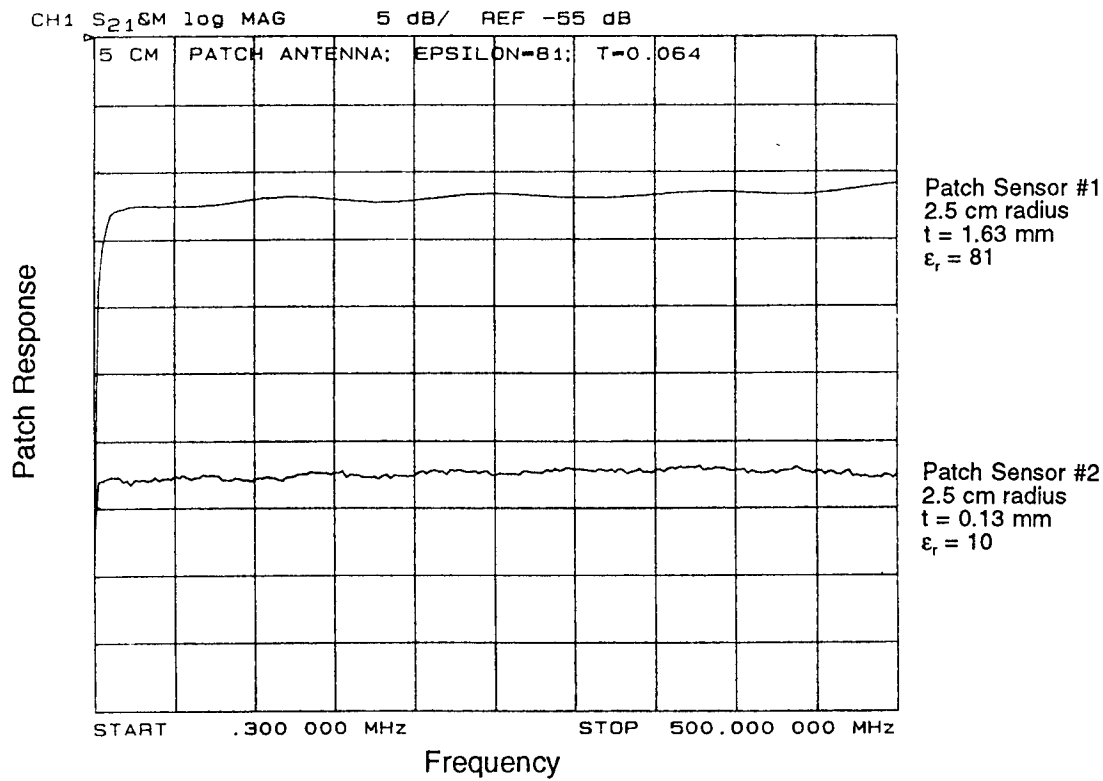


Figure 4: The response of two patch antennas. Although the -3 dB point occurs at a lower frequency for patch #2, approximately 20 dB of sensitivity must be sacrificed to achieve this.

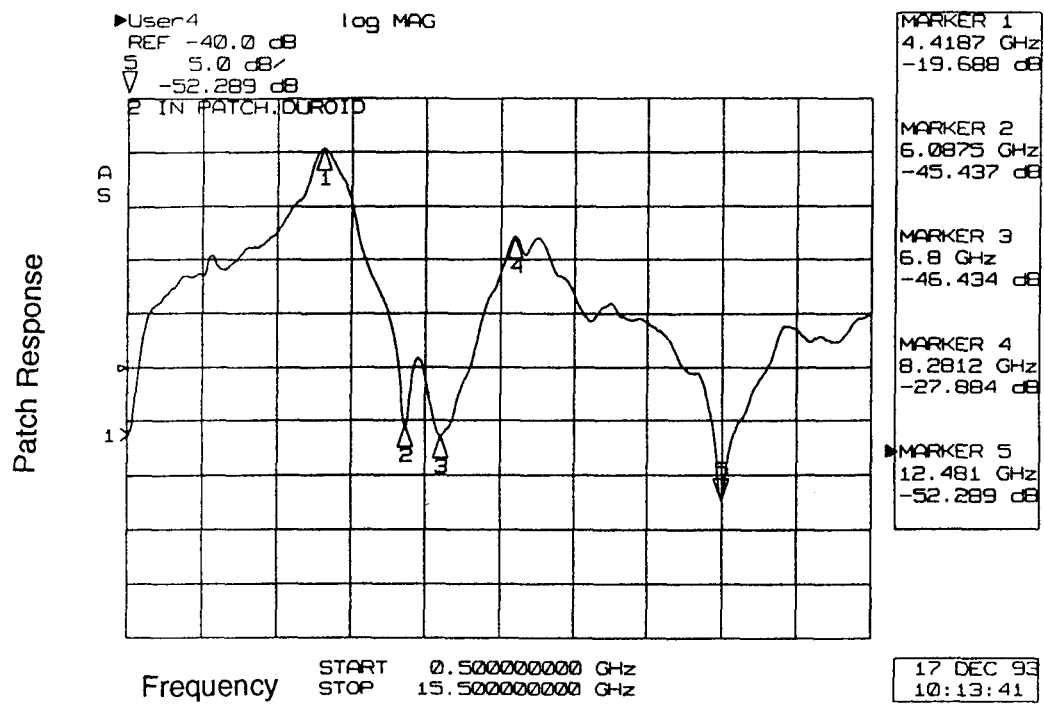


Figure 5: Typical response of a patch antenna. The resonances are due to the various TM_{nm} modes of the patch and make some form of signal processing a necessity.

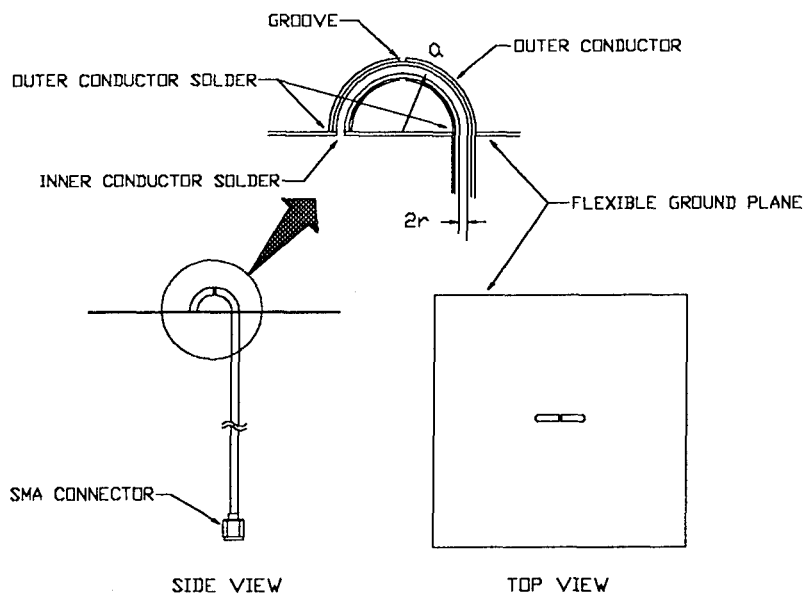


Figure 6: A schematic representation of a surface field probe. This probe responds to a magnetic field but is shielded from the electric field.

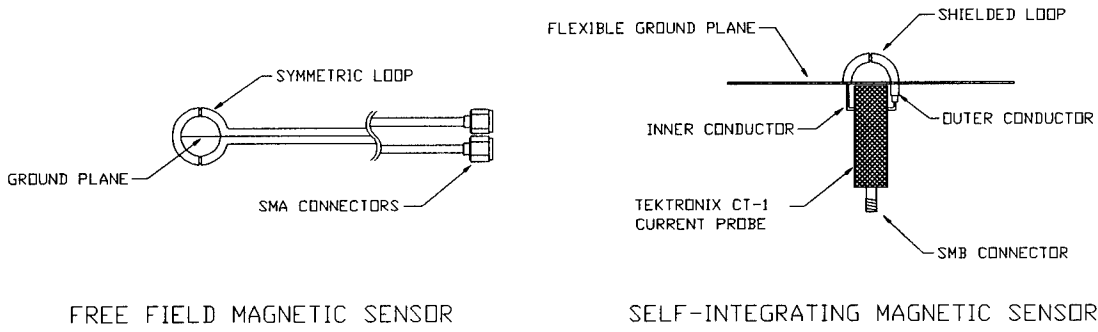


Figure 7: Variations of the surface probe in Figure 6. The first is a free-field version and the second replaces the 50 Ω co-axial cable with a low resistance current probe thus creating a flat response over a larger bandwidth.

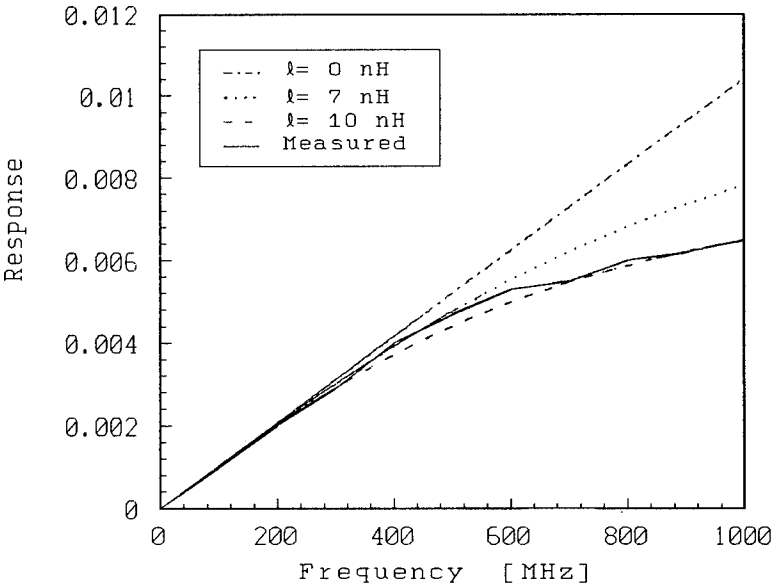


Figure 8: The response of the field probe depicted in Figure 6 when tested in a TEM cell. The inductance, l , of the probe is calculated to be approximately 8 nH.

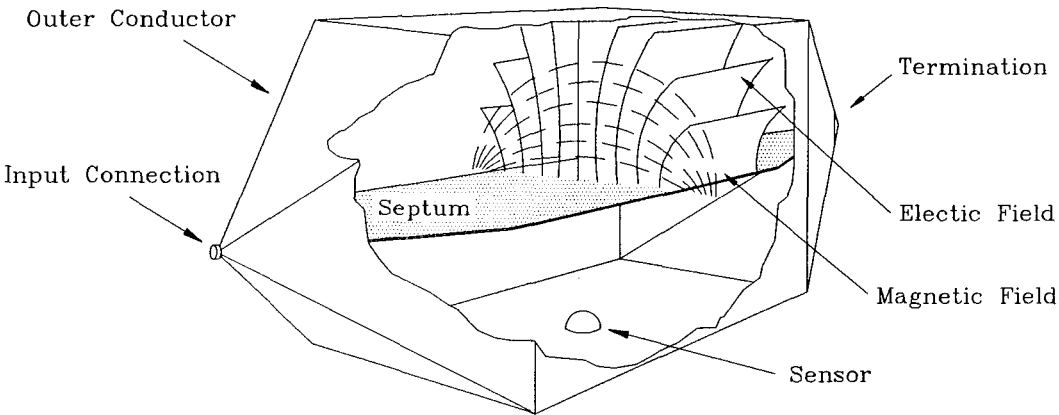


Figure 9: A schematic representation of a TEM cell and its associated fields.

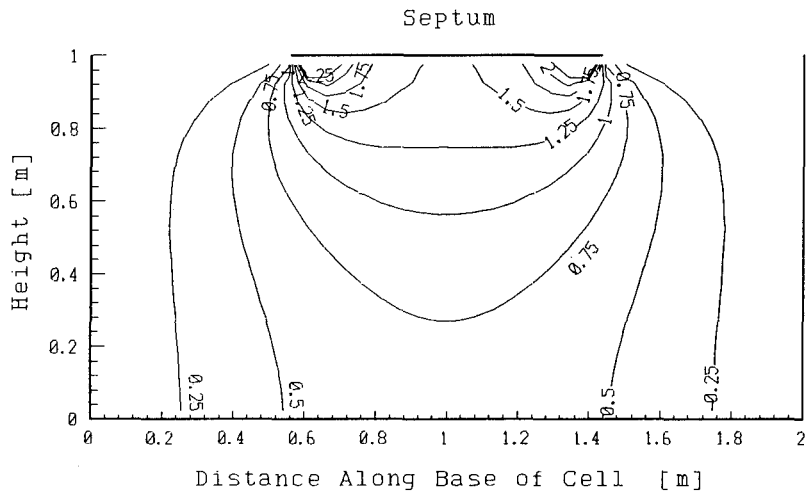


Figure 10: Variation in the vertical electric field in the lower half of a 100 Ω TEM cell. The field level at the base of this cell, as calculated for the static case using Finite Difference, is 65% of the nominal voltage/height value.

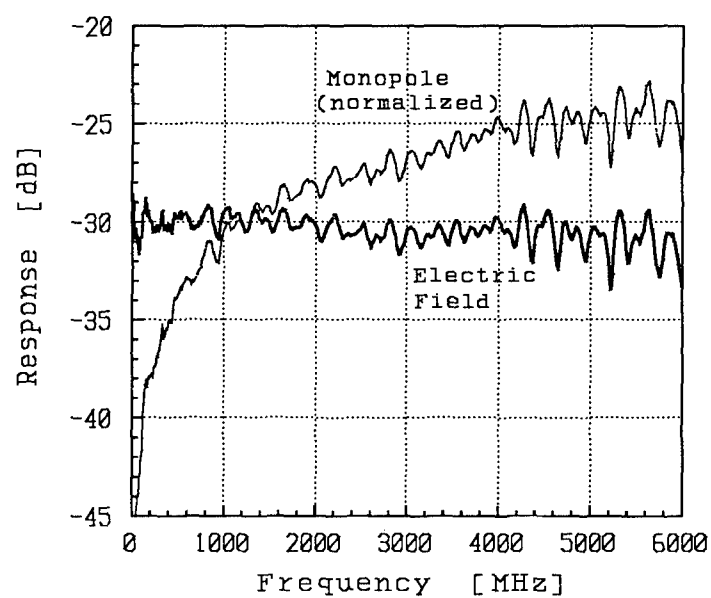


Figure 11: The E-field response of a 1m long GTEM cell as measured by a short monopole. Although the magnitude varies a few dB both spatially (not shown) and with frequency, there are no deep nulls in the response.

DISCUSSION

G.S. BROWN

It seems to me that your talk was primarily concerned with problems associated with very wideband fields measurements. Are there any problems associated with the high power levels attendant with HPM ?

AUTHOR'S REPLY

Yes, it is feasible that one could create a field which is intense enough to generate an arc in or around a critical component of a sensor. A good example of this is patch #2 in figure 4. This sensor is constructed by anodizing an aluminium plate to create the dielectric material (which is inherently thin and porous). As the field strength of a uni-polar pulse is increased, the peak value in the sensor response tends to become non-linear. It is speculated that this is a result of arcing between the top plate and ground plane through the dielectric*. In principle, the same response may be observed (at different field strengths) in a sinusoidal pulse.

(* original observations made by M. Kekez and J. Durr of the NRC in Canada)

P. ZWANBORN

1/ Could you please comment on the fact that your antenna factor decreases if you downsize your sensor.

2/ Have you taken into account that you obtain a mirror image of your sensor when inserted inside a TEM-cell. How does that influence your calibration ?

AUTHOR'S REPLY

1/ In general, a sensor bandwidth is inversely proportional to its dimension and its response is proportional to this dimension. Therefore, as a sensor bandwidth is increased, the magnitude of the response will decrease. This will result in a poorer SNR in the measurement.

2/ A TEM cell can be considered to be a coaxial line and as such, any sensor placed inside it will act as a perturbation in the impedance and cause a reflection to oscillate within the cell. The way we avoid (or minimize) this is to try to keep the sensor less than one tenth of the size at the septum to outer conductor spacing. This should be considered a "rule-of-thumb" and I don't have numerical data to quantify the effects.

A. TAYLOR

Have you investigated temporal dispersion with frequency - ie are high frequencies delayed with respect to low frequencies ?

AUTHOR'S REPLY

No, we have not investigated temporal dispersion.

M.P. CLARKSON

Has phase calibration of the sensors been looked at ?

AUTHOR'S REPLY

My oral response to this question was that we had not investigated the phase response at the various sensors. However, this comment was erroneous because I had mistakenly interpreted the question. We have not looked at a phase calibration in the range of a sensor where the response is very non-linear (ie where a sensor is very resonant). However, in the linear portions the phase response is generally as linear and uniform as the magnitude of the response.

ELECTROMAGNETIC SHIELDING PROPERTIES OF COMPOSITE MATERIALS

C.L. Gardner and R. Apps
Electronic Warfare Division
Defence Research Establishment Ottawa
Ottawa, Ontario, Canada K1A 0Z4

and

A.J. Russell
Composites Group
Defence Research Establishment Pacific
FMO, Victoria, B.C. V0S 1B0

1. SUMMARY

In order to ensure that composite structures have adequate electromagnetic (EM) shielding, a knowledge of the EM properties of anisotropic laminated materials is necessary. In this paper, we provide an overview of work we have carried out to measure the intrinsic EM shielding properties of carbon and non-carbon epoxy laminates. These experimental results are compared with numerical results that have been calculated using the Method of Moments. Finally, results showing the effect of repair of carbon/epoxy composites on shielding properties are presented.

KEYWORDS: Electromagnetic Shielding; Composite Materials; Electric/Magnetic; Carbon/Hybrid/Non-carbon; Repair

2. INTRODUCTION

Composite materials are being used increasingly by the designers of military aircraft, ships and land vehicles. As an example, Figure 1 shows the use of carbon/epoxy composites in the CF-18 aircraft that is in service in the Canadian Forces. Traditionally, the use of composites for the construction of aircraft has been driven by the superior specific strength and stiffness of these materials which allows a significant reduction in weight. More recently, other factors such as the ease of shaping composites has led to their use for the minimization of radar cross-section (RCS). Table 1 gives values of RCS for various aircraft taken from the literature. The reduction of RCS is dramatic.

There is also increasing interest in the use of composites for the construction of ship superstructures. Some of the benefits of the use of composites for this application include: improved stability through a reduction in topside weight; reduced maintenance costs; reduced RCS; and superior fire containment. The use of composites for land vehicles offers improved mobility as a result of weight reduction and improved personnel protection from shells.

3. ELECTROMAGNETIC PROPERTIES OF COMPOSITE MATERIALS

In the previous section, some of the advantages of composite materials, that are leading to an increased use of these materials in military vehicles, have been described. In almost all cases, however, successful operation of these vehicles depends on the reliable operation of sophisticated systems for flight control, navigation, self-defence and fire control. Protection of these systems from the severe electromagnetic environment, including high power microwaves (HPM), that can be encountered is a necessity. The increasing susceptibility of modern microelectronic systems to electromagnetic interference (EMI) makes the job of providing adequate electromagnetic (EM) protection all the more difficult.

To ensure adequate EM shielding, a knowledge of the EM properties of composite materials is necessary. Table 2 provides a summary of some of the electromagnetic properties of composite materials. The conductivity of most of the commonly used reinforcements is poor compared to most metals. Even graphite has a conductivity 2 or 3 orders of magnitude lower than commonly used metals as is seen in Table 2. Other reinforcements such as glass and aramid are

TABLE 1 - AIRCRAFT RADAR SIGNATURES

TARGET	RADAR CROSS SECTION (M ²)
JUMBO JET	100.0
B-52 BOMBER	10.0
LARGE FIGHTERS	5-6
SMALL FIGHTERS	2-3
B-1B BOMBER	1.0
MAN	1.0
F-117A STEALTH FIGHTER	0.1
B-2 STEALTH BOMBER	0.01
SMALL BIRD	0.01
SOURCE: SAMPE Journal, 27, 4 (1991)	

TABLE 2 - EM PROPERTIES OF COMPOSITE MATERIALS

1. EM SHIELDING EFFECTIVENESS IS NOT AS GOOD AS METALS		
CONDUCTIVITY	- COPPER	- $5.8 \cdot 10^7$ MHO/M
	- ALUMINUM	- $3.5 \cdot 10^7$
	- STEEL	- $1.0 \cdot 10^7$
	- GRAPHITE	- $7.0 \cdot 10^4$
	- GLASS	- $1.0 \cdot 10^{-12}$
2. ELECTRICAL BONDING OF COMPOSITES IS DIFFICULT		
CORROSION PROBLEMS		
3. DIFFICULT TO MAINTAIN EM SHIELDING DURING REPAIR		

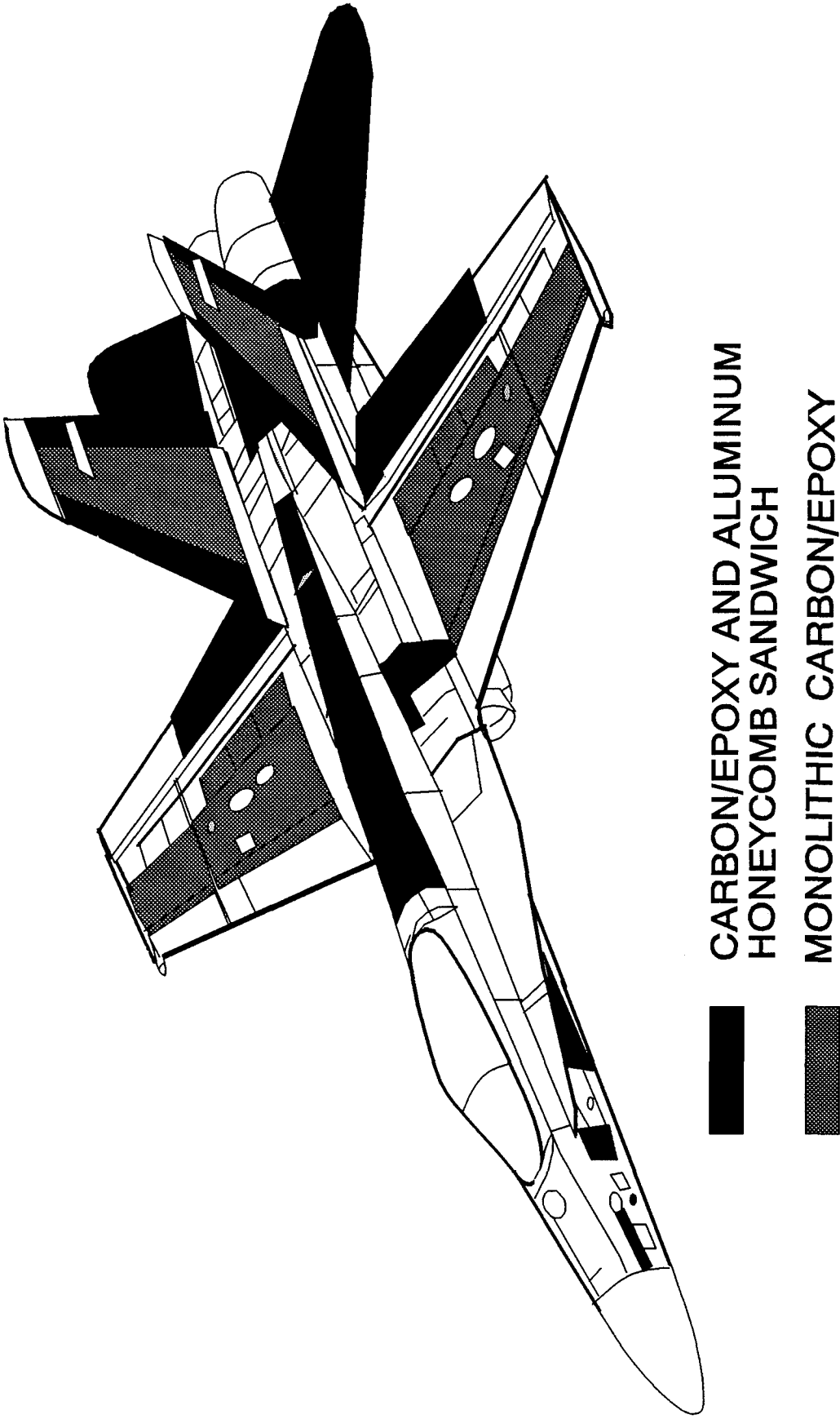


Figure 1 - Use of Composites in the CF-18

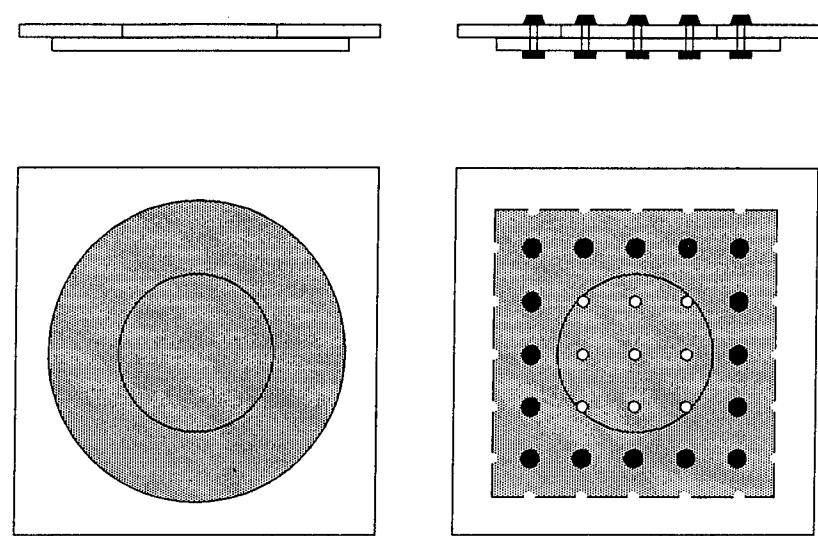


Figure 2 - Methods of Repair. Left-Bonded Epoxy Patch. Right-Bolted Patch

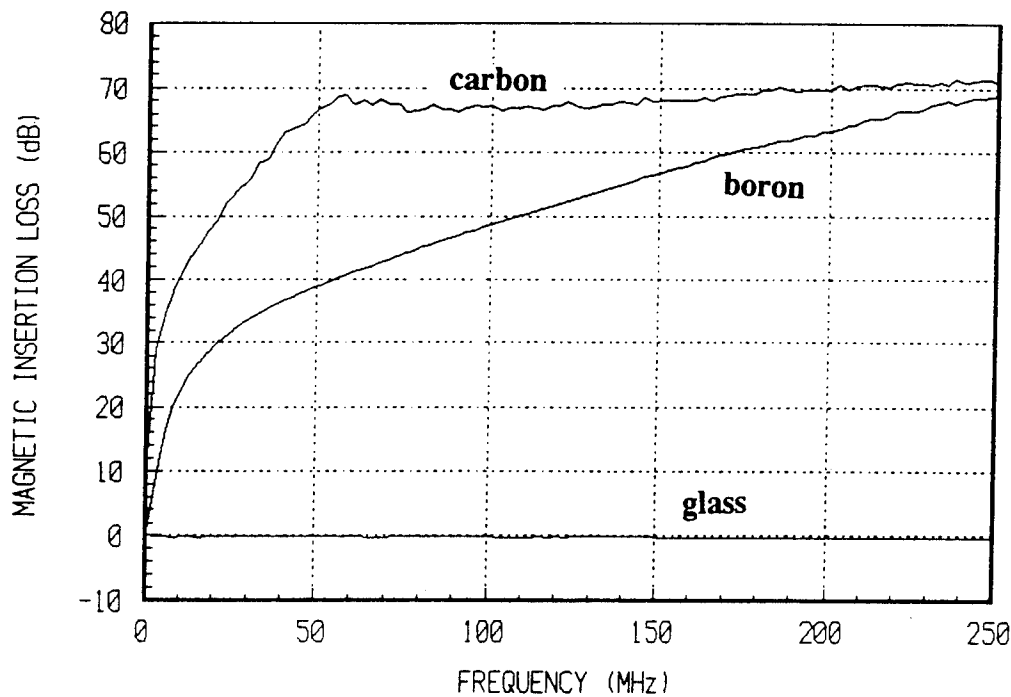


Figure 3 - Effect of Fibre Conductivity on Magnetic Insertion Loss

non-conductive. Because of their limited conductivity, structures made from composite materials generally have poorer EM shielding when compared to metallic structures. For many military applications, it is therefore necessary to either incorporate one or more conductive layers within a laminate or to apply a metal coating to the surface.

EM shielding requirements can also influence the design, construction and life cycle maintenance of composite structures. The need to ensure continuity of conductive pathways wherever composite panels are joined together or connected to adjacent metallic structure can add considerably to the cost and complexity of fabrication. This is especially true where galvanic corrosion concerns would dictate that no electrical contact should exist. Corrosion in fact poses a double threat, reducing the life of the metal components present and slowly degrading the EM shielding by increasing the electrical resistance of the joints. Standard structural repair methods may also have to be modified to ensure electrical continuity between a bonded or bolted patch and the structure itself.

In the following section, we give an overview of the work we have done to measure the intrinsic EM shielding properties of epoxy matrix composite laminates as well as experiments to study the effect of repair on EM shielding. Parts of this work have been published earlier [1,2].

4. EXPERIMENTAL

Measurement Technique

Measurements of the shielding properties of composite materials have been made using a dual transverse electromagnetic (TEM) cell, as described by Wilson and Ma [3]. In this method, two TEM cells are coupled by a common aperture. Measurements are made of the penetration of the EM fields from the driven (lower) cell into the receiving (upper) cell. Insertion loss measurements are made by comparing the results when the aperture is loaded with a composite sample with results for the open (unloaded) aperture.

The theory of the dual TEM cell has been developed by Wilson and Ma [3,4]. Provided the aperture dimension is small compared to the wavelength used, small aperture theory can be used and the penetration of the EM fields into the upper cell treated in terms of the equivalent electric and magnetic polarizabilities of the aperture. The output of the cell in the forward direction is related to the sum of the electric and magnetic polarizabilities and in the

backwards direction, to the difference. Expressions [3] for the forward and backward insertion losses (defined as the ratio of the transmitted power with the material in place to that of an open aperture) are given below.

$$IL_{\text{forward}} = 20 \log \left| \frac{\alpha_{ey} + \alpha_{mx}}{\tilde{\alpha}_{ey} + \tilde{\alpha}_{mx}} \right| \quad (1)$$

and

$$IL_{\text{backwards}} = 20 \log \left| \frac{\alpha_{ey} - \alpha_{mx}}{\tilde{\alpha}_{ey} - \tilde{\alpha}_{mx}} \right| \quad (2)$$

where α_{ey} and α_{mx} are the electric and magnetic polarizabilities of the open aperture and $\tilde{\alpha}_{ey}$ and $\tilde{\alpha}_{mx}$ are the electric and magnetic polarizabilities of the loaded aperture.

Experimentally, [5] it is possible to separate the electric and magnetic properties of the material by adding or subtracting the two outputs of the receiving cell which gives;

$$IL_e = 20 \log \left| \frac{\alpha_{ey}}{\tilde{\alpha}_{ey}} \right| \quad (3)$$

and

$$IL_m = 20 \log \left| \frac{\alpha_{mx}}{\tilde{\alpha}_{mx}} \right| \quad (4)$$

Measurements of the magnetic and electric insertion loss of the materials were made over the frequency range from 0.3 to 500 MHz using a Hewlett Packard HP8753B Network Analyzer. Output data from both ends of the receiving TEM cell were collected using a computer and numerically combined to give either the sum or difference signals.

Sample Preparation

The composite materials used in these studies were made from unidirectional pre-preg of carbon, glass, aramid and boron fibres in an epoxy matrix. The 18 cm square samples were prepared [1] by laminating six or eight plies together using standard composites autoclaving procedures. In some cases the unidirectional plies were aligned while in others they were arranged at different orientations in various stacking sequences (eg $0^\circ, \pm 45^\circ, 90^\circ$). Throughout this paper, fibre orientations are designated with respect to the direction of propagation of the EM waves in the TEM cell.

The degradation in the EM shielding properties of carbon/epoxy components caused by typical structural repairs was investigated to the extent that the geometric

constraints imposed by the TEM cell would allow. Thus while it was not possible to study honeycomb sandwich panels typical of the avionics doors on the CF-18, for example, the same repair materials and procedures normally used for these components were applied to the test samples. Eight ply quasi-isotropic laminates of AS4/3501-6 carbon/epoxy containing a 75 mm diameter hole in the centre were repaired using two different methods. In two of the repairs, 152 mm circular patches of either 6 ply ($0^\circ, \pm 60^\circ$) carbon/epoxy or titanium (Ti-6Al-4V) were adhesively bonded over the hole on one side of the sample using FM-300 epoxy film adhesive from American Cyanamid. The third repair involved a rapid repair technique in which sixteen 7mm diameter blind fasteners were used to attach a thick aluminum patch, drilled with a square array of 7 mm holes equally spaced at 25 mm, to one side of the laminate. These two methods of repair are illustrated in Figure 2.

In order to obtain a proper measurement of the shielding properties of these composite samples, good electrical contact must exist between the sample and the body of the TEM cell used to make the measurements. To achieve this, the edges of all of the samples were copper plated. The use of finger stock and application of pressure to top of the upper cell ensured good electrical contact between the two cells.

Experimental Measurements

While measurements were made of both the magnetic and electric insertion losses for all of the samples examined, in the discussion that follows we only discuss the magnetic shielding properties. The reason for this is that the provision of adequate magnetic shielding at low frequencies is normally of most concern.

Effect of Fibre Type on Magnetic Insertion Loss

The effect of fibre type on the magnetic shielding properties of a number of different materials is shown in Figure 3. The carbon/epoxy laminates provide high levels (>60 dB) of shielding for frequencies above 50 MHz. As anticipated, the glass/epoxy laminate provides essentially no shielding as it is non-conducting. The boron/epoxy laminate on the other hand provides an intermediate degree of shielding.

The dependence of the magnetic insertion loss on frequency and fibre conductivity (Figure 3) is in accordance with theory developed by Casey [6] and Latham and Lee [7].

Effect of Fibre Orientation on Insertion Loss

Fibre orientation has a major influence on magnetic shielding, as seen in Figure 4, which shows the magnetic insertion loss of AS-4 carbon/epoxy laminate having fibres oriented unidirectionally at 0° , 30° , 45° , 60° and 90° to the direction of propagation of the EM wave. Above 60 MHz, the insertion loss measurements for the 0° sample are influenced by the limited dynamic range of the network analyzer which results in a flattening of the 0° curve above this frequency.

Qualitatively these results relate directly to the anisotropic conductivity of the composite laminate. The conductivity is greatest along the fibres and, hence, when they are oriented at 0° , there is very little interruption of the current flow along the body of the cell and shielding is high. By comparison, the conductivity transverse to the fibres is lowest leading to poor shielding when the fibres are oriented at 90° .

Effect of Repair on Magnetic Insertion Loss

Figure 5 shows the magnetic insertion loss of a carbon/epoxy laminate with a 75 mm diameter hole that has been repaired with a bonded carbon/epoxy patch. Also included in this figure are the results for a complete carbon/epoxy laminate and the same laminate with an unfilled 75 mm dia. hole. From these results it is seen that the repaired laminate offers considerably poorer shielding than the undamaged laminate, especially at high frequencies where the difference can be as high as 40 dB. In the application of the bonded patch, no effort is made to electrically connect the graphite fibres in the patch to those in the bulk material. It is interesting therefore that the patch still provides 10 to 20 dB additional shielding over almost all of the frequency range (0.3 - 500 MHz). There is sufficient capacitive coupling apparently between the carbon/epoxy laminate and the patch to allow some current to flow through the patch. This suggestion is supported by the observation that the amount of shielding that the patch provides depends (Figure 6) on the orientation of the patch in the aperture of the dual TEM cell. The shielding provided by the patch is better when the fibres in the upper layer of the carbon/epoxy laminate next to the patch are oriented so that current can flow through this layer (i.e. parallel to the direction of propagation in the TEM cell).

A comparison of the magnetic insertion loss of the three patch types is given in Figure 7. The shielding provided by the bonded carbon and titanium patches is very similar. The bolted patch, on the other hand, provides

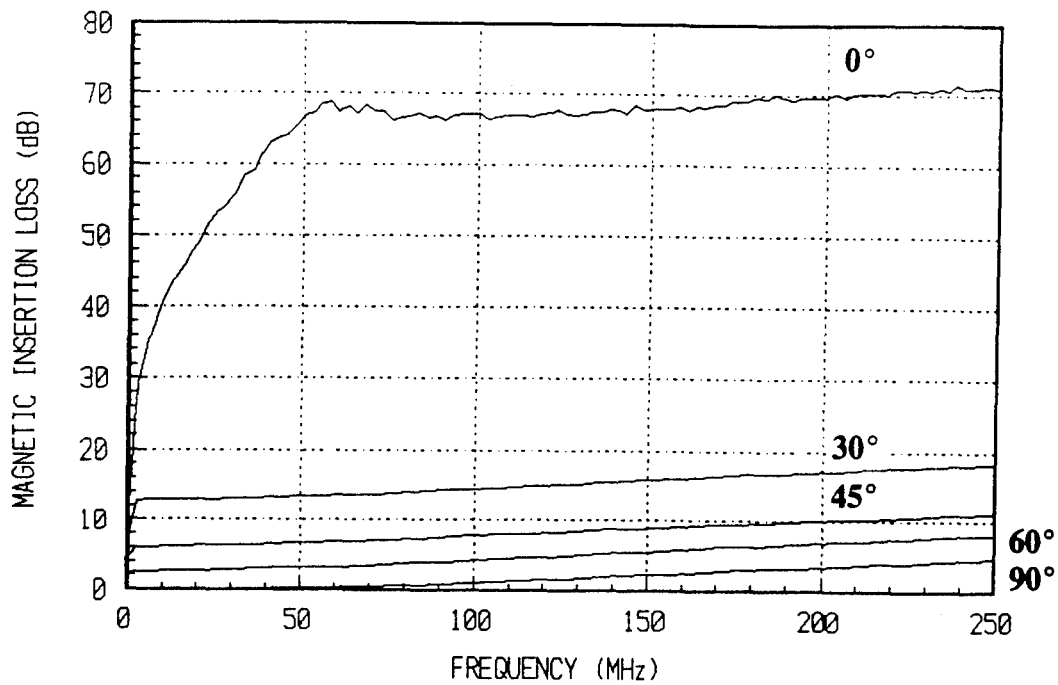


Figure 4 - Effect of Fibre Orientation on Magnetic Insertion Loss

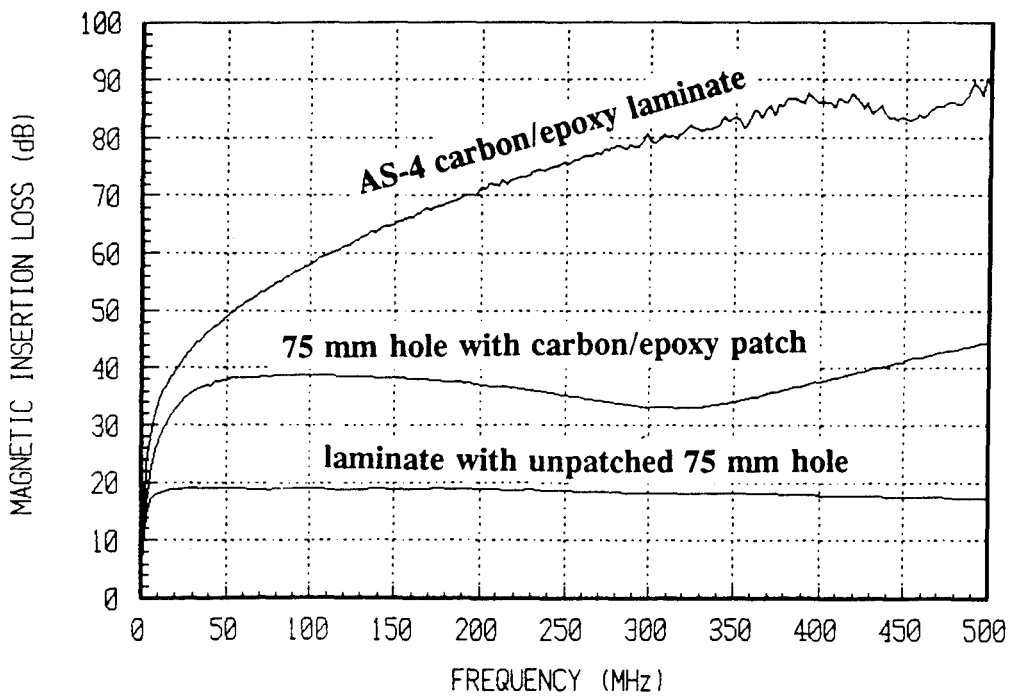


Figure 5 - Effect of Repair on Magnetic Shielding: Carbon/Epoxy Patch

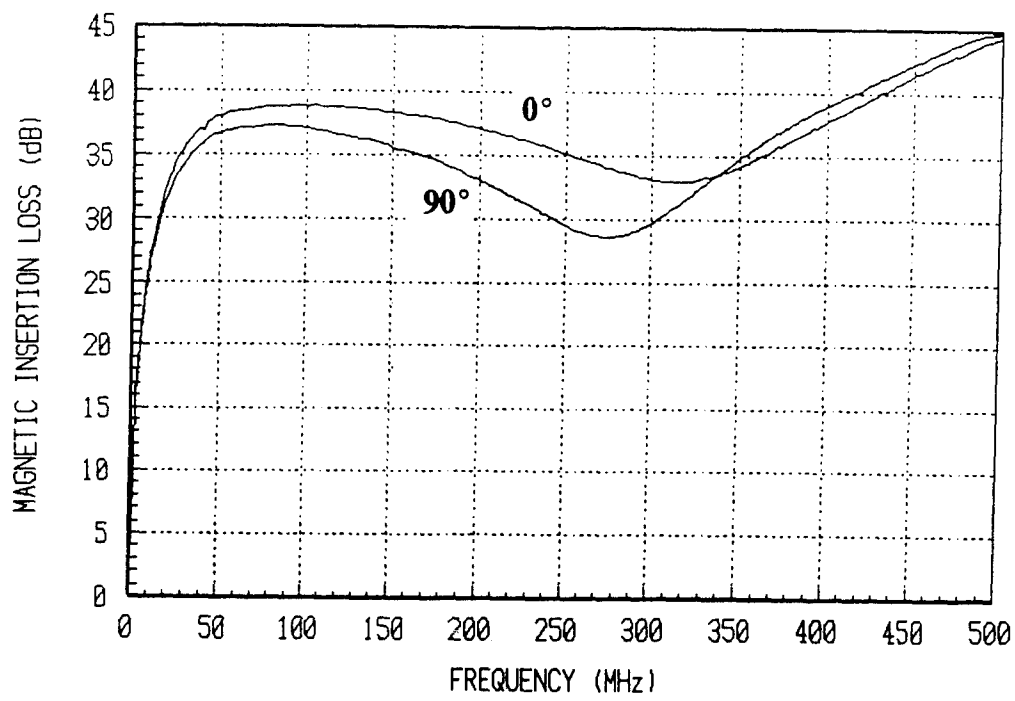


Figure 6 - Effect of Sample Orientation on Magnetic Shielding

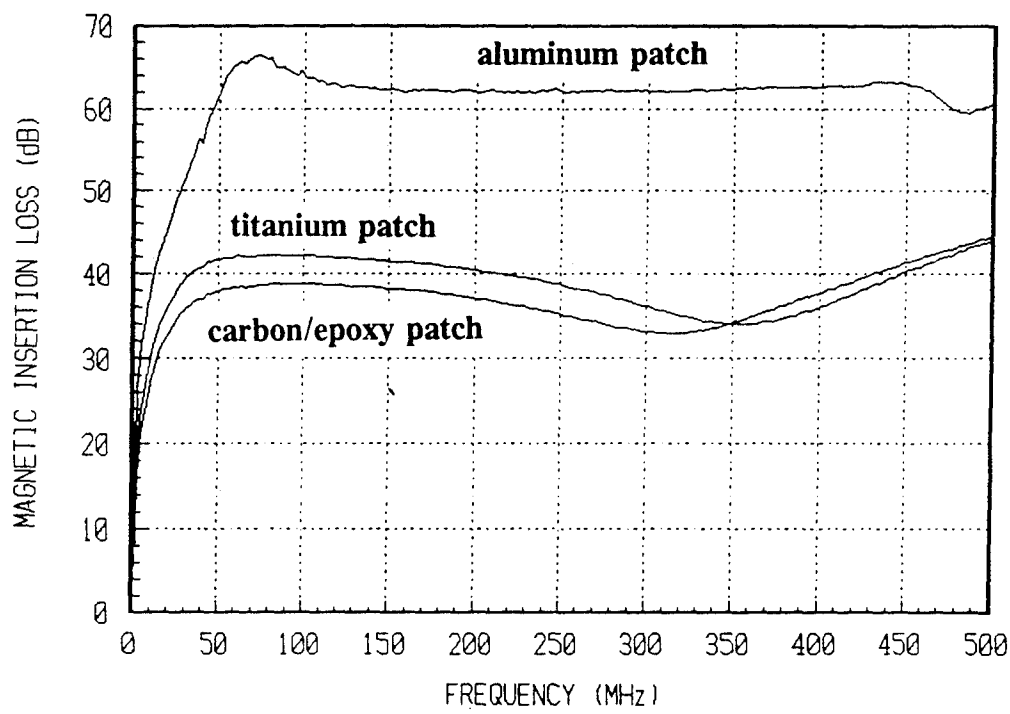


Figure 7 - Effect of Patch Type on Magnetic Shielding

considerably greater shielding. With the bolted patch, electrical contact between the carbon fibres in the carbon/epoxy laminate and the aluminum patch is provided by the bolts. Presumably the shielding would be even higher if the aluminum patch did not contain the 7 mm bolt holes.

5. NUMERICAL CALCULATIONS

In this section, results of numerical studies to calculate the shielding properties of conductive materials are presented and the results compared with experiment. The calculation of the extent of EM penetration through the TEM cell aperture when it is loaded with a composite sample can be best accomplished [8,9] through the calculation of the equivalent magnetic surface currents, \vec{M}_s , that exist over the surface of the aperture. For small apertures, it can be shown that the equivalent magnetic and electric dipole moments (and polarizabilities) are related to the irrotational and solenoidal components of \vec{M}_s respectively.

Isotropic Resistive Material

For an isotropic, resistive material, the integral equations that need to be solved for the irrotational and solenoidal components of \vec{M}_s are the following.

$$\frac{j\omega}{k^2} [\nabla_s \nabla_s \cdot \vec{F}_I + k^2 \vec{F}_I] + \frac{\sigma_s}{2} \vec{M}_{s,I} = \vec{H}_{t,I}^i \quad (5)$$

and

$$j\omega \vec{F}_R + \frac{\sigma_s}{2} \vec{M}_{s,R} = \vec{H}_{t,R}^i \quad (6)$$

where \vec{F}_I and \vec{F}_R are the irrotational and solenoidal components of the electric vector potential defined by

$$\vec{F}_{I,R} = \frac{\epsilon}{4\pi} \iint_A \frac{\vec{M}_{I,R} e^{-jk|\vec{r}-\vec{r}'|}}{|\vec{r}-\vec{r}'|} \quad (7)$$

and $\vec{H}_{t,I}^i$ and $\vec{H}_{t,R}^i$ are the irrotational and solenoidal components of the tangential component of the incident magnetic field.

These equations have been solved using the Method of Moments to determine \vec{M}_s for both the open ($\sigma_s = 0$) and loaded apertures. Once \vec{M}_s is known, the electric and magnetic dipole moments of the open and loaded apertures can be determined from the relationships [10].

$$\vec{p}_e = -\frac{\epsilon}{2} \iint_A \vec{r}' \times \vec{M}_s(\vec{r}') ds' \quad (8)$$

and

$$\vec{p}_m = -\frac{1}{\omega\mu} \iint_A \vec{M}_s(\vec{r}') ds' \quad (9)$$

Figure 8 shows numerical results for the magnetic insertion loss of conductive films having a range of conductivities (in mho) as a function of frequency. These numerical results are in general agreement with the experimental measurements presented earlier (Figure 3) that show that the highly conductive reinforcements provide the highest magnetic shielding.

Anisotropic Resistive Materials

Modification of equation (5) for the case that the aperture is loaded with an anisotropic resistive material is straightforward. In this case the surface conductivity must be expressed in the form of a dyadic, $\vec{\sigma}_s$. For composite materials having unidirectionally oriented fibres (eg. fibres oriented along the x-axis), the conductivity can also be considered to be unidirectional to a good approximation and the only non-zero component of the conductivity dyad is σ_{xx} .

Numerical results for the magnetic insertion loss of a unidirectional composite as a function of orientation is shown in Figure 9. These numerical results are in good agreement with the experimental results shown in Figure 4 that show that the magnetic shielding is greatest when the carbon fibres are oriented at 0° and that the shielding degrades rapidly when the fibres are turned from this orientation. Qualitatively, the shielding behaviour can be understood by noting that the unidirectional composite only shields the component of the magnetic field that is orthogonal to the fibre direction. A simple model for predicting the shielding of unidirectional and multi-directional composite materials was given in [1].

6. CONCLUSIONS

The dual TEM cell technique has been shown to be a valuable method to measure the magnetic and electric insertion loss of conductive materials. Fibre conductivity and fibre orientation were found to control the intrinsic EM shielding characteristics. While carbon fibres have resistivities approximately 3 orders of magnitude higher than good metallic conductors (Al, Cu and Ni), they do possess adequate conductivity to provide substantial

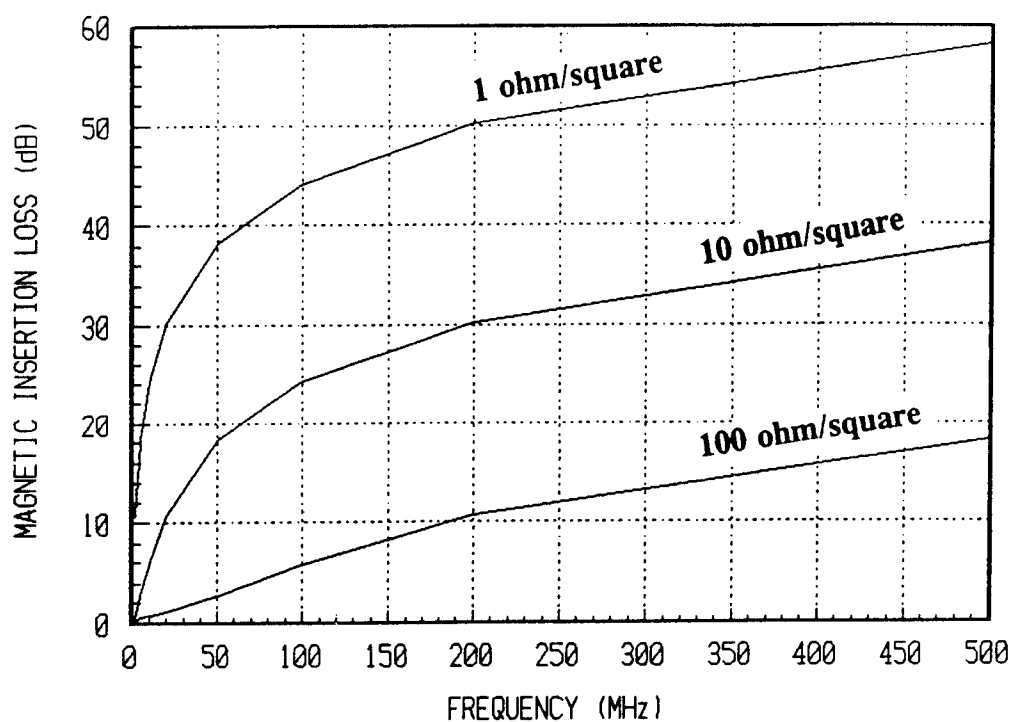


Figure 8 - Effect of Resistivity on Magnetic Insertion Loss

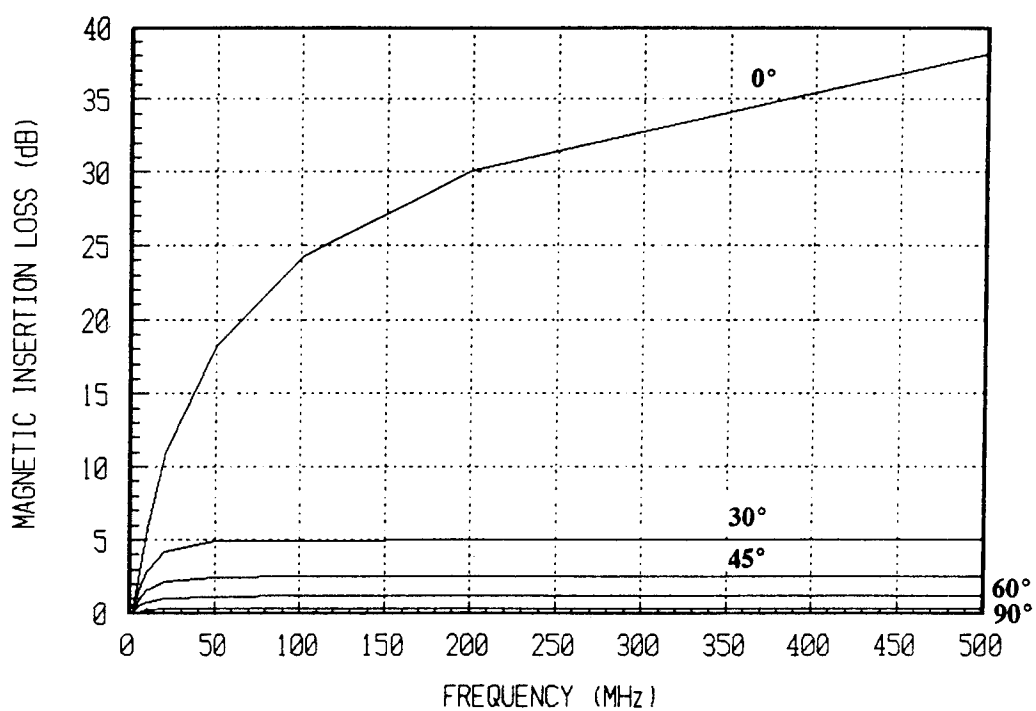


Figure 9 - Effect of Orientation on Magnetic Insertion Loss

shielding to structures made from carbon/epoxy composite materials. However, other common reinforcements such as aramid and glass fibres are incapable of providing adequate shielding unless mixed (hybridised) with carbon fibres.

Repair of composite structures using prescribed techniques for applying bonded patches can result in a substantial degradation of EM shielding. This results because electrical contact is lost between the conductive fibres in the bulk material and those in the patch.

Shielding properties calculated numerically using the Method of Moments are in general agreement with the experimental results presented.

7. ACKNOWLEDGEMENTS

The authors wish to thank Dr. K. Street, Dr. S. Kashyap and Mr. J. Seregelyi for helpful discussions and Mr. E. Jensen for producing the laminates.

7. REFERENCES

- [1] C.L. Gardner and K.N. Street, "Electromagnetic Shielding Properties of Composite Materials", Proc. Eighth Int. Conf. on Composite Materials, 1991.
- [2] C.L. Gardner and G. Costache, "The Penetration of EM Waves Through Loaded Apertures. A Comparison of Analytical and Experimental Results", Proc. 1993 International EMC Symposium, Dallas, August, 1993.
- [3] P.F. Wilson and M.T. Ma, "Shielding Effectiveness Measurements with a Dual TEM Cell", IEEE Trans. EMC, 27, 135 (1985).
- [4] P.F. Wilson and M.T. Ma, "Techniques for Measuring The Electromagnetic Shielding Effectiveness of Materials: Part II", IEEE Trans. Electromagnetic Compatibility, 30, 23 (1988).
- [5] D.F. Higgins, R. Wheeler, and E. Wenaas, "A Comparison of Theoretical and Experimental Data for EM Penetration Through Small Apertures" IEEE Trans. Nuclear Science, NS-32, 4340 (1985).
- [6] K.F. Casey, "Low Frequency Electromagnetic Penetration of Loaded Apertures", IEEE Trans. Electromagnetic Compatibility, EMC-23, 367 (1981).
- [7] R.W. Latham and K.S.H. Lee, "Magnetic Field Leakage into a Semi-Infinite Pipe", Can. J. Phys., 46, 1455 (1968).
- [8] J. van Bladel and C.M. Butler, "Aperture Problems", Theoretical Methods for Determining the Interaction of EM Waves with Structures, NATO Advanced Study Institute Series, J.K. Skwirzynski, Ed., Sythoff and Noordhoff International Publishers, 1979.
- [9] V. Gobin, J.C. Alliot and P. Degauque, "Modelling of Electromagnetic Wave Penetration Through Loaded Apertures", Int. J. Numerical Modelling, 4, 163 (1991).
- [10] C.M. Butler, Y. Rahmat-Samii and R. Mittra, "Electromagnetic Penetration Through Apertures in Conducting Surfaces", IEEE Trans. on Antennas and Propagation, AP-26, 82 (1978).

DISCUSSION

LABAUNE

In your work you consider that the magnetic polarizability of the aperture between the two TEM cell is a function of the conductivity of the sample under test. In fact the contact resistance between the sample and the cells is an important parameter. Have you taken it into account ?

AUTHOR'S REPLY

In carrying out our experiments, we have spent considerable effort to minimise the contact resistance to ensure that it did not influence the measured results. We have copper plated the edges of all of the samples to ensure a low resistance contact between the sample and the cell.

Hardening against a Combined Electromagnetic Threat

M.Dion, C.Gardner, S.Kashyap
 Defence Research Establishment Ottawa
 3701 Carling Avenue
 Ottawa, Ontario, Canada
 K1A 0Z4

1. SUMMARY

Hardening against the electromagnetic environment is usually done by considering each threat separately. In recent years, there has been an increasing interest in methods for unifying electromagnetic standards and procedures to simplify the design and testing of hardening techniques. This approach is appealing as it could reduce the cost of system design as well as the cost of testing.

The objective of this paper is twofold: firstly, to assess the feasibility of combining the various electromagnetic threats to simplify the design of electromagnetic protection; and secondly, to assess the feasibility of using a single test, or at least a minimum number of tests, to verify the electromagnetic hardness of a system.

2. PREFACE

Today's platforms rely heavily on electronic subsystems to perform their mission. The newer technologies used in modern systems are often more susceptible to intentional or unintentional electromagnetic threats, while the electromagnetic environment has become more complex and severe. These threats cover frequencies from DC to 10's of GHz, and include high power microwaves (HPM), nuclear electromagnetic pulse (NEMP), lightning (LEMP), electrostatic discharge (ESD), licensed transmitters and general electromagnetic interference (EMI). The success of the missions now depends on the proper protection of the critical subsystems against any threat which may be encountered during operations.

Over the past decades, techniques were developed for hardening against the various threats, but as they all obey the same Maxwell's equations for propagation and coupling, a single hardening philosophy started to take shape, namely the use of zonal shielding in addition to penetration protection. Although simple, this concept has become costly and inefficient because the procedures of hardening against each threat were developed independently and resulted into standards and survivability steps particular to each threat.

In recent years, there has been an interest in methods for unifying electromagnetic standards and hardening procedures to simplify electromagnetic design and testing

[1]. Benefits would include reductions in costs and time to design, implement and test the required hardening as the result of fewer standards and handbooks and by the avoidance of test redundancies.

3. A UNIFIED APPROACH TO ELECTROMAGNETIC PROTECTION

Conceptually, this approach consists of simply combining the various electromagnetic threats together, propagating them along paths representing the various forms of coupling or filtering, and then comparing the residual levels with the susceptibility thresholds of the individual sensitive components. This approach is particularly well suited to be used along with the concept of electromagnetic topological decomposition [1]. Topological decomposition subdivides a problem into a set of volumes (or localized areas) through which the electromagnetic energy propagates and surfaces through which it penetrates [2] [3]. Although simple in concept, some of the characteristics of the individual threats and coupling functions, as well as the device failure mechanisms have an important impact on our evaluation of whether a system will survive or not. For this reason, it is necessary to discuss the following aspects separately: the electromagnetic environment (EME), the coupling mechanisms, the device failure modes and the simulation of the threats.

The environment is defined by overlaying all the electromagnetic threats across all frequency bands. But, as discussed in detail below, it is necessary to subdivide them into two categories: wideband and narrowband emissions. It is also often the case that a given threat may be specified with some parameters that may vary within some limits. For instance, a narrowband emission may be defined by specifying a range for its carrier frequency or a wideband impulse by a range for its rise time and duration. To be really useful, a design method should allow for such a type of specification.

The coupling mechanisms of the EME may take many forms, such as coupling through intentional receptors (antennas), currents induced in cables, coupling through shielding barriers and apertures, etc. They can usually be approximated by simple transfer functions. As with the EME, they need to be classified as either wideband or narrowband. They may also be specified with some varying parameters (within specified limits).

The propagated electromagnetic signals reaching sensitive components may upset or permanently damage them. In order to properly estimate the system susceptibility, it is important to understand how this energy interacts with electronic components to cause failure.

Once a system is designed and built, it is necessary to verify its hardness but this process is often costly. Therefore, combining some of the EME to reduce the number of tests is attractive. However, this may also result in over-testing the system which may make it impractical in most cases.

A new method for predicting the response of a system to an electromagnetic threat is presented below. This discussion concentrates on the theoretical background of this method, identifying its limits, and suggests an alternate method for describing, combining and propagating electromagnetic signals. It aims at the following goals:

- To keep the error below design margins (typically 10 to 30 dB) — Errors introduced by the approximations are generally less than 10 dB.
- To allow narrowband signals or transfer functions to be specified across a frequency range.
- To readily obtain time-domain parameters such as peak value, rise time, duration, energy, etc., from the frequency domain.
- To allow comparison against failure thresholds in various forms (level-sensitive, power-duration dependency, etc.).
- To allow the computation of optimal shielding based on failure thresholds.

4. FAILURE MODES IN ELECTRONIC SYSTEMS

It is important to understand how the electromagnetic energy is causing equipment damage and upset. Electromagnetic signals can be described in terms of several physically significant parameters which may include the total energy of the signal, its peak value, its duration or its maximum rate of change. The physical mechanism causing failure usually depends primarily on one or two of these parameters. Also, for a given device, the failure mechanism may be different depending on whether upset or damage is considered. The discussion below shows two possible definitions of the threshold curves, one based on a level sensitivity and the other on a power-duration (energy) relationship.

The upset threshold is defined as the minimum signal that will cause a system malfunction, but for which no permanent damage or degradation occurs. Upset thresholds are typically level-sensitive, that is an upset will occur anytime a signal exceeds the threshold, given in volts or amps. This threshold may be frequency-dependant,

hence dependant on the transient duration. Most, if not all, of the EMC design methodologies described in various textbooks are based on level thresholds [4] [5].

The damage threshold is defined as the minimum signal that will cause permanent damage or degradation. This is often the result of an elevated temperature causing meltdown due to the energy deposited by the pulse. For instance, many authors [6]-[8] have related the power a semiconductor may safely absorb to the pulse duration. For short pulses, the energy is deposited adiabatically and failure is determined solely by the total energy content of the pulse. For longer pulses, some of the heat dissipates to the surrounding medium resulting in more power being tolerated before breakdown. For even longer pulses, a steady-state regime is established and the failure level becomes related to peak power instead of total energy. A good model based on the thermodynamics of semiconductor junction meltdown was developed by Wunsch and Bell [6]:

$$P_f = \frac{A}{T} + \frac{B}{\sqrt{T}} + C \quad (1)$$

which relates device failure with the power (P_f) and duration (T) of the applied signal. This type of interaction is not usually taken into account by the classical EMC methodologies.

5. DEFINITION OF ELECTROMAGNETIC QUANTITIES

Most electromagnetic analysis are performed in frequency domain. Furthermore, the phase information is usually not known or difficult to obtain, therefore only the magnitude of the Fourier transform is used. The magnitude is in "/Hz" units and a relation can be found between this function and some time-domain parameters, such as peak value, rise time and duration. For instance, the peak of the magnitude function is not by itself an indication of the peak in time domain, but if multiplied by the bandwidth of the signal, a good approximation may be obtained. The rule-of-thumb that the response of a system is proportional to its bandwidth is well accepted, but may yield to erroneous results, especially when the distinction between wideband and narrowband signals is lost.

White in [5] for instance combines all electromagnetic ambient threats by merging all wideband sources (in V/m/Hz), converted into their equivalent field strength (in V/m), and all narrowband sources, already described by their field strength. Conversion to field strength is done by using a bandwidth adjustment factor applied to every frequency band. This in fact is equivalent to multiplying the spectrum by $\omega/2$. While this approach is apparently widely used, no theoretical proof is given to support it and no guidelines are suggested with respect to its domain of validity. Our work shows that White's approach may give

results which are wrong by several orders of magnitude in the cases of narrowband interactions.

One of the reason why this generally used method fails for narrowband interactions is that the bandwidth information of the signals is not kept. To overcome this problem, a distinction needs to be made between wideband and narrowband electromagnetic quantities (signals or interactions), where narrowband is defined as a quantity demonstrating some resonant features. Wideband quantities are described by a function corresponding to the magnitude of their spectrum, denoted by $H(f)$. In the method proposed, narrowband quantities are described by two discrete values, denoted by $\hat{H}(f_r)$ and $BW_H(f_r)$, corresponding to the peak magnitude and bandwidth at the center frequency. Note that the magnitude $\hat{H}(f_r)$ represents the peak amplitude in time domain for signals or the maximum coupling (at the center frequency) for interactions. By extension, the magnitude and bandwidth may be described by a function, still denoted by $\hat{H}(f_r)$ and $BW_H(f_r)$, which shows the valid range where such an electromagnetic quantity may occur. Alternatively, the bandwidth may be derived, if not specified, from other parameters such as the resonance factor (Q), damping coefficient (z) or duration (T), which are related to one another as:

$$\frac{BW}{f_r} = \frac{1}{Q}, \quad Q = \frac{1}{2z}, \quad BW \approx \frac{1}{T} \quad (2)$$

The last expression is not very accurate (± 10 dB error) and should be avoided to obtain the bandwidth. Wideband and narrowband signals may be combined separately to form two distinct composite signals, which may be further propagated or compared against the predefined failure thresholds. From theoretical and numerical analysis, we can summarize how a signal $E(f)$ or $\hat{E}(f_r)$ is propagated through a transfer function $H(f)$ or $\hat{H}(f_r)$ with the following interaction matrix:

Wideband signal / wideband interaction:

$$R(f) = E(f) \cdot H(f)$$

Wideband signal / narrowband interaction:

$$\hat{R}(f_r) = E(f_r) \cdot \hat{H}(f_r) \cdot 2\pi BW_H$$

$$BW_R(f_r) = BW_H(f_r)$$

Narrowband signal / wideband interaction:

$$\hat{R}(f_r) = \hat{E}(f_r) \cdot H(f_r)$$

$$BW_R(f_r) = BW_E(f_r)$$

Narrowband signal / narrowband interaction:

$$\hat{R}(f_r) = \hat{E}(f_r) \cdot \hat{H}(f_r) \cdot \frac{BW_R(f_r)}{BW_E(f_r)}$$

$$BW_R(f_r) = \min(BW_E(f_r), BW_H(f_r))$$

where R represents the response. $R(f)$ denotes a wideband response while $\hat{R}(f_r)$ and $BW_R(f_r)$ represent the magnitude and bandwidth of a narrowband response. This matrix shows why the standard definition of composite threat as given by White [5] fails when subjected to narrowband interactions. In those cases, the response does not depend on the $E \cdot \hat{H}$ or $\hat{E} \cdot H$ product alone, but also depends on the bandwidth. Note also that wideband signals may become narrowband as they are propagated.

5.1 RELATING TIME AND FREQUENCY DOMAINS

Electromagnetic problems are usually worked out in frequency domain but the failure thresholds are generally specified in terms of time-domain parameters (such as peak value, total energy, etc.). It is therefore of utmost importance to relate those parameters with the frequency-domain spectrum.

With our representation of fields, the peak value in time-domain of narrowband signals is stored and thus obtained directly, and other parameters such as duration or energy may be derived easily from the bandwidth. This relation is not obvious for wideband signals, but it can be proven that for single pulse-type signals, the maximum of the function $H(\omega) \cdot \omega$ is a very good approximation of the peak value of signals in time-domain. This can be easily shown analytically for simple problems, such as for the double exponential, or numerically for more complex problems. For any given spectrum, there is an infinite number of waveforms whose spectrum will approximately fit it, and that may exhibit widely different time-domain characteristics. In particular, it is always possible, for a given spectrum, to choose between high-intensity short signals and lower-intensity longer-duration signals. The estimates obtained from the $H(\omega) \cdot \omega$ product are reasonably accurate for pulse-type signals, ie. signals which concentrate most of their energy into a short burst. Furthermore, the $H(\omega) \cdot \omega$ product identifies the portion of the spectrum that contributes the most to the time-domain function. It can be used to identify the two cutoff frequencies α and β (the -3 dB points below and above the frequency of the maximum) which contribute the most to the signal duration and rise time respectively. The rise time, pulse width and duration may be estimated as $t_r = 2.2/\beta$, $t_w = 0.7/\alpha$ and $t_d = 2.3/\alpha$ respectively. In general, better accuracy is obtained if the curve fits underneath a trapezoid whose sides are steeper than ± 20 dB/decade, but reasonable estimation may be obtained as long as a top portion of the curve can be identified.

5.2 COMPARING RESPONSE AGAINST FAILURE THRESHOLDS

As discussed in previous sections, the failure threshold is defined by the particular physical mechanism involved. The level-sensitive thresholds are the simplest as a failure occurs as soon as the signal reaching the component exceeds the threshold, although that threshold may be frequency-dependant. A simple model of upset threshold

for various logic families is shown on Figure 1, which clearly shows that larger transients are necessary to produce upset above the operating speed of a given family. Narrowband signals $R(f)$ at the susceptible component are simply compared against this threshold for all frequencies while the product $R(\omega)\omega$ is used for comparison for wideband signals. Note that this method is implicitly used by White [4] [5]. Any excess above the threshold curve also represents the additional shielding required to properly harden the system against the threat.

As introduced earlier, other models may be better suited to define the threshold curve. For instance, the Wunsch and Bell model expressed by Equation (1) is more accurate to predict permanent damage in semiconductors. It may be approximated in terms of voltage or current in the form:

$$V_i \approx \frac{A}{\sqrt{f}} + \frac{B}{\sqrt[4]{f}} + C \quad (3)$$

which is shown on Figure 2 for standard TTL logic family. The threshold may also be expressed in terms of bandwidth:

$$V_i \approx A\sqrt{BW} + B\sqrt[4]{BW} + C \quad (4)$$

This threshold can be used directly to compare against narrowband signals. This threshold may be constant if the duration or bandwidth of the signal is constant over its frequency range.

It has been shown that the $H(\omega)\omega$ product can be used to locate the α cutoff frequency and by using $T \approx 0.7/\alpha$, we obtain:

$$V_i \approx A\sqrt{\alpha} + B\sqrt[4]{\alpha} + C \quad (5)$$

and by using $\alpha=2\pi f$, the $H(\omega)\omega$ product may now be compared against the threshold. The signal will not exceed this threshold if its $H(\omega)\omega$ curve lies completely underneath the threshold curve. This is illustrated on Figure 3.

6. THE USE OF COMPOSITE THREAT FOR TESTING

This section presents some considerations about the feasibility of using one or more composite tests to verify the electromagnetic hardness of a system. To qualify as a valid test, a composite waveform must satisfy some basic criteria. Firstly and most importantly, it must guaranty that if a system survives the composite test, it will then survive any of the constituent threats. A composite test is always a form of overtest and thus, there is no guaranty that a system will survive the composite test even though it survives all the individual threats. Therefore the second

criterion is that it should not grossly overtest the system. Finally, the composite waveform should be realizable.

To properly verify the hardness of a system or subsystem, it is necessary to consider it as a 'black box'; that is to assume nothing about how the signal propagates to reach the sensitive components and how it interacts with the components to cause failure. Designing a test (ie. a composite test waveform) based on some assumptions made about a particular type of interaction or failure mode will result in a test that may fail to detect some electromagnetic incompatibilities if some of the assumptions are wrong.

6.1 COMPOSITE WAVEFORMS BASED ON ADDITION OF SPECTRAL COMPONENTS

Adding all individual threats together ($\Sigma e(t)$) would unquestionably result in a composite test that would adequately test the system. Unfortunately, the exact definition of some threats is not always known, but rather defined by some parameters which vary within some limits. Using the superposition property of the transform, $\Sigma e(t) \approx \Sigma E(f)$, the problem can be solved in frequency domain instead. The various threats are not synchronous, therefore taking the maximum of all spectra (or the envelope of the possible spectra if a threat has some varying parameters) instead of adding them defines the spectrum of the composite test. A composite test waveform could then be defined in the time domain. It would seem that any waveform whose spectrum meets or exceeds this composite spectrum would be adequate, but as it will be shown in the example below, some aspects of the system such as particular failure modes may dictate the choice of the composite test waveform. Another problem with this method is that the magnitude of the spectrum is proportional to the duration of a signal (as stated by the time/frequency scaling property of the Fourier transform), yielding to a composite test of very high amplitude. One possible solution is to limit the pulse length to the thermal time constant of the system components.

A simple example will be used through this section to illustrate the discussion. It is an attempt to design a composite test waveform for testing a system according to the CS116 specification of MIL-STD-461C [9]. CS116 specifies a series of damped sinusoid waveforms to be injected at every point of entry. The normalized waveform (peak current $I_p=1$), shown on Figure 4 (top), is defined as:

$$I_0 e^{-2\pi f_0 t} \sin(2\pi f_c t) \quad (6)$$

for frequencies from 10 kHz to 100 MHz with a peak amplitude which is frequency-dependant as shown on the bottom. I_{MAX} is 10 A for Army and Navy procurement and 5 A for Air Force procurement. The corresponding spectrum (for $I_{MAX}=1$) at some frequencies covering the whole possible range is shown on Figure 5, along with the

spectrum of two different composite tests considered. The first is a double exponential, defined as:

$$A(e^{-\alpha t} - e^{-\beta t}) \tag{7}$$

which corresponds in this example to a pulse of 22 A peak amplitude and 0.3 μs duration. The second composite is a frequency-modulated dual sweep (first sweep at constant amplitude up to 1.4 MHz followed by a second sweep, decaying as 1/t, up to 100 MHz), in the form:

$$A_1 \sin(\gamma_1 t^2) \Big|_{t < 60 \mu s} + A_2 \frac{\sin(\gamma_2 (t-t_0)^2)}{t} \Big|_{t > 60 \mu s} \tag{8}$$

which corresponds to a signal of much longer duration (150 μs) and lower peak amplitude (1.2 A).

It is clear from this example that a given spectrum may translate into waveforms having very different characteristics, although they have the same energy. The energy (normalized in 1 Ω) of a real signal e(t) is related to the magnitude of its spectrum by:

$$E_t = 2 \int_0^\infty |H(f)|^2 df \tag{9}$$

from which we may deduce that the energy of the composite test is necessarily larger than any of its constituents. The energy of the two composite tests here is about 40 μJ, which far exceeds the energy of any of the individual CS116 tests (0.5 nJ to 0.7 μJ depending upon the frequency). It is clear that the composite test constitutes a severe overtest of the system. It is conceivable in this case

to build such a source (220 A peak amplitude and 0.3 μs duration for the maximum CS116 specification), but in many cases, it becomes completely unrealistic. For instance, the generator to test for all HPM threats of 1 kV/m and 1 μs duration in the 1-10 GHz band would need to produce a field of 30 MV/m in 10 ps!

If the total energy was the only physical parameter of concern for failure, then we could generalize that any waveform whose spectrum matches the composite would adequately test for all threats at once. Unfortunately, we have seen that failure is often related to other parameters such as peak value and duration. Many waveforms with identical spectrum, thus of comparable energy, will have widely different time-domain characteristics as illustrated by our example above.

Table 1 below summarizes the response of systems of various frequency bands (both wideband and narrowband) to the CS116 waveform (at the maximum resonance) and to the two composite tests. It is clear that the dual FM sweep is not a valid test waveform as it results in smaller responses under some conditions. The system may be underexcited by a factor of as much as Q, the resonance of the interaction. Therefore, failure modes based on a level-sensitive threshold will not be tested appropriately. Also, the responses to this composite are of much longer duration, therefore, failure modes based on power-duration thresholds may not be tested appropriately either. In general, an impulse waveform such as the double exponential tends to concentrate all the energy into a short burst of higher amplitude and shorter duration. Both the level-sensitive and power-duration thresholds failure modes will be tested correctly, but at the expense of overtesting the system and difficulty of design of a suitable source.

Interaction		Peak response to test waveform (A)		
f _c (Hz)	Bandwidth (Hz)	CS116	Double exponential	Dual FM sweep
wideband	4M	1.01	19.78	1.22
1M	1M	0.91	6.85	1.03
1M	100k	0.38	1.25	0.87
1M	10k	.049	0.14	0.21
20M	20M	0.90	10.69	.096
20M	2M	0.49	1.84	.081
20M	200k	0.12	.22	0.066

Table 1. Peak response of various systems to CS116 standard test and two composite test waveforms.

The general conclusion reached from this discussion is that it is not sufficient for a composite pulse to have the same spectral amplitude as the sum (or worst case) of all the threats, but also that some of the time-domain parameters be respected. In particular, it is important that the pulse duration is consistent with the real threats as failures based on a power/duration relationship are very common. An extreme and obvious example is a train of N pulses whose spectrum is comparable to the spectrum of a single pulse of N times the amplitude.

6.2 COMPOSITE WAVEFORMS BASED ON PEAK AMPLITUDE

An alternative method for designing a composite test was described by Podgorski ([10] [11]) who suggested to combining narrowband fields (given in peak time-domain units) with the $H(\omega)\omega$ product of wideband fields in a fashion similar to the procedure used by White [5] for design and analysis. The result is then considered as a $H(\omega)\omega$ product, whose maximum gives the peak value of the composite, and the -3 dB cutoff frequencies give the duration and rise time. What this method fails to take into consideration are the effects of the resonant nature of the threats and/or interactions. In our example, it results in a composite pulse of similar shape and duration (0.3 μ s) but with an amplitude 13 times smaller (1.7 A instead of 22 A). Although this reduces considerably the overtest, it results in an undertest in high-resonance situations. That should also be obvious when considering the energy of this composite (0.23 μ J in this example) which is less than some of the constituent threats (up to 0.7 μ J). Another example (HPM threats in the 1-10 GHz band) revealed undertest situations by 2-3 orders of magnitude.

7. CONCLUSION

To properly design and verify the electromagnetic hardness of an electronic system, it is important to understand the failure mechanism of its electronic components. The two most common failure threshold models were described: one based on level sensitivity and the other based on a power/duration (or level/duration) relation. The conventional methods for EMC/EMI design already use some of the concepts of composite tests implicitly. It is not always understood that these methods are limited to problems involving level-sensitive failure thresholds only and for which no resonant interactions are present.

A new method for EMC/EMI design and analysis was presented. All threats and interactions along a given path may be combined, but a distinction between wideband and narrowband signals and interactions is always preserved. It also allows the definition of narrowband threats or interactions over frequency bands. A simple interaction matrix was presented to model the propagation of electromagnetic signals under various conditions. Simple algorithms for obtaining important time-domain parameters,

such as peak value, rise time and duration, were given. Most importantly, these results may be compared against failure threshold curves (level-sensitive or power/duration) to either calculate a failure index or obtain the optimal additional shielding required to harden the system.

This method may be a very valuable design tool for hardening against multiple threats. However, extreme caution should be used when transposing these results to obtain a composite test waveform for testing. First, a composite test should guaranty that a system will survive any of the threats if it survives the composite test. This implies that the composite test should never undertest the system under any of the normal conditions. It was shown that, based on the energy content, the composite test waveform is a considerable overtest of the system, which would increase the cost of a system if it had a requirement to meet this test. That would be contrary to the prime objective of the whole concept, which is to reduce overall hardening costs, and would not be acceptable by the manufacturer. It was shown that the design of a composite test based on the magnitude of the spectrum alone is not sufficient. Waveforms of same spectrum may have widely different time-domain characteristics, particularly peak value and duration. It may result in a composite test which severely overtests the system under most conditions but may still undertest it under some specific interaction. It was found however that impulse signals such as the double exponential may provide an adequate test, but can be a considerable overtest. In addition, although it is theoretically possible to define a composite test for any problem, in most cases, this proves to be impossible to realize in practice. It may require fields or currents 10 to 1000 times larger than normally required, usually of extremely short duration.

It is concluded that the scope for developing a single electromagnetic simulator for evaluating the hardness of systems against all wideband and narrowband threats is extremely limited. The reason for this is that system upset and damage involve complex physical processes and that no single physical parameter, such as total energy or peak value, is sufficient to determine if failure will occur. To ensure that a system is tested properly, it is not only sufficient that the composite pulse has the same spectral amplitude as the sum of all the threats, but also that some of the time-domain parameters be respected, particularly peak value and duration.

8. REFERENCES

- [1] G. Baker, J.P. Castillo, E.F. Vance, "Potential for a Unified Topological Approach to Electromagnetic Effects Protection", IEEE Transaction on Electromagnetic Compatibility, Vol. 34, No. 3, Aug 1992

- [2] C.E. Baum, "*Electromagnetic Topology for the Analysis and Design of Complex Electromagnetic Systems*", Proceedings of the NATO Advanced Study Institute on Fast Electrical and Optical Diagnostic Principles and Techniques, 1986
- [3] K.S.H. Lee, "*EMP Interaction: Principles, Techniques and Reference Data*", Hemisphere Publishing Corporation, 1986
- [4] D.R.J. White, M. Mardiguian, "*EMI Control - Methodology and Procedures*", 4th edition, Interference Control Technologies, 1985
- [5] D.R.J. White, "*Shielding Design - Methodology and Procedures*", 4th edition, Interference Control Technologies, 1985
- [6] D.C. Wunsch, R.R. Bell, "*Determination of Threshold Failure Levels of Semiconductor Diodes and Transistors Due to Pulse Voltages*", IEEE Transactions on Nuclear Science, Vol. NS-15, No. 6, Dec 1968
- [7] A.H. Kalma, C.J. Fischer, "*Electrical Pulse Burnout Testing of Light-Emitting Diodes*", IEEE Transactions on Nuclear Science, Vol. NS-22, No. 6, Dec 1975
- [8] C.R. Jenkins, D.L. Durgin, "*EMP Susceptibility of Integrated Circuits*", IEEE Transactions on Nuclear Science, Vol. NS-22, No. 6, Dec 1975
- [9] "*Electromagnetic Emission and Susceptibility Requirements for the Control of Electromagnetic Interference*", Military Standard 461C, Department of Defence, USA, 1986
- [10] A.S. Podgorski et al., "*The Implementation of the Composite Electromagnetic Threat Protection Program and the DOD STD 2169*", Proceedings of the 3rd TLG-3 Symposium/Workshop on EMP, Sept 1988
- [11] A.S. Podgorski, "*Composite Electromagnetic Pulse Threat*", Proceedings of the IEEE EMC Conference, 1990

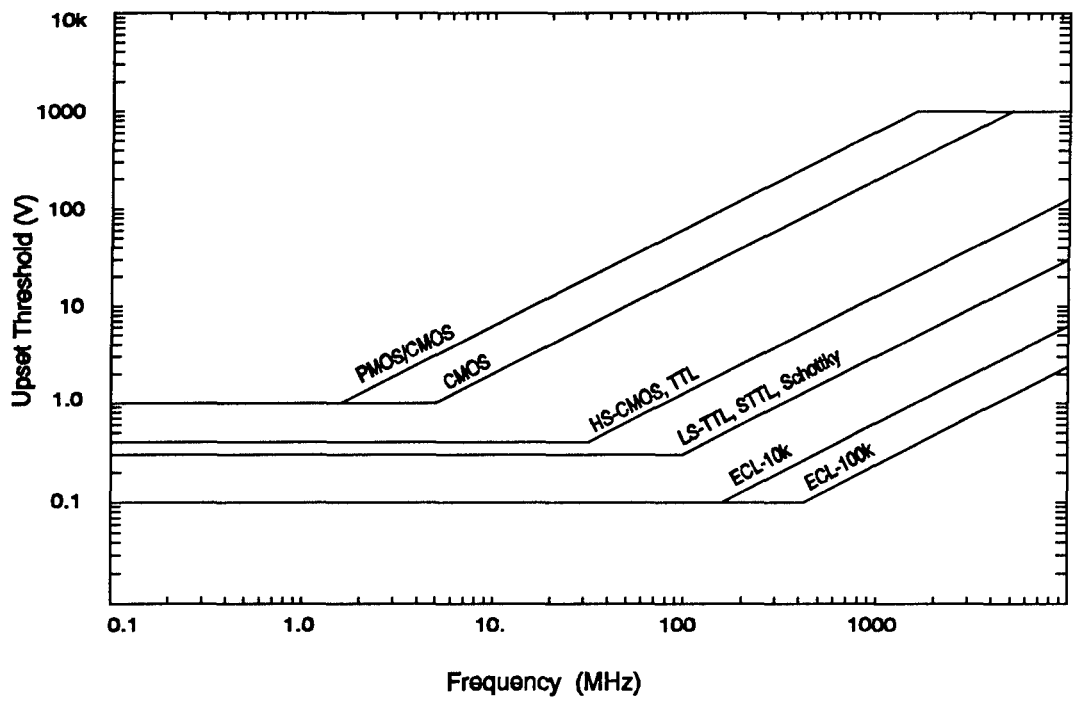


Figure 1. Upset threshold for various logic families.

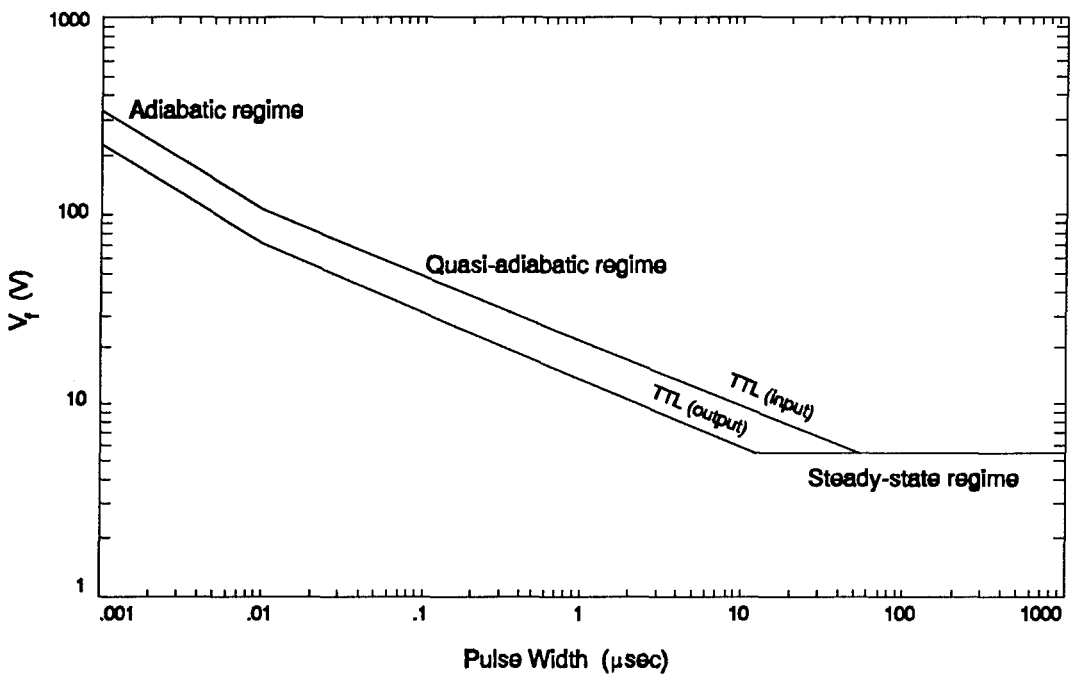


Figure 2. Damage Threshold for TTL logic family.

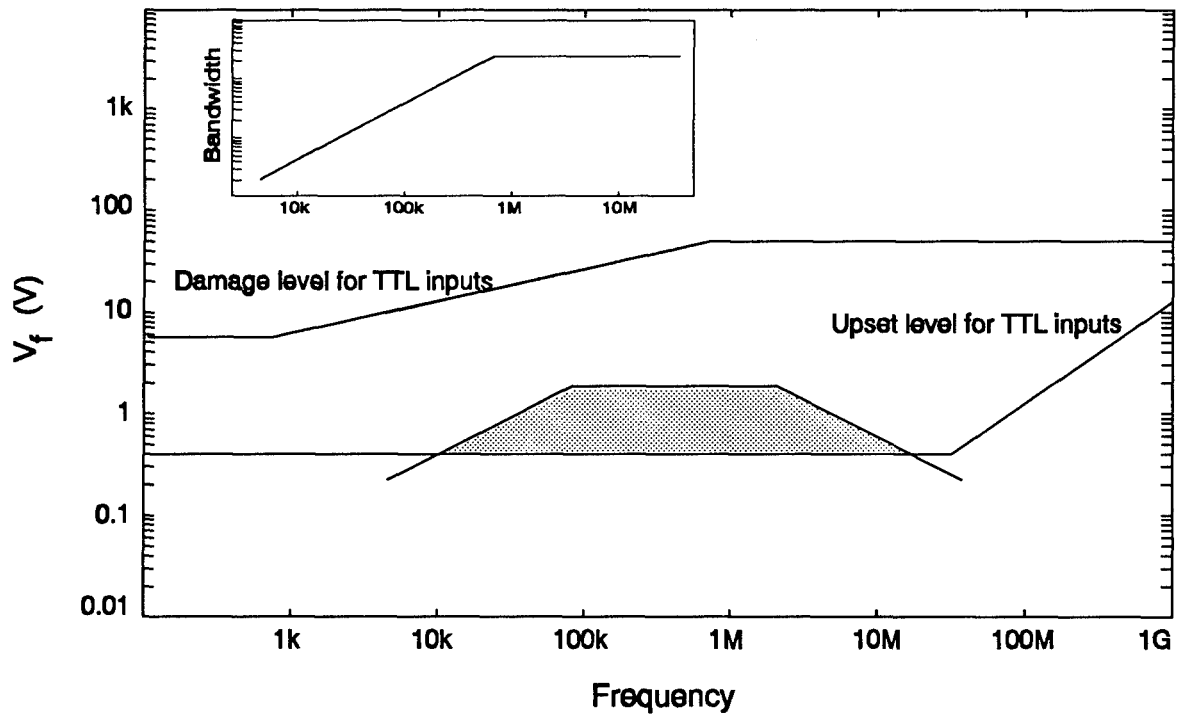
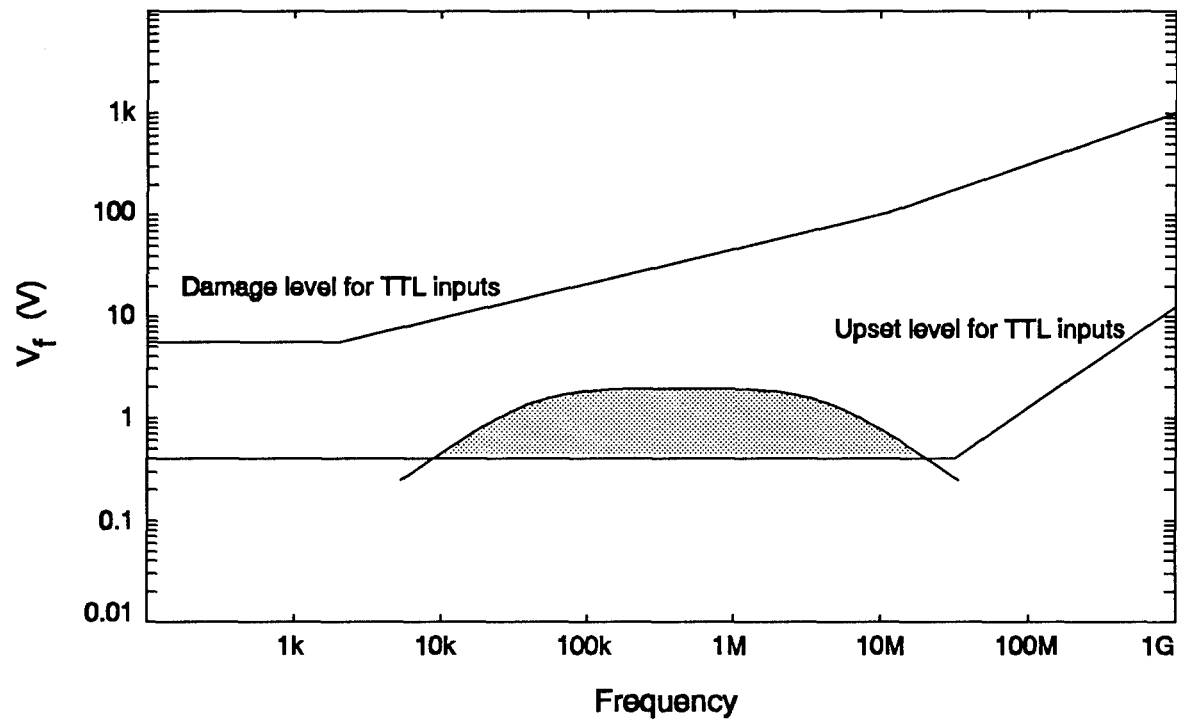


Figure 3. Example of upset and damage threshold comparison of wideband (top) and narrowband (bottom) signal.

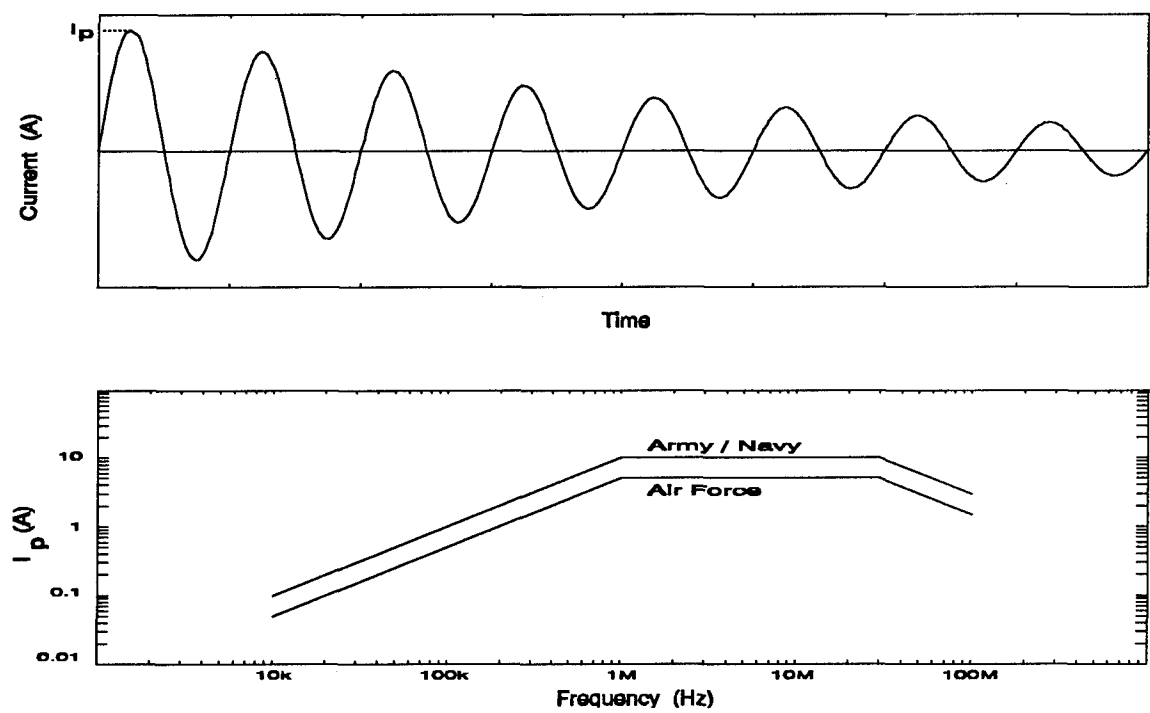


Figure 4. CS116 current injection waveform specification.

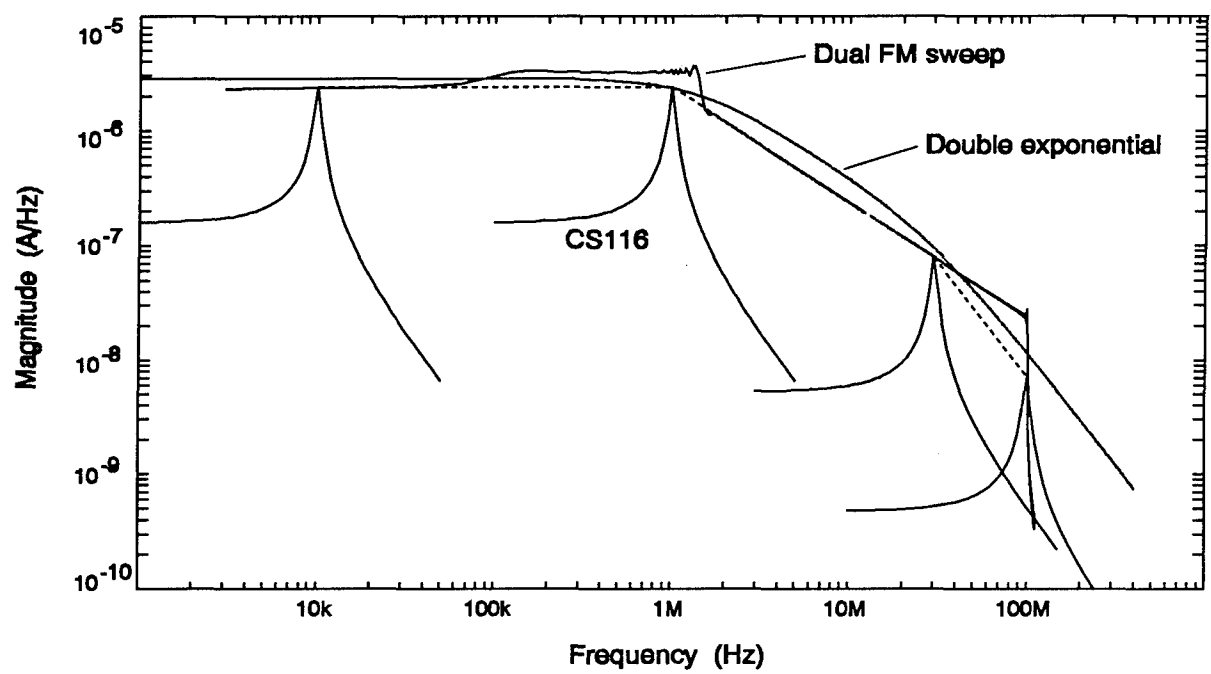


Figure 5. Spectrum of CS116 and two composite waveforms.

Modeling and Numerical Simulation of Microwave Pulse Propagation in Air Breakdown Environment

J. Kim and S.P. Kuo

Weber Research Institute and Department of Electrical Engineering
Polytechnic University, Route 110, Farmingdale, NY 11735, USA

Paul Kossey

Air Force Phillips Laboratory, Hanscom AFB, MA 01731, USA

Summary

It is shown that ionization occurs wherever the field intensity of the pulse exceeds the local breakdown threshold field of the background air. The produced plasma then attenuates the pulse and gives rise to a tail erosion phenomenon that plays the primary role in limiting the energy transfer of the pulse from source to destination.

A theoretical model describing the propagation of an intense microwave pulse in an air breakdown environment is developed and including the possible focusing effect introduced by either using phase array antennas or the other arrangements. The self-consistent description of the propagation process is provided by a set of two modal equations. These include a continuity equation (Poynting's equation) for the energy density of the pulse, and a rate equation of the electron density. A forward wave approximation is used to simplify Poynting's equation, and a semiempirical formula is used for the ionization frequency, ν_i . This frequency provides the coupling between the two modal equations, and is used to express the electron rate equation explicitly. In terms of the relevant parameters of the atmosphere, these two equations are normalized for numerical analysis of pulse propagation in the atmosphere. The dependencies of the propagation characteristics of the pulse on intensity, frequency, width, and shape of the pulse are determined. The numerical simulations lead to an useful empirical relation $p^3w = \alpha = \text{constant}$, where p and w are the incident power and width of the pulse and α depends on the percentage of pulse energy transferred from the source point to a destined position. The density distribution of the pulse's self-generated plasma is also evaluated.

The results also show that for ionization caused by a single unfocused microwave pulse transmitted upwards from the ground, the maximum electron density produced at, for example, 50 km altitude is limited by the tail erosion effect to below 10^6 cm^{-3} . Repetitive pulse and focused beam approaches are also examined. Both approaches can increase the maximum

electron density by no more than an order of magnitude. A scheme using two obliquely propagating pulses intersecting at the destined height, e.g. 50 km, is considered. It is shown that the electron density generated at the lowest intersecting position can easily reach a value of $6.6 \times 10^8 \text{ cm}^{-3}$, which is considered to be high enough for artificial ionospheric mirror (AIM) application.

I. Introduction

Using an artificial ionospheric mirror (AIM) as a reflector of radio signals for over-the-horizon (OTH) communications or radar purposes^[1,2] has several advantages over the conventional approach using the ionosphere as a reflector. 1. it can be produced at a much lower altitude and yet cover a desirable range with tilted setup, 2. it is able to reflect radio signals of much higher frequency and, 3. its stability and location are controllable. The study of the AIM involves the use of intense ground-transmitted microwave pulses for creating localized patches of ionization (AIM) in the stratospheric/ mesospheric altitude range. Thus, these intense microwave pulses have to propagate through the atmosphere, and a variety of physical processes can result. The most significant of these is the ionization process. This occurs when the existing free electrons gain an energy of greater than 12 eV. Moreover, when free electrons are created at a rate faster than their loss rate due to attachment, recombination and diffusion, their density is quickly built up through the process of cascade breakdown in the background gas. These electrons then absorb and/or reflect the energy of the microwave pulses and lead to serious attenuation of pulse energy (so called "tail erosion")^[3-8]. Thus, the pulse energy delivered to the destination can be reduced considerably. The result can be a pulse incapable of producing adequate ionization at the desired altitude for AIM applications. Therefore, a thorough study of microwave pulse propagation through the atmosphere is needed to obtain a better understanding of this phenomenon.

In general, the study concerns two fundamental

issues. One investigates the propagation characteristics of the pulse in the self-generated space-time dependent plasma. The second one seeks determination of the optimum pulse parameters for maximum pulse energy transfer through the background gas. Apparently, these two concerns are interrelated and must be considered together. It suggests that a wide range of pulse parameters including intensity, frequency, width, and shape, etc. would have to be examined.

In our previous work^[9], a theoretical model describing the propagation of an intense microwave pulse in the air was developed. That model was used to perform numerical simulations of our pulse propagation experiments in a chamber. The excellent agreement between the numerical and experimental results validated the theoretical model. A transformation to the local time frame of reference was also introduced to convert the modal equations from a partial differential equation (PDE) form into an ordinary differential equation (ODE) form. Thus, the new set of equations could be solved directly by the available subroutine of an ODE solver and the computation time was reduced considerably. In the present work, this model is further improved by properly including the ionization loss and extended to include the focusing effect. It is then employed to perform a parametrized study of pulse propagation in the atmosphere.

Presented in section II is a brief review of the theoretical model and the set of governing equations for the intense microwave pulse propagation in the air. The results of numerical simulations are presented in section III. Concluding remarks and a discussion of potential applications of the work are given in section IV.

II. Modal Equations describing Pulse Propagation

The propagation of an intense electromagnetic pulse is considered. The plasma along the trail of the pulse is generated by the pulse itself and causes the erosion of the pulse. The pulse-generated plasma is described by the electron density rate equation

$$\frac{\partial}{\partial t} n = (\nu_i - \nu_a) n - \gamma n^2 \quad (1)$$

and the electron momentum equation

$$m_e \frac{\partial}{\partial t} n \bar{v} = -ne\bar{E} - (\eta\nu_i + \nu_a + \gamma n + \nu) m_e n \bar{v} \quad (2)$$

where ν_i , ν_a , γ , and ν are the ionization frequency, attachment frequency, recombination coefficient, and electron-neutral collision frequency respectively; $\eta = (2\varepsilon_i/3T_e)^{1/2}$ is a measure of the effective momentum loss of the plasma fluid in each ionization process, and

ε_i is the ionization energy.

With the aid of (1), (2) is reduced to

$$\frac{\partial}{\partial t} \bar{v} = -e\bar{E}/m_e - [(\eta+1)\nu_i + \nu]\bar{v} \quad (3)$$

The wave equation derived from the Maxwell's equations is given by

$$\left(\frac{\partial^2}{\partial t^2} - c^2 \frac{\partial^2}{\partial z^2} + \omega_{pe}^2\right) \bar{E}(z, t) = -\nu_i \omega_{pe}^2 (m_e/e) \bar{v}(z, t) \quad (4)$$

where the relation $\bar{J} = -en\bar{v}$ has been used,

$\nu_i = \eta\nu_i + \nu_a + \gamma n + \nu$, and $\omega_{pe} = (4\pi e^2/m_e)^{1/2}$ is the electron plasma frequency.

Equations (1), (3), and (4) give a self-consistent description of pulse propagation in an ionizing background. They are coupled through the ionization frequency ν_i , which is modeled to be^[10]

$$\nu_i = 3.83 \times 10^2 \nu_a (\varepsilon^{3/2} + 3.94 \varepsilon^{1/2}) \exp(-7.546/\varepsilon) \quad (5)$$

where $\varepsilon = |A/A_{th}|$ is the wave field normalized to the breakdown (ionization) threshold field, A_{th} . The expression $E(z, t) = A(z, t)e^{-i\phi(z, t)} + c.c.$ for the wave field is assumed with c.c. representing the complex conjugate; $A_{th} \approx 18 p(1 + \omega^2/\nu^2)^{1/2}$ V/cm for a cw wave, in which p is the background pressure measured in torr and ω is the frequency of the wave.

If the pulse is not too short, i.e. it contains many oscillations, slow time and spatial varying envelope approximations can be used to analyze (3) and (4). It is done by first setting $v(z, t) = V(z, t)e^{-i\phi(z, t)} + c.c.$ and $E(z, t) = [A'(z, t)/(1-z/L)]e^{-i\phi(z, t)} + c.c.$ for real A' and ϕ , where $A'/(1-z/L) = A$, L is the focus length of the pulse, and $L \rightarrow \infty$ for an unfocused pulse beam; $V(z, t)$ is, in general, a complex function; the variation of the amplitude functions $A'(z, t)$ and $|V(z, t)|$ in space and time is much slower than that of the phase function $\phi(z, t)$. These expressions for $v(z, t)$ and $E(z, t)$ are then substituted into (3) and (4). Using the facts that $|\partial \ln A' / \partial t| \ll |\partial \phi / \partial t|$, $|\partial \ln A' / \partial z| \ll |\partial \phi / \partial z|$, and $|\partial \ln V / \partial t| \ll |\partial \phi / \partial t|$, and employing the forward-scattering approximation which leads to the definition of local frequency $\omega = \partial \phi / \partial t$, and local wave number $k = -\partial \phi / \partial z$, (3) and (4) are simplified considerably.

Then (3) is solved to yield $V(z, t) \approx -ieA(z, t)$

$/m_e(\omega + iv_2)$, where $v_2 = (\eta + 1)v_1 + v$. This result is used to reduce (4) into a Poynting's equation

$$\frac{\partial}{\partial t} P + \frac{\partial}{\partial z} v_g P = -\beta P + 2v_g P / (L - z) \quad (6)$$

where $P = A^2/2\pi$ is the energy density of the pulse,

$v_g = \partial\omega / \partial k$ is the group velocity, and

$$\beta = v_1 \omega_{pe}^2 / (\omega^2 + v_2^2).$$

The other equation deduced from (4) is the real part of the local dispersion relation of the pulse given by

$$\omega^2 = k^2 c^2 + \omega_{pe}^2 [1 - v_1 v_2 / (\omega^2 + v_2^2)] \quad (7)$$

from which the local group velocity of the pulse can be determined.

In the following analysis, (1) and (6) are the set of modal equations giving a self-consistent description of the pulse propagation in a self-generated plasma. Their coupling is through the ionization frequency given by equation (5), which is rewritten as

$$v_1 / p = 2.5 \times 10^7 [8.8 \bar{P}^{1/4} + 2.236 \bar{P}^{3/4}] \exp[-7.546 / \bar{P}^{1/2}] (\text{sec-torr})^{-1} \quad (8)$$

where $\bar{P} = P / P_{cr}$, $P_{cr} = E_{cr}^2 / 8\pi = A_{th}^2 / 2\pi$ and

$E_{cr} = 2A_{th} = 36.84 p(1 + \omega^2 / v^2)^{1/2}$ V/cm is the breakdown threshold field of the background air of pressure p .

In the practical application of pulse propagation over a long distance, the required computation time becomes an important issue. The large computation time in solving the set of coupled equations (1) and (6) is apparently caused by the simultaneous appearance of spatial and temporal derivatives in (6). Hence, a transformation to the local time frame of reference is introduced to separate the spatial and temporal derivatives from the same equation^[11]. In doing so, computation time for the same propagation distance can be reduced tremendously.

The frame transformation is defined to be^[9]

$$t = t' + \int_0^z dz'' / V_g(t', z'')$$

and

$$z = z'$$

where t' is the local time of the pulse and

$$V_g(t', z') = v_g(t, z).$$

Thus (6) and (1) become

$$\frac{\partial}{\partial t'} V_g P_1 (1 - z' / L)^2 = -[v_1 + c^2 v_a A / 2 V_g^2] (1 - z' / L)^2 P_1 N / n_c \quad (9)$$

and

$$\frac{\partial}{\partial t'} N = v_a A N (V_{g0} P_{10} / V_g P_1) (1 - z' / L)^{-2} \exp [-v_1 \int_0^{z'} dz'' (N / n_c) / V_g] \quad (10)$$

where $P_1(t', z') = P(t, z)$, $N(t', z') = n(t, z)$,

$V_{g0} = V_g(t', z' = 0)$, $P_{10} = P_1(t', z' = 0)$, $\bar{P}_1 = P_1 / P_{cr}$, and

$$A = v_1 / v_a - 1 = 3.83 \times 10^2 (\bar{P}_1^{3/4} + 3.94 \bar{P}_1^{1/4}) \exp (-7.546 / \bar{P}_1^{1/2}) - 1 \quad (11)$$

In the above equations, v , v_1 , v_a , P_{cr} , and n_c are all altitude dependent, and their functional forms are determined as follows. Assuming that the air pressure at 50 km height is 1 torr, and the pressure decays exponentially with the altitude z' . The pressure is given

by $p(z') = 760 e^{-1.346 \times 10^{-3} z'}$ torr, where z' is measured in

meters, and $v = v_0 e^{-1.346 \times 10^{-3} z'}$, where $v_0 = v(z' = 0)$. In terms of the ground level dc breakdown threshold power

$P_{c0} = P_{cr}(z' = 0, \omega = 0)$, then $P_{cr}(z') = P_{c0}(\eta +$

$e^{-2.692 \times 10^{-3} z'})$, where $\eta = \omega^2 / v_0^2$. Similarly,

$n_c(z') = n_{c0}(\eta + e^{-2.692 \times 10^{-3} z'})$, where $n_{c0} = m_e v_0^2 / 4\pi e^2$.

At 1 torr pressure, $v_a = v_{ac} = 1.457 \times 10^5 \text{ sec}^{-1}$ and

$v = v_c = 6 \times 10^9 \text{ sec}^{-1}$ for 1 eV electron temperature.

Including the effect of electron heating by the microwave pulse and assuming that the unperturbed background temperature is about 0.03 eV, a modal

function for v is given by $v = v_c p[\bar{P}_1^{1/2} + 0.03]^{1/2}$, where

$\bar{P}_1 = P_1 / P_{cr} = (P_1 / P_{c0})(\eta + e^{-2.692 \times 10^{-3} z'})^{-1}$. We now

introduce the dimensionless variables and functions as

follows: $(v_c v_{ac})^{1/2} t' \rightarrow t$, $(v_c v_{ac})^{1/2} z' / c \rightarrow z$,

$(v_c v_{ac})^{1/2} L / c \rightarrow L$, $\bar{n} = N / n_c = (N / n_{c0}) h(z) \rightarrow n$,

where $h(z) = (\eta + e^{-2.692 \times 10^{-3} z})^{-1}$, $\bar{P}_1 \rightarrow P_1$,

$\bar{P}_{10} = P_1 / P_{c0} \rightarrow P_{10}$, $Q = (1 - \bar{n})^{1/2} \bar{P}_{10} (1 - z' / L)^2 \rightarrow$

$(1 - n)^{1/2} P_{10} (1 - z / L)^2$, $P_{10} = Q / (1 - n)^{1/2} (1 - z / L)^2$,

and $P_1 = P_{10} h(z) = [Q / (1 - n)^{1/2} (1 - z / L)^2] h(z)$. In

terms of these dimensionless variables and functions,

and the numerical values $(v_c / v_{ac})^{1/2} = 203$ and

$(\nu_c \nu_{ac})^{1/2} = 2.957 \times 10^7 \text{ sec}^{-1}$, equations (9)-(11) become

$$\frac{\partial}{\partial t} n = 3.745 g(z) A n (Q_0 / Q) \exp \left[-1.54 \times 10^5 \int_0^z f(x) dx \right] \quad (12)$$

$$\frac{\partial}{\partial z} Q = -3.745 g(z) \{ (203)^2 [(P_{10} h)^{1/2} + 0.03]^{1/2} + A / 2(1-n) \} n Q / \sqrt{1-n} \quad (13)$$

and

$$A = 3.83 \times 10^2 \{ (P_{10} h)^{3/4} + 3.94 (P_{10} h)^{1/4} \} \exp \left[-7.546 / (P_{10} h)^{1/2} \right] - 1 \quad (14)$$

where $g(z) = e^{-1.346 \times 10^{-2} z}$, $f(x) = g(x) \{ [P_{10}(x) h(x)]^{1/2} + 0.03 \}^{1/2} [n(x) / \sqrt{1-n(x)}]$, and $Q_0 = Q(t, z = 0)$.

Equations (12) and (13) describe vertical propagation of microwave pulse through the atmosphere either from ground to space or from space to ground. If the pulse propagates obliquely with an angle θ with respect to the vertical axis, (12) and (13) must be corrected by replacing V_g with $V_g \cos \theta$, i.e., replacing $\sqrt{1-n}$ by $\sqrt{1-n} \cos \theta$ in these two equations. In terms of z and t , the real distance x and time τ are given by $x = 10.1z$ (m) and $\tau = 33.82t$ (nsec).

III. Numerical Results

The dependencies of the propagation characteristics of a high power unfocused microwave pulse (i.e. $L \rightarrow \infty$) on its power, width and carrier frequency are first investigated by integrating the modal equations numerically. When the pulse power exceeds the breakdown threshold, plasma is generated and causes erosion of the tail part of pulse. This tail erosion phenomenon is demonstrated in Fig. 1(a), in which the shapes of an initially rectangular pulse propagating upwards from ground to four different altitude locations (46.04, 50.75, 52.78 and 56.84 km) are presented. At 46.04 km height, the breakdown threshold is slightly exceeded, but the pulse is almost unperturbed. At other three higher locations, more significant breakdown occurs and causes tail erosion as shown. The corresponding electron densities at the four locations are presented in Fig. 1(b). It shows that the electron density at 46.04 km grows slowly to a very low saturation value. However, at a higher altitude, e.g. 50.75 km, stronger breakdown leads to a faster build-up of electron density to a much higher saturation level of about $8 \times 10^5 \text{ cm}^{-3}$. It is the tail erosion that keeps the

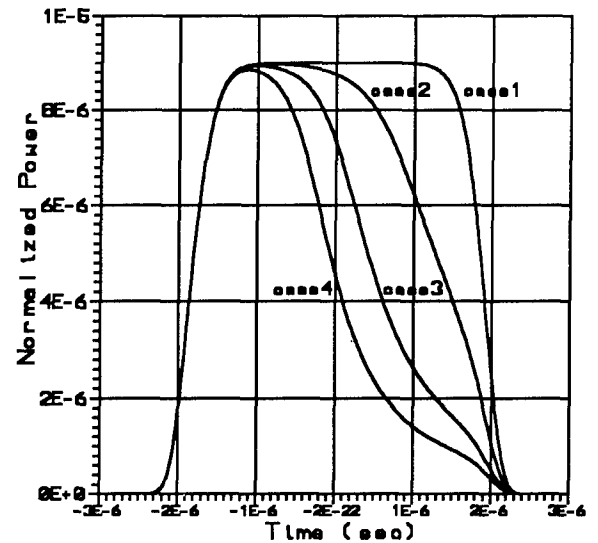


Fig.1(a) Tail erosion of pulse.

[Frequency: 1GHz, Width: 5.4μsec, Altitude: case 1 (46.04km), case 2 (50.75 km), case 3 (52.78km), case 4 (56.84km)]

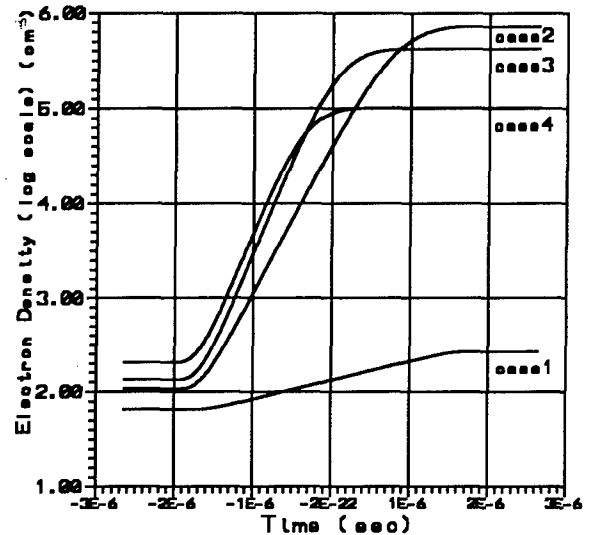


Fig.1(b) Electron density vs time.

[Frequency: 1GHz, Width: 5.4μsec, Normalized Power: 9×10^{-6} , Altitude: case1 (46.04km), case2 (50.75 km), case3 (52.78km), case4 (56.84km)]

electron density from growing. A further increase of the altitude, e.g., at 52.78 and 56.84 km, the breakdown threshold is though reduced, but the pulse power (width) is reduced even faster by the tail erosion process. Thus the electron densities at those two locations grow more quickly, but saturate at lower levels. The distribution of the maximum (in time) electron density along the trail of the pulse is presented in Fig.1(c). It shows that a significant ionization occurs only in a very small spatial region attributed to tail erosion effect. These results suggest that the propagation characteristics of a high power microwave pulse be closely related to the electron density along its propagation path. Presented in Fig.2(a) are the electron

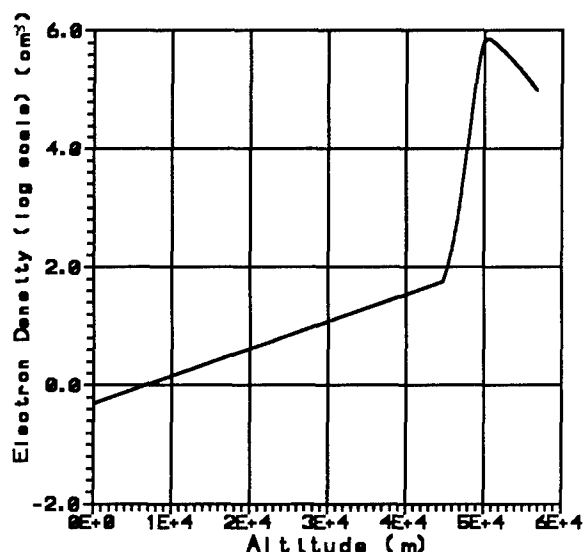


Fig.1(c) Distribution of the maximum (in time) electron density along the trail of the pulse. [Frequency: 1GHz, Width: 5.4 μ sec Normalized Power: 9×10^{-6}]

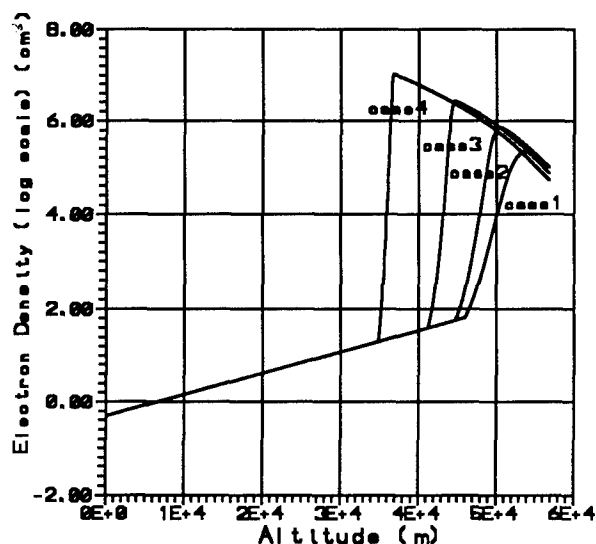


Fig.2(a) The spatial distribution of the maximum (in time) electron density generated by a pulse for four cases of different incident power level. [Frequency: 1GHz, Width: 5.4 μ sec, Normalized Power: case 1 (7×10^{-6}), case 2 (9×10^{-6}), case 3 (5×10^{-5}), case 4 (1×10^{-4})]

density distributions along the trail of the pulses at four different incident power levels: 7×10^{-6} , 9×10^{-6} , 5×10^{-5} and 10^{-4} of the ground level breakdown threshold power. As shown, an increase of pulse power causes the region of cascade breakdown to move downward, and the electron density to grow to a higher saturation level. The pulse is eroded earlier and more severely with increasing power. The power levels of the four pulses in Fig.2(a) at their maximum electron density locations are evaluated respectively to be 2.608, 2.504, 2.286 and 1.553 of the corresponding local breakdown threshold power. One possible way to prevent tail erosion to a high power pulse is to increase

the carrier frequency and the pulse length of the pulse together. The classical breakdown threshold curves for optimized pulse lengths indicate that the breakdown threshold field increases with the carrier frequency ω as the form of $(1 + \omega^2 / \nu^2)^{1/2}$ and has a minimum at $\omega = \nu$. The appearance of this minimum is due to the effect of short pulse length (i.e. Paschen effect). If the pulse is long enough, the breakdown threshold curves tend to become flat at higher altitude and the minimum disappears. Using a long pulse width of 5.4 μ sec and fixing the incident power level of 9×10^{-6} of the breakdown threshold power, but increasing the carrier frequency of the pulse from 0.5 GHz to 1.5 GHz, as demonstrated in Fig.2(b) the breakdown location of the pulse moves upwards (instead of downwards) and

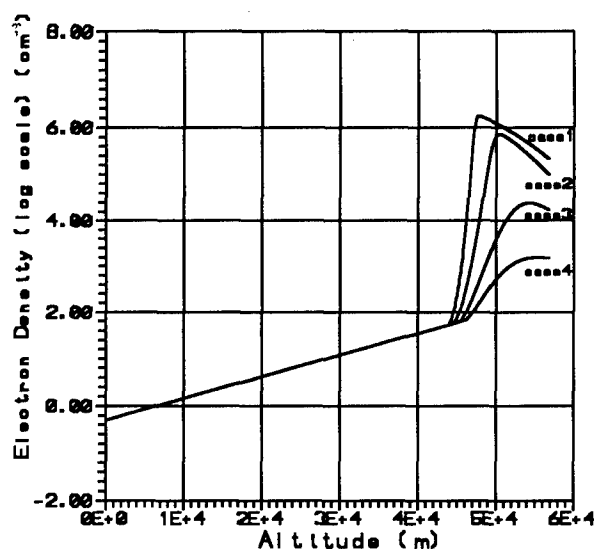


Fig.2(b) The maximum (in time) electron density distribution for four cases of different carrier frequencies. [Normalized Power: 9×10^{-6} , Width: 5.4 μ sec, Frequency: case 1 (0.5GHz), case 2 (1GHz), case 3 (1.3GHz), case 4 (1.5GHz)]

ionization decreases. However, this approach may not be feasible because the required frequency increase is proportional to the field intensity of the pulse.

The dependence of the ionization characteristics on pulse width is also examined. The results are presented in Fig.2(c), which demonstrates that the location of cascade breakdown is not sensitive to the pulse width. In other words, the Paschen effect disappears as the pulse width is wide enough. However, the longer the pulse is the higher the saturation level of the electron density and the thicker the ionization layer are. The numerical results also indicate that the shape of the pulse is not an important factor in determining the electron density distribution and the location of cascade breakdown. This is because a change of the shape of the pulse has the same effect as changing the pulse width. An empirical relationship between the pulse

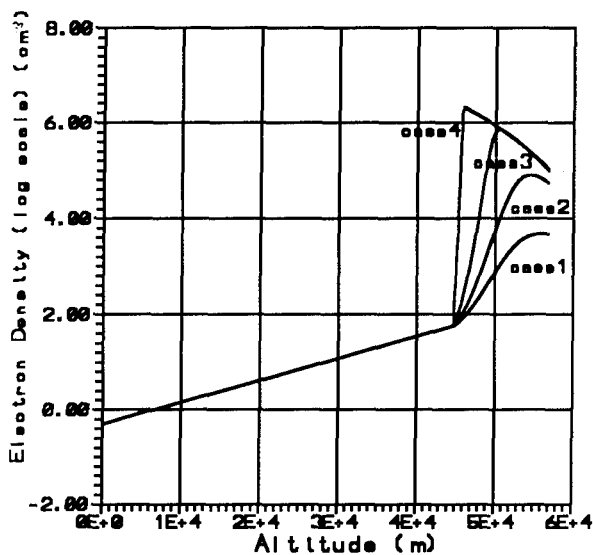


Fig.2(c) The maximum (in time) electron density distribution for four different pulse widths. [Frequency: 1GHz, Normalized Power: 9×10^{-6} , Pulse Width: case 1 (1.68 μ sec), case 2 (2.16 μ sec), case 3 (5.4 μ sec), case 4 (54.1 μ sec)]

width and the pulse power for a fixed percentage of energy transfer from ground to a destined altitude is determined. As shown in Fig.3, three constant power percentages of pulse energy (60%, 68% and 90%)

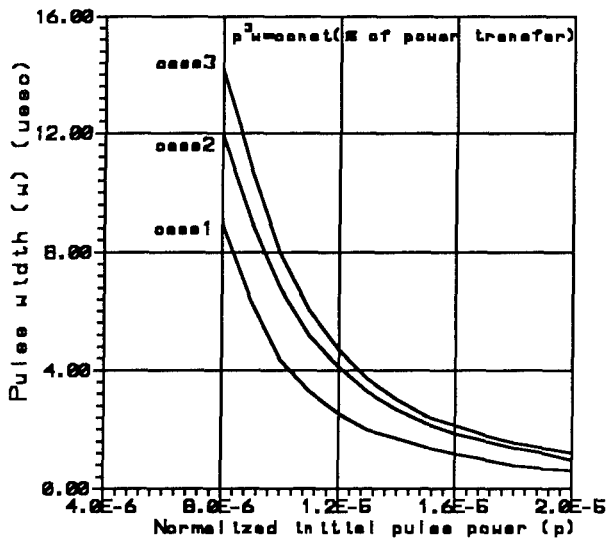


Fig.3. Power transfer from ground to 50 km altitude relationship between pulse width and pulse power leading to a constant percentage pulse. [case 1 (90% power transfer), case 2 (68%), case 3 (60%)]

transmitted to a destined altitude (e.g. 50km) all depend approximately on the product of the third power of the normalized initial pulse power p^3 and pulse width w , i.e. $p^3w=\text{constant} \propto$ the percentage of pulse energy transferred from the source to a destined location. This shows that the pulse power is a more sensitive quantity than the pulse width in determining the energy transfer

of the pulse. Thus, without further treatment of the pulse, such as introducing a focusing phase, the maximum electron density produced by a single pulse at the altitude of interest (e.g. 50 km) is found to be limited to about 10^6 cm^{-3} .

Thus, three different approaches are examined to determine if the ionization at the desired location can be improved. One uses a repetitive pulse approach, and the second uses a focused pulse beam approach. Using periodic pulses with 5.4 μ sec pulse width and a 50% duty cycle, the induced electron density distribution is presented in Fig.4, where only the electron densities

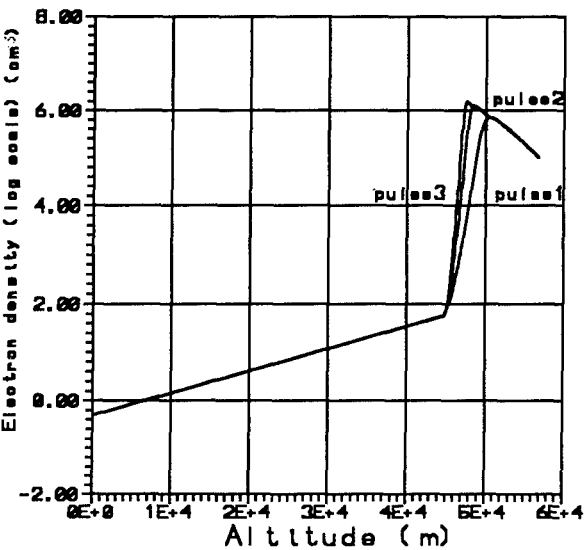


Fig.4 Electron density generated by repetitive pulses of 50% duty cycle; up to three pulses are demonstrated. [Frequency: 1GHz, Normalized Power: 9×10^{-6} , Pulse Width: 5.4 μ sec]

resulting from the first three pulses are included. This is because the electron density distribution remains constant after the third pulse. The results indicate that repetitive pulses can indeed increase electron density at the destined location, but that it still saturates at a relatively low value due to the tail erosion effect. If the focusing effect is limited to a power amplification factor of 10 at 50 km height (i.e. having $L \geq 73 \text{ km}$) for practical reasons, the result presented in Fig.5 shows that the maximum electron density at the desired location (about 50 km height) is only increased by less than an order of magnitude (comparing case3 of Fig.5 and Fig.2c). The saturation level is, again limited by the tail erosion effect and is not enhanced significantly by the increase of the pulse width whose main effect is to increase the spatial width of the ionization layer. Again, this density level is low for considered applications. It is noted that the electron density can be increased to the cutoff density level if the focusing effect is increased by another two orders of magnitude. However, this would be impractical as it requires a very large antenna array, and also the ionization region becomes too small to be a reflector. We, therefore,

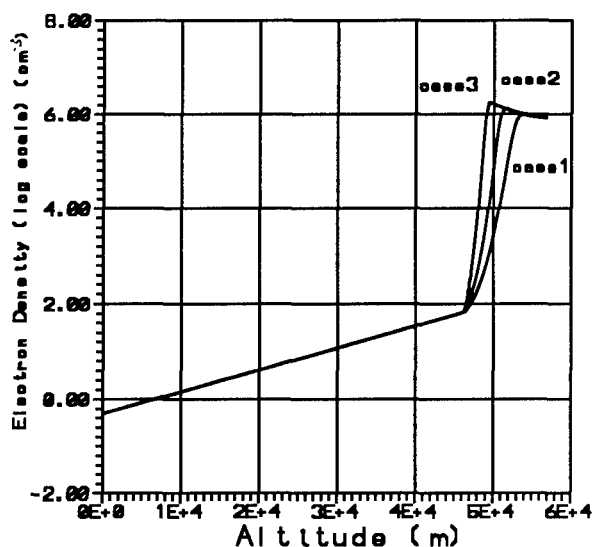


Fig.5 Electron density distribution generated by focused beams of three different widths. [Frequency: 1GHz, Normalized Power: 9×10^{-6} , Width: case 1 (1.68 μ sec), case 2 (2.16 μ sec), case 3 (5.4 μ sec)]

explore a third alternative approach using two intersecting pulse beams^[12,13]. Since the modal equations are not valid in the intersecting region of the two beams (amplitude and phase variation in space become comparable), we only evaluate the intensities of the pulses up to the lower boundary of the intersecting regions and use the added field amplitude at that intersecting point to determine the electron density. Shown in Fig.6, as the two pulses

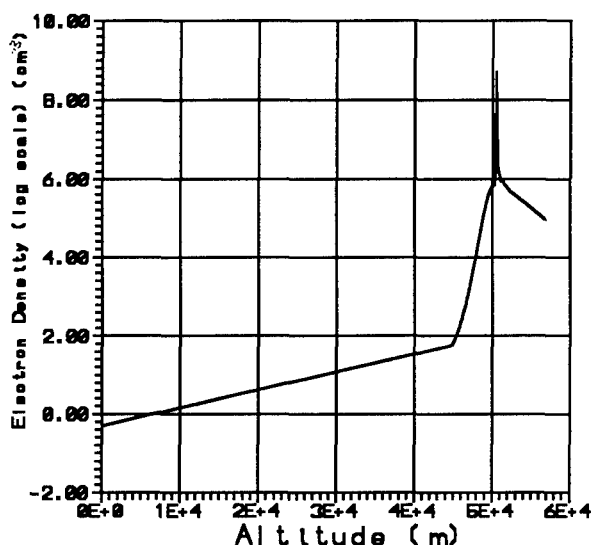


Fig.6 Electron density distribution generated by two pulse beams intersecting at 50km height. [Frequency: 1GHz, Normalized Power: 9×10^{-6} , Pulse Width: 5.4 μ sec]

intersect at about 50.2 km, the electron density increases quickly to about $6.6 \times 10^8 \text{ cm}^{-3}$. This density level is considered to be high enough for practical application.

IV. Summary and conclusion

We have investigated numerically the extent to which the electron density at a desired altitude location can be generated by a high power ground transmitted microwave pulse. This is done by varying the power, width, shape and carrier frequency of the pulse. The results show that once the breakdown threshold field is exceeded in the region between the ground and desired altitude, electron density starts to build up through cascade breakdown in that height region, causing attenuation of the pulse energy (tail erosion) and, thus, deteriorating the energy transmission to the desired altitude. The electron density saturates at a level limited by the pulse width and the tail erosion process. As the pulse continues to travel upward, the breakdown threshold field of the background air decreases, however, the pulse energy (width) is reduced more significantly by the tail erosion process. Thus, the electron density though grows more quickly at the higher altitude, it saturates at a lower level. Consequently, the maximum electron density produced by a single pulse at 50 km altitude, for instance, is found by the present study to be limited to a value below 10^6 cm^{-3} .

A repetitive pulse approach is then considered. The result indicates that using a sequence of pulses can only slightly increase the electron density at the desired location. Again, this limitation is caused by the tail erosion process. This leads to the conclusion that air breakdown in the region below the desired altitude, which causes tail erosion, must be avoided so that sufficient pulse energy can be delivered to this region for plasma generation. This can be done by the following two approaches. One uses a focused beam so that only near the desired altitude the field amplitude exceeds the local breakdown threshold field. However, this approach requires that the beam focusing rate be much greater than the decrease rate of the breakdown threshold field with the altitude. Thus, it requires a very large antenna array that may not be practical. Moreover, to keep the area of the ionization layer a practical size one has to limit the focusing effect to, for instance, a power amplification factor of 10 at the destined altitude. In this case, the ionization is found to be enhanced only by less than an order of magnitude from the unfocused beam case.

The other scheme uses two beams (pulses) intersecting at the desired altitude^[12,13]. Each beam has a field amplitude below the breakdown threshold of the gas at the desired altitude. However, the fields in the intersecting region can interfere constructively and exceed the breakdown threshold. This approach is most effective when the two beams are coherent and have the same polarization. In this case, the intersecting wave fields form a standing wave pattern in the direction perpendicular to the bisecting line of the angle ϕ between the beams. Thus parallel plasma layers

(instead of a single layer) with a separation

$d = \lambda_0 / 2 \sin(\phi/2)$ can be generated, where λ_0 is the wavelength of the two beams^[12]. Using this approach, it is shown that the electron density at the desired altitude (e.g. 50 km) can be increased to about $6.6 \times 10^8 \text{ cm}^{-3}$, which is considered to be high enough for AIM applications. Since a reflector produced by this approach is a set of parallel layers, it can effectively scatter signals even having their frequencies higher than the plasma cutoff frequency as long as the Bragg scattering condition can be approximately matched^[12]. Other advantages of this approach include that the location and the tilted angle of the reflector can be controlled easily by adjusting the incident angles of the two pulse beams.

Acknowledgment

This work was supported in part by the US Air Force System Command, the Air Force Office of Scientific Research grant AFOSR-F49620-94-0076 and in part by National Aeronautics and Space Administration (NASA) grant NAG 5-1051.

Reference

1. Kuo, S.P., Y.S. Zhang, P. Kossey, and R.J. Barker, "On the feasibility of Microwave produced Bragg Reflector: Examined by the Chamber Experiment", NATO AGARD conf. proc., No 485, 18B-1-18B-12, 1990.
2. Kuo, S.P., Y.S. Zhang, M.C. Lee, P. Kossey and R.J. Barker, "Laboratory chamber experiments exploring the potential use of artificially ionized layer of gas as a Bragg reflector for over-the-horizon signals", Radio Sci., 27(6), 851-865, 1992.
3. Bollen, W.M., C.L. Yee, A.W. Ali, M.J. Nagurney, and M.E. Read, "High-power microwave energy coupling to nitrogen during breakdown", J. Appl. Phys. 54, 101-106, 1983.
4. Yee, C.L., A.W. Ali, and W.M. Bollen, "Microwave coupling in a nitrogen-breakdown plasma", J. Appl. Phys., 54, 1278-1283, 1983.
5. Yee, J.H., R.A. Alvarez, D.J. Mayhall, N.K. Madsen, and H.S. Cabayan, "Dynamic characteristics of intense short microwave propagation in an atmosphere", J. Radiation Effects Res. and Eng., 3, 152-160, 1984.
6. Yee, J.H., R.A. Alvarez, D.J. Mayhall, D.P. Byrne, and J. DeGroot, "Theory of intense electromagnetic pulse propagation through the atmosphere", Phys. Fluids, 29, 1238-1244, 1986.
7. Goldstein, B. and Longmire, C., "Microwave absorption and plasma heating due to microwave breakdown in the atmosphere", J. Radiation Effects Res. and Eng., 3, 1626-1628, 1984.
8. Kuo, S.P., Y.S. Zhang, and P. Kossey, "Propagation of high power microwave pulses in air breakdown environment", J. Appl. Phys., 67(6), 2762-2766, 1990a.
9. Kuo, S.P., and Y.S. Zhang, "A theoretical model for intense microwave pulse propagation in an air breakdown environment", Phys. Fluids B, 3(10), 2906-2912, 1991.
10. Lupan, Yu.A., "Refined theory for an RF discharge in air", Sov. Phys. Tech. Phys., 21(11), 1367-1370, 1976.
11. Davidson, R.C., "Methods in Nonlinear Plasma Theory", Academic Press, 1972.
12. Kuo, S.P. and Y.S. Zhang, "Bragg scattering of electromagnetic wave by microwave produced plasma layers", Phys. Fluids B, 2(3), 667-673, 1990.
13. Gurevich, A.V., "Ionization of the lower ionosphere under the effect of strong radio pulses", Geomagn. Aeronom., 19, 428-432, 1979.

DISCUSSION

E. SCHAMILOGLU

Your model neglects the effects of the geomagnetic field. However, at some point along your plasma layer the collision frequency, plasma frequency and electron cyclotron frequency can be comparable. Don't you think that cyclotron effects can be important ?

AUTHOR'S REPLY

Electron cyclotron frequency (≈ 1 MHz) is too low to have any significant effect on pulse propagation (carrier frequency ≥ 1 GHz) in such a collisional plasma ($\nu > 10^9 \text{ sec}^{-1}$, f_p of interest $> 10^8$ Hz) generated in the atmosphere.

U.LAMMERS

What is the rate of decay of your ionospheric mirror and what is a practically useful diameter ?

AUTHOR'S REPLY

A few microseconds due to attachment loss. But attachment process also works to store electrons in the negative ions (O_2^-) which has much lower diffusion loss. Thus, the subsequent HPM pulses for maintainness of plasma layer can be at lower power level since some of the electrons can be provided by the negative ions through detachment process.

The useful diameter of the ionospheric mirror is about 2 hundred meters (depending on the radar frequency) for VHF radars for example.

J. PIGNERET

Similar electron densities can be produced by an ionizing radiation burst which produces black-out and scintillation phenomena on signals transmitted through the disturbed medium (spatial time coherence losses of EM energy). Have you adressed the problem of the quality of the transmission which can be achievable by reflection on such mirror ? (striation development under earth B action).

AUTHOR'S REPLY

As shown by the numerical results the produced plasma layer has sharp boundary, therefore the quality of the reflector is believed to be high. However the roughness of the surface could be an important issue which is not addressed in the present work.

A Review of Nonlinear Electromagnetic Propagation Effects

Joe LoVetri

Department of Electrical Engineering
The University of Western Ontario
London, Ontario, Canada, N6A 5B9
email: joe@gauss.engga.uwo.ca

Marek S. Wartak

Department of Physics and Computing
Wilfrid Laurier University
Waterloo, Ontario, Canada, N2L 3C5
email: mwartak@mach1.wlu.ca

Riaz Siushansian

Department of Electrical Engineering
The University of Western Ontario
London, Ontario, Canada, N6A 5B9
email: riaz@gauss.engga.uwo.ca

1. SUMMARY

It is well known that the presence of intense electromagnetic waves in media which is normally linear will have the effect of producing a nonlinear constitutive relation ($D = \epsilon(E)E$) [1, 2]. This paper will review the fundamentals of non-linear electromagnetic wave propagation with the goal of trying to coalesce the main features of this type of problem. The features of these important nonlinear effects will be summarized and the way in which they manifest themselves mathematically into Maxwell's equations will be reviewed.

For example, in fiber optics the nonlinearities in the permittivity of the fiber have extreme consequences for the governing propagation equations (a nonlinear Schrödinger equation is derived). We will identify important nonlinear mechanisms and analyse their basic physical contents. For that purpose many important analogies between propagation of intense nonlinear pulses in optical fibers and microwave pulses in the atmosphere will be drawn and analysed.

The applications wherein these effects arise will then be surveyed; some of these being intentional while others may be unwanted. The resulting non-linear effects in fiber optics applications are very interesting (soliton propagation) and of practical importance in transoceanic telecommunication [30]. Generation, detection and propagation of optical solitons has been demonstrated over distances as long as 15,000 km [33, 34].

The soliton laser [35], which utilizes Kerr nonlinearity in optical fiber, has also been demonstrated. In the case of the propagation of radio-waves and microwaves through the ionosphere these effects may be undesirable but can be put to use in order to localize or collimate the beam. Thus, for the production of soliton waves in fiber optics and for the collimation of high power microwaves the nonlinearities are essential.

Next, some of the modelling techniques which are available for some of the nonlinear problems will be surveyed and explained [40, 41, 42]. Numerical results for nonlinear electromagnetic propagation will be reviewed. Finally, future problems resulting from the inclusion of nonlinearities will be addressed.

2. NONLINEAR ELECTROMAGNETIC MODELS

2.1 Nonlinear Constitutive Relations

We now investigate nonlinear effects which manifest themselves as nonlinear polarization functions and can be

introduced into the Maxwell equations through the constitutive relations

$$D = \epsilon E \quad (1)$$

$$B = \mu H \quad (2)$$

$$J = \sigma (E + E^i) \quad (3)$$

where E^i is the imposed electric field. The variables which describe the medium are ϵ , the permittivity, μ , the permeability and σ , the conductivity of the medium. The last equation relating the current density, J , to the electric field, E , is sometimes referred to as Ohm's Law. For time invariant inhomogeneous anisotropic media these are tensor variables of space. In this paper, we will mostly be interested in nonlinear isotropic media where the constitutive relations take the new form

$$D = \epsilon_o E + P = \epsilon_o E + P^l + P^{nl} = \epsilon^l E + P^{nl} \quad (4)$$

$$B = \mu_o (H + M) = \mu_o (H + M^l + M^{nl}) \\ = \mu^l H + \mu_o M^{nl} \quad (5)$$

$$J = J^l + J^{nl} + J^i = \sigma^l E + J^{nl} + J^i \quad (6)$$

where P is the polarization vector, $[C/m^2]$, P^l is the polarization term which is linearly dependent on the electric field, and P^{nl} is the polarization vector which is nonlinearly dependent on the electric field. Similar separations of the linear and nonlinear terms have been made in the other two constitutive relations.

If these constitutive relations are introduced into the Maxwell curl equations then the vector wave equation can be derived as

$$\nabla \times \nabla \times E + \mu_o \epsilon_o \partial_{tt} E = -\mu_o \partial_{tt} P - \mu_o \partial_t J - \mu_o \partial_t (\nabla \times M) \quad (7)$$

where the first and last terms on the right hand side can be simplified by introducing the notation

$$J_p = \partial_t P \quad (8)$$

for the polarization current density and

$$J_M = \nabla \times M \quad (9)$$

for the magnetization current density. Now the vector wave equation for the electric field can be written as

$$\nabla \times \nabla \times E + \mu_o \epsilon_o \partial_{tt} E = -\mu_o \partial_t (J + J_p + J_M) \quad (10)$$

where now one can easily see that the source of the electromagnetic wave is made up of different types of current densities. When P and M have nonlinear components which depend on the electric and magnetic fields then these nonlinearities enter the vector wave equation in a nontrivial manner. We will now investigate the forms of these nonlinearities and the effects which they produce.

2.2 Form of Nonlinear Terms

We now consider the mathematical form of these nonlinear terms and the physical effects which arise because of them. Specifically we will look at the way the nonlinear electric polarization depends on the electric field.

First, let us consider the special case of a monochromatic scalar electric field

$$E = E_m \cos(\omega t + \phi_E) = \frac{1}{2} [\underline{E} e^{j\omega t} + \underline{E}^* e^{-j\omega t}] \quad (11)$$

$$= \frac{1}{2} [\underline{E} + \underline{E}^*]$$

where $\underline{E} = E_m e^{j\phi_E}$ is the phasor quantity associated with the wave and $\underline{E}^* = \underline{E} e^{-j\omega t}$. In general the phase, ϕ_E , contains the spatial dependence. Then in a nondispersive medium the nonlinear polarization can be expanded as an infinite power series [2, 33],

$$P^{nl} = \epsilon_0 \sum_n \chi^{(n)} E^n \quad (12)$$

where $\chi^{(n)}$ is the susceptibility associated with the n^{th} power of the electric field. In general, for an electric field strength which is smaller than the internal molecular electric field the magnitude of the susceptibilities decrease with increasing n and only the first few terms in the above expansion will be necessary.

If we substitute (11) into (12) and expand the first 2 terms we get

$$P = \epsilon_0 \left[\chi^{(1)} \frac{1}{2} (\underline{E} + \underline{E}^*) \right. \quad (13)$$

$$\left. + \chi^{(2)} \frac{1}{4} (\underline{E}^2 + 2\underline{E}\underline{E}^* + \underline{E}^{*2}) + \dots \right]$$

and we immediately see that the polarization will have a frequency content different than that of the imposed field since

$$\underline{E}^2 = E_m^2 e^{j2(\omega t + \phi_E)}, \quad \underline{E}^{*2} = E_m^2 e^{-j2(\omega t + \phi_E)} \quad (14)$$

$$\underline{E}^2 + \underline{E}^{*2} = 2E_m^2 \cos(2\omega t + 2\phi_E) \quad (15)$$

$$2\underline{E}\underline{E}^* = 2E_m^2. \quad (16)$$

That is, (15) represents the second harmonic and (16) can be considered a d.c. term. Continuing the expansion for all the terms we can write

$$P = P^l(\omega) + \sum_{n=0}^{\infty} P_m^{nl}(n\omega) \cos(n\omega t + n\phi_E), \quad (17)$$

and it can be shown that the Maxwell equations, and therefore the wave equations, can be cast as an infinite set of coupled partial differential equations. Usually only a finite set of harmonics are of nonnegligible amplitude and so the infinite summation is truncated.

When the imposed field contains two frequency components, say ω_α and ω_β then the resultant fields will contain combination components at combination frequencies $n\omega_\alpha \pm m\omega_\beta$.

For the more general case of a dielectric medium where the polarization of the medium depends on previous values of the electric field (i.e. the matter has *memory*) the linear polarization can be represented as the convolution integral

$$P_i^{(1)}(x, t) = \epsilon_0 \int_0^\infty \kappa_{ij}^{(1)} E_j(t - \tau_1) d\tau_1 \quad (18)$$

and the n^{th} order nonlinear polarization as

$$P_i^{(n)}(x, t) = \epsilon_0 \int_0^\infty \int_0^\infty \dots \int_0^\infty \kappa_{ijkl\dots}^{(n)} E_j(t - \tau_1) E_k(t - \tau_2) E_l(t - \tau_3) \dots \quad (19)$$

where $\kappa_{ijkl\dots}^{(n)}$ is the nonlinear response tensor [3, 36, 37].

A typical first order response function is the Lorentz linear dispersion model [4, 43, 44, 45] where

$$\kappa^{(1)} = \left(\frac{\omega_p^2}{\omega_0} \right) e^{-\frac{\delta t}{2}} \sin(\omega_0 t) \quad (20)$$

In the frequency domain this response function becomes the more familiar

$$\chi^{(1)}(\omega) = \frac{\omega_0^2 (\epsilon_s - \epsilon_\infty)}{\omega_0^2 - j\delta\omega - \omega^2} \quad (21)$$

where $\omega_p^2 = \omega_0^2 (\epsilon_s - \epsilon_\infty)$, and $\nu_0^2 = \omega_0^2 - \delta^2/4$

As an example of the third order response function, the nonlinear characteristics of silica optical fibers have been successfully modelled via the scalar response function [38]

$$g(t) = \alpha \delta(t) + (1 - \alpha) g_R(t) \quad (22)$$

$$g_R(t) = \frac{\tau_1^2 + \tau_2^2}{\tau_1 \tau_2} \exp\left[-\frac{t}{\tau_2}\right] \sin\left[\frac{t}{\tau_1}\right] \quad (23)$$

with the third order nonlinear polarization simplified as

$$P^{nl}(t) = \epsilon_0 \chi^{(3)} E(t) \int_0^\infty g(t-\tau) E^2(t-\tau) d\tau \quad (24)$$

due to the scalar nature of the model.

In these expressions, $g_R(t)$, models the Raman scattering and the Dirac delta function, $\delta(t)$, models the Kerr effect. The parameter α parameterizes the relative strength of each of these in the fiber. The values $\alpha = 0.7$, $\tau_1 = 12.2$ [fs], $\tau_2 = 32$ [fs] were found to give results consistent with experimental results [38].

2.3 Electromagnetic Beam Propagation

When analyzing the propagation of electromagnetic energy in nonlinear media the form of the propagating electromagnetic wave may play an important part in the effects which are produced or seen. That is, should one assume an infinite uniform plane wave, a spherical plane wave, or say a beam of finite cross section? When dealing with laser interactions and aperture type excitations it seems reasonable that a beam model is required where the intensity of the propagating wave varies across a finite cross sectional plane normal to the direction of propagation.

The mathematical form such a beam will take can be derived via the Fresnel Diffraction integral using the paraxial approximation [8]

$$u(x, y, z) \quad (25)$$

$$= \frac{j}{\lambda z} \int_{-\infty}^{\infty} dx' \int_{-\infty}^{\infty} dy' u_0(x', y') e^{-j\left(\frac{k}{2z}\right) [(x-x')^2 + (y-y')^2]}$$

where $u_0(x, y)$ is the cross sectional distribution of the wave at $z = 0$, $k = 2\pi/\lambda = \omega/c$ is the propagation constant, and $u(x, y, z) e^{-jkz}$ is the amplitude of the vector potential in the region $z > 0$. It can be shown, [8], that $u(x, y, z)$ is the solution of the paraxial wave equation

$$\Delta_{\perp} u - 2jk \partial_z u = 0 \quad (26)$$

where $\Delta_{\perp} u$ denotes the Laplacian in the coordinates normal to the assumed direction of propagation, i.e. z . In the derivation of (26) it is assumed that the spatial variation of $u(x, y, z)$ is much less than the carrier e^{-jkz} . This is known as the slowly varying envelope approximation.

The above simple model deals with the time harmonic steady state problem. When the beam energy is not monochromatic, that is when the full time domain problem is considered, the mathematical derivations become more complex. Recently, the case of an ultrawide-bandwidth, space-time Gaussian pulse driving an aperture has been considered by Ziolkowski and Judkins [5]. Analytical and numerical results based on the finite difference time domain method are presented which show that the beam energy and the beam intensity have different diffraction lengths.

When the permittivity, and thus index of refraction, is a function of the local field intensity, a field with varying intensity along the cross-section normal to the direction of propagation will have the effect similar to a medium where the index of refraction varies along the cross-section. Under certain circumstances this has the effect of producing an *optical waveguide* where the natural diffraction effects are countered by the nonlinear effects [6]. If the beam is confined more and more as it progresses through the medium then the phenomena is called *self-focusing* or *spatial solitons*. It can be shown, [7, 8], that if the index of refraction is governed by

$$n = n_0 + n_2 |u|^2 \quad (27)$$

where $n_0 = \sqrt{\epsilon_r}$ is the index of refraction when no field exists, ϵ_r is the dielectric constant of the medium, and n_2 is the coefficient modelling the medium nonlinearity, then the equation governing $u(x, y, z)$ is the *nonlinear Schrödinger equation* (NLS)

$$-j\partial_z u + \Delta_{\perp} u + \kappa |u|^2 u = 0, \quad (28)$$

$$q = \frac{z}{2k_0}, k_0 = \omega \sqrt{\mu_0 \epsilon_0} n_0, \quad (29)$$

and

$$\kappa = 2k_0^2 \frac{n_2}{n_0}. \quad (30)$$

Note that in this model of self-focusing the beam is assumed to be monochromatic and as such the variables in the NLS equation do not involve time.

The relationship given in equation (27) is typical of the Kerr nonlinearity. The phenomena of self-focusing also occurs in the nonlinear interaction of a high power laser beam propagating through a plasma. The effect is mainly attributable to the nonlinear ponderomotive force created by the beam which displaces plasma from the path of the beam and thus increases the dielectric constant inside the beam as compared to the region outside the beam [11]. In regions of high field intensity, the dielectric constant is further increased due to the effective increases in the mass of the plasma electrons which are due to the relativistic electron oscillation (quiver) velocities produced by the field [26]. We will review some of the models which have been used to model these plasma effects in section 4.

The nonlinear Schrödinger equation also comes up in the propagation of an electromagnetic time domain pulse in a dispersive media, that is where the propagation constant is a function of frequency $\beta = \beta(\omega)$, and where the nonlinearity of the medium produces a nonlinear phase modulation of the pulse [10, 8, 39]. In this case, it is typical to include only one spatial variable and time. The time domain pulse is modeled by

$$A(z, t) e^{j\omega_0 t} \quad (31)$$

and the propagation constant is expanded in the first three terms of a Taylor's series about the carrier frequency, ω_0 , as

$$\beta(\omega) = \beta(\omega_0) + \beta'(\omega - \omega_0) + \frac{1}{2}\beta''(\omega - \omega_0)^2. \quad (32)$$

It can be shown (see [8, 10, 30, 39]) that the pulse is governed by

$$j\partial_\zeta A + \frac{1}{2}\beta''\partial_{\tau\tau} A - \kappa|A|^2 A = 0 \quad (33)$$

where

$$\tau = t - \frac{z}{v_g}, \quad \zeta = z, \quad (34)$$

and $A(z, t)$ is assumed to be a slowly varying envelope of the time domain carrier $e^{j\omega_0 t}$. Also in (33),

$$\beta' = \partial_\omega \beta|_{\omega_0} = \frac{1}{v_g} \quad (35)$$

where v_g is the group velocity of the media, and

$$\beta'' = \partial_{\omega\omega} \beta|_{\omega_0} \quad (36)$$

is the second derivative of the propagation constant evaluated at the carrier frequency ω_0 .

Before reviewing, in section 4, some of the many nonlinear models associated with electromagnetic beams propagating in nonlinear media we will consider another physical medium which cannot, in general, be modelled by a simple nonlinear polarization term. This is the propagation of electromagnetic waves in a plasma.

3. PLASMA INTERACTIONS

When an external electromagnetic pulse is applied to a plasma many physical characteristics, such as dielectric constant, and ion and electron densities, exhibit sudden variations and could deviate from their equilibrium values. When the pulse magnitude is small those deviations are usually small; thus, the pulse propagation in plasma can be analyzed using a linear approximation. However, as the amplitude of the electromagnetic wave (pulse) increases, it undergoes a number of changes and nonlinear phenomena become important. Those nonlinear effects can be grouped into three broad categories [11]:

1. Basically nonlinearizable problems,
2. Wave-particle interactions,
3. Wave-wave interactions.

One (and a very important) manifestation of these nonlinearities are solitons [31]. They exist in many branches of physics and engineering. These stable objects owe their existence to two competing effects: first, the nonlinearities that exist in the hydrodynamic equations that lead to steepening and breaking of the waves, and second, the dispersion which causes waves (pulses) to experience broadening in space, and spread of localized dispersion. If the pulse amplitude is such that the interaction in the medium is slightly nonlinear, the competition between these two effects leads to a balance which gives rise to a steady-state pulse (soliton). Actually this balance of dispersion with weak nonlinearity is a general physical process

which arises in a wide variety of problems. The spectacular manifestation of this nonlinearity is the soliton laser which owes its operation to the existence of solitons in optical fibers [32].

For a collisionless plasma composed of cold ions and warm electrons, the basic set of equations for one dimensional motion is expressed in a dimensionless form:

$$\partial_t n + \partial_x(nu) = 0 \quad (37)$$

$$\partial_t u + u\partial_x u = E \quad (38)$$

$$\partial_x n_e = -n_e E \quad (39)$$

$$\partial_x E = n - n_e \quad (40)$$

where n and n_e denote the densities of ions and electrons, respectively, u is the ion velocity, E the electric field, x the space coordinate, and t is the time variable. Dimensionless variables are normalized in terms of the following characteristic quantities:

- 1) characteristic density n_0
- 2) characteristic velocity

$$u_0 = \sqrt{\frac{k_B T_e}{M}} \quad (41)$$

- 3) the Debye length

$$\lambda_D = \sqrt{\frac{k_B T_e}{4\pi e^2 n_0}} \quad (42)$$

- and 4) the characteristic electric potential

$$\psi = \frac{k_B T_e}{e} \quad (43)$$

where k_B is the Boltzmann constant, M is the ion mass, T_e the electrons temperature (assumed to remain constant), and e is elementary charge. In the above equations, (37) and (38) are the continuity and the momentum equations for ions, (39) and (40) are the momentum and Poisson's equation for electrons. The boundary conditions are: $n = n_e = 1$ and $u = 1$ as $x \rightarrow \infty$.

One can introduce new coordinates $\xi = (x - t)\sqrt{\epsilon}$ and $\eta = x\sqrt{\epsilon^3}$, where ϵ is a very small quantity. Expanding n , n_e , u , and E in terms of the power series in ϵ , one can obtain the Korteweg-deVries equation which is often used to describe solitons [11]

$$\partial_\eta u^{(1)} + u^{(1)}\partial_\xi u^{(1)} + \frac{1}{2}\partial_{\xi\xi\xi} u^{(1)} = 0. \quad (44)$$

In equation (44), $u^{(1)}$ is introduced by the following expansion

$$u = \epsilon u^{(1)} + \epsilon^2 u^{(2)} + \dots \quad (45)$$

Similarly, equations can be obtained for other linear coefficients, i.e. $n^{(I)}$ and $n_e^{(I)}$. Those types of solitons have been reviewed extensively in literature [12].

3.1 Fast Switching in Plasma

Another possible application is a picosecond voltage switching in high power systems. The medium in this switch is a high pressure (10-800 atm.) gas. A fast, efficient switch is a basic element in a pulse power accelerator. There we will briefly summarize the results on simple switch working in high pressure gas (10-800 atm.). The switch is triggered by a very short pulse laser. The energy required to drive this switch is much smaller than the energy needed to drive the solid state semiconductor switch and photocathode switch [13].

The principle of that switch is based on the avalanche discharge, with the growth rate described by the Townsend process:

$$N(t) = N_0 e^{\alpha vt} \quad (46)$$

where α is the first Townsend coefficient, v the electron drift velocity, t the time, and N_0 the initial number of electrons present in the field region at the time $t = 0$. The method can be used to switch high power and a high voltage (around 200 kV) on the picosecond scale. The analysis of avalanche discharge process is based on similar equations as these used to describe solitons, i.e. electron fluid equations for continuity, momentum, and energy conservation which are supplemented by Maxwell's equations. Two-dimensional avalanche code has been written and used in [14]. For parallel plate geometry, it predicts a voltage collapse time of 1-10 picosecond for air pressure of 80-500 atm. Simulations at lower voltages and low pressures also gave picosecond scale (1.7-2.1) voltage collapse time.

This system is an example of an electron-ion plasma. Such systems are highly nonlinear. As such, it can support a number of nonlinear phenomena. In [15], the first step was taken towards the understanding of the role of nonlinear phenomena during switching in a Townsend plasma. The theory has been formulated based on continuity equations for electrons and ions with the induction of the Townsend process. The existence of solitary waves of small amplitude described by the Korteweg-deVries equation has been proven.

4. AN OVERVIEW OF NONLINEAR ELECTROMAGNETIC BEAM PROPAGATION MODELS

It is clear that nonlinear electromagnetic beam propagation effects in such media as plasma and optical fibers are many and varied. The detailed mathematical models of these effects are more complicated than those we have given herein. We will now attempt to give an overview of some previous work in the area of self-focusing or spatial solitons.

4.1 Models Based on NLS Equation

In section 2.3 we discussed the nonlinear Schrödinger equation as a model for self-focusing of a beam in a nonlinear medium where the nonlinearity can be modelled as in equation (27). One of the first mathematical expositions of this type of model,

going beyond the initial simple models given in [6] and [7], was presented by Zakharov *et al.* [9, 10].

In [9], the propagation of stationary, that is monochromatic, light beams in nonlinear media was studied using what, in the Soviet literature was known as the parabolic equation

$$2j\partial_z u = \Delta_\perp u + f(|u|^2)u. \quad (47)$$

Today, this equation is generally known as the nonlinear Schrödinger equation, *viz-a-viz* equation (28). The general function $f(|u|^2)$ was used to represent the nonlinearity of the medium. Analytic work was presented for a medium which was close to cubic, and numerical work using the finite difference technique was presented for a cubic medium,

$$f(|u|^2) = \sigma |u|^2 \quad (48)$$

with σ a positive constant, and for a medium modelled by

$$f(|u|^2) = \sigma \kappa^{-1} [1 - \exp(-\kappa |u|^2)] \quad (49)$$

where κ is a positive constant. A axially symmetric Gaussian spatial distribution was imposed at the boundary $z = 0$. It was found that in order for the self-guiding effect to occur, the intensity of the beam must be greater than a critical value, I_0 ,

$$\left(I_1 = \int |u|^2 dr \right) > I_0 = 1.86. \quad (50)$$

Other, more detailed mathematical conditions for the self-guiding effect to occur in this model were also given based on a second functional, I_2 , where

$$I_2 = \int \{ |\nabla u|^2 - F(|u|^2) \} dr, \quad F(\xi) = \int_0^\xi f(\zeta) d\zeta. \quad (51)$$

In Zakharov and Shabat's 1972 paper, [10], an exact solution of the nonlinear Schrödinger equation in two-dimensions was derived using the inverse scattering method.

In [16], the propagation of high power light beam in media with the Kerr non linearity (when conditions are satisfied) has been studied. In addition, some discussion of other non linear optics phenomena has also been included (i.e. Raman scattering, Mandel'shtam-Brillouin scattering, scattering in the wing of a Rayleigh line, and broadening of the spectra of laser pulses). Maxwell's equations are used to model the problem. It is concluded that, typically, the diameter of the foci of a pulse is independent of the incident beam power and duration of the pulse.

4.2 Self-Focusing in Plasma

The self-focusing properties of a plasma on an intense electromagnetic beam have been studied extensively [18-26]. The range of methods used extends from using nonlinear Schrödinger equation [18] already discussed, (28), up to the inclusion of relativistic effects on the electron's mass [26].

The analysis based on the two-dimensional nonlinear Schrödinger equation with both saturable and nonsaturable

nonlinearities has been studied numerically in [18]. In the case of saturable nonlinear medium the simple Gaussian beam produced a complex dynamical structure. As nonlinearity increased, the azimuthal motion was observed and in consequence many cylindrically symmetrical filaments were developed.

Some other self-focusing mechanisms worth mentioning are: ponderomotive self-focusing [19, 20, 21], relativistic self-focusing alone [22, 23], and a combination of relativistic, ponderomotive and thermal self-focusing [24, 25].

Those analyses were driven by the development of powerful lasers and their various applications. Some of them like beat-wave accelerator or the plasma-fiber accelerator require transport of the laser beam with minimal loss in intensity over a considerable distance. A mechanism that allows for such a transport is discussed by Kurki-Suonio [27]. Their model particularly nicely elucidates physical processes responsible for laser-plasma interactions. It is restricted however to short laser pulses propagating in a cool plasma so that the ions, being massive do not have time to respond and thus can be considered as immobile. The basic set of equations consists again of Maxwell's equations and the equation of motion for relativistic electrons. Charge density and plasma current are written in terms of the equilibrium density n_0 and the electron density perturbation δn_e

$$\sum_j e_j n_j = -e \delta n_e \quad (52)$$

$$\mathbf{J} = -e (n_0 + \delta n_e) \mathbf{v} \quad (53)$$

In the Coulomb gauge, i.e. $\nabla \cdot \mathbf{A} = 0$, the electromagnetic field is described by

$$\partial_t \mathbf{A} - c^2 \Delta \mathbf{A} + c \nabla (\partial_t \phi) = 4\pi c \mathbf{J}. \quad (54)$$

Applying the slowly varying envelope approximation they found the equations describing laser beam profiles. They were solved analytically in the slab approximation and compared with computer simulations.

4.3 Overview of Other Work

We now give a brief overview of some other work which has been performed in the modelling of nonlinear electromagnetic processes.

In some work by Yablonovitch, [17], the self-phase modulation in a CO₂ laser is observed to shift up the frequency by 5% due to change in index of refraction from 1 to 0 which is caused by the increase in concentration of electron density. The symmetric spectral broadening of the incident pulse can be obtained using a moderate power lasers or different wavelength lasers.

The relativistic self focusing in plasma has also been investigated by Sprang *et al.*, [26], where an envelope equation was derived which describes the radial evolution of a beam propagation (Gaussian) through plasma. It contains a defocusing term due to diffraction and a focusing term due to the quiver oscillation of the plasma electrons. Under certain

conditions related to the initial slope of the radiation beam radius and to the parameter

$$\alpha = P/P_{crit} \quad (55)$$

where P is the total radiation power,

$$P_{crit} \approx 17 \times 10^9 \left(\frac{\omega}{\omega_{p0}} \right)^2 [\text{W}] \quad (56)$$

and ω_{p0} is the ambient plasma frequency, the beam propagates with constant radius envelope. This happens for $\alpha > 1$ and the initial slope sufficiently small.

The relativistic self-focusing of subpicosecond ultraviolet pulses in a plasma has been considered by Borisov *et al.* [28]. The propagation in both spatially homogeneous plasma and plasma columns was studied. In a mathematical model based on nonlinear Schrödinger equation, it was assumed that for full ionization the gross plasma motion involving ions and the non-inertial Kerr self-focusing effects are insignificant. A clear method of distinguishing relativistic self-focusing from Kerr non-linearity effects was established.

A self-consistent non-linear one dimensional theory has been developed for laser plasma interaction by Sprangle *et al.* [29]. The plasma is modeled as a relativistic fluid using the fluid equations. Some non-linear phenomena such as wake-field generation, relativistic optical guiding, coherent harmonic radiation production, as well as possibility of frequency up-shifting of short and long laser pulses are discussed.

5. TIME DOMAIN MODELLING OF NONLINEAR PROPAGATION AND SOLITONS

Recently, in a series of papers [43, 44, 45], the time domain Maxwell equations, including a differential equation based model for the linear and third-order nonlinear dispersion, have been integrated directly using a finite difference technique. The third-order nonlinear dispersion model used was that based on the scalar response function of Blow and Wood [38], i.e. equations (22)-(24). The computational resources required to evaluate this convolution integral are quite large. To overcome this problem, two coupled ordinary differential equations which properly model the linear and nonlinear dispersive polarization effects were derived for two intermediate functions

$$\begin{aligned} & \frac{1}{\omega_0^2} \frac{d^2 F}{dt^2} + \frac{\delta}{\omega_0^2} \frac{dF}{dt} + \left(1 + \frac{\epsilon_s - \epsilon_\infty}{\epsilon_\infty + \alpha \chi^{(3)} E^2} \right) F \\ & + \left(\frac{(\epsilon_s - \epsilon_\infty)(1 - \alpha) \chi^{(3)} E}{\epsilon_\infty + \alpha \chi^{(3)} E^2} \right) G \\ & = \left(\frac{\epsilon_s - \epsilon_\infty}{\epsilon_\infty + \alpha \chi^{(3)} E^2} \right) D \end{aligned} \quad (57)$$

$$\frac{1}{\omega_0} \frac{d^2 G}{dt^2} + \frac{\bar{\delta}}{\omega_0} \frac{dF}{dt} + \left(1 + \frac{(1-\alpha)\chi^{(3)}E^2}{\epsilon_\infty + \alpha\chi^{(3)}E^2} \right) G + \left(\frac{E}{\epsilon_\infty + \alpha\chi^{(3)}E^2} \right) F = \left(\frac{E}{\epsilon_\infty + \alpha\chi^{(3)}E^2} \right) D \quad (58)$$

where $\bar{\delta} = 2/\tau_2$ and $\omega_0 = (1/\tau_1)^2 + (1/\tau_2)^2$. In [44], the material parameters were chosen as:

$$\epsilon_\infty = 2.25, \epsilon_s = 5.25,$$

$$\omega_0 = 4.0 \times 10^{14} \text{ [rad/s]},$$

$$\bar{\delta} = 2.0 \times 10^9 \text{ [s}^{-1}\text{]},$$

$$\chi^{(3)} = 0.02 \text{ [V}^2\text{/m}^2\text{]},$$

with α , τ_1 , and τ_2 as above and in [38].

The above ordinary differential equations are discretized by a second-order accurate, in time and space, finite difference technique and solved for new time values F^{n+1} and G^{n+1} at each time step of the scheme. The electric flux density, D^{n+1} , and magnetic field intensity H^{n+1} , are updated by the standard interlaced leap-frog finite difference technique. The electric field intensity is found by solving for E , in the equation

$$D = \epsilon_0 \epsilon_\infty E + P^l + P^{nl}. \quad (59)$$

This is accomplished numerically by a Newton iteration at each time step:

$$E^{p+1} = \frac{D^{n+1} - F^{n+1} - (1-\alpha)\chi^{(3)}E^p G^{n+1}}{\epsilon_0 \left(\epsilon_\infty + \alpha\chi^{(3)}(E^p)^2 \right)} \quad (60)$$

where p denotes the index of the Newton's iteration.

Results using this technique have been presented for one and two dimensional problems [44, 45].

6. CONCLUSION

In this paper we have reviewed some of the electromagnetic propagation effects in nonlinear media. We first considered nonlinearities which could be modeled by constitutive relations with physical parameters, ϵ , μ , σ , describing the medium which are functions of the field strengths. We showed that when the permittivity is a nonlinear function of the field strength harmonic frequencies of the incident radiation are produced by the medium. This led to the possibility of spatial (i.e. self-focusing) and temporal solitons being launched into the medium. The modeling of both of these phenomena led to the nonlinear Schrödinger equation. We then reviewed the mathematical models relevant to electromagnetic propagation inside a plasma. We showed that the main mathematical modeling techniques must consider some sort of model for the plasma such as the fluid model. We also saw that the same soliton phenomena are encountered in plasma. Finally, we reviewed some recent numerical work on the solution of the

full vector nonlinear Maxwell equations in the time domain. We conclude that the future modeling of optoelectronic devices which characterized by highly inhomogeneous structures will require the power of this sort of numerical modeling.

7. REFERENCES

Nonlinear optics and electromagnetics:

- [1] L. D. Landau, E.M. Lifshitz and L.P. Pitaevskii, *Electrodynamics of Continuous Media*, 2nd Ed., Pergamon Press, Oxford, 1984.
- [2] A. M. Kugushev, N.S. Golubeva, *Principles of Radio Electronics: Non-linear Electromagnetic Processes*, Mir Publishers, Moscow, 1979.
- [3] A. Yariv, *Quantum Electronics*, third edition, John Wiley & Sons, New York, 1989.
- [4] J. D. Jackson, *Classical Electrodynamics*, 2nd ed., John Wiley, New York, 1975.

Electromagnetic Beam Propagation:

- [5] R. W. Ziolkowski, J. B. Judkins, "Propagation Characteristics of Ultrawide-bandwidth Pulsed Gaussian Beams", *J. Opt. Soc. Am. A*, vol. 9, no. 11, pp. 2021-2030, Nov., 1992.
- [6] R. Y. Cio, E. Garmire, C. H. Townes, "Self-trapping of Optical Beams", *Phys. Rev. Letts.*, vol. 13, no. 15, pp. 479-482, Oct., 1964.
- [7] P. L. Kelley, "Self-focusing of Optical Beams", *Phys. Rev. Letts.*, vol. 15, no. 26, pp. 1005-1008, Dec., 1965.
- [8] H. A. Haus, *Waves and Fields in Optoelectronics*, Prentice-Hall, New Jersey, 1984.
- [9] V. E. Zakharov, V.V. Sobolev, V. C. Synakh, "Behavior of Light beams in Nonlinear Media", *Sov. Phys. JETP*, vol. 33, no. 1, pp. 77-81, July, 1971.
- [10] V. E. Zakharov, A. B. Shabat, "Exact theory of two-dimensional self-focusing and one-dimensional self-modulation of waves in nonlinear media", *Sov. Phys. JETP*, vol. 34, p. 118, 1972.

Electromagnetics in plasma:

- [11] F. F. Chen, *Introduction to Plasma Physics and Controlled Fusion*, second edition, Plenum Press, New York, 1984.
- [12] Y. H. Iahikawa, "Topics on Solitons in Plasmas", *Physica Scripta*, Vol. 20, pp. 256-305, 1975.
- [13] R. E. Cassell, F. Villa, "High Speed Switching in Gases", *IEEE Pulsed Power Conference*, Monterey, CA., June 11-14, 1989.
- [14] D. J. Mayhall, J. H. Yee, F. Villa, "Computer Code Prediction of Picosecond Voltage Switching and TEM Wave Generation in Air Gas Avalanche Switches", *Digest of Technical Papers, Seventh IEEE Pulsed Power Conference*, Monterey, CA, June 11-14, R. White, B. H. Bernstein, Ed.'s, p. 514, 1989.
- [15] M. S. Wartak, A. S. Podgorski, "Propagation of ion-acoustic solitons in the Townsend discharge plasma", *Plasma Physics and Controlled Fusion*, vol. 34, p. 549, 1992.
- [16] V. N. Lugovoi, A. M. Prokhorov, "Theory of the Propagation of High-Power Laser Radiation in a Nonlinear Medium", *Sov. Phys. Usp.*, vol. 16, no. 5, pp. 658-679, March-April, 1974.

- [17] E. Yablonovitch, "Self-Phase Modulation of Light in a Laser-Breakdown Plasma", *Phys. Rev. Lett.*, vol. 32, no. 20, pp. 1101-1104, May, 1974.
- [18] K. Konno, H. Suzuki, "Self-Focusing of Laser Beam in Nonlinear Media", *Physica Scripta (Sweden)* 20, pp. 382-386, 1979.
- [19] C. E. Max, "Strong Self-focusing due to the Ponderomotive Force in Plasmas", *Phys. Fluids*, vol. 19, p. 74, 1976.
- [20] F. S. Felber, "Self-trapping of Intense Optical Beams in Plasmas", *Phys. Fluids*, vol. 23, p. 1410, 1980.
- [21] C. Joshi, C. E. Clayton, F. F. Chen, "Resonant Self-Focusing of Laser Light in Plasma", *Phys. Rev. Letters*, vol. 48, p. 874, 1982.
- [22] C. E. Max, J. Arons, A. B. Langdon, "Self-Modulation and Self-Focusing of Electromagnetic Waves in Plasmas", *Phys. Rev. Letters*, vol. 33, p. 209, 1974.
- [23] P. Sprangle, C. Tang, "Evolution of the Laser Beam Envelope in the Beat Wave Accelerator", in *Laser Acceleration of Particles (AIP Conf. Proc. No. 91)*, C. Joshi and T. Katsouleas, Eds., New York, p. 156, 1985.
- [24] D. A. Jones, E. L. Kane, P. LaLousis, P. Wiles, H. Hora, "Density Modification and Energetic Ion Production at Relativistic Self-focusing of Laser Beams in Plasmas", *Phys. Fluids*, vol. 25, p. 2295, 1982.
- [25] A. Schmitt, R. S. B. Ong, "Theory of Transient Self-Focusing of a CO₂ Laser Pulse in a Cold Dense Plasma", *J. Appl. Phys.*, vol. 54, p. 3003, 1983.
- [26] P. Sprangle, C. Tang, E. Esarey, "Relativistic Self-Focusing of Short-Pulse Radiation Beams in Plasmas", *IEEE Tran. Plasma Sc.*, vol. PS-15, no. 2, pp. 145-153, April, 1987.
- [27] T. Kurki-Suonio, P. J. Morrison, T. Tajima, "Self-focusing of an Optical Beam in a Plasma", *Phys. Rev. A*, vol. 40, no. 6, pp. 3230-3239, September, 1989.
- [28] A. B. Borisov, A. V. Borovskiy, V. V. Korobkin, A. M. Prokhorov, C. K. Rhodes, O. B. Shiryayev, "Stabilization of Relativistic Self-Focusing of Intense Subpicosecond Ultraviolet Pulses in Plasmas", *Phys. Rev. Lett.*, vol. 65, no. 14, pp. 1753-1756, October, 1990.
- [29] P. Sprangle, E. Esarey, A. Ting, "Nonlinear Interaction of Intense Laser pulses in Plasmas", *Phys. Rev. A*, vol. 41, no. 8, pp. 4463-4469, April, 1990.
- [36] A. D. Boardman, P. Egan, T. Twardowski, M. Wilkins, "Nonlinear Surface-Guided Waves in Self-Focusing Optical Media", *Nonlinear Waves in Solid State Physics*, Plenum Press, New York, pp. 1-50, 1990.
- [37] B. Crosignani, P. Di Porto, "The Optical Kerr Effect in Fibers", *Nonlinear Waves in Solid State Physics*, Plenum Press, New York, pp. 275-295, 1990.
- [38] K. J. Blow, D. Wood, "Theoretical Description of Transient Stimulated Raman Scattering in Optical Fibers", *IEEE J. of Quantum Electronics*, vol. 25, no. 12, pp. 2665-2673, Dec. 1989.
- [39] K. J. Blow, N. J. Doran, "Solitons in Optical Fibers", *Nonlinear Waves in Solid State Physics*, Plenum Press, New York, pp. 325-371, 1990.

Numerical solutions and modelling:

Optical fibers, solitons, and soliton laser:

- [40] Q. Chang, G. Wang, "Multigrid and Adaptive Algorithm for Solving the Nonlinear Schrodinger Equation", *J. Comp. Phys.*, vol. 88, p. 362, 1990.
- [41] M. Delfour, M. Fortin, G. Payre, "Finite-Difference Solutions of a Non-linear Schroedinger Equation", *J. Comp. Phys.*, vol. 44, p. 277, 1981.
- [42] T. R. Taha, M. Ablowitz, "Analytical and Numerical Aspects of Certain Nonlinear Evolution Equations. I. Analytical", *J. Comp. Phys.*, vol. 55, p. 192, 1984, "II. Numerical, Nonlinear Schroedinger Equation", *ibid.*, vol. 55, p. 203, 1984, "III. Numerical, Korteweg-de Vries Equation", *ibid.*, vol. 55, p. 231, 1984.
- [43] R. M. Joseph, S. C. Hagness, A. Taflove, "Direct Time Integration of Maxwell's Equations in Linear Dispersive Media with Absorption for Scattering and propagation of femtosecond Electromagnetic Pulses", *Optics Lett.*, vol. 16, pp. 1412-1414, 1991.
- [44] P. M. Goorjian, A. Taflove, R. M. Joseph, S. C. Hagness, "Computational Modeling of Femtosecond Optical Solitons from Maxwell's Equations", *IEEE J. of Quantum Electronics*, vol. 28, no. 10, pp. 2416-2422, Oct. 1992.
- [45] R. M. Joseph, P. M. Goorjian, A. Taflove, "Direct Time Integration of maxwell's Equations in two-dimensional dielectric waveguides for propagation and Scattering of Femtosecond Electromagnetic Solitons", *Optics Letters*, vol. 18, no. 7, pp. 491-493, April 1, 1993.
- [30] G. P. Agrawal, *Nonlinear Fiber Optics*, Academic Press, Inc., Boston, 1989.
- [31] R. K. Bullough, P. J. Caudrey, ed.'s, *Solitons*, Springer-Verlag, Heidelberg, 1980 Progress of Theoretical Physics, Supplement No. 94, 1988.
- [32] P. L. Christiansen, *Nature*, vol. 339, 17, 1989.
- [33] L. F. Mollenauer, "Solitons in optical fibers and soliton laser", *Phil. Tran. R. Soc. Lond.*, v. A 315, 437, 1985.
- [34] L. F. Mollenauer, E. Lichman, G. T. Harvey, M. J. Neubelt, N. M. Nyman, "Demonstration of Error-Free Soliton Transmission Over More Than 15000 km at 5 Gbit/s single/channel and Over More Than 11000 km at 10 Gbit/s in Two Channel WDM", *Electron. Lett.*, vol. 28, p. 792, 1992.
- [35] A. Hasegawa, *Optical Solitons in Fibers*, Springer-Verlag, 1990.

DISCUSSION

P. ZWAMBORN

In the derivation of your non-linear equations you use Taylor-series expansion of field quantities. These Taylor-series will not be valid at locations of discontinuity, how will you model such phenomena ?

AUTHOR'S REPLY

In such a case you will have to model the non-linearities in a different way, for example in the case of spark discharge the discontinuity in the conductivity could not be modeled by a Taylor's series. The addition of a plasma creation model would be necessary.

Spectral Variation of High Power Microwave Pulse Propagating in a Self-generated Plasma

A. Ren and S.P. Kuo

Weber Research Institute and Department of Electrical Engineering
Polytechnic University, Route 110, Farmingdale, NY 11735, USA

Paul Kossey

Air Force Phillips Laboratory, Hanscom AFB, MA 01731, USA

Summary

A systematic study to understand the spectral variation of a high power microwave pulse propagating in a self-generated plasma is carried out in this work. It includes the theoretical formulation, experimental demonstration, and computer simulations and computer experiments.

The experiment of pulse propagation is conducted in a vacuum chamber filled with dry air (~ 0.2 torr), the chamber is made of a 2 ft. cube of Plexiglas. A rectangular microwave pulse (1 μ s pulse width and 3.27 GHz carrier frequency) is fed into the cube through an S band microwave horn placed at one side of the chamber. A second S-band horn placed at the opposite side of the chamber is used to receive the transmitted pulse. The spectra of the incident pulse and transmitted pulse are then compared. As the power of the incident pulse is only slightly ($<15\%$) above the breakdown threshold power of the background air, the peak of the spectrum of the transmitted pulse is upshifted from the carrier frequency 3.27 GHz of the incident pulse. However, as the power of the incident pulse exceeds the breakdown threshold power of the background air by 30%, a different phenomenon appears. The spectrum of the transmitted pulse becomes to have two clearly peaks. One is upshifted and the other one downshifted from the single peak location of the incident pulse. The amount of frequency downshift is comparable to that of the upshifted frequency.

A theoretical model describing the experiment of pulse propagation in a self-generated plasma is developed. There are excellent agreements between the experimental results and computer simulations based on this theoretical model, which is also used to further carry out computer experiments identifying the role of plasma introduced wave loss on the result of frequency downshift phenomenon.

1 Introduction

In using high power microwave pulses for the applications of radar and directed energy system, it is crucial to identify the effect of self-generated plasma on the propagation of the pulses. A considerable research in this aspect has been performed during the past

decade^[1-8]. It is found that the pulse self-generated plasma which is a rapidly space-time function can indeed radically modify wave propagation. For example, it distorts the pulse shape by non-uniform collisional and ionization absorption and may even cause cutoff reflection of the tail portion of the pulse. Such a distortion which usually appears most serious in the tail portion of the pulse is often called "tail erosion" phenomenon. The tail erosion of a pulse limits the energy transfer of the pulse from the source to the target^[6].

On the other hand, the spectral content of the pulse can also be modified significantly during its propagation through the self-generated plasma. This is because the pulse self-generated plasma is a rapidly space-time varying dielectric medium. A change to the index of refraction of the background medium forces the wave to propagate with a different phase velocity and thus to change its spectral content. However, this issue has only been addressed recently^[9,10]. Its effect on many potential applications of HPMs is yet to be explored.

Moreover, the spectral change of the pulse by the self-generated plasma raises a possibility to achieve a "frequency auto-conversion process"^[11-13] for a very powerful microwave pulse propagation through the air without experiencing cutoff reflection by the self-generated plasma. Thus, the tail erosion of the pulse may be significantly reduced. The analysis and preliminary experimental results indeed show that, under the condition that the ionization frequency of the background gas is much larger than the collision frequency of electrons, the carrier frequency ω of the pulse shifts upward to keep $\omega > \omega_{pe}$ during the growth of the plasma density, where ω_{pe} is the electron plasma frequency. Thus, the self-generated plasma is always underdense to the wave and will not introduce cutoff reflection to the wave. This frequency up-shift may be explained qualitatively by the dependence of the phase speed v_p of the wave on the real part of the dielectric constant of the plasma ϵ_r . $v_p = c/\epsilon_r^{1/2}$ is inversely proportional to $\epsilon_r^{1/2}$ and, for a plasma medium, $\epsilon_r = 1 - \omega_{pe}^2/(\omega^2 + \nu^2)$, where ν is the effective collision frequency. Thus, the higher the plasma density, the faster the phase velocity. Since the plasma is generated by the pulse, its

density is expected to be an increasing function from the front to the tail end of the pulse. Thus, the tail portion of the pulse is expected to have higher phase velocity than that of the front portion, consequently, the carrier oscillation of the pulse is squeezed toward the front and has a reduced period. The phase velocity of the wave is also shown to decrease with the collision frequency. Using the similar argument, it explains qualitatively why the carrier frequency of the pulse may also be down-shifted as the collision frequency increases. However, the problem is much more involved and requires computer simulation as will be shown later. The objective of this work is to study the frequency conversion mechanism and the condition under which the frequency up-shift or down-shift occurs. In section II, a theoretical model is developed and discussed. Chamber experiments are performed. Their results confirming the theoretical prediction are presented in section III. Using the developed model, the numerical simulations of the experiments presented in section III are carried out in section IV, in which a comparison between the simulation results and the experimental results is also made. To identify the role of collision frequency on causing frequency down-shift, computer experiments using collision frequency as a key experimental variable are performed. The results are reported in section V. The study is concluded in section VI.

II. Theoretical Model

We consider that an electromagnetic pulse propagates in an ionizable medium (gas) and is intense enough to break down the background gaseous medium. A plasma is generated along the trail of the pulse, and its density is a space-time function depending strongly on the intensity, width, and the shape of the pulse as well as the loss processes including attachment, recombination, and diffusion in the background medium. During the microwave pulse ionizing period, the rate equation of the plasma electron density n_e is given by

$$\frac{\partial}{\partial t} n_e = (v_i - v_a) n_e - \gamma n_e^2 \quad (1)$$

where v_i , v_a , and γ , are the ionization frequency, attachment frequency, and recombination coefficient, respectively. Since the time scale considered is much faster than the time for diffusion to take place the diffusion term is neglected. The ionization frequency is modeled as^[14]:

$$v_i = 3.83 \times 10^2 v_a [\epsilon^{3/2} + 3.94 \epsilon^{1/2}] \exp[-7.546/\epsilon] \quad (2)$$

where $\epsilon = |A/A_{th}|$ is the wave field amplitude A normalized to the breakdown (ionization) threshold field amplitude A_{th} ; $A_{th} \sim 18p(1+\omega^2/v^2)^{1/2}$ V/cm for a continuous wave, p is the background pressure in torr^[15].

The electron momentum equation including the momentum loss from both of elastic and inelastic collision is

$$\frac{\partial}{\partial t} (n_e \bar{v}_e) = -n_e e \bar{E} / m_e - (v + v_a + \gamma n_e + \eta v_i) n_e \bar{v}_e \quad (3)$$

where $\eta = (\epsilon_i / KE)^{1/2}$, the square root of the ratio of the ionization energy ϵ_i of the background gas to the electron average kinetic energy KE , gives a measure of effective momentum loss in each ionization event.

From Maxwell equations, the wave equation is derived to be

$$\frac{\partial^2}{\partial t^2} \bar{E} - c^2 \frac{\partial^2}{\partial z^2} \bar{E} = -4\pi \frac{\partial}{\partial t} \bar{J} \quad (4)$$

where $\bar{J} = -en_e \bar{v}_e$. Using (3), equation (4) becomes

$$\frac{\partial^2}{\partial t^2} \bar{E} - c^2 \frac{\partial^2}{\partial z^2} \bar{E} + \omega_{pe}^2 \bar{E} = -\omega_{pe}^2 (m_e / e) v_i \bar{v}_e \quad (5)$$

where $v_i = v + v_a + \gamma n_e + \eta v_i$. With the aid of (1), (3) can be reduced to

$$\frac{\partial}{\partial t} \bar{v}_e = -e \bar{E} / m_e - [v + (\eta + 1) v_i] \bar{v}_e = -e \bar{E} / m_e - v_2 \bar{v}_e \quad (6)$$

where $v_2 = v + (\eta + 1) v_i$.

Expressing $\bar{E}(z, t) = \hat{X} A(z, t) \exp[-i\phi(z, t)] + c.c.$ and $\bar{v}_e(z, t) = \hat{X} V(z, t) \exp[-i\phi(z, t)] + c.c.$, with real A and ϕ , where c.c. represents the complex conjugate and $V(z, t)$ is, in general, a complex function. If the pulse is not too short, i.e. it carries many oscillations, then the variation of the amplitude functions $A(z, t)$ and $|V(z, t)|$ in space and time is slower than that of the phase function $\exp[-i\phi(z, t)]$. Hence, $|\partial \ln A / \partial t|$ and $|\partial \ln V / \partial t| \ll |\partial \phi / \partial t|$ and $|\partial \ln A / \partial z|$ and $|\partial \ln V / \partial z| \ll |\partial \phi / \partial z|$ which will be employed in the analysis. In addition, the forward-scattering approximation leading to the definition of local frequency $\omega = \partial \phi / \partial t$ and local wave number $k = -\partial \phi / \partial z$ will also be used to simplify the analysis. This approximation is justified because only the portion of the pulse propagating in the forward direction is of interest.

Using these approximations, and the relationship $V(z, t) \sim i e A(z, t) / m_e (\omega + i v_2)$ obtained from (6), (5) leads to

$$\frac{\partial^2}{\partial t^2} \bar{E} - c^2 \frac{\partial^2}{\partial z^2} \bar{E} + \omega_{pe}^2 \bar{E} = i \omega_{pe}^2 v_1 \bar{E} / (\omega + i v_2) \quad (7)$$

Taking the scalar product of \bar{E}^* and (7), and neglecting the two high order terms $A \partial^2 A / \partial t^2$ and $c^2 A \partial^2 A / \partial z^2$, yield

$$\omega^2 - k^2 c^2 = \omega_{pe}^2 [1 - v_1 v_2 / (\omega^2 + v_2^2)] \quad (8)$$

and

$$\frac{\partial}{\partial t} (\omega A^2) + \frac{\partial}{\partial z} (k c^2 A^2) = -[\omega_{pe}^2 v_1 \omega / (\omega^2 + v_2^2)] A^2 \quad (9)$$

Equation (8) is the real part of local dispersion relation of the wave, and equation (9) is the continuity equation for the energy density of the pulse. From their definitions, ω and k are related by the equation $\partial k / \partial t + \partial \omega / \partial z = 0$.

Using (8), (9) is expressed as

$$\begin{aligned} \frac{\partial}{\partial t} P + \frac{\partial}{\partial z} \{ c \{ 1 - [\omega_{pe}^2 / \omega^2] [1 - v_1 v_2 / (\omega^2 + v_2^2)] \}^{1/2} P \} \\ = -[\omega_{pe}^2 v_1 / (\omega^2 + v_2^2)] P \end{aligned} \quad (10)$$

where $P = \omega A^2$ is proportional to the energy density of the microwave pulse.

The phase velocity and the group velocity of the wave in a self-generated plasma can be derived as:

$$v_p = \omega / k = c / \{ 1 - [\omega_{pe}^2 / \omega^2] [1 - v_1 v_2 / (\omega^2 + v_2^2)] \}^{1/2} \quad (11)$$

and

$$\begin{aligned} v_g = \frac{\partial}{\partial k} \omega = c \{ 1 - [\omega_{pe}^2 / \omega^2] [1 - v_1 v_2 / (\omega^2 + v_2^2)] \}^{1/2} \\ / [1 - \omega_{pe}^2 v_1 v_2 / (\omega^2 + v_2^2)^2] \end{aligned} \quad (12)$$

Equation (11) shows that the phase velocity of the wave increases with the plasma frequency and decreases as the term $v_1 v_2 / (\omega^2 + v_2^2)$ increases (i.e. the loss increases). Based on the fact that the phase velocity of the wave decreases as the loss of the medium increases, the frequency down-shift in the spectrum of the wave is possible. It is also noticed from equation (12) that the group velocity of the wave decreases with the plasma frequency. When the plasma frequency ω_{pe} increases to about the value of $(\omega^2 + v_1 v_2)^{1/2}$, the group velocity of the wave reduces to zero, i.e., the wave is cutoff from propagation by the plasma.

Taking the time derivative of (8) and using the relation $\partial k / \partial t + \partial \omega / \partial z = 0$ and (12), yields:

$$\begin{aligned} \frac{\partial}{\partial t} \omega^2 + v_g \frac{\partial}{\partial z} \omega^2 = \{ [1 - v_1 v_2 / (\omega^2 + v_2^2)] \\ / [1 - \omega_{pe}^2 v_1 v_2 / (\omega^2 + v_2^2)^2] \} \frac{\partial}{\partial t} \omega_{pe}^2 \end{aligned} \quad (13)$$

Equations (1), (10) and (13) together with (2) and (12) form a complete set of modal equations describing the dynamic of pulse propagation in the self-generated plasma. The local wave number and phase velocity of the wave can then be obtained from (8) and (11).

In terms of total time derivative, i.e. $d/dt = \partial/\partial t + v_g \partial/\partial z$, (13) can be rewritten as:

$$\begin{aligned} \frac{d}{dt} (\omega^2 - \omega_{pe}^2) = - \{ [v_1 v_2 / (\omega^2 + v_2^2)] [1 - \omega_{pe}^2 / (\omega^2 + v_2^2)] \\ / [1 - \omega_{pe}^2 v_1 v_2 / (\omega^2 + v_2^2)^2] \} \frac{\partial}{\partial t} \omega_{pe}^2 - v_g \frac{\partial}{\partial z} \omega_{pe}^2 \end{aligned} \quad (14)$$

In the case of $v_1 v_2 / (\omega^2 + v_2^2) \ll 1$, the first term on the right-hand side of (14) is negligible, and (14) is reduced to

$$\frac{d}{dt} (\omega^2 - \omega_{pe}^2) = -v_g \frac{\partial}{\partial z} \omega_{pe}^2 \quad (15)$$

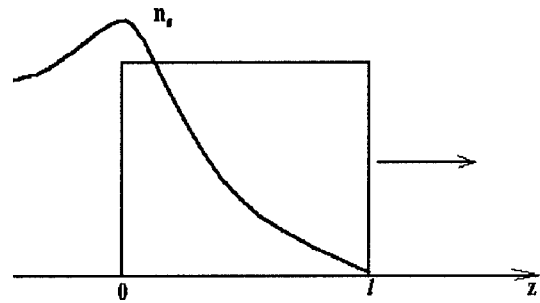


Fig. 1 Envelope of a rectangular pulse and the pulse generated electron plasma density distribution

Considering a rectangular pulse having an envelop as shown in Fig. 1, the density of the generated plasma at a given time is expected to grow nearly exponentially from the background level at the leading edge of the pulse to a peak at the tail end of the pulse. Behind the pulse, plasma density drops from its peak value at a rate depending on the loss mechanisms. The envisioned density profile is also plotted in Fig. 1. It is shown that $\partial \omega_{pe}^2 / \partial z \leq 0$ in the pulse interval and

consequently, $d(\omega^2 - \omega_{pe}^2) / dt > 0$, which means $(\omega^2 - \omega_{pe}^2)$ increases in time. Thus, as long as $\omega > \omega_{pe}$ initially, which is true because the background has very low plasma density, ω keeps greater than ω_{pe} as the microwave pulse propagates. In other words, the carrier frequency of the microwave pulse is up-shifted and keeps greater than the plasma frequency while the ionization increases the plasma density. This frequency up-shift process leads to the reflectionless (without cutoff reflection) propagation of a high power microwave pulse in a self-generated plasma. This conclusion seems trivial for a rectangular pulse propagating in a uniform medium because $d\omega_{pe}^2 / dt < 0$. However, it becomes a significant result for pulse propagating in a non-uniform medium so that $d\omega_{pe}^2 / dt > 0$ can occur. An example of this case is the propagation of a pulse through the atmosphere. It is first noted that the breakdown threshold of the air decreases with the altitude before reaching the altitude having a minimum breakdown threshold field. The

appearance of such a minimum, similar to the Paschen minimum, can be explained as the result of breakdown by a short pulse that is equivalent to DC discharge with a short separation gap between electrodes (i.e., short electron transit time). The pulsed nature of the breakdown field also increases the level of the breakdown threshold because the available ionization time at any point along the trail of the pulse is finite and governed by the pulse duration. Beyond that minimum breakdown threshold altitude, the breakdown threshold starts to increase with the altitude. Thus, if the pulse is transmitted from the ground to the space, ω_{pe}^2 may increase continuously along the trail of the pulse and exceed $\omega_0^2 = \omega^2(t=0, z=0)$ before reaching the altitude of minimum breakdown threshold. However, there is no cutoff reflection throughout the propagation, if $\omega > \omega_{pe}$ initially. It is noted that such a frequency auto-conversion process also works for the pulse propagating from space to the ground since the breakdown threshold again decreases with the propagation distance before passing through the altitude of minimum breakdown threshold.

For the situation that $v_1 v_2 / (\omega^2 + v_2^2) \ll 1$ does not hold, one can show that the frequency down-shift can occur. Let the effective loss $v_1 v_2 / (\omega^2 + v_2^2) = \bar{\nu}$, the relative electron plasma density $\omega_{pe}^2 / (\omega^2 + v_2^2) = n_e / n_c = n$, where n_c is the cutoff plasma density for the wave, equation (14) reduces to

$$\frac{d}{dt}(\omega^2 - \omega_{pe}^2) = -\bar{\nu}[(1-n)/(1-\bar{\nu}n)] \frac{\partial}{\partial t} \omega_{pe}^2 - v_g \frac{\partial}{\partial z} \omega_{pe}^2 \quad (16)$$

where $\bar{\nu}$ and n are both less than 1, and $\partial \omega_{pe}^2 / \partial t \geq 0$ in most of the situations as the pulse is intensive enough to break down the gas. However, if the tail erosion is severe and the plasma loss is high, $\partial \omega_{pe}^2 / \partial t$ may be less than zero. The first term on the right hand side of equation (16) has the opposite sign to $\partial \omega_{pe}^2 / \partial t$, hence, when $\partial \omega_{pe}^2 / \partial t > 0$ and

$$\left| \bar{\nu}[(1-n)/(1-\bar{\nu}n)] \partial \omega_{pe}^2 / \partial t \right| > \left| v_g \partial \omega_{pe}^2 / \partial z \right|,$$

$d(\omega^2 - \omega_{pe}^2)/dt < 0$, the wave frequency is down-shifted. Therefore, in the case of $v_1 v_2 / (\omega^2 + v_2^2) \sim 1$, the frequency conversion may happen in either way, i.e. up- or down-shift, depending on the values of $\bar{\nu}$ and n , and the remaining field intensity whether it is strong enough to continuously breakdown the background gas. On the other hand, these factors are all related to each other. The $\bar{\nu}$ value depends on collision frequency and other loss processes, as well as the wave frequency. When plasma is created by the wave, the ionization loss of the wave also gives rise to the effective collision frequency which modifies the collisionless dispersion relation of

the wave to the form of collisional case. In fact, $\bar{\nu}$ is a measure of total effective loss rate, and is a function of background gas pressure, pulse intensity, electron plasma density and the wave frequency. The electron plasma density n is strongly dependent on intensity, width, shape of the pulse, the background gas breakdown threshold and the loss processes. Hence, only the values of collision frequency and the ratio of the pulse intensity to the breakdown threshold intensity of the background gas need to be considered in studying the frequency conversion process.

III. Experimental demonstrations of frequency conversion

The experiments of pulse propagation are conducted in a vacuum chamber filled with dry air. The chamber is made of a 2 foot cube of Plexiglas with the thickness of one inch. A microwave pulse is fed into the cube through an S-band horn placed at one side of the chamber. A second S-band horn placed at the opposite side of the chamber is used to receive the transmitted pulse. The microwave pulse is generated by a single magnetron tube (QKH 1448) driven by a soft tube modulator. The magnetron produces 1 MW peak output power at a central frequency of 3.27 GHz. The modulator is triggered by a pulse-forming network (PFN) having a pulse width of 1 μ s and a repetition rate ranging between 20 and 60 Hz. An HP 8569B spectrum analyzer is used to record and compare the spectra of the incident and the transmitted pulse.

The block diagram of the experimental setup is shown in Fig. 2. A directional coupler connected to the incident horn is used to monitor the spectrum of the input pulse which is used as a reference. The air pressure in the chamber is set to be about 0.2 torr. At this pressure, the electron-neutral collision frequency is about $1.2 \times 10^9 T_e^{1/2} s^{-1}$, where T_e is the electron temperature measured in eV. In order to avoid the undesired boundary effect, i.e., over ionization to cause cutoff reflection of the incident pulse at the incident boundary, the intensity of the incident pulse is limited to no more than 50% above the breakdown threshold power level. Consequently, the ionization frequency of the background gas is of the same order of magnitude as the electron-neutral collision frequency in the present experiments. Thus the amount of frequency up-shift and down-shift will be of the same order of magnitude and the cause of frequency down-shift can be examined conveniently.

The results of the experiments performed with a sequence of pulses having consecutively increasing incident powers are presented in the following. Shown in Figs. 3 (a)-(f) are the recorded spectra of the incident

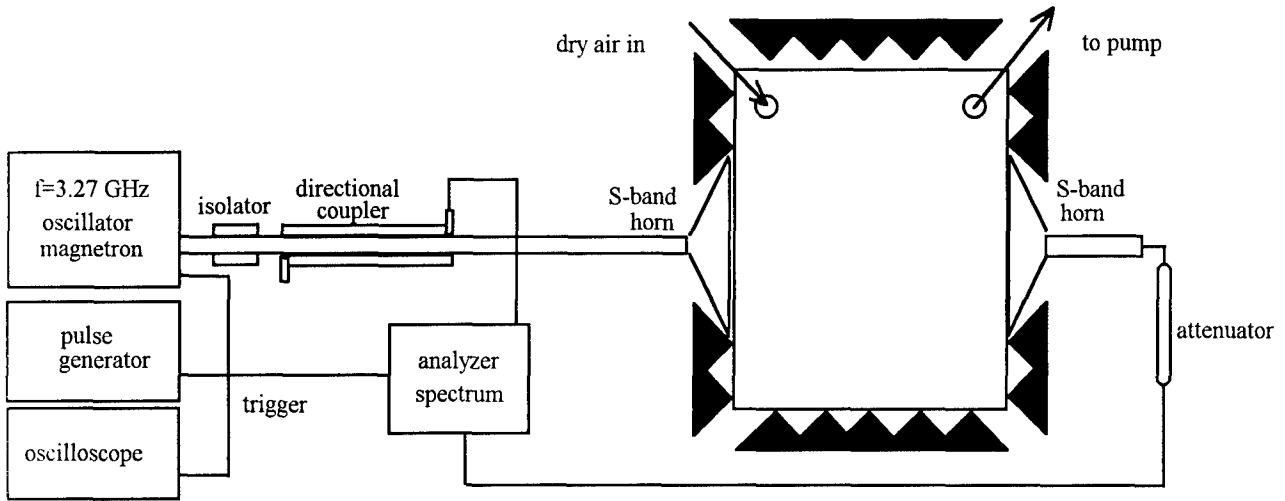


Fig. 2 Experimental setup for the experiment of high power microwave pulse propagating in a self-generated plasma.

and transmitted pulses for $P=1.05P_c$, $P=1.08P_c$, $P=1.14P_c$, $P=1.17P_c$, $P=1.32P_c$, and $P=1.37P_c$, respectively. The peaks of the transmitted pulses in Figs. 3 (a), (b) and (c) are shown to be up-shifted from the carrier frequency 3.27 GHz of the incident pulses. The up-shifted quantities are 0.08 MHz, 0.26 MHz and 0.45 MHz, respectively. Moreover Fig. 3 (c) shows that the spectrum of the transmitted pulse starts to become non-symmetrical and spectrum in Fig. 3 (d) start to break up, a down-shift component emerges. Figs. 3 (e) and (f) show an even more pronounced result. The spectra of the transmitted pulses have two clear peaks. One is up-shifted and the other one down-shifted from the single peak location of the incident pulse. The amount of frequency down-shift is shown to be comparable to that of frequency up-shift in each of the two cases.

IV. Numerical simulation

To solve the equation set of (1), (10) and (13), one first normalizes them into dimensionless forms. Using the following definitions: the cutoff plasma density

$n_c = (\omega^2 + \nu_2^2) m_e / (4\pi e^2)$, which leads to $n = \omega_{pe}^2 / (\omega^2 + \nu_2^2) = n_c / n_c$; $\tau = a\omega_0 t \rightarrow t$, where a is a dimensionless constant scaling number to keep the normalized time within a convenient numerical range; $z' = a\omega_0 z / c \rightarrow z$; $\nu_0 / c \rightarrow \nu_0$; $\nu_1 / \omega_0 \rightarrow \nu_1$; $\nu_a / \omega_0 \rightarrow \nu_a$; $\nu_1 / \omega_0 \rightarrow \nu_1$; $\nu_2 / \omega_0 \rightarrow \nu_2$; $\omega / \omega_0 \rightarrow \omega$; and $P / P_{th} \rightarrow P$. Then equation (1) becomes

$$\frac{\partial}{\partial t} n = (\nu_1 - \nu_a) n / a \quad (17)$$

where the recombination term γn_e^2 has been neglected. Similarly, equations (10) and (13) become

$$\frac{\partial}{\partial t} P + \frac{\partial}{\partial z} \{ [1 - n(1 + \nu_2^2 / \omega^2 - \nu_1 \nu_2 / \omega^2)]^{1/2} P \} = -n \nu_1 P / a \quad (18)$$

and

$$\frac{\partial}{\partial t} \omega^2 + \nu_g \frac{\partial}{\partial z} \omega^2 = \{ [1 - \nu_1 \nu_2 / (\omega^2 + \nu_2^2)] / [1 - n \nu_1 \nu_2 / (\omega^2 + \nu_2^2)] \} \frac{\partial}{\partial t} n \quad (19)$$

where $\partial \ln[1 / (\omega^2 + \nu_2^2)] / \partial t \ll \partial \ln(n) / \partial t$ is assumed, i.e. the density changes much faster than that of the wave frequency and collision frequency. The group velocity (12) is also normalized to

$$\nu_g = [1 - n(1 + \nu_2^2 / \omega^2 - \nu_1 \nu_2 / \omega^2)]^{1/2} / [1 - n \nu_1 \nu_2 / (\omega^2 + \nu_2^2)] \quad (20)$$

Equations (17), (18) and (19) together with (2) and (20) describe the microwave pulse propagating in a self-generated plasma in terms of the dimensionless variables n , P and ω . The normalized initial and boundary conditions are set to be:

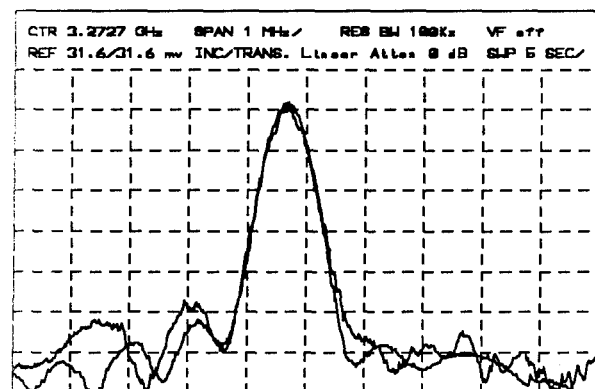
$$\begin{aligned} n(z, t=0) &= n_0, \\ P(z=0, t) &= P_0 \exp\{ -[(t-t_0)/t_0]^{10} \} \exp[0.3 \sin(t/t_0 + 0.35)] \\ \omega(z=0, t) &= 1, \text{ and } \omega(z, t=0) = 1, \end{aligned}$$

where n_0 is the background electron plasma density, P_0 is the power intensity of the pulse, $2t_0$ is the pulse width and $\exp\{ -[(t-t_0)/t_0]^{10} \}$ is used to model the rectangular pulse. The electron plasma density n is initially n_0 everywhere, and n is governed by equation (17) which is coupled to (18) through ν_1 . Since in the experiment, the envelope of the microwave pulse has three wiggles on top of the rectangular pulse, a factor of $\exp[0.3 \sin(t/t_0 + 0.35)]$ is multiplied to the rectangular pulse as the boundary condition of the power intensity $P(z=0, t)$. At the incident boundary $z=0$, P varies in time as a pulse with a width of $2t_0$, and at the initial

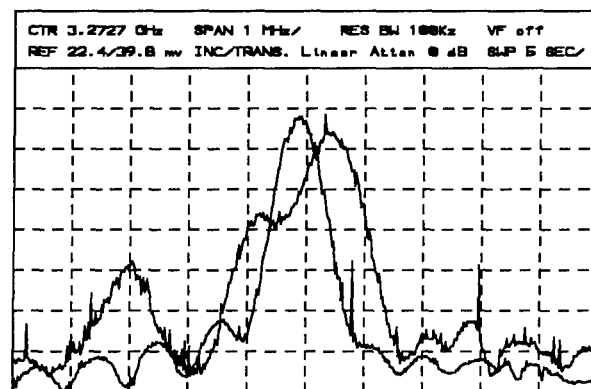
time $t=0$, the front of the pulse is just ready to propagate into the chamber. The frequency ω is 1 at the incident boundary $z=0$ and at the initial time $t=0$, and is governed by equation (19) as time evolves.

A numerical program using the LSODE software package^[16-18] is developed for solving the set of equations with the stated initial and boundary conditions. The parameters are chosen to correspond to those in the experiment, i.e., $t_0=0.5\mu\text{s} \rightarrow 0.5a\omega_0$,

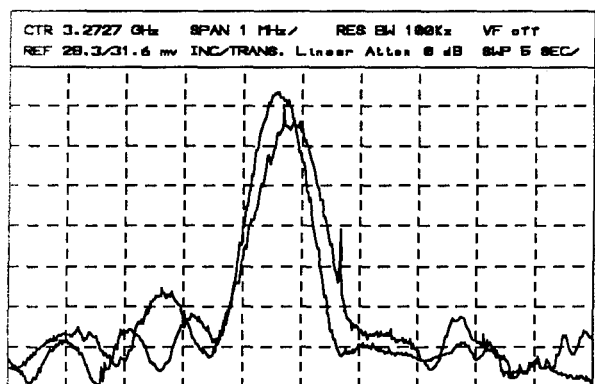
$v_a=6\times 10^4/\omega_0$, $n_0=10^{-5}$, and let the pressure p be 0.2 torr and the collision frequency $\nu=10\nu_0(P+0.03)^{1/2}$, where $\nu_0=4\times 10^9 p/\omega_0 \approx 8\times 10^8/\omega_0$. The spectra of the transmitted pulses corresponding to incident pulses of $P=1.05P_c$, $P=1.08P_c$, $P=1.14P_c$, $P=1.17P_c$, $P=1.32P_c$, and $P=1.37P_c$ are calculated. Figs. 4 (a)-(f) show the results of the numerical simulations. Comparing the spectra in



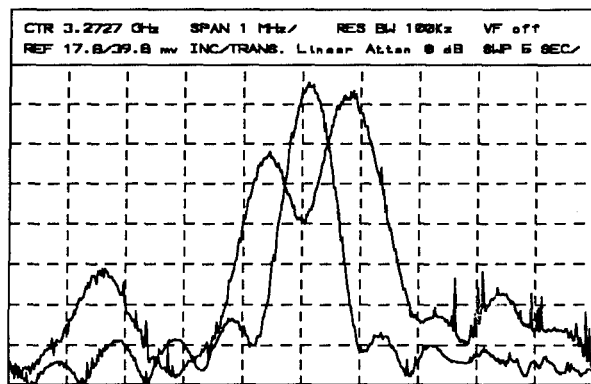
(a) Incident pulse power $P=1.05P_c$



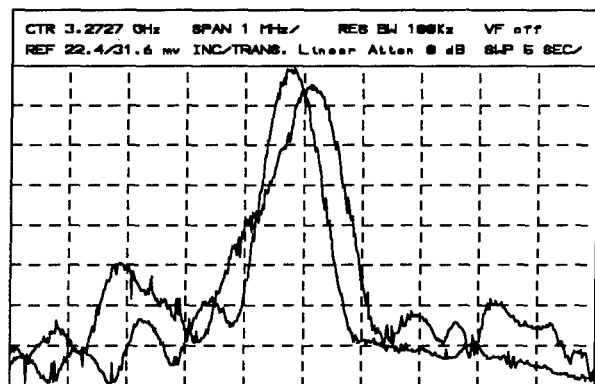
(d) Incident pulse power $P=1.17P_c$



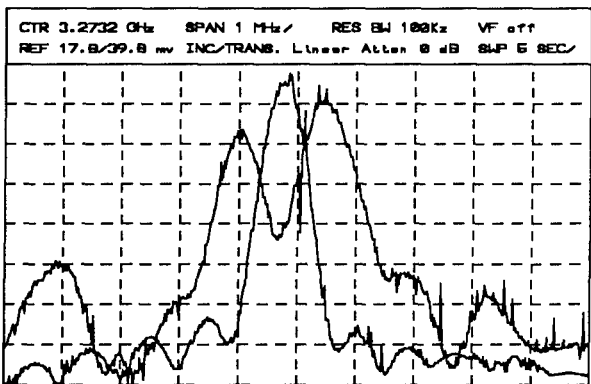
(b) Incident pulse power $P=1.08P_c$



(e) Incident pulse power $P=1.32P_c$



(c) Incident pulse power $P=1.14P_c$



(f) Incident pulse power $P=1.37P_c$

Fig. 3 The recorded spectra of the incident and transmitted pulse.

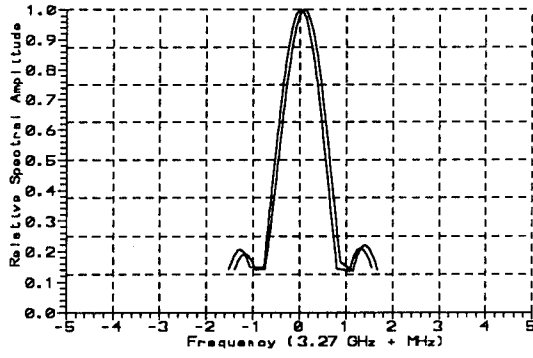
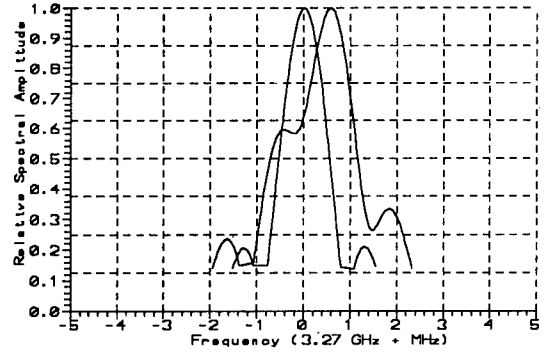
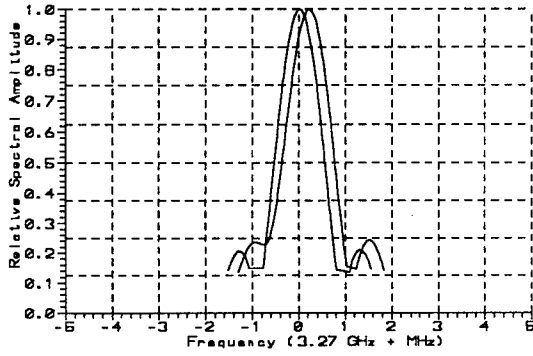
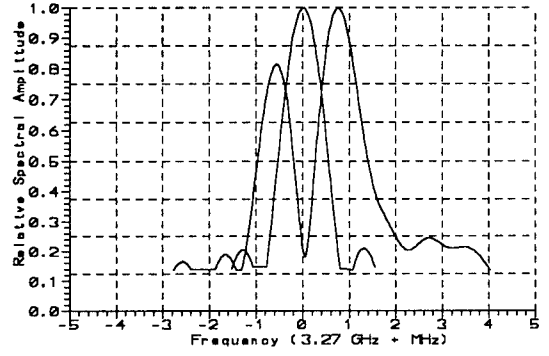
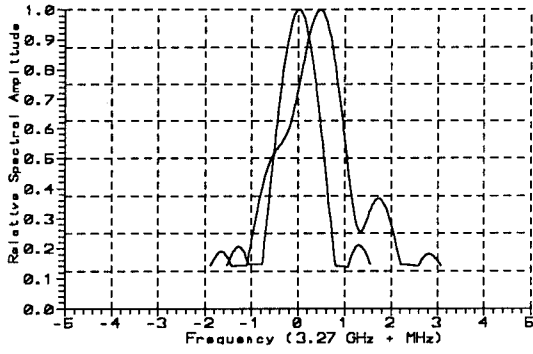
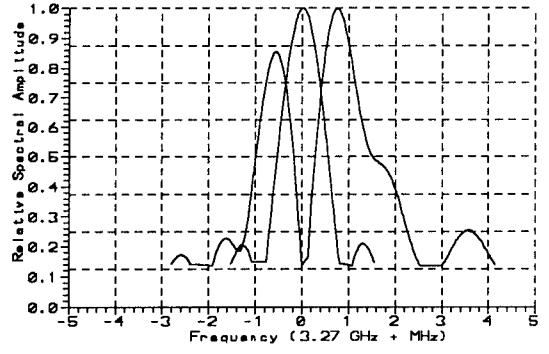
(a) Incident pulse power $P=1.05P_C$ (d) Incident pulse power $P=1.17P_C$ (b) Incident pulse power $P=1.08P_C$ (e) Incident pulse power $P=1.32P_C$ (c) Incident pulse power $P=1.14P_C$ (f) Incident pulse power $P=1.37P_C$

Fig. 4 The numerical results of the spectra of the incident and transmitted pulse.

Figs. 4 (a)-(c) to those in Figs. 3 (a)-(c), good agreements are seen. The amounts of frequency up-shift deduced from Figs. 4 (a)-(c) are 0.08 MHz, 0.23 MHz and 0.45 MHz, respectively, which also agree excellently with the experimental results. The spectral breaking phenomenon shown in Figs. 3 (d)-(f) also appears in the results of the numerical simulation as shown in Figs. 4 (d)-(f). These agreements validate the theoretical model presented in Section 2. To identify the role of effective collision frequency on causing the frequency down-shift and spectral breaking, the developed theoretical model is used to perform a series

of computer experiments. The results are presented in the next section.

V. Computer experiments to identify the collision loss as the cause mechanism of frequency down-shift and spectral breaking

To verify that the collisional loss is indeed the cause frequency down-shift, a series of computer experiments are conducted. It is done by multiplying a variable parameter ξ to the electron-neutral collision frequency ν in equations (17), (18) and (19) and varying ξ from 0.5 to 2. In general, ν_i and ν_a are

proportional to ν , however, their relationships are removed artificially in the computer experiments. In other words, only the electron-neutral collision frequency ν is varied artificially for a fixed background condition. In doing so, the role of ν on frequency down-shift may be identified unambiguously.

Presented in Fig. 5 is the dependencies of the amount of frequency down-shift $-\Delta f_d$ on ξ for different incident power levels. A monotonic increase of $-\Delta f_d$ with ξ is observed for all different incident powers. $-\Delta f_d$ also varies with the power of the incident pulse, P . It increases with P , and then reaches a saturation level as manifested by the overlap of the curves. On the other hand, the dependencies of the amount of frequency up-shift Δf_u on ξ and P presented in Fig. 6 show that Δf_u decreases monotonically with ξ , but increases with P , then reaches a saturation level. The frequency f_m , the minimum between the up-shift peak and down-shift peak of the spectrum of the transmitted pulse, also varies with ξ and P . The dependencies of $\Delta f_m (=f_m - f_c)$ on ξ and P are presented in Fig. 7. Similar to Δf_u , Δf_m decreases with ξ and increases with P , then reaches a saturation level, as shown in Fig. 7. These results clearly demonstrate that ξ plays an important role in determine frequency shift, in particular, in introducing the down-shifted frequency components in the spectrum of the transmitted pulse.

VI. Conclusion

The study of frequency conversion of a high power microwave pulse propagating in a self-generated plasma is presented in this paper. The theoretical model is first presented and the equation describing the frequency auto-conversion process is derived. It indicates that under the condition of $\nu_1 \nu_2 \ll (\omega^2 + \nu_2^2)$ the carrier frequency of the microwave pulse will be up-shifted. If the carrier frequency is greater than the plasma frequency at the incident boundary, during the propagation the carrier frequency of the pulse will be up-shifted continuously to keep higher than the plasma frequency of the self-generated plasma. Thus, the possible cutoff reflection process can be avoid and the erosion of the pulse energy by the self-generated plasma is minimized. Both the chamber experiments and the numerical simulations confirm this theoretical prediction of frequency up-shift phenomenon. In the situation that the loss of the pulse in the self-generated plasma becomes significant, i.e. the effective collision frequency $(\nu_1 \nu_2)^{1/2}$ is high comparing with the plasma frequency, frequency down-shift components appear together with the frequency up-shift components in the spectrum of the transmitted pulse. In other words, the spectrum of the pulse breaks up into two peaks up- and down-shifted from the original carrier frequency. The results of the computer experiments carried out via the developed theoretical model show that the collision frequency and the incident power are the two factors

causing the frequency down-shift and spectral breaking. Since the loss of the pulse increases with the incident power, the two factors are combined into one effective collision frequency determining the amount of frequency down-shift. It is realized qualitatively by the decreasing dependence of the wave phase velocity on the electron collision frequency as indicated qualitatively by the dispersion relation. The increasing dependence of frequency down-shift on electron-neutral collision frequency observed in the computer experiments suggests that the frequency down-shift phenomenon recorded in the experiments is indeed caused by the effective collisionality of the plasma^[19].

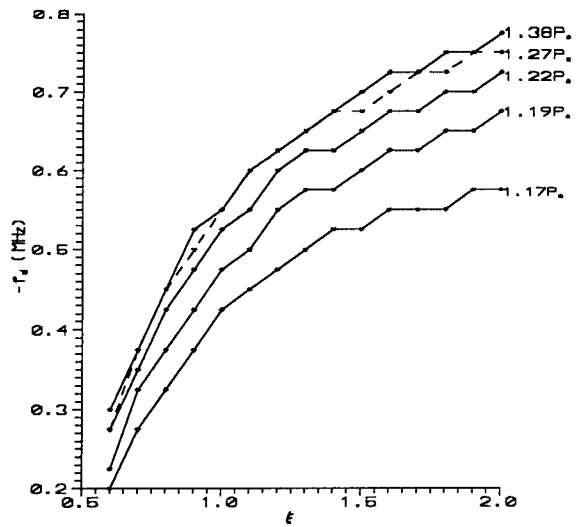


Fig. 5 $-\Delta f_d$ vs ξ and P

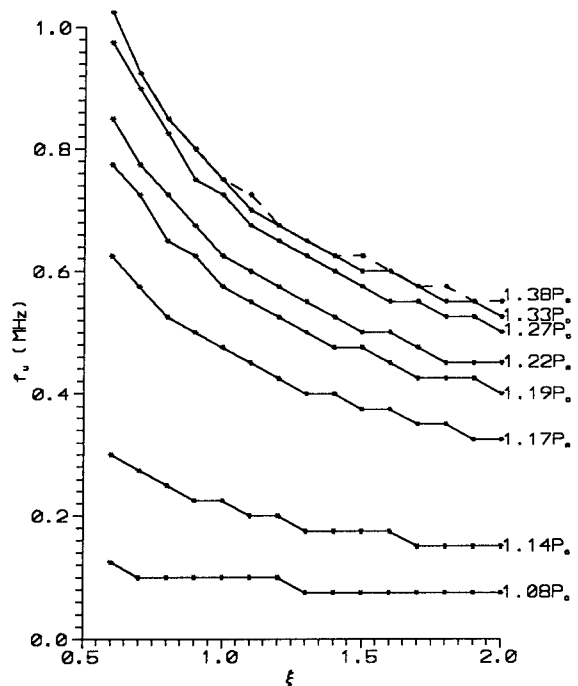


Fig. 6 Δf_u vs ξ and P

Therefore, in order to use the frequency up-conversion process to avoid the cutoff reflection of a high power microwave pulse by the self-generated plasma, one has to be sure that the effective collision frequency of the plasma is low comparing to the plasma frequency of the self-generated plasma. Otherwise, the effective loss process of the microwave pulse will cause part of the frequency spectrum of the pulse to down-shift, and tail erosion of the pulse may be severe.

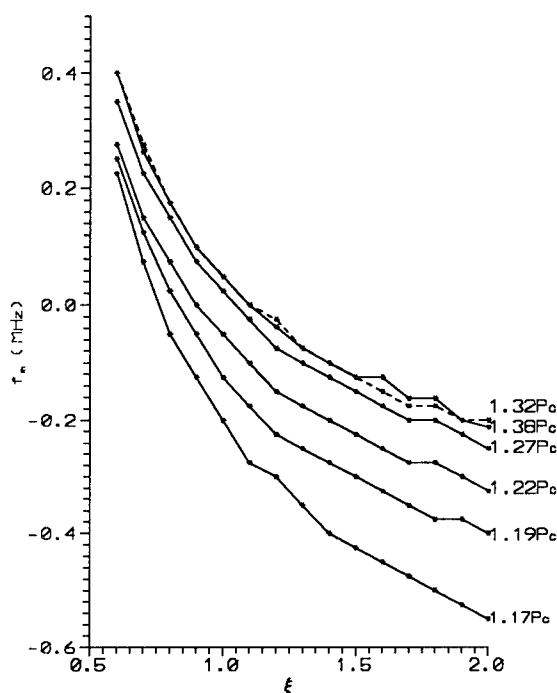


Fig. 7 Δf_m vs ξ and P

Acknowledgments:

This work is supported in part by the U.S. Air Force System Command, the Air Force Office of Scientific Research Grant F49620-94-0076 and in part by National Aeronautics and Space Administration (NASA) Grant NAG5-1051.

References:

1. W.M. Bollen, C.L. Yee, A.W. Ali, M.J. Nagurney, and M.E. Read, "High Power Microwave Energy Coupling to Nitrogen during Breakdown", *J. Appl. Phys.* vol. 54, No. 1, pp.101- , 1983.
2. Wee Woo and J.S. DeGroot, "Microwave Absorption and Plasma Heating due to Microwave Breakdown in the Atmosphere", *Phys. Fluids* 27, No. 2, pp.475-487, 1984.
3. J.H. Yee, R.A. Alvarez, D.J. Mayhall, D.P. Byrne, and J. DeGroot, "Theory of Intense Electromagnetic Pulse Propagation through the Atmosphere", *Phys. Fluids* 29, No. 4, pp.1238-1244, 1986.
4. M.J. Mulbrandon, J. Chen, P.J. Palmadesso, C.A. Sullivan, and A.M. Ali, "A Numerical Solution of the Boltzmann Equation for High-powered Short Pulse Microwave Breakdown in Nitrogen", *Phys. Fluids B* 1, No. 12, pp2507-2515, 1989.
5. S.P. Kuo, and Y.S. Zhang, "Bragg Scattering of Electromagnetic Waves by Microwave-Produced Plasma Layers", *Phys. Fluids B* 2, No. 3, pp.667-673, 1990.
6. S.P. Kuo, Y.S. Zhang, and Paul Kossey, "Propagation of High-power Microwave Pulses in Air Breakdown Environment", *J. Appl. Phys.* Vol. 67, No. 6, pp.2762-2766, 1990.
7. S.P. Kuo, and Y.S. Zhang, "A Theoretical Model for Intense Microwave Pulse Propagation in an Air Breakdown Environment", *Phys. Fluids B* 3, No. 10, pp2906-2912, 1991.
8. J.H. Yee, D.J. Mayhall, G.E. Sieger, and R.A. Alvarez, "Propagation of Intense Microwave Pulse in Air and in a Waveguide", *IEEE. Trans. Antennas and Propagation*, AP-39, pp.1421-1429, 1991.
9. S.P. Kuo, "Frequency Up-conversion of Microwave Pulse in a rapidly Growing Plasma", *Phys. Rev. Lett.*, Vol. 65, No. 8, pp.1000-1003, 1990.
10. S.P. Kuo, and A. Ren, "Experimental Study of Wave Propagation through a Rapidly Created Plasma", *IEEE. Trans. Plasma Science*, Vol. 21, No. 1, pp.53-56, 1993.
11. V.B. Gildenburg, V.A. Krupnov, and V.E. Semenov, "Frequency Autoconversion and Reflectionless Propagation of a Powerful Electromagnetic Pulse in an ionizing medium", *Sov. Tech. Phys. Lett.* 14, pp.783, 1988.
12. S.P. Kuo, Y.S. Zhang, and A. Ren, "Observation of Frequency Up-conversion in the Propagation of a High-power Microwave Pulse in a Self-generated Plasma", *Phys. Lett. A* 150, pp.92-96, 1990.
13. S.P. Kuo, and A. Ren, "Frequency Up-conversion of a High Power Microwave Pulse Propagating in a Self-generated Plasma", *J. Appl. Phys.* 71, No. 11, pp.5376-5380, 1992.
14. Yu. A. Lupan, "Refined Theory for a RF Discharge in Air", *Sov. Phys. Tech. Phys.* Vol. 21, No. 11, pp1367-1370, 1976.
15. A.V. Gurevich, "Ionization of the Lower Ionosphere under the Effect of Strong Radio Pulses", *Geomag. Aeronom.* 19, No. 4, pp.428-432, 1979.
16. A. C. Hindmarsh, "LSODE and LSODI, two initial value ordinary differential equation solvers", *ACM-SIGNUM newsletter*, Vol. 15, No. 4, pp.10-11, 1980.
17. L. R. Petzold, "Automatic Selection of Methods for Solving Stiff and Nonstiff Systems of Ordinary Differential Equations", *Sandia National Lab. Report*, SAND80-8230, Sept., 1980.
18. K. L. Hiebert and L. F. Shampine, "Implicitly Defined Output Points for Solutions of ODE's", *Sandia National Lab. Report*, SAND80-0180, Feb., 1980.
19. S. P. Kuo, A. Ren and G. Schmidt, "Frequency Down-shift in Rapidly ionizing Media", *Phys. Rev. E*, April issue, 1994.

DISCUSSION

LABAUNE

In your paper you have described the ionization process at the tip of the HF beam. This zone of ionization has a size which is a function of the rise time of the plasma formation. Some BF electromagnetic pulse must be radiated by this process (BF means spectral content linked with the plasma formation rise time). What's your opinion ?

AUTHOR'S REPLY

The plasma is highly collisional, if there is any radiation, its intensity is believed to be low. Moreover, the maximum plasma frequency of the experiment is about half of the carrier frequency of the pulse and thus, the radiation can not be included in the recorded spectrum which covers only about 10 MHz around the carrier frequency of the pulse.

In the future experiment we will try to check if there is any significant radiation from the plasma.

Nonlinear Optical Emission and Scattering in Micrometer-Sized Droplets

Gang Chen, Md. Mohiuddin Mazumder, J. Christian Swindal, Karl Schaschek, and Richard K. Chang
 Department of Applied Physics and Center for Laser Diagnostics
 Yale University
 P. O. Box 208284
 New Haven, Connecticut 06520-8284, USA

Summary

Absorption of high peak power microwaves by water droplets can induce a spatially inhomogeneous temperature rise inside the droplet, thereby affecting the droplet evaporation rate and surface tension. A minute decrease of the droplet radius and small amounts of shape distortion can be readily detected by analyzing the changes in the nonlinear optical emission from perturbed droplets. In the visible wavelength region, a micrometer-sized droplet acts as an optical cavity that provides high-Q optical feedback for the nonlinearly generated radiation, such as lasing. Cavity resonances occur at discrete wavelengths that are commensurate with the integer number of wavelengths that can fit into the droplet perimeter.

Intense nonlinear emission occurs whenever the round-trip gain is larger than the round-trip leakage from the droplet rim. A decrease of the droplet radius for example, associated with an increased evaporation rate, will cause all the nonlinear emission peaks to shift to shorter wavelengths. A shape distortion will cause the wavelengths of the nonlinear emission to vary along the droplet rim because the perimeters of the great ellipses change along the rim. Examples will be presented as to how spectral changes in the nonlinear emission can be used as a sensitive diagnostic probe of the size changes and shape distortions of flowing micrometer droplets.

Introduction

The illumination of high-energy electromagnetic radiation in clouds can increase the temperature of the water droplets, should the radiation wavelength λ be within the absorption bands of water or the molecular impurities in the water droplets. The spatial distribution of the heat deposited within the droplet will mimic that of the radiation energy within the droplets.¹ The spatial distribution of the radiation within the droplets¹ is expected to be uniform for small size parameter droplets with $x = 2\pi a/\lambda < 1$, where the droplet radius is a . A uniform deposition of heat will only increase the evaporation rate of droplets and the spatial distribution of the resultant temperature rise is expected to be only a function of the radius. Evaporative cooling will cause the temperature near the droplet surface to be lower than the temperature in the droplet core. For droplets with $x > 1$, the internal intensity or energy distribution is nonuniform and can be calculated with the standard Lorenz-Mie formalism for a droplet with a known complex index of refraction.² A nonuniform deposition of heat will not only increase the evaporation rate³ but also induce a droplet shape change⁴, e.g., destroy the spherical symmetry of an unilluminated droplet.

This paper presents a summary of optical diagnostics techniques that are capable of determining small decreases in the droplet radius⁵ and distortions in the droplet shape⁶. The technique is based on the morphology-dependent resonances (MDRs) of a droplet (with $x \gg 1$) that acts as a

high-Q optical cavity for the probe radiation which has its wavelength in the visible portion of the electromagnetic spectrum. The droplets may have $x < 1$ relative to the perturbing radiation (e.g., with λ in the microwave range), but must have $x \gg 1$ relative to the probe radiation (e.g., with λ in the near-UV to near-IR range). At present, the probe radiation is provided by the lasing radiation resulting from the fluorescent dyes that are purposely added to the droplets at concentration levels of 10^{-5} to 10^{-4} molar. In the future, it may be possible to use the elastic scattering spectrum to deduce small radius changes and distortion amplitudes of droplets that contain no fluorescent dyes. The sharp spectral peaks in the lasing or elastic scattering spectrum is highly sensitive to optical phase changes accumulated after many round trips around the droplet. Hence, it is possible to relate the spectral shifts to changes in the droplet radius and shape.

Resonant Modes of a Sphere

For a perfect sphere, a MDR is specified by three indices² that can be related to the spatial distribution (relative to the standard spherical coordinates) of the internal intensity (see Fig. 1). The first index is the mode order ℓ , which specifies the number of intensity peaks in the radial

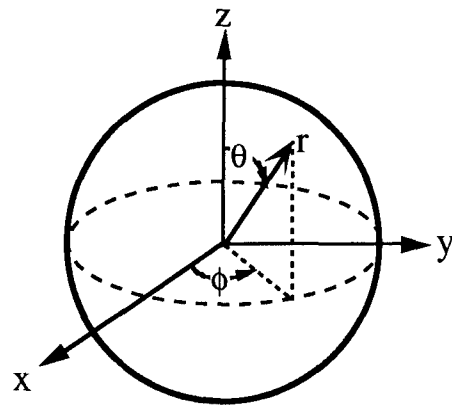


Figure 1 The spherical polar coordinates for the droplet

direction as r increases from 0 to a (see Fig. 2). The intensity distributions of MDRs are localized in a region between $a/n(\omega)$ and a , where $n(\omega)$ is the index of refraction of the liquid, e.g., $n(\omega) = 1.33$ for water. The second index is the mode number n , which specifies the number of intensity peaks in the equatorial plane as the azimuthal angle ϕ is varied from 0° to 180° (see Fig. 3). The third index is the azimuthal mode number m , which describes intensity distribution as a function of the polar angle θ (see Fig. 4). Although each m -mode possesses many intensity peaks in θ , the maximum intensity peak is located at

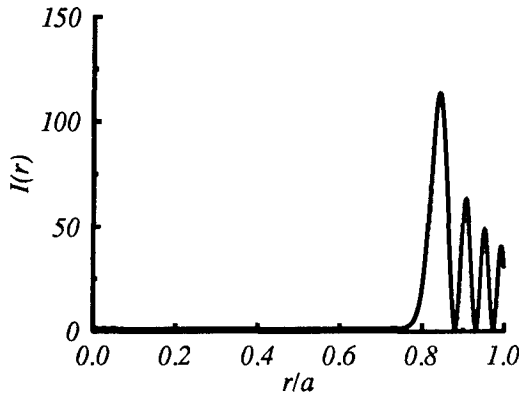


Figure 2 Angle-averaged internal intensity as a function of radial distance, r/a . $\ell = 4$, $n = 116$ and $n(\omega) = 1.36$.

$\theta = \sin^{-1}(m/n)$. The values of m range from $\pm n, \pm(n-1), \dots, 0$. It is convenient to envision the internal radiation to circulate around a great circle inclining at θ .

For a droplet with radius a , the resonant wavelength occurs as $x_{\ell,n,m}$. Because of spherical symmetry, the selection of the z -axis is arbitrary and, hence, the resonant wavelength ought not to be dependent on the azimuthal mode number m . In the Lorenz-Mie treatment of elastic scattering,⁷ the standard convention is to select the z -axis to be along the incident beam direction. For a spherical droplet, it is sufficient to specify the resonant wavelengths by two indices, $x_{\ell,n}$. Each MDR is therefore $(2n+1)$ degenerate. The round trip length around each great circle of a sphere is the same, in the model which assumes the internal radiation to be confined in great circles that are inclined at various θ 's for the different m -MDRs. Depending on the mode order ℓ , the internal radiation can be pictured as circulating in circles with $a/n(\omega) < r < a$.

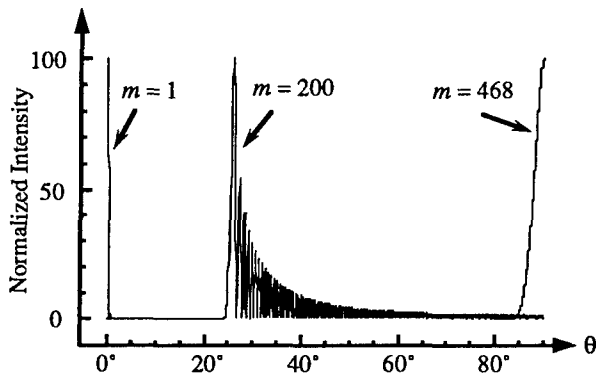


Figure 4 The internal intensity distribution as a function of θ for $n = 468$ MDRs with $|m| = 1, 100$, and 468 .

Resonant Modes of a Spheroid: Oblate or Prolate

For a spheroid, both T-matrix calculations⁸ and perturbation theory⁹ have shown that the m -MDRs are

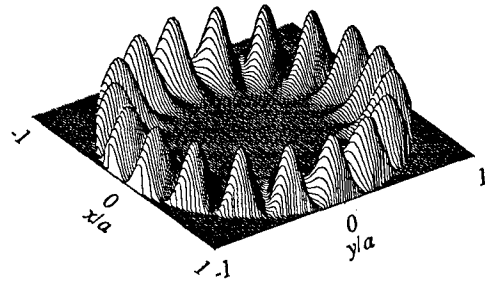


Figure 3 Intensity distribution in the equatorial plane for a MDR having $n = 9$ and $\ell = 1$. The droplet has $n(\omega) = 1.36$.

wavelength or frequency shifted from the $(2n+1)$ degenerate MDR (with $x_{\ell,n}$) of a sphere. When the distortion amplitude is small, the perturbation theory provides an analytical expression⁹ for the MDR frequency of a spheroid that depends on m^2 ;

$$\frac{\Delta\omega(m)}{\omega_0} \approx -\frac{e}{6} \left[1 - \frac{3m^2}{n(n+1)} \right], \quad (1)$$

where ω_0 is the frequency of a MDR at $x_{\ell,n}$, and the distortion amplitude is $e = (r_e - r_p)/a \ll 1$. The droplet polar and equatorial radii are r_p and r_e , respectively. The radius of the equivolume sphere is a .

The frequency shift expressed in Eq. (1) is independent of polarization, mode order ℓ , and droplet radius a . Three features are important in Eq. (1): (1) the frequency shift only depends on m^2 and consequently, there are $n+1$ different m -MDRs, i.e., the shape distortion does not completely lift the degeneracy and the m -MDRs are still doubly degenerate; (2) the frequency splitting for the m -MDRs is not uniform, i.e., the $|m| \approx n$ MDRs are more widely separated in frequency than the $|m| \ll n$ MDRs (see Fig. 5); and (3) the frequency shift from ω_0 for the $|m| \approx n$ MDRs is positive (for prolate spheroid with $r_p > r_e$) and is negative (for oblate spheroid with $r_p < r_e$). Figure 5 shows the frequency shift for the various m -MDRs for both prolate and oblate spheroids that have the same absolute value of e .

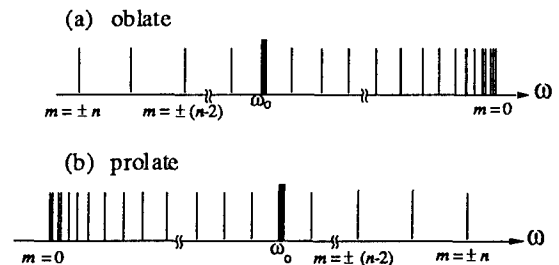


Figure 5 The schematic of the frequency shift expressed by Eq. (1) for (a) oblate and (b) prolate spheroid. ω_0 is the MDR frequency for a sphere with same mode number n .

In principle, by determining whether the frequency shift of $lm \approx n$ MDRs is positive or negative, the sign of e can be determined and hence, be able to determine whether the droplet is a prolate or oblate spheroid.

The evolution of MDRs from a perfect sphere, where each n -MDR is $(2n + 1)$ degenerate, to a slightly distorted oblate spheroid and, finally, to a more distorted oblate spheroid is shown in Fig. 6. The splitting between the n -MDRs can be readily estimated from asymptotic formulae,¹⁰ which for water droplets with $a \approx 50 \mu\text{m}$ is about 26 cm^{-1} . When the distortion amplitude e becomes large, the frequency splittings of the m -MDRs can approach that of the n -MDRs and, consequently, the elastic scattering or lasing spectrum will appear as a continuum.

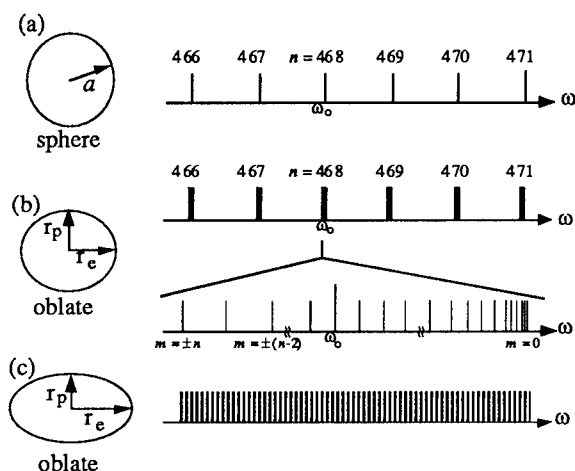


Figure 6 The evolution of MDRs from a perfect sphere (a), to a slightly distorted oblate spheroid (b), and to a severely distorted oblate spheroid (c). For a perfect sphere, all the azimuthal modes of a MDR with mode number n are $(2n + 1)$ degenerate. In (b), these degenerate modes appear to be broadened if spectrally unresolved, or are split if spectrally resolved. In (c), the split azimuthal modes form an overlapping spectrum.

Determination of Evaporation Rate

Direct visualization of the fluorescence from the vapor emanating from the evaporating droplets can be achieved. Figure 7 is a gray-scale image of the randomly spaced acetone droplets and acetone vapor surrounding the droplet stream. The fluorescence is strongest from the acetone droplets. The fluorescence from the acetone vapor trail can be seen for many droplet diameters on both sides of the droplet stream as the vapor diffuses and convects into the surrounding air. A magnified portion of the droplets shows a greater amount of acetone vapor trailing behind the flowing droplets which are traveling some 10 m/sec downward.

The vapor trail of surrounding droplets can affect the evaporation of individual droplets. One method of determining the evaporation rate of interacting droplets involves two separate measurements of the droplet radius at time t_0 and then at a later time $t_0 + \Delta t$. Any change in droplet radii Δa during Δt can be directly related to the decrease in droplet surface area as a result of evaporation.

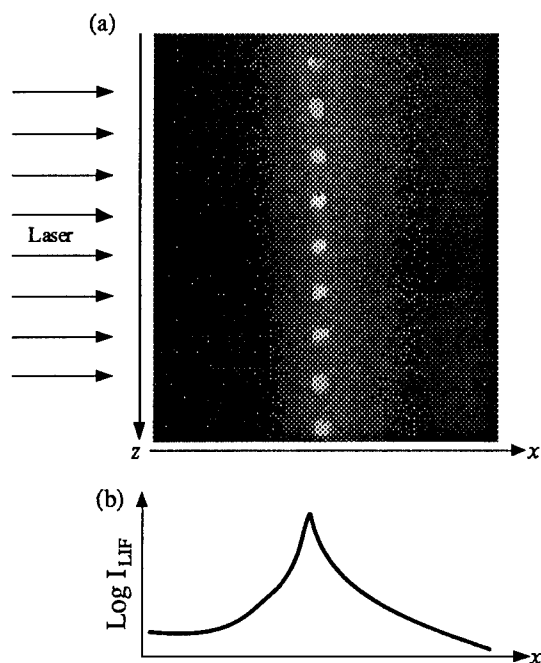


Figure 7 (a) The laser-induced fluorescence image of acetone vapor from a continuous droplet stream. The laser beam is incident from left to right. (b) The fluorescence-intensity profile across the acetone droplet stream (along the x -axis) which is obtained by integrating the data in (a) along the vertical direction (z -axis).

Another method to determine the evaporation rate involves one single measurement of the decrease in the radius of droplets in a linear stream. Because each droplet is produced with the same volume, any differences in the droplet radius must be ascribed to evaporation process. Figure 8 illustrates the relationship between the change in radius Δa with the change in n -MDR wavelength $\Delta\lambda$, i.e., a smaller droplet requires a shorter wavelength to be resonant with the same ℓ, n MDR.

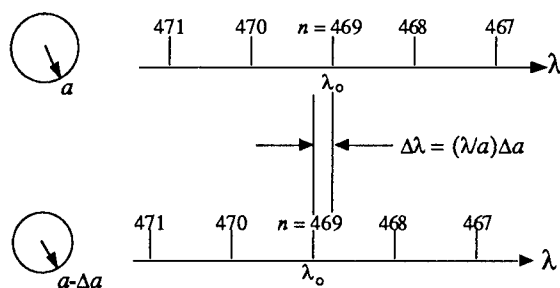


Figure 8 Two sets of MDR peaks with the same mode number n 's from two droplets with different sizes. The consecutive n 's imply that these MDR peaks are associated with the same order number ℓ .

The ethanol droplets used in this experiment contain a laser dye (5×10^{-4} M Rhodamine 6G) chosen for its low lasing threshold and for its orange-red lasing emission. Figure 9

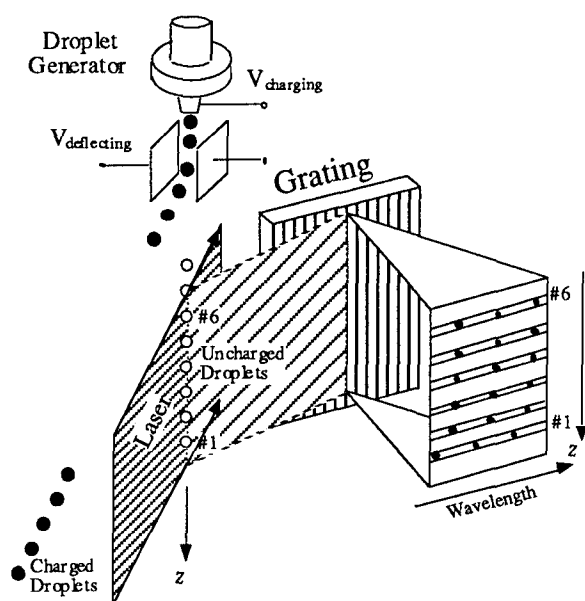


Figure. 9 The experimental arrangement. A laser beam is focused into a sheet and irradiates a continuous droplet stream (not shown) or an isolated segmented droplet stream. The dye-lasing signals from the droplets are collected at 90° with respect to the laser sheet. A CCD camera (not shown) records simultaneously the wavelength dispersed lasing spectra (along the horizontal axis) and the spatial location of each droplet (along the vertical z -axis).

shows the experimental setup that is able to detect simultaneously the MDR peaks in the lasing emission from numerous droplets in a continuous droplet stream or in an isolated droplet-stream segment. The green second-harmonic output of a Q-switched Nd:YAG laser (with wavelength at 532 nm and pulse duration of 7 ns) is focused with a cylindrical lens into a sheet along the droplet stream. Approximately 20 droplets, including the lead droplet in the segment are illuminated simultaneously by the sheet of green pump-laser beam. All the droplets except the lead droplet have a measured $a \approx 40.7 \mu\text{m}$ and $v \approx 10 \text{ m/s}$. The lasing droplets are imaged onto the entrance slit of an image spectrograph which is aligned at 90° with respect to the green-laser sheet. The droplet lasing spectra are dispersed along the spectrograph horizontal axis (wavelength) and the spatial position of the droplets, which is imaged along the entrance slit, is preserved along the vertical z -axis. A CCD camera (not shown in Fig. 9) is positioned at the exit plane of the spectrograph. With a single green-laser shot, a portion of the lasing spectra, consisting of the MDR-related peaks, is recorded while preserving the spatial locations of the droplets.

Figure 10 shows the lasing spectra (in grey scale and for wavelength between 588 and 592 nm) from 24 individual droplets in a continuous linear stream of droplets. For each droplet along the z -axis, the three bright lasing peaks correspond to three MDRs having the same order number ℓ but with consecutive mode numbers $n, n+1$, and $n+2$. The MDRs of a specific n is slightly shifted toward shorter wavelength for the droplets that are progressively further from the orifice (i.e., for the downstream droplets). The

same amount of blue-shift wavelength, for the droplets further downstream, is evident with all the three n -MDRs. Small amount of curvature (or bowing) in the λ versus z (along the stream) data of Fig. 10 is attributed to the inevitable aberration of the spectrograph. For a MDR of fixed ℓ and n and hence, for a fixed $x_{\ell,n}$, a change in the wavelength $\Delta\lambda$ corresponds to a change in the droplet radius, i.e., $\Delta a = (a/\lambda)\Delta\lambda$. This progressive shift of the MDRs to shorter wavelengths indicates that the droplets generated earlier or located further downstream from the orifice are smaller, consistent with the fact that these downstream droplets have had longer time to evaporate. Because all the droplets are in the same environment, the evaporation rate for each droplet in the continuous stream should be identical. We deduce from the spectral shift data that the radius change is approximately 1.4 nm between successive droplets that are temporally generated 0.02 ms apart. Hence, the surface area change per unit time of each droplet in the continuous stream $(dA/dt)_{\text{stream}}$ is equal to $-7.2 \times 10^{-4} \text{ cm}^2/\text{sec}$. Because of the vapor wake effect of the preceding droplets, this evaporation rate is lower than that of a single ethanol droplet which is estimated to be $(dA/dt)_{\text{single}} = -11.4 \times 10^{-4} \text{ cm}^2/\text{sec}$.

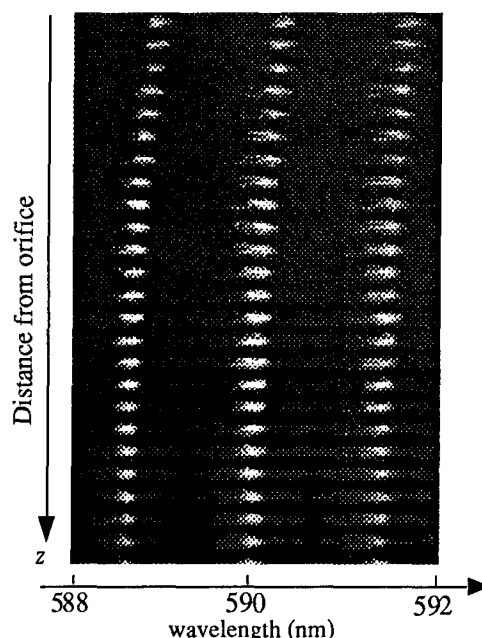


Figure 10 The spectrally and spatially resolved CCD recording of the lasing droplets in a continuous droplet stream. All the droplets are uncharged. The distance between the center of the droplet stream and the orifice is 20 mm.

Evaporation Rate Measurement in a Segmented Stream

Figure 11 shows the spatially resolved MDR-related lasing spectra of an isolated uncharged-droplet segment that includes the lead droplet (droplet #1). Note in Fig. 11 the dark region below the lead droplet indicates that the unwanted charged droplets have been successfully deflected and well separated from the uncharged segmented-droplet stream. In fact, by 20 mm below the orifice, the lateral displacement of the charged-droplet stream is several

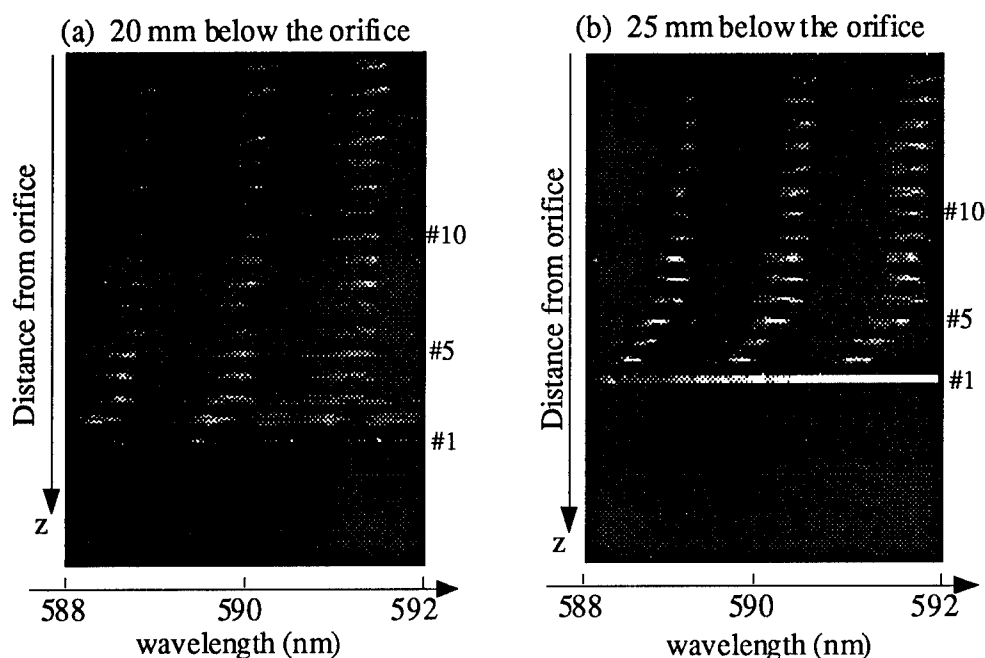


Figure 11 The spectrally and spatially resolved CCD recordings of an isolated segmented droplet stream at (a) 20 mm below the orifice and (b) at 25 mm below the orifice. Between (a) and (b), the time delay of the pump laser pulse is 0.5 ms. The lasing spectrum of the lead droplet is a continuum. Droplet #2, which is distinct in (a), is just about to coalesce with the lead droplet in (b).

millimeters from the uncharged-droplet segment. Figure 11(a) records the MDR-related dye-lasing spectrum of 18 uncharged droplets at 20 mm below the orifice of droplet generator. Figure 11(b) records the MDR-related dye-lasing spectrum at 25 mm below the orifice. This further distance downstream measurement [Fig. 11(b)] is achieved by delaying the green pump-laser pulse for 0.5 ms relative to the charging pulse and by raising the height of the entire droplet generator along with the charging collar and the deflection plates by 5 mm. During the time required to raise the height of the assembly (droplet generator, charging collar, and deflection plates), it is confirmed that the droplet generator is producing the highly stable droplets, e.g., by noting that in Figs. 11(a) and 11(b), the wavelength spacing between MDRs with consecutive n 's are equal.

The position difference of the droplet segment in the CCD pictures in Figs. 11(a) and 11(b) is attributed to the larger drag that effects the droplet segment. When the deflecting voltage is turned off, the uncharged segment travels along the same line as the stream of charged droplets. However, there exists a slight change in the droplet-droplet spacing between the last charged droplet and the first uncharged droplet, i.e., between the transition of the charged and uncharged segments. This slight variation in the droplet-droplet spacing is attributed to the unbalanced Coulomb repulsion among the droplets in the continuous stream, at the transition of the charged and uncharged segments. The distinguishable transition region enables us to keep track of the location of the uncharged droplets even when these droplets form part of the continuous stream. In the CCD pictures (not shown), when the deflecting voltage is off, the uncharged droplets appear at the same position when this segment is at $z = 20$ mm [as in Figs. 11(a)] and at $z = 25$ mm for an extra 0.5 ms delay [as in Fig. 11(b)]. In fact, this is how we determined the droplet flow speed to be

$v \approx 10$ m/s. However, when the downstream charged droplets, along with their vapor wake, are deflected, the increased drag slows down the droplets flow in the uncharged segment. A decrease in droplets flow speed results in the droplets position difference observed between Figs. 11(a) and 11(b).

In Figs. 11(a) and 11(b), for the droplets further upstream in the segmented stream, the progressive wavelength shift to shorter wavelength (e.g., for droplet #18 through droplet #7) is similar to that in the continuous droplet stream shown in Fig. 10. Consequently, we conclude that the evaporation rate for these upstream droplets in the isolated segment is equal to that of a droplet in the continuous stream. However, for droplet #6 to droplet #2 in the isolated segment, the MDRs are shifted more towards the shorter wavelength, implying that the droplet radii for these five droplets are decreasing faster because their evaporation rates are larger than that of the droplets further upstream (e.g., for droplet #18 through droplet #7). Because of the severe shape distortion of the lead droplet, the lasing spectrum of the lead droplet is a continuum. Unfortunately, we are not able to determine the size of the lead droplet from the MDR-related peaks in the continuum lasing spectrum. By viewing through a microscope, we can verify that the lead droplet is much larger (i.e., about 3x the volume of the trailing droplets) and much more distorted than the trailing droplets.

By comparing Figs. 11(a) and 11(b), it is noticed that all the MDRs for the droplets at $z = 25$ mm below the orifice are further shifted to shorter wavelength relative to the corresponding MDRs for the droplets at $z = 20$ mm. In particular, the relative MDR shifts for droplet #6 through droplet #2 at $z = 25$ mm [see Fig. 11(b)] are larger than those at $z = 20$ mm [see Fig. 11(a)]. At a flow speed of 10 m/sec, these droplets at $z = 25$ mm have been out of the

orifice ≈ 0.5 ms longer than when these droplets were at $z = 20$ mm. When the droplets have unequal evaporation rates, the differences in the droplet size become more apparent the further away the droplets are from the orifice or the longer the droplets have been out of the orifice. Also, it can be noticed that droplet #2 is well separated from the lead droplet at $z = 20$ mm from the orifice, and however, droplet #2 is about to coalesce with the lead droplet at $z = 25$ mm below the orifice. At further distance from the orifice ($z > 25$ mm), droplet #2 actually coalesces with the lead droplet, because the lead droplet experiences a larger drag than the trailing droplets.

The droplet evaporation rate dA/dt can be readily deduced from the MDR-related lasing spectra that are shown in Figs. 11(a) and 11(b). Between the droplets at $z = 20$ mm and at $z = 25$ mm, the MDR shift $\Delta\lambda$ for each droplet can be directly related to the droplet size change Δa because $\Delta a = (a/\lambda) \Delta\lambda$. Furthermore, Δa is related to the surface area change because $\Delta A = 8\pi a \Delta a$. In addition, it is known that the relative time difference $\Delta t = 0.5$ ms between the droplets at $z = 20$ mm and at $z = 25$ mm. Hence, we can readily estimate the evaporation rate for each droplet in the isolated segment. The measured evaporation rates for droplet #2 through droplet #7 in the isolated droplet-stream segment are tabulated in Figure 12. We are unable to estimate the evaporation rate of the highly distorted lead droplet because it yields a continuum lasing spectrum. From Fig. 12, it is apparent that the evaporation rates for droplet #2 through droplet #6 in the isolated segment are unequal, i.e., the evaporation rates are progressively smaller for the trailing droplets. However, the evaporation rate for the droplets trailing behind droplet #6 (in the isolated droplet segment) is nearly equal to the evaporation rate for the droplets in the continuous stream.










#n		$\frac{dA}{dt} = -7.2 \times 10^{-4} \text{ cm}^2/\text{sec}$
		
#7		$\frac{dA}{dt} = -7.3 \times 10^{-4} \text{ cm}^2/\text{sec}$
#6		$\frac{dA}{dt} = -7.5 \times 10^{-4} \text{ cm}^2/\text{sec}$
#5		$\frac{dA}{dt} = -8.1 \times 10^{-4} \text{ cm}^2/\text{sec}$
#4		$\frac{dA}{dt} = -8.7 \times 10^{-4} \text{ cm}^2/\text{sec}$
#3		$\frac{dA}{dt} = -9.2 \times 10^{-4} \text{ cm}^2/\text{sec}$
#2		$\frac{dA}{dt} = -11.2 \times 10^{-4} \text{ cm}^2/\text{sec}$
#1		? (continuum spectrum)

Figure 12 The tabulation of droplet evaporation rates (expressed as the decreasing rate of the droplet surface area) for the first several droplets in a segmented droplet stream. Because the lead droplet is so distorted that evaporation rate cannot be determined with the spectroscopic technique.

Determination of Droplet Shape Deformation

The "comet tail" or \hookrightarrow -shaped lasing spectra shown in Figs. 10 and 11 is a manifestation of droplet shape distortion. At low pump intensity ($\approx 5 \text{ MW/cm}^2$), the lasing image from each droplet is an orange ring (the center wavelength of the lasing emission is at 590 nm) that is brighter at the droplet equator and dimmer toward the droplet poles. The intensity variation along the droplet rim is because the equatorial MDRs (with $|m| \approx n$) have better spatial overlap with the internal distribution of the pump radiation. Thus, these $|m| \approx n$ MDRs reach the lasing threshold before the MDRs near the poles. At high-pump intensity ($\approx 10 \text{ MW/cm}^2$), the bright orange ring of lasing droplet image becomes more uniform because the lasing gain is saturated for the equatorial MDRs (with $|m| \approx n$). In addition, the lasing threshold is also reached for those polar MDRs (with $|m| \approx 0$) that have smaller spatial overlap with the internal distribution of the pump intensity. In order to achieve the lasing emission from the entire droplet rim, the input laser intensity is kept at about 10 MW/cm^2 throughout the experiment.

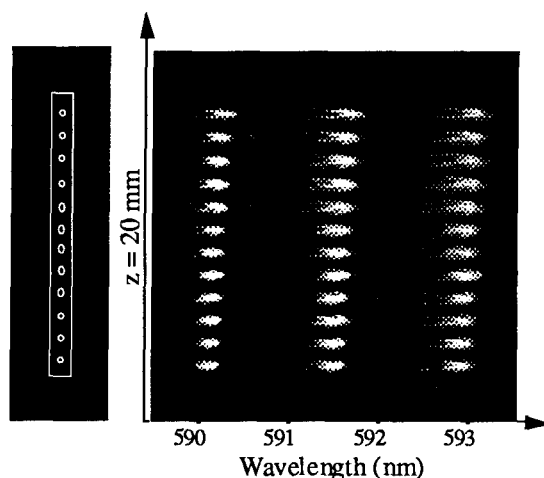


Figure 13 The left side shows at low magnification (2x), the entire image of lasing droplets (20 mm below the orifice) fits into the spectrograph entrance slit (200 μm wide). The right side shows the spatially preserved wavelength-dispersed data captured by a CCD camera. Note that the \hookrightarrow -shaped curve is barely resolved spatially.

The left-hand side of Fig. 13 shows that, with low magnification ($\approx 2\times$), the entire image of twelve droplets (centered at $z = 20$ mm downstream of the orifice) fits into the image spectrograph entrance slit (200 μm wide by 1 cm high). With medium magnification ($\approx 5\times$), only the right-hand or left-hand halves of the circular image of five droplets (centered at $z = 15$ mm) are imaged on the entrance slit (250 μm wide by 1 cm high) [see left-hand side of Figs. 14(a) and 14(b)]. Figure 15(a) shows that with large magnification ($\approx 20\times$), the right half of a single droplet (at $z = 10$ mm) is imaged on the spectrograph entrance slit (800 μm wide by 1 cm high). Figure 15(b) and the right-hand sides of Figs. 13 and 14 display (in grey scale) the CCD recordings of the spectrally dispersed laser emission for the droplet images shown on Fig. 15(a) and on the left-hand sides of Figs. 13 and 14. Notice that all the spatially

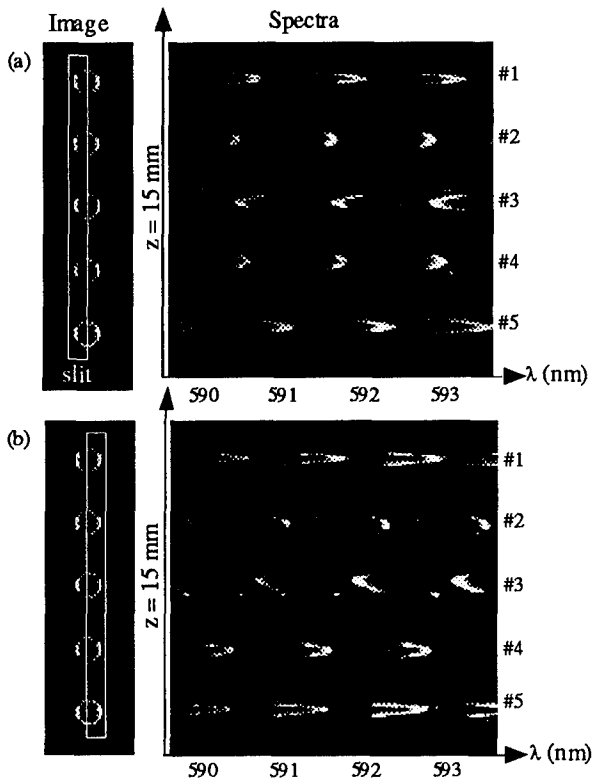


Figure 14 At medium magnification (5x), the CCD image of the lasing droplets (15 mm below the orifice) as they appear at the entrance slit (250 μm wide) of a spectrograph (left column). For (a) the right-half rim and for (b) the left-half rim is imaged onto the slit. The spatially preserved wavelength-dispersed data captured by a CCD camera are shown on the right side. Note the \hookleftarrow - and \hookrightarrow -shaped curves are better resolved spatially than in Fig. 13.

preserved spectra exhibit \hookleftarrow -shaped or \hookrightarrow -shaped curves (similar spectra have been shown in Figs 10 and 11). For the droplet size-parameters ($x \approx 379$) and fixed polarization (TE or TM), the consecutive n -MDRs (for a fixed ℓ) are separated by ≈ 1.25 nm at $\lambda = 591$ nm. At least three n -MDRs are detected in Figs. 7.2 and 7.4(b) and four n -MDRs are detected in Figs. 14(a) and 14(b).

When the entire droplet is imaged into the entrance slit of an image spectrograph (as shown in Fig. 13), the spectral resolution of the spectrograph is limited by the entrance-slit width. However, when the image on the entrance slit is a sharp line source (as the semi-circular rings shown in Figs. 14 and 15), the spectral resolution of the image spectrograph is limited by the source line-thickness, not by the slit width. Hence, the spectral resolutions in Figs. 14 and 15 are better than that in Fig. 13, even though the slit widths in Fig. 14 (500 μm) and Fig. 15 (800 μm) are wider than the slit width in Fig. 13 (200 μm). Consequently, the \hookleftarrow -shaped or \hookrightarrow -shaped curves in Figs. 14 and 15 are sharper than the \hookrightarrow -shaped curves in Fig. 13.

The first cause of the \hookleftarrow -shaped or \hookrightarrow -shaped curves is attributed to the wavelength dispersion of $\lambda(m)$ of the lasing radiation that leaks from the entire droplet rim. The

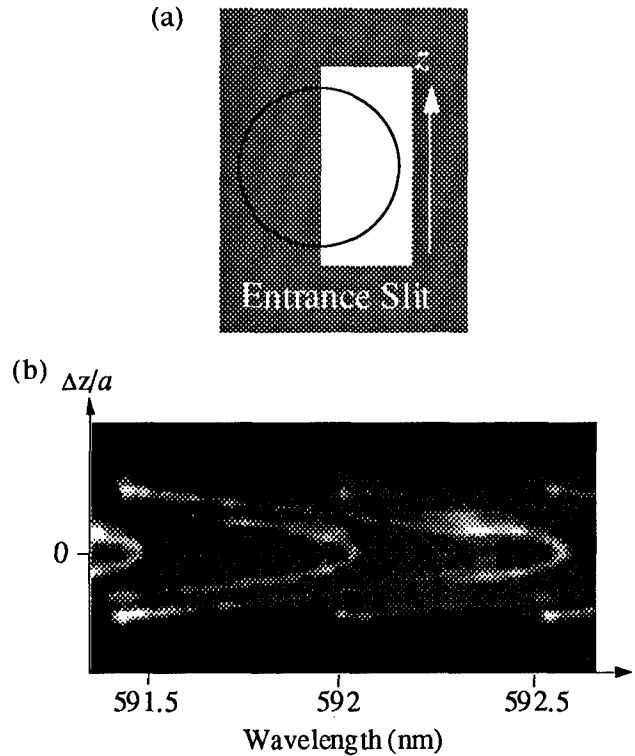


Figure 15 (a) At larger magnification (20x), the right half of circular image of a single droplet (10 mm below the orifice) fits into the entrance slit (800 μm wide) of a spectrograph. (b) The spatially preserved wavelength-dispersed data captured by a CCD camera.

wavelength of the lasing emission extending from the droplet equator ($\theta = 90^\circ$) to the droplet poles ($\theta = 0^\circ$) is associated with the m -mode MDRs ranging from $|m| = n$ to $|m| = 0$, respectively. The energy density of a m -mode MDR with mode number n peaks at $\theta = \sin^{-1}(m/n)$. From geometrical consideration, $\cos\theta = (\Delta z/a)$, where $|\Delta z| \leq a$ is the projection of the rim along the spectrograph slit, measured from the center of each droplet [see Fig. 16(a)]. By using $\omega(m)$ from Eq. (1) [see Fig. 16(c)] and $|m| = n\sin\theta = n[1 - (\Delta z/a)^2]^{1/2}$, the wavelength from various points on the droplet rim can be related to the vertical displacement Δz from the droplet center,

$$\lambda(\Delta z) = \lambda_0 \left[1 - \frac{e}{3} + \frac{e}{2} \left(\frac{\Delta z}{a} \right)^2 \right], \quad (2)$$

where λ_0 is the wavelength of the degenerate MDRs, i.e., $\lambda_0 = 2\pi c/\omega_0$, where c is the speed of light. In deriving Eq. (2), it is assumed that $|e| \ll 1$ and $n/(n+1) \approx 1$, which is valid for the droplet with size parameter $x \gg 1$.

Note that the shape of $\lambda(\Delta z)$ is parabolic with respect to Δz [see Fig. 16(b)]. More importantly, the orientation of the parabola is dependent on the sign of e or on the shape of the droplet, i.e., $\lambda(\Delta z)$ is \hookrightarrow -shaped for an oblate spheroid [shown in Fig. 16(b)] and \hookleftarrow -shaped for a prolate spheroid

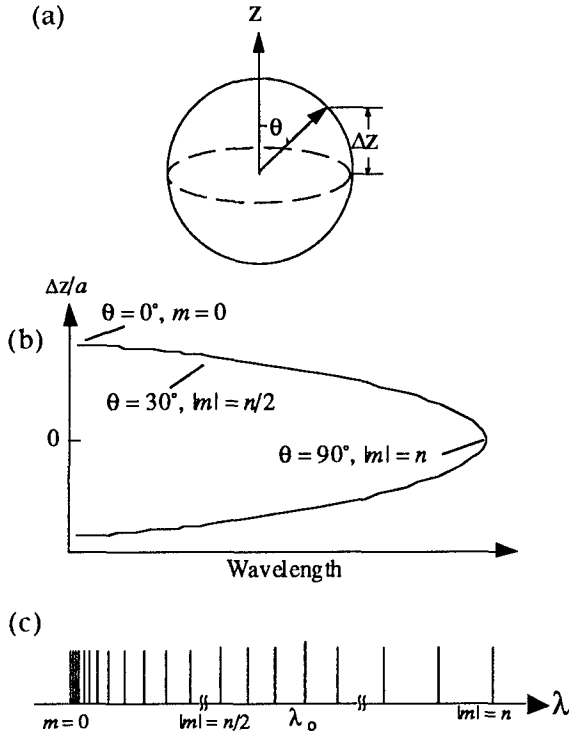


Figure 16 (a) Shows the definition of θ and Δz . (b) Illustrates the wavelength dependence of the light from different positions (with different θ and Δz) on an oblate droplet rim. Various parts of the parabolic $\lambda(\Delta z)$ curve can be related to the different m -MDRs. (c) The MDRs mode splitting and frequency shifts are based on Eq. (1)

(not shown). Figure 16(b) also illustrates the correspondence of three specific m -MDRs (with $|m| = n$, $|m| = n/2$, and $m = 0$) and their specific $\lambda(\Delta z)$ for an oblate spheroid. The \cap -shaped $\lambda(\Delta z)$ curve shown in Fig. 16(b) corresponds to the lasing spectrum of all m -MDRs with a fixed order number ℓ and a fixed mode number n .

The second cause of the \cap -shaped or \cup -shaped curves is associated with the artifact introduced by the semi-circular image of the droplet rim at the entrance slit. In addition to the dispersion, the spectrograph also images the object on the entrance to the exit plane. Because of the combined result of dispersion and imaging, the length of the \cap -shaped or \cup -shaped $\lambda(\Delta z)$ curve is dependent on whether the right half or the left half of the droplet is imaged onto the slit. The image artifact is linearly dependent on the total extent of the image on the entrance slit, e.g., the artifact in the spectrum in Fig. 15 should be about four times larger than that in Fig. 14 because the image on the slit in Fig. 15 extends about four times wider than that in Fig. 14.

Note that in Eq. (2), $\lambda(\Delta z)$ does not depend on n explicitly. Therefore, the droplet distortion e can be determined just from the curvature of $\lambda(\Delta z)$, without knowing or having to determine the mode number n . To determine the magnitude and sign of e from a CCD image in Fig. 15(b), correction is first made for the semi-circular-shape image artifact. The image artifact is determined by setting the spectrograph grating to the zeroth order and taking a CCD picture when

only the semi-circular image artifact is present. However, an angular factor of the grating needs to be taken into account for the image correction, because the grating angle at zeroth order is different from the grating angle when the dispersion of the laser emission is taken. The experimental data points are extracted from the CCD data by selecting peak intensity points along one segment of a \cap -shaped curve shown in Fig. 15(b). Figure 17 shows the semi-circular image-subtracted $\lambda(\Delta z)$ data (designated as + points) which was previously displayed in Fig. 15(b) in the image-uncorrected form and thus, retained the image artifact.

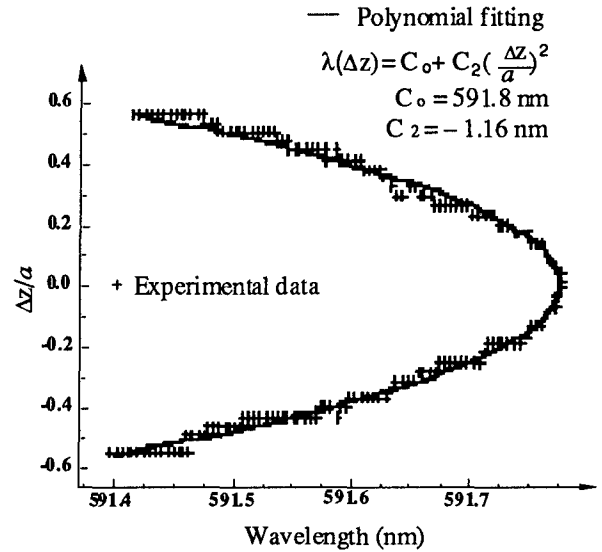


Figure 17 The + symbols designate the image-artifact corrected $\lambda(\Delta z)$ data extracted from one of the \cap -curves shown in Fig. 15(b). The solid curve is the second-order polynomial fit $\lambda(\Delta z) = C_0 + C_2(\Delta z/a)^2$. To reach the least-squared-error, $C_0 = 591.8 \text{ nm}$ and $C_2 = -1.16 \text{ nm}$.

Figure 17 also shows the second order polynomial fit [solid curve for $\lambda(\Delta z) = C_0 + C_2(\Delta z/a)^2$] of the corrected experimental data. C_0 and C_2 are obtained from the least-squared-error fit. By using Eq. (2), $\lambda_0 = 591 \text{ nm}$ and $e = -4 \times 10^{-3}$ are obtained, where the minus sign denotes the oblate shape. At $z = 10 \text{ mm}$, the droplet distortion is caused by the residual quadrupolar shape oscillation induced during the production of the droplets just below the orifice. At the same height ($z = 10 \text{ mm}$), we can also observe the similar parabolic $\lambda(\Delta z)$ lasing spectrum as in Fig. 15(b) but with the opposite orientation, i.e., the $\lambda(\Delta z)$ corresponds to a prolate droplet. By $z = 20 \text{ mm}$, the shape oscillations have all been dampened by viscous forces and the residual steady-state distortion is caused by the inertial force associated with the flowing droplets.

In Fig. 13, the droplet image is so small that the entire image enters the entrance slit (200 μm wide) and spans only a few CCD pixels size in the vertical direction. The actual CCD recording shows that the \cap -shaped $\lambda(\Delta z)$ curve is barely resolved spatially and therefore, we are not able to use the parabolic-curve fitting method to determine the droplet distortion e . However, because the curved-image artifact of the spectrograph is proportional to the entrance-slit width while the dispersion of the spectrograph is

independent on the slit width, the curved-image artifact in Fig. 13 is negligible for small slit widths. Hence, we can approximately attribute the \supset -shaped curve to the spectral extent of m -MDRs ranging from $|m| \approx 0$ to $|m| \approx n$, because the lasing emission is from the *entire* droplet rim. From Eq. (1) or Eq. (2), the frequency extent of all m -MDRs $\Delta\lambda_{all}$ with $|m|$ ranging from 0 to n is found to be:

$$\Delta\lambda_{all} = \lambda_0 \left(\frac{e}{2} \right), \quad (3)$$

where λ_0 is the degenerate MDR wavelength, which can be approximately assumed as the midway wavelength of the \supset -shaped curve. Note again that Eq. (3) is only valid if the lasing emission occurs for all the m -modes, ranging from $|m| = 0$ to $|m| = n$. By using Eq. (3), $e \approx -2 \times 10^{-3}$ is obtained for those droplets in Fig. 13, where the minus sign is deduced from the orientation of barely discernible "comet tails" in the CCD recording.

Conclusion

Both the spherical and spheroidal droplets serve as high-Q optical cavities, when the wavelength of the probe radiation (either of the incident or the fluorescent/lasing) is much smaller than the droplet circumference. We reviewed the nature of the MDRs, which are highly sensitive to the droplet radius and the distortion amplitude of spheroids. From the spectral shifts in the n -MDRs, the droplet radius change can be deduced. From the parabolic-shaped wavelength variation along the droplet rim, the shape-distortion amplitude and its sign (assuming that the droplets are spheroidal) can be determined.

Optical diagnostics techniques based on MDRs may be used to probe the affect of high energy/intensity microwave radiation on clouds of water droplets. The size and shape probing processes can occur during or after the microwave radiation. At present, these MDR-based techniques are limited to laboratory studies and necessitate the addition of dye molecules into the water droplets. In the future, the MDR-based techniques may be extendible to backscattered elastic scattering of clouds in the standard single-ended LIDAR configuration.

We gratefully acknowledge the partial support of this research by the U.S. Army Research Office (DAAH04-94-G-0031) and U.S. Air Force Office of Scientific Research (F49620-94-0135).

References:

1. H. C. van de Hulst, *Light Scattering by Small Particles*, (Dover, New York, 1981)
2. S. C. Hill and R. E. Benner, in *Optical Scattering of Light by Small Particles*, P. W. Barber and R. K. Chang, eds. (World Scientific, Singapore, 1988) pp. 3-61.
3. H.-M. Tzeng, K. F. Wall, M. B. Long, and R. K. Chang, "Evaporation and Condensation Rates of Liquid Droplets Deduced from Structure Resonances in the Fluorescence Spectra," *Opt. Lett.* **9**, 273 (1984).
4. H.-M. Tzeng, M. B. Long, R. K. Chang, and P. W. Barber, "Laser-Induced Shape Distortions of Flowing Droplets Deduced from Morphology-Dependent Resonances in Fluorescence Spectra," *Opt. Lett.* **10**, 209 (1985).
5. G. Chen, A. Serpengüzel, R. K. Chang, W. P. Acker, "Relative Evaporation of Droplets in a Segmented Stream Determined by Cavity Droplet Fluorescence

Peak Shifts," in *Proceedings of the SPIE Conference on Laser Applications in Combustion and Combustion Diagnostics*, **1862** (SPIE, Bellingham, Washington, 1993) p. 200.

6. G. Chen, M. M. Mazumder, Y. R. Chemla, A. Serpengüzel, R. K. Chang, and S. H. Hill, "Wavelength Distribution of Laser Emission Along the Entire Rim of Slightly Deformed Microdroplets," *Opt. Lett.* **18**, 1993 (1993).
7. C. F. Bohren and D. R. Huffman, *Absorption and Scattering of Light by Small Particles* (John Wiley & Sons, New York, 1983).
8. P. W. Barber and S. H. Hill, "Effects of Particle Nonsphericity on Light Scattering," in *Optical Particle Sizing: Theory and Practice*, G. Gouesbet and G. Grehan, eds. (Plenum, New York, 1988) p. 43.
9. H. M. Lai, P. T. Leung, K. Young, P. W. Barber, and S. H. Hill, "Time-Independent Perturbation for Leaking Electromagnetic Modes in Open Systems with Application to Resonances in Microdroplets," *Phys. Rev. A* **41**, 5187 (1990).
10. C. C. Lam, P. T. Leung and K. Young, "Explicit Asymptotic Formulas for the Positions, Widths and Strengths of Resonances in Mie Scattering," *J. Opt. Soc. Am. B* **9**, 1585 (1992)

Micron-Sized Droplets Irradiated with a Pulsed Carbon Dioxide Laser: Measurement of Explosion and Breakdown Thresholds

R. L. Armstrong, and A. Biswas,
Physics Department, Box 3D, New Mexico State University
Las Cruces, NM 88003 (USA)

R. G. Pinnick, and J. D. Pendleton,
Army Research Laboratory, White Sands Missile, NM 88002 (USA)

1. SUMMARY

We present the results of measurements of explosive vaporization and plasma breakdown thresholds of micron-sized droplets irradiated by a pulsed CO₂ laser operating at 10.6 microns. Well-defined explosion and breakdown patterns are observed when the incident laser intensity exceeds the threshold value. In the infrared region, the breakdown threshold is larger than the vaporization threshold by a factor of approximately 10². Although, to the authors knowledge, no analogous measurements of vaporization and breakdown thresholds of individual aerosol particles exist in the microwave region, scaling of our infrared measurements to deduce the corresponding microwave properties is possible using available theoretical models. When this scaling is performed, it suggests that a dramatic reversal of explosion and breakdown thresholds occurs in the microwave region. In this region, the microwave vaporization threshold is larger than the corresponding breakdown threshold by a factor of greater than 10⁴. Recent measurements of breakdown thresholds in aerosol-laden air provide indirect evidence that this reversal

has, in fact, taken place.

2. INTRODUCTION

The propagation of a high-power beam of electromagnetic radiation generally involves strong interactions with matter present along the beam path. In many problems of practical significance, particularly those dealing with the propagation of electromagnetic beams through the atmosphere, interactions with aerosols present along the beam path are of importance. There is great diversity in these interactions, from moderate evaporative heating to explosive vaporization, and from elastic scattering or fluorescence to nonlinear optics and plasma formation. In the regime of high-power radiation, unless the aerosols are exceptionally transparent, heating and plasma interactions will be dominant. Moreover, as discussed below, both explosive vaporization and plasma formation are threshold processes; once the incident beam intensity exceeds the interaction threshold, the interaction exerts a dominant effect on the propagating beam. In this presentation, we summarize our

experimental and theoretical results on the explosive vaporization and plasma thresholds of micron-sized absorbing liquid water aerosol droplets interacting with intense infrared radiation (to our knowledge, no analogous studies exist for the case of microwave radiation). We then briefly discuss the significance of this work for the corresponding case of aerosols interacting with high-power microwave radiation.

Our results indicate that absorbing liquid microdroplets interacting with intense infrared radiation may exhibit either explosive vaporization^{1,2} or spontaneous plasma formation^{3,4}. The processes occur when the fluence exceeds a well-defined threshold, with the plasma threshold larger than the explosive vaporization threshold by a factor of approximately 10^2 . Theoretical analysis of these processes has emphasized the importance of superheating in the initiation of explosive vaporization^{5,6,7}, and the onset of cascade ionization in the formation of a plasma^{8,9}. Several detailed mathematical models of superheating explosions have been developed. These models include the effects of inhomogeneous laser irradiation⁶, and thermodynamic transport^{5,7}; however, these models follow the temporal development of the superheating process only to the time where the internal temperature in some region within the droplet reaches the superheat, or spinodal, temperature, thereby avoiding the difficulties associated with modeling the superheating explosion itself. Recently, however, a model calculation was performed¹⁰ describing the superheating explosion. This model will be useful in correlating the "fate" of the irradiated droplet (e. g., whether it explodes as vapor or as a spray of smaller droplets) with beam parameters such as laser wavelength, intensity, and pulse duration, and droplet characteristics such as composition and size.

A common feature of the experimental observations of microdroplets irradiated by intense infrared radiation (in the present experiment, this radiation is provided by a pulsed CO₂ laser operating at a wavelength $\lambda = 10.6$ microns), is the initiation of superheating or plasma emission on either the "illuminated" or "shadow" side of the droplet, depending on whether the emission initially occurs on the hemisphere closest to, or furthest from, the incident laser beam. Weakly absorbing droplets generally exhibit shadow side emissions, whereas emissions on the illuminated side occur for more strongly absorbing droplet media. These observations are in agreement with the results of the several model calculations cited above.

3. EXPERIMENT

Our measurements consist of observing superheating explosions and plasma plumes in micron-sized droplets of water and other liquids, following irradiation by an intense beam of CO₂ laser radiation (temporal pulse length about 100 nsec). Figure 1 illustrates the experimental arrangement (for additional experimental details, see reference 11). The microdroplets, which are produced repetitively using a vibrating orifice aerosol generator (not shown), are subsequently irradiated by the CO₂ laser. Time-resolved observations of the irradiated droplets are obtained with the aid of an auxiliary Nd:YAG laser, focussed directly below the droplet stream with sufficient intensity to generate an air plasma. This plasma, visible for approximately 100 nsec, and capable of being initiated at selected times after onset of the CO₂ pulse, serves as a fast strobe light with which to view the irradiated droplets. The droplets may either be observed directly using the microscope, or photographed by the camera. Figures 2 and 3 display typical photographs of

irradiated droplets obtained using our apparatus. The photographs give both temporal sequences (obtained by varying the delay of the YAG pulse), and fluence sequences (obtained by attenuating the CO₂ pulse). It is noteworthy that, corresponding to a fixed set of laser and droplet characteristics, droplet explosions display well-defined and reproducible explosion patterns.

Inspection of the photographs, such as those shown in Figs. 2 and 3, reveal several features of interest. First, since water is more absorbing than ethanol at 10.6 microns, water explosions initiate on the illuminated side whereas ethanol explosions initiate on the shadow side. Figure 4 shows the normalized source function (i.e., the ratio of the internal energy density to the incident energy density) for water and ethanol droplets. These source function plots clearly suggest that water heating should occur on the illuminated side whereas ethanol should heat on the shadow side. Second, there exists a fluence threshold for superheating explosions. This feature is suggested in both Figs. 2 and 3; below a well-defined fluence, denoted by F_{th} , no explosions are observed. Third, even for fluences above this threshold, superheating explosions initiate after a well-defined delay (e. g., Fig. 2 gives a delay of approximately 2 microseconds for the case of water droplets). The presence of a delay may be modeled on the basis of homogeneous nucleation of vapor bubbles in superheated regions of the droplet, and therefore provides compelling evidence that the observed droplet explosions are, in fact, caused by superheating¹². Fourth, the character of the explosions depends on the liquid medium; water, which is more absorbing than ethanol at 10.6 microns, explodes more violently. The recently developed¹⁰ model discussed above is

capable of describing the characteristics of the explosion products.

In an attempt to model the threshold fluence for droplet explosions, we assume that the threshold fluence corresponds to the situation where some portion of the droplet reaches the superheat temperature. In the absence of heat transport effects, this fluence is simply given by⁶

$$(1) \quad F_{th} = \lambda \rho c_p \Delta T / 4 \pi n k S_{max}$$

where ρ and c_p are the density and specific heat, ΔT is the difference between superheat and ambient temperatures, n and k are the real and imaginary parts of the complex refractive index, and S_{max} is the maximum value of the normalized source function. The normalized source function at some point \mathbf{r} in the droplet is

$$(2) \quad S = |\mathbf{E}(\mathbf{r})|^2 / |\mathbf{E}_0|^2$$

where \mathbf{E}_0 and \mathbf{E} are the incident and internal electric fields. Heat transport effects, of course, exist in the irradiated droplet; however, for the case of the pulsed laser sources considered here, droplet heating corresponds to the so-called "fast heating" regime⁷, for which Eq. (1) represents an excellent approximation. Consequently, we use Eq. (1) to model the threshold fluence. Figure 5 provides a comparison of threshold fluence measurements; data from this work are presented, as well as the results of others^{1,13,14}. Two theoretical comparisons are given, using either ambient or temperature-dependent material properties; the use of temperature-dependent material properties evidently provides better agreement. The pronounced "dip" in the model threshold fluence evident at small droplet sizes arises because of the transition from shadow-to-illuminated side heating; additional data at these sizes is needed to

experimentally confirm this feature. Considering the large uncertainty in the determination of the CO₂ laser spot size (approximately 50%), as well as shot-to-shot fluctuations in the laser pulse length, there is satisfactory agreement between theoretical and experimental values of the threshold fluence for droplet explosions. We did not attempt to model threshold fluence values for other liquids studied in these experiments (e.g., ethanol, shown in Fig.3) because of the lack of knowledge of temperature-dependent material properties. We conclude that the agreement between measured and predicted threshold fluence values for droplet explosions, in addition to the observed delays in the explosions themselves¹², provide strong evidence that superheating is the dominant mechanism responsible for explosive vaporization in intensely irradiated microdroplets.

We also measured threshold fluences for plasma initiation. We defined this threshold by the requirement that a visible spark be observed on approximately 50% of the laser shots. We also note that an audible acoustical "snap" accompanies the observation of the spark, providing an additional diagnostic test for the presence of a plasma. Figure 6 compares our data for water droplets with measurements of others^{3,14}. Note that the thresholds for plasma initiation are larger by a factor of approximately 10² than the thresholds for explosive vaporization, but still a factor of about 4 below the threshold for "clean" air (i. e., aerosol-free air) breakdown. Figure 7 presents the results of our measurements on other liquids, and compares them with the results of others^{3,4}. Observations for the "diesel cylinder" were made using the droplet generator with the piezoelectric shutter, responsible for producing droplets, turned off.

4. MICROWAVE IRRADIATION OF WATER DROPLETS

Since, to the authors knowledge, no experiments analogous to those described above have been performed for microwaves, in this section we shall discuss the scaling of our results from infrared to microwave radiation. For the case of explosive vaporization, Eq. (1) may readily be scaled. Inspection of Figure 4 shows that the source function is approximately unity for water at 10.6 microns in the region of maximum heating (i. e., near the illuminated surface). We suggest that source function enhancement will likewise be small at the longer microwave wavelengths, where the internal electromagnetic field distribution approaches uniformity; moreover, at microwave wavelengths, significant absorption also tends to suppress the field variability. We therefore assume $S_{\max} = 1$ in Eq. (1). Then, using available values of the complex refractive index¹⁵, we find, e. g., that at an assumed microwave wavelength of 10 cm,

$$(3) \quad F_{\text{th}, 10 \text{ cm}}/F_{\text{th}, 10.6 \text{ microns}} = 171$$

From Fig. 5, we see that F_{th} is approximately 3 J/cm² at 10.6 microns. Hence, the scaled explosive vaporization fluence threshold at a microwave wavelength of 10 cm is approximately 513 J/cm². (Note that, if $S_{\max} > 1$ in the microwave region, this represents an upper bound for the fluence threshold). Assuming a microwave pulse length of 100 nsec gives the corresponding scaled microwave irradiance threshold of approximately 5.1 GW/cm² at a wavelength of 10 cm.

Scaling infrared measurements of breakdown thresholds of water droplets to the microwave region may also be accomplished on the basis of an available

model¹⁶. This model provides a theoretical expression for the breakdown irradiance threshold as a function of laser and droplet parameters; however, the model threshold expression exhibits a complex dependence on these parameters. Special cases of the general threshold expression do provide simple scaling rules, and we concentrate on these cases here. The model, which provides good agreement with measured aerosol breakdown thresholds in the infrared, assumes that cascade ionization is the dominant mechanism responsible for aerosol breakdown. This is a good assumption in the infrared, where the multi-photon ionization process is weak because of the large number of simultaneously absorbed infrared photons required for ionization. This assumption has increased validity in the microwave region, where photon energies are smaller. Other important model characteristics depend on the ratio of the temporal pulse length, t_p , to the characteristic breakdown time, t_c (the time interval between successive ionizing collisions), and on the dominant loss mechanisms for free electrons in the plasma. For laser pulse lengths greater than about 100 nsec (the so-called "long pulse" regime), with electron diffusion assumed to be the dominant loss mechanism, the breakdown irradiance threshold assumes the simple form¹⁶

$$(4) \quad I_{BD} = (\text{Constant})/\lambda t_p^{1/2} a^{1/2},$$

where a is the droplet radius. This expression provides good agreement with measured infrared breakdown thresholds¹⁶. From Fig. 6, we see that 1 GW/cm² is a typical breakdown threshold for approximately 50 micron water droplets irradiated by 10.6 micron infrared radiation (with $t_p = 100$ nsec). For an assumed microwave wavelength of 10 cm, and the same assumed values for t_p and a , the

corresponding scaled microwave irradiance breakdown threshold is approximately 10⁵ W/cm². Multiplying this scaled microwave irradiance threshold by the assumed value of $t_p = 100$ nsec, we obtain the corresponding scaled microwave fluence threshold of approximately 10 mJ/cm².

Comparison of the above scaling results reveals that there is a dramatic reversal in the magnitudes of the explosive vaporization and plasma breakdown thresholds when the transition from infrared to microwave radiation is made. By keeping the temporal pulse length and droplet size the same in the two wavelength regions, we have emphasized the importance of wavelength scaling. This results in the breakdown threshold being smaller than the explosive vaporization threshold by a factor of approximately 10⁴ at a wavelength of 10 cm (i. e., 10 mJ/cm²/513 J/cm²), whereas it is greater than the explosive vaporization threshold by a factor of nearly 10² at 10.6 microns (i. e., 200 J/cm²/3 J/cm²). Since the initiation time for plasma breakdown is faster than that for explosive vaporization^{8,12,16}, we suggest that this result further implies that explosive vaporization will not be observed in droplets irradiated by microwave radiation; however, slow evaporative vaporization will still occur.

Although studies of individual droplets irradiated by microwave radiation have not, to the authors knowledge, been performed, breakdown thresholds of gases have been measured. In a recent study¹⁷, breakdown thresholds of laboratory air were measured at a microwave wavelength of approximately 10.5 cm. Discussions by one of us (RGP) with the author of this paper revealed that the breakdown threshold measurements were performed on unfiltered laboratory air, which generally contains aerosol particles similar to those found in

the free troposphere. The measurements should therefore approximately apply to aerosol-laden air. The measured¹⁷ breakdown thresholds lie in the mJ range (approximately 50 mJ at a pressure of 1 atmosphere) for pulse lengths of the order of 100 nsec. These thresholds are similar to our scaled microwave aerosol breakdown thresholds of 10 mJ/cm² at a comparable wavelength of 10 cm, and, significantly, they are smaller by a factor of approximately 10⁴ than the corresponding scaled microwave explosive vaporization thresholds at this wavelength.

5. CONCLUSIONS

In this paper, we have presented the results of measurements of explosive vaporization and plasma breakdown thresholds for aerosol particles in air, irradiated by intense CO₂ laser radiation at 10.6 microns. At this wavelength, vaporization thresholds are significantly lower than the corresponding breakdown thresholds; hence, as the incident laser intensity is raised, explosive vaporization will occur at a lower intensity. However, plasma breakdown will still be observed in the infrared, for intensities above the breakdown threshold, since the time scale for explosive vaporization is slower than that for plasma formation. Then, using our infrared data and theoretical models of the explosive vaporization and plasma breakdown thresholds, we obtained scaled explosive vaporization and plasma breakdown thresholds in the microwave region. In this region, the scaled vaporization thresholds are significantly higher than the scaled breakdown thresholds. Moreover, the time scale for plasma breakdown remains faster than that for explosive vaporization. This suggests that explosive vaporization will not be observed in the microwave region. Hence, plasma breakdown will be the only

remaining threshold process for absorbing aerosol particles in the microwave region. Recent measurements of aerosol - laden air exhibit breakdown thresholds consistent with our scaled breakdown threshold values. However, we conclude that threshold measurements of individual aerosol particles, similar to those we have made in the infrared region, are needed to provide greater understanding of these important threshold processes that will effect the propagation of high - power microwave radiation through the atmosphere.

6. REFERENCES

1. Kafalas, P., and Ferdinand, A. P., "Fog Droplet Vaporization and Fragmentation by a 10.6 Micron Laser Pulse", *Appl. Opt.* **12**, 29 (1973).
2. Wood, C. F., Leach, D. H., Zhang, J.-G., Chang, R. K., and Barber, P. W., "Time-Resolved Shadowgraphs of Large Individual Water and Ethanol Droplets Vaporized by a Pulsed CO₂ Laser", *Appl. Opt.* **27**, 2279 (1988).
3. Lencioni, D. E., "The Effect of Dust on 10.6 Micron Laser-Induced Air Breakdown", *Appl. Phys. Lett.* **23**, 12 (1973).
4. Smith, D. C., and Brown, R. T., "Aerosol-Induced Air Breakdown with CO₂ Laser Radiation", *J. Appl. Phys.* **46**, 1146 (1975).
5. Prishivalko, A. P., "Heating and Destruction of Water Drops on Exposure to Radiation with Inhomogeneous Heat Evolution", *Sov. Phys. J.* **26**, 142 (1983).
6. Pendleton, J. D., "Water Droplets Irradiated by a Pulsed CO₂ Laser: Comparison of Computed Temperature Contours with Explosive Vaporization Patterns", *Appl. Opt.* **24**, 1631 (1985).
7. Park, B.-S., and Armstrong, R. L., "Laser-Droplet Heating: Fast and Slow Heating Regimes", *Appl. Opt.* **28**, 3671 (1989).
8. Armstrong, R. L., "Interactions of Absorbing Aerosols with Intense Light Beams", *J. Appl. Phys.* **56**, 2142 (1984).
9. Pinnick, R. G., Chylek, P., Jarzembski, M., Creegan, E., Srivastava, V., Fernandez, G., Pendleton, J. D., and Biswas, A., "Aerosol-Induced Laser Breakdown Thresholds: Wavelength Dependence", *Appl. Opt.* **27**, 987 (1988).
10. Geints, Yu. E., Zemlyanov, A. A., and Armstrong, R. L., "Explosive Boiling of Water Droplets Irradiated with Intense CO₂-Laser Radiation: Numerical Experiments", *Applied Optics* (in press).
11. Pinnick, R. G., Biswas, A., Armstrong, R. L., Jennings, S. G., Pendleton, J. D., and Fernandez, G., "Micron-Sized Droplets Irradiated with a Pulsed CO₂ Laser: Measurement of Explosion and Breakdown Thresholds" *Appl. Opt.* **29**, 918 (1990).
12. Park, B.-S., Biswas, A., Armstrong, R. L., and Pinnick, R. G., "Delay of Explosive Vaporization in Pulsed Laser-Heated Droplets", *Opt. Lett.* **15**, 206 (1990).
13. Alexander, D. R., and Armstrong, J. G., "Explosive Vaporization of Aerosol Drops under Irradiation by a CO₂ Laser Beam", *Appl. Opt.* **26**, 533 (1987).
14. Kwok, H. S., Rossi, T. M., Lau, W. S., and Shaw, D. T., "Enhanced Transmission in CO₂ - Laser Aerosol Interactions", *Opt. Lett.* **13**, 192 (1988).
15. Ray, P. S., "Broadband Complex Refractive Indices of Ice and Water", *Appl. Opt.* **11**, 1836 (1972).
16. Smith, D. C., "Gas Breakdown Initiated by Laser Radiation Interaction with Aerosols and Solid Surfaces", *J. Appl. Phys.* **48**, 2217 (1977).
17. Alvarez, R. A., "Statistical Sneakthrough" Effects in High - Power Microwave Pulse Propagation at Low Altitudes", Lawrence Livermore Nat'l Laboratory Rep. DDV-89-0037, Nov., 1989.

7. FIGURE CAPTIONS

Fig. 1 - Schematic of experimental apparatus for measurement of droplet explosion and breakdown thresholds. Infrared radiation from a pulsed CO_2 laser is focussed by a 38mm focal length germanium lens onto single droplets produced by a vibrating-orifice generator (not shown). Exploding droplets are viewed or photographed through the microscope using back-illumination from an air plasma generated by a pulsed Nd:YAG laser operating synchronously with the CO_2 laser and the generator. The synchronization allows time-resolved photographs of exploding droplets to be made at selectable times after initiation of the CO_2 laser pulse.

Fig. 2 - Time-resolved photographs of exploding water droplets irradiated with a pulsed CO_2 laser. The left column shows a time sequence at a fixed laser fluence approximately equal to the threshold fluence for explosive vaporization, F_{th} ; the right shows a fluence sequence at a fixed time after initiation of the CO_2 laser pulse.

Fig. 3 - Same as Fig. 3, except for ethanol droplets.

Fig. 4 - Upper trace - Normalized electromagnetic energy distribution (source function) inside a 52 micron water droplet irradiated along the negative z-axis with unpolarized radiation, 10.6 micron wavelength. A normalized radius is used for both y- and z- axes. Energy density and heating are highest on the illuminated side, causing the explosion to be initiated there (see Fig. 2).

Lower trace - Same as upper trace except for ethanol droplets with 16.6

micron radius. In this case, absorption is less, allowing radiation to penetrate and be focussed by the droplet; peak heating (and droplet explosion) occurs on the shadow side (see Fig. 3).

Fig. 5 - Measurement of CO_2 laser fluence required to explode water droplets compared to predictions of superheat fluence.

Fig. 6 - Measurements of water droplet-induced CO_2 laser breakdown thresholds obtained in the present work and by other investigators.

Fig. 7 - Measurements of CO_2 laser-breakdown thresholds for various liquid droplet materials (this work), and for solid particles (previous work). Solid particles are seen to have lower thresholds than for liquid droplets.

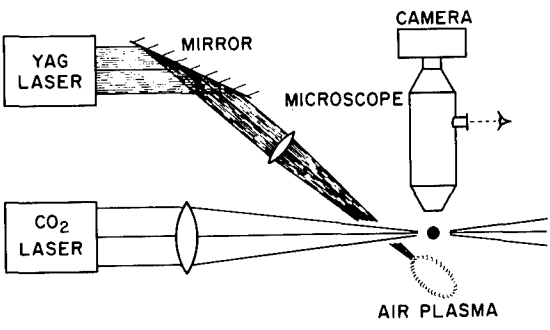


Fig. 1

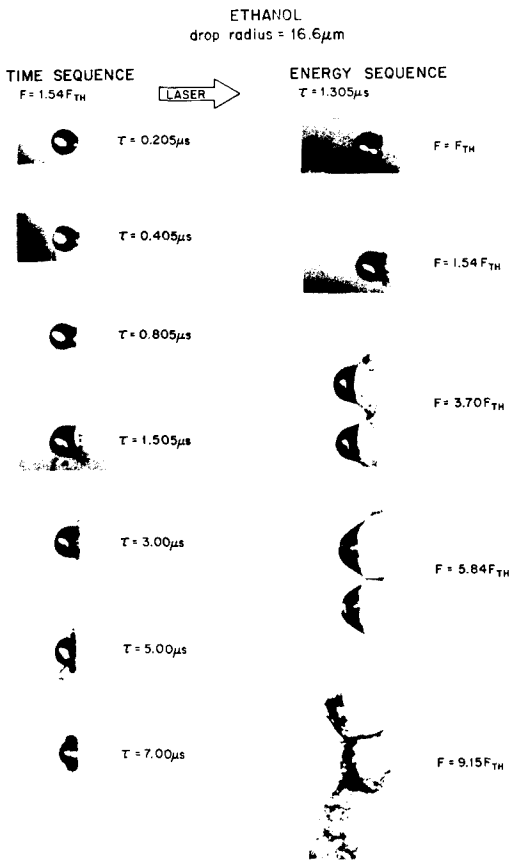


Fig. 3

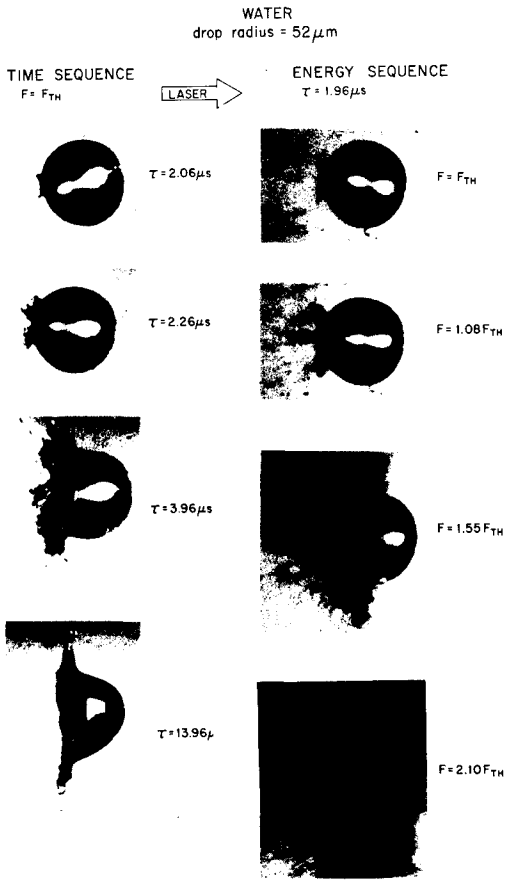


Fig. 2

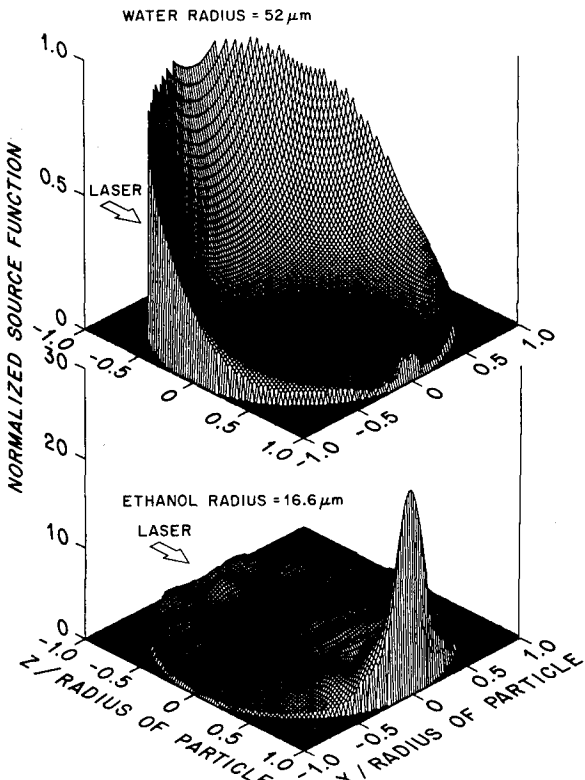


Fig. 4

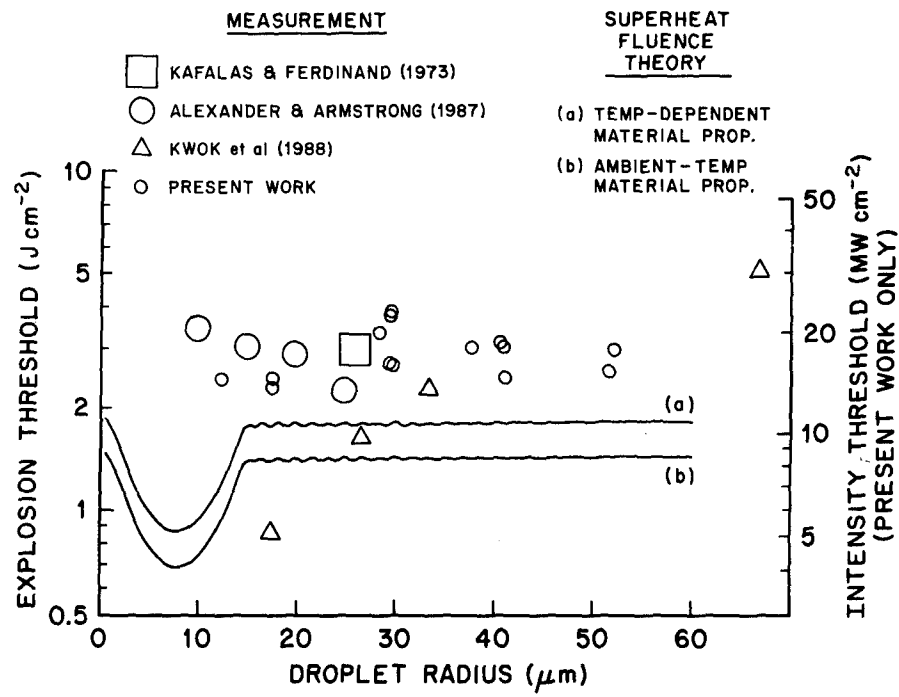


Fig. 5

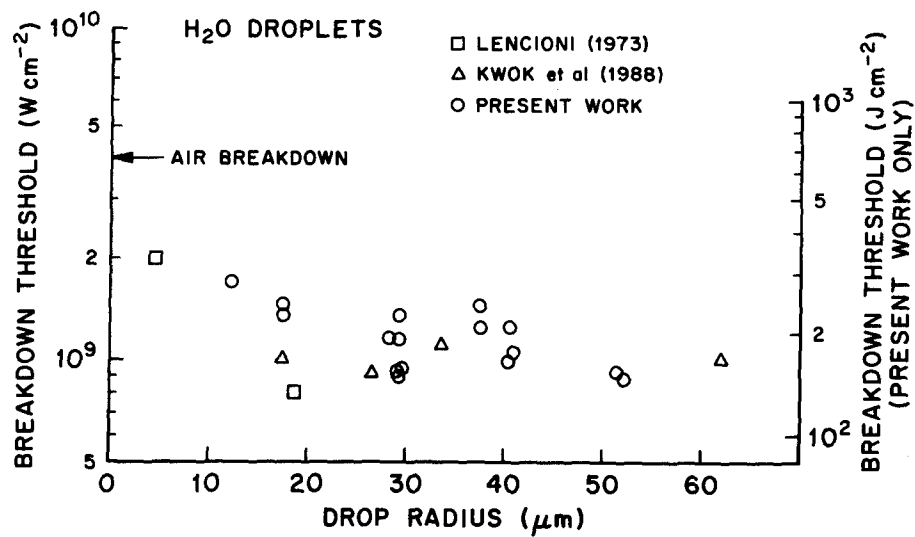


Fig. 6

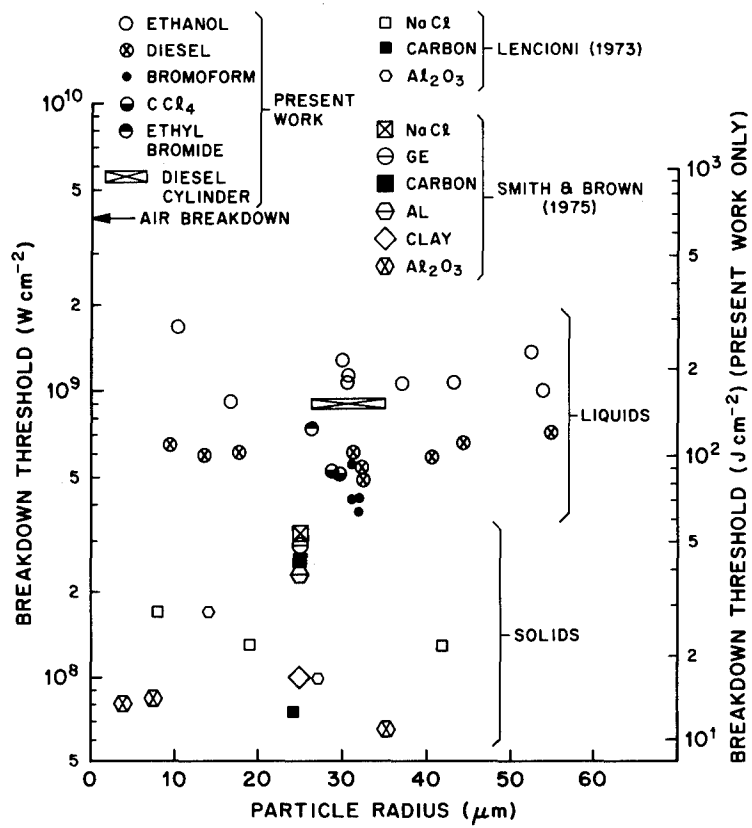


Fig. 7

Calculating the 3-D Absorbed Power Distribution Inside a Human Body that is Illuminated by an Incident EM Field Using the WCG-FFT Method

A. Peter M. Zwamborn
TNO Physics & Electronics Laboratory
P.O. Box 96864
2509 JG The Hague, The Netherlands.
E-mail: A.P.M.Zwamborn@fel.tno.nl

1. ABSTRACT

During the past several years considerable effort has been put into the development of computational techniques for handling the scattering and diffraction of electromagnetic waves by an object. We can distinguish between global techniques (e.g., the use of wave function expansion and integral equation) and local techniques (finite-difference and finite-elements methods).

In this paper we present a global technique to solve the full three-dimensional scattering problem by strongly inhomogeneous objects. This domain-integral is formulated in the frequency-domain. The strong form is weakened by using appropriate test functions and expansion functions. Subsequently, the domain-integral equation obtained is then solved using an iterative Conjugate Gradient scheme combined with an efficient computation of the convolutional integral involved by using the Fast Fourier Transform algorithm (WCG-FFT method). In order to show the accuracy of the method we first compare the numerical results associated with the scattering problem by an inhomogeneous dielectric sphere with the Mie-series solution. Then, numerical computations are carried out on a MRI-scan generated model of a human body inside a metallic enclosure with apertures. Here, we present the absorbed power density inside the human body.

2. WEAK FORM OF THE DOMAIN INTEGRAL EQUATION

The domain integral equation that is obtained in its strong form is weakened by testing it with appropriate testing functions and expanding the electric vector potential with appropriate expansion functions. The advantages of this procedure are, firstly, that the grad-div operator acting on the vector potential is integrated analytically over the domain of the object only, and secondly,

that we have maintained the simple convolution structure of the vector potential. The integral equation is formulated in terms of the electric flux density. The continuity of the normal component of the electric flux density yields a correct implementation of the normal component of the electric field at the interfaces of (strong) discontinuity. No surface integrals that are directly related to surface-charges are introduced. The weak domain integral equation is solved using an iterative conjugate gradient scheme in which the convolution integral is computed efficiently by using the Fast Fourier Transform algorithm. This procedure is introduced by Zwamborn and van den Berg in [1] and we shall only resume the results.

We consider the problem of scattering by a lossy inhomogeneous dielectric object with complex permittivity

$$\epsilon(\mathbf{x}) = \epsilon_r(\mathbf{x})\epsilon_0 + i\frac{\sigma(\mathbf{x})}{\omega}, \quad (1)$$

where ϵ_r denotes the relative permittivity of the object with respect to the lossless and homogeneous embedding with permittivity ϵ_0 , and where σ denotes the electric conductivity of the object. The incident electric field is denoted as $\mathbf{E}^i = (E_1^i, E_2^i, E_3^i)$. In this paragraph, we formulate the scattering problem as a domain-integral equation for the unknown electric flux density $\mathbf{D} = (D_1, D_2, D_3)$ over the object domain \mathbf{D}^S as

$$\mathbf{E}^i(\mathbf{x}) = \frac{\mathbf{D}(\mathbf{x})}{\epsilon(\mathbf{x})} - (k_0^2 + \text{grad div})\mathbf{A}(\mathbf{x}), \quad \mathbf{x} \in \mathbf{D}^S, \quad (2)$$

where $k_0 = \omega(\epsilon_0\mu_0)^{1/2}$ and the vector potential $\mathbf{A} = (A_1, A_2, A_3)$ is given by

$$\mathbf{A}(\mathbf{x}) = \frac{1}{\epsilon_0} \int_{\mathbf{x}' \in \mathbf{D}^S} G(\mathbf{x} - \mathbf{x}') \chi(\mathbf{x}') \mathbf{D}(\mathbf{x}') d\mathbf{x}', \quad (3)$$

in which the normalized contrast function χ is defined as

$$\chi(\mathbf{x}) = \frac{\epsilon(\mathbf{x}) - \epsilon_0}{\epsilon(\mathbf{x})}. \quad (4)$$

Further, the three-dimensional Green's function G is given by

$$G(\mathbf{x}) = \frac{\exp(ik_0|\mathbf{x}|)}{4\pi|\mathbf{x}|}, \quad \mathbf{x} \in \mathbb{R}^3. \quad (5)$$

Testing and expansion procedure

We first introduce a discretization in the spatial domain $\mathbf{x} = (x_1, x_2, x_3)$. We use a uniform mesh with grid widths of Δx_1 , Δx_2 and Δx_3 in the x_1 , x_2 and x_3 directions, respectively.

In order to cope with the grad-div operator in Eq. (2), we test the strong form of Eq. (2) by multiplying both sides of the equality sign by a vectorial testing function $\Psi_{M,N,P}^{(p)}(\mathbf{x})$, $p = 1, 2, 3$, and integrate the result over the domain $\mathbf{x} \in \mathbb{D}^S$. The testing function $\Psi_{M,N,P}^{(p)}(\mathbf{x}) = \psi_{M,N,P}^{(p)}(\mathbf{x})\mathbf{i}_p$ is a volumetric rooftop function.

Using these functions we obtain the following weak formulation of the domain-integral equation

$$\mathbf{e}_{M,N,P}^{i,(p)} = \sum_{I,J,K \in \mathbb{B}^3} \sum_{q=1}^3 \left\{ \mathbf{D}_{I,J,K}^{(q)} u_{M,N,P;I,J,K}^{(p,q)} - \mathbf{A}_{I,J,K}^{(q)} \left[k_0^2 v_{M,N,P;I,J,K}^{(p,q)} + w_{M,N,P;I,J,K}^{(p,q)} \right] \right\}, \quad (6)$$

in which \mathbb{B}^3 denotes the set of discrete points located inside the object domain and

$$\mathbf{e}_{M,N,P}^{i,(p)} = \sum_{I,J,K \in \mathbb{B}^3} \sum_{q=1}^3 \mathbf{E}_{I,J,K}^{i,(q)} v_{M,N,P;I,J,K}^{(p,q)}, \quad (7)$$

$$u_{M,N,P;I,J,K}^{(p,q)} = \int_{\mathbf{x} \in \mathbb{D}^S} \varepsilon^{-1}(\mathbf{x}) \Psi_{M,N,P}^{(p)}(\mathbf{x}) \cdot \Psi_{I,J,K}^{(q)}(\mathbf{x}) d\mathbf{x}, \quad (8)$$

$$v_{M,N,P;I,J,K}^{(p,q)} = \int_{\mathbf{x} \in \mathbb{D}^S} \Psi_{M,N,P}^{(p)}(\mathbf{x}) \cdot \Psi_{I,J,K}^{(q)}(\mathbf{x}) d\mathbf{x}, \quad (9)$$

$$w_{M,N,P;I,J,K}^{(p,q)} = \int_{\mathbf{x} \in \mathbb{D}^S} \text{div} \Psi_{M,N,P}^{(p)}(\mathbf{x}) \cdot \text{div} \Psi_{I,J,K}^{(q)}(\mathbf{x}) d\mathbf{x}. \quad (10)$$

In order to cope with the singularity of the Green's function we employ the spherical mean of Eq. (5) and compute the vector potential by using a FFT algorithm. More details can be found in [1].

3. NUMERICAL RESULTS

In this chapter we briefly discuss the applicability of WCG-FFT for the numerical approximation of three-

dimensional scattering problems, such as the scattering by a strongly inhomogeneous dielectric sphere and the computation of the absorbed power distribution inside a human body that is illuminated by an incident plane wave. The human body is located inside a metallic structure with apertures. The human model is obtained from a MRI-scan generated dataset [3]. It should be noted that is not the objective of the paper to discuss countermeasures against an electromagnetic health treat. Instead, we want to show the applicability of the method for complex electromagnetic scattering problems or studies concerning the analysis of possible hazards caused by non-ionizing radiation.

3.1 Scattering by the Dielectric Sphere

In this paragraph, we present the case of a plane wave incident on a radially inhomogeneous lossy dielectric sphere. For this test case, analytical results are available. The electric field is polarized parallel to the x_1 -axis and propagates along the negative x_3 -axis. The origin of the sphere is located in $\{0, 0, 0\}$. We present the magnitude of the electric field strength inside a lossy inhomogeneous sphere with $\varepsilon_{r,1} = 72$, $\sigma_1 = 0.9$ S/m and $k_0 r_1 = 0.163$ and $\varepsilon_{r,2} = 7.5$, $\sigma_2 = 0.05$ S/m and $k_0 r_2 = 0.314$, where r_1 and r_2 denote the radius.

In the WCG-FFT method we have used mesh sizes of $15 \times 15 \times 15$ and $29 \times 29 \times 29$ to discretize the sphere. For the $29 \times 29 \times 29$ case, the WCG-FFT method needed 404 iterations to obtain a residual error less than 0.1 percent. On the Convex C230 this calculation took 15500 s CPU time and required 18 Mbyte of storage.

In Figures 1a and 1b we present the magnitude of the electric field inside the sphere. Compared to the Mie-series solution, it has been observed that the iterative WCG-FFT method produces very accurate results, even for a coarse mesh. In case the mesh becomes more dense, it has been shown that the numerical scheme approximates the analytical solution more accurate.

3.2 Scattering by a Complex Strongly Inhomogeneous Structure

Let us yet consider a human body located inside a metallic enclosure. This enclosure has three apertures. One small aperture in front of the eyes and the other two apertures at both hand-sides. With respect to the human body the Cartesian reference frame is chosen such that the x_1 -axis is parallel with front to back, the x_2 -axis is parallel with left to right and the x_3 -axis is parallel with feet to head. The frequency of operation is taken to be 450 MHz. The electromagnetic field is polarized parallel to the x_2 -axis and propagates along the positive x_1 -axis. The human body is discretized into $21 \times 31 \times 53$ subdivisions with mesh widths $\Delta x_1 = 1.676$ cm, $\Delta x_2 = 1.601$ cm and $\Delta x_3 = 3.123$ cm. For muscle we have taken $\varepsilon_{r,M} = 71.5$, $\sigma_M = 0.83$ S/m, for

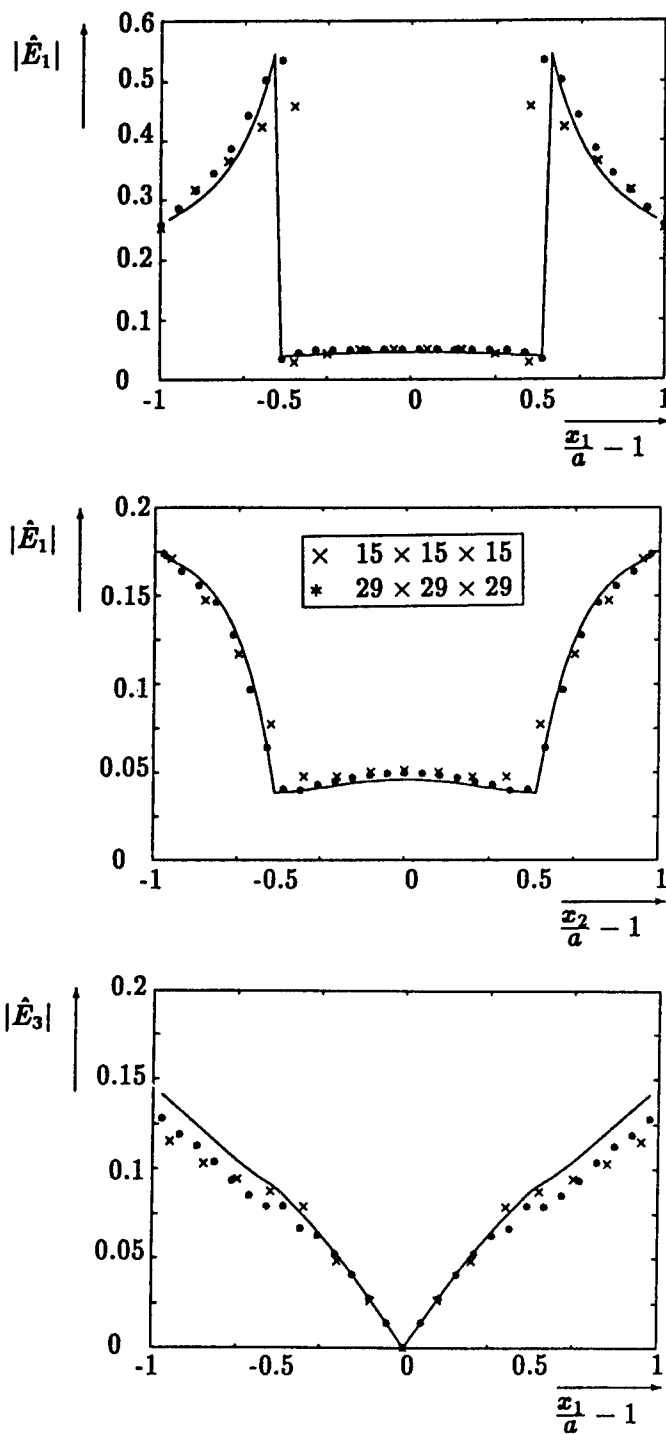


Figure 1: The magnitude of the electric field inside a strongly inhomogeneous sphere with $\epsilon_{r,1}=72$, $\sigma_1=0.9$ S/m and $k_0 r_1=0.163$ and $\epsilon_{r,1}=7.5$, $\sigma_1=0.05$ S/m and $k_0 r_1=0.314$. The results pertaining to a mesh of $15 \times 15 \times 15$ are presented by the symbols x and the results pertaining to a mesh of $29 \times 29 \times 29$ are presented by the symbols *. The analytical solution (Mie series) is presented by the solid line.

fat we have taken $\epsilon_{r,F}=15$, $\sigma_F=0.22$ S/m and for metal we have taken $\epsilon_{r,I}=1$, $\sigma_I=1000$ S/m. Note that the subscripts M, F and I denote muscle, fat and metal, respectively. The WCG-FFT method needed 862 iterations to obtain a residual error norm of less than 0.1 percent. On the Convex C230 this calculation took about 59000 s CPU time and required 37 Mbyte of storage.

In Figure 2 we present the absorbed power density normalized to the maximum occurring power density in the human body. It should be noted that the absorbed power density is calculated as follows

$$\dot{w} = \frac{1}{2} \sigma |\mathbf{E}|^2. \quad (11)$$

Figure 2a shows the $x_1 x_2$ -plane at $x_3 = 78.2$ cm and in Figure 2b the $x_2 x_3$ plane is shown at $x_1 = -1.676$ cm. It has been observed that the maximum values of the absorbed power density are located in the direct surroundings of the eye and brain tissue. Further, the absorbed power density is located at the outer boundary of the human body. This is expected because the penetration depth in the human body is limited for electromagnetic fields at 450 MHz.

4. CONCLUSIONS AND FUTURE DEVELOPMENTS

In this paper we have presented a weak formulation of the domain integral equation for solving three-dimensional scattering problems by strongly inhomogeneous dielectric objects. It has been shown that the iterative WCG-FFT method is an accurate and powerful tool to solve the frequency-domain integral equation and produces very accurate frequency-domain results. In order to obtain time-domain results, the WCG-FFT method could be extended in a fast marching-on-in-frequency procedure [2]. Subsequently, we use an inverse Fourier transform. This matter is under investigation at the moment. Further, it is anticipated that a considerable saving of CPU time could be obtained by using a hardware implementation of the FFT algorithm.

Acknowledgement

The author gratefully acknowledges the assistance of his colleague, Fred T.C. Koenis, in reading and correcting the manuscript as well as preparing the camera-ready manuscript during the author's sabbatical leave.

REFERENCES

- [1] A.P.M. Zwamborn and P.M. van den Berg, "The three-dimensional weak form of the conjugate gradient FFT method for solving scattering problems," *IEEE Trans. Microwave Theory Techn.*, MTT-40, pp. 1757-1766, September 1992.

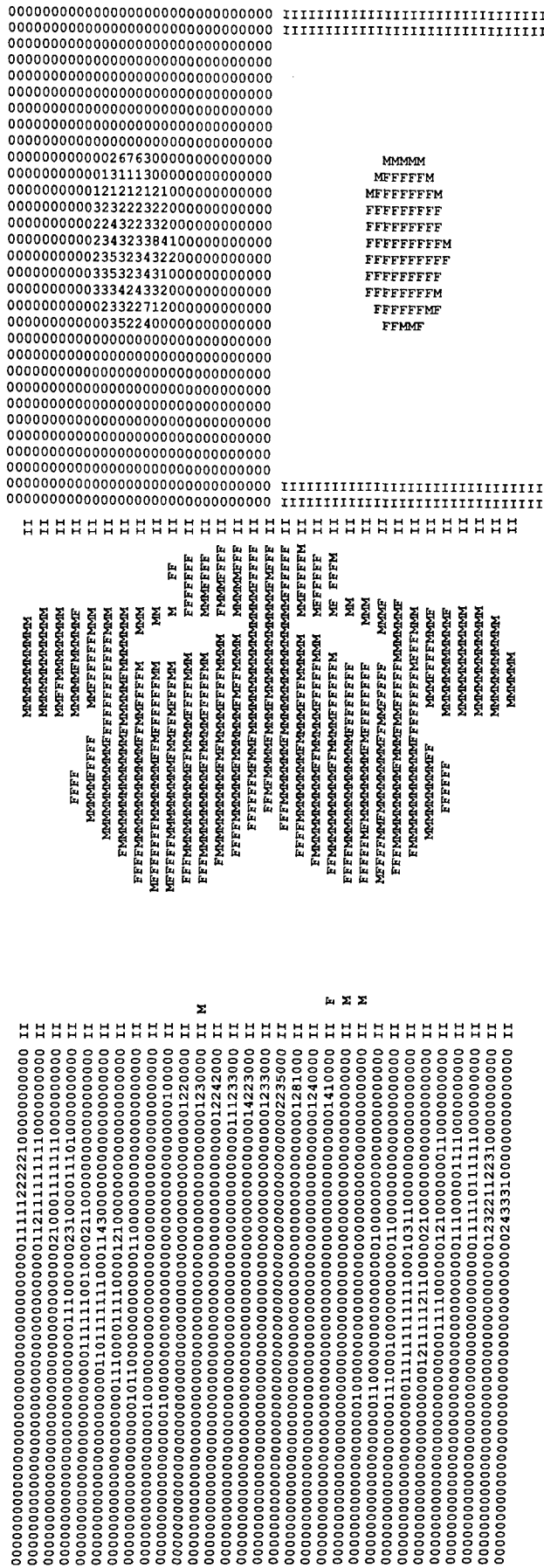


Figure 2: The normalized absorbed power density inside a human body.

[2] A.G. Tijhuis and Z.Q. Peng, "Marching-on-in-frequency method for solving integral equations in transient electromagnetic scattering," *IEE Proc. H*, Vol. 138, pp. 347-355, August 1991.

[3] A.P.M. Zwamborn, P.M. van den Berg, J. Mooibroek and F.T.C. Koenis, "Computation of three-dimensional electromagnetic-field distributions in a human body using the weak form of the CGFFT method," *Applied Computational Electromagnetics Society Journal*, vol. 7, no. 2, pp. 26-42, winter 1992.

DISCUSSION

J. NITSCH

- 1/ Did you also calculate the local and whole body SAR (Specific Absorption Rates) values in your model ?
- 2/ Did you compare your numerical results with those obtained by different numerical approaches for the same human-model ? Is there agreement ?

AUTHOR'S REPLY

- 1/ The model only calculates the total electric field. Once the field has been calculated one can calculate related quantities easily.
- 2/ At the moment we are comparing the numerical results of this model with outer schemes such as FD-TD. However, there is some agreement and disagreement between the results. Hence, there is still some research to be done in this field.

CRITICAL HEAT FLUX PANEL EXPERIMENTS

J.E. Beraun, K.F. Raymond, J.S. Orlins, and F.A. Rigby
Phillips Laboratory WSAE
3550 Aberdeen Avenue S.E.
Kirtland AFB
NM 87117-5776
UNITED STATES

ABSTRACT

The Phillips Laboratory's Laser Effects Branch, PL/WSAE, performs laser interaction experiments on a wide range of materials, components, and subsystems, to understand the physics of interaction at high heating rates and to explore for any synergistic phenomenology in components and subsystems. This paper covers one such recently completed project: Critical Heat Flux Panel Experiments. The goal of the Critical Heat Flux Panel Experiments is to determine the necessary threshold laser irradiance to induce film boiling on the inside surface of a fuel tank. Film boiling describes the phenomena whereby a thin continuous vapor layer is formed on the heated surface, such as the inside surface of a fuel tank and effectively insulates the wall from the liquid within. Film boiling, once established, interferes with heat transfer by insulating the wall from the liquid, which allows laser energy to remain within the wall raising its temperature quickly to failure level. At heating rates below those required for film boiling, vapor bubbles form and detach continuously from the heated surface, a process referred to as nucleate boiling. This leaves both, plenty of liquid in contact with the wall and actually stirs up the liquid providing massive heat transfer from the wall. Thus, nucleate boiling is a very effective heat transfer mechanism. The Critical Heat Flux Panel Experiments have successfully established laser irradiance thresholds for achieving film boiling and ultimate failure of a metal tank. This paper describes in detail test design and special procedures utilized for this test series. The paper also presents experimental results and its implications to theoretical models.

1. INTRODUCTION

In the later part of 1992 and early 1993, testing was performed at the Phillips Laboratory to investigate the critical heat flux for film boiling of JP-8. These tests were performed using the Electric Discharge Coaxial Laser (EDCL) II, a carbon-dioxide laser at Kirtland AFB NM.

The critical heat flux is important because it represents the maximum rate at which the liquid can cool the metal wall of a tank. Thus, if a laser can deposit more heat flux on the tank skin than the liquid's critical heat flux, the metal skin will rapidly heat up and fail due to internal pressure.

The particular interest of these experiments is to determine the critical heat flux for JP-8 in a fuel tank. This information is not available in literature. In fact, complete JP-8 property information is very difficult to find, and in some cases unobtainable. Additionally, the vast majority of information on critical heat flux is for pool boiling where the bottom surface is being heated. The orientation of interest in these experiments is for fluid adjacent to a heated vertical wall. The physics of film and nucleate boiling is discussed in detail in the next section.

2. PHENOMENOLOGY

As laser energy is deposited on the metal wall of a tank, the metal begins to heat up and lose some of its thermal energy to the liquid. When heat is transferred through the wall of the tank to the initially static liquid, convective motion develops in the liquid driven by the density difference between hot and cool liquid. This removes hot liquid from contact with the heated portion of the wall and replaces it with cold liquid, thereby increasing heat transport. The velocity of motion, however, is limited due to the usually small density variation available in the liquid state, and heat transfer rates for simple convection are generally low compared to the heating rates of interest, which are for boiling. Therefore, the temperature of the wall will continue to rise as the laser provides more heat than can be carried away, until the wall temperature rises above the saturation temperature of the liquid (determined by the pressurization of the tank). At this point, small bubbles of vapor form (nucleate) against the hot tank wall, and a new heat transfer regime develops, called nucleate boiling.

A vapor bubble will grow against the wall of the tank until the buoyant force on the bubble overcomes the surface tension that holds it to the wall. As the bubble begins to rise, fresh liquid fills the space it occupied and comes in contact with the wall, so that the process of bubble formation begins again. Heat transfer rates for nucleate boiling can be far higher than for simple convection for two reasons. First, the density difference between vapor and liquid is much greater than the difference between hot and cold liquid (unless tank pressure approaches the critical point of the material) which drives much faster fluid movement. Second, the heat absorbed by the boiling liquid includes the heat of vaporization in addition to the "sensible" heat required to heat the liquid from its initial temperature to saturation. Thus, the material leaving the heated wall is both, moving faster and carrying more heat per unit mass than in simple convection.

Although nucleate boiling can sustain a much higher rate of heat transfer from the wall than can simple convection, the process is still limited. An essential requirement of the nucleate boiling process is that the bubbles of vapor leave the hot surface and be replaced by liquid. Thus it is necessary to have simultaneous movement of liquid to the surface and vapor away from it. The larger the heat flux that is being transferred from the heated surface, the greater the mass fluxes of liquid and vapor must be. For relatively low rates of nucleate boiling heat transfer, the movement of liquid toward the hot surface is slow, the volume of vapor bubbles is small, and there is minimal interference between the two motions. As the heating rate is increased, this situation changes. A point must be reached when the flow of liquid toward the hot surface will be strong enough to begin to restrict the movement of vapor bubbles away from the surface, and equivalently, the total cross-section area filled by vapor begins to restrict the flow path available to the liquid. Increasing the heat transfer rate beyond this level means further increasing the volume of vapor leaving the surface, which, in turn, interferes with the supply of liquid that can be converted to vapor. Clearly, there is a limiting maximum heat transfer rate that can be achieved.

When the heat flux through the wall exceeds this limit, vapor is created at the wall more rapidly than it can leave the wall in the form of bubbles. This means that the bubbles of vapor forming against the heated wall will grow until they begin to coalesce, covering large areas of the wall surface with vapor. The limit of this process is the formation of a continuous film of vapor between the wall and the liquid. This is called film boiling.

The critical heat flux can be viewed as the rate of heat transfer through the wall that is required to produce film boiling. In an area covered by vapor, heat can be removed from the wall only by transfer to and through the vapor. The primary processes at work are heat conduction through the thin layer of gas and radiative heat transfer from the wall to the liquid. Convective heat transfer through relatively low density gas, however, is much more difficult than by direct contact of the liquid with the wall; also, radiative heat transfer is ineffective until high wall temperatures are reached, being a function of T_w^4 . The vapor film serves, in effect, as an insulating layer separating the wall from the liquid volume. As a result, the wall temperature increases tremendously (usually thousands of degrees) until

an equilibrium heat transfer rate is reached and the wall temperature stabilizes. Normally, internal pressure will cause a failure of the metal before this equilibrium is reached. Thus to summarize, in nucleate boiling, the wall temperature can never very greatly exceed the saturation temperature of the liquid because the wall is continuously cooled by direct contact with the liquid; but in film boiling, only a small excess in heat flux above the critical heat flux can force the wall temperature to rise to failure.

Formation and detachment of vapor bubbles at the wall is an unsteady process that includes some degree of randomness and is influenced by conditions at the wall, such as surface roughness. Geometry of the container may also influence the value of critical heat flux. Thus, critical heat flux is not a unique and precise material property of the liquid the way that density or viscosity is. Equations for predicting critical heat flux from fluid properties, as shown in the next section, should be recognized as approximations for a process that is subject to some variability.

3. THEORETICAL FORMULATION

In the above section, the discussion given of the mechanisms of boiling included the transfer of both sensible heat to warm the liquid up to the saturation temperature and the heat involved in vaporizing the liquid (latent heat of vaporization, H_v). When discussing quantitative descriptions of critical heat flux, it is useful to separate these two processes, and begin by considering the case of the initial fluid temperature being equal to the saturation temperature, so that all the heat transfer occurs in the form of latent heat of vaporization.

3.1 SATURATED BOILING

From basic physics, the flux of latent heat transported by vapor leaving the heated surface, q_{sat} , is the mass flux times the latent heat of vaporization, H_v . The mass flux is the vapor density, ρ_v , times the vapor mean effective velocity, u_e . Thus,

$$q_{sat} = \rho_v H_v u_e \quad (1)$$

The value of this effective velocity associated with critical heat flux must be determined semi-empirically. A number of different formulas can be found in the literature on pool boiling (Ref. 1). Four are shown below:

$$q_{sat} = 0.18 \rho_v H_v \left[\frac{\sigma(\rho_l - \rho_v)g}{\rho_v^2} \right]^{1/4} \left[\frac{\rho_l}{\rho_l + \rho_v} \right]^{1/2} \quad (2)$$

$$q_{sat} = 0.16 \rho_v H_v \left[\frac{\sigma(\rho_l - \rho_v)g}{\rho_v^2} \right]^{1/4} \quad (3)$$

$$q_{sat} = 0.145 \rho_v H_v \left[\frac{\sigma(\rho_l - \rho_v)g}{\rho_v^2} \right]^{1/4} \left[\frac{\rho_l + \rho_v}{\rho_l} \right]^{1/2} \quad (4)$$

$$q_{sat} = 0.13 \rho_v H_v \left[\frac{\sigma(\rho_l - \rho_v)g}{\rho_v^2} \right]^{1/4} \left[\frac{\rho_l}{\rho_l + \rho_v} \right]^{1/2} \quad (5)$$

The first quantity in brackets represents the mean effective velocity. The second term in brackets represents additional, dimensionless, correction factors used by some authors to improve the fit for behavior at high pressures. Specifically, q_{sat} is the heat flux to the saturated liquid, ρ_v and ρ_l are the densities of the vapor and liquid at saturation respectively, σ is the surface tension for saturated conditions, H_v is the latent heat of vaporization, and g is the acceleration due to gravity.

The majority of the work that has been done on critical heat flux in pool boiling has involved heat transfer to liquid lying over a heated horizontal surface. The geometry of interest for this series of experiments is liquid lying adjacent to a heated vertical surface.

Reference 2 presents a formula for critical heat flux which is at once simple and is based on testing done with boiling occurring around the exterior of a horizontal heated pipe of circular cross-section. Portions of the surface of the pipe present high inclination angles, so this result might be expected to represent behavior similar to that on a vertical plate. This formula is the same as the first equation presented above for the horizontal case (equation 2), the only difference being a different coefficient:

$$q_{sat} = 0.116\rho_v H_v \left[\frac{\sigma(\rho_l - \rho_v)g}{\rho_v^2} \right]^{1/4} \quad (6)$$

NOTE: The units of all equations above for heat flux - latent heat of vaporization are Watts/meter². This paper presents all data in Watts/centimeter².

When the initial temperature of the liquid is less than the saturation temperature, the liquid is said to be "subcooled." The critical heat flux is larger for a subcooled case than it is for the saturated case because the liquid will take up sensible heat in addition to the heat of vaporization. However, the effect of subcooling is greater than can be accounted for by just the extra heat that must be added to the liquid that is vaporized. This is because the strong convective motions involved in nucleate boiling bring much more liquid into contact with the wall than is actually vaporized. When the liquid is subcooled, all this unvaporized liquid also carries away heat.

3.2 SUBCOOLING

Because the heat transfer associated with subcooling is driven by the same fluid motions that transport vapor (and the heat of vaporization) away from the wall, both the flux of sensible heat and the flux of latent heat of vaporization tend to vary in proportion to the vapor flux off the wall. As a result, they also vary in proportion to one another. Consequently, the effect of subcooling is commonly represented by a factor that is multiplied by the saturated critical heat flux. The subcooling correction presented in Reference 2 is:

$$q_c = q_{sat} \left[1 + \frac{0.1}{\rho_v H_v} \left(\frac{\rho_v}{\rho_l} \right)^{1/4} C_{pl} \rho_l (T_{sat} - T_o) \right] \quad (7)$$

where q_c is the critical heat flux, C_{pl} is the liquid specific heat, T_{sat} is the saturation temperature of the fluid, and T_o is the initial bulk temperature of the liquid. Note, that the initial bulk liquid temperature is valid only so long as the mass of liquid in the pool is large enough or the time of nucleate boiling is short enough that any bulk heating of the liquid can be neglected. The complete equation is obtained by multiplying equation (7) with the previous equations; for example, from Reference 2 equation (6) and (7) give:

$$q_c = 0.116\rho_v H_v \left[\frac{\sigma(\rho_l - \rho_v)g}{\rho_v^2} \right]^{1/4} \left[1 + \frac{0.1}{\rho_v H_v} \left(\frac{\rho_v}{\rho_l} \right)^{1/4} C_{pl} \rho_l (T_{sat} - T_o) \right] \quad (8)$$

4. PRE-TEST PREDICTIONS

This section presents pre-test calculations and also includes a discussion of material properties because they had such a large and important effect on the pre-test predictions. Therefore, this section begins with material properties and finishes with their effect on numerical predictions.

4.1 MATERIAL PROPERTY ISSUES

Two studies were conducted to provide information on the properties of JP-8 in July 1992 and October 1992. Several significant uncertainties were identified. One of these was saturation pressure. This is obviously an important parameter for test planning, and it also has a significant impact on the calculation of critical heat flux from equation 7. Actually, JP-8, also known as commercial Jet-A fuel is made up of 40 percent kerosene and 60 percent aromatics-distillates. Kerosene is a mixture of a number of hydrocarbon liquids, and the distillates further complicate matters. Both studies found sources in the literature giving a "bubble point" for kerosene at one atmosphere of about 170 degrees C, but information for higher pressures was not found. One of the studies estimated a "saturation" temperature for 65 psia (446 kPa) by making a calculation for a mixture for octane and dodecane that would have a one atmosphere vapor pressure at 170 degrees C. The other one used the same approach, but assumed a mixture of octane and nonane. Both studies predicted a temperature of 260 degrees C for 65 psia.

For the specific heat of the liquid, the first study used data for RP-1 (References 3) showing a specific heat of 1349 J/Kg-C at 140 degrees C. The second effort utilized a Russian source (Reference 4) indicating a value of 3210 J/Kg-C for a kerosene based liquid that is similar to JP-8. The latter value is therefore treated as the preferred estimate for specific heat. Surface tension at elevated temperature and pressure is also a source of uncertainty. The second study sites a specific value for 192 degrees C, which is used as the preferred estimate, while the first one identifies a broad range of uncertainty. Table 1 summarizes the material properties estimates given by in both studies.

TABLE 1. PROPERTIES

			<u>ONE</u>	<u>TWO</u>
ρ_v	density of vapor	Kg/m ³	11.5	12.5
ρ_l	density of liquid	Kg/m ³	800	628
σ	surface tension	N/m	.002-.01	.0088
H_v	heat of vaporization	J/Kg	246,541	250,000
C_{pl}	liquid specific heat	J/Kg-°C	1349	3210
T_{sat}	saturation temp. for 14.7psia °C		170	170
T_{sat}	saturation temp. for 65 psia °C		260	260
T_o	initial liquid temp.	°C	30	30
g	acceleration of gravity	M/sec ²	9.8	9.8

4.2 PRE-TEST PREDICTIONS: NUMERICAL CALCULATIONS

The pre-test predictions are summarized in Table 2. The initial pre-test predictions were made using the Science Applications International Corp.

material properties (referred to as study one); using equations (4) and (7) above over a full range of surface tension values. The results were:

For 65 psia: Critical Heat Flux = $86 - 129 \text{ W/cm}^2$

Later, material properties considered more accurate became available from Physical Sciences Inc. (referred to as study two) and were utilized for an updated pre-test prediction. Additionally, equation (6), which included a vertical orientation, was included. Table 2 summarizes the pre-test predictions. Pressures of 12 and 65 psia are shown. Table 2 also shows the calculated temperature values that went into these predictions.

TABLE 2. PRE-TEST PREDICTIONS

Q_{sat}	Subcooling	14.7 PSIA	65 PSIA
Eq 6'	Eq 7	121.5 W/cm^2	181.9 W/cm^2
Eq 2	Eq 7	186.8 W/cm^2	279.5 W/cm^2
Eq 3	Eq 7	167.7 W/cm^2	250.9 W/cm^2
Eq 4	Eq 7	153.4 W/cm^2	229.6 W/cm^2
Eq 5	Eq 7	134.9 W/cm^2	201.9 W/cm^2
<u>Temperature Predictions</u>		<u>14.7 PSIA</u>	<u>65 PSIA</u>
T_{sat} (saturation/boiling)		170°C	260°C
T_o (initial)		30°C	30°C

5. DESCRIPTION OF TESTS

This section describes the test series in detail. It includes a detailed discussion of the test apparatus used, the various diagnostics used to determine the laser conditions at the target plane, and the test procedure.

5.1 TEST APPARATUS

A test apparatus was designed and fabricated for measuring the critical heat flux of various liquids for a wide range of pressures. The test unit is a stainless steel container capable of holding fluid at pressures of interest (several atmospheres), it has built-in feed-throughs for accessing the instrumentation leads. Its inside dimensions are approximately 12.5 cm in length and a diameter of approximately 10 cm. One of the end walls of the test unit is removable; this feature allows the inside of the test wall material to be in direct contact with the liquid, and the outer surface exposed to the laser, while containing the liquid at various pressures. In addition, this design feature makes it possible to instrument and replace the test wall material, thus allowing a variety of wall materials to be tested.

One side of the test unit has a plexiglass window which permits observation of the interior of the unit during laser irradiation using high speed cameras. This provision on the container allows for excellent diagnostics of the phenomenology of bubble formation on the vertical wall.

The EDCL II laser at Kirtland AFB was used for the experiments. The sample wall material used in this test series was a stainless steel, 2 mm thick. The laser beam was directed at the center of the sample wall material. Spotsizes were chosen to be large compared to the thickness to allow 1-D heat transfer through the wall.

5.2 DIAGNOSTICS

Test diagnostics and measurements included the following:

- Laser Output Power: The output power is measured using a water cooled calorimeter. Power versus time measurements for the entire duration of laser run time are performed for every laser firing.

- Power at Target Plane: This measurement is performed using a calorimeter located at the target plane. Power measurements at this location provides direct measurement after the laser beam has gone through the relay optics of the experimental setup. This measurement is performed each time the beam train optics are repositioned or changed to ensure that power requirements on target is achieved.

- Laser Shutter Open/Close Times: The laser shutter is used in a pre-programmed fashion to irradiate the target for pre-determined times. This instrument along with a fast infrared detector allow exact measurement of the irradiation time and power on target.

- Plexiglass Burn: A plexiglass material is used to quantify the laser spotsize at the target plane. When the laser interacts with this material it leaves a footprint, this footprint is then later profiled using a laser profilometer to quantify the exact size of the laser beam at the target plane.

- Thermocouples: Six thermocouples were soldered to the back of the sample wall material. Four made the shape of a diamond; the fifth was in the middle of the diamond pattern, and the sixth was directly above the diamond. The middle thermocouple was positioned to be at the center of the laser spot.

- Infrared Camera: A Hughes Infrared camera was used to record the front surface temperature of the sample wall material. This camera provides an in-situ measurement and it has a dynamic range up to 1000 C.

- Overview Video: One video camera was placed to record the entire test chamber and act as a test overview camera.

- Close-up Video: One video camera was placed to look through the side window in the chamber and record when nucleate or film boiling was achieved.

- Chamber Pressure: A pressure transducer was used to monitor the chamber pressure duration of each test.

5.3 TEST PROCEDURE

During a typical test sequence the following steps are followed. Detailed alignment of all the optics of the beam train in order to obtain the desired spot size and beam profile on target. The next step, and this is done at the start of each test day, do a plexiglass burn and verify laser spot size and beam profile at the target plane. Then calorimeter measurement at the target plane was performed to accurately determine the irradiance level at the target. Once laser conditions were determined at the target plane the next step was to place the instrumented sample material in the chamber, fill and pressurize the chamber to the desired pressure. Then a sequence check is performed to verify that all instrumentation and diagnostic systems are properly functioning.

The test unit was located in a fireproof enclosure especially constructed for these tests, and personnel were on standby with fire extinguishers in case of a fire. The test conductor had access to a pickle switch to terminate laser irradiation whenever film boiling was achieved, or after 15 to 20 seconds if only nucleate boiling was achieved. Film boiling was easy to determine from either the closeup video camera or from the Hughes Infrared camera (which was color coded so that the color would change when the metal sample wall material rose above the liquid saturation temperature). The metal temperature rises very rapidly to failure after film boiling is achieved, so it was important to shut the laser off quickly to prevent failure of the metal wall.

The test series was performed to determine the threshold of film boiling. Tests were performed over a wide range of irradiances in an effort to quantify the threshold to film boiling. The irradiance conditions were gradually adjusted to determine the threshold as accurately as possible. This was repeated at five different pressures to determine the film boiling threshold as a function of pressure.

6. RESULTS

The experimental results are presented, discussed and compared to theory. This section starts with a discussion of how some of the critical test parameters are calculated. A discussion of the importance of preventing bulk heating from skewing the experimental results follows. Experimental results are then presented. Final comments on the results are then provided to conclude this section.

6.1 DISCUSSION

Laser Coupling: Previous to this series of critical heat flux experiments, a series of laser tests were performed to determine the laser coupling to the sample wall material at the wavelength of the EDCL II laser. The laser coupling is the ratio of the energy absorbed by the metal to the energy incident on the metal sample.

Film Boiling: The transition to film boiling was determined in three different ways. As mentioned earlier, the Hughes Infrared camera was used to monitor the front surface temperature of the sample and when the front surface of the metal sample exceeded the saturation temperature of the liquid, the test was stopped. In addition, a close-up video camera was used to monitor the back surface of the metal sample and the liquid. Nucleate boiling appeared as a steady stream of small bubbles. Film boiling appeared as one large bubble the same shape as the laser spot. Film and nucleate boiling were also determined from the thermocouple data. Nucleate boiling appeared as a rapid level off in temperature, while film boiling appeared as a rapid rise after the level off for nucleate boiling. Thus, all diagnostics used were very effectively for determining when film boiling occurred.

Bulk Heating: These critical heat flux experiments were conducted at ambient conditions, which resulted in an initial liquid temperature T_0 of approximately 20 degrees C. For JP-8 at these conditions, the critical heat flux is dominated by subcooling. This can be seen in equation (7), the correction factor for subcooling. Values of equation (7) ranged from 4 to 8, meaning that 75 to almost 90 percent of the critical heat flux went to warm the liquid up to saturation temperature. It is clear in equation (7) that the higher the initial temperature T_0 , the smaller the temperature difference $T_{sat} - T_0$, and the smaller the critical heat flux required to achieve film boiling. Thus, care was needed in these experiments to keep the bulk initial liquid temperature at one value and not allow too much variation. Thus, care was taken to achieve film boiling quickly, in order not to add too much heat energy to the bulk liquid and, in effect, raise its initial bulk temperature, while nucleate boiling was occurring. In the analysis of the results, if more than 10 seconds elapsed between laser on target and the onset of film boiling, T_0 was regarded as uncertain (it was not specifically measured during each test) and the result was not used.

6.2 EXPERIMENTAL RESULTS

The experimental results are shown in Figure 1. Each point represents a test shot. The open squares represent tests where film boiling was achieved; the filled circles represent tests where only nucleate boiling was observed. Also, the pre- and post-test predictions for equations (6) and (7), which included a vertical orientation, are shown as a diamond and "x" respectively.

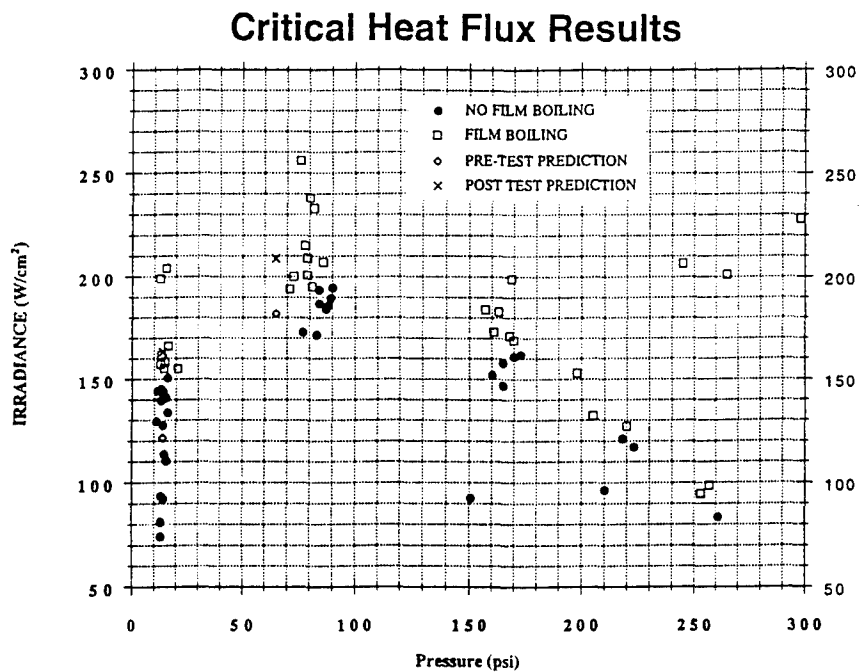


Figure 1. The Critical Heat Flux for JP-8 versus Pressure.

The experimental results are very consistent. A smooth curve can be drawn that cleanly separates the great majority of the film boiling cases from the nucleate ones. In a few cases, the tests would be slightly on the wrong side of the line. This can be explained by the accuracy of the laser power, laser coupling, spot size, pressure, and initial temperature measurements. Additionally, the tests were conducted over a period of three months and the initial temperature was allowed to be ambient, which varied some. Overall, the results were very good.

6.3 COMPARISON TO THEORETICAL PREDICTIONS

Table 3 summarizes the comparison of the pre-test estimates of saturation temperature versus the experimentally measured temperatures. An average of the effective saturation temperature found from the tests conducted at 14.7 psia is shown. The saturation temperature for 65 psia was not directly observed from the experimental data. However, a graph of saturation temperature versus pressure was made from the experimental data. A curve fit was made to this data. The value for 65 psia was taken from the graph and is shown in Table 3 below.

TABLE 3. RESULTS: TEMPERATURE PREDICTIONS

Temperature Predictions	14.7 PSIA	14.7 PSIA	65 PSIA	65 PSIA
	Pre-Test	Experiment	Pre-Test	Experiment
T _{sat} (saturation)	170°C	222°C	260°C	290°C
T _o (initial)	30°C	20°C	30°C	20°C
(T _{sat} - T _o)	140°C	202°C	230°C	270°C

The observed effective saturation point of JP-8 was significantly higher than the 170 degree C value found in the literature for kerosene or RP-1. The estimated values for 65 psia are considerably closer, but still fall below the experimentally obtained value, which is not surprising because these estimates were made for liquid mixtures that would fit the 170 degree C for one atmosphere pressure.

Given the substantial differences between the expected and observed saturation temperatures, the pre-test calculations of critical heat flux should be expected to depart significantly from the observations. To account for the difference in saturation temperatures, the critical heat flux predictions were recalculated using the observed effective saturation temperatures. These results are shown in Table 4 and 5.

Atmospheric Pressure: Results are summarized in Table 4. The pre-test prediction for equation (6), which included a vertical orientation, was too low - 121.5 W/cm² compared to an experimentally measured 150 W/cm². This was because the calculated saturation temperature was too low. When the experimentally obtained temperatures are used, the result improves to a very good match - 163 W/cm², versus 150 W/cm² from the experiment. The results from the other equations for pool boiling are shown to emphasize the range that current theory would predict. Note that there is a fair amount of spread when the experimentally obtained temperatures are used - 163 W/cm² to 251 W/cm².

TABLE 4. RESULTS: CRITICAL HEAT FLUX AT 14 PSIA

q_{sat}	<u>Subcooling</u>	<u>Pre-Test</u>	<u>Experimental</u>	<u>Post Test</u>
Eq 6'	Eq 7	121.5 W/cm ²	150 W/cm ²	163.1 W/cm ²
Eq 2	Eq 7	186.8 W/cm ²		250.6 W/cm ²
Eq 3	Eq 7	167.7 W/cm ²		225.0 W/cm ²
Eq 4	Eq 7	153.4 W/cm ²		205.9 W/cm ²
Eq 5	Eq 7	134.9 W/cm ²		181.0 W/cm ²

Post Test corrections were for measured ($T_{sat} - T_o$)

Pressure of 65 PSIA: Results are summarized in Table 5. The pre-test prediction for equation (6), which included the vertical orientation, was very close - 181.9 W/cm² compared to an experimentally measured 185 W/cm². Again, the calculated saturation temperature was too low. When the experimentally obtained temperatures are used, the result is - 209 W/cm² versus 185 W/cm² from the experiment. In reality, many of the properties shown in table 1 would change as the pressure was raised from atmospheric to 65 psia. This data was not available, so only the saturation temperature was changed. This accounts for the slightly larger error, as compared to the atmospheric pressure case. The results for the other pool boiling equations again are higher and are shown to emphasize the range that current theory would predict. Again, the overall range with experimentally obtained temperatures is fairly large - 209 W/cm² to 321 W/cm².

TABLE 5. RESULTS: CRITICAL HEAT FLUX AT 65 PSIA

q_{sat}	<u>Subcooling</u>	<u>Pre-Test</u>	<u>Experimental Result</u>	<u>Post Test</u>
Eq 6'	Eq 7	181.9 W/cm ²	185 W/cm ²	208.8 W/cm ²
Eq 2	Eq 7	279.5 W/cm ²		320.8 W/cm ²
Eq 3	Eq 7	250.9 W/cm ²		288.0 W/cm ²
Eq 4	Eq 7	229.6 W/cm ²		263.6 W/cm ²
Eq 5	Eq 7	201.9 W/cm ²		231.7 W/cm ²

Post Test corrections were for measured ($T_{sat} - T_o$)

The pool boiling equations all produced larger values of critical heat flux than did the equation that included the vertical orientation. This is expected to some degree because the pool boiling equations were based on a bottom horizontally heated surface. In the horizontal case, as vapor bubbles are formed, they move up directly away from the bottom wall, which is the one being heated. This allows cold fresh liquid to come in contact with the wall. In the vertical case, as vapor bubbles are formed, they move up tangent to the wall being heated. Thus, the section of heated wall just above has a lot of hot vapor bubbles in the region adjacent to it, making it easier to obtain a region of continuous vapor. These same type convective currents also form during the subcooling phase with hot and cold liquid. Thus, it is easier to obtain film boiling on a vertical rather than horizontal bottom wall, and thus the critical heat flux is lower.

Theoretical predictions are not shown for any pressure above 65 psia. This is because JP-8 vapor properties are changing significantly, and complete data at these elevated pressures could not be obtained. The downward trend at higher pressures is expected. As the pressure increases, the critical pressure of JP-8 is approached. As the critical pressure is approached, the properties of the liquid and vapor approach the same value, and the value of critical heat flux, as seen in equations (2) through (6), approaches zero.

7. CONCLUSION

Experimental results correlated very well with theoretical predictions, particularly at atmospheric pressure where the most accurate properties were available. Theoretical equations for horizontal pool boiling predicted too high of a critical heat flux, as expected. The trend of critical heat flux versus pressure was just as expected. Good theoretical predictions of critical heat flux at high pressures are difficult without accurate property data at these pressures. Overall, the experimental results were very good and a close match with theory was obtained for lower pressures, which was the primary area of interest.

8. REFERENCES

1. Rhosenow, W. M. and Hartnett, J. P., Handbook of Heat Transfer, McGraw-Hill, 1973.
2. Whalley, P. B., Boiling Condensation and Gas Liquid Flow, Oxford University Press, 1987.
3. Kit, G. and Eversed, D. S., Rocket Propellant Handbook, MacMillan, New York, 1960.
4. Vargaftick, N. B., Handbook of Physical Properties of liquids and Gases, English Translation, published by Hemisphere Publishing Corp., 1975. Originally published by Nanka Press, Moscow.

NOTE:

The discussion following Paper 27 is printed in the Classified Supplement of these Conference Proceedings.

UPGRADING OF THE RF TUBES OF THE PRESENT STATE OF THE ART.

Georges FAILLON
THOMSON TUBES ELECTRONIQUES
2, rue Latécoère
B.P. 121
78141 VELIZY Cedex, France

SUMMARY

Although basic studies are far from completion, the microwave levels requested for the vulnerability test benches are far below those expected on HPM weapons. At the same time, the main requirements of the test benches are accuracy and reliability, therefore the sources to be used can be derived from the existing high power sources commonly used in several fields such as radars, particle accelerators, thermonuclear fusion... For example, the development of klystron amplifiers delivering 100 to 200 MW in S band with μ s pulse length are in progress.

In shorter pulses (10s of ns) relativistic magnetrons (below the X or C band) and BWOs (beyond the X band) begin to be easy to bring into operation.

Nevertheless amplifiers seem more attractive because their pulses shapes, their frequencies and their phases are entirely controlled. The bandwidth is also an important technical characteristic.

Devices such as pulse compressors upgrade existing tubes. The single cavity, plasma switch compressor transforms for example a 50 kW 2 μ s pulse into 3 MW, 5 ns in X band and the same principle can be applied to provide up to 50 to 200 MW according to the frequency.

1. INTRODUCTION

For several years, new developments in the field of microwave tubes have been in progress. For instance :

- . Millimeter waves generation at low and high power levels.
- . Very small size and compact devices associated to their supplies.
- . CW Megawatt tubes in decimetric band.
- . Considerable high peak power devices from L to X bands.

2. HPM VULNERABILITY TESTS

At the same time, a long term question has been raised by several Defence Agencies about the HPM concept. Many branches of the physics and many technologies are involved in the development of systems able to generate and to launch very intense microwave pulses or bursts through the atmosphere, in order to reach and to perturb - or at least to jam - a moving or a fixed target. On the battlefield, many situations have to be faced and it is well understood that the specifications of such systems are not yet defined, although in progress. Moreover, basic researches are still needed, for instance, we have to know how many millijoules are requested to perturb a given solid state component or to investigate the dependance of the pulse length and the repetition rate. In longer words, high power experiments are or will be necessary to conduct these studies and to determine the final specifications.

Such experiments are planned to be made in large chambers or in open fields and, in any case, at relatively small distances. Therefore, the microwave power levels requested for these experiments can be set to "only" hundreds of MW - when ten(s) of GW are likely necessary on the futur real HPM launchers, assuming a range of 10 or a few tens of km - Of course, in both cases, the frequencies are the same (.3 to 10 or 20 GHz) and although not yet assessed the pulse lengths also will be the same (tens of ns up to 1 or a few μ s).

3. HIGH PEAK POWER KLYSTRONS.

Such characteristics are still far from the conventional tubes capabilities, nevertheless closer. Figure 1 shows the state of the art concerning for example the klystron peak powers versus frequencies with pulse lengths of a few μ s.

The klystrons are mainly used on particle accelerators and they seem to be one of the most fitted tubes for the vulnerability test benches. Their linear electron beams, which are produced by 1 to 2 10^{-6} AV- $3/2$ Pierce type guns, are modulated by a first cavity; then the density modulation is enhanced by an assembly of intermediate cavities and drift tubes and finally the last (or output) cavity transfers the kinetic energy of such bunched beams into electromagnetic waves which are directly sent through window(s) and waveguides to the load. In our case this load is, of course, an antenna.

The increase of the peak power encounters several difficulties, among which the most obvious are the breakdowns arising in the gun and in the output cavity or structure. In the gun, extensive experimental studies [1] give now the limits of the most critical characteristic, which is not the electric field on electrodes, but the product $E \cdot V$, as shown on the curve of Figure 2. Therefore, by redesigning the gun in order to decrease E , the curve is only slightly shifted. Taking these difficulties into consideration, we have designed a 20 MW (220 kV) L band tube at 100 μ s, and several other tubes: 120 kV 2 ms, 300 kV 5-10 μ s and 600 kV 1 μ s. The first two devices are already in operation and the last two are under construction. Of course, these rules are valid for every kind of tube.

The second type of arcing concerns the RF structures. The particle accelerator community and the industry have conducted in this area some specific measurements and it is commonly admitted that 50 kV/mm in S band is a limit, with a pulse length of 1-2 μ s and 50% better in X band [2]. Therefore to get 50 to 70 MW or more in X band, or 150 to 200 MW in S band, a new structure is needed. This is the reason why coupled cavities or, better, travelling wave sections have been introduced: roughly the RF electric field is divided by the number of cells, but at the expenses of possible parasitic oscillations and a more complicated geometry.

The cathodes of the present tubes are thermoionic and made of impregnated tungsten. Progress is on the way to achieve within 1 μ s pulse current densities up to 80 to 150 A/cm², (Figure 3) [3] thanks to Os-W thin

coatings or optimized Os percentage inside the W matrix itself. In spite of the high temperature and of the heater, such thermoionic cathodes give more constant and homogeneous electron beams, compared to the field emission guns. These last ones must be devoted to much higher powers and very short pulses, and usually they have to be removed quite often.

Up to now the windows are made of ceramics and are able to transmit, for example, 100 MW and more in S band - 3 μ s pulses, but their reliability must be improved. The choices of the ceramic purity and the crystallography are important, added to the surface treatment. But, in any case, an increase of the diameter seems attractive and the window will be located in the output horn antenna. This explains why efforts have been successfully achieved in brazing 30 to 40 cm disks inside copper sleeves and why a better knowledge of the overmoded waveguides becomes necessary.

Of course, as already pointed out, these improvements in the technology can be extended to any kind of microwave tubes. But they are presently focused on the development of klystrons such as 60-80 MW 2 to 3 μ s, 100-200 MW 1 to 2 μ s, both in S band, and several laboratories are already working to get 50 to 80 MW .5 to 1 μ s around 11 GHz.

4. AMPLIFIERS-OSCILLATORS.

Klystron means amplifier. As a matter-of-fact, compared to oscillators, amplifiers are more helpful in the vulnerability measurements. The main reasons are the ability to easily control not only the shape of the output pulses but also their phase and their frequency. For instance, thanks to a 1.5 μ s voltage pulse, the RF output can be as small as 30 to 40 ns with a very abrupt (10-20 ns) or - if requested - a long (100's ns) rise time. It can be also a burst of ten 50 ns pulses, also spaced by 50 ns... Moreover, several tubes can be used in parallel, providing a perfect summation of their microwave pulses and a first approach of a phase array transmitter. The frequency can be changed from pulse to pulse at the repetition rate - tens to thousands of pps - or varied inside the pulse itself. Therefore, thanks to these flexibilities, many measurement methods can be implemented in order to increase the accuracy of the results.

5. MULTIBEAMS.

The frequency bandwidth is also one major characteristic. The conventional klystrons present instantaneous bandwidths of a few % and in some cases up to 15% [4]. But it is doubtful whether such bandwidths could be achieved with 500-700 kV electron beams. Therefore, we have to engage studies in this direction and the multibeam tubes appear as one of the best solutions [5][6]. The number of cavities remains the same but each one is crossed by several (n) electron beams (Fig. 4). The currents (i) carried by these individual beams are small and the low values of their space charge forces favour high efficiencies. The total current ($I = n i$) is several times greater than the current of the corresponding one beam tube. Therefore, the cavities are strongly loaded and present large natural instantaneous bandwidths. The decrease of the cathode voltage which are 2 to 3 times lower than usual brings several main advantages in terms of size, cost, x-rays shielding, etc... ; but, above all, the DC and RF breakdowns limit is strongly pushed away whether in the electron guns or in the microwave output circuits. The 100 kW CW 6 beams prototype we have developed at 426 MHz confirms our point of view. At frequencies higher than roughly 2 GHz overmoded cavities will be required or, at least, cavities with entirely different shapes.

6. MAGNETRONS.

Although the magnetrons are basically oscillators, their significant capabilities must be shown to advantage. Usual magnetrons used on the Radar transmitters or on the radiotherapy accelerators are limited to 5 to 10 MW in S band and to 1 or 2 MW in X bands, with several μ s pulse lengths. To overpass these power limits, the straps which connect the cavities in the anode must be eliminated because of breakdown difficulties. Therefore parasitic oscillations arise more easily, but this problem is solved by reducing the number of cavities, at the expense, of course, of the efficiency. These magnetrons called "relativistic" have been successfully developed, for example, in S band, 900 MW, 40 ns can be achieved with a beam power of 750 kV 12 kA ($\text{eff} = 10\%$). As usually in these devices, we note a narrow pulse length, which is explained by the advent of an arc between the cathode and the anode and by the shift of the radial electron

trajectories under the influence of the azimuthal magnetic field induced by the strong current flowing inside the cathode. The pulses are noisy and non precisely reproducible but, beyond all questions, powerful.

7. BWO

The Backward Wave Oscillators belong to the TWT family. The slow wave structure is easy to manufacture but much more difficult to design. As a matter-of-fact, this structure is, on principle, overmoded and consists of a large diameter cylindrical waveguide, which is smoothly corrugated in order to propagate modes whose phase velocity is slightly lower than the electron beam velocity. Usually, this electron beam is hollow and travels near the wall. The group velocity is negative, giving a better efficiency and therefore the output power is extracted near the gun side or better reflected and transmitted across the tube, up to the final taper and antenna, through the window.

The main difficulty, which slows down the development of the BWOs, is the control of the oscillations on the right mode, and is mainly related to the electron beam characteristics : this electron beam is unfortunately hollow - as already said - and also produced by a field emission cathode. The matching of the RF structure is quite critical.

Commercial compact BWOs exist in Ku and Ka bands at a power level of about 40-50 MW / 4 ns. If needed, improvements can be foreseen in order to enlarge the energy per pulse ($P \tau$) and to decrease the operating frequency down to the X band. On the other hand, the pulse repetition frequency seems to be increased much more easily.

8. PULSE COMPRESSORS

The general principle of the pulse compressors is to exchange power P for pulse length τ , while the energy $P\tau$ remains nearly the same. To our knowledge, three types of pulse compressors exist :

1. Passive compressor with double resonator.
2. Single cavity with plasma switch.
3. Dispersive line pulse compressors.

A schematic description is given on Figure 5. The klystron output feeds 2 overmoded high Q_0 cavities (TM₀₃₈...).

Thanks to the 3 dB coupler, the phases of the 2 reflected waves are opposite and the klystron is perfectly protected. As soon as the 2 cavities are filled up (3 to 4 μ s), the phase of the driver is abruptly changed by 180° and the stored energy rushes towards the load, presenting a high power peak and a decay time related to the Q_{xs} .

Although more and more experimented in scientific particle accelerators such as Trieste (210 MW, S band, 700 ns) these compressors require accurate manufacturing ($Q_0 = 2 \cdot 10^5$, intense fields in the coupling holes) and many mechanical and electrical adjustments and tunings. For instance, a change of the cavities temperature greater than 3°C cannot be tolerated because of frequency shift and mismatching. The basic reason of this complexity is more the large pulse width than the peak power itself.

This leads up to the second type of pulse compressor, which is the simplest and, then, less expensive. The power ratios or the gains, $G = P_{out} / P_{in}$ being about 50 or 100, commercial and almost available tubes - magnetrons and klystrons - can be chosen to equip the first stage, just before the compressor, according to Figure 6. Then the energy delivered by the tube is transmitted, through an isolator, to a cavity. This cavity is simply made by a short-circuited waveguide. The output side short-circuit is generated by a real metallic short circuit in a lateral coupled waveguide. When the cavity is filled up, an arc is triggered at $\lambda_g/4$ in this lateral waveguide and the stored energy is radiated by the antenna, directly connected to the cavity.

Of course, to minimize the Joule losses, we must adjust the metallic short circuit as tightly as possible during the filling time and then we have to create the open circuit in an extremely very short time, in the order of the ns.

These difficulties begin to be overcome and the objective of our first experiment, now in progress, is to get 2.5 - 3 MW, 5-10 ns in X band from a 50 kW 1-2 μ s magnetron ($G=50-60$). The

next step could be 200 MW-5 ns from a 4 MW S band magnetron or 50 MW from a .5 MW X band magnetron.

The use of amplifier klystrons in the place of oscillator magnetrons would be favourable not only to get higher powers, but also to be able to control the phase and the frequency, and then to organize devices in parallel (phase array). Also, the same klystron for instance could feed several compressors. Because the expected low costs, the use of several devices to illuminate - at the same time or not - the measurement area brings great and new advantages : many configurations can be imagined according to the number, the locations, the frequencies, the phases and the powers of the pulse compressors.

Finally, it is expectable to enlarge the output pulse lengths by changing the couplings either during the manufacturing stage or during the measurements themselves ; and in this context, the present experience of the passive compressors with 2 resonators will be very useful.

Up to now the dispersive line pulse compressors have been only used in the intermediate stages of some radars. A frequency modulated signal is sent into a dispersive line. The lowest frequencies - at the beginning of the pulse - are overcome by the faster ones. In the microwave range and at high powers, the expected result is a compression rate of 10 to 15 in pulse lengths and a power gain of 8 to 10. Of course, the main problem remains the choice and the design of the dispersive travelling wave structure, and this type of compressor is now only under paper studies.

CONCLUSION

The requirements of the vulnerability test benches are mainly focused on precise and reliable measurements ; therefore, to provide their high power microwave output stage, we have proposed solutions not so far from the conventional tubes.

First, the klystrons extrapolated from the present state of the art will be able to deliver 100 to 200 MW / 1 μ s in S band or 50 to 100 MW in X band.

Regarding the high voltages (700 kV), their behaviour will be more reliable, thanks to major changes - now in progress - in the electron gun and in the output cavity. Multibeam tubes with significantly lower cathode voltages can also be proposed; moreover, the instantaneous bandwidths of these tubes are very attractive (10 to 15% expected).

Secondly, magnetrons are already designed to get GWs but only in short pulses (10s of ns) and at one single frequency. The BWOs still need time to be proposed into realistic operation at 100s of MW levels beyond the X band; nevertheless, commercial tubes exist with 4 ns pulses and a few tens of MW.

We also have to take into account that amplifiers are more attractive than

oscillators, because their frequencies, their phases and their amplitudes can be easily and instantaneously controlled, even during the pulse itself. Moreover they can be used in parallel.

Finally, pulse compressors are sometimes forgotten, although they are unexpensive and they upgrade existing tubes such as magnetrons or - better - klystrons. The one cavity plasma switch compressor presents power gains in excess of 50 and, after the present experiment on the MWs level, 100 to 200 MW can be expected.

In any case, these comments are not applicable at all to the real future HPM systems but only to the vulnerability test benches.

[1] The technology of high voltage vacuum devices and systems, Chapter 12 : Electron Vacuum Tubes.

A.J. DURAND, A.M. SHROFF
Editor: Prof. R.V. LATHAM Acad. Plan. Book

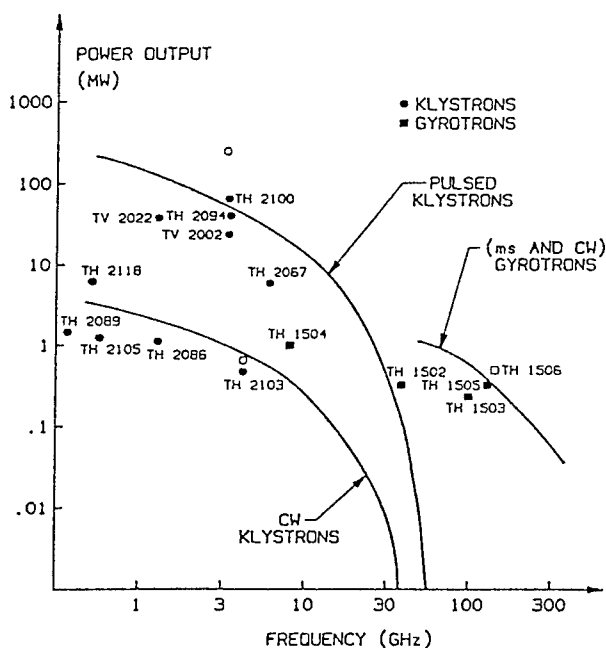
[2] International Workshop on pulsed RF power sources for Linear Colliders.
Dubna, Russia, July 5-9, 1993

[3] Thermoionic sources for high-brightness electron beams.
R.E. THOMAS et al.
IEEE Trans. on E.D. Vol. 37 N°3 (1990)

[4] 15% Bandwidth high power S band klystron.
A.J. DURAND
Radar'94 Conf. 3-6 May 94 Paris.

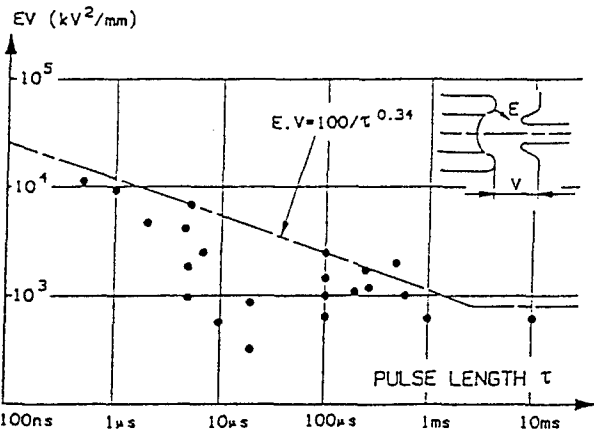
[5] Compact multibeam klystron
M. BRES, G. FAILLON, D.T. TRAN
IEDM L.A. Dec. 86

[6] Advantages of multibeam klystrons.
C. BEARZATTO, M. BRES, G. FAILLON
ITG 92 GARMISCH P. May 92.



PRESENT TECHNOLOGY LIMITS FOR PULSED AND CW HIGH POWER MICROWAVE TUBES

FIGURE 1.



BREAKDOWN LIMIT IN ELECTRON GUNS
FIGURE 2.

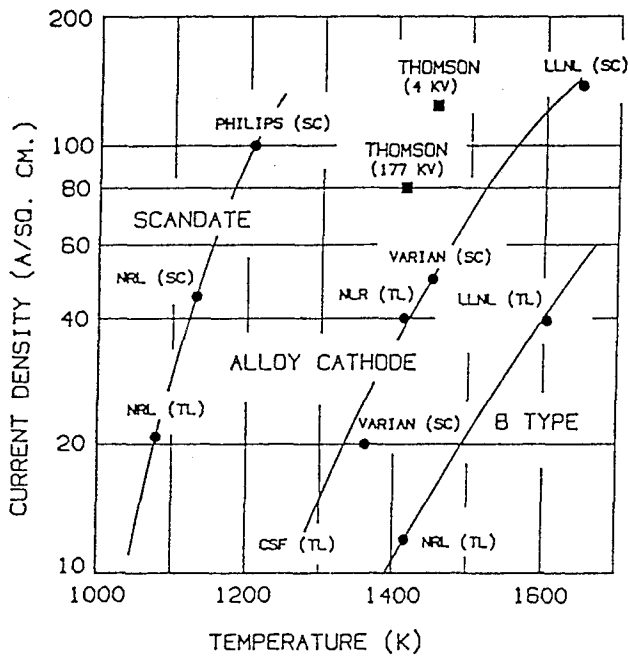
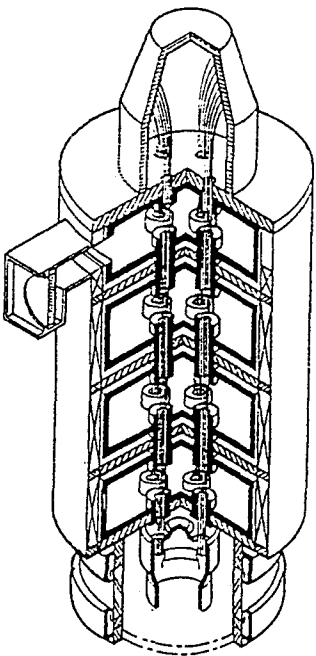
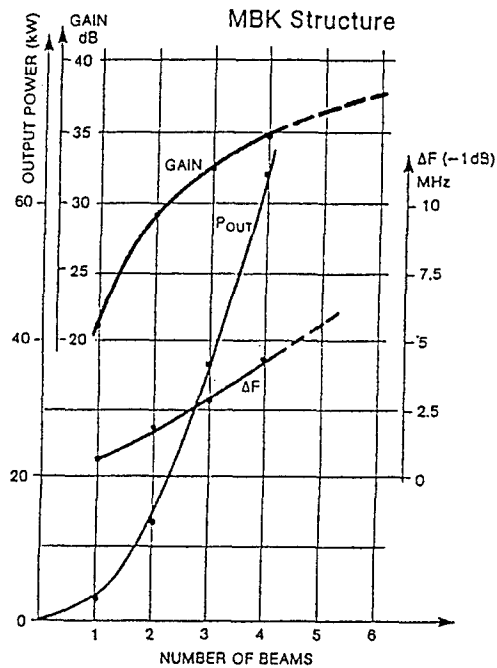


Fig. 3. THERMOIONIC CATHODES [3]
CURRENT DENSITIES VS TEMPERATURE



Measured performances vs number of beams
FIGURE 4.

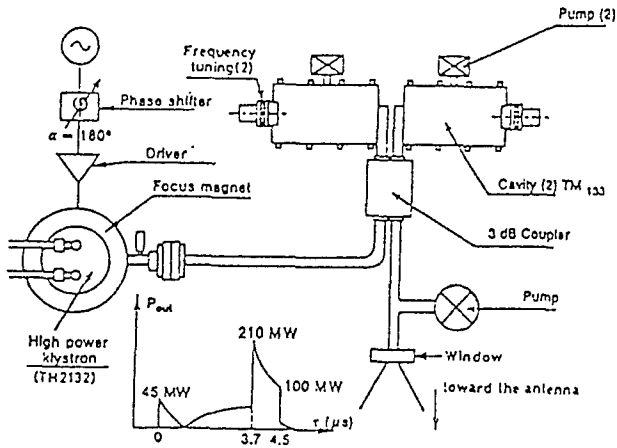


FIGURE 5.
DOUBLE RESONATOR PASSIVE PULSE COMPRESSOR

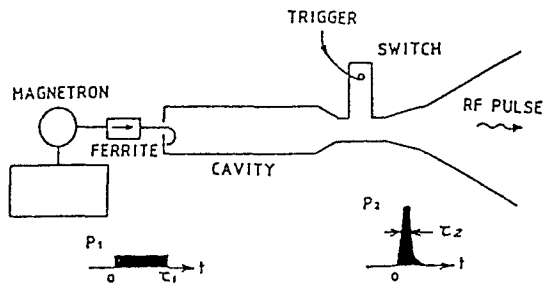


Fig. 6.
SINGLE CAVITY-PLASMA SWITCH COMPRESSOR

DISCUSSION

E. SCHWEICHER

1/ Peut-on éviter les arcs en mettant les cavités sous pression de SF₆ derrière une fenêtre de verre ?

2/ Avec 500 kV il y a danger de production de rayons X durs. Comment protéger l'environnement de ces rayons X durs ?

AUTHOR'S REPLY

1/ L'idée est bonne, mais pour de multiples raisons, des électrons vont percuter le verre, le charger et il se produira alors un claquage catastrophique.

2/ C'est la raison pour laquelle nous avons introduit les tubes multifaisceaux, dont la caractéristique essentielle est une tension cathode beaucoup plus faible (200 kV ou 250 au lieu de 5 ou 600 kV).

The Numerical Modelling of Near-Field HPM Target Coupling

A. Soubeyran, J.P. Estienne
MATRA MARCONI SPACE FRANCE
31 rue des Cosmonautes
Z.I. du Palays
31055 Toulouse Cedex
France

J.P. Boeuf
Centre de Physique Atomique de TOULOUSE
Université Paul Sabatier
118 route de Narbonne
F-31062 Toulouse Cedex
France

A. Ravier
MATRA DEFENSE
37 av. Louis Breguet, B.P. 1
78146 Vélizy-Villacoublay Cedex
France

1. SUMMARY

The numerical simulation of the coupling of HPM waves on targets is investigated either in vacuum (e.g. satellites) or in the atmosphere (e.g. aircraft's) using integral methods for unstructured meshing.

2. INTRODUCTION

The present paper describes the development of new numerical methods optimised for the prediction of HPM/target coupling in various environments. The numerical simulation of the coupling of HPM waves with a complex target body, either in vacuum (e.g. satellites) or in the atmosphere (e.g. aircrafts) requires especially efficient methods, in order to permit the treatment of realistic configurations.

As part of its ElectroMagnetic Compatibility management program, the European leading space company MMS is developing an integrated set of advanced codes, basically adapted to the description of intricate geometry and material patchwork found on satellites [1]. These prediction softwares are integrated in the global framework TDAS-EMC (Test Data Analysis System for ElectroMagnetic Compatibility) which combines the analysis of specification, prediction and measurement data together with a database management adapted to large space project evolution [2].

In any homogeneous medium, a Boundary Integral Equation formulation like the Method of Moments appears best suited to optimise the computer storage when describing complex bodies by an unstructured finite element surface mesh. This is typically the case in vacuum or more generally in the absence of any space charge and/or current distribution.

If a non-uniform plasma environment, either pre-existent or generated by field enhancement in the atmosphere (e.g.

around target slits) is to be accounted for, volume resolutions must be envisaged to solve the coupled equations of fields and charge distribution. The original problem for which we developed such schemes consisted in the electrostatic discharge charge transport, resulting field propagation and coupling around a spacecraft.

The classical Finite Difference method with regular mesh becomes rapidly unusable on limited workstations (e.g. DEC alpha) when considering several hundred megahertz emissions with tens of meter size calculation domain and body details down to a few centimetres. The electromagnetic field computation developed in MMS is therefore based on an integral method of Finite Volumes, allowing for the resolution in an optimised unstructured volume mesh, directly connected to the surface mesh used in vacuum.

A fully new method is then being developed to describe the charge transport resulting from field acceleration, using a direct integration of the VLASOV statistical equation. By judicious integration based on first and second moments, we transform it into an hyperbolic system, finally solved in the same way as the MAXWELL system.

The extension of this numerical method to the BOLTZMANN equation, including collision terms (necessary in the atmosphere and for pulse series) is under way.

Finally, in the dense atmosphere where transport phenomena become negligible in front of collisions, synthetic relations can be used to deduce the charge density and current distributions from the local electric field.

3. COUPLING IN VACUUM

In vacuum or any homogeneous medium, the physical problem of electromagnetic wave interactions is fully defined

by boundary (i.e. interface) conditions (i.e. charge and current distributions) and propagation medium dielectric properties (i.e. ϵ_0 and μ_0 in vacuum). Therefore, Boundary Integral Equation formulation is well adapted to optimise computer requirements. Among them, most used are surface finite elements and Method of Moments. This latest numerical scheme has been chosen in MMS because of its much simpler way to code, at the expense of increased matrix storage [3].

3.1 Method of Moments

As a result from the signal type, a time resolution is considered here. Two formulations are possible, either based on magnetic fields (i.e. Magnetic Field Integral Equation = MFIE) or based on electric fields (i.e. EFIE). The second one was chosen in MMS because of simpler implementation of geometry flexibility : thin open surfaces and wires. When considering the interaction between electromagnetic waves and solid bodies, it is always possible to separate the total radiations (T index) into incident waves (I index) and scattered waves (S index) :

$$\mathbf{E}^T = \mathbf{E}^I + \mathbf{E}^S$$

$$\mathbf{H}^T = \mathbf{H}^I + \mathbf{H}^S$$

The introduction of potentials leads to the following formulation :

$$\frac{d\mathbf{E}(r,t)}{dt} = -\nabla_r \cdot \frac{dV(r,t)}{dt} - \frac{\partial^2 \mathbf{A}(r,t)}{\partial t^2}$$

with scalar and vector potentials V and A, defined only by diffraction involved currents J (see figure 1) :

$$\begin{cases} \frac{dV(r,t)}{dt} = \int_s \frac{-\text{div} \bar{\mathbf{J}}(r', t - \frac{R}{c})}{R(r,r')} ds \\ \frac{d^2 \mathbf{A}(r,t)}{dt^2} = \frac{d^2}{dt^2} \int_s \frac{\bar{\mathbf{J}}(r', t - \frac{R}{c})}{R(r,r')} ds \end{cases} \quad \text{with: } \bar{\mathbf{R}} = \bar{\mathbf{r}} - \bar{\mathbf{r}}'$$

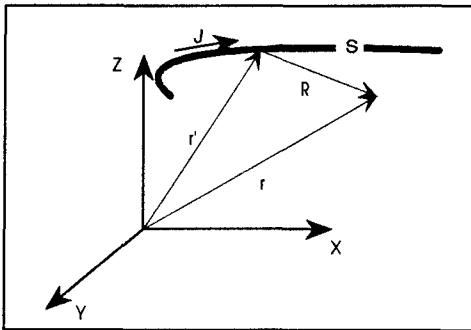


Figure 1 : coordinate system for EFIE method

The scattered field can therefore be expressed in the following way :

$$\frac{d\bar{\mathbf{E}}^S(r,t)}{dt} = \int_s \frac{\text{div} \bar{\mathbf{J}}(r', t')}{R} ds' - \frac{\partial^2}{\partial t^2} \cdot \int_s \frac{\bar{\mathbf{J}}(r', t')}{R} ds'$$

Using appropriate base functions (i.e. "roof top" functions), depending on the type of problem and verifying several properties (e.g. continuity, etc...), it is possible to develop this formulation in a matrix form, when applied on a finite element discretised geometry :

$$\sum_{2,k} Z_{u,k} \cdot I_k^n = V_k^n$$

where :

k and u define element indices

n defines the time step

Z matrix contains all the scattering interactions depending on the geometry and the various loads.

I is the current matrix for every elements

V is the matrix containing the source terms (voltage, current sources and incident field) and the retarded scattering interaction terms.

This linear system is solved by a conjugate gradient method to give currents everywhere on the scattering bodies. Then, starting from the MoM (i.e. Method of Moments) unknowns (i.e. normal component of edge currents), the fields can be expanded everywhere in the surrounding space, according to EFIE equation [3, 4].

This numerical simulation scheme was successfully applied to the prediction of the HPM field emitted by a small radiating device and its coupling on a missile-like target situated in near field zone [13].

However, due to the high electrical fields generated near the target edges, it becomes necessary to evaluate the possibility of air breakdown if we consider an atmospheric coupling. It is the aim of the next paragraph.

4. COUPLING IN THE ATMOSPHERE

A dramatic illustration of the above breakdown limitation, is presented on figure 4, where it is apparent that an HPM pulse will freely propagate and couple only at altitudes higher than about 50 km.

Below 50 km some local breakdowns occur at the place of "hot points" where the field is especially high; this does not mean however that no propagation exists anymore in a three dimensional configuration. In order to consider the HPM coupling at altitudes below the breakdown threshold atmospheric pressure, it becomes necessary to take into account the plasma creation around the target and possibly around the antenna in the modelling. Only near-field coupling will be envisaged here, so that no propagation absorption is accounted for because of the proximity between antenna and target (< 50 m).

The appropriate numerical simulation requires now to integrate simultaneously MAXWELL field propagation equations together with electron transport equation in an accurate 3D representation of coupling region. Due to inhomogeneous and variable propagation conditions in the vicinity of the target, it becomes necessary to consider a volume space meshing, contrary to the previous case in vacuum.

Mean power (MW.cm⁻²)

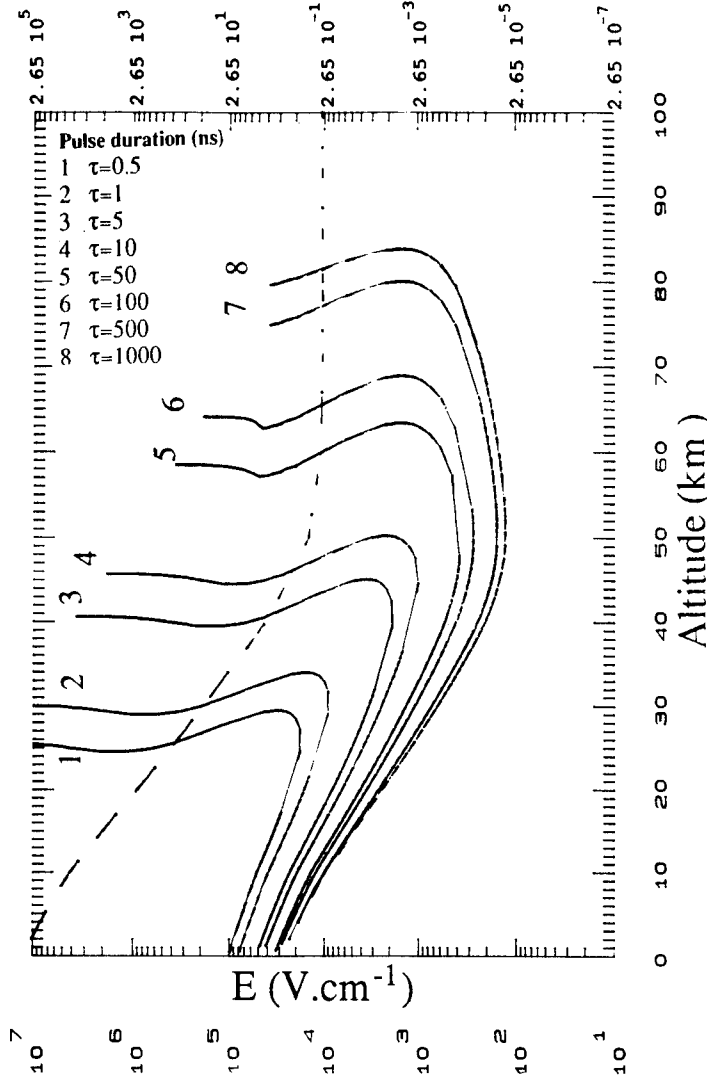


Figure 4 : Breakdown field and power with relativistic effects at 1 GHz

4.1 MAXWELL Equation : Finite Volume Resolution

In order to minimise computer memory requirements, the choice of the numerical method was based on the compatibility with an unstructured finite element (i.e. tetrahedral) space meshing which can be adapted to any specific case. MAXWELL equations are therefore solved by means of a finite volume formulation, essentially similar to flux-splitting methods used in Computational Fluid Dynamic [5]. The MAXWELL equation system is shown to be a linearly set of hyperbolic equations, which integration is based on a one step explicit scheme. The method is first order accurate in time and space, what is quite sufficient when using small enough time and space discretisation steps, as permitted by unstructured mesh.

In order to apply the finite volume numerical integration scheme, MAXWELL equations must be put in a conservative form. This method is derived from CFD where it is quite usual, to transform a set of partial differential equations into an hyperbolic conservative system [6, 7, 8].

Conservative form (simplified in 2D) :

$$\begin{cases} \frac{\partial u}{\partial t} + \frac{\partial f}{\partial x} + \frac{\partial g}{\partial y} = R & \text{in } \Omega \times (0, T) \\ u(x, y, 0) = u_0(x, y) & \text{in } \Omega \\ u(x, y, t) = \Phi(x, y, t) & \text{in } \partial\Omega \times (0, T) \end{cases}$$

with :

$$\begin{cases} \Omega \subset \mathbb{R}^2 \\ u = (E_x, E_y, B_z)^T \\ f = (0, c^2 B_z, E_y)^T \\ g = (-c^2 B_z, 0, -E_x)^T \\ R = (-\mu c^2 J_x, -\mu c^2 J_y, 0)^T \end{cases}$$

Note that matrix R contains local source terms of current density 'J' deduced from electron transport calculations (see below).

The domain Ω is discretised with an unstructured mesh of triangular (i.e. tetrahedral in 3D) elements, so that the conservative integral form of MAXWELL's equations reads :

$$\frac{\partial}{\partial t} \int_{\Omega} u \, d\Omega + \int_{\Gamma} (f, g) \cdot n \, d\Gamma = \int_{\Omega} R \, d\Omega$$

where Γ is the boundary of Ω and 'n' the outer normal. In every triangular mesh K_i we have then :

$$\frac{\partial}{\partial t} \left(\int_{K_i} u \, dK_i \right) + \sum_{k=1}^3 \int_{\Gamma_{K_i}} (f, g) \cdot n_{\Gamma_{K_i}} \, d\Gamma_{K_i} = \int_{K_i} R \, dK_i$$

The discretisation grid is constant in time. To evaluate the flux vectors f and g , for each edge Γ_{K_i} of cell K_i , we consider the field states u_L and u_R on each side (Left and Right):

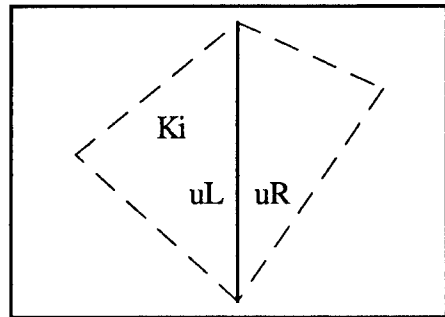


Figure 5 : Γ_{K_i} cell boundary with Left and Right field vectors

The homogeneous condition reads :

$$f = A u \text{ and } g = B u$$

with A and B the Jacobean matrix :

$$A = \frac{\partial f}{\partial u} \text{ and } B = \frac{\partial g}{\partial u}$$

We show below the computation of flux vector 'f', similar to a method of characteristics. It would be the same for 'g'.

Let's call $\lambda_1, \lambda_2, \lambda_3$ the eigenvalues of the matrix A , r_1, r_2, r_3 the right eigenvectors and l_1, l_2, l_3 the left eigenvectors associated. The difference between f_L and f_R comes both from propagation conditions (e.g. local current) and interface

constraint, like a dielectric film. To compute f_R and f_L , u_R and u_L are multiplied by right and left eigenvectors :

$$\begin{cases} f_L = \sum_{i=1}^3 (l_i, u_L) \lambda_i r_i \\ f_R = \sum_{i=1}^3 (l_i, u_R) \lambda_i r_i \end{cases}$$

The time integration is then based on an explicit scheme. For every K_i cell :

$$u_i^{n+1} = u_i^n + S(u_i^n, R_i^n)$$

with :

$$S(u_i^n, R_i^n) = \frac{-1}{\text{surface}(K_i)} \left(\sum_{j=1}^3 (f_{r_{K_i}^j}, g_{r_{K_i}^j}) \right) + \Delta t R_i^n$$

The numerical stability is ensured by the CFL condition on the time step : $\lambda_{\max} \frac{\Delta t}{h_{\min}} \leq 1$ with λ_{\max} the largest eigenvalue of matrixes A and B, and h_{\min} the minimum triangle height found in the mesh.

4.2 Electron distribution

It is interesting here to distinguish two limiting regimes :

- 1- Collisional plasma : when the electron collision rate largely exceed the HPM frequency
- 2- Non-collisional plasma : in the opposite case...

4.2.1 Collisional plasma : local field model

This is typically the case for altitudes below about 50 km (depends on the frequency), where the ionising frequency is much higher than the HPM frequency, leading to a very efficient energy transfer [9]. It becomes here possible to simplify drastically the plasma distribution computation by neglecting transport terms in the BOLTZMANN equation. This simplification is based on a local equilibrium between the electric field and the electron kinetic [10] :

$$\begin{cases} \frac{\partial n}{\partial t} = D \cdot \Delta n + n \cdot \left(v_i \left(\frac{E}{N} \right) - v_a \left(\frac{E}{N} \right) \right) - r \cdot n^2 \\ \frac{\partial \vec{v}}{\partial t} = -\frac{e}{m} \cdot \vec{E} - v_i \cdot \vec{v} \end{cases}$$

with :

- n = electron density
- \vec{v} = electron drift velocity
- $v_i(E/N)$ = ionising frequency
- $v_a(E/N)$ = attachment frequency
- r = recombination coefficient
- D = diffusion coefficient; it is a combination between free diffusion without plasma and ambipolar diffusion within a plasma :

$$D = D_a \cdot \frac{1 + \xi^2}{1 + D_a/D_e \cdot \xi^2} \quad \text{with : } \xi = \frac{\lambda_{\text{Debye}}}{L}$$

- E = electric field
- N = neutral gas density
- e = elementary electron charge (negative)
- m = electron mass

This simplified model leads to an exponential growth of the local electron density with time, in a constant amplitude electric field. The space charge remains zero because of negligible macroscopic separation between positive and negative charges before attachment or recombination. It is called the "local field" model, from which the local current density is easily deduced by : $\vec{J} = e \cdot n \cdot \vec{v}$. This is the coupling term with MAXWELL equations.

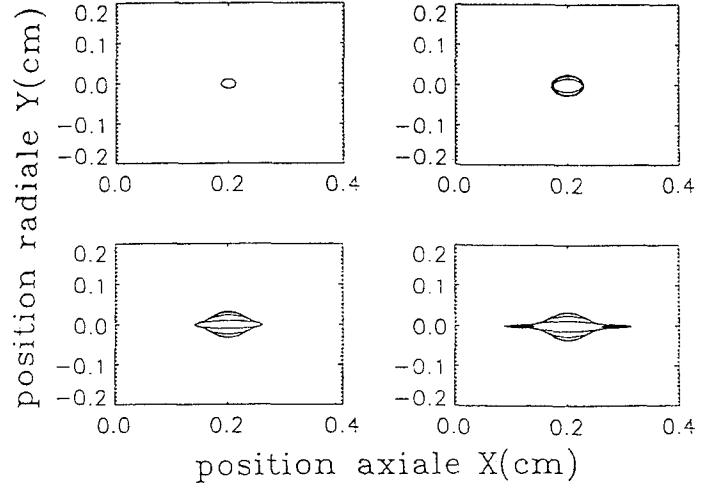


Figure 6 : Electron density distribution of a "plasmoid" in logarithm scale (between 10^{10} and 10^{14} cm^{-3}) at four times (8, 12, 16 and 18 ns) in a 4.5 MV/m average field, in ambient atmosphere

The ion current is neglected, due to the high inertia of ions. In MAXWELL electric field equation, the dielectric permittivity of space is modified by the presence of the plasma :

$$\epsilon_r = 1 - j \cdot \frac{e^2}{m \cdot \epsilon_0 \cdot \omega \cdot v_i} \cdot n$$

with : ω being the HPM pulsation.

With such a model it is possible to simulate the growth of local plasma zones or "plasmoids" at increased field places, as shown on figure 6. The figure 4 was also deduced from the same model, however improved by accounting for relativistic effects when the electron energy exceed about 10 keV, and defining a breakdown threshold when the electron multiplication exceed 10^8 .

4.2.2 Uncollisional plasma : BOLTZMANN equation

When the ionising frequency is small compared to the HPM frequency it becomes necessary to include the transport terms in the electron distribution equation, so that the full BOLTZMANN equation is required to be solved. This condition arises at high altitudes, typically above 60 km altitude.

MMS is currently developing an advanced numerical method to solve this type of electron distribution function equation, in the limiting case of absence of collisional source terms, i.e. the VLASOV equation, basically to describe accurately electrostatic discharge propagation around spacecrafts [1].

$$\frac{\partial f}{\partial t} + \bar{v} \cdot \nabla_{\bar{x}} f + \frac{e}{m} \cdot (\bar{E} + \bar{v} \wedge \bar{B}) \cdot \nabla_{\bar{v}} f = 0$$

with : $f(\bar{x}, \bar{v}, t)$ the distribution function (i.e. statistical presence probability)

This equation derives exactly from the more general BOLTZMANN equation, without collision effects. In order to overcome the well-known difficulties arising with standard particle tracking methods (e.g. Particle In Cell), like numerical instabilities due to particle trapping and "granular" charge distribution, we developed a new numerical scheme : ETS (Enhanced Transport Solver), which guiding principles follow [11].

The electron transport is here calculated by a direct integration of the statistical VLASOV equation, using a development of the distribution function over a series of appropriate functions, where the velocity space is described using a limited set of parameters. Thanks to this representation, the VLASOV equation can be transformed in a linear set of hyperbolic equations, which integration is undertaken by the same method as used for MAXWELL equations and with equivalent efficiency, much higher than traditional particle tracking methods [12]. Moreover, the direct integration of the distribution function allows to get a very good accuracy on charge density and current, with a dynamic range over at least five orders of magnitude between smallest and largest meaningful values [13].

The distribution function is split into a linear combination of functions f_i with appropriate integration properties, which are separately solution of the VLASOV equation, to statistically move particles according to applied forces.

$$f(\bar{x}, \bar{v}, t) = \sum_{i=1}^{m(t)} f_i(\bar{x}, \bar{v}, t)$$

$$\text{with : } \frac{df_i}{dt} = 0 \text{ for } i = 1, \dots, m \text{ (} m \leq 10 \text{)}$$

The form of f_i functions is chosen such that the non-linear 'v' dependency in VLASOV equation is removed :

$$f_i(\bar{x}, \bar{v}, t) = g_i(\alpha_i(\bar{x}, t), \beta_i(\bar{x}, t), \xi_i(\bar{x}, t), \bar{v})$$

The proper integration in phase space, involving first and second moment of the VLASOV equation, permits to obtain a conservative formulation, formally similar to the one obtained with MAXWELL equations (here in 2D) :

$$\frac{\partial W_i}{\partial t} + \frac{\partial H_i}{\partial x} + \frac{\partial P_i}{\partial y} = T_i$$

with :

W_i = vector of α_i , β_i and ξ_i

H_i and P_i = vectors of scalar product between $\text{div} W_i$ and a pseudo velocity vector.

T_i = vector of acceleration terms

The coupling variables with the MAXWELL system are currents and space charge densities, which are deduced as it follows :

$$\begin{cases} n(\bar{x}, t) = e \int_{\bar{v}} f d\bar{v} = \sum_{i=1}^m \varphi_i(\alpha_i(\bar{x}, t), \beta_i(\bar{x}, t)) \text{ in } \Omega \times (0, T) \\ J(\bar{x}, t) = e \int_{\bar{v}} \bar{v} f d\bar{v} = \sum_{i=1}^m \psi_i(\alpha_i(\bar{x}, t), \beta_i(\bar{x}, t), \xi_i(\bar{x}, t)) \text{ in } \Omega \times (0, T) \end{cases}$$

$n(\bar{x}, 0)$ and $J(\bar{x}, 0)$ are given (at $t = 0$)

The time integration scheme is then quite similar to the one used for MAXWELL's equations :

$$W_i^{n+1} = W_i^n + \Delta t \cdot S(W_i^n, T_i^n)$$

with :

$$S(W_i^n, T_i^n) = \frac{-1}{\text{surface}(K_i)} \left(\sum_{j=1}^3 (H_{\Gamma_{K_i}^j}, P_{\Gamma_{K_i}^j}) \right) + T_i^n$$

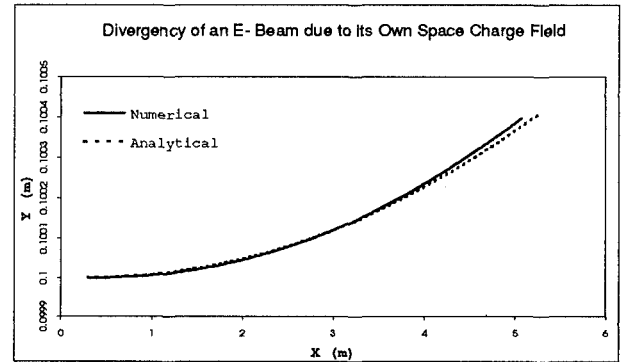


Figure 7 : Charge transport by direct VLASOV equation integration

The resulting code is today running with two-dimensional rectangular coordinates and was applied to various types of wave/charge interactions. The figure 7 shows the case of an electron beam diverging under its self-induced space charge field, for which an analytical solution can be found.

In the case where collisional effects are not negligible but do not inhibit sufficiently transport phenomena, it becomes necessary to introduce corresponding ionising and recombination source terms in the transport equation. This case is supposed to occur between about 50 and 80 km altitudes. It is then proposed to use a FOKKER-PLANCK formulation of the BOLTZMANN equation with collisional terms approximated by B-G-K operators :

$$\frac{\partial f}{\partial t} + \bar{v} \cdot \nabla_{\bar{x}} f + \frac{e}{m} \cdot (\bar{E} + \bar{v} \wedge \bar{B}) \cdot \nabla_{\bar{v}} f = \nu_i \cdot (F_n - f) + \nu_r \cdot (F_i - f)$$

with :

f = electron distribution function

F_n = Maxwellian distribution function

$$= n \cdot \left(\frac{m}{2\pi k T_n} \right)^{\frac{3}{2}} \cdot \exp \left\{ - \left[\frac{m(\bar{v} - \bar{u}_n)^2}{2k T_n} \right] \right\}$$

F_i = Maxwellian distribution function

$$= n \cdot \left(\frac{m}{2\pi k T_i} \right)^{\frac{3}{2}} \cdot \exp \left\{ - \left[\frac{m(\bar{v} - \bar{u}_i)^2}{2k T_i} \right] \right\}$$

ν_i = ionising frequency

ν_r = recombination frequency

Preliminary numerical analysis are under way to introduce this type of terms into the previous formulation developed for the simpler VLASOV equation.

5. CONCLUSION

The coupling between HPM waves and a general target as been investigated from the numerical point of view. It was found that an optimal approach is possible by choosing different numerical schemes according to different physical regimes, which allow various approximations :

① At altitudes higher than 100 km : it can be considered that no ionisation takes place anymore (fully ionised ambient low density plasma) and wave/target interaction can be approximated by field scattering in vacuum. No electron distribution is to be calculated and only MAXWELL equations are to be solved, best optimised using a BIE formulation in the time domain. Numerical calculations using a Method of Moment indicate strong field enhancement around the target.

At lower altitudes, collisional phenomena take place, dense plasma is locally produced and therefore requires :

- resolution of an electron distribution equation
- volume resolution of MAXWELL equations due to inhomogeneous propagation conditions : this part is now realised using a Finite Volume resolution scheme, based on a CFD-like algorithm, taking advantage of unstructured meshing of space. Current and space charge source terms can be introduced everywhere.

② Between 100 and 50 km : collisional effects are competing with charge transport and it is necessary to account for both. These are the worst conditions for numerical simulations where both currents and space charge are to be evaluated. A new advanced method is proposed to solve the FOKKER-PLANCK equation, based on a numerical scheme developed for the VLASOV equation : this equation is transformed into a conservative system and solved similarly to the MAXWELL equations (i.e. Finite Volume method).

③ Below 50 km altitude : collisional effects become preponderant and the electron drift becomes negligible during the HPM pulse transit. Transport terms in BOLTZMANN equation are then negligible and the macroscopic space charge collapse to near zero. Current source terms for MAXWELL equation resolution are possible to approximate using the simplified "local field" model. Such a numerical simulation permits to predict the formation of "plasmoids" in zones of enhanced electric field due to target coupling.

6. ACKNOWLEDGEMENTS

Developments and results presented in this paper have been gained thanks to the support of following organisms :

- DGA/Direction des Recherches et Etudes Techniques
- Centre d'Etude de Gramat
- Centre National d'Etudes Spatiales
- European Space Agency

7. REFERENCES

- [1] "Electrostatic Charge and Discharge : Space Charge Evolution and Associated Electromagnetic Fields on Complex 3-D Spacecrafts in the GEO Environment" Soubeyran A., Estienne J.P., Aouizerate A., Talaalout L., Clementz D., Proc. of 3rd ESA Eur. Workshop on EMC and CEM, PISA (Italy), 26-28 Oct. 93, p. 135.
- [2] "TDAS-EMC : An Engineering Tool for Electromagnetic Compatibility Control on Large Systems" Inzoli L., Garres C., Granger J.P., Ferrante J.G., Marino M.F., Seillé J., Proc. of 3rd ESA Eur. Workshop on EMC and CEM, PISA (Italy), 26-28 Oct. 93, p. 93.
- [3] "The Method of Moments in Time and Frequency Domain, a New Technique Applied to Transient Electromagnetics" J.P. Estienne, Proc. of 3rd ESA Eur. Workshop on EMC and CEM, PISA (Italy), 26-28 Oct. 93, p. 24.
- [4] "Intégrales de Frontière en Régime Instationnaire" Estienne J.P., Gravelle L., Proc. CEM 94, Toulouse (France) 2-4 Mars 94, p. 323.
- [5] "A CFD-Based Finite-Volume Procedure for Computational Electromagnetic - Inter disciplinary Applications of CFD Methods" V. Shankar, W. Hall, A. Mohammadian, AIAA-89-1987, 9th Comp. Fluid Dyn. Conf., Buffalo New-York, Jun. 1989.
- [6] "Hyperbolic Systems of Conservation Laws" E. Godlewski, P. Raviard, S.M.A.I., Vol. 3, 1991
- [7] "Difference Schemes for Hyperbolic Equations, with High Order of Accuracy" P. Lax, B. Wendroff, Com. on Pure Math., Vol. 17, 1964.
- [8] "Trajectographie des électrons d'une Décharge Electrostatique : Resolution des Equations de MAXWELL en 2D" L. Talaalout, A. Soubeyran, J.P. Estienne, Contrat CNES No 896/ CNES/91/1251/00, Ref. MMS S413/NT/15.93, May 1993.
- [9] "Physical Phenomena Induced by Passage of Intense Electromagnetic Pulse in the Atmosphere" Yee J.H., Mayhall D.J., Alvarez R., LLNL Report, 1984.
- [10] "Propagation d'Impulsions Micro-Onde dans l'Atmosphère" J.P. Boeuf, Rapport Interne N°1, CPAT (France), 1992.
- [11] "Résolution des Equations de MAXWELL et VLASOV" L. Talaalout, Y. Haugazeau, A. Soubeyran, J.P. Estienne, Proc. JEE'93, Toulouse, 17-19 Nov. 93, p.109-118.
- [12] "Trajectographie des électrons d'une Décharge Electrostatique : MATESD 2D : Document de Référence" L. Talaalout, J.P. Estienne, A. Soubeyran, Contrat CNES No 896/ CNES/91/1251/00, Ref. MMS S413/NT/19.93, Jun. 1993.
- [13] "Numerical Modelling of Charged Particle Emission Effects" A. Soubeyran, J.P. Estienne, MMS-F Technical Note Ref. S413/NT/12.93, Feb. 1993.
- [13] "Générateur Pyrotechnique" J.P. Estienne, Compte Rendu de la Journée Micro-Ondes de Forte Puissance, C.E.Gramat, 10 Dec. 92.

DISCUSSION

G.LABAUNE

A-t-on des lois d'évolution de l'ionisation en fonction des champs incidents et de leurs fréquences et temps d'application ?

AUTHOR'S REPLY

Il existe des lois basées sur une analyse physique et dont les paramètres font l'objet d'ajustements empiriques.

E. SCHWEICHER

Vous semblez avoir négligé l'influence du champ magnétostatique terrestre qui rendrait votre plasma anisotrope. Envisagez-vous d'en tenir compte dans l'avenir ?

AUTHOR'S REPLY

C'est exact, le champ magnétique terrestre est négligé aujourd'hui. Pour un plasma de petite dimension ($< R_{\text{Larmor}}$) ce n'est pas important. Sinon il faudra considérer ce champ, ce qui est possible dans le futur.

LABORATOIRE D'ESSAIS FIER DE FORT NIVEAU HYPERFRÉQUENCE

JP. BRASILE, G. JEAN-FRANÇOIS, M. SIMON

THOMSON SHORTS SYSTEMES

9, rue des Mathurins - BP 150 - 92223 BAGNEUX CEDEX (FRANCE)

1- INTRODUCTION

Un laboratoire de forte puissance hyperfréquence a été étudié et réalisé par THOMSON SHORTS SYSTEMES. Cette installation produit :

- de fortes puissances hyperfréquence (1GW crête),
- des champs forts rayonnés.

Les possibilités de cette installation permettent :

- de réaliser des essais de vulnérabilité en champ forts hyperfréquence,
- d'être utilisé comme démonstrateur technologique mettant en oeuvre de fortes tensions pulsées (1 MV) de forts courants (quelques dizaines de kA) et de grandes puissances hyperfréquences rayonnées (1 GW).

2- DESCRIPTION

L'installation est constituée de :

2-1- L'ENSEMBLE GÉNÉRATEUR HAUTE TENSION COMPRENANT :

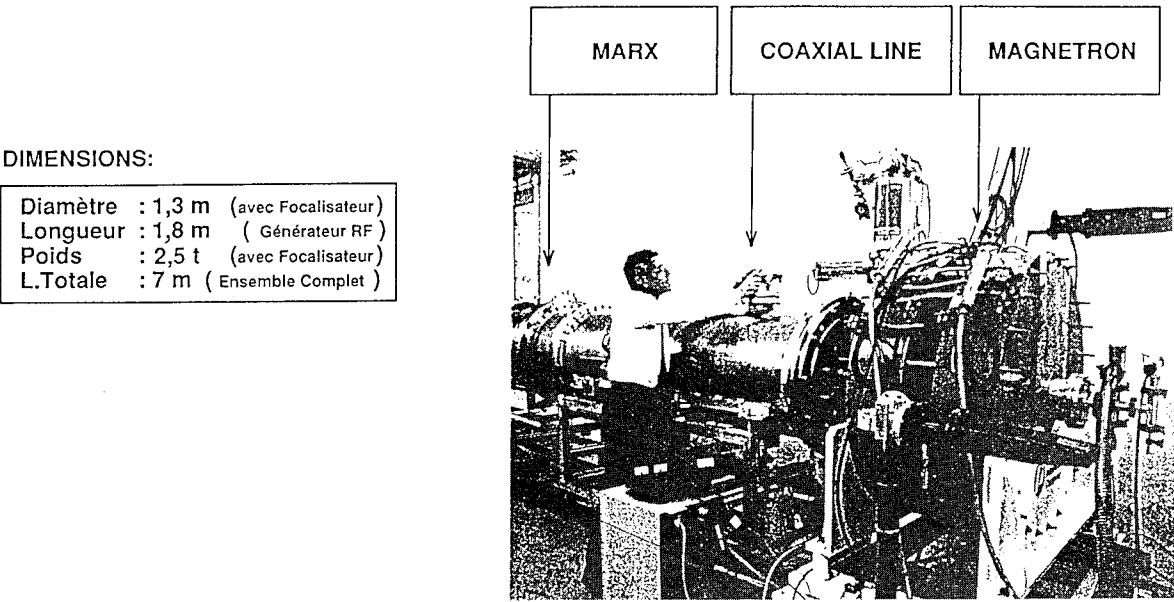
- une Alimentation 100 kV,
- un générateur de Marx compact délivrant de 0,4 à 1,2 MV pour 20 kA. L'énergie stockée est de 3 kJ pour une capacité équivalente de 4,17 nF avec 12 étages. L'isolement électrique est assuré par du gaz SF6 sous pression. (O. BECLE et al, 8th IEEE Internation Pulse Power Conf. pp. 998-1000 San Diego 1991), et le fonctionnement est monocoup,
- une ligne coaxiale de mise en forme des impulsions de tension.

2-2- L'ENSEMBLE GÉNÉRATEUR HYPERFRÉQUENCE :

- Un magnétron relativiste en bande S (type 6 vannes de Physics International.),
- un ensemble de focalisation (champ magnétique jusqu'à 1,2 Tesla)
- 1 à 3 antennes de type cornet (16 dB de gain),
- des moyens annexes (vide, refroidissement,.....)

Cet ensemble est installé dans une casemate permettant la protection contre les rayons X.

La figure ci-après représente l'installation:

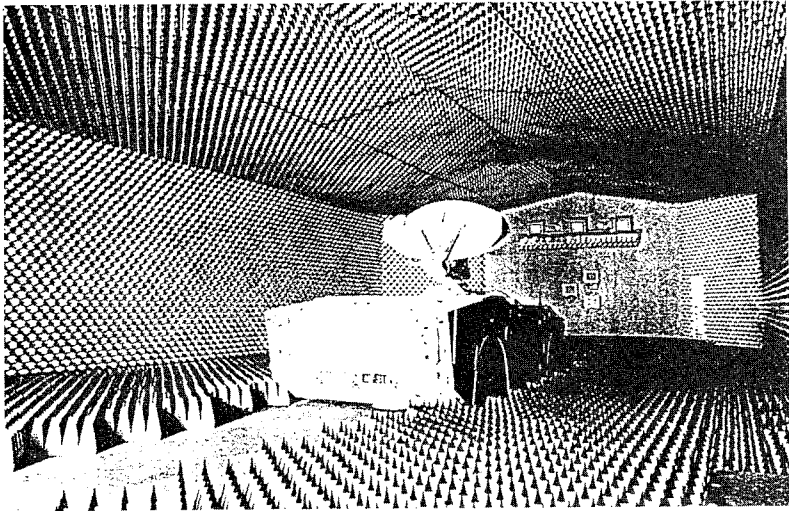


2-3- UNE CHAMBRE DE RAYONNEMENT R.F.

Cet ensemble consiste en une chambre anéchoïde de dimensions :

**CHAMBRE D'ESSAIS pour Fortes
Puissances Hyperfréquences**

Longueur : 22 m
Largeur : 10 m
Hauteur : 5,5 m



2-4- DES MOYENS DE CONTRÔLE COMMANDE ET DE DIAGNOSTICS.

ces moyens sont implantés dans une cage de Faraday.

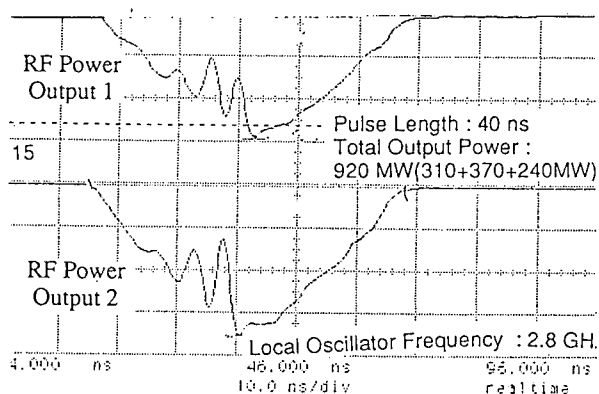
3- RÉSULTATS

Les performances obtenues avec l'installation d'essais FIER sont :

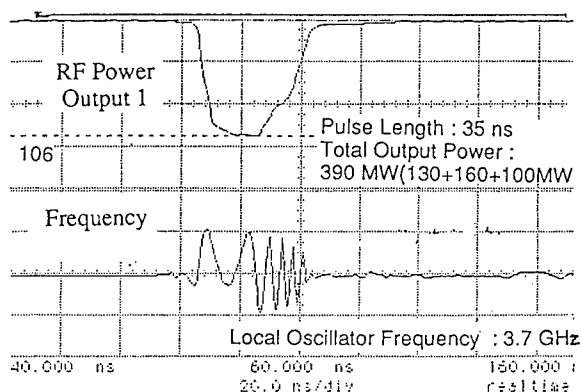
- Puissance hyperfréquence : gamme de 60 MW à 1 GW sur 1 à 3 sorties hyperfréquences avec une énergie maximale de 25 J par impulsion. La durée des impulsions varie de 20 ns à 100 ns en fonction de régime de fonctionnement et des fréquences utilisées.
- Fréquences : 2,8 GHz ; 3,2 GHz et 3,7 GHz,
- courant magnétron (4 à 20 kA),
- champ magnétique axial 0,4 à 1T
- Tension appliquée : 400 kV à 900 kV.

La forme typique des impulsions pour la puissance de sortie R.F. en fonction du temps est illustrée par les figures ci-dessous :

Fréquence à 2,8 GHz



Fréquence : 3,7 GHz

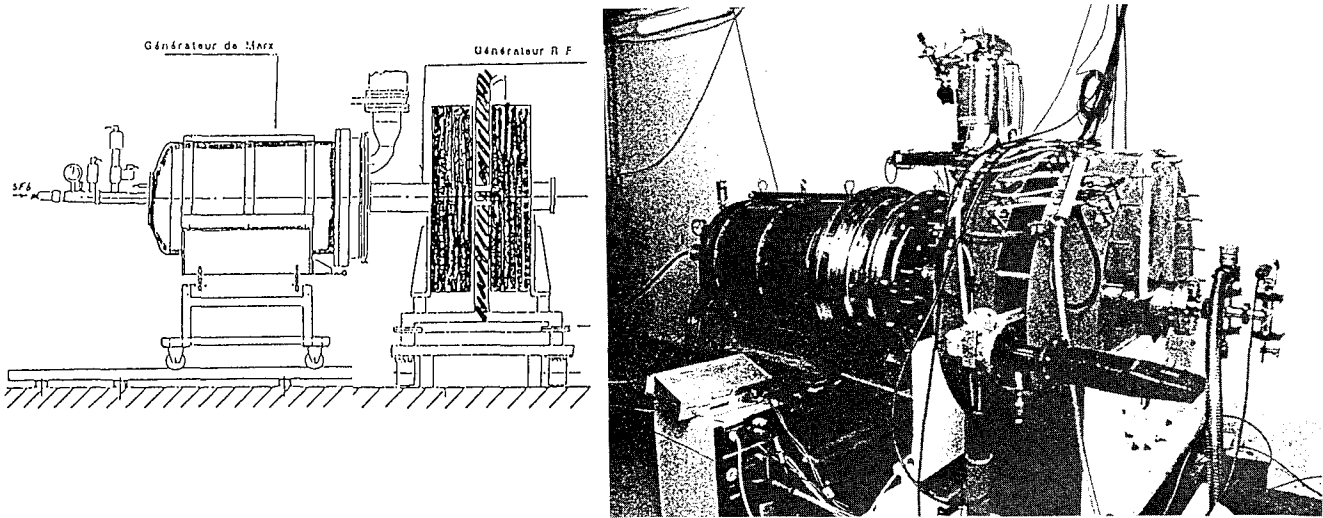


La puissance hyperfréquence générée par le magnétron est transportée par guides d'ondes jusqu'à trois cornets de 16 dB de gain qui rayonnent dans la chambre. Les caractéristiques principales rayonnées sont indiquées dans le tableau ci-après :

Fréquence (GHz)	2,8	3,2	3,7
Puissance Crête (MW)	350	150	200
Largeur Impulsion (ns)	55	40	40
Front de montée (ns)	3 à 20	5 to 8	3 à 15
Surface éclairée (3dB) (m ²)			
- à 3m	1,4	1	0,8
- à 6 m	5,5	4,2	3,1
- à 10 m	15,3	11,6	8,6
- à 14 m	30	22,7	16,8
Densité de puissance / Champ crête (W / m ²) (kV / m)			
- à 3m	13570 / 320	7600 / 240	13550 / 320
- à 6 m	3400 / 160	1900 / 120	3390 / 160
- à 10 m	1220 / 95	680 / 70	1220 / 95
- à 14 m	620 / 70	350 / 50	620 / 70

4- ENSEMBLE COMPACT

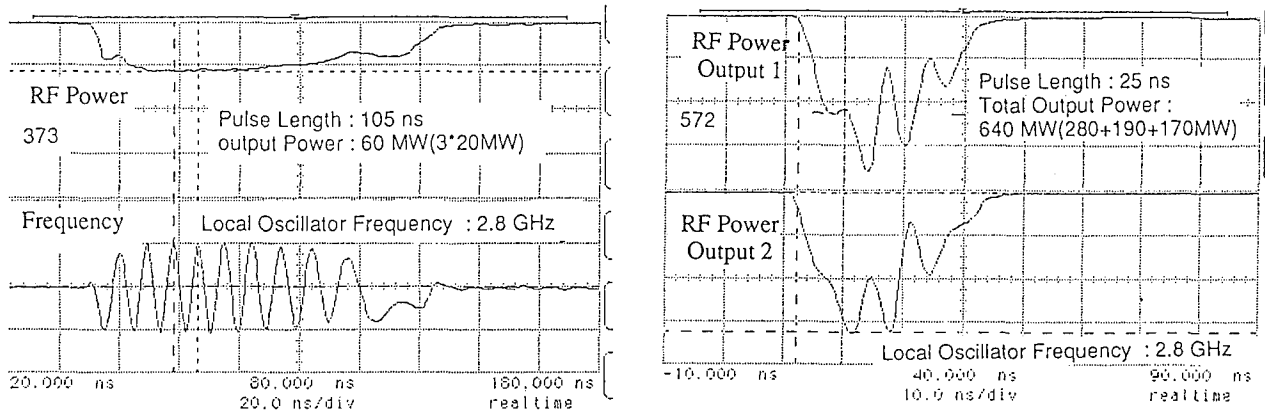
Dans le but de réaliser un ensemble compact de génération MFP le fonctionnement du magnétron relativiste directement connecté au générateur de MARX a été testé avec succès. Le MARX compact développé par TSS est de faible self (front de montée inférieur à < 50 ns sur 50 Ω à 900 kV) et de petites dimensions (volume inférieur à 0,6 m³) pour une énergie stockée de 3kJ. L'installation réalisée est représentée ci-dessous.



Le fonctionnement dans cette configuration fait apparaître deux gammes de fonctionnement :

- Impulsions longues (de l'ordre de 100 ns) à faible puissance (≈ 60 MW),
- Impulsions courtes (de l'ordre de 20 à 30 ns) à forte puissance (≈ 600 MW).

Une illustration de ces deux régimes de fonctionnement est donnée ci-dessous :



5- EVOLUTIONS :

Il est prévu de faire évoluer l'installation champs forts FIER sur les points suivants :

- Répétitivité : trains d'impulsions de 30 s à quelques hertz (les premiers essais sont satisfaisants),
- Compacité : générateur de MARX de 2,25 kJ à 800 kV dans 150 à 200 litres,
- Fréquence : Etude d'un amplificateur bande X de forte puissance (GW).

6- CONCLUSION

Le laboratoire d'essais FIER permet la génération de champs forts jusqu'à 13 kW/m^2 pour plusieurs fréquences en bande S.

La durée des impulsions hyperfréquences générées peut être variable de 100 ns à 15 ns.

La chambre de rayonnement est dimensionnée pour accepter des objets de grandes dimensions.

Les évolutions futures envisagées en font un outil pour l'étude de vulnérabilité de systèmes dans une gamme de fonctionnement encore élargie.

E. SCHWEICHER

1/ A 10 m, la densité de puissance est-elle de 10 kW/cm^2 ou bien 10 kW/m^2 ?

2/ Quel est l'encombrement quand le Marx est connecté directement au magnétron ?

AUTHOR'S REPLY

1/ Elle est de 10 kW/cm^2

2/ Longueur = 3 m ; diamètre = 1,3 m

Translation:

Q.

1. At 10 m, is power density 10 kW/cm^2 or 10 kW/m^2 ?

2. What are the dimensions when the Marx is connected directly to the magnetron ?

A.

1. It is 10 kW/cm^2 .

2. Length = 3m ; diameter = 1.3m.

RADIAL ACCELETRON, A NEW LOW-IMPEDANCE HPM SOURCE

Moe Joseph Arman

PHILLIPS LABORATORY

Electromagnetic Sources Division, PL/WSR

3550 Aberdeen Ave. SE

Kirtland AFB, New Mexico, 87117-5776

SUMMARY

Under a grant from the National Research Council and in collaboration with the Phillips Laboratory, the author was tasked to explore and analyze the proposed concept of using transit-time effects in a coaxial geometry to develop a low-impedance HPM source that uses no external magnetic field and no confining foils. This source will work in the 1-20 GHz range and will have a power output of no less than 1 GW. The input will be a low-voltage dc pulse of only 350kV or less with a flat top of approximately 200ns. The dc pulse is launched into a coaxial structure that is the diode, the oscillator, and the buncher all in one. Strong impedance mismatch between the diode section and the body of the device provides enough reflection to have a well defined coaxial cavity of high Q to support cavity characteristic modes. Electrons are emitted from the inner conductor of the structure and as they accelerate towards the anode they interact with a selected characteristic mode of the structure, on the average losing kinetic energy to the mode. This process continues until the RF fields are strong enough to modify the transit time away from the optimal value thus leading to saturation. The source offers significant improvements in power, repetition rate, size, and efficiency. Because of the coaxial structure, the diode impedance may be

reduced to a few ohms thus allowing larger input and output powers. With no foils to erode, the only thing limiting the repetition rate is the vacuum ability, and since there is no external magnetic field required, the device is simple, lightweight and inexpensive. Because of the strong bunching the efficiency is high. As is the case with all transit-time oscillators, the signal is stable and monochromatic. The device may be used as a buncher or as an oscillator. In what follows I present the progress made so far and show that all goals set forth in this project are achieved. In addition it is shown that the gated emission of electrons, a process basic to high power rf-amplification, is a natural by-product of the mechanism used in this device.

1. INTRODUCTION

Accelerated motion of electric charges is the source of all electromagnetic radiations. Fields of characteristic modes of high Q conducting structures can be used as an accelerating mechanism for coherent radiation from charged particle beams in the microwave range(1-6). For instance when streaming charged particles cross a cavity resonating at one of its characteristic modes, decelerating fields of the mode, under certain conditions, can cause the charges to radiate coherently

thereby losing some of their kinetic energy and enhancing the fields. This process, known as 'Transit-Time' effect, has been understood since the 1930's. However, mainly because of very low growth rate and partly because of low saturation levels, no significant amount of microwave radiation has been produced with the nonrelativistic charged particle beams available until now. An attempt in increasing the beam current in order to increase the power would result in strong space charge depression and formation of virtual cathode. Recent advancements in pulse-power technology has made relativistic giga-amp beams possible thereby reviving the Transit-Time Oscillators (TTO) as a possible source of HPM radiation. Since the resonating structure has a strong stabilizing effect on the process, HPM sources based on TTO's are robust, stable, monochromatic, and efficient.

Radial acceletron is one such new source but in addition because of its cylindrical structure it is of a very low impedance (high power) and because it combines the oscillator with the diode, it uses no foil so it can be repeated at a very high rate. Furthermore for the modes explored here, the radial acceletron uses no external magnetic field so it is very compact and light. In section 2 the theory involved in radial acceletron is explored. The results of numerical simulations are presented in section 3. Section 4 is the conclusion and suggestions for follow-up work.

2. THEORY

We start with a brief qualitative description of the theory of transit-time oscillators. When charged particles cross a structure with standing RF waves they undergo a series of accelerations and decelerations. If the particles' transit-time is close to the period of the RF and the radiation is the lowest mode in the direction of the transit, there will be one acceleration and one deceleration in an order that depends on the phase at the time of entry.

Those particles who accelerate first and decelerate next will travel faster than the average and have gained some kinetic energy upon leaving. Those particles that enter at a decelerating phase however will spend more time in the cavity than the average transit time. These particles lose more kinetic energy than those of the opposite phase gained. The overall result is a net flow of energy from the beam to the fields. This process continues until the average transit time becomes significantly different from the initial transit time and the fields cease to grow any further.

In an acceletron this process takes place in a diode and the particles are, in addition to the RF fields, also subject to the dc fields of the diode. This not only allows for a more compact system because the diode and the resonating cavity are combined into one, the uniform acceleration due to the dc fields raises the space charge limited current thus allowing more current at a lower voltage. Combining the diode and the resonator also eliminates the need for foils in the path of the beam thus allowing for very high repetition rate.

In a *radial* acceletron, in addition, the diode/resonator has a coaxial structure that allows for much smaller diode impedances and consequently higher power for any given voltage. Figure 1 is a schematic drawing of a radial acceletron with coaxial loading. It consists of two coaxial lines sharing the same outer conductor. The inner conductor to the left is the cathode, enlarged at the emission area to enhance the fields and to increase the emission surface. The dc pulse is launched from the left. The electrons move radially towards the anode and radiate in the process. The radiation is extracted through the coaxial line to the right.

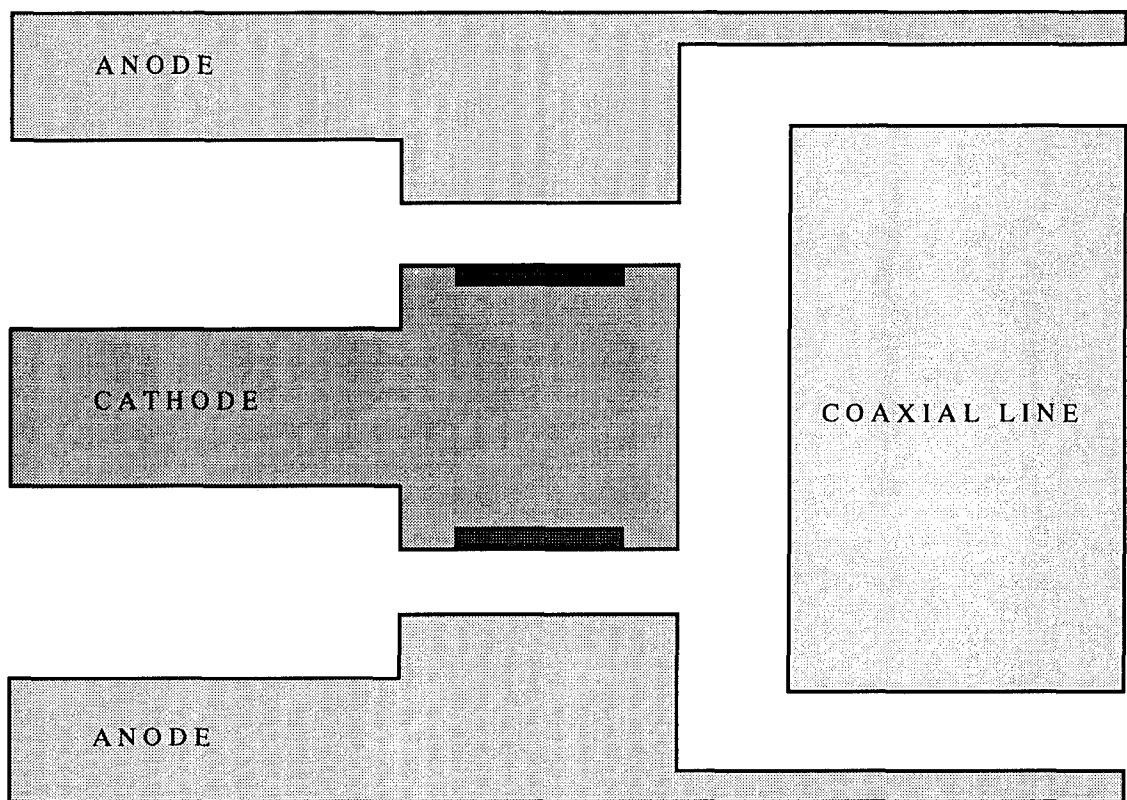


Figure 1. Schematic plot of the radial accelatron with radial loding. The dc pulse is launched from the left.

2.1 SMALL-SIGNAL ANALYSIS

The most complete solution to the radial accelatron problem is to solve the maxwell's equations for the entire system and find the fields and the current self-consistently as a function of time. This approach is however intractable because of the complicated boundary conditions involved. In the small-signal gain approximation the fields are initially assumed known, eigenmodes of the system, and the current assumed fixed. The nonlinear effects, if any, and the space charge effect are ignored in this approximation, and the saturation mechanism can not be addressed. In this approximation, the energy exchange between the beam and the rf radiation may be described by

$$\frac{d(\text{Energy})}{dt} = \int_{\text{beam}} (\vec{J} \cdot \vec{E}) dV \quad (1)$$

where \vec{J} is the beam current, \vec{E} is the sum of the d.c. field and the electric field of the eigenmode assumed present in the cavity, and the integration is over the beam volume. Furthermore, to assure analytic solution, non-relativistic approximation is used and the calculation is carried out for a single particle. Generalization to a stream is trivial.

Assuming a TM_{001} mode and a rectangular

approximation to the eigenmode in the coaxial cavity, we integrate the equation of motion to get

$$v = \frac{eV}{md}t + \frac{eE_0}{m\omega} (\sin(\omega t + \phi) - \sin\phi) \quad (2)$$

where v is the velocity of the electron as a function of time, e is the electron charge, V is the dc voltage, m is the electron mass, d is the diode gap, E_0 is the amplitude of the assumed rf field, ω is the angular frequency of the rf, and ϕ is the phase at which the particle was emitted. Integrating (2) with respect to t over the gap gives

$$d = \frac{eV}{2md}\tau^2 - \frac{eE_0\sin\phi}{m\omega}\tau - \frac{eE_0}{m\omega^2} (\cos(\omega\tau + \phi) - \cos\phi) \quad (3)$$

where τ is the transit time of the electron. If we further assume that the transit time τ is comparable to the period T of the rf, equation (3) reduces to

$$d = \frac{eV}{2md}\tau^2 - \frac{eE_0\sin\phi}{m\omega}\tau \quad (4)$$

Solving for τ and assuming $E_0 \ll (V/d)$ we have

$$\tau = \left(\frac{E_0\sin\phi}{\omega V} - \sqrt{\frac{2m}{eV}} \right) d. \quad (5)$$

Substituting (5) in (2) gives the final velocity

v_f as a function of ϕ , V , and d

$$v_f = \left(\frac{eE_0\sin\phi}{m\omega} - \sqrt{\frac{2eV}{m}} \right) + \frac{eE_0}{m\omega} * \left[\sin \left(\frac{E_0 d \sin\phi}{V} - \omega d \sqrt{\frac{2m}{eV}} + \phi \right) - \sin\phi \right]. \quad (6)$$

v_d , the velocity gain due to the rf, is given by

$$v_d = v_{dc} - v_f = \sqrt{\frac{2eV}{m}} - v_f \quad (7)$$

where v_{dc} is the final velocity in the absence of rf. v_d averaged over ϕ changes sign with d , displaying alternating regions of growth and damping as a function of d . v_d is a measure of how much energy is being exchanged between the beam and the rf. This quantity may be summed over all electrons to find the growth rate for the rf radiation.

3. SIMULATION

The TM_{001} mode of the radial acceletron has been studied rather extensively using the 2-D PIC codes ISIS and MAGIC and the 3-D PIC code SOS. The 2-D simulations were carried out to verify the principle behind the radial acceletron and to confirm its viability as a high power source of microwave. The 3-D simulations were performed to rule out the presence of non-axisymmetric modes that could disturb the TM_{001} mode. A tentative axial loading of the device was also modeled using the 2-D code MAGIC. An unoptimized rms efficiency of 15% has been observed.

3.1 2-D SIMULATIONS

The 2-D simulations were carried out for a device designed to produce the TM_{001} mode at 3.1 GHz. operating at 300kv. The choice of the TM_{001} mode was arbitrary, other modes and other frequencies are equally achievable. The radius of the inner conductor at the emission surface, Figure 1., is 23.4 cm, the radius of the anode is 27.0 cm, and the cavity is 6.4 cm long. The emission surface is 3.2 cm long. The input line impedance is $20\ \Omega$, the load impedance is $4\ \Omega$, and the gap between the diode and the load is 8 cm. A short risetime of 5 ns for the dc pulse was applied to speed up the simulation. In some simulations Bragg reflectors were used in the input line to increase the Q of the cavity.

Figure 2 is a plot of particles trajectories as they move towards the anode. This corresponds to a time when the instability has saturated and the emission is fully modulated by the rf's electric field. In addition to this modulation, interaction with the rf has further bunched the beam to very high densities, an indication of possible high efficiency. Figure 3 is a perspective plot of the radial electric field showing the rf propagating along the gap and down the coaxial load to the right. The Bragg reflectors in the input line have reduced the backward going rf to a very low level. Notice that the peak values of the rf amplitude in the coaxial load is larger than the dc amplitude in the input line.

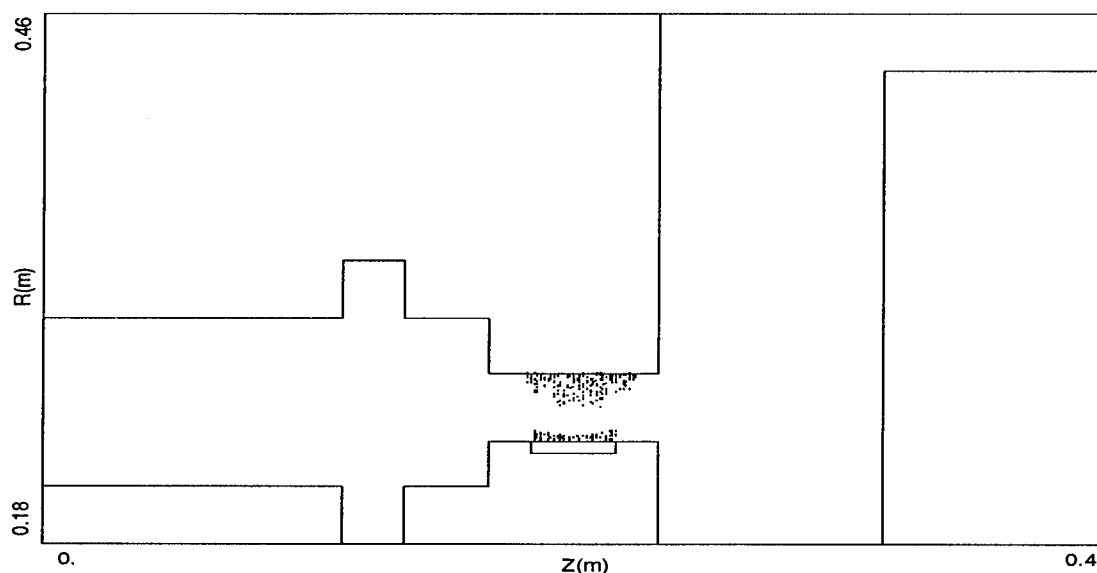


Figure 2. Computer simulation of the radial acceletron showing the electron in a gated emission pattern. The Bragg reflectors in the input line are for confining the rf fields. Only the upper portion of the device is modeled.

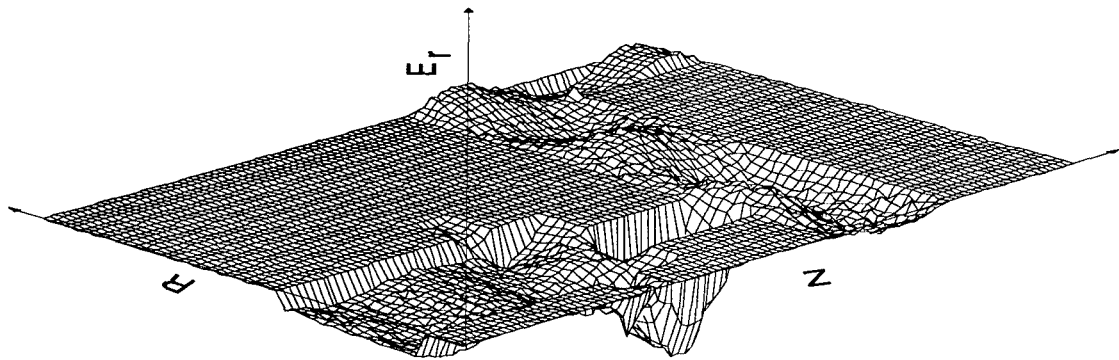


Figure 3. Perspective plot of the radial electric field showing the rf being generated in the cavity, propagating radially outward towards the coaxial line and leaving the system through the coax.

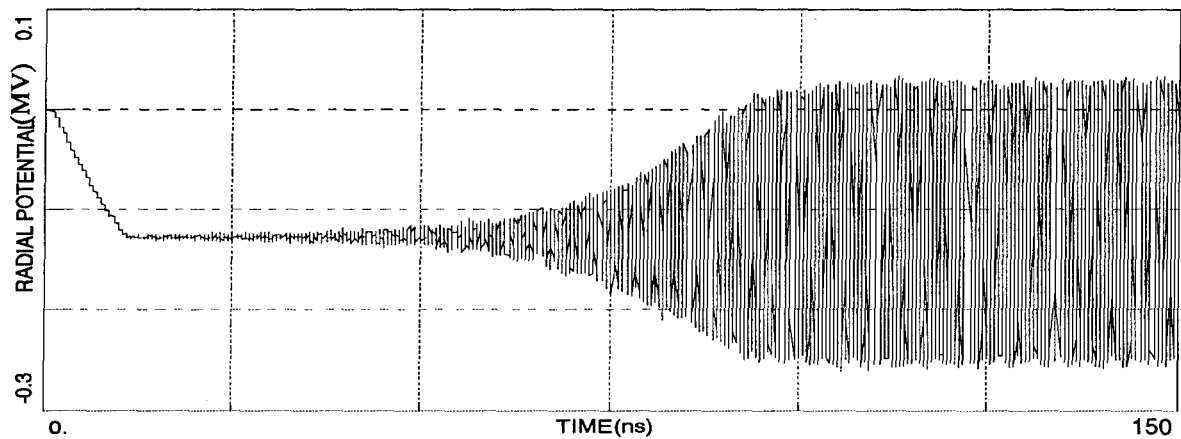


Figure 4a. Time plot of the radial potential at the center of the resonator cavity. The amplitude of the ac voltage exceeds the dc value by a small fraction.

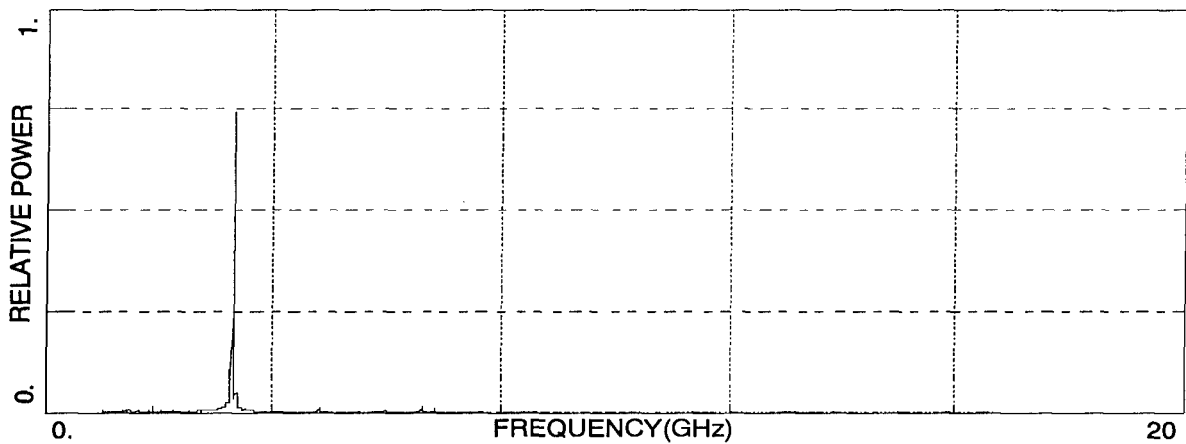


Figure 4b. The fourier transform of 4a showing a stable signal at approximately 3.1 GHz.

Figure 4a is the voltage in the center of the diode (i.e. E_r at the center integrated along the radius) plotted as a function of time. The amplitude of the rf is slightly larger than the magnitude of the input pulse. Figure 4b is the fourier transform of 4a. It shows a pure TM_{001} mode with no indication of any mode competition. Figure 5a is the time plot of the radial current density in a/m. The total dc current, $2\pi r j_r$, is approximately 10ka. The peak rf current is approximately 4 times that, indicating very strong bunching. The fourier analysis of the current time plot, Figure 5b, shows up to 4 harmonics present. The enlargement of the current plot shows regions of zero current caused by emission turn-off due to strong rf fields at the cathode. This modulated emission feature is similar to the gated emission patterns much desired in many rf related applications of intense electron beams.

Figure 6a is a plot of the extracted rf power as a function of time. The peak power is approximately 500mw, leading to an rms efficiency of 15%. No effort so far has been made in optimizing the loading and the extraction mechanism. Based on the bunching properties of the beam, the author is confident an overall rms efficiency of 25% is readily possible. Figure 6b is the fourier transform of 6a showing the main peak at twice the frequency of the rf radiation. This indicates the extracted power is almost entirely ac radiation.

3.2 3-D SIMULATIONS

The purpose of the 3-D simulations was to rule out the possibility of mode competition due to non-axisymmetric modes. The acceletron with the TM_{001} mode is basically a two-dimensional problem. However to model the non-axisymmetric modes one needs to model the entire device. The device modeled in two dimensions was also modeled in three dimensions with the azimuthal angle ranging from 0 to 360 degrees, in cylindrical geometry. The gridding was chosen to

resolve any modes at TM_{333} or lower. No modes other than the TM_{001} mode was observed for the parameters used. Figure 7 is a plot of the fourier transform of the beam current from the 3-D simulation indicating there are no mode other than the mode observed in the 2-D simulation.

The 2-D Particle-In-Cell (PIC) codes MAGIC and ISIS, and the 3-D PIC code SOS were used extensively in this work.

4. CONCLUDING REMARKS AND FUTURE WORK

Radial acceletron being a transit-time oscillator latches onto a characteristic mode of the structure supporting it and as such it produces a stable monochromatic radiation at a fixed frequency with little possibility of mode shifting or mode mixing. Furthermore, being an acceletron it allows the source to work at lower voltages (~250 KV) without forming virtual cathode. *Radial* acceletron in particular because of its radial mode of operation allows much lower impedances for the diode, leading to higher input/output powers at lower voltages (~10ka of current for a 250KV pulse). In addition because there is no external magnetic field, the source is small, light, and portable. Also because there are no foils necessary, potentially high repetition rate are possible.

Numerical simulations have confirmed the viability of the concepts involved. The bunching and the gated emission features of the device are particularly encouraging. Switching to much higher frequencies with little or no drop in the power output is possible. The efficiency(rms), based on preliminary loading simulation results and bunching levels observed, could exceed 50%. The author believes a 2GW source in the x-band operating at 250KV with a repetition rate of 1 khz is possible.

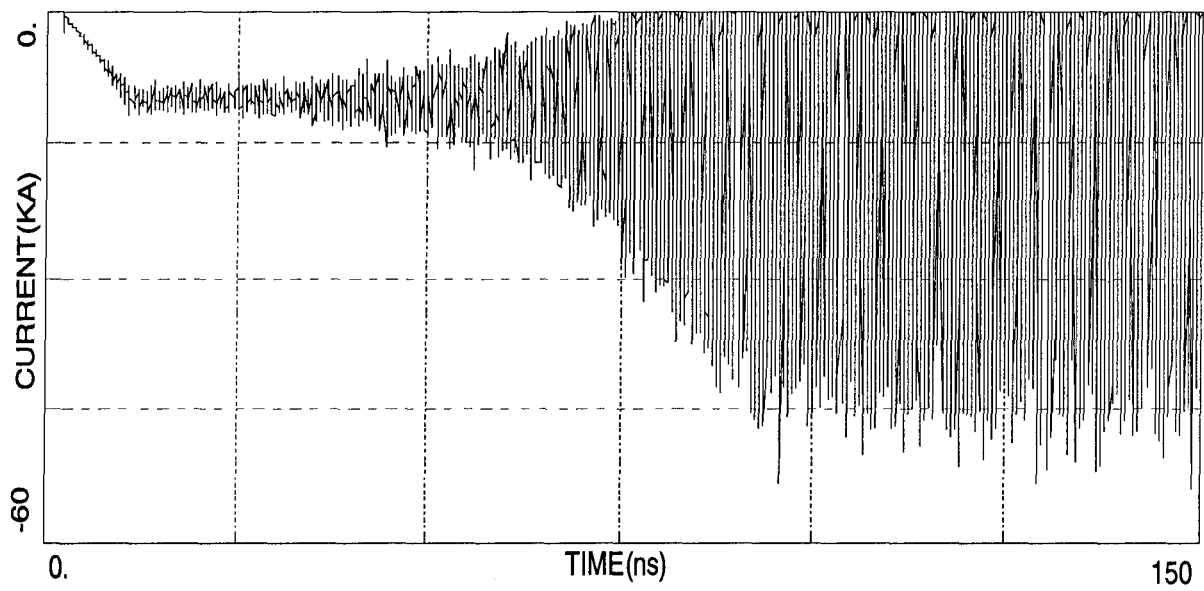


Figure 5a. The time plot of the total radial current in the resonator cavity. The peak ac current is at least four times the dc level.

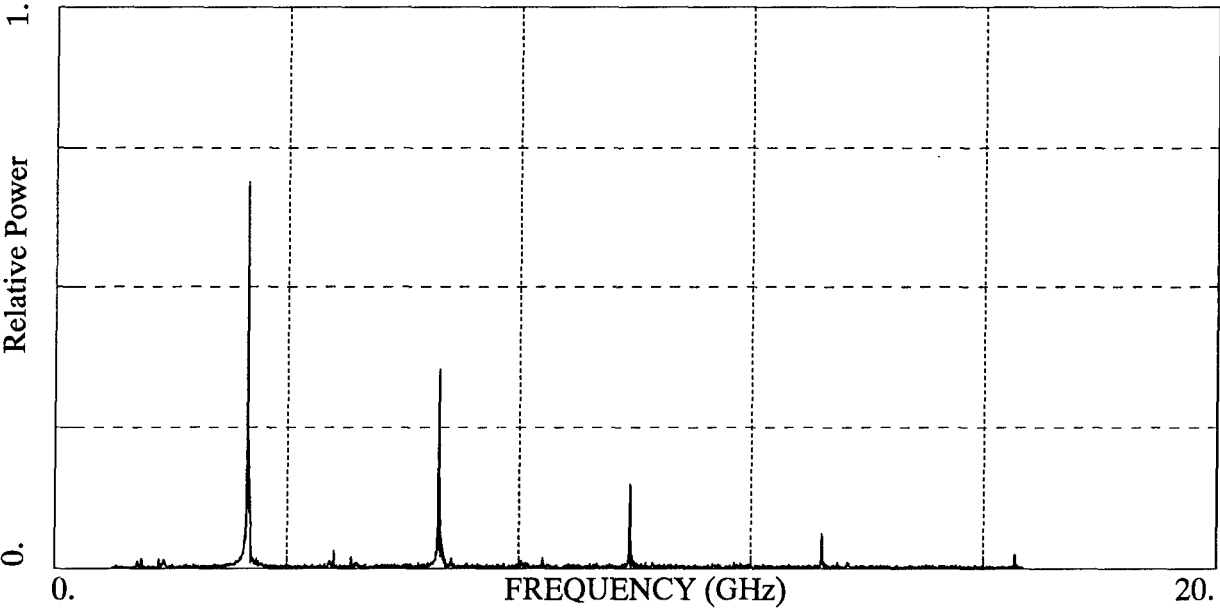


Figure 5b. The fourier transform of 5a showing up to five harmonics, an indication of strongly bunched beam.

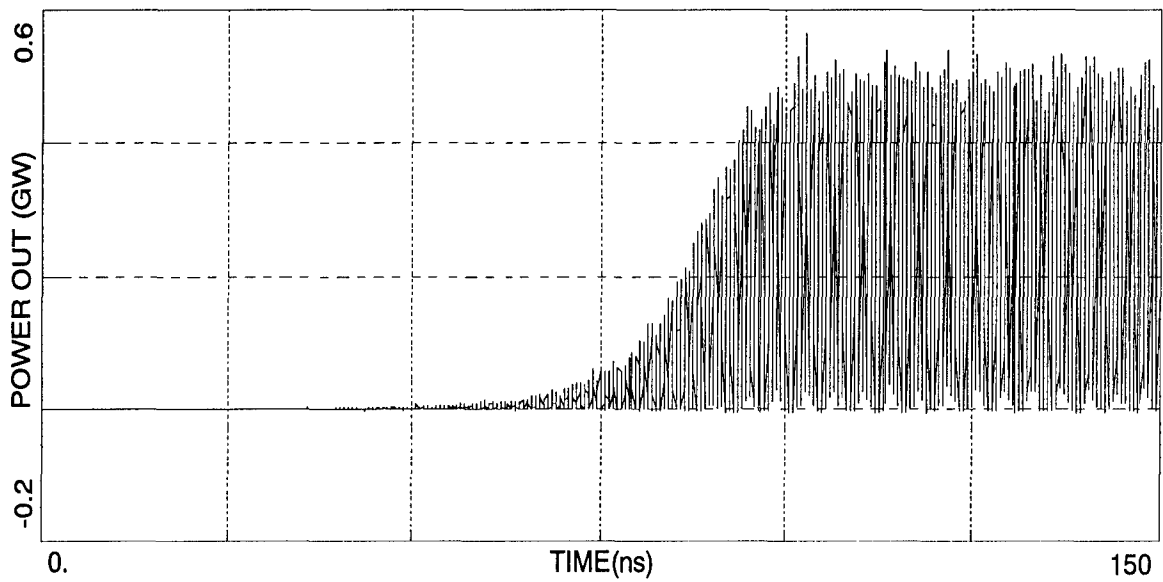


Figure 6a. The time plot of the extracted power through a coaxial load showing a stable rf signal. The axial load is not optimized and the choice of axial extraction is not final.

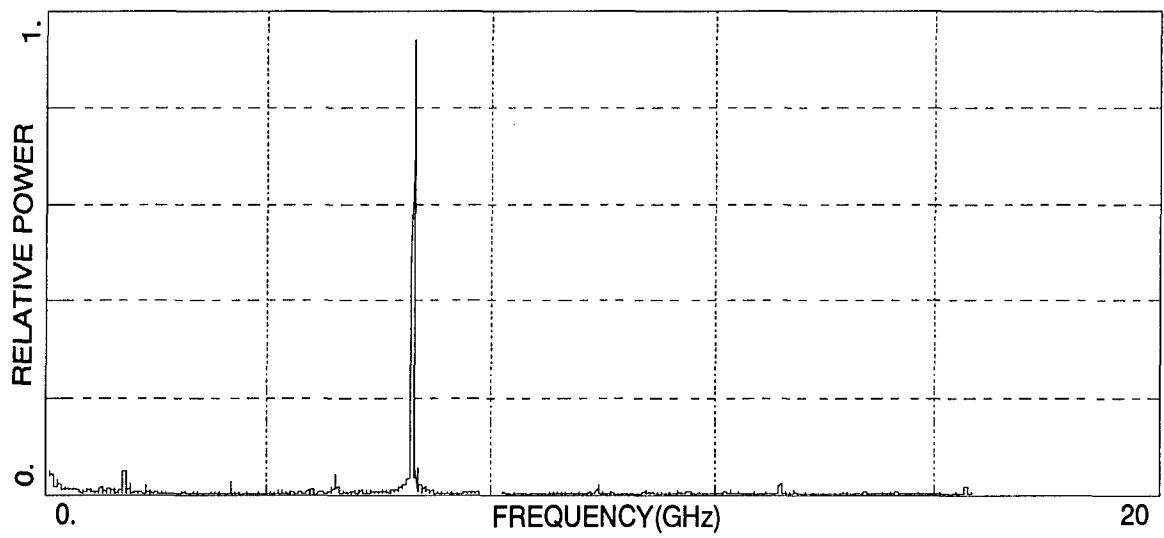


Figure 6b. The fourier transform of 6a showing a monochromatic rf signal at twice the frequency of the rf fields.

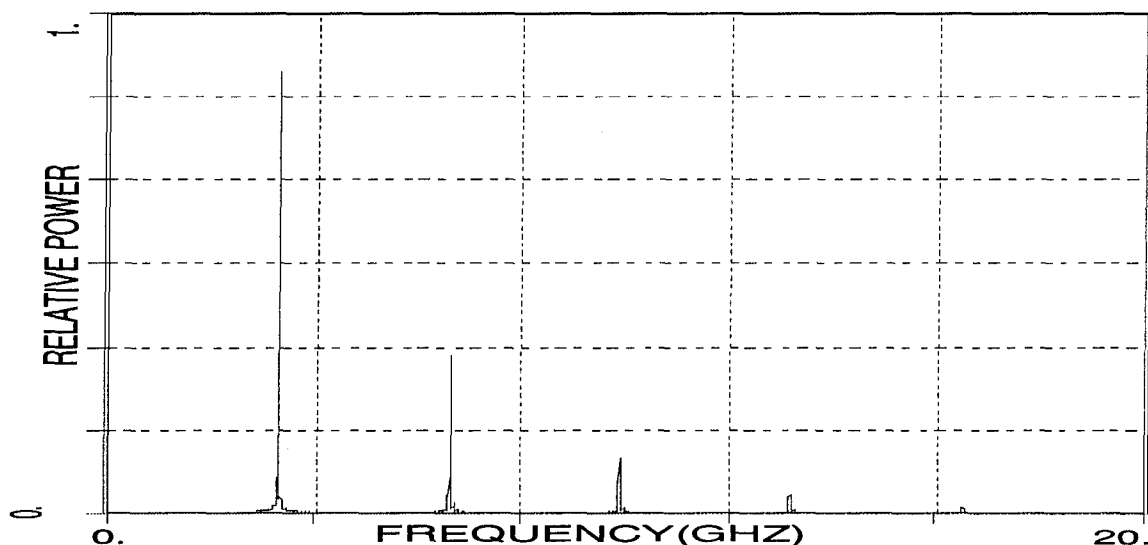


Figure 7. The fourier transform of the modulated total current in the 3-D simulation. This plot confirms the absence of non-axisymmetric modes in the cavity.

Future work on radial acceletron is basically optimization and load configuration. Once the loading is designed, a prototype for experimental testing can be built. Integration of the source into the pulser system and the antenna should not present any major problems. The Phillips laboratory is planning an experimental test of the radial acceletron for early 1994.

REFERENCES

1. D. Marcuse, "Principles of Quantum Electronics", pp. 125-144, Academic Press, New York (1980).
2. J. Marcum, "Interchange of Energy Between an Electron Beam and an Oscillating Electric Field", J. Appl. Phys. 17, 4 (1946)
3. B.B. Godfrey, "Oscillatory Nonlinear Electron Flow in a Pierce Diode", Phys. Fluids 30, 1553 (1987).
4. M.J. Arman, D.J. Sullivan, B.B. Godfrey, R.E. Clark, J.E. Walsh, "Analytical Study and Numerical Simulation of High Power Vircator and Transvertron Microwave Sources", MRC/ABQ-R-1029, Mission Research Corporation, Albuquerque, New Mexico (1988).
5. D.J. Sullivan, J.E. Walsh, M.J. Arman, B.B. Godfrey, "Simulation of Transvertron High Power Microwave Sources", SPIE's OE/LAS'89 (1988).
6. M.J. Arman, D.J. Sullivan, "High Power Transit-time rf Amplifier for Super Accelerators", AIP Conference Proceedings 297, Computational Accelerator Physics, (1993), pp 219.

DISCUSSION

E. SCHWEICHER

Your Bragg reflector seems to me comparable to the grating of a DFB laser. Does it mean that the width of the groove (which constitutes the Bragg reflector) is exactly half a wavelength ?

AUTHOR'S REPLY

They work like grating of a DFB lasers, but the ratios are not exactly like those of the DFB laser.

J. PIGNERET

- 1/ What is the mechanism which controls the growth rate of the AC E field ?
- 2/ Can you input external EM energy, synchronously, to speed up the growth ?

AUTHOR'S REPLY

- 1/ Many parameters are involved like the dimensions, the dc pulse parameters and the time of flight for the electrons crossing the gap. The growth rate is rather small here because of the low Q-factor in the cavity.
- 2/ Yes, that will help.

H. BOTTOLLIER-CURTET

Is the plasma gap closure a potential limitation of this device ?

AUTHOR'S REPLY

Yes, it could be but this problem requires a lot of CPU time. Will be examined numerically.

J. NITSCH

- 1/ How did you match the outer part of your coaxial line with the air ?
- 2/ How does the radiation pattern looks like ?

AUTHOR'S REPLY

- 1/ It will depend on the kind of loading.
- 2/ Not investigated.

REPORT DOCUMENTATION PAGE			
1. Recipient's Reference	2. Originator's Reference	3. Further Reference	4. Security Classification of Document
	AC/243 (Panel 1) TP/4, Vol I (AGARD-CP-564)	ISBN 92-836-0012-6	UNCLASSIFIED/ UNLIMITED
5. Originator	Defence Research Group, North Atlantic Treaty Organisation, B-1110 Brussels, Belgium		
6. Title	High Power Microwaves (HPM)		
7. Presented at	the joint AGARD Sensor and Propagation Panel and Defence Research Group meeting, Ottawa, Canada, 2-5 May 1994.		
8. Author(s)/Editor(s)	Multiple		9. Date
			March 1995
10. Author's/Editor's Address	Multiple		11. Pages
			296
12. Distribution Statement	There are no restrictions on the distribution of this document. Information about the availability of this and other DRG publications is given on the back cover.		
13. Keywords/Descriptors	<div>High power microwaves</div> <div>Vulnerability</div> <div>Microwave transmission</div> <div>Microwave equipment</div> <div>Microwave antennas</div> <div>Radiation hardening</div> <div>Hardening (systems)</div> <div>Coupling circuits</div> <div>High energy</div> <div>Electromagnetic weapons</div> <div>Electronic warfare</div>		
14. Abstract	<p>This publication (also published as AGARD-CP-564) contains the unclassified papers presented to a specialists' meeting sponsored jointly by the AGARD Sensor and Propagation Panel and the Defence Research Group (DRG) of NATO.</p> <p>The topics covered on the occasion of that meeting on the subject of "High Power Micro-Waves (HPM)" included:</p> <ul style="list-style-type: none">— High Peak Power Generators— Transmission Line and Antenna Peak Power Handling— Atmospheric Microwave Breakdown— Target Coupling Mechanisms— Components and Subsystems Vulnerability— Hardening Against HPM— Test Facilities		

DRG DOCUMENT CENTRES

NATO does not hold stocks of DRG publications for general distribution. NATO initiates distribution of all DRG documents from its Central Registry. Nations then send the documents through their national NATO registries, subregistries, and control points. One may sometimes obtain additional copies from the registries. The DRG Document Centres listed below can supply copies of previously issued technical DRG publications upon request.

BELGIUM

EGM-JSRL
Quartier Reine Elisabeth
Rue d'Evere, 1140 Bruxelles
Tel:(02)243 3163, Fax:(02)243 3655

THE NETHERLANDS

IDL/TDCK
P.O. Box 20701
2500 ES Den Haag
Tel:(015)152 691, Fax:(015)152 728

CANADA

Directorate of Scientific Information Services
National Defence Headquarters
MGen. George R. Pearkes Building
Ottawa, Ontario, K1A 0K2
Tel:(613)992-2263, Fax:(613)996-0392

NORWAY

Norwegian Defence Research Establishment
Central Registry
P.O. Box 25
2007 Kjeller
Tel:(06)80 71 41 Fax:(06)80 71 15

DENMARK

Forsvarets Forskningstjeneste
Ved Idrætsparken 4
2100 København Ø
Tel:3927 8888 + 5660,
Fax:3543 1086

PORTUGAL

Direcção-General de Armamento
Ministério da Defesa Nacional
Avenida da Ilha da Madeira
1499 Lisboa
Tel:(01)610001 ext. 4425, Fax:(01)611970

FRANCE

CEDOCAR
00460 Armées
Tel:(1)4552 4500, Fax:(1)4552 4574

SPAIN

DGAM
C/ Arturo Soria 289
28033 Madrid
Tel:(91)2020640, Fax (91)2028047

GERMANY

DOKFIZBw
Friedrich-Ebert-Allee 34
5300 Bonn 1
Tel:(0228)233091, Fax:(0228)125357

TURKEY

Genelkurmay Genel Plân Prensipier
Savunma Araştırma Daire Başkanlığı
Ankara
Tel:(4)1176100 ext. 1684, Fax:(4)1176 3386

GREECE

National Defence Headquarters
R+T Section (D3)
15561 Holargos, Athens
Tel:(01)64 29 008

UNITED KINGDOM

DRIC
Kentigern House, 65 Brown Street
Glasgow G2 8EX
Tel:(0141)224 2435, Fax:(0141)224 2145

ITALY

MOD Italy
SEGREDIFESA IV Reparto PF.RS
Via XX Settembre, 123/A
00100 Roma
Tel:(06)735 3339, Fax:(06)481 4264

UNITED STATES

DTIC
Cameron Station
Alexandria, VA 22304-6145
Tel:(202)274-7633, Fax:(202)274-5280

DEFENCE RESEARCH SECTION

NATO HEADQUARTERS

B 1110 BRUSSELS

BELGIUM

Telephone [32](2)728 4285 - Telefax [32](2)728 4103
(not a DRG Document Distribution Centre)

Aucun stock de publications n'a existé à AGARD. A partir de 1993, AGARD détiendra un stock limité des publications associées aux cycles de conférences et cours spéciaux ainsi que les AGARDographies et les rapports des groupes de travail, organisés et publiés à partir de 1993 inclus. Les demandes de renseignements doivent être adressées à AGARD par lettre ou par fax à l'adresse indiquée ci-dessus. *Veuillez ne pas téléphoner.* La diffusion initiale de toutes les publications de l'AGARD est effectuée auprès des pays membres de l'OTAN par l'intermédiaire des centres de distribution nationaux indiqués ci-dessous. Des exemplaires supplémentaires peuvent parfois être obtenus auprès de ces centres (à l'exception des Etats-Unis). Si vous souhaitez recevoir toutes les publications de l'AGARD, ou simplement celles qui concernent certains Panels, vous pouvez demander à être inclut sur la liste d'envoi de l'un de ces centres. Les publications de l'AGARD sont en vente auprès des agences indiquées ci-dessous, sous forme de photocopie ou de microfiche.

CENTRES DE DIFFUSION NATIONAUX

ALLEMAGNE

Fachinformationszentrum,
Karlsruhe
D-76344 Eggenstein-Leopoldshafen 2

BELGIQUE

Coordonnateur AGARD-VSL
Etat-major de la Force aérienne
Quartier Reine Elisabeth
Rue d'Evere, 1140 Bruxelles

CANADA

Directeur, Services d'information scientifique
Ministère de la Défense nationale
Ottawa, Ontario K1A 0K2

DANEMARK

Danish Defence Research Establishment
Ryvangs Allé 1
P.O. Box 2715
DK-2100 Copenhagen Ø

ESPAGNE

INTA (AGARD Publications)
Pintor Rosales 34
28008 Madrid

ETATS-UNIS

NASA Headquarters
Code JOB-1
Washington, D.C. 20546

FRANCE

O.N.E.R.A. (Direction)
29, Avenue de la Division Leclerc
92322 Châtillon Cedex

GRECE

Hellenic Air Force
Air War College
Scientific and Technical Library
Dekelia Air Force Base
Dekelia, Athens TGA 1010

ISLANDE

Director of Aviation
c/o Flugrad
Reykjavik

ITALIE

Aeronautica Militare
Ufficio del Delegato Nazionale all'AGARD
Aeroporto Pratica di Mare
00040 Pomezia (Roma)

LUXEMBOURG

Voir Belgique

NORVEGE

Norwegian Defence Research Establishment
Attn: Biblioteket
P.O. Box 25
N-2007 Kjeller

PAYS-BAS

Netherlands Delegation to AGARD
National Aerospace Laboratory NLR
P.O. Box 90502
1006 BM Amsterdam

PORTUGAL

Força Aérea Portuguesa
Centro de Documentação e Informação
Alfragide
2700 Amadora

ROYAUME-UNI

Defence Research Information Centre
Kentigern House
65 Brown Street
Glasgow G2 8EX

TURQUIE

Millî Savunma Başkanlığı (MSB)
ARGE Dairesi Başkanlığı (MSB)
06650 Bakanlıklar-Ankara

Le centre de distribution national des Etats-Unis ne détient PAS de stocks des publications de l'AGARD.

D'éventuelles demandes de photocopies doivent être formulées directement auprès du NASA Center for AeroSpace Information (CASI) à l'adresse ci-dessous. Toute notification de changement d'adresse doit être fait également auprès de CASI.

AGENCES DE VENTE

NASA Center for
AeroSpace Information (CASI)
800 Elkridge Landing Road
Linthicum Heights, MD 21090-2934
Etats-Unis

ESA/Information Retrieval Service
European Space Agency
10, rue Mario Nikis
75015 Paris
France

The British Library
Document Supply Division
Boston Spa, Wetherby
West Yorkshire LS23 7BQ
Royaume-Uni

Les demandes de microfiches ou de photocopies de documents AGARD (y compris les demandes faites auprès du CASI) doivent comporter la dénomination AGARD, ainsi que le numéro de série d'AGARD (par exemple AGARD-AG-315). Des informations analogues, telles que le titre et la date de publication sont souhaitables. Veuillez noter qu'il y a lieu de spécifier AGARD-R-nnn et AGARD-AR-nnn lors de la commande des rapports AGARD et des rapports consultatifs AGARD respectivement. Des références bibliographiques complètes ainsi que des résumés des publications AGARD figurent dans les journaux suivants:

Scientific and Technical Aerospace Reports (STAR)
publié par la NASA Scientific and Technical
Information Division
NASA Headquarters (JTT)
Washington D.C. 20546
Etats-Unis

Government Reports Announcements and Index (GRA&I)
publié par le National Technical Information Service
Springfield
Virginia 22161
Etats-Unis
(accessible également en mode interactif dans la base de données bibliographiques en ligne du NTIS, et sur CD-ROM)



AGARD holds limited quantities of the publications that accompanied Lecture Series and Special Courses held in 1993 or later, and of AGARDographs and Working Group reports published from 1993 onward. For details, write or send a telefax to the address given above. *Please do not telephone.*

AGARD does not hold stocks of publications that accompanied earlier Lecture Series or Courses or of any other publications. Initial distribution of all AGARD publications is made to NATO nations through the National Distribution Centres listed below. Further copies are sometimes available from these centres (except in the United States). If you have a need to receive all AGARD publications, or just those relating to one or more specific AGARD Panels, they may be willing to include you (or your organisation) on their distribution list. AGARD publications may be purchased from the Sales Agencies listed below, in photocopy or microfiche form.

NATIONAL DISTRIBUTION CENTRES**BELGIUM**

Coordonnateur AGARD — VSL
Etat-major de la Force aérienne
Quartier Reine Elisabeth
Rue d'Evere, 1140 Bruxelles

CANADA

Director Scientific Information Services
Dept of National Defence
Ottawa, Ontario K1A 0K2

DENMARK

Danish Defence Research Establishment
Ryvangs Allé 1
P.O. Box 2715
DK-2100 Copenhagen Ø

FRANCE

O.N.E.R.A. (Direction)
29 Avenue de la Division Leclerc
92322 Châtillon Cedex

GERMANY

Fachinformationszentrum
Karlsruhe
D-76344 Eggenstein-Leopoldshafen 2

GREECE

Hellenic Air Force
Air War College
Scientific and Technical Library
Dekelia Air Force Base
Dekelia, Athens TGA 1010

ICELAND

Director of Aviation
c/o Flugrad
Reykjavik

ITALY

Aeronautica Militare
Ufficio del Delegato Nazionale all'AGARD
Aeroporto Pratica di Mare
00040 Pomezia (Roma)

LUXEMBOURG

See Belgium

NETHERLANDS

Netherlands Delegation to AGARD
National Aerospace Laboratory, NLR
P.O. Box 90502
1006 BM Amsterdam

NORWAY

Norwegian Defence Research Establishment
Attn: Biblioteket
P.O. Box 25
N-2007 Kjeller

PORTUGAL

Força Aérea Portuguesa
Centro de Documentação e Informação
Alfragide
2700 Amadora

SPAIN

INTA (AGARD Publications)
Pintor Rosales 34
28008 Madrid

TURKEY

Millî Savunma Başkanlığı (MSB)
ARGE Dairesi Başkanlığı (MSB)
06650 Bakanlıklar-Ankara

UNITED KINGDOM

Defence Research Information Centre
Kentigern House
65 Brown Street
Glasgow G2 8EX

UNITED STATES

NASA Headquarters
Code JOB-1
Washington, D.C. 20546

The United States National Distribution Centre does NOT hold stocks of AGARD publications.

Applications for copies should be made direct to the NASA Center for AeroSpace Information (CASI) at the address below.

Change of address requests should also go to CASI.

SALES AGENCIES

NASA Center for
AeroSpace Information (CASI)
800 Elkridge Landing Road
Linthicum Heights, MD 21090-2934
United States

ESA/Information Retrieval Service
European Space Agency
10, rue Mario Nikis
75015 Paris
France

The British Library
Document Supply Centre
Boston Spa, Wetherby
West Yorkshire LS23 7BQ
United Kingdom

Requests for microfiches or photocopies of AGARD documents (including requests to CASI) should include the word 'AGARD' and the AGARD serial number (for example AGARD-AG-315). Collateral information such as title and publication date is desirable. Note that AGARD Reports and Advisory Reports should be specified as AGARD-R-nnn and AGARD-AR-nnn, respectively. Full bibliographical references and abstracts of AGARD publications are given in the following journals:

Scientific and Technical Aerospace Reports (STAR)
published by NASA Scientific and Technical
Information Division
NASA Headquarters (JTT)
Washington D.C. 20546
United States

Government Reports Announcements and Index (GRA&I)
published by the National Technical Information Service
Springfield
Virginia 22161
United States
(also available online in the NTIS Bibliographic
Database or on CD-ROM)



Printed by Canada Communication Group
45 Sacré-Cœur Blvd., Hull (Québec), Canada K1A 0S7